Elements of MOM4p1

STEPHEN M. GRIFFIES
NOAA Geophysical Fluid Dynamics Laboratory
Princeton, USA

WITH CONTRIBUTIONS FROM
MARTIN SCHMIDT (WARNEMÜNDE, GERMANY)
MIKE HERZFELD (CSIRO-HOBART, AUSTRALIA)

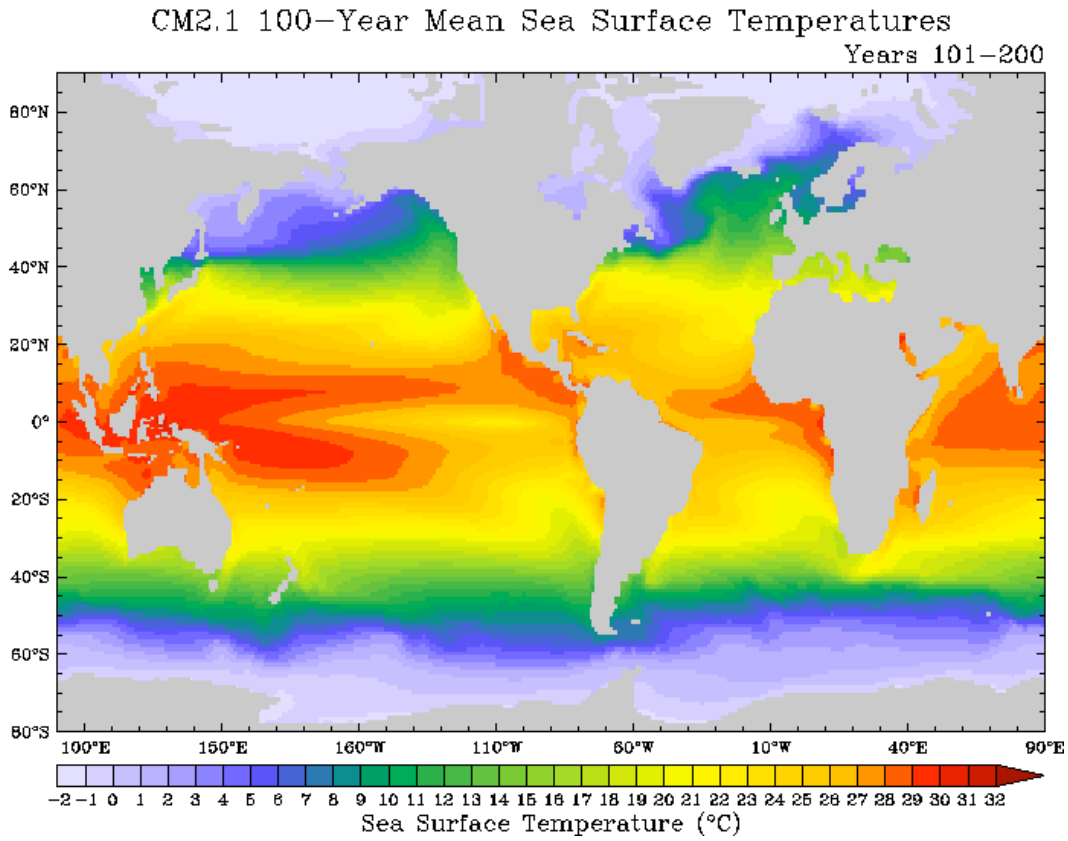

This document is freely distributed for ocean scientists interested in understanding the fundamentals of version 4.1 of the Modular Ocean Model (MOM). This document should be referenced as

ELEMENTS OF MOM4P1
GFDL OCEAN GROUP TECHNICAL REPORT NO. 6
Stephen M. Griffies
NOAA/Geophysical Fluid Dynamics Laboratory
444 pages
Version prepared on December 16, 2009
Code and documentation available online at `www.gfdl.noaa.gov/fms`.

Information about how to download and run MOM4 can be found at the GFDL Flexible Modeling System (FMS) web site accessible from `www.gfdl.noaa.gov/fms`.

CONTENTS

1 Executive summary of MOM4p1 **13**
1.1 General features . . . 13
1.2 Relating MOM4p1 to MOM4.0 . . . 18

2 Synopsis of MOM4p1 **19**
2.1 What is MOM? . . . 19
2.2 First release of MOM4.0: October 2003 . . . 20
2.3 First release of MOM4p1: Early 2007 . . . 20
2.4 MOM4p1 release December 2009 . . . 21
2.5 Fundamentals of MOM4p1 . . . 21
2.6 Tracer features . . . 24
2.7 Subgrid scale parameterizations . . . 27
2.8 Miscellaneous features . . . 30
2.9 Short bibliography of MOM4 documents . . . 31
2.10 The future of MOM . . . 31

I. Formulation of the ocean equations **33**

3 Fundamental equations **35**
3.1 Fluid kinematics . . . 35
3.1.1 Mass conserving fluid parcels . . . 35
3.1.2 Volume conserving fluid parcels . . . 37
3.1.3 Mass conservation for finite domains . . . 38
3.1.4 Evolution of ocean sea level . . . 39
3.1.5 Solid earth kinematic boundary condition . . . 41
3.1.6 Generalized vertical coordinates . . . 42
3.1.7 Upper surface kinematic condition . . . 44
3.1.8 Dia-surface transport . . . 47
3.2 Mass conservation and the tracer equation . . . 50
3.2.1 Eulerian form of mass conservation . . . 50
3.2.2 Mass conservation for parcels . . . 52
3.2.3 Mass conservation for constituents: the tracer equation . . . 52

3.3 Thermodynamical tracers . . . 53
3.3.1 Potential temperature . . . 53
3.3.2 Potential enthalpy . . . 54
3.4 Material time changes over finite regions . . . 56
3.5 Basics of the finite volume method . . . 58
3.6 Mass and tracer budgets over finite regions . . . 60
3.6.1 General formulation . . . 60
3.6.2 Budget for an interior grid cell . . . 61
3.6.3 Fresh water budget . . . 64
3.6.4 The ideal age tracer . . . 64
3.6.5 Budgets without dia-surface fluxes . . . 65
3.6.6 Cells adjacent to the ocean bottom . . . 66
3.6.7 Cells adjacent to the ocean surface . . . 67
3.6.8 Compatability between vertically integrated mass and tracer budgets . . . 69
3.7 Forces from pressure . . . 70
3.7.1 The accumulation of contact pressure forces . . . 70
3.7.2 Pressure gradient body force in hydrostatic fluids . . . 74
3.8 Linear momentum budget . . . 75
3.8.1 General formulation . . . 76
3.8.2 An interior grid cell . . . 76
3.8.3 Cell adjacent to the ocean bottom . . . 78
3.8.4 Cell adjacent to the ocean surface . . . 78
3.8.5 Horizontal momentum equations for hydrostatic fluids . . . 79
3.9 The Boussinesq budgets . . . 80

4 The hydrostatic pressure force 83
4.1 Hydrostatic pressure forces at a point . . . 83
4.2 Pressure gradient body force . . . 84
4.2.1 Depth based vertical coordinates . . . 85
4.2.2 A test case for zero cross-coordinate flow . . . 88
4.2.3 Pressure based vertical coordinates . . . 89
4.3 Pressure gradient body force in B-grid MOM4p1 . . . 90
4.3.1 Depth based vertical coordinates . . . 91
4.3.2 Pressure based vertical coordinates . . . 92

5 Parameterizations with generalized level coordinates 93
5.1 Friction . . . 93
5.1.1 Vertical friction . . . 93
5.1.2 A comment on nonlinear vertical friction . . . 94
5.1.3 Lateral friction . . . 95
5.1.4 Bottom stress . . . 96
5.1.5 Summary of the linear momentum budget . . . 97
5.2 Diffusion and skew diffusion . . . 97
5.2.1 Vertical diffusion . . . 97
5.2.2 Horizontal diffusion . . . 98
5.2.3 Neutral physics . . . 98

6 Depth and pressure based vertical coordinates **105**
6.1 Depth based vertical coordinates . . . 105
6.1.1 Depth coordinate . . . 105
6.1.2 An example of depth coordinates . . . 107
6.1.3 Depth deviation coordinate . . . 108
6.1.4 Zstar coordinate . . . 109
6.1.5 Depth sigma coordinate . . . 110
6.1.6 Summary of the depth based vertical coordinates . . . 111
6.2 Pressure based coordinates . . . 112
6.2.1 Pressure coordinate . . . 113
6.2.2 Pressure deviation coordinate . . . 114
6.2.3 Pstar coordinate . . . 114
6.2.4 Pressure sigma coordinate . . . 115
6.2.5 Summary of the pressure based vertical coordinates . . . 116

II. Numerical formulations **117**

7 Quasi-Eulerian Algorithms **119**
7.1 Pressure and geopotential at tracer points . . . 119
7.1.1 Pressure at tracer point: energetic method . . . 120
7.1.2 Pressure at a tracer point: finite volume considerations . . . 120
7.1.3 Discrete geopotential based on energetic considerations . . . 121
7.1.4 Discrete geopotential based on finite volume considerations . . . 121
7.2 Initialization issues . . . 121
7.3 Vertical dimensions of grid cells . . . 123
7.3.1 Thickness of a grid cell . . . 123
7.3.2 Vertical distance between tracer points . . . 124
7.3.3 Summary of grid increments . . . 125
7.3.4 Surface height diagnosed in pressure based models . . . 131
7.3.5 Bottom pressure diagnosed in depth based models . . . 131
7.4 Vertically integrated volume/mass budgets . . . 132
7.4.1 Vertically integrated volume budget . . . 132
7.4.2 Vertically integrated mass budget . . . 132
7.4.3 Summary of the vertically integrated volume/mass budgets . . . 133
7.5 Compatibility between tracer and mass . . . 134
7.6 Diagnosing the dia-surface velocity component . . . 134
7.6.1 Depth based vertical coordinates . . . 135
7.6.2 Pressure based vertical coordinates . . . 137
7.6.3 Comments about diagnosing the dia-surface velocity component . . . 141
7.7 Vertically integrated horizontal momentum . . . 141
7.7.1 Budget using contact pressures on cell boundaries . . . 141
7.7.2 Budget using the pressure gradient body force . . . 141
7.7.3 Depth based vertical coordinates . . . 142
7.7.4 Pressure based vertical coordinates . . . 143

8 Time stepping schemes **145**
8.1 Split between fast and slow motions . . . 145
8.2 Time stepping the model equations as in MOM4.0 . . . 146
8.2.1 The standard scheme used in OM3.0 . . . 147
8.2.2 Problems related to tracer conservation . . . 148
8.2.3 The time staggered scheme used in OM3.1 . . . 149
8.2.4 Sensitivity to the time stepping scheme . . . 150
8.2.5 Dissipative aspects of the predictor-corrector . . . 151
8.3 Surface height and bottom pressure smoothing . . . 152
8.4 Introduction to time stepping in MOM4p1 . . . 154
8.5 Basics of staggered time stepping in MOM4p1 . . . 154
8.6 Predictor-corrector for the barotropic system . . . 155
8.7 The Griffies (2004) scheme . . . 157
8.8 Algorithms motivated from predictor-corrector . . . 158
8.8.1 Barotropic time stepping and surface height on integer time steps . . . 158
8.8.2 Surface height on half-integer time steps . . . 159
8.8.3 Method A: $\mathbf{U}(\tau + \Delta\tau) = \overline{\mathbf{U}}$ . . . 161
8.8.4 Method B: $\mathbf{U}(\tau + \Delta\tau/2) = \overline{\mathbf{U}}$ . . . 162
8.9 Algorithms enforcing compatibility . . . 163
8.9.1 Method I: Griffies (2004) . . . 163
8.9.2 Method II: Algorithm based on barotropic predictor-corrector . . . 164
8.9.3 Method III: Modified Griffies (2004) . . . 165

9 Equation of state and related quantities **169**
9.1 Introduction . . . 169
9.2 Linear equation of state . . . 170
9.3 Jackett et al. equation of state . . . 171

10 Mechanical energy budgets and conversions **175**
10.1 Energetic conversions in the continuum . . . 175
10.1.1 Pressure work conversions in Boussinesq fluids . . . 176
10.1.2 Pressure work conversions in non-Boussinesq fluids . . . 177
10.1.3 Boussinesq kinetic energy advection conversion . . . 177
10.1.4 Non-Boussinesq kinetic energy advection conversion . . . 178
10.2 Conservation, consistency, and accuracy . . . 178
10.3 Thickness weighted volume and mass budgets . . . 179
10.4 Discrete Boussinesq pressure work conversions . . . 179
10.4.1 The vertically integrated term $\mathcal{P}_1$ . . . 181
10.4.2 Advection velocity components for tracers . . . 181
10.4.3 Completing the manipulations for $\mathcal{P}_2$ . . . 183
10.4.4 The geopotential gradient term $\mathcal{P}_3$ . . . 184
10.4.5 Summary for the Boussinesq pressure conversion . . . 186
10.5 Discrete non-Boussinesq pressure work conversions . . . 186
10.5.1 The vertically integrated term $\mathcal{P}_1$ . . . 188
10.5.2 Defining the advection velocities . . . 188
10.5.3 Completing the manipulations for $\mathcal{P}_3$ . . . 189

10.5.4 The pressure gradient term $\mathcal{P}_2$ . . . 191
10.5.5 Summary for the non-Boussinesq pressure conversion . . . 191
10.6 Discrete Boussinesq kinetic energy advection . . . 192
10.6.1 Coriolis force . . . 193
10.6.2 Horizontal convergence . . . 193
10.6.3 Diagnosing the vertical transport for U-cells . . . 194
10.6.4 Discrete integration by parts on horizontal convergence . . . 194
10.6.5 Discrete integration by parts on vertical convergence . . . 196
10.6.6 Final result . . . 196
10.7 Discrete non-Boussinesq kinetic energy advection . . . 197

11 Temporal treatment of the Coriolis force 199
11.1 Inertial oscillations . . . 199
11.2 Explicit temporal discretization with leap frog . . . 200
11.3 Semi-implicit time discretization with leap frog . . . 201
11.4 Semi-implicit time discretization with forward step . . . 202
11.5 As implemented in MOM4 . . . 202
11.5.1 Algorithm in the code . . . 202
11.5.2 Namelist parameters . . . 203
11.5.3 Energy analysis . . . 204

12 Open boundary conditions 205
12.1 Introduction . . . 205
12.2 Types of open boundary conditions . . . 206
12.2.1 Open boundaries in the ARAKAWA B-grid . . . 206
12.2.2 Sommerfeld radiation condition . . . 208
12.2.3 Clamped boundary conditions . . . 209
12.2.4 No gradient boundary conditions . . . 209
12.2.5 Interior cell no gradient boundary conditions . . . 210
12.2.6 Enhanced friction and diffusion near the boundary . . . 210
12.3 Implementation of sea level radiation conditions . . . 210
12.3.1 Sign convention for the phase speed . . . 210
12.3.2 Gravity wave radiation condition for the phase speed . . . 210
12.3.3 Orlanski radiation condition for the phase speed . . . 211
12.3.4 Camerlengo and O'Brien radiation condition . . . 211
12.3.5 Radiation condition after Miller & Thorpe . . . 212
12.3.6 Raymond and Kuo radiation condition . . . 212
12.3.7 The IOW-radiation condition . . . 213
12.3.8 Phase speed smoothing . . . 214
12.3.9 Relaxation to data . . . 214
12.4 OBC for tracers . . . 215
12.4.1 Reduced tracer equations at open boundaries . . . 215
12.4.2 Upstream advection of tracers near the boundary . . . 217
12.4.3 Relaxation towards external data . . . 217
12.4.4 Flow relaxation scheme of Martinsen and Engedahl . . . 218
12.4.5 Radiation conditions . . . 218

12.4.6 Vertical mixing and viscosity co-efficients . . . 219
12.4.7 Enhanced horizontal mixing and viscosity co-efficients . . . 219
12.5 The namelist obc_nml . . . 219
12.6 Topography generation - Preparation of boundary data . . . 220
12.6.1 Topography generation with open boundaries . . . 220
12.6.2 Preparation of input data files . . . 221
12.6.3 Consistency of input data and model configuration . . . 223

13 Tidal forcing from the moon and sun 225
13.1 Tidal consituents and tidal forcing . . . 225
13.2 Formulation in nonBoussinesq models . . . 226
13.3 Implementation in MOM4 . . . 226

III. Subgrid scale parameterizations 229

14 Mixing related to tidal energy dissipation 231
14.1 Formulation . . . 231
14.2 Mixing from internal wave breaking . . . 232
14.2.1 Simmons etal (2004) scheme . . . 233
14.2.2 Some considerations for testing the implementation . . . 235
14.3 Dianeutral diffusivities from bottom drag . . . 237

15 Calculation of buoyancy forcing 239
15.1 Fundamentals . . . 239
15.2 The formulation as in Large et al. (1994) . . . 242
15.3 Buoyancy forcing for KPP in MOM . . . 243
15.4 Bug in MOM4.0 . . . 244

16 Neutral physics and boundary layers 245
16.1 Notes on implementation as of June 2008 . . . 245
16.2 Regions affecting neutral physics . . . 246
16.2.1 Upper turbulent boundary layer . . . 247
16.2.2 Transition between surface boundary layer and interior . . . 247
16.2.3 Ocean interior . . . 248
16.2.4 Transition between the interior and bottom boundary layer . . . 249
16.2.5 Bottom turbulent boundary layer . . . 249
16.2.6 Comments on the treatment in MOM4p0 . . . 249
16.3 Quasi-Stokes streamfunction . . . 250
16.3.1 Surface turbulent boundary layer . . . 251
16.3.2 Surface transition region . . . 252
16.3.3 Bottom transition region . . . 253
16.3.4 Bottom turbulent boundary layer . . . 253
16.3.5 Summary of the streamfunction algorithm . . . 254
16.4 Specializing the quasi-Stokes streamfunction . . . 255
16.4.1 GM90 streamfunction . . . 255

16.4.2 Streamfunction in completely unstratified regions . . . 255
16.4.3 Local N^2 dependent diffusivity . . . 256
16.5 Discussion of some details . . . 257
16.5.1 Step-like features in the upper ocean . . . 257
16.5.2 Handling the triads of slopes . . . 257
16.5.3 Ensuring there are no negatively stratified regions . . . 258
16.6 Lateral diffusive parameterization . . . 258
16.7 Computation of the Rossby radius . . . 259
16.8 Method for obtaining low pass filtered fields . . . 260
16.9 Regularized slopes . . . 261

17 Parameterization of form drag 263
17.1 Regarding the TEM approach . . . 263

18 Restratification effects by submesoscale eddies 265
18.1 Basics of the scheme . . . 265
18.2 Skew tracer flux components . . . 267
18.3 Eddy induced transport . . . 268

19 Overflow schemes 271
19.1 Motivation for overflow schemes . . . 271
19.2 The sigma transport scheme . . . 272
19.2.1 Sigma diffusion . . . 272
19.2.2 Sigma advection . . . 274
19.2.3 Implementation of sigma transport . . . 278
19.3 The Campin and Goosse (1999) scheme . . . 278
19.3.1 Finding the depth of neutral buoyancy . . . 279
19.3.2 Prescribing the downslope flow . . . 280
19.3.3 Mass conservation and tracer transport . . . 281
19.3.4 Implementation in MOM4 . . . 281
19.4 Neutral depth over extended horizontal columns . . . 283
19.5 Sigma friction . . . 285

20 Cross-land mixing 287
20.1 Introduction . . . 287
20.2 Tracer and mass/volume compatibility . . . 287
20.3 Tracer mixing in a Boussinesq fluid with fixed boxes . . . 288
20.4 Mixing of mass/volume . . . 289
20.4.1 Instantaneous and complete mixing . . . 290
20.4.2 A finite time incomplete mixing . . . 290
20.4.3 A finite time incomplete mixing for surface cells . . . 291
20.5 Tracer and mass mixing . . . 291
20.6 Formulation with multiple depths . . . 292
20.6.1 MOM1 formulation of cross-land tracer mixing . . . 292
20.6.2 Generalizing to free surface and non-Boussinesq . . . 293
20.7 Suppression of B-grid null mode . . . 295

21 Implicit treatment of vertical mixing **297**
21.1 General form of discrete vertical diffusion . . . 297
21.2 Discretization of vertical fluxes . . . 298
21.3 A generic form: Part A . . . 299
21.3.1 Surface cells . . . 299
21.3.2 Interior cells . . . 299
21.3.3 Bottom cells . . . 299
21.3.4 Form appropriate for Numerical Recipes . . . 300
21.4 A generic form with implicit bottom drag . . . 300
21.4.1 Surface cells . . . 301
21.4.2 Interior cells . . . 301
21.4.3 Bottom cells . . . 301
21.4.4 Form appropriate for Numerical Recipes . . . 302
21.5 Implicit bottom drag again . . . 302
21.6 Caveat for implicit bottom drag . . . 303

IV. Diagnostic capabilities **305**

22 Streamfunctions **307**
22.1 Brief on notation . . . 307
22.2 Meridional-overturning streamfunction . . . 307
22.2.1 Summary of mas conservation for a finite region . . . 307
22.2.2 Zonally integrated mass transport . . . 308
22.2.3 Mass transport streamfunction . . . 309
22.2.4 Transport beneath an arbitrary surface . . . 311
22.2.5 Transport from GM90 . . . 312
22.2.6 Diagnosing the streamfunction in Ferret from MOM4 output . . . 313
22.3 Vertically integrated transport . . . 313
22.3.1 Summary of the rigid lid . . . 314
22.3.2 General case of divergent flow in non-Boussinesq fluids . . . 314

23 Effective dianeutral diffusivity **317**
23.1 Potential energy and APE in Boussinesq fluids . . . 317
23.2 Effective dianeutral mixing . . . 319
23.2.1 Global effective dianeutral diffusivity . . . 319
23.2.2 Finite difference approximation . . . 320
23.2.3 Relevant vertical stratification range . . . 321
23.2.4 A useful test case . . . 321
23.2.5 Computational precision . . . 322
23.2.6 Negative κ_{eff} . . . 322
23.2.7 A comment on convection . . . 322
23.2.8 The experimental design . . . 323
23.3 Modifications for time dependent cell thicknesses . . . 323
23.4 An example with vertical density gradients . . . 323
23.4.1 Evolution of the unsorted state . . . 324

23.4.2 Evolution of the sorted state . . . 325
23.4.3 Caveat about weakly stratified regions . . . 329
23.5 An example with vertical and horizontal gradients . . . 329
23.5.1 Vertical diffusion . . . 329
23.5.2 Horizontal diffusion . . . 334

24 Spurious dissipation from numerical advection 339
24.1 Formulation of the method for Boussinesq fluid . . . 339
24.2 Formulation for MOM4p1 . . . 341
24.3 Comparing to physical mixing . . . 343

25 Diagnosing the dianeutral velocity component 345
25.1 A brief on the model formulation . . . 345
25.2 Dianeutral velocity component . . . 346
25.2.1 Kinematics . . . 347
25.2.2 Physical Processes . . . 348
25.2.3 Diagnosing $w^{(\gamma)}$ in finite grid cells . . . 349
25.2.4 Spurious mixing from numerical advection . . . 351

26 Diagnosing the contributions to sea level evolution 353
26.1 Mass budget for a column of water . . . 353
26.2 Evolution of sea level . . . 355
26.3 Diagnosing terms contributing to the surface height . . . 356
26.3.1 Pressure based vertical coordinates . . . 356
26.3.2 Depth based vertical coordinates . . . 357
26.4 Global averaged sea level . . . 357

27 Balancing the hydrological cycle in ocean-ice models 361
27.1 Transfer of water between sea ice and ocean . . . 361
27.2 Balancing the hydrological cycle . . . 361
27.3 Water mass flux from salt mass flux . . . 362

28 Gyre and overturning contributions to tracer transport 365
28.1 Formulation . . . 365
28.2 Enabling the diagnostic . . . 366

V. Test Cases 369

29 Torus test case 371

30 Symmetric box test case 375

31 Box sector test case 379

32 Wind driven gyre test case 385

33 DOME test case 389

34 Bowl test case **395**

35 Indian Ocean Model **401**

36 CSIRO Mark 3.5 test **403**

37 Global ocean ice model with tripolar grid **405**
37.1 Three different vertical coordinates 405
37.1.1 Initialization of the p^* simulation 406
37.1.2 Brief analysis for the simulations 406
37.2 Age tracer and sensitivity to overflow parameterizations 407

38 Global ocean-ice-biogeochemistry model **417**

39 Global coupled model CM2.1 **419**

40 Eastern upwelling area test case **421**

BIBLIOGRAPHY **431**

CHAPTER

ONE

Executive summary of MOM4p1

MOM4p1 is a B-grid hydrostatic nonBoussinesq ocean model, with a Boussinesq option. This chapter provides an itemized summary of various code features. More discussion is provided in subsequent chapters. Note that items written in small capitals are new or substantially updated relative to MOM4.0.

1.1 General features

- GENERALIZED DEPTH AND PRESSURE BASED LEVEL VERTICAL COORDINATES.
  - Full support for the quasi-horizontal coordinates

$$
\begin{aligned}
s &= z \\
s &= z^* = H \left(\frac{z - \eta}{H + \eta} \right) \\
s &= p \\
s &= p^* = p_{\mathrm{b}}^o \left(\frac{p - p_{\mathrm{a}}}{p_{\mathrm{b}} - p_{\mathrm{a}}} \right)
\end{aligned}
$$

  - Partial support for the terrain following coordinates

$$
\begin{aligned}
s &= \sigma^{(z)} = \frac{z - \eta}{H + \eta} \\
s &= \sigma^{(p)} = \frac{p - p_{\mathrm{a}}}{p_{\mathrm{b}} - p_{\mathrm{a}}}
\end{aligned}
$$

    There is presently no support for terrain following coordinates using neutral physics, KPP vertical mixing, nor for sophisticated horizontal pressure gradient algorithms.

- Generalized orthogonal horizontal coordinates, with the tripolar grid of Murray (1996) supported in test cases. Other orthogonal grids have been successfully employed with MOM4.

- Parallel programming: MOM4p1 follows the parallel programming approach of MOM4.0, and is written with arrays ordered `(i,j,k)` for straightforward processor domain decomposition. As with MOM4.0, MOM4p1 relies on the GFDL Flexible Modeling System (FMS) (`http://www.gfdl.noaa.gov/fms`) infrastructure and superstructure code for computations on multiple parallel machines, with the code having been successfully run on dozens of computer platforms.

- EXPLICIT FREE SURFACE AND EXPLICIT BOTTOM PRESSURE SOLVER: MOM4 employs a split-explicit time stepping scheme where fast two-dimensional dynamics is sub-cycled within the slower three dimensional dynamics. The method follows ideas detailed in Chapter 12 of Griffies (2004), which are based on Killworth et al. (1991) and Griffies et al. (2001). Chapter 7 in this document presents further details for MOM4p1.

- Time stepping schemes: The time tendency for tracer and baroclinic velocity can be discretized two ways.

  - The first approach uses the traditional leap-frog method for the dissipation-less portion of the dynamics, along with a Robert-Asselin time filter (Haltiner and Williams, 1980). This method is retained solely for legacy purposes. It is *not* reccomended for general use.
  - The preferred time steppng method discretizes the time tendency with a two-level forward step, which eliminates the time splitting mode and so eliminates the need for a Robert-Asselin time filter. Tracer and velocity are staggered in time, thus providing, ideally, a second order time accurate method. For certain model configurations, this scheme has been found to be twice as efficient as the leap-frog based scheme since one can take twice the time step with the two-level approach (e.g., the global climate model test case presented in Chapter 37). Furthermore, without the time filtering needed with the leap-frog, the new scheme conserves total tracer to within numerical roundoff. This scheme is discussed in Griffies (2004), Griffies et al. (2005), and in Chapter 7 of this document.

- EQUATION OF STATE: The equation of state in MOM4p1 follows the formulation of Jackett et al. (2006), where the coefficients from McDougall et al. (2003) are updated to new empirical data.

- UPDATED FREEZING TEMPERATURE FOR FRAZIL: Accurate methods for computing the freezing temperature of seawater are provided by Jackett et al. (2006). These methods allow, in particular, for the computation of the freezing point at arbitrary depth, which is important for ice shelf modelling.

- CONSERVATIVE TEMPERATURE: MOM4p1 time steps the conservative temperature described by McDougall (2003) to provide a measure of heat in the ocean (see Section 3.3.2). This variable is about 100 times more conservative than the traditional potential temperature variable. An option exists to set either conservative temperature or potential temperature prognostic, with the alternative temperature variable carried as a diagnostic tracer.

- PRESSURE GRADIENT CALCULATION: The pressure gradient calculation has been updated in MOM4p1 to allow for the use of generalized level coordinates. A description of the formulation is given in Chapter 4. None of the sophisticated methods described by Shchepetkin and McWilliams (2002) are implemented in MOM4p1, and so terrain following vertical coordinates may suffer from unacceptably large pressure gradients errors in MOM4p1.

- Partial bottom steps: MOM4p1 employs the partial bottom step technology of Pacanowski and Gnanadesikan (1998) to facilitate the representation of bottom topography. This approach is implemented for all of the vertical coordinates.

- TRACER ADVECTION: MOM4p1 comes with the following array of tracer advection schemes. Note that centred schemes are stable *only* for the leap-frog version of MOM4p1. We thus partition the advection schemes according to the corresponding time stepping schemes.

  - Schemes available for either time stepping method

    1. First order upwind
    2. Quicker scheme is third order upwind biased and based on the Leonard (1979). Holland et al. (1998) and Pacanowski and Griffies (1999) discuss implementations in ocean climate models. This scheme does not have flux limiters, so it is not monotonic.
    3. Quicker-MOM3: The Quicker scheme in MOM4p1 differs slightly from that in MOM3, and so the MOM3 algorithm has also been ported to MOM4p1.
    4. Multi-dimensional third order upwind biased approach of Hundsdorfer and Trompert (1994), with Super-B flux limiters.
    5. Multi-dimensional third order upwind biased approach of Hundsdorfer and Trompert (1994), with flux limiters of Sweby (1984).
    6. The second moment scheme of Prather (1986) has been implemented in MOM4p1. It is available without limiters, or with the limiters of Merryfield and Holloway (2003).
    7. The piece-wise parabolic method has been implemented in MOM4p1.

  - Schemes available only for leap-frog time stepping

    1. Second order centred differences
    2. Fourth order centred differences: This scheme assumes the grid is uniformly spaced (in metres), and so is less than fourth order accurate when the grid is stretched, in either the horizontal or vertical.
    3. Sixth order centred differences: This scheme assumes the grid is uniformly spaced (in metres), and so is less than sixth order accurate when the grid is stretched, in either the horizontal or vertical. This scheme is experimental, and so *not* supported for general use.

- TRACER PACKAGES: MOM4p1 comes with an array of tracer packages of use for understanding water mass properties and for building more sophisticated tracer capabilities, such as for ocean ecosystem models. These packages include the following.

- Idealized passive tracer module with internally generated initial conditions. These tracers are ideal for testing various advection schemes, for example, as well as to diagnose pathways of transport.
- An ideal age tracer, with various options for specifying the initial and boundary conditions.
- The OCMIP2 protocol tracers (CO_2, CFC, biotic).
- iBGC: An intermediate complexity ocean biogeochemistry model.
- BLING: Another ocean biogeochemistry model. This model has been written in a *generic* format to allow for its use with both MOM4p1 and GFDL's isopycnal model GOLD.
- TOPAZ: A comprehensive model of oceanic ecosystems and biogeochemical cycles is a state of the art model that considers 22 tracers including three phytoplankton groups, two forms of dissolved organic matter, heterotrophic biomass, and dissolved inorganic species for C, N, P, Si, Fe, $CaCO_3$ and O_2 cycling. The model includes such processes as gas exchange, atmospheric deposition, scavenging, N_2 fixation and water column and sediment denitrification, and runoff of C, N, Fe, O_2, alkalinity and lithogenic material. The phytoplankton functional groups undergo co-limitation by light, nitrogen, phosphorus and iron with flexible physiology. Loss of phytoplankton is parameterized through the size-based relationship of Dunne et al. (2005). Particle export is described through size and temperature based detritus formation and mineral protection during sinking with a mechanistic, solubility-based representation alkalinity addition from rivers, $CaCO_3$ sedimentation and sediment preservation and dissolution. This model has been written in a *generic* format to allow for its use with both MOM4p1 and GFDL's isopycnal model GOLD.

- Penetration of shortwave radiation as discussed in Sweeney et al. (2005) using various attenuation options.

- Horizontal friction: MOM4p1 has a suite of horizontal friction schemes, such as Smagorinsky laplacian and biharmonic schemes described in Griffies and Hallberg (2000) and the anisotropic laplacian scheme from Large et al. (2001) and Smith and McWilliams (2003).

- Convection: There are various convective methods available for producing a gravitationally stable column. The scheme used most frequently at GFDL for certain idealized studies is that due to Rahmstorf (1993).

- NEUTRAL PHYSICS AND BOUNDARY REGIONS: There are new options available for treating neutral physics within boundary regions, as motivated from ideas proposed by Ferrari et al. (2008). The MOM4p1 formulation is given in Chapter 16

- FORM DRAG: MOM4p1 has various options associated with the parameterization of form drag arising from unresolved mesoscale eddies, as proposed by Greatbatch and Lamb (1990), Aiki et al. (2004), and Ferreira and Marshall (2006).

- RESTRATIFICATION EFFECTS FROM SUBMESOSCALE EDDIES: There is a new option available for parameterizing the restratification effects from submesoscale eddies, as proposed by Fox-Kemper et al. (2008b). The MOM4p1 formulation is given in Chapter 18.

- TIDAL MIXING PARAMETERIZATION: The Simmons et al. (2004) parameterization has been implemented as a means to parameterize the diapycnal mixing effects from breaking internal gravity waves, especially those waves influenced by rough bottom topography. Additionally, this scheme has been combined with that used by Lee et al. (2006), who discuss the importance of barotropic tidal energy on shelves for dissipating energy and producing tracer mixing. Chapter 14 presents the MOM4p1 formulation.

- Other vertical mixing schemes: MOM4p1 comes with an array of vertical mixing schemes, such as the following.

  - Constant background diffusivity proposed by Bryan and Lewis (1979).
  - The Pacanowski and Philander (1981) Richardson number dependent scheme.
  - The KPP scheme of Large et al. (1994).
  - GENERAL OCEAN TURBULENCE MODEL (GOTM): MOM4p1 has a wrapper enabling a 3d general circulation simulation to employ the one-dimensional physics closures available from (Umlauf et al., 2005).

- UPDATE OF OVERFLOW SCHEMES: MOM4p1 comes with various methods of use for parameterizing, or at least facilitating the representation of, dense water moving into the abyss. These schemes are documented in Chapter 19.

- REFINED OPEN BOUNDARY CONDITIONS MODULE: The open boundary conditions module has been updated for MOM4p1 to facilitate its use for regional modelling as described by Herzfeld et al. (2010). Chapter 12 presents some details. This scheme has been developed for use only with depth based vertical coordinates, with z and z^* the two coordinates that have been tested. No development has been given to pressure based vertical coordinates. Pressure based coordinates solve for the bottom pressure rather than the surface height. Hence, there are algorithm development issues required to extend the present OBC code to handle pressure based vertical coordinates.

- UPDATED SPURIOUS MIXING DIAGNOSTIC: Griffies et al. (2000b) describe an empirical diagnostic method to diagnose the levels of mixing occurring in a model. This diagnostic required some upgrades to allow for the use of thickness weighting for time stepping the prognostic fields. This diagnostic is described in Chapter 23. Also, the method of Burchard and Rennau (2008) is available in MOM4p1 to diagnose the dissipation associated with numerical advection. Details of the MOM4p1 implementation of this diagnostic are provided in Chapter 24.

- STERIC SEA LEVEL DIAGNOSTIC: We provide some added diagnostics for understanding how sea level evolves. Preliminary formulation is given in Chapter 26.

- REVISED TEST CASES: All of the test cases have been revised as well as the addition of some new tests. Documentation of these tests is presented in Part V of this document.

- UPDATED FMS INFRASTRUCTURE AND PREPROCESSING TOOLS: As with all releases of mom4, it comes with updated infrastructure, preprocessing code, coupling code, etc. supported by an array of scientists and engineers at GFDL.

1.2 Relating MOM4p1 to MOM4.0

- Backward compatibility

  There is *no option* that will provide bitwise agreement between MOM4p1 simulations and MOM4.0 simualations. Providing this feature was deemed too onerous on the development of MOM4p1, in which case many of the algorithms were rewritten, reorganized, and modified.

  Nonetheless, some features have been preserved, with the aim to provide a reasonable path towards backward checking. In particular, the mom4p0 neutral physics algorithm has been retained, and indeed is recommended for production runs. Additionally, changes to KPP mentioned below are provided in the MOM4p1 version of this module, with the MOM4.0 version ported to MOM4p1 for legacy purposes.

- Bug fixes

  1. The shortwave penetration module in MOM4.0 failed to account for the undulating surface height when computing the attenuation of shortwave entering the ocean. For many cases this bug is of minor consequence. But when refining the vertical resolution, the surface height undulations must be accounted for when attentuating shortwave. Additionally, for general vertical coordinates, undulating depths are the norm, so the shortwave algorithm needed to be updated.
  2. The KPP vertical mixing scheme included many places where the vertical grid was assumed to be rigid and one dimensional. As for the shortwave, this code was originally developed for a rigid lid z-model. When generalizing to free surface, partial bottom steps, and vertical coordinates, the vertical grid becomes a dynamic three dimensional array, which required some modifications to the code.

- General cleanup and additions

  1. Numerous additional diagnostic features;
  2. Basic code clean up with bit more tidy code style in most places;
  3. Thoroughly updated documentation of MOM4p1 as a complement to the MOM4 Technical Guide of Griffies et al. (2004).

CHAPTER
TWO

Synopsis of MOM4p1

The purpose of this document is to detail the formulation, methods, and selected SGS parameterizations of MOM4p1. This document complements many of the discussions in the MOM3 Manual of Pacanowski and Griffies (1999), the MOM4 Technical Guide of Griffies et al. (2004), and the monograph by Griffies (2004).

The equations and methods of MOM4p1 are based on the hydrostatic and nonBoussinesq equations of the ocean along with a selection of subgrid scale (SGS) parameterizations. The model is written with rudimentary general level coordinate capabilities employing a quasi-Eulerian algorithm. Notably, this approach precludes it from running as a traditional isopycnal layered model, which generally use quasi-Lagrangian algorithms. Nonetheless, the generalized level coordinate features of MOM4p1 distinguish it most noticeably from MOM4.0. The purpose of this chapter is to summarize the basic elements of MOM4p1. Features new relative to MOM4.0 are highlighted in smallcaps.

2.1 What is MOM?

The Modular Ocean Model (MOM) is a numerical representation of the ocean's hydrostatic primitive equations. It is designed primarily as a tool for studying the ocean climate system. Additionally, MOM has been used in regional and coastal applications, with many new features in MOM4p1 aimed at supporting this work. The model is developed by researchers from around the world, with the main algorithm development and software engineering provided by NOAA's Geophysical Fluid Dynamics Laboratory (GFDL). The model is freely available via

`http://www.gfdl.noaa.gov/fms`

MOM evolved from numerical ocean models developed in the 1960's-1980's by Kirk Bryan and Mike Cox at GFDL. Most notably, the first internationally released and supported primitive equation ocean model was developed by Mike Cox (Cox (1984)). It cannot be emphasized enough how revolutionary it was in 1984 to freely release, support, and document code for use in numerical ocean climate modeling. The Cox-code provided scientists worldwide with a powerful tool to investigate basic and applied questions about the ocean and its interactions with other components of the climate system. Previously, rational investigations of such questions by most scientists were limited to restrictive idealized models and analytical methods. Quite simply, the Cox-code started

what has today become a right-of-passage for every high-end numerical model of dynamical earth systems.

Upon the untimely passing of Mike Cox in 1990, Ron Pacanowski, Keith Dixon, and Tony Rosati rewrote the Cox code with an eye on new ideas of modular programming using Fortran 77. The result was the first version of MOM (Pacanowski et al. (1991)). Version 2 of MOM (Pacanowski (1995)) introduced the memory window idea, which was a generalization of the vertical-longitudinal slab approach used in the Cox-code and MOM1. Both of these methods were driven by the desires of modelers to run large experiments on machines with relatively small memories. The memory window provided enhanced flexibility to incorporate higher order numerics, whereas slabs used in the Cox-code and MOM1 restricted the numerics to second order. MOM3 (Pacanowski and Griffies (1999)) even more fully exploited the memory window with a substantial number of physics and numerics options.

The Cox-code and each version of MOM came with a manual. Besides describing the elements of the code, these manuals aimed to provide transparency to the rationale underlying the model's numerics. Without such, the model could in many ways present itself as a black box, thus greatly hindering its utility to the scientific researcher. This philosophy of documentation saw its most significant realization in the MOM3 Manual, which reaches to 680 pages. The present document is written with this philosophy in mind, yet allows itself to rely somewhat on details provided in the previous manuals as well as theoretical discussions given by Griffies (2004).

The most recent version of MOM is version 4. The origins of MOM4 date back to a transition from vector to parallel computers at GFDL, starting in 1999. Other models successfully made the transition some years earlier (e.g., The Los Alamos Parallel Ocean Program (POP) and the OCCAM model from Southampton, UK). New computer architectures generally allow far more memory than previously available, thus removing many of the reasons for the slabs and memory window approaches used in earlier versions of MOM. Hence, we concluded that the memory window should be jettisoned in favor of a straightforward horizontal 2D domain decomposition. Thus began the project to redesign MOM for use on parallel machines.

2.2 First release of MOM4.0: October 2003

When physical scientists aim to rewrite code based on software engineering motivations, more than software issues are addressed. During the writing of MOM4, numerous algorithmic issues were also addressed, which added to the development time. Hence, the task of rewriting MOM3 into MOM4.0 took roughly four years to complete.

2.3 First release of MOM4p1: Early 2007

Griffies spent much of 2005 in Hobart, Australia as a NOAA representative at the CSIRO Marine and Atmospheric Research Laboratory, as well as with researchers at the University of Tasmania. This period saw focused work to upgrade MOM4 to include certain features of generalized level coordinates. An outline of these, and other features, is given in the following sections.

By allowing for the use of a suite of vertical coordinates, MOM4p1 is algorithmically more flexible than any previous version of MOM. This work, however, did not fundamentally alter the overall computational structure relative to the last release of MOM4.0 (the MOM4p0d release in

May 2005). In particular, MOM4p1 is closer in "look and feel" to MOM4p0d than MOM4p0a is to MOM3.1. Given this similarity, it was decided to retain the MOM4 name for the MOM4p1 release, rather switch to MOM5. Many of the newer features in MOM4p1 should be considered experimental, and worthy of use mainly for research purposes.

2.4 MOM4p1 release December 2009

The MOM4p1 release of December 2009 represents a major upgrade to the code, especially those areas related to the open boundary conditions (Chapter 12 and Herzfeld et al. (2010)), various physical parameterizations, diagnostics, and FMS infrastructure. This public release also provides the community with a *test case* consisting of the CM2.1 configuration used by GFDL for the IPCC AR4 assessment, as documented by Griffies et al. (2005), Gnanadesikan et al. (2006a), Delworth et al. (2006), Wittenberg et al. (2006), and Stouffer et al. (2006). Although CM2.1 for the AR4 assessement actually used MOM4.0, the setup in the CM2.1-MOM4p1 test case is backwards compatibile.

2.5 Fundamentals of MOM4p1

In this section, we outline fundamental features of MOM4p1; that is, features that are always employed when using the code.

- GENERALIZED LEVEL COORDINATES: Various vertical coordinates have been implemented in MOM4p1. We have focused attention on vertical coordinates based on functions of depth or pressure, which means in particualar that MOM4p1 *does not* support thermodynamic or isopycnal based vertical coordinates.[1]

  The following list summarizes vertical coordinates presently implemented in MOM4p1. Extensions to other vertical coordinates are straightforward, given the framework available for the coordinates already present. Full details of the vertical coordinates are provided in Chapter 6.

  - Geopotential coordinate as in MOM4.0, including the undulating free surface at $z = \eta$ and bottom partial cells approximating the bottom topography at $z = -H$

$$s = z. \tag{2.1}$$

  - Quasi-horizontal rescaled height coordinate of Stacey et al. (1995) and Adcroft and Campin (2004)

$$\begin{aligned} s &= z^* \\ &= H \left(\frac{z - \eta}{H + \eta} \right). \end{aligned} \tag{2.2}$$

[1]The Hallberg Isopycnal Model (HIM) is available from GFDL for those wishing to use layered models. HIM is a Fortran code that is fully supported by GFDL scientists and engineers. Information about HIM is available at `http://www.gfdl.noaa.gov/fms/`.

– Depth based terrain following "sigma" coordinate, popular for coastal applications

$$\begin{aligned} s &= \sigma^{(z)} \\ &= \frac{z-\eta}{H+\eta}. \end{aligned} \tag{2.3}$$

– Pressure coordinate

$$s = p \tag{2.4}$$

was shown by Huang et al. (2001), DeSzoeke and Samelson (2002), Marshall et al. (2004), and Losch et al. (2004) to be a useful way to transform Boussinesq z-coordinate models into nonBoussinesq pressure coordinate models.

– Quasi-horizontal rescaled pressure coordinate

$$\begin{aligned} s &= p^* \\ &= p_{\mathrm{b}}^o \left(\frac{p-p_{\mathrm{a}}}{p_{\mathrm{b}}-p_{\mathrm{a}}} \right), \end{aligned} \tag{2.5}$$

where p_{a} is the pressure applied at the ocean surface from the atmosphere and/or sea ice, p_{b} is the hydrostatic pressure at the ocean bottom, and p_{b}^o is a time independent reference bottom pressure.

– Pressure based terrain following coordinate

$$\begin{aligned} s &= \sigma^{(p)} \\ &= \left(\frac{p-p_{\mathrm{a}}}{p_{\mathrm{b}}-p_{\mathrm{a}}} \right). \end{aligned} \tag{2.6}$$

Note the following points:

– All depth based vertical coordinates implement the volume conserving, Boussinesq, ocean primitive equations.

– All pressure based vertical coordinates implement the mass conserving, nonBoussinesq, ocean primitive equations.

– There has little effort focused on reducing pressure gradient errors in the terrain following coordinates (Section 4.2). Researchers intent on using terrain following coordinates may find it necessary to implement one of the more sophisticated pressure gradient algorithms available in the literature, such as that from Shchepetkin and McWilliams (2002).

– Use of neutral physics parameterizations (Section 5.2.3 and Chapter 16) with terrain following coordinates is not recommended with the present implementation. There are formulation issues that have not been addressed, since the main focus of neutral physics applications at GFDL centres on vertical coordinates that are quasi-horizontal.

– Most of the vertical coordinate dependent code is in the

`mom4/ocean_core/ocean_thickness`

module, where the thickness of a grid cell is updated according to the vertical coordinate choice. The developer intent on introducing a new vertical coordinate may find it suitable to emulate the steps taken in this module for other vertical coordinates. The remainder of the model code is generally transparent to the specific choice of vertical coordinate, and such has facilitated a straightforward upgrade of the code from MOM4.0 to MOM4p1.

- Generalized orthogonal horizontal coordinates: MOM4p1 is written using generalized horizontal coordinates, with the coordinates assumed to be locally orthogonal. The formulation in this document follows this approach as well. For global ocean climate modelling, MOM4p1 comes with test cases (the OM3 test case in Chapter 37) using the tripolar grid of Murray (1996). Other orthogonal grids have been successfully employed with MOM4.0.

  Code for reading in the grid and defining MOM4 specific grid factors is found in the module

  `mom4/ocean_core/ocean_grids`.

  MOM comes with preprocessing code suitable for generating grid specification files of various complexity, including the Murray (1996) tripolar grid. Note that the horizontal grid in MOM4 is static (time independent), whereas the vertical grid is generally time dependent. Hence, there is utility in separating the horizontal from the vertical grids.

- Parallel programming: MOM4p1 follows the parallel programming approach of MOM4.0, and is written with arrays ordered `(i,j,k)` for straightforward processor domain decomposition.

- EXPLICIT FREE SURFACE AND EXPLICIT BOTTOM PRESSURE SOLVER: MOM4 employs a split-explicit time stepping scheme where fast two-dimensional dynamics is sub-cycled within the slower three dimensional dynamics. The method follows ideas detailed in Chapter 12 of Griffies (2004), which are based on Killworth et al. (1991) and Griffies et al. (2001). Chapter 7 presents the details for MOM4p1, and the code is on the module

  `mom4/ocean_core/ocean_barotropic`.

- Time stepping schemes: The time tendency for tracer and baroclinic velocity can be discretized two ways.

  1. The first approach uses the traditional leap-frog method for the inviscid/dissipationless portion of the dynamics, along with a Robert-Asselin time filter.
  2. The preferred method discretizes the time tendency with a two-level forward step, which eliminates the need to time filter. Tracer and velocity are staggered in time, thus providing second order accuracy in time. For certain model configurations, this scheme has been found to be twice as efficient as the leap-frog based scheme since one can take twice the time step with the two-level approach. Furthermore, without the time filtering needed with the leap-frog, the new scheme conserves total tracer to within numerical roundoff. This scheme is discussed in Griffies et al. (2005) and Griffies (2004) (see Chapter 12), as well as in Chapter 7 of this document.

The code implementing these ideas in MOM4p1 can be found in

`mom4/ocean_core/ocean_velocity`
`mom4/ocean_tracers/ocean_tracer`

- Time stepping the Coriolis force: As discussed in Chapter 11, there are various methods available for time stepping the Coriolis force on the B-grid used in MOM4. The most commonly used method for global climate simulations at GFDL is the semi-implicit approach in which half the force is evaluated at the present time and half at the future time.

- EQUATION OF STATE: As discussed in Chapter 9, the equation of state in MOM4p1 follows the formulation of Jackett et al. (2006), where the coefficients from McDougall et al. (2003) are updated to new empirical data. The code for computing density is found in the module

  `mom4/ocean_core/ocean_density`.

- CONSERVATIVE TEMPERATURE: MOM4p1 time steps the conservative temperature described by McDougall (2003) to provide a measure of heat in the ocean (see Section 3.3.2). This variable is about 100 times more conservative than the traditional potential temperature variable. An option exists to set either conservative temperature or potential temperature prognostic, with the alternative temperature variable carried as a diagnostic tracer. This code for computing conservative temperature is within the module

  `mom4/ocean_tracers/ocean_tempsalt`.

- PRESSURE GRADIENT CALCULATION: The pressure gradient calculation has been updated in MOM4p1 to allow for the use of generalized vertical coordinates. A description of the formulation is given in Chapter 4, and the code is in the module

  `mom4/ocean_core/ocean_pressure`.

  Notably, none of the sophisticated methods described by Shchepetkin and McWilliams (2002) are implemented in MOM4p1, and so terrain following vertical coordinates may suffer from unacceptably large pressure gradients errors in MOM4p1. Researchers are advised to perform careful tests prior to using these coordinates.

- Partial bottom steps: MOM4p1 employs the partial bottom step technology of Pacanowski and Gnanadesikan (1998) to facilitate the representation of bottom topography, with the code in the module

  `mom4/ocean_core/ocean_topog`.

2.6 Tracer features

Here, we outline some of the features available for tracers in MOM4p1.

- TRACER ADVECTION: MOM4p1 comes with the following array of tracer advection schemes. Note that centred schemes are stable *only* for the leap-frog version of MOM4p1. We thus partition the advection schemes according to the corresponding time stepping schemes. The code for tracer advection schemes are in the module

  `mom4/ocean_tracers/ocean_tracer_advect`.

  - Schemes available for either time stepping method
    1. First order upwind
    2. Quicker scheme is third order upwind biased and based on the Leonard (1979). Holland et al. (1998) and Pacanowski and Griffies (1999) discuss implementations in ocean climate models. This scheme does not have flux limiters, so it is not monotonic.
    3. Quicker-MOM3: The Quicker scheme in MOM4p1 differs slightly from that in MOM3, and so the MOM3 algorithm has also been ported to MOM4p1.
    4. Multi-dimensional third order upwind biased approach of Hundsdorfer and Trompert (1994), with Super-B flux limiters.[2] The scheme is available in MOM4p1 with either time stepping scheme.
    5. Multi-dimensional third order upwind biased approach of Hundsdorfer and Trompert (1994), with flux limiters of Sweby (1984).[3] It is available in MOM4p1 with either time stepping scheme.
    6. The second moment scheme of Prather (1986) has been implemented in MOM4p1. It is available without limiters, or with the limiters of Merryfield and Holloway (2003).
    7. The piece-wise parabolic method has been implemented in MOM4p1.

    Both of the MIT-based schemes are non-dispersive, preserve shapes in three dimensions, and preclude tracer concentrations from moving outside of their natural ranges in the case of a purely advective process. They are modestly more expensive than the Quicker scheme, and it do not significantly alter the simulation relative to Quicker in those regions where the flow is well resolved. The Sweby limiter code was used for the ocean climate model documented by Griffies et al. (2005).
  - Schemes available only for leap-frog time stepping
    1. Second order centred differences
    2. Fourth order centred differences: This scheme assumes the grid is uniformly spaced (in metres), and so is less than fourth order accurate when the grid is stretched, in either the horizontal or vertical.
    3. Sixth order centred differences: This scheme assumes the grid is uniformly spaced (in metres), and so is less than sixth order accurate when the grid is stretched, in

[2] This scheme was ported to MOM4 by Alistair Adcroft, based on his implementation in the MITgcm. The online documentation of the MITgcm at `http://mitgcm.org` contains useful discussions and details about this advection scheme.

[3] This scheme was ported to MOM4 by Alistair Adcroft, based on his implementation in the MITgcm. The online documentation of the MITgcm at `http://mitgcm.org` contains useful discussions and details about this advection scheme.

either the horizontal or vertical. This scheme is experimental, and so *not* supported for general use.

- TRACER PACKAGES: MOM4p1 comes with an array of tracer packages of use for understanding water mass properties and for building more sophisticated tracer capabilities, such as for ocean ecosystem models. Modules for these tracers are in the directories

  `mom4/ocean_tracers`
  `mom4/ocean_bgc`
  `ocean_shared/generic_tracers`.

  The tracer packages include the following.

  - Idealized passive tracer module with internally generated initial conditions. These tracers are ideal for testing various advection schemes, for example, as well as to diagnose pathways of transport.
  - An ideal age tracer, with various options for specifying the initial and boundary conditions.
  - The OCMIP2 protocol tracers (CO_2, CFC, biotic).
  - iBGC: A simple ocean biogeochemistry model.
  - BLING: An intermediate complexity ocean biogeochemistry model. This model has been written in a *generic* format to allow for its use with both MOM4p1 and GFDL's model code GOLD.
  - TOPAZ: A comprehensive model of oceanic ecosystems and biogeochemical cycles is a state of the art model that considers 22 tracers including three phytoplankton groups, two forms of dissolved organic matter, heterotrophic biomass, and dissolved inorganic species for C, N, P, Si, Fe, $CaCO_3$ and O_2 cycling. The model includes such processes as gas exchange, atmospheric deposition, scavenging, N_2 fixation and water column and sediment denitrification, and runoff of C, N, Fe, O_2, alkalinity and lithogenic material. The phytoplankton functional groups undergo co-limitation by light, nitrogen, phosphorus and iron with flexible physiology. Loss of phytoplankton is parameterized through the size-based relationship of Dunne et al. (2005). Particle export is described through size and temperature based detritus formation and mineral protection during sinking with a mechanistic, solubility-based representation alkalinity addition from rivers, $CaCO_3$ sedimentation and sediment preservation and dissolution. This model has been written in a *generic* format to allow for its use with both MOM4p1 and GFDL's isopycnal model GOLD.

- UPDATED FREEZING TEMPERATURE FOR FRAZIL: Accurate methods for computing the freezing temperature of seawater are provided by Jackett et al. (2006). These methods allow, in particular, for the computation of the freezing point at arbitrary depth, which is important for ice shelf modelling. These methods have been incorporated into the frazil module

  `mom4/ocean_tracers/ocean_frazil`,

  with heating due to frazil formation treated as a diagnostic tracer.

- PENETRATION OF SHORTWAVE RADIATION: The following modules are available for computing shortwave penetration into the ocean

  `mom4/ocean_param/sources/ocean_shortwave`
  `mom4/ocean_param/sources/ocean_shortwave_csiro`
  `mom4/ocean_param/sources/ocean_shortwave_gfdl`
  `mom4/ocean_param/sources/ocean_shortwave_jerlov`

  with the reader referred to each module for full documentation. In brief, these modules provide the following options.

  - `ocean_shortwave`: This module drives the other shortwave modules.
  - `ocean_shortwave_csiro`: This module implements a simple exponential decay for the penetrative shortwave radiation. This module was prepared at CSIRO Marine and Atmospheric Research in Australia.
  - `ocean_shortwave_gfdl`: This module implements the optical model of Morel and Antoine (1994) as well as that of Manizza et al. (2005).
    * Sweeney et al. (2005) compile a seasonal climatology of chlorophyll based on measurements from the NASA SeaWIFS satellite, and this climatology is available with the distribution of MOM4. They used this data to develop two parameterizations of visible light absorption based on the optical models of Morel and Antoine (1994) and Ohlmann (2003). The two models yield quite similar results when used in global ocean-only simulations, with very small differences in heat transport and overturning.
    * The Morel and Antoine (1994) method for attenuating shortwave radiation was employed in the CM2 coupled climate model, as discussed by Griffies et al. (2005). In MOM4p1, we updated the implementation of this algorithm relative to MOM4.0 by including the time dependent nature of the vertical position of a grid cell. The MOM4.0 implementation used the vertical position appropriate only for the case of a static ocean free surface.
    * In more recent model development, especially that associated with interactive biogeochemistry, GFDL modelers have employed the scheme from Manizza et al. (2005) rather than Morel and Antoine (1994).
  - `ocean_shortwave_jerlov`: This module implements yet another exponential decay formulation (actually, a double exponential) for the penetrative shortwave radiation.

2.7 Subgrid scale parameterizations

Here, we outline some features of the subgrid scale parameterizations available in MOM4p1.

- Horizontal friction: MOM4p1 has a suite of horizontal friction schemes, such as Smagorinsky laplacian and biharmonic schemes described in Griffies and Hallberg (2000) and the

anisotropic laplacian scheme from Large et al. (2001) and Smith and McWilliams (2003). Code for these schemes is found in the modules

`mom4/ocean_param/mixing/ocean_lapgen_friction`
`mom4/ocean_param/mixing/ocean_bihgen_friction`.

- Convection: There are various convective methods available for producing a gravitationally stable column, with the code found in the module

  `mom4/ocean_param/mixing/ocean_convect`.

  The scheme used most frequently at GFDL is that due to Rahmstorf (1993).

- NEUTRAL PHYSICS AND BOUNDARY REGIONS: There are new options available for treating neutral physics within boundary regions, as motivated from ideas proposed by Ferrari et al. (2008). A discussion of these ideas is given in Chapter 16 of this document, and the code is available in the module

  `mom4/ocean_param/mixing/ocean_nphysicsB`,

  with the MOM4.0 methods remaining in

  `mom4/ocean_param/mixing/ocean_nphysicsA`.

  There are also some further methods implemented in

  `mom4/ocean_param/mixing/ocean_nphysicsC`

  based on the work of Ferrari et al. (2009). Note that the nphysicsC module remains experimental, and so should *not* be used for general applications.

- RESTRATIFICATION EFFECTS FROM SUBMESOSCALE EDDIES: There is an option available for parameterizing the restratification effects from submesoscale eddies, as proposed by Fox-Kemper et al. (2008b). The MOM4p1 formulation is given in Chapter 18, and the code is available in the module

  `mom4/ocean_param/mixing/ocean_submesoscale`.

- FORM DRAG: MOM4p1 has various options associated with the parameterization of form drag arising from unresolved mesoscale eddies, as proposed by Greatbatch and Lamb (1990), Aiki et al. (2004), and Ferreira and Marshall (2006). The code is available in the module

  `mom4/ocean_param/mixing/ocean_form_drag`,

  and documentation is given in Chapter 17. The form drag parameterization schemes are experimental and have not been thoroughly used at GFDL.

- TIDAL MIXING PARAMETERIZATION: The tidal mixing parameterization of Simmons et al. (2004) has been implemented as a means to parameterize the diapycnal mixing effects from breaking internal gravity waves, especially those waves influenced by rough bottom topography. Additionally, this scheme has been combined with that used by Lee et al. (2006), who discuss the importance of barotropic tidal energy on shelves for dissipating energy and producing tracer mixing. Chapter 14 presents the model formulation, and

  `mom4/ocean_param/mixing/ocean_vert_tidal`

  contains the code.

- Other vertical mixing schemes: MOM4p1 comes with an array of vertical mixing schemes, such as the following.

  – Constant background diffusivity proposed by Bryan and Lewis (1979)

    `mom4/ocean_param/mixing/ocean_vert_mix`

  – Richardson number dependent scheme from Pacanowski and Philander (1981)

    `mom4/ocean_param/mixing/ocean_vert_pp`

  – The KPP scheme from Large et al. (1994)

    `mom4/ocean_param/mixing/ocean_vert_kpp`
    `mom4/ocean_param/mixing/ocean_vert_kpp_mom4p0`

    The module `ocean_vert_kpp` maintains code provides some code updates relative to MOM4.0, such as to allow for the use of generalized vertical coordinates; features found useful in fresh inland seas; and modifications introduced by Danabasoglu et al. (2006). The module `ocean_vert_kpp_mom4p0` maintains code compatibility with the implementation of MOM4.0 necessary to allow for backwards compatiblity with the CM2.1 coupled model documented in Griffies et al. (2005).

  – GENERAL OCEAN TURBULENCE MODEL (GOTM): Coastal simulations require a suite of vertical mixing schemes beyond those available in most ocean climate models. GOTM (Umlauf et al., 2005) is a public domain Fortran90 free software used by a number of coastal ocean modellers

    `http://www.gotm.net/`

    GOTM includes many sophisticated turbulence closure schemes, and is updated periodically. It thus provides users of MOM4p1 access to most updated methods for computing vertical diffusivities and vertical viscosities. GOTM has been coupled to MOM4p1 by scientists at CSIRO in Australia in collaboration with German and GFDL scientists.
    The MOM4p1 wrapper for GOTM is

    `mom4/ocean_param/mixing/ocean_vert_gotm`

    with the GOTM source code in the directory

    `mom4/ocean_param/gotm`.

- UPDATE OF OVERFLOW SCHEMES: MOM4p1 comes with various methods of use for parameterizing, or at least facilitating the representation of, dense water moving into the abyss. These schemes are documented in Chapter 19, with the following modules implementing these methods

  `mom4/ocean_param/mixing/ocean_sigma_transport`
  `mom4/ocean_param/mixing/ocean_mixdownslope`
  `mom4/ocean_param/sources/ocean_overflow`
  `mom4/ocean_param/sources/ocean_overexchange`.

2.8 Miscellaneous features

Here, we outline some miscellaneous features of MOM4p1.

- REFINED OPEN BOUNDARY CONDITIONS MODULE: Much of the appeal of MOM4p1 is related to its enhanced facilities for regional ocean modeling, with Herzfeld et al. (2010) documenting certain of these features. Central to this utility is the enhanced open boundary condition module

  `mom4/ocean_core/ocean_obc`

  which is documented in Chapter 12 as well as Herzfeld et al. (2010).

- UPDATED SPURIOUS MIXING DIAGNOSTIC: Griffies et al. (2000b) describe an empirical diagnostic method to diagnose the levels of mixing occurring in a model. This diagnostic required some upgrades to allow for the use of thickness weighting for time stepping the prognostic fields (see Chapter 23, especially Section 23.3). This code is available in the module

  `mom4/ocean_diag/ocean_tracer_diag`.

  Also, the method of Burchard and Rennau (2008) is available in MOM4p1 to diagnose the dissipation associated with numerical advection. Details of the MOM4p1 implementation of this diagnostic are provided in Chapter 24.

- STERIC SEA LEVEL DIAGNOSTIC: We compute the steric sea level diagnostically for the case when running a Boussinesq model. The formulation is given in Chapter 26.

- REVISED TEST CASES: All of the test cases have been revised as well as the addition of some new tests. As in MOM4.0, the tests are **not sanctioned for their physical realism.** Instead, they are provided for computations and numerical evaluation, and as starting points for those wishing to design and implement their own research models.

- UPDATED FMS INFRASTRUCTURE AND PREPROCESSING TOOLS: As with all releases of MOM4, it comes with updated infrastructure, preprocessing code, coupling code, etc. supported by an array of scientists and engineers at GFDL.

2.9 Short bibliography of MOM4 documents

The following is an incomplete list of documents that may prove useful for those wishing to learn more about the MOM4 code, and some of its uses at GFDL.

- The MOM3 Manual of Pacanowski and Griffies (1999) continues to contain useful discussions about issues that remain relevant for MOM4.
- The MOM4 Technical Guide of Griffies et al. (2004) aims to document the MOM4.0 code and its main features.
- The present document, Griffies (2009), presents the fundamental formulation and model algorithms of use for the generalized vertical coordinate code MOM4p1.
- The monograph by Griffies (2004) presents a pedagogical treatment of many areas relevant for ocean climate modellers.
- The paper by Griffies et al. (2005) provides a formulation of the ocean climate model used in the GFDL CM2 climate model for the study of global climate variability and change. The ocean code is based on MOM4.0.
- The paper by Gnanadesikan et al. (2006a) describes the ocean simulation characteristics from the coupled climate model CM2.
- The paper by Delworth et al. (2006) describes the coupled climate model CM2.
- The paper by Wittenberg et al. (2006) focuses on the tropical simulations in the CM2 coupled climate model.
- The paper by Stouffer et al. (2006) presents some idealized climate change simulations with the coupled climate model CM2.
- The paper by Herzfeld et al. (2010) documents the use of MOM4p1 for regional modeling.

2.10 The future of MOM

MOM has had a relatively long and successful history. The release of MOM4p1 represents a major step at GFDL to move into the world of generalized level coordinate models, as well as regional modeling. It is anticipated that MOM4p1 will be used at GFDL and abroad for many process, coastal, regional, and global studies. It is, quite simply, the most versatile of the MOM codes produced to date.

Nonetheless, there are many compelling reasons to move even further along the generalization path, in particular to include isopycnal layered models in the same code base as the level vertical coordinates enabled in MOM4p1. As discussed in Griffies et al. (2000a), there remain many systematic problems with each vertical coordinate class, and such warrants the development of a single code base that can examine these issues in a controlled setting.

GFDL employs the developers of three of the world's most successful ocean model codes: (1) Alistair Adcroft, who developed the MITgcm, which has non-hydrostatic and hydrostatic options;

(2) Bob Hallberg, who developed the Hallberg Isopycnal Model, which has been used for process studies and global coupled modelling, and (3) Stephen Griffies, who has been working on MOM development. A significant step forward in ocean model code will be found by merging various features of the MITgcm, HIM, and MOM. Therefore, Adcroft, Griffies, and Hallberg have each agreed to evolve their efforts towards the goal of producing a GFDL Unified Ocean Model. Public release of this code will occur at an uncertain date, likely after 2012.

PART I
Formulation of the ocean equations

Descriptive methods provide a foundation for physical oceanography. Indeed, many observational oceanographers are masters at weaving a physical story of the ocean. Once a grounding in observations and experimental science is established, it is the job of the theorist to rationalize the phenomenology using fundamental principles of physics. For oceanography, these fundamentals largely rest in the realm of classical physics. That is, for a fundamental understanding, it is necessary to combine the descriptive, and more generally the experimental, approaches with theoretical methods based on mathematical physics. Together, the descriptive/experimental and theoretical methods render deep understanding of physical phenomena, and allow us to provide rational, albeit imperfect, predictions of unobserved phenomena, including the state of future ocean climate.

Many courses in physics introduce the student to mathematical tools required to garner a quantative understanding of physical phenomena. Mathematical methods add to the clarity, conciseness, and precision of our description of physical phenomena, and so enhance our ability to unravel the essential physical processes involved with a phenomenon.

The purpose of this part of the document is to mathematically formulate the fundamental equations providing the rational basis of the MOM4p1 ocean code. It is assumed in this section that the reader has a basic understanding of calculus and fluid mechanics.

CHAPTER
THREE

Fundamental equations

The purpose of this chapter is to formulate the kinematic and dynamic equations that form the basis for MOM4p1. Much of this material is derived from lectures of Griffies (2005) at the 2004 GODAE School on Operational Oceanography. The proceedings of this school have been put together by Chassignet and Verron (2005), and this book contains many pedagogical reviews of ocean modelling. Additional discussions can be found in Griffies and Adcroft (2008) and Griffies (2004).

3.1 Fluid kinematics

The purpose of this section is to derive some of the basic equations of fluid kinematics applied to the ocean. Kinematics is the study of the intrinsic properties of motion, without concern for dynamical laws. As considered here, fluid kinematics is concerned with balances of mass for infinitesimal fluid parcels or finite regions of the ocean. It is also concerned with the behaviour of a fluid as it interacts with geometrical boundaries of the domain, such as the land-sea and air-sea boundaries of an ocean basin.

3.1.1 Mass conserving fluid parcels

Consider an infinitesimal parcel of seawater contained in a volume[1]

$$\mathrm{d}V = \mathrm{d}x\,\mathrm{d}y\,\mathrm{d}z \tag{3.1}$$

with a mass

$$\mathrm{d}M = \rho\,\mathrm{d}V. \tag{3.2}$$

[1] A parcel of fluid is macroscopically small yet microscopically large. That is, from a macroscopic perspective, the parcel's thermodynamic properties may be assumed uniform, and the methods of continuum mechanics are applicable to describing the mechanics of an infinite number of these parcels. However, from a microscopic perspective, these fluid parcels contain many molecules, and so it is safe to ignore the details of molecular interactions. Regions of a fluid with length scales on the order of 10^{-3}cm satisfy these properties of a fluid parcel. See Section 2.2 of Griffies (2004) for further discussion.

In these equations, ρ is the *in situ* mass density of the parcel and $\mathbf{x} = (x, y, z)$ is the Cartesian coordinate of the parcel with respect to an arbitrary origin. As the parcel moves through space-time, we measure its velocity

$$\mathbf{v} = \frac{\mathrm{d}\mathbf{x}}{\mathrm{d}t} \tag{3.3}$$

by considering the time changes in its position.[2]

The time derivative $\mathrm{d}/\mathrm{d}t$ introduced in equation (3.3) measures time changes of a fluid property as one follows the parcel. That is, we place ourselves in the parcel's moving frame of reference. This time derivative is thus directly analogous to that employed in classical particle mechanics (Landau and Lifshitz, 1976; Marion and Thornton, 1988). Describing fluid motion from the perspective of an observer moving with fluid parcels affords us with a *Lagrangian* description of fluid mechanics. For many purposes, it is useful to take a complementary perspective in which we measure fluid properties from a fixed space frame, and so allow fluid parcels to stream by the observer. The fixed space frame affords one with an *Eulerian* description of fluid motion. To relate the time tendencies of scalar properties measured in the moving and fixed frames, we perform a coordinate transformation, the result of which is (see Section 2.3.3 of Griffies (2004) for details)

$$\boxed{\frac{\mathrm{d}}{\mathrm{d}t} = \partial_t + \mathbf{v} \cdot \nabla,} \tag{3.4}$$

where

$$\partial_t = \frac{\partial}{\partial t} \tag{3.5}$$

measures time changes at a fixed space point. The *transport* term

$$\mathbf{v} \cdot \nabla = \mathbf{u} \cdot \nabla_s + w^{(s)} \, \partial_z \tag{3.6}$$

reveals the fundamentally nonlinear character of fluid dynamics. In this relation, ∇_z is the horizontal gradient operator taken on surfaces of constant generalized vertical coordinate s, and $w^{(s)}$ measures the transport of fluid crossing these surfaces. We provide further discussion of this expression in Section 3.1.8. In general, the operator $\mathbf{v} \cdot \nabla$ is known as the *advection* operator in geophysical fluids, whereas it is often termed *convection* in the classical fluids literature.[3]

It is convenient, and conventional, to formulate the mechanics of fluid parcels that conserve mass. Choosing to do so allows many notions from classical particle mechanics to transfer over to continuum mechanics of fluids, especially when formulating the equations of motion from a Lagrangian perspective. We thus focus on kinematics satisfied by mass conserving fluid parcels. In this case, the mass of a parcel changes only if there are sources within the continuous fluid, so that

$$\frac{\mathrm{d}}{\mathrm{d}t} \ln(\mathrm{d}M) = \mathcal{S}^{(M)} \tag{3.7}$$

where $\mathcal{S}^{(\mathcal{M})}$ is the rate at which mass is added to the fluid, per unit mass. Mass sources are often assumed to vanish in textbook formulations of fluid kinematics, but they can be nonzero in certain cases for ocean modelling, so it is convenient to carry them around in our formulation.

[2]The three dimensional velocity vector is written $\mathbf{v} = (\mathbf{u}, w)$ throughout these notes, with $\mathbf{u} = (u, v)$ the horizontal components and w the vertical component.

[3]*Convection* in geophysical fluid dynamics generally refers to the rapid vertical motions that act to stabilize fluids that are gravitationally unstable.

Equation (3.7) expresses mass conservation for fluid parcels in a Lagrangian form. To derive the Eulerian form of mass conservation, start by substituting the mass of a parcel given by equation (3.2) into the mass conservation equation (3.7) to derive

$$\frac{\mathrm{d}}{\mathrm{d}t} \ln \rho = -\nabla \cdot \mathbf{v} + \mathcal{S}^{(M)}. \tag{3.8}$$

That is, the density of a parcel increases when the velocity field converges onto the parcel. To reach this result, we first note the expression

$$\frac{\mathrm{d}}{\mathrm{d}t} \ln (\mathrm{d}V) = \nabla \cdot \mathbf{v}, \tag{3.9}$$

which says that the infinitesimal volume of a fluid parcel increases in time if the velocity of the parcel diverges from the location of the parcel. Imagine the parcel expanding in response to the diverging velocity field.

Upon deriving the material evolution of density as given by equation (3.8), rearrangement renders the Eulerian form of mass conservation

$$\boxed{\rho_{,t} + \nabla \cdot (\rho \, \mathbf{v}) = \rho \, \mathcal{S}^{(M)}.} \tag{3.10}$$

A comma is used here as shorthand for the partial time derivative taken at a fixed point in space

$$\rho_{,t} = \frac{\partial \rho}{\partial t}. \tag{3.11}$$

We use an analogous notation for other partial derivatives throughout these notes. Rewriting mass conservation in terms of the density time tendency

$$\rho_{,t} = -\nabla \cdot (\rho \, \mathbf{v}) + \rho \, \mathcal{S}^{(M)}, \tag{3.12}$$

reveals that at each point in the fluid, the mass density increases if the linear momentum per volume of the fluid parcel,

$$\mathbf{p} = \rho \, \mathbf{v}, \tag{3.13}$$

converges to the point.

3.1.2 Volume conserving fluid parcels

Fluids that are comprised of parcels that conserve their mass, as considered in the previous discussion, satisfy *non-Boussinesq* kinematics. In ocean climate modelling, it has been traditional to exploit the large degree to which the ocean fluid is incompressible, in which case the volume of fluid parcels is taken as constant. These fluids are said to satisfy *Boussinesq* kinematics.

For the Boussinesq fluid, conservation of volume for a fluid parcel leads to

$$\frac{\mathrm{d}}{\mathrm{d}t} \ln(\mathrm{d}V) = \mathcal{S}^{(V)}, \tag{3.14}$$

where $\mathcal{S}^{(V)}$ is the volume source per unit volume present within the fluid. It is numerically the same as the mass source $\mathcal{S}^{(M)}$ defined in equation (3.7). This statetment of volume conservation

is equivalent to the mass conservation statement (3.7) *if* we assume the mass of the parcel is given by

$$\mathrm{d}M = \rho_o \, \mathrm{d}V, \tag{3.15}$$

where ρ_o is a constant reference density.

Using equation (3.9) in the Lagrangian volume conservation statement (3.14) leads to the following *constraint* for the Boussinesq velocity field

$$\boxed{\nabla \cdot \mathbf{v} = \mathcal{S}^{(V)}.} \tag{3.16}$$

Where the volume source vanishes, the three dimensional velocity field is non-divergent

$$\nabla \cdot \mathbf{v} = 0 \quad \text{for Boussinesq fluids with } \mathcal{S}^{(V)} = 0. \tag{3.17}$$

3.1.3 Mass conservation for finite domains

Now consider a finite sized region of ocean extending from the free surface at $z = \eta(x, y, t)$ to the solid earth boundary at $z = -H(x, y)$, and allow the fluid within this region to respect the mass conserving kinematics of a non-Boussinesq fluid. The total mass of fluid inside the region is given by

$$M = \int \mathrm{d}x \, \mathrm{d}y \int_{-H}^{\eta} \rho \, \mathrm{d}z. \tag{3.18}$$

Conservation of mass for this region implies that the time tendency

$$M_{,t} = \int \mathrm{d}x \, \mathrm{d}y \, \partial_t \left(\int_{-H}^{\eta} \mathrm{d}z \, \rho \right) \tag{3.19}$$

changes due to imbalances in the flux of seawater passing across the domain boundaries, and from sources within the region.[4] For a region comprised of a vertical fluid column, the only means of affecting the mass are through fluxes crossing the ocean free surface, convergence of mass brought in by horizontal ocean currents through the vertical sides of the column, and sources within the column. These considerations lead to the balance

$$M_{,t} = \int \mathrm{d}x \, \mathrm{d}y \left(q_{\mathrm{w}} \, \rho_{\mathrm{w}} + \int_{-H}^{\eta} \mathrm{d}z \, \rho \, \mathcal{S}^{(M)} - \nabla \cdot \int_{-H}^{\eta} \mathrm{d}z \, \rho \, \mathbf{u} \right). \tag{3.20}$$

The term $q_{\mathrm{w}} \, \rho_{\mathrm{w}} \, \mathrm{d}x \, \mathrm{d}y$ represents the mass flux of water (mass per unit time) crossing the free surface, where ρ_{w} is the *in situ* density of the water crossing the surface.[5] We provide a more detailed accounting of this flux in Section 3.1.7. Equating the time tendencies given by equations (3.19) and (3.20) leads to a mass balance within each vertical column of fluid

$$\boxed{\partial_t \left(\int_{-H}^{\eta} \mathrm{d}z \, \rho \right) + \nabla \cdot \mathbf{U}^{\rho} = q_{\mathrm{w}} \, \rho_{\mathrm{w}} + \int_{-H}^{\eta} \mathrm{d}z \, \rho \, \mathcal{S}^{(M)},} \tag{3.21}$$

[4] We assume no water enters the domain through the solid-earth boundaries.

[5] Water crossing the ocean surface is typically quite fresh, such as for precipitation or evaporation. However, rivers and ice melt can generally contain a nonzero salinity.

where

$$\mathbf{U}^{\rho} = \int_{-H}^{\eta} \mathrm{d}z \, \rho \, \mathbf{u} \tag{3.22}$$

is a shorthand notation for the vertically integrated horizontal momentum per volume.

Setting density factors in the mass conservation equation (3.21) to the constant reference density ρ_o renders the volume conservation equation

$$\boxed{\eta_{,t} + \nabla \cdot \mathbf{U} = q_{\mathrm{w}} + \int_{-H}^{\eta} \mathrm{d}z \, \mathcal{S}^{(V)}} \tag{3.23}$$

appropriate for a Boussinesq fluid, where fluid parcels conserve volume rather than mass. In this equation

$$\mathbf{U} = \int_{-H}^{\eta} \mathrm{d}z \, \mathbf{u} \tag{3.24}$$

is the vertically integrated horizontal velocity. In the next section, we highlight an important difference between mass and volume conserving fluids.

3.1.4 Evolution of ocean sea level

By introducing the vertically averaged density

$$\overline{\rho} = D^{-1} \int_{-H}^{\eta} \mathrm{d}z \, \rho \tag{3.25}$$

to the mass conservation equation (3.21), we can derive the following prognostic equation for the thickness

$$D = H + \eta \tag{3.26}$$

of a fluid column

$$\boxed{D_{,t} = \frac{1}{\overline{\rho}} \left(-\nabla \cdot \mathbf{U}^{\rho} + q_{\mathrm{w}} \, \rho_{\mathrm{w}} + \int_{-H}^{\eta} \mathrm{d}z \, \rho \, \mathcal{S}^{(M)} \right) - D \, \partial_t \, \ln \overline{\rho}.} \tag{3.27}$$

This equation partitions the time evolution for the total thickness of a column of seawater into a set of distinct, though not fully independent, physical processes. These processes are the following.

- **Dynamical effects**: The term $-\overline{\rho}^{-1} \nabla \cdot \mathbf{U}^{\rho}$ increases the column thickness when ocean currents cause mass to converge onto the column. We term this a *dynamical* effect, as it is largely a function of the changing ocean currents. Notably, however, if the currents have no convergence, yet the density has a nontrivial gradient, this term remains nonzero as well. So the appellation *dynamical* should be taken with this caveat. When considering a Boussinesq fluid, the analog is the term $-\nabla \cdot \mathbf{U}$ (see the volume conservation equation (3.23)), which vanishes only when the currents are divergence-free. Hence, the name *dynamical* is precise for the Boussinesq fluid.

- **Mass exchange with other components of the climate system**: The term $\overline{\rho}^{-1}\, q_{\mathrm{w}}\, \rho_{\mathrm{w}}$ alters the column thickness when water is transported across the ocean surface via interactions with other components of the climate system, such as rivers, precipitation, evaporation, ice melt, etc. This effect has its analog in Boussinesq models, in which a nonzero q_{w} alters the volume of the fluid.
- **Mass sources**: The term $\overline{\rho}^{-1} \int_{-H}^{\eta} \mathrm{d}z\, \rho\, \mathcal{S}^{(M)}$ increases the column thickness whenever there are mass sources within the column, and similarly for the Boussinesq case with volume sources.
- **Steric effect**: The term $-D\, \partial_t\, \ln \overline{\rho}$ adds a positive contribution to the column thickness when the vertically averaged *in situ* density within a column decreases. Conversely, when the vertically averaged density increases, the column thickness shrinks. We term this a *steric effect*, as it arises only from changes in the ocean hydrography within a fluid column. Hydrography changes are affected by movements of the ocean fluid (advection), small scale processes such as mixing, or local sources. Notably, the steric term is absent in the Boussinesq fluid's prognostic equation for its surface height, as can be seen by its absence in the volume conservation equation (3.23).

Anthropogenic ocean warming causes the thickness of ocean columns to expand, thus raising sea level. This effect is contained in the steric term. Changes in the mass transport into the ocean due to glacial melt water are also important, and likely will increase in importance as more land ice melts. Fluctuations in the mass convergence cause fluctuations in sea level, and such may be systematic if the surface forcing, say from the atmospheric winds, has a trend.

In many modelling studies of sea level rise due to global warming, only the global averaged sea level is considered, as this provides a single number for comparison between various model projections of future climate change. It is also something that can be diagnosed in either the Boussinesq or non-Boussinesq ocean models used in the climate projections. Reconsidering equation (3.27), the mass budget for the global ocean is given by

$$\partial_t \langle \overline{\rho}\, D \rangle = \langle q_{\mathrm{w}}\, \rho_{\mathrm{w}} \rangle, \tag{3.28}$$

where we dropped the source term for simplicity, and

$$\langle F \rangle = \frac{\int \mathrm{d}x\, \mathrm{d}y\, F}{\int \mathrm{d}x\, \mathrm{d}y} \tag{3.29}$$

is the global area average of a field. Without sources, the global seawater mass will change only when there is mass entering the ocean via a nonzero q_{w}. Performing the time derivative in equation (3.28) allows us to isolate the column thickness

$$\langle \overline{\rho}\, D_{,t} \rangle = -\langle D\, \overline{\rho}_{,t} \rangle + \langle q_{\mathrm{w}}\, \rho_{\mathrm{w}} \rangle. \tag{3.30}$$

Focusing on the steric effect by setting $q_{\mathrm{w}} = 0$ leads to

$$\langle \overline{\rho}\, D_{,t} \rangle = -\langle D\, \overline{\rho}_{,t} \rangle. \tag{3.31}$$

To garner an approximate sense for the effects from steric changes on the globally averaged column thickness, we approximate this equation with

$$\begin{aligned} \langle D_{,t} \rangle &\approx -\langle D\, \partial_t\, \ln \overline{\rho} \rangle \\ &\approx -\frac{\langle D\, \overline{\rho}_{,t} \rangle}{\rho_o} \end{aligned} \tag{3.32}$$

These expressions are accurate to within a few percent, and they are readily diagnosed in either a non-Boussinesq or Boussinesq model.

3.1.5 Solid earth kinematic boundary condition

To continue with our presentation of fluid kinematics, we establish expressions for the transport of fluid through a specified surface. The specification of such transport arises in many areas of oceanography and ocean model design. We start with the simplest surface: the time independent solid earth boundary. This surface is commonly assumed to be impenetrable to fluid.[6] The expression for fluid transport at the lower surface leads to the *solid earth kinematic boundary condition.*

As there is no fluid crossing the solid earth lower boundary, a no-normal flow condition is imposed at the solid earth boundary at the depth

$$z = -H(x, y). \tag{3.33}$$

To develop a mathematical expression for the boundary condition, we note that the outward unit normal pointing from the ocean into the underlying rock is given by[7] (see Figure 3.1)

$$\hat{\mathbf{n}}_{\mathrm{H}} = -\frac{\nabla(z+H)}{|\nabla(z+H)|}. \tag{3.34}$$

Furthermore, we assume that the bottom topography can be represented as a continuous function $H(x, y)$ that does not possess "overturns." That is, we do not consider caves or overhangs in the bottom boundary where the topographic slope becomes infinite. Such would make it difficult to consider the slope of the bottom in our formulations. This limitation is common for ocean models.[8]

A no-normal flow condition on fluid flow at the ocean bottom implies

$$\mathbf{v} \cdot \hat{\mathbf{n}}_{\mathrm{H}} = 0 \qquad \text{at} \quad z = -H(x, y).v \tag{3.35}$$

Expanding this constraint into its horizontal and vertical components yields

$$\mathbf{u} \cdot \nabla H + w = 0 \qquad \text{at} \quad z = -H(x, y). \tag{3.36}$$

Furthermore, introducing a material time derivative (3.4) allows us to write this boundary condition as

$$\frac{\mathrm{d}(z+H)}{\mathrm{d}t} = 0 \qquad \text{at} \quad z = -H(x, y). \tag{3.37}$$

Equation (3.37) expresses in a material or Lagrangian form the impenetrable nature of the solid earth lower surface, whereas equation (3.36) expresses the same constraint in an Eulerian form.

[6]This assumption may be broken in some cases. For example, when the lower boundary is a moving sedimentary layer in a coastal estuary, or when there is seeping ground water. We do not consider such cases here.

[7]The three dimensional gradient operator $\nabla = (\partial_x, \partial_y, \partial_z)$ reduces to the two dimensional horizontal operator $\nabla_z = (\partial_x, \partial_y, 0)$ when acting on functions that depend only on the horizontal directions. To reduce notation clutter, we do not expose the z subscript in cases where it is clear that the horizontal gradient is all that is relevant.

[8]For hydrostatic models, the solution algorithms rely on the ability to integrate vertically from the ocean bottom to the top, uninterrupted by rock in between. Non-hydrostatic models do not employ such algorithms, and so may in principle allow for arbitrary bottom topography, including overhangs.

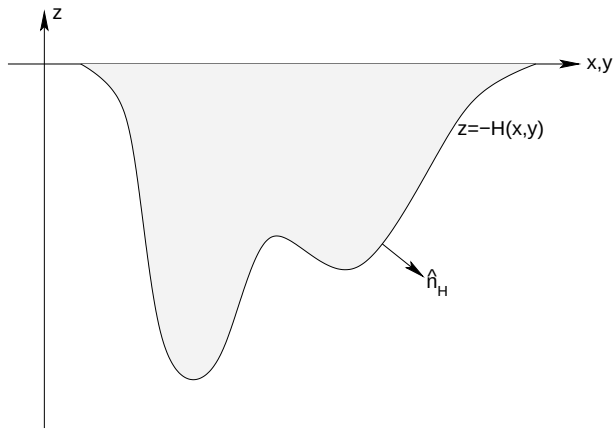

Figure 3.1: Schematic of the ocean's bottom surface with a smoothed undulating solid earth topography at $z = -H(x, y)$ and outward normal direction $\hat{\mathbf{n}}_{\mathrm{H}}$. Undulations of the solid earth can reach from the ocean bottom at 5000m-6000m to the surface over the course of a few kilometers (slopes on the order of 0.1 to 1.0). These ranges of topography variation are far greater than the surface height (see Figure 3.2). It is important for simulations to employ numerics that facilitate an accurate representation of the ocean bottom.

3.1.6 Generalized vertical coordinates

We now consider the form of the bottom kinematic boundary condition in generalized vertical coordinates. Generalized vertical coordinates provide the ocean theorist and modeler with a powerful set of tools to describe ocean flow, which in many situations is far more natural than the more traditional geopotential coordinates (x, y, z) that we have been using thus far. Therefore, it is important for the student to gain some exposure to the fundamentals of these coordinates, as they are ubiquitous in ocean modelling today.

Chapter 6 of Griffies (2004) develops a calculus for generalized vertical coordinates. Experience with these methods is useful to nurture an understanding for ocean modelling in generalized vertical coordinates. Most notably, these coordinates, when used with the familiar horizontal coordinates (x, y), form a non-orthogonal triad, and thus lead to some relationships that may be unfamiliar. To proceed in this section, we present some salient results of the mathematics of generalized vertical coordinates, and reserve many of the derivations for Griffies (2004).

When considering generalized vertical coordinates in oceanography, we always assume that the surfaces cannot overturn on themselves. This constraint means that the Jacobian of transformation between the generalized vertical coordinate

$$s = s(x, y, z, t) \tag{3.38}$$

and the geopotential coordinate z, must be one signed. That is, the specific thickness

$$\frac{\partial z}{\partial s} = z_{,s} \tag{3.39}$$

is of the same sign throughout the ocean fluid. The name *specific thickness* arises from the property that

$$\mathrm{d}z = z_{,s}\, \mathrm{d}s \tag{3.40}$$

is an expression for the thickness of an infinitesimal layer of fluid bounded by two constant s surfaces.

Deriving the bottom kinematic boundary condition in s-coordinates requires a relation between the vertical velocity component used in geopotential coordinates, $w = \mathrm{d}z/\mathrm{d}t$, and the pseudo-velocity component $\mathrm{d}s/\mathrm{d}t$. For this purpose, we refer to some results from Section 6.5.5 of Griffies (2004). As in that discussion, we derive the isomorphic relations

$$\dot{z} = (\partial_t + \mathbf{u} \cdot \nabla_s + \dot{s}\,\partial_s)\, z \tag{3.41}$$

$$\dot{s} = (\partial_t + \mathbf{u} \cdot \nabla_z + \dot{z}\,\partial_z)\, s, \tag{3.42}$$

where

$$\dot{z} = \frac{\mathrm{d}z}{\mathrm{d}t} \tag{3.43}$$

$$\dot{s} = \frac{\mathrm{d}s}{\mathrm{d}t} \tag{3.44}$$

are useful shorthands for the vertical velocity components, motivated from similar notation used in classical particle mechanics. Note that the partial time derivative appearing in each of the expressions is taken with the corresponding space variables held fixed. That is, ∂_t in equation (3.41) is taken with s held fixed, whereas ∂_t in equation (3.42) is taken with z held fixed.

Rearrangement of equations (3.41) and (3.42) leads to

$$\dot{z} = z_{,s}\,(\mathrm{d}/\mathrm{d}t - \partial_t - \mathbf{u} \cdot \nabla_z)\, s. \tag{3.45}$$

This expression is relevant when measurements are taken on surfaces of constant geopotential, or depth. To reach this result, we made use of the triple product identities

$$z_{,t} = -s_{,t}\, z_{,s} \tag{3.46}$$

$$z_{,x} = -s_{,x}\, z_{,s} \tag{3.47}$$

$$z_{,y} = -s_{,y}\, z_{,s}. \tag{3.48}$$

A derivation of these identities is given in Section 6.5.4 of Griffies (2004). These relations should be familiar to those having studied thermodynamics, where the analogous expressions are known as the Maxwell relations (Callen, 1985).

We now apply relation (3.45) to the ocean bottom, which is generally not a surface of constant depth. It is thus necessary to transform the constant depth gradient ∇_z to a horizontal gradient taken along the bottom. To do so, proceed as in Section 6.5.3 of Griffies (2004) and consider the time-independent coordinate transformation

$$(\overline{x}, \overline{y}, \overline{z}, \overline{t}) = (x, y, -H(x, y), t). \tag{3.49}$$

The horizontal gradient taken on constant depth surfaces, ∇_z, and the horizontal gradient along the bottom, $\nabla_{\overline{z}}$, are thus related by

$$\nabla_{\overline{z}} = \nabla_z - (\nabla H)\, \partial_z. \tag{3.50}$$

Using this result in equation (3.45) yields

$$s_{,z}\,(w + \mathbf{u} \cdot \nabla H) = (\mathrm{d}/\mathrm{d}t - \partial_t - \mathbf{u} \cdot \nabla_{\overline{z}})\, s \qquad \text{at} \quad z = -H. \tag{3.51}$$

The left hand side vanishes due to the kinematic boundary condition (3.36), which then leads to

$$\mathrm{d}s/\mathrm{d}t = (\partial_t + \mathbf{u} \cdot \nabla_{\bar{z}})\, s \qquad \text{at} \quad s = s(x, y, z = -H(x, y), t). \tag{3.52}$$

The value of the generalized coordinate at the ocean bottom can be written in the shorthand form

$$s_{\text{bot}}(x, y, t) = s(x, y, z = -H, t) \tag{3.53}$$

which leads to

$$\boxed{\frac{\mathrm{d}\,(s - s_{\text{bot}})}{\mathrm{d}t} = 0 \qquad \text{at} \quad s = s_{\text{bot}}.} \tag{3.54}$$

This relation is analogous to equation (3.37) appropriate to z-coordinates. Indeed, it is actually a basic statement of the impenetrable nature of the solid earth lower boundary, which is true regardless the vertical coordinates.

The various mathematical steps that led to the very simple result (3.54) could have been dispensed with if we already understood some notions of generalized vertical coordinates. Nonetheless, the steps introduced some of the formalism required to work with generalized vertical coordinates, and as such provide a useful testing ground for later manipulations where the answer is less easy to anticipate. This strategy is highly recommended to the student working with new formalisms. That is, first test your mathematical skills with problems where the answer is either known, or can be readily judged correct with basic physical understanding. After garnering experience and confidence, one may then approach genuinely new problems using the methods.

3.1.7 Upper surface kinematic condition

To formulate budgets for mass, tracer, and momentum in the ocean, we consider the upper ocean surface to be a time dependent permeable membrane through which precipitation, evaporation, ice melt, and river runoff[9] pass. The expression for fluid transport at the upper surface leads to the *upper ocean kinematic boundary condition.*

To describe the kinematics of water transport into the ocean, it is useful to introduce an effective transport through a smoothed ocean surface, where smoothing is performed via an ensemble average. We assume that this averaging leads to a surface absent overturns or breaking waves, thus facilitating a mathematical description analogous to the ocean bottom just considered. The vertical coordinate takes on the value

$$z = \eta(x, y, t) \tag{3.55}$$

at this idealized ocean surface.

We furthermore assume that density of the water crossing the ocean surface ρ_{w} is a function of the temperature, salinity, and pressure. There are generally different water densities for precipitation, evaporation, runoff, and ice melt. Such level of detail is generally not considered, and we

[9] River runoff generally enters the ocean at a nonzero depth rather than through the surface. Many global models, however, have traditionally inserted river runoff to the top model cell. Such can become problematic numerically and physically when the top grid cells are refined to levels common in coastal modelling. Hence, more applications are now considering the input of runoff throughout a nonzero depth. Likewise, sea ice can melt at depth, thus necessitating a mass transport to occur within the ocean between the liquid and solid water masses.

make approximations below. For now, we note that the mass transport crossing the ocean surface can be written

$$\begin{aligned}(\text{MASS/TIME}) \text{ THROUGH SURFACE} = \\ -\mathrm{d}A_\eta\, \hat{\mathbf{n}}_\eta \cdot (\hat{\mathbf{n}}_\mathrm{P}\, P\, \rho_\mathrm{P} + \hat{\mathbf{n}}_\mathrm{E}\, E\, \rho_\mathrm{E} + \hat{\mathbf{n}}_\mathrm{R}\, R\, \rho_\mathrm{R} + \hat{\mathbf{n}}_\mathrm{I}\, I\, \rho_\mathrm{I}).\end{aligned} \tag{3.56}$$

In this expression, $\hat{\mathbf{n}}_\mathrm{P}\, P\, \rho_\mathrm{P}$ is the mass per time per area of precipitation oriented in the direction specified by $\hat{\mathbf{n}}_\mathrm{P}$, where ρ_P is the mass density of the precipitation and P is the volume per time per area of precipitation. Likewise, $\hat{\mathbf{n}}_\mathrm{E}\, E\, \rho_\mathrm{E}$ is the evaporative mass flux, $\hat{\mathbf{n}}_\mathrm{R}\, R\, \rho_\mathrm{R}$ is the river mass flux, and $\hat{\mathbf{n}}_\mathrm{I}\, I\, \rho_\mathrm{I}$ is the ice melt mass flux. The unit normal

$$\hat{\mathbf{n}}_\eta = \frac{\nabla\,(z-\eta)}{|\nabla\,(z-\eta)|} \tag{3.57}$$

points from the ocean surface at $z = \eta$ into the overlying atmosphere (see Figure 3.2). Finally, the area element $\mathrm{d}A_\eta$ measures an infinitesimal area element on the ocean surface $z = \eta$, and it is given by (see Section 20.13.2 of Griffies (2004))

$$\mathrm{d}A_\eta = |\nabla(z-\eta)|\, \mathrm{d}x\, \mathrm{d}y. \tag{3.58}$$

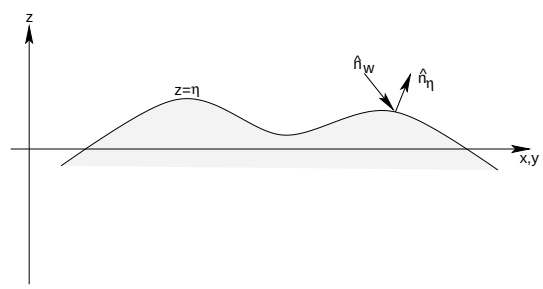

Figure 3.2: Schematic of the ocean's upper surface with a smoothed undulating surface at $z = \eta(x, y, t)$, outward normal direction $\hat{\mathbf{n}}_\eta$, and normal direction $\hat{\mathbf{n}}_\mathrm{w}$ orienting the passage of water across the surface. Undulations of the surface height are on the order of a few metres due to tidal fluctuations in the open ocean, and order 10m-20m in certain embayments (e.g., Bay of Fundy in Nova Scotia). When imposing the weight of sea ice onto the ocean surface, the surface height can depress even further, on the order of 5m-10m, with larger values possible in some cases. It is important for simulations to employ numerical schemes facilitating such wide surface height undulations.

We now make a common assumption about the orientation of the water transported across the surface. Namely, precipitation generally enters the ocean, so that we write

$$P\, \hat{\mathbf{n}}_\eta \cdot \hat{\mathbf{n}}_\mathrm{P} \approx -P \tag{3.59}$$

since $\hat{\mathbf{n}}_\eta \cdot \hat{\mathbf{n}}_\mathrm{P} \approx -1$. We make similar approximations for the other mass flux components, with the conventions that $P > 0$ is the volume per time per area of precipitation entering the ocean, $E > 0$ is the evaporation leaving the ocean, $R > 0$ is the river runoff entering the ocean, and $I > 0$ is the ice melt entering the ocean (signs are reversed on each of these fluxes for cases where water

fluxes are in opposite directions). Additionally, for notational convenience, we assume the density of the water transported across the surface is generically written ρ_{w}. Hence, the mass flux takes the more compact form

$$(\text{MASS/TIME}) \text{ THROUGH SURFACE} = (P - E + R + I)\ \rho_{\mathrm{w}}\, \mathrm{d}A_\eta. \tag{3.60}$$

We next exploit the assumption that the ocean surface has no overturns. In this case, we can define

$$q_{\mathrm{w}}\, \mathrm{d}A = (P - E + R + I)\, \mathrm{d}A_\eta, \tag{3.61}$$

where

$$\mathrm{d}A = \mathrm{d}x\, \mathrm{d}y \tag{3.62}$$

is the horizontal projection of the surface area element $\mathrm{d}A_\eta$. The volume per time per horizontal area of fluid crossing the ocean surface is therefore defined by

$$\boxed{\begin{aligned} q_{\mathrm{w}} &= \frac{(P - E + R + I)\, \mathrm{d}A_\eta}{\mathrm{d}A} \\ &= \frac{(\text{VOLUME/TIME}) \text{ THROUGH FREE SURFACE}}{\text{HORIZONTAL AREA UNDER FREE SURFACE}}. \end{aligned}} \tag{3.63}$$

This is the surface water flux that appears in ocean model budgets for mass, tracer, and momentum. The assumptions leading up to this simple expression can be readily dropped in cases where more information is available (e.g., separate densities for the precipitation, evaporation, runoff, ice melt). Indeed, in realistic climate models, these densities may be available. However, for purposes of mathematical formulation, it is more convenient to employ the terse expression derived here. Note that in Section 3.6.7, we derive an alternative expression (3.189) for q_{w} that connects it to the dia-surface velocity component discussed in Section 3.1.8.

To develop the surface kinematic boundary condition, return to the expression (3.21) for mass conservation, rewritten here for completeness

$$\partial_t \left(\int_{-H}^{\eta} \mathrm{d}z\, \rho \right) + \nabla \cdot \left(\int_{-H}^{\eta} \mathrm{d}z\, \rho\, \mathbf{u} \right) = q_{\mathrm{w}}\, \rho_{\mathrm{w}} + \int_{-H}^{\eta} \mathrm{d}z\, \rho\, \mathcal{S}^{(M)}. \tag{3.64}$$

Next, we perform the derivative operations on the integrals, keeping in mind Leibnitz's Rule when differentiating an integral. The first step of the derivation leads to

$$\begin{aligned} [\rho\, (\partial_t + \mathbf{u} \cdot \nabla)\, \eta]_{z=\eta} + [\rho\, \nabla H \cdot \mathbf{u}]_{z=-H} + \int_{-H}^{\eta} \mathrm{d}z\, [\rho_{,t} + \nabla \cdot (\rho\, \mathbf{u})] = \\ \rho_{\mathrm{w}}\, q_{\mathrm{w}} + \int_{-H}^{\eta} \mathrm{d}z\, \rho\, \mathcal{S}^{(M)}. \end{aligned} \tag{3.65}$$

The Eulerian mass conservation relation (3.10) and bottom kinematic boundary condition (3.36) render the surface kinematic boundary condition

$$\boxed{\rho\, (\partial_t + \mathbf{u} \cdot \nabla)\, \eta = \rho_{\mathrm{w}}\, q_{\mathrm{w}} + \rho\, w \qquad \text{at} \quad z = \eta.} \tag{3.66}$$

This relation can also be written in the material form

$$\boxed{\rho \left(\frac{\mathrm{d}(z-\eta)}{\mathrm{d}t} \right) = -\rho_{\mathrm{w}}\, q_{\mathrm{w}} \qquad \text{at} \quad z = \eta.} \tag{3.67}$$

Contrary to the solid earth condition (3.37), where $z + H$ is materially constant, permeability of the ocean surface leads to a nontrivial material evolution of $z - \eta$.

To derive the analogous s-coordinate boundary condition, we proceed as for the bottom in Section 3.1.6. Here, the coordinate transformation is time dependent

$$(\overline{x}, \overline{y}, \overline{z}, \overline{t}) = (x, y, \eta(x, y, t), t). \tag{3.68}$$

The horizontal gradient and time derivative operators are therefore related by

$$\nabla_{\overline{z}} = \nabla_z + (\nabla\, \eta)\, \partial_z \tag{3.69}$$

$$\partial_{\overline{t}} = \partial_t + \eta_{,t}\, \partial_z. \tag{3.70}$$

Hence, the relation (3.45) between vertical velocity components takes the following form at the ocean surface

$$w = z_{,s}\, (\mathrm{d}/\mathrm{d}t - \partial_{\overline{t}} - \mathbf{u} \cdot \nabla_{\overline{z}})\, s + (\partial_t + \mathbf{u} \cdot \nabla)\eta \qquad \text{at} \quad z = \eta. \tag{3.71}$$

Substitution of the z-coordinate kinematic boundary condition (3.66) leads to

$$\rho\, z_{,s}\, \left(\mathrm{d}/\mathrm{d}t - \partial_{\overline{t}} - \mathbf{u} \cdot \nabla_{\overline{z}}\right)\, s = -\rho_{\mathrm{w}}\, q_{\mathrm{w}} \qquad \text{at} \quad s = s_{\mathrm{top}} \tag{3.72}$$

where $s_{\mathrm{top}} = s(x, y, z = \eta, t)$ is the value of the generalized vertical coordinate at the ocean surface. Reorganizing the result (3.72) leads to the material time derivative form

$$\boxed{\rho\, z_{,s} \left(\frac{\mathrm{d}(s - s_{\mathrm{top}})}{\mathrm{d}t} \right) = -\rho_{\mathrm{w}}\, q_{\mathrm{w}} \qquad \text{at} \quad s = s_{\mathrm{top}}} \tag{3.73}$$

which is analogous to the z-coordinate result (3.67). Indeed, it can be derived trivially by noting that $\mathrm{d}z/\mathrm{d}t = z_{,s}\, \mathrm{d}s/\mathrm{d}t$. Even so, just as for the bottom kinematic boundary condition considered in Section 3.1.6, it is useful to have gone through these manipulations to garner experience and confidence with the formalism. Such confidence is of particular use in the next section focusing on the dia-surface flux.

3.1.8 Dia-surface transport

A surface of constant generalized vertical coordinate, s, is of importance when establishing the balances of mass, tracer, and momentum within a layer of fluid whose upper and lower bounds are determined by surfaces of constant s. Fluid transport through this surface is said to constitute the *dia-surface* transport. This transport plays a fundamental role in generalized vertical coordinate modelling.

At an arbitrary point on a surface of constant generalized vertical coordinate (see Figure 3.3), the flux of fluid in the direction normal to the surface is given by

$$\text{SEAWATER FLUX IN DIRECTION } \hat{\mathbf{n}} = \mathbf{v} \cdot \hat{\mathbf{n}}, \tag{3.74}$$

with

$$\hat{\mathbf{n}} = \nabla s \, |\nabla s|^{-1} \tag{3.75}$$

the surface unit normal direction. Introducing the material time derivative $\mathrm{d}s/\mathrm{d}t = s_{,t} + \mathbf{v} \cdot \nabla s$ leads to the equivalent expression

$$\mathbf{v} \cdot \hat{\mathbf{n}} = |\nabla s|^{-1} \left(\mathrm{d}/\mathrm{d}t - \partial_t \right) s. \tag{3.76}$$

That is, the normal component to a fluid parcel's velocity is proportional to the difference between the material time derivative of the surface and its partial time derivative.

Since the surface is generally moving, the net flux of seawater penetrating the surface is obtained by subtracting the velocity of the surface $\mathbf{v}^{(\mathrm{ref})}$ in the $\hat{\mathbf{n}}$ direction from the velocity component $\mathbf{v} \cdot \hat{\mathbf{n}}$ of the fluid parcels

$$\text{FLUX OF SEAWATER THROUGH SURFACE} = \hat{\mathbf{n}} \cdot \left(\mathbf{v} - \mathbf{v}^{(\mathrm{ref})} \right). \tag{3.77}$$

The velocity $\mathbf{v}^{(\mathrm{ref})}$ is the velocity of a reference point fixed on the surface, and it is written

$$\mathbf{v}^{(\mathrm{ref})} = \mathbf{u}^{(\mathrm{ref})} + w^{(\mathrm{ref})} \, \hat{\mathbf{z}}. \tag{3.78}$$

Since the reference point remains on the same $s = \text{const}$ surface, $\mathrm{d}s/\mathrm{d}t = 0$ for the reference point. Consequently, we can write the vertical velocity component $w^{(\mathrm{ref})}$ as

$$w^{(\mathrm{ref})} = -z_{,s} \left(\partial_t + \mathbf{u}^{(\mathrm{ref})} \cdot \nabla_z \right) s, \tag{3.79}$$

where equation (3.45) was used with $\mathrm{d}s/\mathrm{d}t = 0$. This result then leads to

$$\begin{aligned} \hat{\mathbf{n}} \cdot \mathbf{v}^{(\mathrm{ref})} &= \hat{\mathbf{n}} \cdot \mathbf{u}^{(\mathrm{ref})} + \hat{\mathbf{n}} \cdot \hat{\mathbf{z}} \, w^{(\mathrm{ref})} \\ &= -s_{,t} \, |\nabla s|^{-1}, \end{aligned} \tag{3.80}$$

which says that the normal component of the surface's velocity vanishes when the surface is static, as may be expected. When interpreting the dia-surface velocity component below, we find it useful to note that relation (3.80) leads to

$$z_{,s} \, \nabla s \cdot \mathbf{v}^{(\mathrm{ref})} = z_{,t}. \tag{3.81}$$

To reach this result, we used the identity $s_{,t} \, z_{,s} = -z_{,t}$, with $z_{,t}$ the time tendency for the depth of a particular constant s surface.

Expression (3.80) then leads to the following expression for the net flux of seawater crossing the surface

$$\boxed{\begin{aligned} \hat{\mathbf{n}} \cdot \left(\mathbf{v} - \mathbf{v}^{(\mathrm{ref})} \right) &= |\nabla s|^{-1} \left(\partial_t + \mathbf{v} \cdot \nabla \right) s \\ &= |\nabla s|^{-1} \, \mathrm{d}s/\mathrm{d}t. \end{aligned}} \tag{3.82}$$

Hence, the material time derivative of the generalized surface vanishes if and only if no water parcels cross it. This important result is used throughout ocean theory and modelling. It measures the volume of seawater crossing a generalized surface, per time, per area. The area normalizing the volume flux is that area $\mathrm{d}A_{(\hat{\mathbf{n}})}$ of an infinitesimal patch on the surface of constant generalized vertical coordinate with outward unit normal $\hat{\mathbf{n}}$. This area can be written (see equation (6.58) of Griffies (2004))

$$\boxed{\mathrm{d}A_{(\hat{\mathbf{n}})} = |z_{,s} \, \nabla s| \, \mathrm{d}A,} \tag{3.83}$$

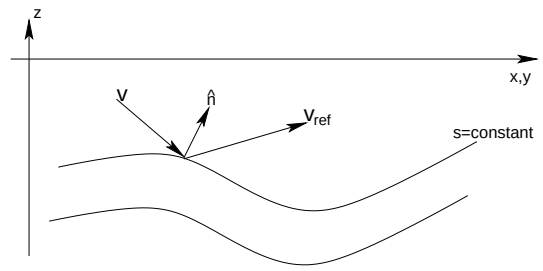

Figure 3.3: Surfaces of constant generalized vertical coordinate living interior to the ocean. An upward normal direction $\hat{\mathbf{n}}$ is indicated on one of the surfaces. Also shown is the orientation of a fluid parcel's velocity $\mathbf{v}$ and the velocity $\mathbf{v}^{(\mathrm{ref})}$ of a reference point living on the surface.

where

$$\mathrm{d}A = \mathrm{d}x\,\mathrm{d}y \tag{3.84}$$

is the horizontal projection of the area element. Hence, the volume per time of fluid passing through the generalized surface is

$$\begin{aligned}(\text{VOLUME/TIME}) \text{ THROUGH SURFACE} &= \hat{\mathbf{n}} \cdot (\mathbf{v} - \mathbf{v}^{(\mathrm{ref})})\,\mathrm{d}A_{(\hat{\mathbf{n}})} \\ &= |z_{,s}|\,(\mathrm{d}s/\mathrm{d}t)\,\mathrm{d}x\,\mathrm{d}y,\end{aligned} \tag{3.85}$$

and the magnitude of this flux is

$$|\hat{\mathbf{n}} \cdot (\mathbf{v} - \mathbf{v}^{(\mathrm{ref})})\,\mathrm{d}A_{(\hat{\mathbf{n}})}| \equiv |w^{(s)}|\,\mathrm{d}x\,\mathrm{d}y. \tag{3.86}$$

We introduced the expression

$$w^{(s)} = z_{,s}\,\frac{\mathrm{d}s}{\mathrm{d}t}, \tag{3.87}$$

which measures the volume of fluid passing through the surface, per unit area $\mathrm{d}A = \mathrm{d}x\,\mathrm{d}y$ of the horizontal projection of the surface, per unit time. That is,

$$\boxed{\begin{aligned} w^{(s)} &\equiv \frac{\hat{\mathbf{n}} \cdot (\mathbf{v} - \mathbf{v}^{(\mathrm{ref})})\,\mathrm{d}A_{(\hat{\mathbf{n}})}}{\mathrm{d}A} \\ &= \frac{(\text{VOLUME/TIME}) \text{ OF FLUID THROUGH SURFACE}}{\text{AREA OF HORIZONTAL PROJECTION OF SURFACE}}. \end{aligned}} \tag{3.88}$$

The quantity $w^{(s)}$ is called the dia-surface velocity component. It is directly analogous to the fresh water flux q_{w} defined in equation (3.61), which measures the volume of freshwater crossing the ocean surface, per unit time per horizontal area. To gain some experience with the dia-surface velocity component, it is useful to write it in the equivalent forms

$$\boxed{\begin{aligned} w^{(s)} &= z_{,s}\,\mathrm{d}s/\mathrm{d}t \\ &= z_{,s}\,\nabla s \cdot (\mathbf{v} - \mathbf{v}^{(\mathrm{ref})}) \\ &= (\hat{\mathbf{z}} - \nabla_s z) \cdot \mathbf{v} - z_{,t} \\ &= w - (\partial_t + \mathbf{u} \cdot \nabla_s)\,z \end{aligned}} \tag{3.89}$$

where the penultimate step used the identity (3.81), and where

$$\begin{aligned} \mathbf{S} &= \nabla_s z \\ &= -z_{,s} \, \nabla_z s \end{aligned} \tag{3.90}$$

is the slope of the s surface as projected onto the horizontal directions. For example, if the slope vanishes, then the dia-surface velocity component measures the flux of fluid moving vertically relative to the motion of the generalized surface. When the surface is static and flat, then the dia-surface velocity component is simply the vertical velocity component $w = \mathrm{d}z/\mathrm{d}t$.

The expression (3.87) for $w^{(s)}$ brings the material time derivative (3.4) into the following equivalent forms

$$\frac{\mathrm{d}}{\mathrm{d}t} = \left(\frac{\partial}{\partial t}\right)_z + \mathbf{u} \cdot \nabla_z + w \left(\frac{\partial}{\partial z}\right) \tag{3.91}$$

$$= \left(\frac{\partial}{\partial t}\right)_s + \mathbf{u} \cdot \nabla_s + \frac{\mathrm{d}s}{\mathrm{d}t} \left(\frac{\partial}{\partial s}\right) \tag{3.92}$$

$$= \left(\frac{\partial}{\partial t}\right)_s + \mathbf{u} \cdot \nabla_s + w^{(s)} \left(\frac{\partial}{\partial z}\right), \tag{3.93}$$

where

$$\partial_s = z_{,s} \, \partial_z, \tag{3.94}$$

relates the vertical coordinate partial derivatives. The form given by equation (3.93) motivates some to refer to $w^{(s)}$ as a vertical velocity component that measures the rate at which fluid parcels penetrate the surface of constant generalized coordinate (see Appendix A to McDougall (1995)). One should be mindful, however, to distinguish $w^{(s)}$ from the generally different vertical velocity component $w = \mathrm{d}z/\mathrm{d}t$, which measures the water flux crossing constant geopotential surfaces.

We close with a few points of clarification for the case where no fluid parcels cross the generalized surface. Such occurs, in particular, in the case of adiabatic flows with $s = \rho$ an isopycnal coordinate. In this case, the material time derivative (3.93) only has a horizontal two-dimensional advective component $\mathbf{u} \cdot \nabla_s$. This result *should not* be interpreted to mean that the velocity of a fluid parcel is strictly horizontal. Indeed, it generally is not, as the form (3.91) should make clear. Rather, it means that the transport of fluid properties occurs along surfaces of constant s, and such transport is measured by the convergence of horizontal advective fluxes as measured along surfaces of constant s. We revisit this point in Section 3.6.2 when discussing tracer transport (see in particular Figure 3.5).

3.2 Mass conservation and the tracer equation

We revisit here the mathematical description of a mass conserving fluid parcel for the purpose of introducing the evolution equation for trace material within a parcel.

3.2.1 Eulerian form of mass conservation

Seawater consists of many material constituents, such as freshwater, salts and biogeochemical components, with the possibility also for chemical reactions to take place. For brevity, we ignore

chemical reactions, though note that the following discussion can be generalized to such cases (see, for example, Section II-2 in DeGroot and Mazur, 1984).

The mass density of each constituent within a parcel of seawater is given by

$$\rho_n = \frac{\text{mass of component n}}{\text{volume of seawater parcel}}, \tag{3.95}$$

with the total density in a parcel given by the sum over all N constituents

$$\begin{aligned} \rho &= \sum_{n=1}^{N} \left(\frac{\text{mass of component n}}{\text{volume of seawater parcel}} \right) \\ &= \sum_{n=1}^{N} \rho_n . \end{aligned} \tag{3.96}$$

Observe that the mass of a seawater parcel is the sum of individual constituent masses (numerator in equation (3.96)), whereas the volume of the parcel is a complicated function of the temperature, pressure, and material constituents.

For an arbitrary finite region within the fluid, conservation of mass for each constituent takes the form

$$\partial_t \left(\int \rho_n \, \mathrm{d}V \right) = - \int \rho_n \, \mathbf{v}_n \cdot \mathrm{d}\mathbf{A}, \tag{3.97}$$

where

$$\mathrm{d}\mathbf{A} = \hat{\mathbf{n}} \, \mathrm{d}A \tag{3.98}$$

is the area element on the region boundary, with $\hat{\mathbf{n}}$ the outward normal, and $\mathbf{v}_n$ is the velocity of constituent n. Equation (3.97) says that the mass of each constituent within a region is affected by the flow of that constituent through the region boundaries.

Now apply the mass budget (3.97) to a static volume, in which case we can bring the time derivative inside the integral, and use Gauss' Theorem on the boundary integral to render

$$\int \mathrm{d}V \, \left(\partial_t \, \rho_n + \nabla \cdot (\rho_n \, \mathbf{v}_n) \right) = 0. \tag{3.99}$$

Since the volume is arbitrary, this relation leads to the local expression of mass balance for each constituent

$$\partial_t \, \rho_n = - \nabla \cdot (\rho_n \, \mathbf{v}_n). \tag{3.100}$$

Summing over all constituents then leads to the familiar Eulerian expression of mass conservation

$$\boxed{\partial_t \, \rho = - \nabla \cdot (\rho \, \mathbf{v}),} \tag{3.101}$$

where

$$\mathbf{v} = \rho^{-1} \sum_{n=1}^{N} \rho_n \, \mathbf{v}_n \tag{3.102}$$

is the velocity for the center of mass of the parcel.

The density of seawater is often well approximated by

$$\rho \approx \rho_{\text{salt}} + \rho_{\text{fresh}}, \tag{3.103}$$

where ρ_{salt} is the mass of ocean "salt" per mass of seawater, and ρ_{fresh} is the mass of fresh water per mass of seawater. Other material constituents occur in such small concentrations that their contributions to the seawater density are generally ignored for purposes of ocean modeling.

3.2.2 Mass conservation for parcels

The material time derivative

$$\frac{\mathrm{d}}{\mathrm{d}t} = \partial_t + \mathbf{v} \cdot \nabla, \tag{3.104}$$

measures time changes of a fluid property for an observer moving with the center of mass velocity $\mathbf{v}$. Mass conservation (3.101) in the moving, or *Lagrangian*, frame then takes the form

$$\frac{\mathrm{d}\rho}{\mathrm{d}t} = -\rho \, \nabla \cdot \mathbf{v}, \tag{3.105}$$

indicating that the density of a fluid parcel increases in regions where currents converge, and density decreases where currents diverge.

3.2.3 Mass conservation for constituents: the tracer equation

Introducing the material time derivative to the constituent mass balances (3.100) leads to the material budget

$$\frac{\mathrm{d}\rho_n}{\mathrm{d}t} = -\rho_n \, \nabla \cdot \mathbf{v} - \nabla \cdot \left[\rho_n \left(\mathbf{v}_n - \mathbf{v}\right)\right]. \tag{3.106}$$

Now define the *relative mass flux*

$$\mathbf{J}_n = \rho_n \left(\mathbf{v}_n - \mathbf{v}\right) \tag{3.107}$$

to render an expression for the material evolution of the density for each constituent

$$\frac{\mathrm{d}\rho_n}{\mathrm{d}t} = -\rho_n \, \nabla \cdot \mathbf{v} - \nabla \cdot \mathbf{J}_n. \tag{3.108}$$

The flux $\mathbf{J}_n$ is nonzero for those motions where the constituent n moves relative to the parcel's center of mass. This motion can be caused by many effects, with molecular diffusion the canonical example, in which case we parameterize $\mathbf{J}_n$ as a downgradient diffusive flux.[10] Notably, the total mass flux vanishes

$$\mathbf{J} = \sum_{n=1}^{N} \mathbf{J}_n = 0, \tag{3.109}$$

which follows since we choose to measure the parcel motion with respect to its center of mass. Hence, there is no subgrid scale flux for the full density ρ; i.e., the mass conservation equation (3.101) is exact, even in the presence of subgrid scale processes.

As a final step in our development of mass conservation, introduce the concentration of a material constituent, defined by

$$\begin{aligned} C_n &= \frac{\text{mass of component n}}{\text{mass of seawater parcel}} \\ &= \frac{\rho_n}{\rho}. \end{aligned} \tag{3.110}$$

[10] For an ocean model, whose grid spacing is far greater than that appropriate for molecular diffusion, the relative motion of a constituent is also affected by far larger subgrid scale processes, such as unresolved eddy advective and diffusive transport.

Substituting this *tracer concentration* into the constituent density equation (3.108) leads to the material form of the *tracer equation*

$$\boxed{\rho \frac{\mathrm{d}C_n}{\mathrm{d}t} = -\nabla \cdot \mathbf{J}_n,} \tag{3.111}$$

with the Eulerian form given by

$$\boxed{\partial_t \left(\rho\, C_n\right) = -\nabla \cdot \left(\rho\, \mathbf{v}\, C_n + \mathbf{J}_n\right).} \tag{3.112}$$

3.3 Thermodynamical tracers

Heating and cooling of the ocean, as well as mass exchange, predominantly occur near the ocean surface. In contrast, transport in the interior is nearly adiabatic and isohaline (and so nearly isentropic). Hence, the surface ocean experiences irreversible processes that set characteristics of the water masses moving quasi-isentropically within the ocean interior. Useful labels for these water masses maintain their values when moving within the largely ideal ocean interior. Salinity is a good tracer for such purposes since it is altered predominantly by mixing between waters of varying concentrations. This constitutes a basic property of material tracers considered in Section 3.2. We discuss here desirable properties of a thermodynamic tracer that tags the heat within a water parcel and evolves analogously to material tracers. Much of this material follows from Chapter 5 of Griffies (2004).

3.3.1 Potential temperature

Vertical adiabatic and isohaline motion in the ocean changes a fluid parcel's hydrostatic pressure, which thus causes its *in situ* temperature to change in proportion to the adiabatic lapse rate as given by

$$\mathrm{d}T = \Gamma \mathrm{d}p. \tag{3.113}$$

Consequently, *in situ* temperature is not a useful thermodynamic variable to label water parcels of common origin. Instead, it is more useful to remove the adiabatic pressure effects.

Removing adiabatic pressure effects from *in situ* temperature leads to the concept of *potential temperature*. Potential temperature is the *in situ* temperature that a water parcel of fixed composition would have if it were isentropically transported from its *in situ* pressure to a reference pressure p_r, with the reference pressure typically taken at the ocean surface. Mathematically, the potential temperature θ is the reference temperature obtained via integration of $\mathrm{d}T = \Gamma \mathrm{d}p$ for an isentropic *in situ* temperature change with respect to pressure (e.g., Apel, 1987):

$$T = \theta(s, T, p_r) + \int_{p^r}^{p} \Gamma(s, \theta, p')\, \mathrm{d}p', \tag{3.114}$$

with Γ the lapse rate defined in terms of pressure changes. By definition, the *in situ* temperature T equals the potential temperature θ at the reference pressure $p = p_r$. Elsewhere, they differ by an amount determined by the adiabatic lapse rate. Beneath the diabatic surface mixed layer, a vertical profile of potential temperature is far more constant than *in situ* temperature.

As shown in Section 5.6.1 of Griffies (2004), the potential temperature of a parcel is constant when the parcel's specific entropy ζ and material composition are constant. Mathematically, this result follows by noting that when entropy changes at a fixed pressure and composition, $p = p_r$ so that temperature equals potential temperature. Equation (5.41) of Griffies (2004) then leads to

$$\mathrm{d}\zeta = C_p \, \mathrm{d} \ln \theta, \tag{3.115}$$

implying $\mathrm{d}\zeta = 0$ if and only if $\mathrm{d}\theta = 0$.

3.3.2 Potential enthalpy

Potential temperature has proven useful for many oceanographic purposes. However, we have yet to ask whether it is a convenient variable to mark the heat content in a parcel of seawater. Traditionally, it is the potential temperature multiplied by the heat capacity that is used for this purpose. Bacon and Fofonoff (1996) provide a review with suggestions for this approach. In contrast, McDougall (2003) argues that potential temperature multiplied by heat capacity is less precise, by some two orders of magnitude, than an alternative thermodynamic tracer called *potential enthalpy*.

To understand this issue from a mathematical perspective, consider the evolution equation for potential temperature

$$\rho \, \frac{\mathrm{d}\theta}{\mathrm{d}t} = -\nabla \cdot \mathbf{J}_\theta + \Sigma_\theta, \tag{3.116}$$

where $\mathbf{J}_\theta$ is a flux due to molecular diffusion, and Σ_θ is a source. That potential temperature evolves in this manner is ensured by its being a scalar field. Consider the mixing of two seawater parcels at the same pressure where the parcels have different potential temperature and salinity. In the absence of the source term, the equilibrated state consists of a single parcel with mass equal to the sum of the two separate masses, and potential temperature and salinity determined by their respective mass weighted means. Does this actually happen in the real ocean? That is, can source terms be ignored? Fofonoff (1962) and McDougall (2003) note that it is indeed the case for salinity (and any other material tracer due to conservation of matter), yet it is not the case for potential temperature. Instead, potential temperature contains source terms that alter the mass weighted average equilibrated state. In contrast, potential enthalpy (discussed below) maintains the desired conservative behavior when mixing at constant reference pressure, and nearly maintains this behavior if mixing parcels at a different pressure. Hence, ocean models which set the source term to zero upon mixing potential temperature are in error. McDougall (2003) quantifies this error.

Potential enthalpy is defined analogously to potential temperature. What motivates the use of potential enthalpy is the observation that the fundamental relation between thermodynamic state variables takes a nearly conservative form when written in terms of potential enthalpy. To see this point, consider the evolution of internal energy (see equation (5.94) in Griffies, 2004), and introduce the enthalpy per mass (specific enthalpy)

$$\mathcal{H} = \mathcal{I} + p/\rho \tag{3.117}$$

leads to

$$\rho \, \frac{\mathrm{d}\mathcal{H}}{\mathrm{d}t} = -\nabla \cdot \mathbf{J}_q + \frac{\mathrm{d}p}{\mathrm{d}t} + \rho \, \epsilon. \tag{3.118}$$

Dropping the frictional dissipation term arising from molecular friction leads to the approximate statement

$$\rho \frac{\mathrm{d}\mathcal{H}}{\mathrm{d}t} - \frac{\mathrm{d}p}{\mathrm{d}t} \approx -\nabla \cdot \mathbf{J}_q. \tag{3.119}$$

To proceed, the fundamental thermodynamic relation (see equation (5.31) Griffies, 2004, in) becomes

$$\mathrm{d}\mathcal{H} = T\,\mathrm{d}\zeta + \rho^{-1}\,\mathrm{d}p + \mu\,\mathrm{d}C \tag{3.120}$$

in terms of enthalpy. Thus, enthalpy can be written as a function of entropy, salt concentration, and pressure,

$$\mathcal{H} = \mathcal{H}(\zeta, C, p). \tag{3.121}$$

Transport of a seawater parcel without changing heat, salt, or momentum occurs without change in entropy, thus rendering

$$\left(\frac{\partial \mathcal{H}}{\partial p}\right)_{\zeta,C} = \rho^{-1}. \tag{3.122}$$

Keeping salinity and entropy fixed (or equivalently fixed salinity and potential temperature) leads to

$$\mathcal{H}(\theta, s, p) = \mathcal{H}^o(\theta, s, p_r) + \int_{p^r}^{p} \rho^{-1}(\theta, s, p')\,\mathrm{d}p' \tag{3.123}$$

with $\mathcal{H}^o(\theta, s, p_r)$ defining the potential enthalpy of a parcel with potential temperature θ and salinity s. Taking the time derivative and using the approximate relation (3.119) yields

$$\frac{\mathrm{d}\mathcal{H}^o}{\mathrm{d}t} \approx -\rho^{-1}\,\nabla\cdot\mathbf{J}_q + \int_{p}^{p^r} \mathrm{d}p'\,\frac{\mathrm{d}\rho^{-1}(\theta, s, p')}{\mathrm{d}t}. \tag{3.124}$$

McDougall (2003) shows that for the ocean, the integral

$$\begin{aligned}\int_{p}^{p^r} \mathrm{d}p'\,\frac{\mathrm{d}\rho^{-1}(\theta, s, p')}{\mathrm{d}t} &= \int_{p}^{p^r} \mathrm{d}p'\,\left(\frac{\partial\rho^{-1}}{\partial\theta}\,\frac{\mathrm{d}\theta}{\mathrm{d}t} + \frac{\partial\rho^{-1}}{\partial s}\,\frac{\mathrm{d}s}{\mathrm{d}t}\right)\\ &= \frac{\mathrm{d}\theta}{\mathrm{d}t}\int_{p}^{p^r} \mathrm{d}p'\,\rho^{-1}\,\alpha - \frac{\mathrm{d}s}{\mathrm{d}t}\int_{p}^{p^r} \mathrm{d}p'\,\rho^{-1}\,\beta\end{aligned} \tag{3.125}$$

has magnitude on the order of the ocean's tiny levels of dissipation arising from molecular viscosity. These expressions introduced the thermal expansion coefficient $\alpha = -\partial\ln\rho/\partial\theta$ and saline contraction coefficient $\beta = \partial\ln\rho/\partial s$. The time derivatives of potential temperature and salinity can be removed from the pressure integrals, since they are each independent of pressure. Given the smallness of $\int_p^{p^r}\,\mathrm{d}p'\,\mathrm{d}\rho^{-1}/\mathrm{d}t$, one can write the approximate potential enthalpy equation

$$\rho\,\frac{\mathrm{d}\mathcal{H}^o}{\mathrm{d}t} \approx -\nabla\cdot\mathbf{J}_q. \tag{3.126}$$

Hence, potential enthalpy is a state function that approximately specifies the heat in a parcel of seawater, and it evolves analogously to a material tracer such as salinity. See McDougall (2003) for a proof that $\mathcal{H}^o$ more accurately sets the heat for a parcel of seawater than does $C_p\,\theta$. Given that it does, McDougall suggests that *conservative temperature*

$$\Theta \equiv \frac{\mathcal{H}^o(\theta, s, p_r)}{C_p^o} \tag{3.127}$$

with $p_r = 0$ is more appropriate than potential temperature as a thermodynamic tracer for use in an ocean model, and generally for measuring heat in the ocean. In this equation

$$\begin{aligned} C_p^o &= \frac{\mathcal{H}(\theta = 25^\circ C, s = 35\text{psu}, p_r = 0)}{25^\circ C} \\ &= 3989.245\,\text{J}\,\text{kg}^{-1}\,{}^\circ\text{K}^{-1} \end{aligned} \tag{3.128}$$

is a heat capacity chosen to minimize the difference between $C_p^o\,\theta$ and potential enthalpy $\mathcal{H}^o(\theta, s, p_r)$ when averaged over the sea surface.[11] In the remainder of these notes, we maintain the notation θ, recognizing the fact that Θ may instead be used. All formulas for density and thermodynamic fluxes can be generalized, as shown by McDougall (2003). From a fundamental perspective, McDougall (2003) provides a compelling case for the use of conservative temperature. Nonetheless, it remains a research topic to determine the significance to simulated ocean circulation of errors made in numerical models using potential temperature rather than conservative temperature.

3.4 Material time changes over finite regions

In the following sections, we focus on the mass, tracer, and momentum budgets formulated over a finite domain. The domain, or control volume, of interest is that of an ocean model grid cell. The budget for a grid cell is distinct from budgets for infinitesimal mass conserving Lagrangian fluid parcels moving with the fluid. Mass conserving fluid parcels form the fundamental *system* for which the budgets of mass, tracer, momentum, and energy are generally formulated from first principles (see, for example, chapters 3-5 in Griffies, 2004). Grid cell budgets are then derived from the fundamental parcel budgets.

The grid cells of concern for MOM4p1 have vertical sides fixed in space-time, but with the top and bottom generally moving. In particular, the top and bottom either represent the ocean top, ocean bottom, or a surface of constant generalized vertical coordinate. We furthermore assume that at no place in the fluid do the top or bottom surfaces of the grid cell become vertical. This assumption allows for a one-to-one relation to exist between geopotential depth z and the generalized vertical coordinate s introduced in Section 3.1.6 (i.e., the relation is invertible).

To establish the grid cell budget, we integrate the budget for mass conserving fluid parcels over the volume of the cell. This section is focused on the mathematics required for integrating the density weighted material time derivative acting on an arbitrary field ψ

$$\rho\,\frac{\mathrm{d}\,\psi}{\mathrm{d}t} = (\rho\,\psi)_{,t} + \nabla\cdot(\rho\,\mathbf{v}\,\psi). \tag{3.129}$$

We start with the partial time derivative on the right hand side, and introduce Cartesian coordi-

[11] The value quoted by McDougall (2003) is $C_p^o = 3989.24495292815\,\text{J}\,\text{kg}^{-1}\,{}^\circ\text{K}^{-1}$.

nates (x, y, z) for the purpose of performing the grid cell integral

$$\begin{aligned}\iiint \mathrm{d}V\,(\rho\,\psi)_{,t} &= \iiint \mathrm{d}x\,\mathrm{d}y\,\mathrm{d}z\,(\rho\,\psi)_{,t} \\ &= \iint \mathrm{d}x\,\mathrm{d}y \int_{z_1}^{z_2} \mathrm{d}z\,(\rho\,\psi)_{,t} \\ &= \iint \mathrm{d}x\,\mathrm{d}y \left[-(\rho\,\psi)_2\,\partial_t\,z_2 + (\rho\,\psi)_1\,\partial_t\,z_1 + \partial_t \left(\int_{z_1}^{z_2} \mathrm{d}z\,(\rho\,\psi) \right) \right].\end{aligned} \tag{3.130}$$

The second equality follows by noting that the horizontal extent of a grid cell remains static, thus allowing for the horizontal integral to be brought outside of the time derivative. In contrast, the vertical extent has a time dependence, which necessitates the use of Leibniz's Rule. We now use equation (3.46)

$$z_{,t} = -s_{,t}\,z_{,s} \tag{3.131}$$

which relates time tendencies of the depth of a generalized surface to time tendencies of the surface itself. Equation (3.80) is next used to write

$$\begin{aligned} z_{,t} &= -s_{,t}\,z_{,s} \\ &= z_{,s}\,|\nabla s|\,\hat{\mathbf{n}}\cdot\mathbf{v}^{(\mathrm{ref})}, \end{aligned} \tag{3.132}$$

in which we introduced the reference velocity $\mathbf{v}^{(\mathrm{ref})}$ for a point sitting on the generalized surface. Finally, recall equation (3.83), which relates the area element on the surface to the horizontal projection $\mathrm{d}A = \mathrm{d}x\,\mathrm{d}y$ of the surface

$$\mathrm{d}A_{(\hat{\mathbf{n}})} = |z_{,s}\,\nabla s|\,\mathrm{d}A. \tag{3.133}$$

Introducing this area then renders

$$\boxed{z_{,t}\,\mathrm{d}A = \hat{\mathbf{n}}\cdot\mathbf{v}^{(\mathrm{ref})}\mathrm{d}A_{(\hat{\mathbf{n}})}.} \tag{3.134}$$

This equation relates the time tendency of the depth of the generalized surface to the normal component of the velocity at a point on the surface. The two are related through the ratio of the area elements. This result is now used for the top and bottom boundary terms in relation (3.130), yielding

$$\boxed{\iiint \mathrm{d}V\,(\rho\,\psi)_{,t} = \partial_t \left(\iiint \rho\,\mathrm{d}V\,\psi \right) - \iint \mathrm{d}A_{(\hat{\mathbf{n}})}\,\hat{\mathbf{n}}\cdot\mathbf{v}^{(\mathrm{ref})}\,(\rho\,\psi).} \tag{3.135}$$

Hence, the domain integrated Eulerian time tendency of the density weighted field equals the time tendency of the density weighted field integrated over the domain, minus an integral over the domain boundary associated with transport of material across that domain, with proper account taken for time dependence of the domain boundary.

The next step needed for volume integrating the density weighted material time derivative in equation (3.129) involves the divergence of the density weighted field

$$\iiint \mathrm{d}V\,\nabla\cdot(\rho\,\mathbf{v}\,\psi) = \iint \mathrm{d}A_{(\hat{\mathbf{n}})}\,\hat{\mathbf{n}}\cdot\mathbf{v}\,(\rho\,\psi), \tag{3.136}$$

which follows from Gauss' Law. Combining this result with equation (3.135) leads to the relation

$$\boxed{\iiint \rho \, \mathrm{d}V \, \frac{\mathrm{d}\,\psi}{\mathrm{d}t} = \partial_t \left(\iiint \rho \, \mathrm{d}V \, \psi \right) + \iint \mathrm{d}A_{(\hat{\mathbf{n}})} \, \hat{\mathbf{n}} \cdot (\mathbf{v} - \cdot \mathbf{v}^{(\mathrm{ref})}) \, (\rho \, \psi).} \tag{3.137}$$

Hence, the mass weighted grid cell integral of the material time derivative of a field is given by the time derivative of the mass weighted field integrated over the domain, plus a boundary term that accounts for the transport across the domain boundaries, with allowance made for moving domain boundaries. The manipulations leading to this result focused on an interior grid cell. The result, however, holds in general for a cell that abuts either the ocean surface or ocean bottom. For the ocean bottom, the boundary term vanishes since the bottom has a zero reference velocity, and there is no normal flow of fluid across the bottom. For the ocean surface, we employ relation (3.189) that defines the dia-surface transport of mass across the ocean surface in a manner analogous to the dia-surface transport (3.88) across an interior surface.

3.5 Basics of the finite volume method

The finite volume method for formulating the discrete equations of an ocean model has been incorporated to the ocean modelling literature only since the late 1990's. The work of Adcroft et al. (1997) is a canonical example of how this method can be used to garner a better representation of the solid earth boundary. In this section, we briefly outline the basis for this method. The interested reader may wish to look at chapter 6 of the book by Hirsch (1988), or the chapter by Machenhauer et al. (2009) for a more thorough introduction, or one of the growing number of monographs devoted exclusively to the method.

The general equations of fluid mechanics can be represented as conservation equations for scalar quantities (e.g., seawater mass and tracer mass) and vector quantities (e.g., linear momentum). As just detailed in Section 3.4, the conservation law for a scalar Ψ over an arbitrary fluid region can be put in the form

$$\partial_t \left(\iiint \Psi \, \mathrm{d}V \right) = - \iint \mathrm{d}A_{(\hat{\mathbf{n}})} \, \hat{\mathbf{n}} \cdot \mathbf{F} + \iiint \mathcal{S} \, \mathrm{d}V. \tag{3.138}$$

The volume integral is taken over an arbitrary fluid region, and the area integral is taken over the bounding surface to that volume, with outward normal $\hat{\mathbf{n}}$. The flux $\mathbf{F}$ penetrates the surface and acts to alter the scalar, whereas internal sources $\mathcal{S}$ contribute to changes in the scalar throughout the interior of the domain. The budget for the vector linear momentum can be written in this form, with the addition of body forces that act similar to the source term written here (see Section 3.8). Fundamental to the finite volume method is that the fluxes contribute *only* at the boundary to the domain, and not within the interior as well. Hence, the domain can be subdivided into arbitrary shapes, with budgets over the subdivisions summing to recover the global budget.

A discrete finite volume analog to equation (3.138), for a region labeled with the integer J, takes the form

$$\partial_t \left(V_J \, \Psi_J \right) = - \sum_{\text{sides}} \left(A_{(\hat{\mathbf{n}})} \, \hat{\mathbf{n}} \cdot \mathbf{F} \right) + V_J \, \mathcal{S}_J. \tag{3.139}$$

Quantities with the integer J subscript refer to the discrete analogs to the continuum fields and the geometric factors in equation (3.138). In particular, we define the discrete finite volume quantities

$$V_J \equiv \iiint \mathrm{d}V \tag{3.140}$$

$$\Psi_J \equiv \frac{\iiint \mathrm{d}V\,\Psi}{\iiint \mathrm{d}V} \tag{3.141}$$

$$\mathcal{S}_J \equiv \frac{\iiint \mathrm{d}V\,\mathcal{S}}{\iiint \mathrm{d}V}. \tag{3.142}$$

Again, it is due to the conservation form of the fundamental fluid dynamic equation (3.138) that allows for a straightforward finite volume interpretation of the discrete equations. Notably, once formulated as such, the problem shifts from fundamentals to details, with details differing on how one represents the subgrid scale behaviour of the continuum fields. This shift leads to the multitude of discretization methods available for such processes as transport, time stepping, etc. In the following, we endeavour to write the fluid equations of the ocean in the conservation form (3.138). Doing so then renders a finite volume framework for the resulting discrete or semi-discrete equations.

When working with nonBoussinesq budgets, the finite volume interpretation applies directly to the tracer mass per volume, ρC, rather than to the tracer concentration C. The same applies to the linear momentum per volume, $\rho\,\mathbf{v}$, rather than to the velocity $\mathbf{v}$. That is, the finite volume model carries the discrete fields ρ_J, $(\rho C)_J$ and $(\rho\,\mathbf{v})_J$, defined as

$$\rho_J \equiv \frac{\iiint \mathrm{d}V\,\rho}{\iiint \mathrm{d}V} \tag{3.143}$$

$$(\rho C)_J \equiv \frac{\iiint \mathrm{d}V\,\rho C}{\iiint \mathrm{d}V} \tag{3.144}$$

$$(\rho\,\mathbf{v})_J \equiv \frac{\iiint \mathrm{d}V\,\rho\,\mathbf{v}}{\iiint \mathrm{d}V}. \tag{3.145}$$

As we will see in the discussions in Sections 3.6 and 3.8, we actually work with a slightly modified finite volume suite of variables, whereby the finite volume interpretation applies to the seawater mass per horizontal area, the tracer mass per horizontal area and linear momentum per horizontal area

$$(\mathrm{d}z\,\rho)_J \equiv \frac{\iint \mathrm{d}A \int \mathrm{d}z\,\rho}{\iint \mathrm{d}A} \tag{3.146}$$

$$(\mathrm{d}z\,\rho C)_J \equiv \frac{\iint \mathrm{d}A \int \mathrm{d}z\,\rho C}{\iint \mathrm{d}A} \tag{3.147}$$

$$(\mathrm{d}z\,\rho\,\mathbf{v})_J \equiv \frac{\iint \mathrm{d}A \int \mathrm{d}z\,\rho\,\mathbf{v}}{\iint \mathrm{d}A}, \tag{3.148}$$

where $\mathrm{d}z$ is the thickness of a grid cell, and $\mathrm{d}A = \mathrm{d}x\,\mathrm{d}y$ is the horizontal projection of its area. The inclusion of thickness facilitates the treatment of grid cells whose thickness is a function of

time, such as in MOM4p1. Note that to reduce notational clutter, we employ the same symbol for the continuum field as for the discrete, so we drop the J subscript in the following.

3.6 Mass and tracer budgets over finite regions

The purpose of this section is to extend the kinematics discussed in the previous sections to the case of mass and tracer budgets for finite domains within the ocean fluid. In the formulation of ocean models, these domains are thought of as discrete model grid cells.

3.6.1 General formulation

As described in Section 3.2, the tracer concentration C represents a mass of tracer per mass of seawater for *material tracers* such as salt or biogeochemical tracers. Mathematically, this definition means that for each fluid parcel,

$$\begin{aligned} C &= \frac{\text{mass of tracer}}{\text{mass of seawater}} \\ &= \frac{\rho_C \, \mathrm{d}V}{\rho \, \mathrm{d}V}, \end{aligned} \tag{3.149}$$

where ρ_C is the mass density of tracer within the fluid parcel. In addition to material tracers, we are concerned with a thermodynamical tracer that measures the heat within a fluid parcel. In this case, C is typically taken to be the potential temperature. However, the work of McDougall (2003) prompts us to consider a modified temperature known as *conservative temperature*, which more accurately measures the heat within a fluid parcel *and* is transported, to within a very good approximation, in a manner directly analogous to material tracers. We discussed these temperature variables in Section 3.3.

Given these considerations, the total tracer mass within a finite region of seawater is given by the integral.

$$\begin{aligned} \text{tracer mass in a region} &= \iiint \rho_C \, \mathrm{d}V \\ &= \iiint C \, \rho \, \mathrm{d}V. \end{aligned} \tag{3.150}$$

Correspondingly, the evolution of tracer mass within a Lagrangian parcel of mass conserving fluid is given by (see Section 5.1 of Griffies, 2004)

$$\rho \frac{\mathrm{d}C}{\mathrm{d}t} = -\nabla \cdot \mathbf{J} + \rho \, \mathcal{S}^{(\mathrm{C})}, \tag{3.151}$$

where $\mathcal{S}^{(\mathrm{C})}$ is a tracer source in the region, with units of tracer concentration per time. The tracer flux $\mathbf{J}$ arises from subgrid scale transport of tracer in the absence of mass transport. Such transport in MOM4p1 consists of diffusion and/or unresolved advection. As discussed in Section 3.2.3, this flux is computed with respect to the center of mass of a fluid parcel. It therefore vanishes when the tracer concentration is uniform, in which case the tracer budget reduces to the mass budget (3.7).

We now develop a regional budget for tracer mass over a grid cell. For this purpose, apply the general result (3.137) relating the material time derivative to a regional budget, to render

$$\partial_t \left(\iiint C \, \rho \, \mathrm{d}V \right) = \iiint \mathcal{S}^{(\mathrm{C})} \, \rho \, \mathrm{d}V - \iint \mathrm{d}A_{(\hat{\mathbf{n}})} \, \hat{\mathbf{n}} \cdot [(\mathbf{v} - \mathbf{v}^{\mathrm{ref}}) \, \rho \, C + \mathbf{J}]. \tag{3.152}$$

Again, the left hand side of this equation is the time tendency for tracer mass within the finite sized grid cell region. When the tracer concentration is uniform, the SGS flux vanishes, in which case the tracer budget (3.152) reduces to the finite domain mass budget

$$\partial_t \left(\iiint \rho \, \mathrm{d}V \right) = \iiint \mathcal{S}^{(\mathrm{M})} \, \rho \, \mathrm{d}V - \iint \mathrm{d}A_{(\hat{\mathbf{n}})} \, \hat{\mathbf{n}} \cdot [(\mathbf{v} - \mathbf{v}^{\mathrm{ref}}) \, \rho \,]. \tag{3.153}$$

In addition to the tracer flux $\mathbf{J}$, it is convenient to define the *tracer concentration flux* $\mathbf{F}$ via

$$\mathbf{J} = \rho \, \mathbf{F}, \tag{3.154}$$

where the dimensions of $\mathbf{F}$ are velocity $\times$ tracer concentration.

In a manner analogous to our definition of a dia-surface velocity component in Section 3.1.8, it is useful to introduce the dia-surface SGS flux component. For this purpose, consider the tracer mass per time crossing a surface of constant generalized vertical coordinate, where this transport arises from SGS processes. Manipulations similar to those used to derive the dia-surface velocity component lead to

$$\begin{aligned} (\text{SGS tracer mass through surface})/(\text{time}) &= \mathrm{d}A_{(\hat{\mathbf{n}})} \, \hat{\mathbf{n}} \cdot \mathbf{J} \\ &= z_{,s} \, \nabla s \cdot \mathbf{J} \, \mathrm{d}x \, \mathrm{d}y \\ &= (\hat{\mathbf{z}} - \mathbf{S}) \cdot \mathbf{J} \, \mathrm{d}x \, \mathrm{d}y, \end{aligned} \tag{3.155}$$

where $\mathbf{S}$ is the slope vector for the generalized surface defined in equation (3.90). We are therefore led to introduce the dia-surface SGS tracer flux

$$\boxed{\begin{aligned} J^{(s)} &\equiv \frac{\mathrm{d}A_{(\hat{\mathbf{n}})} \, \hat{\mathbf{n}} \cdot \mathbf{J}}{\mathrm{d}A} \\ &= z_{,s} \, \nabla s \cdot \mathbf{J} \\ &= (\hat{\mathbf{z}} - \mathbf{S}) \cdot \mathbf{J}, \end{aligned}} \tag{3.156}$$

where $\mathrm{d}A = \mathrm{d}x \, \mathrm{d}y$ is the horizontal cross-sectional area. In words, $J^{(s)}$ is the tracer mass per time per horizontal area penetrating surfaces of constant generalized vertical coordinate via processes that are unresolved by the dia-surface velocity component $w^{(s)}$.

3.6.2 Budget for an interior grid cell

Consider the budget for a region bounded away from the ocean surface and bottom, such as that shown in Figure 3.4. We have in mind here a grid cell within a discrete numerical model. There are two assumptions that define a grid cell for our purposes.

- The sides of the cell are vertical, so they are parallel to $\hat{\mathbf{z}}$ and aligned with the horizontal coordinate directions $(\hat{\mathbf{x}}, \hat{\mathbf{y}})$. Their horizontal positions are fixed in time.

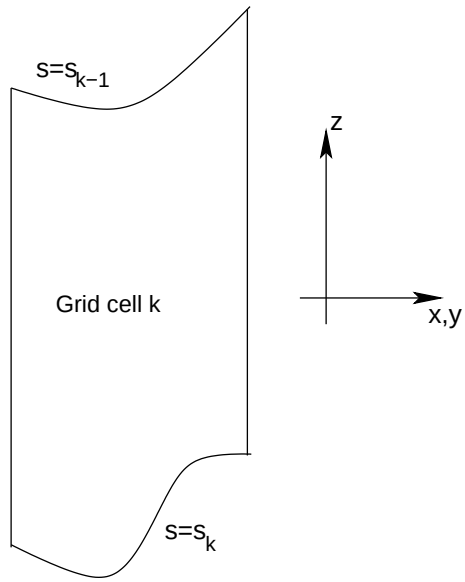

Figure 3.4: Schematic of an ocean grid cell labeled by the vertical integer k. Its sides are vertical and oriented according to $\hat{\mathbf{x}}$ and $\hat{\mathbf{y}}$, and its horizontal position is fixed in time. The top and bottom surfaces are determined by constant generalized vertical coordinates s_{k-1} and s_k, respectively. Furthermore, the top and bottom are assumed to always have an outward normal with a nonzero component in the vertical direction $\hat{\mathbf{z}}$. That is, the top and bottom are never vertical. We take the convention that the discrete vertical label k increases as moving downward in the column, and grid cell k is bounded at its upper face by $s = s_{k-1}$ and lower face by $s = s_k$.

- The top and bottom of the cell are defined by surfaces of constant generalized vertical coordinate $s = s(x, y, z, t)$. The generalized surfaces do not overturn, which means that $s_{,z}$ is single signed throughout the ocean.

These assumptions lead to the following results for the sides of the grid cell

$$\text{TRACER MASS ENTERING CELL WEST FACE} = \iint\limits_{x=x_1} \mathrm{d}y\,\mathrm{d}z\,(u\,\rho\,C + \rho\,F^x) \tag{3.157}$$

$$\text{TRACER MASS LEAVING CELL EAST FACE} = -\iint\limits_{x=x_2} \mathrm{d}y\,\mathrm{d}z\,(u\,\rho\,C + \rho\,F^x) \tag{3.158}$$

where $x_1 \le x \le x_2$ defines the domain boundaries for the east-west coordinates.[12] Similar results hold for the tracer mass crossing the cell in the north-south directions. At the top and bottom of the grid cell

$$\text{TRACER MASS ENTERING CELL BOTTOM FACE} = \iint\limits_{s=s_k} \mathrm{d}x\,\mathrm{d}y\;\rho\,(w^{(s)}\,C + F^{(s)}) \tag{3.159}$$

[12]We use generalized horizontal coordinates, such as those discussed in Griffies (2004). Hence, the directions east, west, north, and south may not correspond to the usual geographic directions. Nonetheless, this terminology is useful for establishing the budgets, whose validity is general.

$$\text{TRACER MASS LEAVING CELL TOP FACE} = -\iint\limits_{s=s_{k-1}} \mathrm{d}x\,\mathrm{d}y\;\rho\,(w^{(s)}\,C + F^{(s)}). \tag{3.160}$$

To reach this result, we used a result from Section 3.1.8 to write the volume flux passing through the top face of the grid cell

$$\mathrm{d}A_{(\hat{\mathbf{n}})}\,\hat{\mathbf{n}}\cdot(\mathbf{v}-\mathbf{v}^{\mathrm{ref}}) = w^{(s)}\,\mathrm{d}x\,\mathrm{d}y, \tag{3.161}$$

with $w^{(s)} = z_{,s}\,\mathrm{d}s/\mathrm{d}t$ the dia-surface velocity component. A similar relation holds for the bottom face of the cell. The form of the SGS flux passing across the top and bottom is correspondingly given by

$$\mathrm{d}A_{(\hat{\mathbf{n}})}\,\hat{\mathbf{n}}\cdot\mathbf{J} = J^{(s)}\,\mathrm{d}x\,\mathrm{d}y, \tag{3.162}$$

which follows from the general expression (3.156) for the dia-surface tracer flux.

In a model using the generalized coordinate s for the vertical, it is sometimes convenient to do the vertical integrals over s instead of z. For this purpose, recall that with $z_{,s}$ single signed, the vertical thickness of a grid cell is given by equation (3.40), repeated here for completeness

$$\mathrm{d}z = z_{,s}\,\mathrm{d}s. \tag{3.163}$$

Bringing these results together, and taking the limit as the volume of the cell in (x, y, s) space goes to zero (i.e., $\mathrm{d}x\,\mathrm{d}y\,\mathrm{d}s \to 0$) leads to

$$\partial_t(z_{,s}\,\rho\,C) = z_{,s}\,\rho\,\mathcal{S}^{(\mathrm{C})} - \nabla_s\cdot[z_{,s}\,\rho\,(\mathbf{u}\,C+\mathbf{F})] - \partial_s\,[\,\rho\,(w^{(s)}\,C + F^{(s)})] \tag{3.164}$$

Notably, the horizontal gradient operator ∇_s is computed on surfaces of constant s, and so it is distinct generally from the horizontal gradient ∇_z taken on surfaces of constant z.

As indicated at the end of Section 3.5, we prefer to work with thickness weighted quantities, given the general time dependence of a model grid cell in MOM4p1. Hence, as an alternative to taking the limit as $\mathrm{d}x\,\mathrm{d}y\,\mathrm{d}s \to 0$, consider instead the limit as the time independent horizontal area $\mathrm{d}x\,\mathrm{d}y$ goes to zero, thus maintaining the time dependent thickness $\mathrm{d}z = z_{,s}\,\mathrm{d}s$ inside the derivative operators. In this case, the thickness weighted tracer mass budget takes the form

$$\boxed{\partial_t(\mathrm{d}z\,\rho\,C) = \mathrm{d}z\,\rho\,\mathcal{S}^{(\mathrm{C})} - \nabla_s\cdot[\mathrm{d}z\,\rho\,(\mathbf{u}\,C+\mathbf{F})] - [\rho\,(w^{(s)}\,C+F^{(s)})]_{s=s_{k-1}} + [\rho\,(w^{(s)}\,C+F^{(s)})]_{s=s_k}.} \tag{3.165}$$

Similarly, the thickness weighted mass budget is

$$\boxed{\partial_t(\mathrm{d}z\,\rho) = \mathrm{d}z\,\rho\,\mathcal{S}^{(\mathrm{M})} - \nabla_s\cdot(\mathrm{d}z\,\rho\,\mathbf{u}) - (\rho\,w^{(s)})_{s=s_{k-1}} + (\rho\,w^{(s)})_{s=s_k}.} \tag{3.166}$$

For clarity, we note that the horizontal divergence operator acting on the mass transport takes the form

$$\nabla_s\cdot(\mathrm{d}z\,\rho\,\mathbf{u}) = \frac{1}{\mathrm{d}y}\,\frac{\partial}{\partial x}\,(\mathrm{d}y\,\mathrm{d}z\,\rho\,u) + \frac{1}{\mathrm{d}x}\,\frac{\partial}{\partial y}\,(\mathrm{d}x\,\mathrm{d}z\,\rho\,v). \tag{3.167}$$

The mass source $\mathcal{S}^{(\mathrm{M})}$ has units of inverse time that, for self-consistency, must be related to the tracer source via

$$\mathcal{S}^{(\mathrm{M})} = \mathcal{S}^{(\mathrm{C})}(C=1). \tag{3.168}$$

Additionally, the SGS tracer flux vanishes with a uniform tracer

$$\mathbf{F}(C=1) = 0. \tag{3.169}$$

Note that by setting the tracer concentration in equation (3.165) to a uniform constant, SGS transort fluxes vanish, thus revealing the mass conservation budget. This procedure for deriving the mass budget from the tracer budget follows trivially from the definition of the tracer concentration given by equation (3.149). It represents a *compatibility condition* between the discrete budgets, and this condition is critical to maintain within a numerical model in order to respect tracer and mass conservation in the simulation. We have more to say about the compatibility condition in Section 3.6.8.

One reason that the thickness weighted budget given by equation (3.165) is more convenient than equation (3.164) is that equation (3.165) expresses the budget in terms of the grid cell thickness $\mathrm{d}z$, rather than the specific thickness $z_{,s}$. Nonetheless, this point is largely one of style and convenience, as there is no fundamental reason to prefer one form over the other for purposes of developing the discrete equations of an ocean model.

3.6.3 Fresh water budget

Seawater is comprised of freshwater with a relatively fixed ratio of various salts. It is common to consider the budget for the concentration of these salts, which is described by the tracer equation (3.165). As a complement, it may be of interest to formulate a budget for freshwater. In this case, we consider the mass of fresh water within a fluid parcel

$$\begin{aligned} \text{mass of fresh water} &= \text{mass of seawater} - \text{mass of salt} \\ &= \rho \, \mathrm{d}V \, (1 - S) \\ &= \rho \, \mathrm{d}V \, W, \end{aligned} \tag{3.170}$$

where S is the salinity (mass of salt per mass of seawater), and

$$W \equiv 1 - S \tag{3.171}$$

is the mass of fresh water per mass of seawater. Results from the tracer budget considered in Section 3.6.2 allow us to derive the following budget for fresh water within an interior ocean model grid cell

$$\begin{aligned} \partial_t(\mathrm{d}z \, \rho \, W) = \mathrm{d}z \, \rho \, (\mathcal{S}^{(\mathrm{M})} - \mathcal{S}^{(\mathrm{S})}) - \nabla_s \cdot [\mathrm{d}z \, \rho \, (\mathbf{u} \, W - \mathbf{F})] \\ - [\rho \, (w^{(s)} \, W - F^{(s)})]_{s=s_{k-1}} + [\rho \, (w^{(s)} \, W - F^{(s)})]_{s=s_k}. \end{aligned} \tag{3.172}$$

In these relations, the SGS tracer flux components $\mathbf{F}$ and $F^{(s)}$ are those for salt, and $\mathcal{S}^{(S)}$ is the salt source. Equation (3.172) is very similar to the tracer equation (3.165), with modified source term and negative signs on the SGS flux components.

3.6.4 The ideal age tracer

Thiele and Sarmiento (1990) and England (1995) consider an ideal age tracer for Boussinesq fluids. We consider the generalization here to nonBoussinesq fluids, in which

$$\rho \, \frac{\mathrm{d}A}{\mathrm{d}t} + \nabla \cdot \mathbf{J} = \rho \, \mathcal{S}^{(A)}, \tag{3.173}$$

where the age tracer A has dimensions of time and it is initialized globally to zero. It is characterized by the dimensionless *clock* source $\mathcal{S}^{(A)}$, which takes the values

$$\mathcal{S}^{(A)} = \begin{cases} 0 & \text{if } z = \eta \\ 1 & \text{if } z < \eta, \end{cases} \tag{3.174}$$

In a finite difference model, the boundary condition at $z = \eta$ is applied at the top grid cell $k = 1$. In MOM4p1, various age tracers can be defined that differ by the region that their boundary condition is set to zero. Given these prescriptions, A measures the age, in units of time, that a water parcel has spent away from the region where it was set to zero. Therefore, visual maps of A are useful to deduce such physically interesting properties as ventilation times.

From equation (3.165), the budget for tracer mass per area in a grid cell is given by

$$\begin{aligned} \partial_t(\mathrm{d}z\,\rho\,A) = \mathrm{d}z\,\rho\,\mathcal{S}^{(\mathrm{A})} - \nabla_s \cdot [\mathrm{d}z\,\rho\,(\mathbf{u}\,A + \mathbf{F})] \\ - [\rho\,(w^{(s)}\,A + F^{(s)})]_{s=s_{k-1}} + [\rho\,(w^{(s)}\,A + F^{(s)})]_{s=s_k}. \end{aligned} \tag{3.175}$$

In practice, the clock source is added to the age tracer at the very end of the time step, so that it is implemented as an adjustment process. In this way, we remove the ambiguity regarding the time step to evaluate the $\rho\,\mathrm{d}z$ factor that multiplies the age source.

3.6.5 Budgets without dia-surface fluxes

To garner some experience with tracer budgets, it is useful to consider the special case of zero dia-surface transport, either via advection or SGS fluxes, and zero tracer/mass sources. In this case, the thickness weighted mass and tracer mass budgets take the simplified form

$$\partial_t(\mathrm{d}z\,\rho) = -\,\nabla_s \cdot (\mathrm{d}z\,\rho\,\mathbf{u}) \tag{3.176}$$

$$\partial_t(\mathrm{d}z\,\rho\,C) = -\,\nabla_s \cdot [\mathrm{d}z\,\rho\,(\mathbf{u}\,C + \mathbf{F})]. \tag{3.177}$$

The first equation says that the time tendency of the thickness weighted density (mass per area) at a point between two surfaces of constant generalized vertical coordinate is given by the horizontal convergence of mass per area onto that point. The transport is quasi-two-dimensional in the sense that it is only a two-dimensional convergence that determines the evolution. The tracer equation has an analogous interpretation. We illustrate this situation in Figure 3.5. As emphasized in our discussion of the material time derivative (3.93), this simplification of the transport equation does not mean that fluid parcels are strictly horizontal. Indeed, such is distinctly not the case when the surfaces are moving.

A further simplification of the mass and tracer mass budgets ensues when considering adiabatic and Boussinesq flow in isopycnal coordinates. We consider ρ now to represent the constant potential density of the finitely thick fluid layer. In this case, the mass and tracer budgets reduce to

$$\partial_t(\mathrm{d}z) = -\,\nabla_\rho \cdot (\mathrm{d}z\,\mathbf{u}) \tag{3.178}$$

$$\partial_t(\mathrm{d}z\,C) = -\,\nabla_\rho \cdot [\mathrm{d}z\,(\mathbf{u}\,C + \mathbf{F})]. \tag{3.179}$$

Equation (3.178) provides a relation for the thickness of the density layers, and equation (3.179) is the analogous relation for the tracer within the layer. These expressions are commonly used in the construction of adiabatic isopycnal models, which are often used in the study of geophysical fluid mechanics of the ocean.

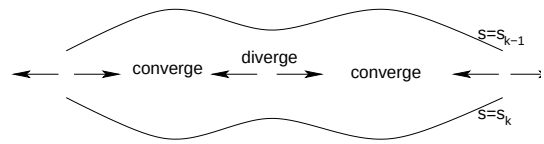

Figure 3.5: Schematic of the horizontal convergence of mass between two surfaces of constant generalized vertical coordinates. As indicated by equation (3.176), when there is zero dia-surface transport, it is just the horizontal convergence that determines the time evolution of mass between the layers. Evolution of thickness weighted tracer concentration in between the layers is likewise evolved just by the horizontal convergence of the thickness weighted advective and diffusive tracer fluxes (equation (3.177)). In this way, the transport is quasi-two-dimensional when the dia-surface transports vanish. A common example of this special system is an adiabatic ocean where the generalized surfaces are defined by isopycnals.

3.6.6 Cells adjacent to the ocean bottom

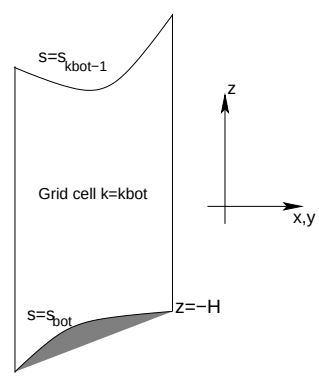

Figure 3.6: Schematic of an ocean grid cell next to the ocean bottom labeled by $k = k_{\text{bot}}$. Its top face is a surface of constant generalized vertical coordinate $s = s_{\text{kbot}-1}$, and the bottom face is determined by the ocean bottom topography at $z = -H$ where $s_{\text{bot}}(x, y, t) = s(x, y, z = -H, t)$.

For a grid cell adjacent to the ocean bottom (Figure 3.6), we assume that just the bottom face of this cell abuts the solid earth boundary. The outward normal $\hat{\mathbf{n}}_{\text{H}}$ to the bottom is given by equation (3.34), and the area element along the bottom is

$$\mathrm{d}A_{\text{H}} = |\nabla(z + H)|\, \mathrm{d}x\, \mathrm{d}y. \tag{3.180}$$

Hence, the transport across the solid earth boundary is

$$-\iint \mathrm{d}A_{\text{H}}\, \hat{\mathbf{n}}_{\text{H}} \cdot (\mathbf{v}\, \rho\, C + \mathbf{J}) = \iint \mathrm{d}x\, \mathrm{d}y\, (\nabla H + \hat{\mathbf{z}}) \cdot (\mathbf{v}\, \rho\, C + \mathbf{J}). \tag{3.181}$$

We assume that there is zero advective mass flux across the bottom, in which case the advective flux drops out since $\mathbf{v} \cdot (\nabla H + \hat{\mathbf{z}}) = 0$ (equation (3.36)). However, the possibility of a nonzero

geothermal tracer transport warrants a nonzero SGS tracer flux at the bottom, in which case the bottom tracer flux is written

$$Q^{(\mathrm{C})}_{(\mathrm{bot})} = (\nabla H + \hat{\mathbf{z}}) \cdot \mathbf{J}. \tag{3.182}$$

The corresponding thickness weighted budget is given by

$$\boxed{\partial_t \left(\mathrm{d}z\, \rho\, C\right) = \mathrm{d}z\, \rho\, \mathcal{S}^{(\mathrm{C})} - \nabla_s \cdot \left[\mathrm{d}z\, \rho\, (\mathbf{u}\, C + \mathbf{F})\right] - \Big[\rho\, (w^{(s)}\, C + z_{,s}\, \nabla s \cdot \mathbf{F})\Big]_{s=s_{kbot-1}} + Q^{(\mathrm{C})}_{(\mathrm{bot})},} \tag{3.183}$$

and the corresponding mass budget is

$$\boxed{\partial_t \left(\mathrm{d}z\, \rho\right) = \mathrm{d}z\, \rho\, \mathcal{S}^{(\mathrm{M})} - \nabla_s \cdot (\mathrm{d}z\, \rho\, \mathbf{u}) - (\rho\, w^{s)})_{s=s_{kbot-1}} + Q^{(\mathrm{M})}_{(\mathrm{bot})},} \tag{3.184}$$

where $Q^{(\mathrm{M})}_{(\mathrm{bot})}$ allows for the possibility of mass entering through geothermal boundary sources. For brevity, we drop this term in the following, since it generally is ignored for ocean climate modeling.

3.6.7 Cells adjacent to the ocean surface

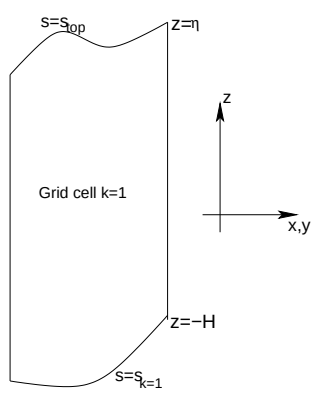

Figure 3.7: Schematic of an ocean grid cell next to the ocean surface labeled by $k = 1$. Its top face is at $z = \eta$, and the bottom is a surface of constant generalized vertical coordinate $s = s_{k=1}$.

For a grid cell adjacent to the ocean surface (Figure 3.7), we assume that just the upper face of this cell abuts the boundary between the ocean and the atmosphere or sea ice. The ocean surface is a time dependent boundary with $z = \eta(x, y, t)$. The outward normal $\hat{\mathbf{n}}_\eta$ is given by equation (3.57), and its area element $\mathrm{d}A_\eta$ is given by equation (3.58).

As the surface can move, we must measure the advective transport with respect to the moving surface. Just as in the dia-surface transport discussed in Section 3.1.8, we consider the velocity of a reference point on the surface

$$\mathbf{v}^{\mathrm{ref}} = \mathbf{u}^{\mathrm{ref}} + \hat{\mathbf{z}}\, w^{\mathrm{ref}}. \tag{3.185}$$

Since $z = \eta$ represents the vertical position of the reference point, the vertical component of the velocity for this point is given by

$$w^{\mathrm{ref}} = (\partial_t + \mathbf{u}^{\mathrm{ref}} \cdot \nabla)\, \eta \tag{3.186}$$

which then leads to

$$\mathbf{v}^{\text{ref}} \cdot \nabla (z - \eta) = \eta_{,t}. \tag{3.187}$$

Hence, the advective transport leaving the ocean surface is

$$\begin{aligned} \iint\limits_{z=\eta} \mathrm{d}A_{(\hat{\mathbf{n}})}\, \hat{\mathbf{n}} \cdot (\mathbf{v} - \mathbf{v}^{\text{ref}})\, \rho\, C &= \iint\limits_{z=\eta} \mathrm{d}x\, \mathrm{d}y\, (-\eta_{,t} + w - \mathbf{u} \cdot \nabla \eta)\, \rho\, C \\ &= - \iint\limits_{z=\eta} \mathrm{d}x\, \mathrm{d}y\, \rho_{\text{w}}\, q_{\text{w}}\, C, \end{aligned} \tag{3.188}$$

where the surface kinematic boundary condition (3.66) was used. The negative sign on the right hand side arises from our convention that $q_{\text{w}} > 0$ represents an input of water to the ocean domain. We can summarize this result with the local relation

$$\boxed{\rho_{\text{w}}\, q_{\text{w}} = -\frac{\rho\, \mathrm{d}A_{(\hat{\mathbf{n}})}\, \hat{\mathbf{n}} \cdot (\mathbf{v} - \mathbf{v}^{\text{ref}})}{\mathrm{d}A} \qquad \text{at} \quad z = \eta,} \tag{3.189}$$

where again $\mathrm{d}A = \mathrm{d}x\, \mathrm{d}y$ is the horizontal area element. This relation exposes the connection between the water flux q_{w} at the ocean surface, and the more general dia-surface velocity component defined by equation (3.88). In summary, the tracer flux leaving the ocean free surface is given by

$$\iint\limits_{z=\eta} \mathrm{d}A_{(\hat{\mathbf{n}})}\, \hat{\mathbf{n}} \cdot [(\mathbf{v} - \mathbf{v}^{\text{ref}})\, \rho\, C + \mathbf{J}] = \iint\limits_{z=\eta} \mathrm{d}x\, \mathrm{d}y\, (-\rho_{\text{w}}\, q_{\text{w}}\, C + \nabla (z - \eta) \cdot \mathbf{J}). \tag{3.190}$$

In equation (3.190), we formally require the tracer concentration precisely at the ocean surface $z = \eta$. However, as mentioned at the start of Section 3.1.7, it is actually a fiction that the ocean surface is a smooth mathematical function. Furthermore, seawater properties precisely at the ocean surface, known generally as *skin properties*, are generally not what an ocean model carries as its prognostic variable in its top grid cell. Instead, the model carries a bulk property averaged over roughly the upper few tens of centimeters.

To proceed in formulating the boundary condition for an ocean climate model, we consider there to be a boundary layer model that provides us with the total tracer flux passing through the ocean surface. Developing such a model is a nontrivial problem in air-sea and ice-sea interaction theory and phenomenology. For present purposes, we do not focus on these details, and instead just introduce this flux in the form

$$Q^{(\text{C})} = -\rho_{\text{w}}\, q_{\text{w}}\, C_{\text{w}} + Q^{(\text{C})}_{(\text{turb})} \tag{3.191}$$

where C_{w} is the tracer concentration within the incoming water q_{w}. The first term on the right hand side represents the advective transport of tracer through the surface with the fresh water (i.e., ice melt, rivers, precipitation, evaporation). The term $Q^{(\text{C})}_{(\text{turb})}$ arises from parameterized turbulence and/or radiative fluxes, such as sensible, latent, shortwave, and longwave heating appropriate for the temperature equation. A positive value for $Q^{(\text{C})}_{(\text{turb})}$ signals tracer leaving the ocean through its surface. In the special case of zero fresh water flux, then

$$\nabla (z - \eta) \cdot \mathbf{J} = Q^{(\text{C})}_{(\text{turb})} \qquad \text{if} \quad q_{\text{w}} = 0. \tag{3.192}$$

In general, it is not possible to make this identification. Instead, we must settle for the general expression

$$\iint\limits_{z=\eta} \mathrm{d}A_{(\hat{\mathbf{n}})}\, \hat{\mathbf{n}} \cdot [(\mathbf{v} - \mathbf{v}^{\mathrm{ref}})\, \rho\, C + \mathbf{J}] = \iint\limits_{z=\eta} \mathrm{d}x\, \mathrm{d}y\, (-\rho_{\mathrm{w}}\, q_{\mathrm{w}}\, C_{\mathrm{w}} + Q^{(\mathrm{C})}_{(\mathrm{turb})}). \tag{3.193}$$

The above results lead to the thickness weighted tracer budget for the ocean surface grid cell

$$\boxed{\begin{aligned} \partial_t\, (\mathrm{d}z\, \rho\, C) &= \mathrm{d}z\, \rho\, \mathcal{S}^{(\mathrm{C})} - \nabla_s \cdot [\mathrm{d}z\, \rho\, (\mathbf{u}\, C + \mathbf{F})] \\ &\quad + \Big[\rho\, (w^{(s)}\, C + z_{,s}\, \nabla s \cdot \mathbf{F})\Big]_{s=s_{k=1}} + (\rho_{\mathrm{w}}\, q_{\mathrm{w}}\, C_{\mathrm{w}} - Q^{(\mathrm{turb})}_{(\mathrm{C})}), \end{aligned}} \tag{3.194}$$

and the corresponding mass budget

$$\boxed{\partial_t\, (\mathrm{d}z\, \rho) = \mathrm{d}z\, \rho\, \mathcal{S}^{(\mathrm{M})} - \nabla_s \cdot (\mathrm{d}z\, \rho\, \mathbf{u}) + (\rho\, w^{(s)})_{s=s_{k=1}} + \rho_{\mathrm{w}}\, q_{\mathrm{w}}.} \tag{3.195}$$

3.6.8 Compatability between vertically integrated mass and tracer budgets

In Section 3.6.2, we considered issues of compatibility between the tracer and mass budgets within a grid cell. Such compatibility follows trivially from the definition of tracer concentration given in Section 3.6.1. We briefly revisit compatibility here, by focusing on the vertically integrated tracer and mass budgets.

Combining the surface tracer budget (3.195), the bottom budget (3.183), and interior budget (3.165), renders the vertically integrated tracer budget

$$\begin{aligned} \partial_t \left(\sum_k \mathrm{d}z\, \rho\, C \right) &= \sum_k \mathrm{d}z\, \rho\, \mathcal{S}^{(\mathrm{C})} - \nabla_s \cdot \left(\sum_k \mathrm{d}z\, \rho\, (\mathbf{u}\, C + \mathbf{F}) \right) \\ &\quad + \left(\rho_{\mathrm{w}}\, q_{\mathrm{w}}\, C_{\mathrm{w}} - Q^{(\mathrm{turb})}_{(\mathrm{C})} + Q^{(\mathrm{bott})}_{(\mathrm{C})} \right). \end{aligned} \tag{3.196}$$

As expected, the only contributions from vertical fluxes come from the top and bottom boundaries. Furthermore, by setting the tracer concentration to a uniform constant, in which case the SGS turbulent terms vanish, the tracer budget reduces to the vertically integrated mass budget

$$\partial_t \left(\sum_k \mathrm{d}z\, \rho \right) = \sum_k \mathrm{d}z\, \rho\, \mathcal{S}^{(\mathrm{M})} - \nabla_s \cdot \mathbf{U}^{\rho} + \rho_{\mathrm{w}}\, q_{\mathrm{w}}, \tag{3.197}$$

where

$$\mathbf{U}^{\rho} = \sum_k \mathrm{d}z\, \rho\, \mathbf{u} \tag{3.198}$$

is the discrete form of the vertically integrated horizontal momentum per volume defined by equation (3.22). As for the individual grid cells, this vertically integrated compatiblity between tracer and mass budgets must be carefully maintained by the space and time discretizations used in an ocean model. Otherwise, conservation properties of the model will be compromised (Griffies et al., 2001).

3.7 Forces from pressure

Pressure is a contact force per area that acts in a compressive manner on the boundary of a finite fluid domain (e.g., see Figure 3.8). Mathematically, we have

$$\mathbf{F}_{\text{press}} = -\iint \mathrm{d}A_{(\hat{\mathbf{n}})}\, \hat{\mathbf{n}}\, p, \tag{3.199}$$

where p is the pressure (with units of a force per area) acting on the boundary of the domain with outward normal $\hat{\mathbf{n}}$ and area element $\mathrm{d}A_{(\hat{\mathbf{n}})}$. The minus sign accounts for the compressive behaviour of pressure. The accumulation of contact pressure forces acting over the bounding area of the domain leads to a net pressure force acting on the domain.

Through use of the Green-Gauss theorem of vector calculus, we can equivalently consider pressure to exert a body force per area at each point within the domain, so that

$$\mathbf{F}_{\text{press}} = -\iiint \mathrm{d}V\, \nabla\, p, \tag{3.200}$$

where $\mathrm{d}V$ is the volume element. That is, the volume integral of the pressure gradient body force over the domain yields the net pressure force.

In the continuum, the two formulations (3.199) and (3.200) yield identical pressure forces. Likewise, in a finite volume discretization, the two forms are identical (e.g., Section 6.2.2 of Hirsch, 1988). But with finite differences, as used in earlier versions of MOM for pressure forces, the two forms can lead to different numerical methods. In the remainder of this section, we further explore the computation of pressure forces according to the two different formulations. Further details of discrete expressions are presented in Chapter 4.

3.7.1 The accumulation of contact pressure forces

Pressure acts as a contact or interfacial stress on the sides of a finite region of fluid. In particular, the total pressure force acting on the grid cell in Figure 3.8 is given by summing the pressure forces acting on the six cell faces

$$\mathbf{F}_{\text{pressure}} = \mathbf{F}_{x=x_1} + \mathbf{F}_{x=x_2} + \mathbf{F}_{y=y_1} + \mathbf{F}_{y=y_2} + \mathbf{F}_{s=s_1} + \mathbf{F}_{s=s_2}. \tag{3.201}$$

The pressure acting on faces with a zonal normal can be written

$$\mathbf{F}_{x=x_1} = \hat{\mathbf{x}} \left(\int \mathrm{d}y \int_{z_2}^{z_1} \mathrm{d}z\, p \right)_{x=x_1} \tag{3.202}$$

$$\mathbf{F}_{x=x_2} = -\hat{\mathbf{x}} \left(\int \mathrm{d}y \int_{z_2}^{z_1} \mathrm{d}z\, p \right)_{x=x_2} \tag{3.203}$$

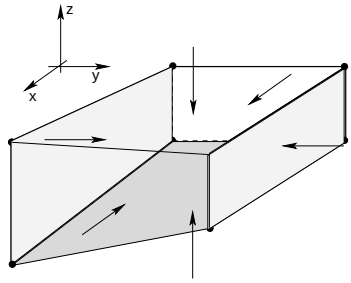

Figure 3.8: Schematic of a grid cell bounded at its top and bottom in general by sloped surfaces and vertical side walls. The top and bottom surfaces can represent linear piecewise approximations to surfaces of constant generalized vertical coordinates, with $s = s_1$ at the top surface and $s = s_2$ at the bottom surface. They could also represent the ocean surface (for the top face) or the ocean bottom (for the bottom face). The arrows represent the pressure contact forces that act in a compressive manner along the boundaries of the grid cell and in a direction normal to the boundaries. These forces arise from contact between the shown fluid volume and adjacent regions. Due to Newton's Third Law, the pressure acting on an arbitrary fluid parcel **A** due to contact with a parcel **B** is equal and opposite to the pressure acting on parcel **B** due to contact with parcel **A**. If coded according to finite volume budgets, as in Lin (1997) or Adcroft et al. (2008), this law extends to the pressure forces acting between grid cells in an ocean model.

where the vertical integral extends from the bottom face at $z_2 = z(x, y, s = s_2, t)$ to the top face at $z_1 = z(x, y, s = s_1, t)$. Likewise, the meridional pressure forces are

$$\mathbf{F}_{y=y_1} = \hat{\mathbf{y}} \left(\int \mathrm{d}x \int_{z_2}^{z_1} \mathrm{d}z \, p \right)_{y=y_1} \tag{3.204}$$

$$\mathbf{F}_{y=y_2} = -\hat{\mathbf{y}} \left(\int \mathrm{d}x \int_{z_2}^{z_1} \mathrm{d}z \, p \right)_{y=y_2} . \tag{3.205}$$

On the top face, the pressure force is given by

$$\begin{aligned} \mathbf{F}_{s=s_1} &= -\left(\int \mathrm{d}y \int \mathrm{d}x \, p \, z_{,s} \, \nabla s \right)_{s=s_1} \\ &= -\left(\int \mathrm{d}y \int \mathrm{d}x \, p \, (-\nabla_s z + \hat{\mathbf{z}}) \right)_{s=s_1} . \end{aligned} \tag{3.206}$$

Note the contribution from the generally non-horizontal top face as represented by the two dimensional vector

$$\nabla_s z = \mathbf{S}, \tag{3.207}$$

which is the slope of the surface of constant generalized vertical coordinate relative to the horizontal plane. The pressure force on the bottom face has a similar appearance

$$\mathbf{F}_{s=s_2} = \left(\int \mathrm{d}y \int \mathrm{d}x \, p \, (-\nabla_s z + \hat{\mathbf{z}}) \right)_{s=s_2} . \tag{3.208}$$

If the top and bottom faces are horizontal, as for z-models, the pressure force acting at $s = s_1$ and $s = s_2$ acts solely in the vertical direction. More generally, the pressure force per area on the top and bottom faces is oriented according to the slope of the faces and so has a nontrivial projection into all three directions.

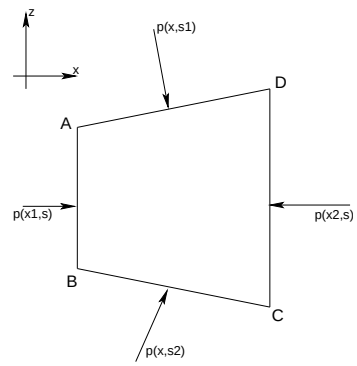

Figure 3.9: The sides of the grid cell, with the slopes top and bottom surfaces more enhanced here than in Figure 3.9. The corners are denoted A, B, C, and D, and oriented in a counterclockwise manner. This is the orientation appropriate for performing a contour integral in order to compute the pressure force acting on the area.

To garner a sense for how pressure acts on the face of a grid cell, consider the case where the top surface of a grid cell rises to the east as shown in Figure 3.9. In this case, the pressure force per area in the $x - z$ plane takes the form

$$\text{PRESSURE FORCE PER AREA ON TOP FACE} = -p\,[\hat{\mathbf{z}} - (\partial z/\partial x)_s\,\hat{\mathbf{x}}]. \tag{3.209}$$

Since $(\partial z/\partial x)_s > 0$ for this example, the pressure force per area has a positive component in the $\hat{\mathbf{x}}$ direction, as indicated by the arrow normal to the top surface in Figure 3.9.

When the top surface represents the surface of the ocean at $z = \eta$, the pressure p is the applied pressure p_a arising from any media above the ocean, such as the atmosphere and sea ice. In this case,

$$\begin{aligned}\text{PRESSURE FORCE PER AREA ON OCEAN SURFACE} &= -p_\mathrm{a}\,\nabla\,(z - \eta)\\ &= -p_\mathrm{a}\,(\hat{\mathbf{z}} - \nabla\eta),\end{aligned} \tag{3.210}$$

where $\nabla\eta$ is the slope of the ocean surface. Likewise, if the bottom of the grid cell is bounded by the solid earth boundary,

$$\begin{aligned}\text{PRESSURE FORCE PER AREA ON OCEAN BOTTOM} &= p_\mathrm{b}\,\nabla\,(z + H)\\ &= p_\mathrm{b}\,(\hat{\mathbf{z}} + \nabla H),\end{aligned} \tag{3.211}$$

where ∇H is the bottom slope.

A sum of the pressure forces acting on the six faces of the grid cell determines the acceleration

due to pressure acting on a grid cell. Organizing the forces into the three directions leads to

$$F^x_{\text{pressure}} = \left(\int \mathrm{d}y \int_{z_2}^{z_1} \mathrm{d}z\, p \right)_{x=x_1} - \left(\int \mathrm{d}y \int_{z_2}^{z_1} \mathrm{d}z\, p \right)_{x=x_2} \tag{3.212}$$

$$+ \left(\int \mathrm{d}y \int_{x_1}^{x_2} \mathrm{d}x\, z_{,x}\, p \right)_{s=s_1} - \left(\int \mathrm{d}y \int_{x_1}^{x_2} \mathrm{d}x\, z_{,x}\, p \right)_{s=s_2} \tag{3.213}$$

$$F^y_{\text{pressure}} = \left(\int \mathrm{d}x \int_{z_2}^{z_1} \mathrm{d}z\, p \right)_{y=y_1} - \left(\int \mathrm{d}x \int_{z_2}^{z_1} \mathrm{d}z\, p \right)_{y=y_2} \tag{3.214}$$

$$+ \left(\int \mathrm{d}x \int_{y_1}^{y_2} \mathrm{d}y\, z_{,y}\, p \right)_{s=s_1} - \left(\int \mathrm{d}x \int_{y_1}^{y_2} \mathrm{d}y\, z_{,y}\, p \right)_{s=s_2} \tag{3.215}$$

$$F^z_{\text{pressure}} = \left(\iint \mathrm{d}x\, \mathrm{d}y\, p \right)_{s=s_2} - \left(\iint \mathrm{d}x\, \mathrm{d}y\, p \right)_{s=s_1} . \tag{3.216}$$

Making the hydrostatic approximation, whereby the vertical momentum equation maintains the inviscid hydrostatic balance, allows us to note that the difference in pressure between the top and bottom surfaces of the region is determined by the weight of fluid between the surfaces,

$$\iint_{s=s_2} \mathrm{d}x\, \mathrm{d}y\, p - \iint_{s=s_1} \mathrm{d}x\, \mathrm{d}y\, p = g \int \rho\, \mathrm{d}V. \tag{3.217}$$

It is notable that this expression relates the difference in contact forces acting on the domain boundaries to the integral of a body force (the gravitational force) acting throughout the domain interior.

We now work on reformulating the horizontal pressure forces into a manner amenable to finite volume discretization. Referring to Figure 3.9, we can write the horizontal forces in a manner than builds in the orientation of pressure via a counterclockwise contour integral

$$\begin{aligned} F^x_{\text{pressure}} &= - \left(\int \mathrm{d}y \int_{z_1}^{z_2} \mathrm{d}z\, p \right)_{x=x_1} - \left(\int \mathrm{d}y \int_{x_1}^{x_2} \mathrm{d}x\, z_{,x}\, p \right)_{s=s_2} \\ &\quad - \left(\int \mathrm{d}y \int_{z_2}^{z_1} \mathrm{d}z\, p \right)_{x=x_2} - \left(\int \mathrm{d}y \int_{x_2}^{x_1} \mathrm{d}x\, z_{,x}\, p \right)_{s=s_1} \\ &= - \left(\int \mathrm{d}y \int_{z_1}^{z_2} \mathrm{d}z\, p \right)_{x=x_1} - \left(\int \mathrm{d}y \int_{x_1}^{x_2} \mathrm{d}z\, p \right)_{s=s_2} \\ &\quad - \left(\int \mathrm{d}y \int_{z_2}^{z_1} \mathrm{d}z\, p \right)_{x=x_2} - \left(\int \mathrm{d}y \int_{x_2}^{x_1} \mathrm{d}z\, p \right)_{s=s_1} \\ &= - \int \mathrm{d}y \oint_{ABCD} \mathrm{d}z\, p. \end{aligned} \tag{3.218}$$

In the penultimate step, we set $z_{,x}\,\mathrm{d}x = \mathrm{d}z$, which is an relation valid along the particular contour $ABCD$. That is, in all the integrals, the differential increment $\mathrm{d}z$ is taken along the contour surrounding the cell. The counter-clockwise orientation of the integral follows from the compressive nature of pressure. Since the contour of integration is closed, we have the identity

$$\boxed{\begin{aligned} F^x_{\text{pressure}} &= -\int \mathrm{d}y \oint_{ABCD} p\,\mathrm{d}z \\ &= \int \mathrm{d}y \oint_{ABCD} z\,\mathrm{d}p. \end{aligned}} \tag{3.219}$$

The contour integral form of the pressure force is key to providing a finite volume discretization that is consistent with Newton's Third Law (Lin, 1997; Adcroft et al., 2008). What is needed next is an assumption about the subgrid profiles for pressure and geopotential $\Phi = g\,z$ in order to evaluate the contour integral.

3.7.2 Pressure gradient body force in hydrostatic fluids

In the early finite difference formulations of the pressure force, modelers discretized the gradient of pressure and performed certain grid averages so that the gradient occurs at the appropriate grid point. Guidance to the discretization details was provided by concerns of energetic consistency (Chapter 10), whereby work done by pressure in the discrete algorithm is balanced by buoyancy work (Bryan, 1969). This general philosophy *still* guides the formulation of the pressure force in MOM4p1.

As with the contact forces formulation, in a hydrostatic fluid we are only concerned with horizontal pressure gradients, since the vertical momentum equation is reduced to the inviscid hydrostatic balance. Hence, we are concerned with the horizontal acceleration arising from pressure differences in a hydrostatic and non-Boussinesq fluid, and this acceleration can be written[13]

$$\boxed{\begin{aligned} \rho^{-1}\,\nabla_z p &= \rho^{-1}\,(\nabla_s - \nabla_s\,z\,\partial_z)\,p \\ &= \rho^{-1}\,\nabla_s\,p + g\,\nabla_s\,z \\ &= \rho^{-1}\,\nabla_s\,p + \nabla_s\,\Phi, \end{aligned}} \tag{3.220}$$

where the hydrostatic relation $p_{,z} = -\rho\,g$ was used to reach the second equality, and

$$\Phi = g\,z \tag{3.221}$$

is the geopotential. To reach this result, we used the expression

$$\boxed{\nabla_z = \nabla_s - \nabla_s\,z\,\partial_z,} \tag{3.222}$$

which relates the lateral gradient operator acting on constant depth surfaces, ∇_z, to the lateral operator acting on surfaces of constant generalized vertical coordinate, ∇_s.

Depending on the choice for the vertical coordiante s, discretizations of the pressure gradient body force can result in both terms in equation (3.220) being large and of opposite sign in many

[13] For a Boussinesq fluid, equation (3.220) is modified by a factor of ρ/ρ_o.

regions. This issue is especially pernicious for terrain following coordinates in regions of nontrivial topographic slope (e.g., Griffies et al., 2000a). Hence, this calculation exposes the discrete pressure gradient force to nontrivial numerical truncation errors which can lead to spurious numerical pressure gradients and thus to incorrect simulated currents. Significant effort has gone into reducing such *pressure gradient errors*, especially in terrain following models where undulations of the coordinate surfaces can be large with realistic topography (e.g., see Figure 6.3). Some of these issues are summarized in Section 2 of Griffies et al. (2000a).

The pressure gradient force acting at a point represents the infinitesimal limit of a body force. We see this fact by multiplying the pressure gradient acceleration by the mass of a fluid parcel, which leads to the pressure force acting at a point in the continuum

$$\begin{aligned} \text{PRESSURE GRADIENT FORCE} &= -(\rho\, \mathrm{d}V)\, \rho^{-1}\, \nabla_z p \\ &= -\mathrm{d}V\, \nabla_z p \\ &= -\mathrm{d}V\, (\nabla_s\, p + \rho\, \nabla_s\, \Phi). \end{aligned} \tag{3.223}$$

Hence, the pressure force acting on a finite region is given by the integral over the extent of the region

$$\begin{aligned} \text{PRESSURE GRADIENT FORCE OVER REGION} &= -\iiint (\rho\, \mathrm{d}V)\, \rho^{-1}\, \nabla_z p \\ &= -\iiint \mathrm{d}V\, \nabla_z p. \end{aligned} \tag{3.224}$$

As stated earlier, a finite volume discretization of this force will take the same form as the finite volume discretization of the pressure contact force discussed in Section 3.7.1, as it should due to the Green-Gauss Theorem invoked to go from equation (3.199) to (3.200). However, these formulations generally *do not* provide for a clear energetic interpretation as promoted by the finite difference formulation of Bryan (1969).

3.8 Linear momentum budget

The purpose of this section is to formulate the budget for linear momentum over a finite region of the ocean, with specific application to ocean model grid cells. The material here requires many of the same elements as in Section 3.6, but with added richness arising from the vector nature of momentum, and the additional considerations of forces from pressure, friction, gravity, and planetary rotation. Note that we initially formulate the equations using the pressure contact force, as this provides a general formulation. Afterwards, we specialize to hydrostatic fluids, and thus write the pressure force as a gradient (Section 3.7.2), as commonly done in primitive equation ocean models

3.8.1 General formulation

The budget of linear momentum for a finite region of fluid is given by the following relation based on Newton's second and third laws

$$\begin{aligned}\partial_t \left(\iiint \mathrm{d}V \, \rho \, \mathbf{v} \right) = \iiint \mathrm{d}V \, \mathcal{S}^{(\mathbf{v})} - \iint \mathrm{d}A_{(\hat{\mathbf{n}})} \, [\, \hat{\mathbf{n}} \cdot (\mathbf{v} - \mathbf{v}^{\mathrm{ref}})] \, \rho \, \mathbf{v} \\ + \iint \mathrm{d}A_{(\hat{\mathbf{n}})} \, (\hat{\mathbf{n}} \cdot \boldsymbol{\tau} - \hat{\mathbf{n}} \, p) - \iiint \mathrm{d}V \, \rho \, [\, g \, \hat{\mathbf{z}} + (f + \mathcal{M}) \, \hat{\mathbf{z}} \wedge \mathbf{v}].\end{aligned} \tag{3.225}$$

The left hand side is the time tendency of the region's linear momentum. The first term on the right hand side, $\mathcal{S}^{(\mathbf{v})}$, is a momentum source, with units momentum per volume per time. This term is nonzero if, for example, the addition of mass to the ocean via a source occurs with a nonzero momentum. Often, it is assumed that mass is added with zero velocity, and so does not appear as a momentum source. The second term is the advective transport of linear momentum across the boundary of the region, with recognition that the region's boundaries are generally moving with velocity $\mathbf{v}^{\mathrm{ref}}$. The third term is the integral of the contact stresses due to friction and pressure. These stresses act on the boundary of the fluid domain. We already discussed the forces from pressure in Section 3.7. The stress tensor $\boldsymbol{\tau}$ is a symmetric second order tensor that parameterizes subgrid scale transport of momentum. The final term on the right hand side is the volume integral of body forces due to gravity and the Coriolis force.[14] In addition, there is a body force arising from the nonzero curvature of the spherical space. This curvature leads to the advection metric frequency (see equation (4.49) of Griffies (2004))

$$\mathcal{M} = v \, \partial_x \ln \mathrm{d}y - u \, \partial_y \ln \mathrm{d}x. \tag{3.226}$$

In spherical coordinates where

$$\mathrm{d}x = (r \, \cos \phi) \, \mathrm{d}\lambda \tag{3.227}$$

$$\mathrm{d}y = r \, \mathrm{d}\phi, \tag{3.228}$$

with r the distance from the earth's center, λ the longitude, and ϕ the latitude, the advective metric frequency takes the form

$$\mathcal{M} = (u/r) \, \tan \phi. \tag{3.229}$$

The advection metric frequency arises since linear momentum is not conserved on the sphere.[15] Hence, the linear momentum budget picks up this extra term that is a function of the chosen lateral coordinates.

3.8.2 An interior grid cell

At the west side of a grid cell, $\hat{\mathbf{n}} = -\hat{\mathbf{x}}$ whereas $\hat{\mathbf{n}} = \hat{\mathbf{x}}$ on the east side. Hence, the advective transport of linear momentum entering through the west side of the grid cell and that which is

[14] The wedge symbol $\wedge$ represents a vector cross product, also commonly written as $\times$. The wedge is typically used in the physics literature, and is preferred here to avoid confusion with the horizontal coordinate x.

[15] Linear momentum is not conserved for ideal flow on a sphere. Instead, angular momentum is conserved for ideal fluid flow on the sphere in the absence of horizontal boundaries (see Section 4.11.2 of Griffies (2004)).

leaving through the east side are given by

$$\text{TRANSPORT ENTERING FROM WEST} = \iint\limits_{x=x_1} \mathrm{d}y\,\mathrm{d}s\; z_{,s}\, u\,(\rho\,\mathbf{v}) \tag{3.230}$$

$$\text{TRANSPORT LEAVING THROUGH EAST} = -\iint\limits_{x=x_2} \mathrm{d}y\,\mathrm{d}s\; z_{,s}\, u\,(\rho\,\mathbf{v}). \tag{3.231}$$

Similar results hold for momentum crossing the cell boundaries in the north and south directions. Momentum crossing the top and bottom surfaces of an interior cell is given by

$$\text{TRANSPORT ENTERING FROM THE BOTTOM} = \iint\limits_{s=s_2} \mathrm{d}x\,\mathrm{d}y\; w^{(s)}\,(\rho\,\mathbf{v}) \tag{3.232}$$

$$\text{TRANSPORT LEAVING FROM THE TOP} = -\iint\limits_{s=s_1} \mathrm{d}x\,\mathrm{d}y\; w^{(s)}\,(\rho\,\mathbf{v}). \tag{3.233}$$

Forces due to the contact stresses at the west and east sides are given by

$$\text{CONTACT FORCE ON WEST SIDE} = -\iint\limits_{x=x_1} \mathrm{d}y\,\mathrm{d}s\; z_{,s}\,(\hat{\mathbf{x}}\cdot\boldsymbol{\tau} - \hat{\mathbf{x}}\,p) \tag{3.234}$$

$$\text{CONTACT FORCE ON EAST SIDE} = \iint\limits_{x=x_2} \mathrm{d}y\,\mathrm{d}s\; z_{,s}\,(\hat{\mathbf{x}}\cdot\boldsymbol{\tau} - \hat{\mathbf{x}}\,p) \tag{3.235}$$

with similar results at the north and south sides. At the top of the cell, $\mathrm{d}A_{(\hat{\mathbf{n}})}\,\hat{\mathbf{n}} = \nabla s\,\mathrm{d}x\,\mathrm{d}y$ whereas $\mathrm{d}A_{(\hat{\mathbf{n}})}\,\hat{\mathbf{n}} = -\nabla s\,\mathrm{d}x\,\mathrm{d}y$ at the bottom. Hence,

$$\text{CONTACT FORCE ON CELL TOP} = \iint\limits_{s=s_{k-1}} \mathrm{d}x\,\mathrm{d}y\; z_{,s}\,(\nabla s\cdot\boldsymbol{\tau} - p\,\nabla s) \tag{3.236}$$

$$\text{CONTACT FORCE ON CELL BOTTOM} = -\iint\limits_{s=s_k} \mathrm{d}y\,\mathrm{d}s\; z_{,s}\,(\nabla s\cdot\boldsymbol{\tau} - p\,\nabla s). \tag{3.237}$$

Bringing these results together, and taking limit as the time independent horizontal area $\mathrm{d}x\,\mathrm{d}y \to 0$, leads to the thickness weighted budget for the momentum per horizontal area of an interior grid cell

$$\boxed{\begin{aligned}\partial_t\,(\mathrm{d}z\,\rho\,\mathbf{v}) = {} & \mathrm{d}z\,\mathcal{S}^{(\mathbf{v})} - \nabla_s\cdot[\,\mathrm{d}z\,\mathbf{u}\,(\rho\,\mathbf{v})] + (w^{(s)}\,\rho\,\mathbf{v})_{s=s_k} - (w^{(s)}\,\rho\,\mathbf{v})_{s=s_{k-1}} \\ & + \partial_x\,[\,\mathrm{d}z\,(\hat{\mathbf{x}}\cdot\boldsymbol{\tau} - \hat{\mathbf{x}}\,p)] + \partial_y\,[\,\mathrm{d}z\,(\hat{\mathbf{y}}\cdot\boldsymbol{\tau} - \hat{\mathbf{y}}\,p)] \\ & + [z_{,s}\,(\nabla s\cdot\boldsymbol{\tau} - p\,\nabla s)]_{s=s_{k-1}} - [z_{,s}\,(\nabla s\cdot\boldsymbol{\tau} - p\,\nabla s)]_{s=s_k} \\ & - \rho\,\mathrm{d}z\,[\,g\,\hat{\mathbf{z}} + (f+\mathcal{M})\,\hat{\mathbf{z}}\wedge\mathbf{v}].\end{aligned}} \tag{3.238}$$

Note that both the time and horizontal partial derivatives are for positions fixed on a constant generalized vertical coordinate surface. Also, the pressure force as written here is a shorthand for

the more complete contour integral formulation provided in Section 3.7 (e.g., equation (3.219)). Additionally, we have yet to take the hydrostatic approximation, so these equations are written for the three components of the velocity.

The first term on the right hand side of the thickness weighted momentum budget (3.238) is the momentum source, and the second is the convergence of advective momentum fluxes occurring within the layer. We discussed the analogous flux convergence for the tracer and mass budgets in Section 3.6.5. The third and fourth terms arise from the transport of momentum across the upper and lower constant s interfaces. The fifth and sixth terms arise from the horizontal convergence of pressure and viscous stresses. The seventh and eigth terms arise from the frictional and pressure stresses acting on the constant generalized surfaces. These forces provide an interfacial stress between layers of constant s. Note that even in the absence of frictional stresses, interfacial stresses from pressure acting on the generally curved s surface can transmit momentum between vertically stacked layers. The final term arises from the gravitational force, the Coriolis force, and the advective frequency.

3.8.3 Cell adjacent to the ocean bottom

As for the tracer and mass budgets, we assume zero mass flux through the ocean bottom at $z = -H(x, y)$. However, there is generally a nonzero stress at the bottom due to both the pressure between the fluid and the bottom, and unresolved features in the flow which can correlate or anti-correlate with bottom topographic features (Holloway (1999)). The area integral of the stresses lead to a force on the fluid at the bottom

$$\mathbf{F}_{\text{bottom}} = -\iint\limits_{z=-H} \mathrm{d}x\,\mathrm{d}y\,[\,\nabla(z+H)\cdot\boldsymbol{\tau} - p\,\nabla(z+H)]. \tag{3.239}$$

Details of the stress term requires fine scale information that is generally unavailable. For present purposes we assume that some boundary layer model provides information that is schematically written

$$\boldsymbol{\tau}^{\text{bot}} = \nabla(z+H)\cdot\boldsymbol{\tau} \tag{3.240}$$

where $\boldsymbol{\tau}^{\text{bot}}$ is a vector bottom stress. Taking the limit as the horizontal area vanishes leads to the thickness weighted budget for momentum per horizontal area of a grid cell next to the ocean bottom

$$\boxed{\begin{aligned}\partial_t\,(\mathrm{d}z\,\rho\,\mathbf{v}) = {} & \mathrm{d}z\,\mathcal{S}^{(\mathbf{v})} - \nabla_s\cdot[\,\mathrm{d}z\,\mathbf{u}\,(\rho\,\mathbf{v})] - (w^{(s)}\,\rho\,\mathbf{v})_{s=s_{kbot-1}} \\ & + \partial_x\,[\,\mathrm{d}z\,(\hat{\mathbf{x}}\cdot\boldsymbol{\tau} - \hat{\mathbf{x}}\,p)] + \partial_y\,[\,\mathrm{d}z\,(\hat{\mathbf{y}}\cdot\boldsymbol{\tau} - \hat{\mathbf{y}}\,p)] \\ & + [z_{,s}\,(\nabla s\cdot\boldsymbol{\tau} - p\,\nabla s)]_{s=s_{kbot-1}} \\ & - \boldsymbol{\tau}^{\text{bot}} + p_{\text{b}}\,\nabla(z+H) \\ & - \rho\,\mathrm{d}z\,[\,g\,\hat{\mathbf{z}} + (f+\mathcal{M})\,\hat{\mathbf{z}}\wedge\mathbf{v}].\end{aligned}} \tag{3.241}$$

3.8.4 Cell adjacent to the ocean surface

There is a nonzero mass and momentum flux through the upper ocean surface at $z = \eta(x, y, t)$, and contact stresses are applied from resolved and unresolved processes involving interactions with the atmosphere and sea ice. Following the discussion of the tracer budget at the ocean surface in

Section 3.6.7 leads to the expression for the transport of momentum into the ocean due to mass transport at the surface

$$-\iint \mathrm{d}A_{(\hat{\mathbf{n}})}\,\hat{\mathbf{n}}\cdot[(\mathbf{v}-\mathbf{v}^{\mathrm{ref}})\,\rho\,\mathbf{v} = \iint\limits_{z=\eta}\mathrm{d}x\,\mathrm{d}y\,\rho_{\mathrm{w}}\,q_{\mathrm{w}}\,\mathbf{v}. \tag{3.242}$$

The force arising from the contact stresses at the surface is written

$$\mathbf{F}_{\mathrm{contact}} = \iint\limits_{z=\eta}\mathrm{d}x\,\mathrm{d}y\,[\,\nabla\,(z-\eta)\cdot\boldsymbol{\tau} - p\,\nabla\,(z-\eta)]. \tag{3.243}$$

Bringing these results together leads to the force acting at the ocean surface

$$\mathbf{F}_{\mathrm{surface}} = \iint\limits_{z=\eta}\mathrm{d}x\,\mathrm{d}y\,[\,\nabla\,(z-\eta)\cdot\boldsymbol{\tau} - p\,\nabla\,(z-\eta) + \rho_{\mathrm{w}}\,q_{\mathrm{w}}\,\mathbf{v}]. \tag{3.244}$$

Details of the various terms in this force are generally unknown. Therefore, just as for the tracer at $z=\eta$ in Section 3.6.7, we assume that a boundary layer model provides information about the total force, and that this force is written

$$\mathbf{F}_{\mathrm{surface}} = \iint\limits_{z=\eta}\mathrm{d}x\,\mathrm{d}y\,[\,\boldsymbol{\tau}^{\mathrm{top}} - p_{\mathrm{a}}\,\nabla\,(z-\eta) + \rho_{\mathrm{w}}\,q_{\mathrm{w}}\,\mathbf{v}_{\mathrm{w}}], \tag{3.245}$$

where $\mathbf{v}_{\mathrm{w}}$ is the velocity of the fresh water. This velocity is typically taken to be equal to the velocity of the ocean currents in the top cells of the ocean model, but such is not necessarily the case when considering the different velocities of, say, river water and precipitation. The stress $\boldsymbol{\tau}^{\mathrm{top}}$ is that arising from the wind, as well as interactions between the ocean and sea ice. Letting the horizontal area vanish leads to the thickness weighted budget for a grid cell next to the ocean surface

$$\boxed{\begin{aligned}\partial_t\,(\mathrm{d}z\,\rho\,\mathbf{v}) = {}& \mathrm{d}z\,\mathcal{S}^{(\mathbf{v})} - \nabla_s\cdot[\,\mathrm{d}z\,\mathbf{u}\,(\rho\,\mathbf{v})] + (w^{(s)}\,\rho\,\mathbf{v})_{s=s_{k=1}} \\ & + \partial_x\,[\,\mathrm{d}z\,(\hat{\mathbf{x}}\cdot\boldsymbol{\tau} - \hat{\mathbf{x}}\,p)] + \partial_y\,[\,\mathrm{d}z\,(\hat{\mathbf{y}}\cdot\boldsymbol{\tau} - \hat{\mathbf{y}}\,p)] \\ & - [z_{,s}\,(\nabla s\cdot\boldsymbol{\tau} - p\,\nabla s)]_{s=s_{k=1}} \\ & + [\,\boldsymbol{\tau}^{\mathrm{top}} - p_{\mathrm{a}}\,\nabla\,(z-\eta) + \rho_{\mathrm{w}}\,q_{\mathrm{w}}\,\mathbf{v}_{\mathrm{w}}] \\ & - \rho\,\mathrm{d}z\,[\,g\,\hat{\mathbf{z}} + (f+\mathcal{M})\,\hat{\mathbf{z}}\wedge\mathbf{v}].\end{aligned}} \tag{3.246}$$

3.8.5 Horizontal momentum equations for hydrostatic fluids

We now assume the fluid to maintain a hydrostatic balance, which is the case for primitive equation ocean general circulation models. In this case, we exploit the pressure gradient body force as discussed in Section 3.7.2. Specializing the momentum budgets from Sections 3.8.2, 3.8.3, and 3.8.4 to use the hydrostatic pressure gradient force (again, interpreted according to the finite volume form given in Section 3.7) leads to the horizontal linear momentum budget for interior, bottom,

and surface grid cells

$$\boxed{\begin{aligned}[\partial_t + (f+\mathcal{M})\,\hat{\mathbf{z}}\wedge]\,(\rho\,\mathrm{d}z\,\mathbf{u}) = {} & \mathrm{d}z\,\mathcal{S}^{(\mathbf{u})} - \nabla_s\cdot[\,\mathrm{d}z\,\mathbf{u}\,(\rho\,\mathbf{u})] \\ & - \mathrm{d}z\,(\nabla_s\,p + \rho\,\nabla_s\,\Phi) \\ & + \partial_x\,(\mathrm{d}z\,\hat{\mathbf{x}}\cdot\boldsymbol{\tau}) + \partial_y\,(\mathrm{d}z\,\hat{\mathbf{y}}\cdot\boldsymbol{\tau}) \\ & - [w^{(s)}\,\rho\,\mathbf{u} - z_{,s}\,\nabla s\cdot\boldsymbol{\tau}]_{s=s_{k-1}} \\ & + [w^{(s)}\,\rho\,\mathbf{u} - z_{,s}\,\nabla s\cdot\boldsymbol{\tau}]_{s=s_k}.\end{aligned}} \tag{3.247}$$

$$\boxed{\begin{aligned}[\partial_t + (f+\mathcal{M})\,\hat{\mathbf{z}}\wedge]\,(\rho\,\mathrm{d}z\,\mathbf{u}) = {} & \mathrm{d}z\,\mathcal{S}^{(\mathbf{u})} - \nabla_s\cdot[\,\mathrm{d}z\,\mathbf{u}\,(\rho\,\mathbf{u})] \\ & - \mathrm{d}z\,(\nabla_s\,p + \rho\,\nabla_s\,\Phi) \\ & + \partial_x\,(\mathrm{d}z\,\hat{\mathbf{x}}\cdot\boldsymbol{\tau}) + \partial_y\,(\mathrm{d}z\,\hat{\mathbf{y}}\cdot\boldsymbol{\tau}) \\ & - [w^{(s)}\,\rho\,\mathbf{u} - z_{,s}\,\nabla s\cdot\boldsymbol{\tau}]_{s=s_{kbot-1}} \\ & - \boldsymbol{\tau}^{\mathrm{bottom}}\end{aligned}} \tag{3.248}$$

$$\boxed{\begin{aligned}[\partial_t + (f+\mathcal{M})\,\hat{\mathbf{z}}\wedge]\,(\rho\,\mathrm{d}z\,\mathbf{u}) = {} & \mathrm{d}z\,\mathcal{S}^{(\mathbf{u})} - \nabla_s\cdot[\,\mathrm{d}z\,\mathbf{u}\,(\rho\,\mathbf{u})] \\ & - \mathrm{d}z\,(\nabla_s\,p + \rho\,\nabla_s\,\Phi) \\ & + \partial_x\,(\mathrm{d}z\,\hat{\mathbf{x}}\cdot\boldsymbol{\tau}) + \partial_y\,(\mathrm{d}z\,\hat{\mathbf{y}}\cdot\boldsymbol{\tau}) \\ & + [\,\boldsymbol{\tau}^{\mathrm{wind}} + \rho\,q_{\mathrm{w}}\,\mathbf{u}_{\mathrm{w}}] \\ & + [\,w^{(s)}\,\rho\,\mathbf{u} - z_{,s}\,\nabla s\cdot\boldsymbol{\tau}]_{s=s_1}.\end{aligned}} \tag{3.249}$$

3.9 The Boussinesq budgets

We consider various depth-based vertical coordinates in Section 6.1. These coordinates are used to discretize the Boussinesq model equations where the volume of a parcel is conserved rather than the mass. A detailed discussion of the interpretation of the Boussinesq equations in terms of density weighted fields is given by McDougall et al. (2002) and Griffies (2004). For now, we gloss over those details by quoting the Boussinesq equations for volume, tracer, and momentum as arising from setting all density factors to the constant ρ_o, except when multiplied by the gravitational acceleration in the hydrostatic balance (i.e., for calculation of pressure and geopotential, the full density is used). The density ρ_o is a representative density of the ocean fluid. In MOM4 we set

$$\boxed{\rho_o = 1035\,\mathrm{kg/m^3},} \tag{3.250}$$

although this value can be changed via altering a parameter statement and thus recompiling the code). For much of the ocean, the *in situ* density deviates less than 3% from $1035\,\mathrm{kg\,m^{-3}}$ (see page 47 of Gill (1982)).

The replacement of density in the mass, tracer, and linear momentum budgets over a grid cell

in the ocean interior leads to the following budgets for the hydrostatic model

$$
\begin{aligned}
\partial_t(\mathrm{d}z) &= \mathrm{d}z\,\mathcal{S}^{(\mathrm{V})} - \nabla_s\cdot(\mathrm{d}z\,\mathbf{u}) - (w^{(s)})_{s=s_{k-1}} + (w^{(s)})_{s=s_k} \\
\partial_t(\mathrm{d}z\,C) &= \mathrm{d}z\,\mathcal{S}^{(\mathrm{C})} - \nabla_s\cdot[\mathrm{d}z\,(\mathbf{u}\,C+\mathbf{F})] \\
&\quad - (w^{(s)}\,C + F^{(s)})_{s=s_{k-1}} \\
&\quad + (w^{(s)}\,C + F^{(s)})_{s=s_k} \\
[\partial_t + (f+\mathcal{M})\,\hat{\mathbf{z}}\wedge]\,(\rho_o\,\mathrm{d}z\,\mathbf{u}) &= \mathrm{d}z\,\mathcal{S}^{(\mathbf{u})} - \nabla_s\cdot[\,\mathrm{d}z\,\mathbf{u}\,(\rho_o\,\mathbf{u})] \\
&\quad - \mathrm{d}z\,(\nabla_s\,p + \rho\,\nabla_s\,\Phi) \\
&\quad + \partial_x\,(\mathrm{d}z\,\hat{\mathbf{x}}\cdot\boldsymbol{\tau}) + \partial_y\,(\mathrm{d}z\,\hat{\mathbf{y}}\cdot\boldsymbol{\tau}) \\
&\quad - [w^{(s)}\,\rho_o\,\mathbf{u} - z_{,s}\,\nabla s\cdot\boldsymbol{\tau}]_{s=s_{k-1}} \\
&\quad + [w^{(s)}\,\rho_o\,\mathbf{u} - z_{,s}\,\nabla s\cdot\boldsymbol{\tau}]_{s=s_k}.
\end{aligned}
\tag{3.251}
$$

The first equation reduces to a volume budget rather than a mass budget found for the non-Boussinesq system. In this equation, $\mathcal{S}^{(\mathrm{V})}$ is a volume source with units of inverse time. Likewise, $\mathcal{S}^{(\mathbf{u})}$ is a velocity source (with units of acceleration). The Boussinesq equations for a grid cell adjacent to the ocean bottom are given by

$$
\begin{aligned}
\partial_t(\mathrm{d}z) &= \mathrm{d}z\,\mathcal{S}^{(\mathrm{V})} - \nabla_s\cdot(\mathrm{d}z\,\mathbf{u}) - (w^{(s)})_{s=s_{kbot-1}} \\
\partial_t(\mathrm{d}z\,C) &= \mathrm{d}z\,\mathcal{S}^{(\mathrm{C})} - \nabla_s\cdot[\mathrm{d}z\,(\mathbf{u}\,C+\mathbf{F})] \\
&\quad - (w^{(s)}\,C + F^{(s)})_{s=s_{kbot-1}} \\
&\quad + Q^{(\mathrm{C})}_{(\mathrm{bot})} \\
[\partial_t + (f+\mathcal{M})\,\hat{\mathbf{z}}\wedge]\,(\rho_o\,\mathrm{d}z\,\mathbf{u}) &= \mathrm{d}z\,\mathcal{S}^{(\mathbf{u})} - \nabla_s\cdot[\,\mathrm{d}z\,\mathbf{u}\,(\rho_o\,\mathbf{u})] \\
&\quad - \mathrm{d}z\,(\nabla_s\,p + \rho\,\nabla_s\,\Phi) \\
&\quad + \partial_x\,(\mathrm{d}z\,\hat{\mathbf{x}}\cdot\boldsymbol{\tau}) + \partial_y\,(\mathrm{d}z\,\hat{\mathbf{y}}\cdot\boldsymbol{\tau}) \\
&\quad - [w^{(s)}\,\rho_o\,\mathbf{u} - z_{,s}\,\nabla s\cdot\boldsymbol{\tau}]_{s=s_{kbot-1}} \\
&\quad - \boldsymbol{\tau}^{\mathrm{bottom}}
\end{aligned}
\tag{3.252}
$$

and the equations for a cell next to the ocean surface are

$$
\begin{aligned}
\partial_t\,(\mathrm{d}z) &= \mathrm{d}z\,\mathcal{S}^{(\mathrm{V})} - \nabla_s\cdot(\mathrm{d}z\,\mathbf{u}) + (w^{(s)})_{s=s_{k=1}} + \rho_o\,q_{\mathrm{w}} \\
\partial_t\,(\mathrm{d}z\,C) &= \mathrm{d}z\,\mathcal{S}^{(\mathrm{C})} - \nabla_s\cdot[\mathrm{d}z\,(\mathbf{u}\,C+\mathbf{F})] \\
&\quad + (w^{(s)}\,C + F^{(s)})_{s=s_{k=1}} \\
&\quad + (\rho_o\,q_{\mathrm{w}}\,C_{\mathrm{w}} - Q^{(\mathrm{turb})}_{(\mathrm{C})}) \\
[\partial_t + (f+\mathcal{M})\,\hat{\mathbf{z}}\wedge]\,(\rho_o\,\mathrm{d}z\,\mathbf{u}) &= \mathrm{d}z\,\mathcal{S}^{(\mathbf{u})} - \nabla_s\cdot[\,\mathrm{d}z\,\mathbf{u}\,(\rho_o\,\mathbf{u})] \\
&\quad - \mathrm{d}z\,(\nabla_s\,p + \rho\,\nabla_s\,\Phi) \\
&\quad + \partial_x\,(\mathrm{d}z\,\hat{\mathbf{x}}\cdot\boldsymbol{\tau}) + \partial_y\,(\mathrm{d}z\,\hat{\mathbf{y}}\cdot\boldsymbol{\tau}) \\
&\quad + [\,\boldsymbol{\tau}^{\mathrm{wind}} + \rho_o\,q_{\mathrm{w}}\,\mathbf{u}_{\mathrm{w}}] \\
&\quad + [\,w^{(s)}\,\rho_o\,\mathbf{u} - z_{,s}\,\nabla s\cdot\boldsymbol{\tau}]_{s=s_1}.
\end{aligned}
\tag{3.253}
$$

CHAPTER
FOUR

The hydrostatic pressure force

The purpose of this chapter is to detail issues related to computing the pressure force in hydrostatic ocean models. Care is taken to split the pressure force into its slow and fast components, thus facilitating a split of the momentum equation for use in an explicit time stepping scheme for the momentum equation.

In Section 3.7, we encountered two formulations of the pressure force. The first computes the pressure gradient body force (Section 3.7.2), and considers the pressure force to be acting at a point. This interpretation follows from a finite difference interpretation of the velocity equation, following the energetic approach of Bryan (1969) and all versions of MOM. The second formulation applies a finite volume interpretation advocated in Chapter 3, with particular attention given to the contour integral form of pressure as derived in Section 3.7.1. The finite volume approach does *not* lend itself to straightforward energetic conversion arguments (Chapter 10). It is for this reason that we maintain the finite difference approach of Bryan (1969) in MOM4p1.

4.1 Hydrostatic pressure forces at a point

A hydrostatic fluid maintains the balance

$$p_{,z} = -\rho\, g. \tag{4.1}$$

This balance means that the pressure at a point in a hydrostatic fluid is determined by the weight of fluid above this point. This relation is maintained quite well in the ocean on spatial scales larger than roughly 1km. Precisely, when the squared ratio of the vertical to horizontal scales of motion is small, then the hydrostatic approximation is well maintained. In this case, the vertical momentum budget reduces to the hydrostatic balance, in which case vertical acceleration and friction are neglected. If we are interested in explicitly representing such motions as Kelvin-Helmholtz billows and flow within a convective chimney, vertical accelerations are nontrivial and so the non-hydrostatic momentum budget must be used.

The hydrostatic balance greatly affects the algorithms used to numerically solve the equations of motion. Marshall et al. (1997) highlight these points in the context of developing an algorithm suited for both hydrostatic and non-hydrostatic simulations. However, so far no long-term global

climate simulations have been run at resolutions sufficiently refined to require the non-hydrostatic equations. Additionally, many regional and coastal models, even some with grid resolutions finer than 1km, still maintain the hydrostatic approximation, and thus they must parameterize the unrepresented non-hydrostatic motions.

As discussed in Section 3.7.2, at a point in the continuum, the horizontal acceleration arising from pressure differences in a hydrostatic and non-Boussinesq fluid can be written[1]

$$\begin{aligned} \rho^{-1} \nabla_z p &= \rho^{-1} \left(\nabla_s - \nabla_s z \, \partial_z \right) p \\ &= \rho^{-1} \nabla_s p + g \, \nabla_s z \\ &= \rho^{-1} \left(\nabla_s p + \rho \, \nabla_s \Phi \right) \end{aligned} \tag{4.2}$$

where the hydrostatic relation $p_{,z} = -\rho g$ was used to reach the second equality, and

$$\Phi = g z \tag{4.3}$$

is the geopotential. The general expression for the horizontal pressure gradient to evaluate in an ocean model is thus given by

$$\boxed{\nabla_z p = \nabla_s p + \rho \, \nabla_s \Phi} \tag{4.4}$$

For cases where the density is constant on s surfaces, we can combine the two terms on the right hand side into the gradient of a scalar, thus rendering a horizontal pressure gradient force with a zero curl. This special case holds for geopotential and pressure coordinates and isopycnal coordinates in the special case of an idealized linear equation of state. However, it does not hold in the more general case, in which the difficulty of numerically computing the acceleration from pressure arises when there are contributions from *both* terms. Generally, both terms can be large and of opposite sign in many regions. In this case, the simulation is exposed to nontrivial numerical truncation errors that can, for example, lead to spurious pressure gradients that spin up an unforced fluid with initially flat isopycnals. However, in certain cases one term dominates, in which case an accurate pressure gradient is simpler to compute numerically.

Significant effort has gone into reducing such *pressure gradient errors*, especially in terrain following models where undulations of the coordinate surfaces can be large with realistic bottom topography (e.g., see Figure 6.3). Some of these issues are summarized in Section 2 of Griffies et al. (2000a). Perhaps the most promising approach is that proposed by Shchepetkin and McWilliams (2002). It is notable that difficulties with pressure gradient errors have largely been responsible for the near absence of sigma models being used for long term global ocean climate simulations.[2]

4.2 Pressure gradient body force

As stated above, the presence of both terms on the right hand side of equation (4.4) complicates the numerical implementation of the horizontal pressure gradient force. The problem is that numerical errors in one term are often not compensated by the other term, and such can lead to spurious flows. For the quasi-horizontal depth based and pressure based coordinates supported by MOM4p1 (i.e., $s = z$, $s = z^*$, $s = p$, or $s = p^*$; see Chapter 6), these errors are quite small.

[1] To obtain this result for a Boussinesq fluid, multiply both sides of equation (4.2) by ρ/ρ_o.

[2] The work of Diansky et al. (2002) is the only case known by the author of a global sigma model used for climate purposes.

The reason is that these choices ensure that one of the two terms appearing in equation (4.4) is significantly smaller than the other. Nonetheless, it is useful to provide a formulation that even further reduces the potential for errors for both the quasi-horizontal coordinates, as well as the terrain following coordinates $\sigma^{(z)}$ and $\sigma^{(p)}$ (Chapter 6).

In addition to reducing errors associated with a numerical computation of the pressure gradient, we aim to split the pressure gradient into two terms associated with the slowly evolving internal modes and the faster barotropic mode. Details of this split are a function of the vertical coordinate. This split in the pressure gradient then facilitates our treatment of the vertically integrated momentum equations, as discussed in Section 7.7.

In the following, we are motivated by the formulation of the pressure gradient commonly applied to z-models. Adcroft and Campin (2004) extended this treatment to the z^* vertical coordinate. We take it one more step in order to handle all vertical coordinates supported by MOM4p1. Hallberg (1997) goes further by treating the pressure gradient in isopycnal layered models using a realistic equation of state, and Adcroft et al. (2008) present a more accurate approach for generlized vertical coordinate models.

4.2.1 Depth based vertical coordinates

As mentioned on page 47 of Gill (1982), *in situ* density in the bulk of the ocean deviates less than 3% from the constant density

$$\rho_o = 1035\,\mathrm{kg/m^3}. \tag{4.5}$$

The hydrostatic pressure associated with this constant density has no horizontal gradients, and so it does not contribute to horizontal pressure gradient forces. For increased accuracy computing the horizontal pressure gradient, it is useful to remove this term from the calculation of hydrostatic pressure. For this purpose, we write the hydrostatic balance as

$$\begin{aligned} p_{,z} &= -g\,\rho \\ &= -g\,(\rho_o + \rho'), \end{aligned} \tag{4.6}$$

which has an associated split in the hydrostatic pressure field

$$p = p_\mathrm{a} + p_o(z) + p'(x, y, z, t). \tag{4.7}$$

We can solve for the pressures by assuming

$$p_o(z = \eta) = 0 \tag{4.8}$$

$$p'(z = \eta) = 0, \tag{4.9}$$

which leads to

$$\boxed{\begin{aligned} p_o &= -g\,\rho_o\,(z - \eta) \\ &= -\rho_o\,\Phi + g\,\rho_o\,\eta, \end{aligned}} \tag{4.10}$$

$$\boxed{p' = g \int_z^\eta \rho'\,\mathrm{d}z,} \tag{4.11}$$

and thus

$$\boxed{p = p_\mathrm{a} + g\,\rho_o\,\eta - \rho_o\,\Phi + p'.} \tag{4.12}$$

Splitting off the free surface height is advantageous as it allows for a split of the pressure gradient into its fast two dimensional barotropic contributions and slow three dimensional baroclinic contributions. This split in pressure gradient facilitates the development of a split-explicit time stepping method for the momentum equations considered in Section 7.7. Details of the split in pressure are dependent on the vertical coordinate choice. We now discuss the three depth based vertical coordinates used in MOM4p1.

4.2.1.1 Geopotential vertical coordinates

We first consider the horizontal pressure gradient realized with geopotential vertical coordinates. We are here motivated by the desire to split the dynamics into fast and slow portions, as approximated by depth integrating the momentum equation (Section 7.7).

The anomalous pressure p' maintains a dependence on surface height through the upper limit on the vertical integral in equation (4.11). When working with geopotential vertical coordinates, it is very convenient to isolate this dependence by exploiting a very accurate approximation described below. This split then allows us to exclusively place the surface height dependent pressure gradient into the vertically integrated momentum equation. The slow component to the pressure gradient then has no dependence on the surface height; it is instead just a function of the anomalous density. The slow pressure gradient component thus vanishes when the density is horizontally unstratified; i.e., when there is no baroclinicity.

To facilitate the split described above, we proceed in the following manner

$$\begin{aligned} p' =& g \int_z^{\eta} \rho' \, \mathrm{d}z \\ =& g \int_z^{0} \rho' \, \mathrm{d}z + g \int_0^{\eta} \rho' \, \mathrm{d}z \\ \approx& g \int_z^{0} \rho' \, \mathrm{d}z + g \, \eta \, \rho'_{\mathrm{surf}} \\ \equiv& p'_{\mathrm{clinic}} + p'_{\mathrm{surf}}. \end{aligned} \tag{4.13}$$

The approximation made in the third step remains good where density is well mixed between $z = 0$ and $z = \eta$, and this is generally the case for large scale modelling. Here, density in the surface region of the ocean is assumed to take on the value

$$\rho_{\mathrm{surf}} = \rho_o + \rho'_{\mathrm{surf}}, \tag{4.14}$$

which is a function of horizontal position and time. The anomalous pressure p' has therefore been separated into two pressures, where the anomalous *surface pressure*

$$p'_{\mathrm{surf}} = \rho'_{\mathrm{surf}} \, g \, \eta \tag{4.15}$$

is a function of the surface height and surface density, and the pressure

$$p'_{\mathrm{clinic}} = g \int_z^{0} \rho' \, \mathrm{d}z \tag{4.16}$$

is the anomalous hydrostatic *baroclinic pressure* within the region from a depth $z < 0$ to $z = 0$. Again, the baroclinic pressure is independent of the surface height, and so its horizontal gradients are only a function of density.

This split of pressure thus renders the horizontal pressure gradient (equation (4.4))

$$\boxed{\begin{aligned}(\nabla_z\, p)_{\text{approx}} &= \nabla_s\, p + \rho\, \nabla_s\, \Phi \\ &= \nabla_s\, (p_{\text{a}} + g\, \rho_o\, \eta - \rho_o\, \Phi + p') + \rho\, \nabla_s\, \Phi \\ &\approx \nabla\, (p_{\text{a}} + g\, \rho_o\, \eta + p'_{\text{surf}}) + \nabla_s\, p'_{\text{clinic}} + (\rho - \rho_o)\, \nabla_s\, \Phi \\ &= \underbrace{\nabla\, (p_{\text{a}} + g\, \rho_{\text{surf}}\, \eta)}_{\text{fast}} + \underbrace{\nabla_s\, p'_{\text{clinic}} + \rho'\, \nabla_s\, \Phi}_{\text{slow}}.\end{aligned}} \tag{4.17}$$

In a geopotential vertical coordinate model, interior grid cells are discretized at levels of constant geopotential. Hence, the gradient ∇_s reduces to the constant geopotential gradient ∇_z. In this case the horizontal gradient of the geopotential vanishes, $\nabla_z\, \Phi = 0$. At the bottom, however, MOM4p1 employs bottom partial step topography (Pacanowski and Gnanadesikan, 1998). The bottom cells are thus *not* discretized along a constant geopotential. Hence, just at the bottom, there is a nontrivial gradient of the geopotential Φ (see Figure 6.1). In general, note how the geopotential is multiplied by the anomalous density $\rho' = \rho - \rho_o$, thus minimizing the impact of this term.

4.2.1.2 z^* and $\sigma^{(z)}$ vertical coordinate

The new issue that arises when moving away from geopotential coordinates is that the geopotential $\Phi = g\, z$ has a nonzero along coordinate gradient in the interior, whereas with geopotential coordinates it remains nonzero only along the partial bottom stepped topography. The presence of Φ gradients in the interior is fundamental.

Following the discussion in Section 4.2.1, we are led to the following expressions for the horizontal pressure gradient. The exact expression relevant for the z^* and $\sigma^{(z)}$ coordinates is given by

$$\boxed{\begin{aligned}(\nabla_z\, p)_{\text{exact}} &= \nabla_s\, p + \rho \nabla_s\, \Phi \\ &= \nabla_s\, (p_{\text{a}} + p_o + p') + \rho\, \nabla_s\, \Phi \\ &= \nabla_s\, (p_{\text{a}} - \rho_o\, \Phi + g\, \rho_o\, \eta + p') + \rho\, \nabla_s\, \Phi \\ &= \underbrace{\nabla\, (p_{\text{a}} + g\, \rho_o\, \eta)}_{\text{fast}} + \underbrace{\nabla_s\, p' + \rho'\, \nabla_s\, \Phi}_{\text{slow}}.\end{aligned}} \tag{4.18}$$

Note that we have *assumed* that the geopotential falls inside the slow portion of the pressure gradient. This assumption is made *even though* the depth of a grid point is a function of the undulating surface height. The validity of this assumption can be assessed by the integrity and stability of the simulation.

To facilitate a unified treatment in subsequent manipulations, we define

$$\begin{aligned} p_{\text{surf}} &= \rho_{\text{surf}}\, g\, \eta \quad & s = z \\ p_{\text{surf}} &= \rho_0\, g\, \eta \quad & s = z^*, \sigma^{(z)} \end{aligned} \tag{4.19}$$

and

$$\begin{aligned} p' &= g\, \textstyle\int_z^0 \rho'\, \mathrm{d}z \quad & s = z \\ p' &= g\, \textstyle\int_z^\eta \rho'\, \mathrm{d}z \quad & s = z^*, \sigma^{(z)}. \end{aligned} \tag{4.20}$$

In both the exact and aproximated pressure gradient expressions, the geopotential gradient $\nabla_s \Phi$ in the ocean interior is weighted by the small density deviation $\rho' = \rho - \rho_o$. For quasi-horizontal depth-based vertical coordinates supported in MOM4p1 (Section 6.1), the horizontal gradient of the geopotential is small, and the ρ' weighting further reduces its contribution. For terrain following coordinates, the horizontal gradient term is not small, and the ρ' weighting is essential to reduce its magnitude.

4.2.2 A test case for zero cross-coordinate flow

In the development of generalized vertical coordinates, a useful test case was suggested by Alistair Adcroft. We focus here on the special case of $s = z^*$. In this test, initialize the density field as a function only of the vertical coordinate z^*. The domain is flat bottomed and doubly periodic in the horizontal, thus precluding pressure gradients due to side boundaries or topography. In a state of rest, there is no horizontal pressure gradients, and so no motion. As a body force is applied to the barotropic equations, such as through an ideal tidal forcing, there will now be a nontrivial surface height field η as well as a nontrivial barotropic velocity. Both pieces of the slow contribution to the horizontal pressure gradient (4.18) develop a nontrivial vertical structure, and this will initiate baroclinic structure and thus a nonzero cross coordinate vertical velocity $w^{(s)}$. This cross coordinate velocity will be much smaller in the $s = z^*$ case than with $s = z$, given than z^* follows the motion of the free surface.

In order to further test the integrity of the z^* implementation, we wish to truncate the pressure calculation in this test so that there will be no slow pressure gradients developed when the tidal forcing is applied, and hence there will be no cross coordinate motion. For this purpose, truncate the slow piece of the horizontal pressure gradient (4.18) as

$$\nabla_s p' + \rho' \nabla_s \Phi \rightarrow \nabla_s p'_{\text{truncate}}. \tag{4.21}$$

In this truncation, we drop the geopotential term $\rho' \nabla_s \Phi$, as this term will produce nontrivial horizontal gradients as the surface height undulates. We also introduce a truncated perturbation pressure determined by

$$\begin{aligned} p' &= g \int_z^{\eta} \rho' \, \mathrm{d}z \\ &= g \int_{s(z)}^{s(\eta)} \rho' \, z_{,s} \, \mathrm{d}s \\ &= g \, (1 + \eta/H) \int_{z^*}^{0} \rho' \, \mathrm{d}z^* \\ &= p'_{\text{truncate}} + (g \, \eta/H) \int_{z^*}^{0} \rho' \, \mathrm{d}z^*. \end{aligned} \tag{4.22}$$

To reach the penultimate step, we used $z_{,s} = (1 + \eta/H)$ for $s = z^*$. The coordinate increments used to define the pressure field p'_{truncate} are static in a model discretizing the vertical according to $s = z^*$. Hence, $\nabla_s p'_{\text{truncate}} = 0$ if the density is a function only of z^*. So when the model's slow pressure field is comprised of just p'_{truncate}, the ideal tidal test in the torus should maintain zero cross coordinate flow, $w^{z^*} = 0$, even as the surface height fluctuates. Testing to see that this property is maintained is a useful means for evaluating the integrity of the algorithm.

4.2.3 Pressure based vertical coordinates

A complementary discussion to the above is now given for pressure based vertical coordinates. Since for pressure based vertical coordinates we solve for the bottom pressure, it is useful to formulate the geopotential in terms of the bottom pressure rather than the atmospheric pressure. For this purpose, consider the following identities

$$\begin{aligned}
\Phi + g\,H &= g \int_{-H}^{z} \mathrm{d}z \\
&= g \int_{p_\mathrm{b}}^{p} z_{,p}\,\mathrm{d}p \\
&= -\int_{p_\mathrm{b}}^{p} \rho^{-1}\,\mathrm{d}p \\
&= -\int_{p_\mathrm{b}}^{p} (\rho_o^{-1} + \rho^{-1} - \rho_o^{-1})\,\mathrm{d}p \\
&= (p_\mathrm{b} - p)/\rho_o + \rho_o^{-1} \int_{p_\mathrm{b}}^{p} (\rho'/\rho)\,\mathrm{d}p \\
&= (p_\mathrm{b} - p)/\rho_o - (g/\rho_o) \int_{-H}^{z} \rho'\,\mathrm{d}z.
\end{aligned} \tag{4.23}$$

We are thus led to

$$\boxed{\rho_o\,\Phi = p_\mathrm{b} - p + \rho_o\,(\Phi_\mathrm{b} + \Phi'),} \tag{4.24}$$

where

$$\boxed{\rho_o\,\Phi' = -g \int_{-H}^{z} \rho'\,\mathrm{d}z.} \tag{4.25}$$

is an anomalous geopotential similar to the anomalous hydrostatic pressure introduced in Section 4.2.1, and

$$\Phi_\mathrm{b} = -g\,H \tag{4.26}$$

is the geopotential at the ocean bottom. The horizontal pressure force is therefore written

$$\boxed{\begin{aligned}
\nabla_s\,p + \rho\,\nabla_s\,\Phi &= \nabla_s\,p + (\rho/\rho_o)\,\nabla\,(p_\mathrm{b} + \rho_o\,\Phi_\mathrm{b}) - (\rho/\rho_o)\,\nabla_s\,p + \rho\,\nabla_s\,\Phi' \\
&= \underbrace{(\rho/\rho_o)\,\nabla\,(p_\mathrm{b} + \rho_o\,\Phi_\mathrm{b})}_{\text{fast}} + \underbrace{\rho\,\nabla_s\,\Phi' - (\rho'/\rho_o)\,\nabla_s\,p}_{\text{slow}}.
\end{aligned}} \tag{4.27}$$

Note that the three-dimensional pressure term $(\rho'/\rho_o)\,\nabla_s\,p$ is weighted by the generallly very small density deviation $\rho' = \rho - \rho_o$. For the non-terrain following quasi-horizontal pressure-based vertical coordinates supported in MOM4p1 (Section 6.2), the horizontal gradient of the pressure

is small, and the weighting by (ρ'/ρ_o) further reduces its contribution. Also note that the *fast* contribution is here weighted by the density, and so this term may appear to require further splitting into $\rho = \rho_o + \rho'$ before identifying the fast two dimensional contribution. However, as the nonBoussinesq formulation here considers momentum per area, the baroclinic velocity includes density weighting (see equation (8.1)). This is how we are to split the horizontal momentum equations into fast two dimensional motions and slow three dimensional motions for purposes of time stepping. We consider these issues further in Sections 7.7 and 8.1.

During the testing of this formulation for the pressure gradient, we found it useful to write the anomalous geopotential in the following form

$$\begin{aligned} -(\rho_o/g)\,\Phi' &= \int_{-H}^{z} \rho'\,\mathrm{d}z \\ &= \int_{-H}^{\eta} \rho'\,\mathrm{d}z - \int_{z}^{\eta} \rho'\,\mathrm{d}z \\ &= \frac{p_\mathrm{b} - p_\mathrm{a}}{g} - \rho_o\,(H+\eta) - \int_{z}^{\eta} \rho'\,\mathrm{d}z \\ &= \frac{p_\mathrm{b} - p_\mathrm{a} - p'}{g} - \rho_o\,(H+\eta). \end{aligned} \tag{4.28}$$

To reach this result, we used the hydrostatic balance for the full ocean column,

$$\int_{-H}^{\eta} \rho'\,\mathrm{d}z = \frac{p_\mathrm{b} - p_\mathrm{a}}{g} - \rho_o\,(H+\eta) \tag{4.29}$$

as well as the definition (4.11) of the anomalous hydrostatic pressure

$$p' = g \int_{z}^{\eta} \rho'\,\mathrm{d}z \tag{4.30}$$

used in Section 4.2.1 for the depth based vertical coordinates. These results then lead to the identiy

$$p_\mathrm{b} + \rho_o\,(\Phi_\mathrm{b} + \Phi') = p' + p_\mathrm{a} + \rho_o\,g\,\eta. \tag{4.31}$$

4.3 Pressure gradient body force in B-grid MOM4p1

We now detail how the pressure gradient body force is represented in the B-grid generalized level coordinate version of MOM4p1. As the pressure force acts to accelerate a fluid parcel, our aim is to determine the pressure force acting at the velocity cell point. Much in the derivation of the pressure force depends on assumptions regarding where pressure is computed in the discrete model. For the B-grid version of MOM4p1, hydrostatic pressure is coincident with the tracer fields as shown in Figure 3.9, which illustrates a typical case where a grid cell is bounded by vertical sidewalls with generally nonhorizontal tops and bottoms.

As mentioned in Section 3.7.2, we prefer to discretize the pressure gradient body force as it facilitates the splitting of the pressure force into fast and slow components. The result here is a derivation of the Pacanowski and Gnanadesikan (1998) discrete pressure gradient body force as originally implemented for the treatment of partial step bottom topography. Their discussion is relevant here, since the pressure gradient force in the presence of partial step bottoms must account for the pressure between cells that live at different depths. This is also the essential issue for the treatment of pressure with the generalized level coordinates of MOM4p1.

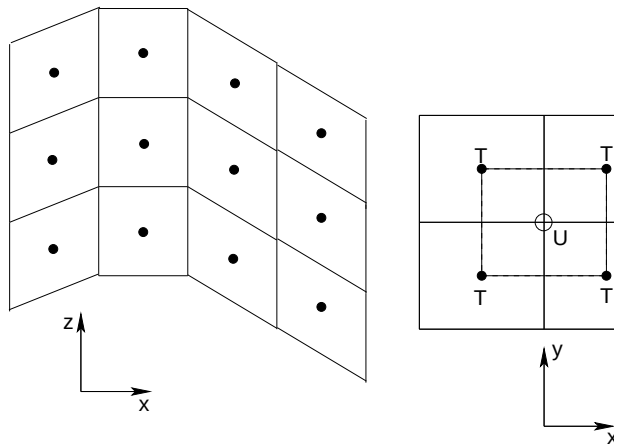

Figure 4.1: The left panel shows a set of grid cells in the x-z plane for a generalized level coordinate version of MOM4p1. The center point represents a tracer point. As active tracers determine density, and as density determines hydrostatic pressure, the hydrostatic pressure is coincident with tracer. For the x-y plane shown in the right panel, the velocity and tracer are offset, with the velocity at the northeast corner of the tracer cell according to the B-grid arrangement. The velocity cell, shown surrounding the velocity point, has a thickness set according to the minimum of the surrounding four tracer cell thicknesses. Hence, a velocity point and tracer point with the same discrete vertical index k generally live at different depths.

4.3.1 Depth based vertical coordinates

The aim here is to discretize the pressure gradient body force written in the forms (4.18) and (4.17)

$$\nabla_s\, p + \rho \nabla_s\, \Phi = \nabla\, (p_{\mathrm{a}} + p_{\mathrm{surf}}) + \nabla_s\, p' + \rho'\, \nabla_s\, \Phi, \tag{4.32}$$

where p_{surf} and p' are defined according to equations (4.19) and (4.20), respectively. Our focus here is the slowly evolving three dimensional terms $\nabla_s\, p' + \rho'\, \nabla_s\, \Phi$. The first term is straightforward to discretize according to the assumptions regarding the placement of pressure given in Figure 4.1. In the right panel of this figure, we see that pressure is available at the corners of the velocity cell. Hence, to approximate pressure at the west and east faces of the cell, one can average the pressure found at the corners. A grid weighted average may be appropriate, but the simplest method is an unweighted average in which

$$\boxed{\nabla_s\, p' \approx \hat{\mathbf{x}}\, FDX_NT(FAY(p')) + \hat{\mathbf{y}}\, FDY_ET(FAX(p'))} \tag{4.33}$$

The averaging operators are defined according to

$$\begin{aligned} 2\,\overline{a_i}^{x} &= (a_{i+1} + a_i) \\ &= FAX(a) \end{aligned} \tag{4.34}$$

and

$$\begin{aligned} 2\,\overline{a_j}^{y} &= (a_{j+1} + a_j) \\ &= FAY(a) \end{aligned} \tag{4.35}$$

with the second expression in each equation exposing the notation used in the ocean model code. Additionally, finite difference operators have been introduced

$$\begin{aligned} FDX_NT(a) &= \frac{a_{i+1} - a_i}{dxu_{i,j}}. \\ FDY_ET(a) &= \frac{a_{j+1} - a_j}{dyu_{i,j}}. \end{aligned} \tag{4.36}$$

These operators are used for fields that live at the north face and east face, respectively, of a tracer cell.

The geopotential contribution in (4.32) is computed using the geopotential values at the tracer points, and so its gradient is located at the tracer cell faces. To have the density multiplier at the same point requires that it be averaged prior to multiplying. Finally, an orthogonal spatial average is required to place the product onto the velocity point. The result is given by

$$\boxed{\rho'\,\nabla_s\,\Phi \approx \hat{\mathbf{x}}\left[FAY[\delta_i\Phi\;FAX(\rho')]/dxu_{i,j}\right] + \hat{\mathbf{y}}\left[FAX[\delta_j\Phi\;FAY(\rho')]/dyu_{i,j}\right].} \tag{4.37}$$

4.3.2 Pressure based vertical coordinates

The aim is to discretize the pressure gradient body force written in the form (4.27)

$$\nabla_s\,p + \rho\,\nabla_s\,\Phi = (\rho/\rho_o)\,\nabla\,(p_{\mathrm{b}} + \rho_o\,\Phi_{\mathrm{b}}) + \rho\,\nabla_s\,\Phi' - (\rho'/\rho_o)\,\nabla_s\,p \tag{4.38}$$

and to do so in a manner analogous to the Boussinesq case. In particular, we consider here the slow three dimensional contribution $\rho\,\nabla_s\,\Phi' - (\rho'/\rho_o)\,\nabla_s\,p$ and write for the pressure term

$$\boxed{\rho'\,\nabla_s\,p \approx \hat{\mathbf{x}}\left[FAY[\delta_i p\;FAX(\rho')]/dxu_{i,j}\right] + \hat{\mathbf{y}}\left[FAX[\delta_j p\;FAY(\rho')]/dyu_{i,j}\right],} \tag{4.39}$$

which is analogous to the discrete $\rho'\,\nabla_s\,\Phi$ contribution in equation (4.37). The geopotential term is discretized as

$$\boxed{\rho\,\nabla_s\,\Phi' \approx \hat{\mathbf{x}}\,\rho\;FDX_NT\,(FAY(\Phi')) + \hat{\mathbf{y}}\,\rho\;FDY_ET\,(FAX(\Phi')),} \tag{4.40}$$

which is analogous to the discrete version of $\nabla_s\,p'$ in equation (4.33). Note that the density ρ in equation (4.40) is centered on the velocity cell.

CHAPTER
FIVE

Parameterizations with generalized level coordinates

The parameterization of subgrid scale (SGS) processes is of fundamental importance to ocean models. Details of how these processes are parameterized depend on the choice of vertical coordinates. The purpose of this chapter is to describe how various SGS parameterizations are formulated with generalized level coordinates of MOM4p1. As we will see, by diagnosing the vertical grid cell thicknesses according to the methods described in Section 7.3, parameterizations implemented in the geopotential MOM4.0 code remain algorithmically unaltered when converting to the generalized level coordinate MOM4p1.

5.1 Friction

The convergence of frictional stress leads to a friction force acting on fluid parcels. The purpose of this section is to detail the form of friction appearing in the generalized level coordinates of MOM4p1. For this purpose, we follow much of the discussion in Chapter 17 of Griffies (2004). In particular, Section 17.3.4 leads us to take the physical components to the frictional stress tensor in the form

$$\boldsymbol{\tau} = \begin{pmatrix} \tau^{xx} & \tau^{xy} & \rho\,\kappa\,u_{,z} \\ \tau^{xy} & -\tau^{xx} & \rho\,\kappa\,v_{,z} \\ \rho\,\kappa\,u_{,z} & \rho\,\kappa\,v_{,z} & 0 \end{pmatrix}, \tag{5.1}$$

where κ is a non-negative viscosity with units $\mathrm{m}^2\,\mathrm{s}^{-1}$. Taking $\tau^{33} = 0$ is consistent with use of the hydrostatic approximation, which reduces the vertical momentum equation to the inviscid hydrostatic balance. We comment in Section 5.1.3 on the form of the two-dimensional transverse elements τ^{xx} and τ^{xy}.

5.1.1 Vertical friction

As the gravitational force is so critical to stratified fluids close to a hydrostatic balance, it is typical in ocean modelling to single out the vertical direction. In particular, closures for the unresolved vertical exchange of momentum are usually taken to be proportional to the vertical derivative, or shear, of the horizontal velocity field. This argument leads to the form of the stress tensor given by equation (5.1). For a generalized level coordinate model, the vertical shear elements take the

form

$$\rho\,\kappa\,\mathbf{u}_{,z} = \rho\,\kappa\,s_{,z}\,\mathbf{u}_{,s}. \tag{5.2}$$

In MOM4p1, the left hand side of this expression is numerically evaluated for purposes of computing the vertical shear. That is, vertical derivatives are computed for arbitrary vertical coordinates just as in geopotential coordinates. This result follows by diagnosing the vertical grid cell thicknesses using the methods described in Section 7.3, where we make use of the relation between vertical coordinates

$$\mathrm{d}z = z_{,s}\,\mathrm{d}s. \tag{5.3}$$

Now return to the thickness weighted momentum budget for a grid cell discussed in Section 3.8. The above considerations lead us to write the frictional stress acting on a generalized surface as

$$\begin{aligned} z_{,s}\,\nabla s\cdot\boldsymbol{\tau} &= (\hat{\mathbf{z}}-\mathbf{S})\cdot\boldsymbol{\tau} \\ &\approx \hat{\mathbf{z}}\cdot\boldsymbol{\tau} \\ &= \rho\,\kappa\,\mathbf{u}_{,z}. \end{aligned} \tag{5.4}$$

The second step used the small angle approximation to drop the extra slope term. Alternatively, we can interpret the dia-surface frictional stress $z_{,s}\,\nabla s\cdot\boldsymbol{\tau}$ as parameterized by $\rho\,\kappa\,\mathbf{u}_{,z}$. Either way, the result (5.4) is the form that vertical frictional stress is implemented in MOM4p1.

5.1.2 A comment on nonlinear vertical friction

As noted above, we choose in MOM4p1 to implement vertical friction, and vertical tracer diffusion (Section 5.2.1) just as in a geopotential coordinate model. This method is facilitated by diagnosing the vertical thickness of a grid cell according to equation (5.3) (see Section 7.3), prior to computing vertical derivatives.

We now mention an alternative method, *not implemented in MOM4p1*, since this method is often seen in the literature. The alternative is to compute the vertical shear according to the right hand side of equation (5.2). The density weighted inverse specific thickness $\rho/z_{,s}$ adds a nonlinear term to the vertical friction, and this complicates the numerical treatment (Hallberg, 2000). It is reasonable to approximate this factor by a constant for the dimensionful quasi-horizontal coordinates considered in Sections 6.1 and 6.2.[1] For the Boussinesq case with depth-based vertical coordinates, this approximation results in

$$\rho\,\kappa/z_{,s} \approx \rho_o\,\kappa, \tag{5.5}$$

where $z_{,s}\approx 1$ follows from the results for all but the sigma coordinate in Table 6.1. The vertical friction therefore becomes

$$\begin{aligned} (\rho\,\kappa\,\mathbf{u}_{,z})_{,z} &\approx \rho_o\,s_{,z}\,(\kappa\,s_{,z}\,\mathbf{u}_{,s})_{,s} \\ &\approx \rho_o\,(\kappa\,\mathbf{u}_{,s})_{,s}. \end{aligned} \tag{5.6}$$

Likewise, dimensionful pressure-based coordinates used for non-Boussinesq fluids have

$$\rho\,\kappa/z_{,s} \approx -g\,\rho_o^2\,\kappa, \tag{5.7}$$

[1] Terrain following sigma coordinates, which are dimensionless, are notable exceptions to this result.

as follows for all but the sigma coordinate in Table 6.2. The vertical friction therefore becomes

$$(\rho\,\kappa\,\mathbf{u}_{,z})_{,z} \approx \rho_o\,(g\,\rho_o)^2\,(\kappa\,\mathbf{u}_{,s})_{,s}. \tag{5.8}$$

The above approximations are well motivated physically since the value of the vertical viscosity is not known to better than 10%, and the above approximations are well within this range for vertical coordinates whose iso-surfaces are quasi-horizontal. Similar arguments were presented by Losch et al. (2004). Additionally, the approximations are very conveinent numerically since they allow us to continue implementing vertical physical processes in a linear manner as traditionally handled in z-models. Such facilitates straightforward time implicit methods to stably handle large vertical viscosities. Without these approximations, or without use of the geopotential-based approach described above in Section 5.1.1, vertical physical processes are nonlinear. Arbitrarily stable numerical methods for such processes require an iterative scheme such as that discussed by Hallberg (2000) employed in isopycnal models.

5.1.3 Lateral friction

There is no fundamental theory to prescribe the form of lateral friction at the resolutions available for large scale ocean modelling. Indeed, many argue that the form commonly used in models is wrong (Holloway, 1992). We take the perspective that lateral friction in ocean models provides a numerical closure. This perspective motivates us to prescribe friction in a manner that maintains basic symmetry properties of the physical system, and which is convenient to implement.

The deformation rates are a basic element of the lateral frictional stress. Using generalized orthogonal horizontal coordinates and z for the vertical, the deformation rates given in Section 17.7.1 of Griffies (2004) take the form

$$e_{\mathrm{T}} = (\mathrm{d}y)\,(u/\mathrm{d}y)_{,x} - (\mathrm{d}x)\,(v/\mathrm{d}x)_{,y} \tag{5.9}$$

$$e_{\mathrm{S}} = (\mathrm{d}x)\,(u/\mathrm{d}x)_{,y} + (\mathrm{d}y)\,(v/\mathrm{d}y)_{,x} \tag{5.10}$$

where $\mathrm{d}x$ and $\mathrm{d}y$ are the infinitesimal horizontal grid increments. Consistent with lateral friction being considered a numerical closure, we place no fundamental importance on the horizontal derivatives being taken on constant z surfaces. Hence, we propose to use the *same* mathematical form for the deformation rates regardless the vertical coordinate. That is, for the generalized level coordinate MOM4p1, the deformation rates are computed according to the lateral strains within surfaces of constant vertical coordinate.

As shown in the Appendix to Griffies and Hallberg (2000), and further detailed in Section 17.10 of Griffies (2004), the divergence of the thickness weighted lateral stress within a layer, $\nabla \cdot \boldsymbol{\tau}$, leads to the thickness weighted forces per volume acting in the generalized horizontal directions

$$\begin{aligned} \mathrm{d}z\,\rho\,F^x &= (\mathrm{d}y)^{-2}\,[(\mathrm{d}y)^2\,\mathrm{d}z\,\tau^{xx}]_{,x} + (\mathrm{d}x)^{-2}\,[(\mathrm{d}x)^2\,\mathrm{d}z\,\tau^{xy}]_{,y} \\ \mathrm{d}z\,\rho\,F^y &= (\mathrm{d}x)^{-2}\,[(\mathrm{d}x)^2\,\mathrm{d}z\,\tau^{yy}]_{,y} + (\mathrm{d}y)^{-2}\,[(\mathrm{d}y)^2\,\mathrm{d}z\,\tau^{xy}]_{,x}. \end{aligned} \tag{5.11}$$

We extend the forms for the stress tensor given in Chapter 17 of Griffies (2004) by assuming that all horizontal derivatives appearing in the stress tensor are taken along surfaces of constant generalized level coordinate. Notably, the forms all have an overall density factor, such as the general form given by equation (17.119) in Griffies (2004)

$$\begin{pmatrix} \tau^{xx} & \tau^{xy} \\ \tau^{xy} & -\tau^{xx} \end{pmatrix} = \rho \begin{pmatrix} (A\,e_{\mathrm{T}} + D\,\Delta\,R^x_x) & (A\,e_{\mathrm{S}} + D\,\Delta\,R^x_y) \\ (A\,e_{\mathrm{S}} + D\,\Delta\,R^y_x) & (-A\,e_{\mathrm{T}} + D\,\Delta\,R^y_y) \end{pmatrix}, \tag{5.12}$$

with R a rotation matrix

$$R^{(m)}_{(n)} = \begin{pmatrix} \sin 2\theta & -\cos 2\theta \\ -\cos 2\theta & -\sin 2\theta \end{pmatrix}, \tag{5.13}$$

$A \geq 0$ is a non-negative viscosity weighting the isotropic stress tensor, and $D \geq 0$ is a non-negative viscosity weighting the aniostropic stress tensor. For the Boussinesq fluid, the density factor in the stress tensor is set to the constant ρ_o. Furthermore, recall that the specific thickness $z_{,s}$ is a depth independent function when using the vertical coordinates discussed in Section 6.1. For the non-Boussinesq cases which use pressure-based vertical coordinates, the density weighted specific thickness $\rho\, z_{,s}$ is a depth independent function, which then simplifies the density weighted thickness of a grid cell $\rho\, \mathrm{d}z = \rho\, z_{,s}\, \mathrm{d}s$. These results are familiar from the analogous simplifications arising for other terms in the scalar and momentum budgets discussed in Chapter 3.

5.1.4 Bottom stress

We exposed the form of bottom stress in Section 3.8.3, and it generally leads to a bottom force given by

$$\begin{aligned} \mathbf{F}_{\text{bottom}} &= -\iint\limits_{z=-H} \mathrm{d}x\, \mathrm{d}y\, \nabla(z+H) \cdot \boldsymbol{\tau} \\ &= -\iint\limits_{z=-H} \mathrm{d}x\, \mathrm{d}y\, \boldsymbol{\tau}^{\text{bottom}}. \end{aligned} \tag{5.14}$$

A common method to parameterize this force is to consider unresolved small scale processes to give rise to a dissipative drag written in the form

$$\mathbf{F}_{\text{bottom}} = -\iint\limits_{z=-H} \mathrm{d}x\, \mathrm{d}y\, [\, \rho\, C_D\, \mathbf{u}_{\text{b}} (\mathbf{u}_{\text{b}}^2 + \mathbf{u}_{\text{tide}}^2)^{1/2}], \tag{5.15}$$

where it is only the horizontal bottom force that appears in hydrostatic models. In this equation, C_D is a dimensionless drag coefficient with common values taken as

$$C_D \approx 10^{-3}. \tag{5.16}$$

Because the precise value of C_D is not well known, the product $\rho\, C_D$ is approximated in MOM4p1 as

$$\rho\, C_D \approx \rho_o\, C_D. \tag{5.17}$$

The velocity $\mathbf{u}_{\text{tide}}$ represents a residual horizontal velocity that is not resolved in models running without tidal forcing. Hence, even with the bottom flow weak, the residual velocity keeps the drag nontrivial. A common value for the residual velocity is

$$|\mathbf{u}_{\text{tide}}| \approx 0.05\, \mathrm{m\, s^{-1}}. \tag{5.18}$$

The velocity $\mathbf{u}_{\text{b}}$ is formally the velocity within the bottom boundary layer, but it is commonly taken in models as the velocity at the grid cell adjacent to the bottom. Note that our assumed form of the unresolved bottom stresses take the form of a *bottom drag*. See Holloway (1999) for more general forms where the unresolved bottom stresses may act to accelerate the resolved flow field.

5.1.5 Summary of the linear momentum budget

The horizontal linear momentum budgets for interior, bottom, and surface grid cells are given by equations (3.238), (3.241), and (3.246). We rewrite them here for future reference, incorporating the more detailed form for friction appropriate for hydrostatic models

$$\boxed{\begin{aligned}[\partial_t + (f+\mathcal{M})\,\hat{\mathbf{z}}\wedge]\,(\mathrm{d}z\,\rho\,\mathbf{u}) = \rho\,\mathrm{d}z\,\mathcal{S}^{(\mathbf{u})} &- \nabla_s\cdot[\,\mathrm{d}z\,\mathbf{u}\,(\rho\,\mathbf{u})] \\ &- \mathrm{d}z\,(\nabla_s\,p + \rho\,\nabla_s\,\Phi) + \mathrm{d}z\,\rho\,\mathbf{F} \\ &- [\,\rho\,(w^{(s)}\,\mathbf{u} - \kappa\,\mathbf{u}_{,z})\,]_{s=s_{k-1}} \\ &+ [\,\rho\,(w^{(s)}\,\mathbf{u} - \kappa\,\mathbf{u}_{,z})\,]_{s=s_k}\end{aligned}} \tag{5.19}$$

$$\boxed{\begin{aligned}[\partial_t + (f+\mathcal{M})\,\hat{\mathbf{z}}\wedge]\,(\mathrm{d}z\,\rho\,\mathbf{u}) = \rho\,\mathrm{d}z\,\mathcal{S}^{(\mathbf{u})} &- \nabla_s\cdot[\,\mathrm{d}z\,\mathbf{u}\,(\rho\,\mathbf{u})] \\ &- \mathrm{d}z\,(\nabla_s\,p + \rho\,\nabla_s\,\Phi) + \mathrm{d}z\,\rho\,\mathbf{F} \\ &- [\,\rho\,(w^{(s)}\,\mathbf{u} - \kappa\,\mathbf{u}_{,z})\,]_{s=s_{kbot-1}} \\ &- \boldsymbol{\tau}^{\mathrm{bottom}}\end{aligned}} \tag{5.20}$$

$$\boxed{\begin{aligned}[\partial_t + (f+\mathcal{M})\,\hat{\mathbf{z}}\wedge]\,(\mathrm{d}z\,\rho\,\mathbf{u}) = \rho\,\mathrm{d}z\,\mathcal{S}^{(\mathbf{u})} &- \nabla_s\cdot[\,\mathrm{d}z\,\mathbf{u}\,(\rho\,\mathbf{u})] \\ &- \mathrm{d}z\,(\nabla_s\,p + \rho\,\nabla_s\,\Phi) + \mathrm{d}z\,\rho\,\mathbf{F} \\ &+ [\,\boldsymbol{\tau}^{\mathrm{wind}} + \rho_{\mathrm{w}}\,q_{\mathrm{w}}\,\mathbf{u}_{\mathrm{w}}\,] \\ &+ [\,\rho\,(w^{(s)}\,\mathbf{u} - \kappa\,\mathbf{u}_{,z})\,]_{s=s_{k=1}}.\end{aligned}} \tag{5.21}$$

As discussed in Section 3.7.2, we prefer to work with the pressure gradient body force acting within the grid cell of a primitive equation ocean model, rather than the accumulation of contact pressures acting at the faces. This formulation in terms of body forces is convenient in a hydrostatic fluid as it facilitates a numerical treatment of pressure in the discrete ocean climate model (Section 4.3).

5.2 Diffusion and skew diffusion

Some of the results for friction are also applicable for diffusion. However, neutral diffusion and skew diffusion require some added considerations.

5.2.1 Vertical diffusion

Dianeutral tracer transport is often parameterized with a diffusive closure, and these closures require the dianeutral derivative of tracer. For most parameterizations, dianeutral derivatives are computed with a vertical derivative (see Section 7.4 of Griffies (2004)), and these derivatives are computed in MOM4p1 just as done for the velocity shears for vertical friction described in Section 5.1.1. Hence, vertical diffusion of tracer concentration is implemented by a direct computation of the finite differenced vertical derivative

$$(\rho\,\kappa\,C_{,z})_{,z} \approx \delta_z\,(\rho\,\kappa\,C_{,z}) \tag{5.22}$$

where C is the tracer concentration and κ is the vertical diffusivity.

5.2.2 Horizontal diffusion

Horizontal diffusion is used infrequently in the interior regions of the ocean in climate simulations with MOM4, since neutral physics is preferred for physical reasons. However, near the surface boundary, arguments presented in Section 16.2 motivate orienting lateral diffusive processes along surfaces of constant generalized level coordinate when in the surface turbulent boundary, and along topography following coordinates for the bottom turbulent boundary layer. Hence, it is useful to consider the form that horizontal diffusion takes in generalized level coordinates.

When computing the horizontal fluxes as downgradient along surfaces of constant vertical coordinate s, we consider

$$\rho \mathbf{F} = -\rho A \nabla_s C, \tag{5.23}$$

with A a horizontal diffusivity. The thickness weighted horizontal diffusion operator is therefore given by

$$R^{\text{horz}} = -\nabla_s \cdot (\mathrm{d}z \, \rho \mathbf{F}). \tag{5.24}$$

5.2.3 Neutral physics

As for horizontal and vertical diffusion, we compute the tracer flux from neutral physics as $\rho \mathbf{F}$, where $\mathbf{F}$ is the tracer concentration flux formulated as in a Boussinesq model, and ρ is the *in situ* density for a non-Boussinesq model and ρ_o for a Boussinesq model. This approach requires a bit of justification for the neutral skewsion from Gent and McWilliams (1990), and we provide such in this section. The bottomline is there are no nontrivial issues involved with implementing this scheme in a non-Boussinesq model. The only issue arising with generalized level coordinates thus relates to the computation of neutral direction slopes.

Neutral diffusion fluxes are oriented relative to neutral directions. Hence, the slope of the neutral direction relative to the surface of constant vertical coordinate is required to construct the neutral diffusion flux.

The scheme of Gent and McWilliams (1990) requires the slope of the neutral direction relative to the geopotential surface, since this slope provides a measure of the available potential energy. For simplicity, we use the same slope for both neutral diffusion and skew diffusion in MOM4p1. Doing so facilitates a straightforward extension of the neutral physics technology employed in the z-model MOM4.0 to the generalized coordinates supported for MOM4p1. It however produces a modified Gent and McWilliams (1990) scheme in which skew diffusion relaxes neutral directions toward surfaces of constant vertical coordinate rather than constant geopontential surfaces. For surfaces of constant vertical coordinate that are quasi-horizontal, the modified skew diffusion scheme should act in a manner quite similar to that in a z-model. However, for the terrain following coordinates $\sigma^{(z)}$ and $\sigma^{(p)}$, novel issues arise which have *have not* been considered in the MOM4p1 formulation of Gent and McWilliams (1990) skewsion. Hence, the use of neutral physics parameterizations with terrain following vertical coordinates is *not* recommended in MOM4p1.

5.2.3.1 The velocity field from Gent and McWilliams (1990)

As formulated by Gent et al. (1995), the parameterization of Gent and McWilliams (1990) is typically considered from the perspective of a Boussinesq ocean model. For the purposes of advective transport of tracer, we add a non-divergent velocity $\mathbf{v}^* = \nabla \wedge \mathbf{\Psi}$ to the non-divergent resolved

scale velocity $\mathbf{v}$. The parameterized vector streamfunction is given by

$$\mathbf{\Psi} = -\kappa\,\mathbf{S} \wedge \hat{\mathbf{z}}, \tag{5.25}$$

where $\mathbf{S}$ is the neutral slope and $\kappa > 0$ is a kinematic diffusivity. In this way, volume conservation remains unchanged, thus removing the need to modify the model's kinematic relations used to diagnose the vertical velocity component w.

The above results can be seen from a finite volume perspective by considering the volume conservation equation for an interior model grid cell (Section 3.9), in which

$$\partial_t(\mathrm{d}z) = \mathrm{d}z\,\mathcal{S}^{(\mathrm{V})} - \nabla_s \cdot (\mathrm{d}z\,\mathbf{u}) - (w^{(s)})_{s=s_{k-1}} + (w^{(s)})_{s=s_k}, \tag{5.26}$$

where $\mathcal{S}^{(\mathrm{V})}$ is a volume source, and $w^{(s)}$ is the dia-surface velocity component. Use of the Gent et al. (1995) advective velocity

$$\mathbf{u}^* = -\partial_z\,(\kappa\,\mathbf{S}) \tag{5.27}$$

leads to the finite volume result

$$\int_{z_k}^{z_{k-1}} \mathrm{d}z\,\mathbf{u}^* = -(\kappa\,\mathbf{S})_{k-1} + (\kappa\,\mathbf{S})_k, \tag{5.28}$$

which renders

$$\begin{aligned} -\nabla_s \cdot \left(\int_{z_k}^{z_{k-1}} \mathrm{d}z\,\mathbf{u}^* \right) - w^*_{k-1} + w^*_k &= \nabla_s \cdot (\kappa\,\mathbf{S})_{k-1} - \nabla_s \cdot (\kappa\,\mathbf{S})_k - w^*_{k-1} + w^*_k \\ &= 0. \end{aligned} \tag{5.29}$$

Hence, there is no modification of the volume in a grid cell from the Gent et al. (1995) velocity field.

We now extend the formulation to a non-Boussinesq fluid, in which case the mass conservation takes the form (see equation (3.166) in Section 3.6.2)

$$\partial_t(\mathrm{d}z\,\rho) = \mathrm{d}z\,\rho\,\mathcal{S}^{(\mathrm{M})} - \nabla_s \cdot (\mathrm{d}z\,\rho\,\mathbf{u}) - (\rho\,w^{(s)})_{s=s_{k-1}} + (\rho\,w^{(s)})_{s=s_k}, \tag{5.30}$$

with $\mathcal{S}^{(\mathrm{M})}$ a mass source. Define a density weighted horizontal advection velocity according to

$$\rho\,\mathbf{u}^* = -\partial_z\,(\rho\,\kappa\,\mathbf{S}), \tag{5.31}$$

in which case the vector streamfunction from the Boussinesq case is extended to the non-Boussinesq merely by introducing a density weighting

$$\rho\,\mathbf{\Psi} = -\rho\,\kappa\,\mathbf{S} \wedge \hat{\mathbf{z}}. \tag{5.32}$$

This result then leads to

$$\begin{aligned} &-\nabla_s \cdot \left(\int_{z_k}^{z_{k-1}} \rho\,\mathrm{d}z\,\mathbf{u}^* \right) - (\rho\,w^*)_{s=s_{k-1}} + (\rho\,w^*)_{s=s_k} = \\ &\quad \nabla_s \cdot (\rho\,\kappa\,\mathbf{S})_{k-1} - \nabla_s \cdot (\rho\,\kappa\,\mathbf{S})_k - (\rho\,w^*)_{s=s_{k-1}} + (\rho\,w^*)_{s=s_k} \\ &\quad = 0, \end{aligned} \tag{5.33}$$

which means there is no modification to the mass of a grid cell through the introduction of the non-Boussinesq Gent et al. (1995) parameterization.

Note that in the continuum, the above finite volume results mean that the non-Boussinesq Gent et al. (1995) velocity satisfies

$$\nabla_s \cdot (\rho\, z_{,s}\, \mathbf{u}^*) + \partial_s\, (\rho\, z_{,s}\, w^*) = 0, \tag{5.34}$$

where s is the vertical coordinate. For the geopotential case with $s = z$, we have

$$\nabla_z \cdot (\rho\, \mathbf{u}^*) + \partial_z\, (\rho\, w^*) = 0, \tag{5.35}$$

which reduces to the familiar non-divergence condition

$$\nabla_z \cdot \mathbf{u}^* + \partial_z\, w^* = 0 \tag{5.36}$$

in the Boussinesq case.

5.2.3.2 Neutral slopes

A key to the implementation of neutral physics is the slope of a neutral direction relative to either the geopotential or a surface of constant generalized level coordinate. Implicit in the following is the assumption that the neutral slope is finite relative to each surface.

The neutral slope relative to the geopotential is

$$\begin{aligned} \mathbf{S}_{(\rho/z)} &= \nabla_\rho\, z \\ &= -z_{,\rho}\, \nabla_z \rho \end{aligned} \tag{5.37}$$

with ρ the locally referenced potential density. The (ρ/z) subscript notation highlights that the neutral slope is computed relative to a geopotential. The relation between this slope and the others can be seen by noting that in generalized vertical coordinates, the horizontal gradient ∇_z is computed using the transformation (6.33) in Griffies (2004) so that

$$\begin{aligned} \mathbf{S}_{(\rho/z)} &= -z_{,\rho}\, (\nabla_s - \mathbf{S}_{(s/z)} \partial_z)\, \rho \\ &= \mathbf{S}_{(\rho/s)} + \mathbf{S}_{(s/z)}. \end{aligned} \tag{5.38}$$

This equation identifies the slope of the vertical coordinate surface relative to the geopotential

$$\begin{aligned} \mathbf{S}_{(s/z)} &= \nabla_s z \\ &= -z_{,s}\, \nabla_z\, s \end{aligned} \tag{5.39}$$

and the slope of the neutral direction relative to the vertical coordinate surface

$$\begin{aligned} \mathbf{S}_{(\rho/s)} &= \nabla_\rho\, s \\ &= -z_{,\rho}\, \nabla_s\, \rho \\ &= -z_{,s}\, s_{,\rho}\, \nabla_s\, \rho. \end{aligned} \tag{5.40}$$

In words, equation (5.38) says that the slope of the neutral direction relative to the geopotential equals to the slope of the neutral direction relative to the vertical coordinate surface plus the slope

of the vertical coordinate surface relative to the geopotential. In isopycnal models, the slope $\mathbf{S}_{(\rho/s)}$ is very small for much of the ocean. Except for the sigma coordinates, each of the depth-based and pressure-based vertical coordinates discussed in Sections 6.1 and 6.2 have $\mathbf{S}_{(s/z)}$ typically less than 10^{-4} and $\mathbf{S}_{(\rho/s)}$ less than 10^{-2}. For sigma coordinates, both $\mathbf{S}_{(\rho/s)}$ and $\mathbf{S}_{(s/z)}$ can be nontrivial in much of the model domain affected by topography.

Figure 5.1 illustrates the relation (5.38) between slopes. This figure shows a particular zonal-vertical slice, with slope given by the tangent of the indicated angle. That is, the x-component of the slope vectors are given by

$$\begin{aligned} S_{(s/z)} &= \tan \alpha_{(s/z)} \\ S_{(\rho/z)} &= \tan \alpha_{(\rho/z)} \\ S_{(\rho/s)} &= \tan \alpha_{(\rho/s)}. \end{aligned} \tag{5.41}$$

In this example, $S_{(s/z)} < 0$ whereas $S_{(\rho/z)} > 0$. Note that the angle between the generalized surface and the isopycnal surface, $S_{(\rho/s)}$, is larger in absolute value for this example than $S_{(\rho/z)}$. This case may be applicable to certain regions of σ-models, whereas for isopycnal models $S_{(\rho/s)}$ will generally be smaller than $S_{(\rho/z)}$. The generally nontrivial angle $S_{(\rho/s)}$ found in sigma models is yet another reason we do not recommend the use of neutral physics as implemented in MOM4p1 along with terrain following vertical coordinates. Significant work is required to ensure a proper treatment of neutral physics with terrain following coordinates, and we are not prepared to support such in MOM4.

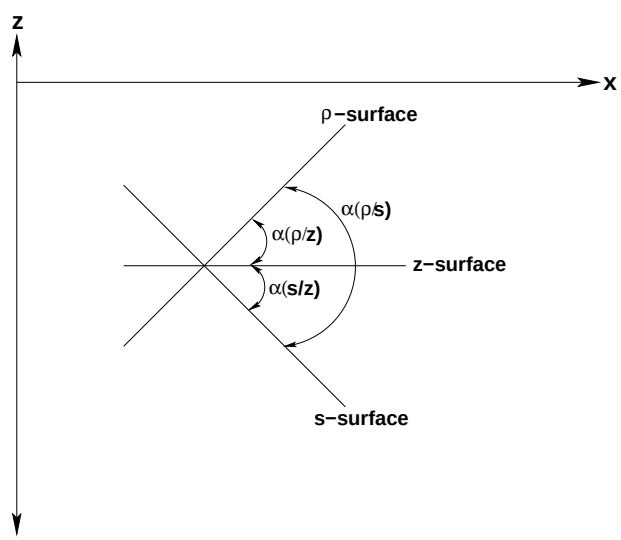

Figure 5.1: Relationship between the slopes of surfaces of constant depth, constant generalized vertical coordinate s, and potential density ρ. Shown here is a case where the slope is projected onto a single horizontal direction, so that the slope is given by the tangent of the indicated angle. This figure is taken from Figure 6.5 of Griffies (2004).

5.2.3.3 Fluxes for neutral diffusion

The relative slope between the neutral direction and vertical coordinate is required to compute the neutral diffusion flux. We assume here that this slope is small, thus allowing us to approximate the full diffusion tensor of Redi (1982) with the small slope approximated tensor of Gent and McWilliams (1990). To lend mathematical support for these comments, we start with the neutral diffusion flux as written for the small slope approximation in z-models. As discussed in Section 14.1.4 of Griffies (2004), this flux has horizontal and vertical components given by

$$\mathbf{F}^{(h)} = -A_I \, \nabla_\rho C \tag{5.42}$$

$$F^{(z)} = -A_I \, \mathbf{S}_{(\rho/z)} \cdot \nabla_\rho C. \tag{5.43}$$

Converting this flux to a form appropriate for general vertical coordinates requires a transformation of the gradient operator

$$\begin{aligned} \nabla_\rho &= \nabla_z + \mathbf{S}_{(\rho/z)} \, \partial_z \\ &= \nabla_s + [\mathbf{S}_{(\rho/z)} - \mathbf{S}_{(s/z)}] \, \partial_z \\ &= \nabla_s + \mathbf{S}_{(\rho/s)} \, \partial_z. \end{aligned} \tag{5.44}$$

The third equality used the slope relation (5.38).

As seen in Section 3.6, the thickness weighted tracer budget contains a contribution from the convergence of a SGS flux in the form

$$R = -\nabla_s \cdot (\mathrm{d}z \, \rho \, \mathbf{F}) - [\rho \, z_{,s} \, \nabla s \cdot \mathbf{F}]_{s=s_{k-1}} + [\rho \, z_{,s} \, \nabla s \cdot \mathbf{F}]_{s=s_k}. \tag{5.45}$$

We are therefore led to consider the dia-surface flux component

$$\begin{aligned} F^{(s)} &= z_{,s} \, \nabla s \cdot \mathbf{F} \\ &= (\hat{\mathbf{z}} - \mathbf{S}_{(s/z)}) \cdot \mathbf{F} \\ &= -A_I \, (\mathbf{S}_{(\rho/z)} - \mathbf{S}_{(s/z)}) \cdot \nabla_\rho \, C \\ &= -A_I \, \mathbf{S}_{(\rho/s)} \cdot \nabla_\rho \, C \\ &= \mathbf{S}_{(\rho/s)} \cdot \mathbf{F}^{(h)}. \end{aligned} \tag{5.46}$$

This flux component, as well as the horizontal flux component, take forms isomorphic to those for the specific case of $s = z$ given by equations (5.42) and (5.43). This isomorphism follows from the need to only have information about the relative slope between the generalized surfaces of constant s and the neutral directions.

5.2.3.4 Fluxes for skew diffusion

An arbitrary tracer has a Gent and McWilliams (1990) skew flux in the form

$$\mathbf{F} = A_{\mathrm{gm}} \, (\mathbf{S}_{(\rho/z)} \, C_{,z} - \hat{\mathbf{z}} \, \mathbf{S}_{(\rho/z)} \cdot \nabla_z \, C), \tag{5.47}$$

where A_{gm} is a non-negative skew diffusivity. The horizontal component of this flux is converted to general coordinates via

$$\begin{aligned} \mathbf{F}^{(h)} &= A_{\mathrm{gm}} \, (\mathbf{S}_{(\rho/s)} + \mathbf{S}_{(s/z)}) \, C_{,z} \\ &\approx A_{\mathrm{gm}} \, \mathbf{S}_{(\rho/s)} \, C_{,z}. \end{aligned} \tag{5.48}$$

Consistent with this same approximation, we are led to the dia-surface component of the skew flux

$$
\begin{aligned}
z_{,s}\,\nabla s\cdot\mathbf{F} &= \left(\hat{\mathbf{z}}-\mathbf{S}_{(s/z)}\right)\cdot\mathbf{F}\\
&= -A_{\mathrm{gm}}\left(\mathbf{S}_{(\rho/z)}\cdot\nabla_z+\mathbf{S}_{(\rho/z)}\cdot\mathbf{S}_{(s/z)}\,\partial_z\right)C\\
&= -A_{\mathrm{gm}}\,\mathbf{S}_{(\rho/z)}\cdot\left(\nabla_s-\mathbf{S}_{(s/z)}\,\partial_z\,\right)C-A_{\mathrm{gm}}\,\mathbf{S}_{(\rho/z)}\cdot\mathbf{S}_{(s/z)}\,\partial_z\,C\\
&= -A_{\mathrm{gm}}\,\mathbf{S}_{(\rho/z)}\cdot\nabla_s\,C\\
&\approx -A_{\mathrm{gm}}\,\mathbf{S}_{(\rho/s)}\cdot\nabla_s\,C.
\end{aligned}
\tag{5.49}
$$

These approximations are reasonable where $|\mathbf{S}_{(s/z)}|$ is much smaller than $|\mathbf{S}_{(\rho/z)}|$ if $\mathbf{S}_{(\rho/z)}$ is non-trivial. When the neutral slope $\mathbf{S}_{(\rho/z)}$ vanishes, as for regions of zero baroclinicity, this approximation may not be valid when $s \neq z$. However, in regions of vanishing baroclinicity, we expect the error to be of minimal consequence to the simulation since either the z or s based skew fluxes are close to zero. In general, approximating the slope as proposed here leads the modified Gent and McWilliams (1990) scheme to dissipate neutral slopes as they deviate from surfaces of constant generalized vertical coordinate. So long as these surfaces are quasi-horizontal, the modified scheme should perform in a physically relevant manner.

5.2.3.5 Summary of the neutral fluxes

The horizontal and dia-surface components to the small angle neutral diffusion flux take the form

$$
\boxed{
\begin{aligned}
\mathbf{F}^{(h)} &= -A_I\left(\nabla_s+\mathbf{S}_{(\rho/s)}\,\partial_z\right)C\\
F^{(s)} &= \mathbf{S}_{(\rho/s)}\cdot\mathbf{F}^{(h)}
\end{aligned}
}
\tag{5.50}
$$

where the slope is given by

$$
\boxed{
\begin{aligned}
\mathbf{S}_{(\rho/s)} &= \nabla_\rho\, s\\
&= -z_{,\rho}\,\nabla_s\,\rho.
\end{aligned}
}
\tag{5.51}
$$

The horizontal and dia-surface skew flux components are approximated by

$$
\boxed{
\begin{aligned}
\mathbf{F}^{(h)} &\approx A_{\mathrm{gm}}\,\mathbf{S}_{(\rho/s)}\,C_{,z}\\
F^{(s)} &\approx -A_{\mathrm{gm}}\,\mathbf{S}_{(\rho/s)}\cdot\nabla_s\,C.
\end{aligned}
}
\tag{5.52}
$$

Each of these neutral fluxes are isomorphic to the fluxes used in the z-model MOM4.0. This isomorphism enables us to transfer the neutral physics technology from MOM4.0 directly to MOM4p1.

CHAPTER
SIX

Depth and pressure based vertical coordinates

The purpose of this chapter is to document issues related to the choice of vertical coordinates. In MOM4p1, only depth-based and pressure-based coordinates are supported. Isopycnal coordinates are not supported. Furthermore, terrain following sigma coordinates are coded in MOM4p1. However, more work is required to reduce pressure gradient errors (Section 4.2) and consistently employ neutral physics (Section 5.2.3 and Chapter 16). Much in this chapter is derived from lectures of Griffies (2005) at the 2004 GODAE School.

6.1 Depth based vertical coordinates

We use depth based vertical coordinates in this section to discretize the Boussinesq equations.[1] Depth based coordinates are also known as *volume based* coordinates, since for a Boussinesq model that uses depth as the vertical coordinate, the volume of interior grid cells is constant in the absence of sources. Correspondingly, depth based coordinates are naturally suited for Boussinesq fluids.

6.1.1 Depth coordinate

With a free surface, the vertical domain over which the z-coordinate

$$s = z \tag{6.1}$$

ranges is given by the time dependent interval

$$-H \leq z \leq \eta. \tag{6.2}$$

Consequently, the sum of the vertical grid cell increments equals to the total depth of the column

$$\sum_k \mathrm{d}z = H + \eta. \tag{6.3}$$

[1] Greatbatch and McDougall (2003) discuss an algorithm for non-Boussinesq dynamics in a z-model. Their methods are implemented in mom4p0a and mom4p0b of Griffies et al. (2004). This approach may be of special use for non-Boussinesq non-hydrostatic z-models. However, when focusing on hydrostatic models as we do here, pressure based vertical coordinates discussed in Section 6.2 are more convenient to realize non-Boussinesq dynamics.

The trivial form of the specific thickness $z_{,s} = 1$ greatly simplifies the Boussinesq budgets.

The depth coordinate is very useful for many purposes in global climate modelling, and models based on depth are the most popular ocean climate models. Their advantages include the following.

- Simple numerical methods have been successfully used in this framework.
- For a Boussinesq fluid, the horizontal pressure gradient can be easily represented in an accurate manner.
- The equation of state for ocean water can be accurately represented in a straightforward manner (e.g., Jackett et al. (2006)).
- The upper ocean mixed layer is well parameterized using a z-coordinate.

Unfortunately, these models have some well known disadvantages, which include the following.

- Representation of tracer transport within the quasi-adiabatic interior is cumbersome, with problems becoming more egregious as mesoscale eddies are admitted (Griffies et al. (2000b)).
- Representation and parameterization of bottom boundary layer processes and flow are unnatural.

Grid cells have static vertical increments $\mathrm{d}s = \mathrm{d}z$ when $s = z$, except for the top where $\partial_t (\mathrm{d}z) = \eta_{,t}$. The time dependent vertical range of the coordinate slightly complicates a numerical treatment of the surface cell in z-models (see Griffies et al. (2001) for details of one such treatment).

Placing all changes in ocean thickness in the top gric cell exposes the free surface geopotential coordinate models to two pesky problems. First, when adding fresh water to the ocean, such as for with simulations of land ice melting, the top cell thickens, which means the representation of vertical processes is coarsened. Conversely, the surface cell can be lost (i.e., can become dry) if the free surface depresses below the depth of the top grid cell's bottom face. This is a very inconvenient feature that limits the use of z-coordinates.[2] In particular, the following studies may require very refined vertical resolution and/or large undulations of the surface height, and so would not be accessible with a conventional free surface z-model.

- Process studies of surface mixing and biological cycling may warrant very refined upper ocean grid cell thickness, some as refined as 1m.
- Realistic tidal fluctuations in some parts of the World Ocean can reach 10m-20m.
- Coastal models tend to require refined vertical resolution to represent shallow coastal processes along the continental shelves and near-shore.
- When coupled to a sea ice model, the weight of the ice will depress the ocean free surface.

[2] Linearized free surfaces, in which the budgets for tracer and momentum are formulated assuming a constant top cell thickness, avoid problems with vanishing top cells. However, such models do not conserve total tracer or volume, and so are of limited use for long term climate studies (see Griffies et al. (2001) and Campin et al. (2004) for discussion).

6.1.2 An example of depth coordinates

In some of the following discussion, we illustrate aspects of vertical coordinates by diagnosing the values for the coordinates from a realistic z-model run with partial step thicknesses. *Partial steps* have arbitrary thickness set to accurately represent the bottom topography. The partial step technology was introduced by Adcroft et al. (1997) in the C-grid MITgcm, and further discussed by Pacanowski and Gnanadesikan (1998) for the B-grid Modular Ocean Model (MOM). Figure 6.1 compares the representation of topography in a z-model using partial steps as realized in the MOM code of Griffies et al. (2004). Many z-models have incorporated the partial step technology as it provides an important facility to accurately represent flow and waves near topography.

Because of partial steps, the level next to the ocean bottom has grid cell centers that are generally at different depths. Hence, the bottom cell in a partial step z-model computes its pressure gradient with two terms: one due to gradients across cells with the same grid cell index k, and another due to slopes in the bottom topography. Details of the pressure gradient calculation are provided in Chapter 4. All other cells, including the surface, have grid cell centers that are at fixed depths. Figure 6.2 illustrates the lines of constant partial step depth for this model.

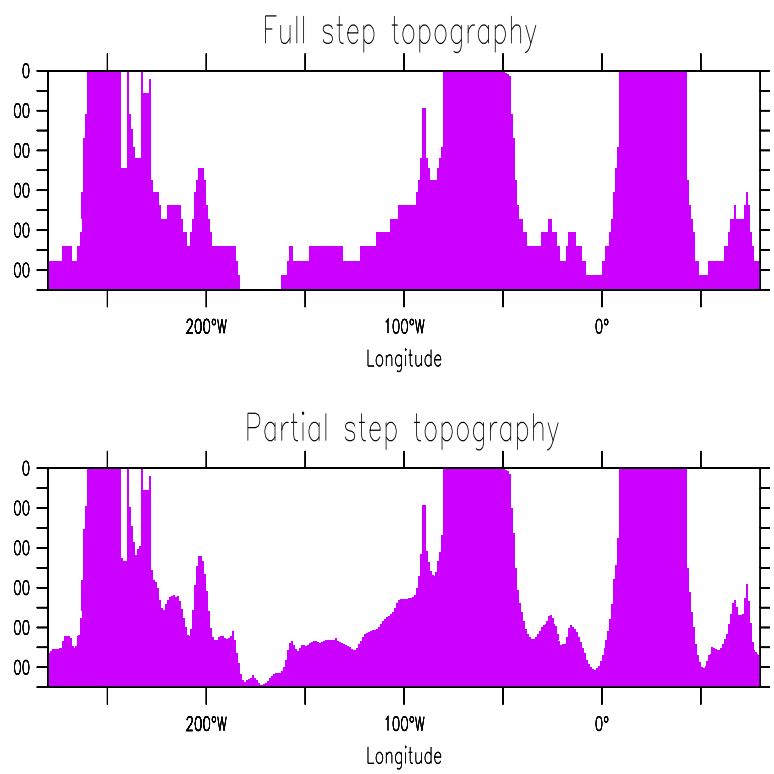

Figure 6.1: Comparison of the partial step versus full step representation of topography as realized in the z-model discussed by Griffies et al. (2005). This vertical section is taken along the equator. The model horizontal grid has one degree latitudinal resolution. The main differences are in the deep ocean in regions where the topographic slope is gradual. Steep sloped regions, and those in the upper ocean with refined vertical resolution, show less distinctions.

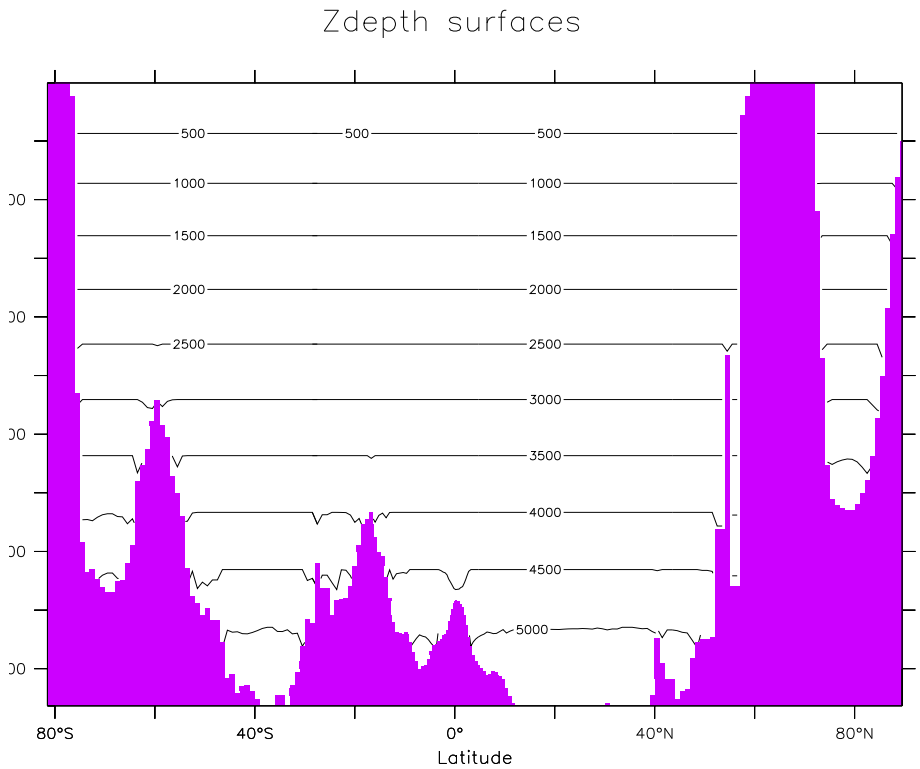

Figure 6.2: This figure contours the depth of grid cell centers used in a modern geopotential ocean model. Deviations from the horizontal occur next to the bottom due to use of a partial bottom step representation of topography, as illustrated in Figure 6.1. In this case, the bottom cell has an arbitrary thickness according to the methods of Adcroft et al. (1997) and Pacanowski and Gnanadesikan (1998). This technology is common in modern geopotential ocean models, as it provides a more faithful and robust representation of the ocean bottom. Shown here is a north-south section along $150°W$.

6.1.3 Depth deviation coordinate

The depth deviation coordinate

$$s = z - \eta \tag{6.4}$$

removes the restriction on upper ocean grid cell resolution present with $s = z$. That is, $s = 0$ is the time independent coordinate value of the ocean surface, no matter how much the free surface depresses or grows. Hence, no surface cells vanish so long as $\eta > -H$. If $\eta < -H$, the bottom topography is exposed, in which case the model's land-sea boundaries are altered. Such necessitates a model that can allow for wetting and drying of grid cells. Alternatively, it requires a model where ocean is extended globally, with infinitesimally thin ocean layers present over land. We do not have such features in MOM4p1.

The depth deviation coordinate ranges between $-(H + \eta) \leq s \leq 0$. The only time dependent interface in s-space is at the bottom of the column. Consequently, by solving the problem at the ocean surface, the deviation coordinate introduces a problem to the ocean bottom where bottom cells can now vanish. To see this problem, discretize the deviation coordinate s according to time

independent values s_k. For example, the s_k values can be set as the depths of cells in a model with $s = z$. When η evolves, depth z and $s = z - \eta$ become different, and so the depth of a grid cell must be diagnosed based on the time independent value of s_k and the time dependent surface height

$$z_k = s_k + \eta. \tag{6.5}$$

If the time dependent depth of the upper interface of a bottom grid cell is diagnosed to be deeper than the actual bottom depth $z = -H$, then we know that the bottom grid cell has vanished and so there are problems. To maintain nonvanishing cells requires a limit on how negative η can become. For example, if the upper interface of a bottom cell is -5000m and the bottom interface (at the ocean bottom) is $H = 5005$m, then the bottom cell is lost if $\eta < -5$m. This restriction is of some consequence when aiming to use partial bottom steps (see Figure 6.1) along with tides and sea ice. In practice, if one is interested in allowing thick sea ice and nontrivial tidal fluctuations, then it will be necessary to keep the bottom partial steps thicker than roughly 10m-20m. This is arguably a less onerous constraint on the model's vertical grid spacing than the complementary problem at the ocean surface encountered with the traditional z-coordinate $s = z$.

In summary, grid cells have static grid increments $\mathrm{d}s = \mathrm{d}z$ for all cells except the bottom. At the bottom, $\partial_t(\mathrm{d}z) = \partial_t(\mathrm{d}s) = \eta_{,t}$. Hence, the thickness of the bottom cell grows when the surface height grows, and it thins when the surface height becomes negative. The bottom cell can be lost if η becomes too negative. The sum of the vertical increments yields the total depth of the column $\sum_k \mathrm{d}s = (H + \eta)$. Because the surface height fluctuations are so much smaller than changes in bottom topography, the depth deviation coordinate appears nearly the same as the depth coordinate when viewed over the full depth range of a typical model such as in Figure 6.2.

The author knows of no model routinely using the depth deviation coordinate. It does appear to have advantages for certain applications over the depth coordinate. However, the zstar coordinate discussed next resolves problems at *both* the top and bottom, and so is clearly preferable. The depth deviation coordinate is *not* implemented in MOM4p1 for these reasons.

6.1.4 Zstar coordinate

To overcome problems with vanishing surface and/or bottom cells, we consider the *zstar* coordinate

$$z^* = H\left(\frac{z - \eta}{H + \eta}\right). \tag{6.6}$$

This coordinate is closely related to the "eta" coordinate used in many atmospheric models (see Black (1994) for a review of eta coordinate atmospheric models). It was originally used in ocean models by Stacey et al. (1995) for studies of tides next to shelves, and it has been recently promoted by Adcroft and Campin (2004) for global climate modelling.

The surfaces of constant z^* are quasi-horizontal. Indeed, the z^* coordinate reduces to z when η is zero. In general, when noting the large differences between undulations of the bottom topography versus undulations in the surface height, it is clear that surfaces constant z^* are very similar to the depth surfaces shown in Figure 6.2. These properties greatly reduce difficulties of computing the horizontal pressure gradient relative to terrain following sigma models discussed next. Additionally, since $z^* = z$ when $\eta = 0$, no flow is spontaneously generated in an unforced ocean starting from rest, regardless the bottom topography.[3] This behavior is in contrast to the case with

[3]Because of the use of partial bottom steps, there are two terms contributing to horizontal pressure gradients within

sigma models, where pressure gradient errors in the presence of nontrivial topographic variations can generate nontrivial spontaneous flow from a resting state, depending on the sophistication of the pressure gradient solver.[4] The quasi-horizontal nature of the coordinate surfaces also facilitates the implementation of neutral physics parameterizations in z^* models using the same techniques as in z-models (see Chapters 13-16 of Griffies (2004) for a discussion of neutral physics in z-models, as well as Section 5.2.3 and Chapter 16 in this document for treatment in MOM4p1).

The range over which z^* varies is time independent

$$-H \leq z^* \leq 0. \tag{6.7}$$

Hence, all cells remain nonvanishing, so long as the surface height maintains $\eta > -H$. This is a minor constraint relative to that encountered on the surface height when using $s = z$ or $s = z - \eta$.

Because z^* has a time independent range, all grid cells have static increments $\mathrm{d}s$, and the sum of the vertical increments yields the time independent ocean depth

$$\sum_k \mathrm{d}s = H. \tag{6.8}$$

The z^* coordinate is therefore invisible to undulations of the free surface, since it moves along with the free surface. This property means that no spurious vertical transport is induced across surfaces of constant z^* by the motion of external gravity waves. Such spurious transport can be a problem in z-models, especially those with tidal forcing. Quite generally, the time independent range for the z^* coordinate is a very convenient property that allows for a nearly arbitrary vertical resolution even in the presence of large amplitude fluctuations of the surface height, again so long as $\eta > -H$.

6.1.5 Depth sigma coordinate

The depth-sigma coordinate

$$\begin{aligned} \sigma &= z^*/H \\ &= \left(\frac{z-\eta}{H+\eta}\right) \end{aligned} \tag{6.9}$$

is the canonical *terrain following* coordinate. Figure 6.3 illustrates this coordinate in a realistic model. The sigma coordinate has a long history of use in coastal modelling. For reviews, see Greatbatch and Mellor (1999) and Ezer et al. (2002). Models based on the sigma coordinate have also been successfully extended to basinwide studies, as well as recent global work by Diansky et al. (2002).

Just as for z^*, the range over which the sigma coordinate varies is time independent. Here, it is given by the dimensionless range

$$-1 \leq \sigma \leq 0. \tag{6.10}$$

the bottom level when $s = z$. As discussed by Pacanowski and Gnanadesikan (1998), these two terms lead to modest pressure gradient errors. These errors, however, are far smaller than those encountered with σ coordinates.

[4] Shchepetkin and McWilliams (2002) provide a thorough discussion of pressure gradient solvers along with methods for reducing the pressure gradient error.

Hence, all cells have static grid increments $\mathrm{d}s$, and the sum of the vertical increments yields unity

$$\sum_k \mathrm{d}s = 1. \tag{6.11}$$

So long as the surface height is not depressed deeper than the ocean bottom (i.e., so long as $\eta > -H$), then all cells remain nonvanishing.[5]

Some further key advantages of the sigma coordinate are the following.

- It provides a natural framework to represent bottom influenced flow and to parameterize bottom boundary layer processes.
- Thermodynamic effects associated with the equation of state are well represented with this coordinate.

However, some of the disadvantages are the following:

- As with the z-models, representation of the quasi-adiabatic interior is cumbersome due to numerical truncation errors inducing unphysically large levels of spurious mixing, especially in the presence of vigorous mesoscale eddies. Parameterization of these processes using neutral physics schemes may be more difficult numerically than in the z-models. The reason is that neutral directions generally have slopes less than 1/100 relative to the horizontal, but can have order unity slopes relative to sigma surfaces. The larger relative slopes precludes the *small slope approximation* commonly made with z-model implementations of neutral physics. The small slope approximation provides for simplification of the schemes, and improves computational efficiency.
- Sigma models have difficulty accurately representing the horizontal pressure gradient in the presence of realistic topography, where slopes are commonly larger than 1/100 (see Section 3.7 for a discussion of the pressure gradient calculation).

Griffies et al. (2000a) notes that there are few examples of global climate models running with terrain following vertical coordinates. Diansky et al. (2002) is the only exception known to the author. This situation is largely due to problems representing realistic topography without incurring unacceptable pressure gradient errors, as well as difficulties implementing parameterizations of neutral physical processes. There are notable efforts to resolve these problems, such as the pressure gradient work of Shchepetkin and McWilliams (2002). Continued efforts along these lines may soon facilitate the more common use of terrain following coordinates for global ocean climate modelling. At present, the sigma coordinate is coded in MOM4p1 in hopes that it will motivate researchers to further investigate its utility for ocean modelling.

6.1.6 Summary of the depth based vertical coordinates

Depth based vertical coordinates are natural for Boussinesq equations. These coordinates and their specific thicknesses $z_{,s}$ are summarized in Table 6.1. Notably, both the sigma and zstar coordinates have time independent ranges, but time dependent specific thicknesses. In contrast, the

[5] If $\eta < -H$, besides drying up a region of ocean, the specific thickness $z_{,s} = H + \eta$ changes sign, which signals a singularity in the vertical grid definition. The same problem occurs for the z^* coordinate.

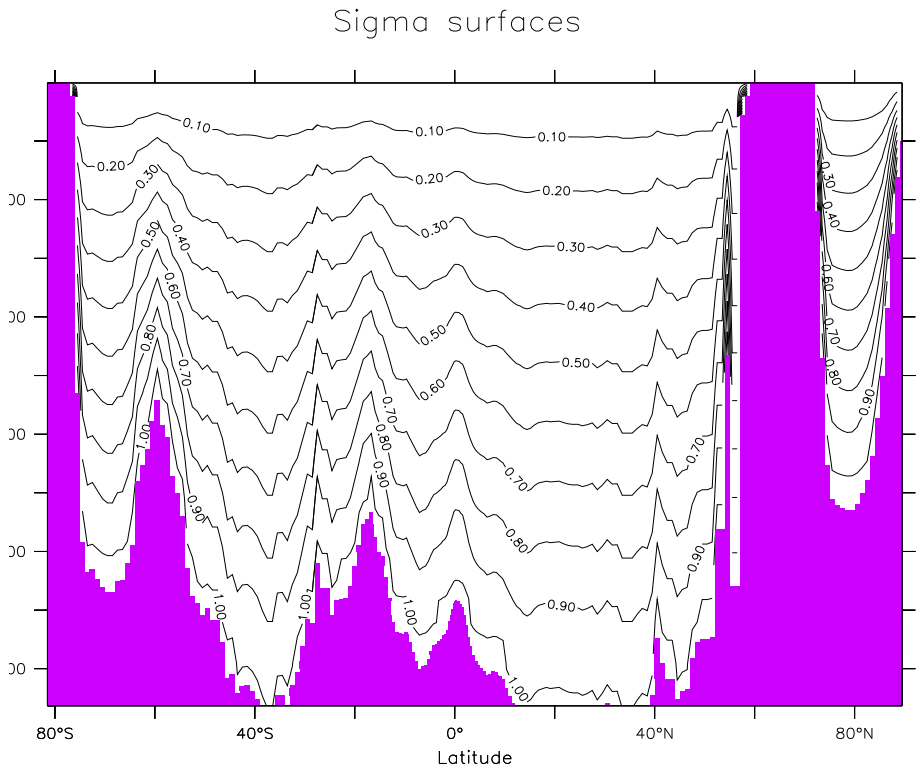

Figure 6.3: Constant sigma surfaces as diagnosed in a z-model. Shown here is a section along $150°W$, as in Figure 6.2. Note the strong variations in the contours, as determined by changes in the bottom topography.

depth and depth deviation coordinates have time dependent depth ranges and time independent specific thicknesses. If plotted with the same range as those given in Figure 6.2, surfaces of constant depth deviation and constant zstar are indistinguishable from surfaces of constant depth. This result follows since the surface height undulations are so much smaller than undulations in the bottom topography, thus making the depth deviation and zstar coordinates very close to horizontal in most parts of the ocean.

6.2 Pressure based coordinates

The second class of vertical coordinates that we discuss is based on pressure. Pressure-based coordinates are used to discretize the non-Boussinesq equations, and these coordinates are also known as *mass based* coordinates. This name is based on noting that for a non-Boussinesq fluid using pressure, the mass of interior grid cells is constant without sources (e.g., see equation (3.217)).

Pressure coordinates provide a straightforward way to generalize Boussinesq z-models to non-Boussinesq pressure models (Huang et al., 2001; DeSzoeke and Samelson, 2002; Marshall et al., 2004; Losch et al., 2004). The reason is that there is an isomorphism between the Boussinesq equations written in depth based coordinates and non-Boussinesq equations written in pressure based coordinates. The root of this isomorphism is the simplification of the density weighted specific thickness $\rho\, z_{,s}$ for pressure based coordinates. We detail this point in the following discussions.

COORD	DEFINITION	RANGE	$z_{,s}$
geopotential	z	$-H \leq z \leq \eta$	1
z-deviation	$z' = z - \eta$	$-(H+\eta) \leq z' \leq 0$	1
z-star	$z^* = H\,(z-\eta)/(H+\eta)$	$-H \leq z^* \leq 0$	$1+\eta/H$
z-sigma	$\sigma^{(z)} = (z-\eta)/(H+\eta)$	$-1 \leq \sigma \leq 0$	$H+\eta$

Table 6.1: Table of vertical coordinates based on depth. These coordinates are naturally used for discretizing the Boussinesq equations. Note that the specific thickness $z_{,s}$ is depth independent. This property proves to be important for developing numerical algorithms in Section 7.6. The coordinates $s = z$, $s = z^*$, and $s = \sigma^{(z)}$ are coded in MOM4p1, whereas the depth deviation coordinate *is not*.

Pressure based vertical coordinates that we consider include the following:

$$s = p \qquad \text{pressure} \tag{6.12}$$

$$s = p - p_{\mathrm{a}} \qquad \text{pressure-deviation} \tag{6.13}$$

$$s = \left(\frac{p - p_{\mathrm{a}}}{p_{\mathrm{b}} - p_{\mathrm{a}}}\right) \qquad \text{pressure-sigma} \tag{6.14}$$

$$s = p_{\mathrm{b}}^{o}\left(\frac{p - p_{\mathrm{a}}}{p_{\mathrm{b}} - p_{\mathrm{a}}}\right) \qquad \text{pressure-star.} \tag{6.15}$$

In these equations, p is the hydrostatic pressure at some depth within the ocean fluid, p_{a} is the pressure applied at the ocean surface $z = \eta$ from any media above the ocean, such as the atmosphere and sea ice, p_{b} is the hydrostatic pressure at the solid-earth lower boundary arising from all fluid above the bottom (ocean water and p_{a} above the ocean), and p_{b}^{o} is a time independent reference pressure, usually taken to be the bottom pressure in a resting ocean.[6] Since $p_{,z} = -\rho\, g < 0$ is single signed for the hydrostatic fluid, pressure provides a well defined vertical coordinate. Strengths and weaknesses of the corresponding depth based coordinates also hold for the pressure based coordinates, with the main difference being that pressure based models are non-Boussinesq.

6.2.1 Pressure coordinate

With a free surface, the vertical domain over which the p-coordinate

$$s = p \tag{6.16}$$

ranges is given by

$$p_{\mathrm{a}} \leq p \leq p_{\mathrm{b}}. \tag{6.17}$$

Hence, the surface and bottom boundaries are time dependent, whereas the density weighted specific thickness is constant

$$\rho\, z_{,s} = -g^{-1} \tag{6.18}$$

[6]Note that equation (11.64) of Griffies (2004) used the time dependent p_{b} rather than the time independent reference pressure p_{b}^{o}. The former vertical coordinate has not been used in practice, and so we focus here on that coordinate defined with the reference pressure p_{b}^{o}.

where the hydrostatic equation $p_{,z} = -\rho\, g$ was used. Relation (6.18) is the root of the isomorphism between Boussinesq depth based models and non-Boussinesq pressure based models.

The time dependent range for the pressure coordinate complicates the treatment of both the top and bottom cells. In particular, if the bottom pressure is less than the time independent discrete pressure level at the top interface of the lowest cell, then there is no mass within the bottom cell. Likewise, if the applied pressure is greater than the discrete pressure level at the bottom interface of the top cell, then there is no mass in the top cell. These results mean that grid cells have static vertical coordinate increments $\mathrm{d}s = \mathrm{d}p$ for all cells except the top and bottom. At the top, $\partial_t\,(\mathrm{d}s) = \partial_t\, p_\mathrm{a}$ and at the bottom $\partial_t\,(\mathrm{d}s) = -\partial_t\, p_\mathrm{b}$. The associated mass per unit area in the cells evolves according to $\partial_t\,(\rho\,\mathrm{d}z) = -g^{-1}\,\partial_t\, p_\mathrm{a}$ at the surface, and $\partial_t\,(\rho\,\mathrm{d}z) = g^{-1}\,\partial_t\, p_\mathrm{b}$ at the bottom. Hence, the mass within the top cell decreases when the applied pressure increases, and the mass in the bottom cell increases when the bottom pressure increases. Both the surface and the bottom cells can therefore vanish depending on the applied and bottom pressures.

The sum of the vertical coordinate increments can be found by noting the total mass per area is given by

$$\begin{aligned} g^{-1}\,(p_\mathrm{b} - p_\mathrm{a}) &= \sum \rho\,\mathrm{d}z \\ &= \sum \rho\, z_{,s}\,\mathrm{d}s \\ &= -g^{-1} \sum \mathrm{d}s, \end{aligned} \tag{6.19}$$

thus yielding the time dependent result

$$\sum \mathrm{d}s = -(p_\mathrm{b} - p_\mathrm{a}). \tag{6.20}$$

6.2.2 Pressure deviation coordinate

The pressure deviation coordinate

$$s = p - p_\mathrm{a} \tag{6.21}$$

removes the restriction on upper ocean grid cell resolution since $s = 0$ is the time independent value of the ocean surface. That is, this coordinate ranges between

$$0 \le s \le p_\mathrm{b} - p_\mathrm{a}. \tag{6.22}$$

This coordinate is isomorphic to the depth deviation coordinate $s = z - \eta$ discussed in Section 6.1.3, and shares the same limitations which prompt us *not* to have this coordinate coded in MOM4p1.

In summary, grid cells have static vertical coordinate increments $\mathrm{d}s$ for all cells except the bottom. At the bottom $\partial_t\,(\mathrm{d}s) = -\partial_t\,(p_\mathrm{b} - p_\mathrm{a})$. The associated mass per unit area in the bottom cell evolves according to $\partial_t\,(\rho\,\mathrm{d}z) = g^{-1}\,\partial_t\,(p_\mathrm{b} - p_\mathrm{a})$. As for the pressure coordinate, the sum of the vertical coordinate increments yields

$$\sum \mathrm{d}s = -(p_\mathrm{b} - p_\mathrm{a}). \tag{6.23}$$

6.2.3 Pstar coordinate

The pstar coordinate is given by

$$p^* = p_\mathrm{b}^o \left(\frac{p - p_\mathrm{a}}{p_\mathrm{b} - p_\mathrm{a}} \right), \tag{6.24}$$

where p_{b}^{o} is a time independent reference pressure. Two possible choices for p_{b}^{o} include

$$p_{\mathrm{b}}^{o} = g \int_{-H}^{0} \mathrm{d}z \, \rho^{\mathrm{init}}, \tag{6.25}$$

or the simpler case of

$$p_{\mathrm{b}}^{o} = g \, \rho_o \, H. \tag{6.26}$$

The p^* coordinate is isomorphic to the z^* coordinate, with p^* extending over the time independent range

$$0 \leq p^* \leq p_{\mathrm{b}}^{o}. \tag{6.27}$$

The sum of the vertical coordinate increments can be found by noting the total mass per area is given by

$$\begin{aligned} g^{-1} \left(p_{\mathrm{b}} - p_{\mathrm{a}} \right) &= \sum \rho \, \mathrm{d}z \\ &= \sum \rho \, z_{,s} \, \mathrm{d}s \\ &= - \left(\frac{p_{\mathrm{b}} - p_{\mathrm{a}}}{g \, p_{\mathrm{b}}^{o}} \right) \sum \mathrm{d}s, \end{aligned} \tag{6.28}$$

thus yielding the time independent result

$$\sum \mathrm{d}s = -p_{\mathrm{b}}^{o}. \tag{6.29}$$

6.2.4 Pressure sigma coordinate

The pressure-sigma terrain following coordinate

$$\sigma^{(p)} = \left(\frac{p - p_{\mathrm{a}}}{p_{\mathrm{b}} - p_{\mathrm{a}}} \right) \tag{6.30}$$

is the pressure analog to the depth based sigma coordinate $\sigma^{(z)} = (z - \eta)/(H + \eta)$. This coordinate has been used by Huang et al. (2001), and it shares the same advantages and disadvantages as the depth-based sigma coordinate. Grid cells have static vertical coordinate increments $\mathrm{d}s$ for all cells. The associated mass per unit area never vanishes in any cell, so long as the bottom pressure is greater than the applied pressure.

The sum of the vertical coordinate increments can be found by noting the total mass per area is given by

$$\begin{aligned} g^{-1} \left(p_{\mathrm{b}} - p_{\mathrm{a}} \right) &= \sum \rho \, \mathrm{d}z \\ &= \sum \rho \, z_{,s} \, \mathrm{d}s \\ &= -g^{-1} \left(p_{\mathrm{b}} - p_{\mathrm{a}} \right) \sum \mathrm{d}s, \end{aligned} \tag{6.31}$$

thus yielding the time independent result

$$\sum \mathrm{d}s = -1. \tag{6.32}$$

COORD	DEFINITION	RANGE	$g\,\rho\,z_{,s}$
pressure	p	$p_{\mathrm{a}} \le p \le p_{\mathrm{b}}$	-1
p-deviation	$p' = p - p_{\mathrm{a}}$	$0 \le p' \le p_{\mathrm{b}} - p_{\mathrm{a}}$	-1
pstar	$p^* = p_{\mathrm{b}}^o\,(p - p_{\mathrm{a}})/(p_{\mathrm{b}} - p_{\mathrm{a}})$	$0 \le p^* \le p_{\mathrm{b}}^o$	$-(p_{\mathrm{b}} - p_{\mathrm{a}})/p_{\mathrm{b}}^o$
p-sigma	$\sigma^{(p)} = (p - p_{\mathrm{a}})/(p_{\mathrm{b}} - p_{\mathrm{a}})$	$0 \le \sigma \le 1$	$-(p_{\mathrm{b}} - p_{\mathrm{a}})$

Table 6.2: Table of vertical coordinates based on pressure. These coordinates are naturally used for non-Boussinesq dynamics. Note that the density weighted specific thickness $\rho\,z_{,s}$ is depth independent. This property proves to be important for developing numerical algorithms in Section 7.6. The coordinates $s = p$, $s = p^*$, and $s = \sigma^{(p)}$ are coded in MOM4p1, whereas the pressure deviation coordinate *is not*.

6.2.5 Summary of the pressure based vertical coordinates

A technical reason that the pressure based coordinates considered here are so useful for non-Boussinesq hydrostatic modelling is that $\rho\,z_{,s}$ is either a constant or a two-dimensional field. In contrast, for depth based models $\rho\,z_{,s}$ is proportional to the three-dimensional *in situ* density ρ, thus necessitating special algorithmic treatment for non-Boussinesq z-models (see Greatbatch and McDougall (2003) and Griffies (2004)). Table 6.2 summarizes the pressure-based coordinates discussed in this section. The pressure and pressure deviation coordinates have time dependent ranges but time independent specific thicknesses $\rho\,z_{,s}$. The sigma and pstar coordinates have time independent range but time dependent specific thickness.

As Table 6.2 reveals, the specific thickness $z_{,s}$ is negative for the pressure-based coordinates, whereas it is positive for the depth-based coordinate (Table 6.1). The sign change arises since upward motion in a fluid column increases the geopotential coordinate z yet decreases the hydrostatic pressure p. To establish a convention, we assume that the thickness of a grid cell in z space is always positive

$$\mathrm{d}z = z_{,s}\,\mathrm{d}s > 0 \tag{6.33}$$

as is the case in the conventional z-models. With $z_{,s} < 0$ for the pressure-based vertical coordinates, the thickness of grid cells in s space is negative

$$\mathrm{d}s < 0 \qquad \text{for pressure-based coordinates with } z_{,s} < 0. \tag{6.34}$$

PART II
Numerical formulations

The purpose of this part of the document is to describe algorithms used to numerically solve the ocean primitive equations in MOM4p1.

CHAPTER
SEVEN

Quasi-Eulerian Algorithms

There are two types of ocean models as distinguished by their solution algorithms (Adcroft and Hallberg, 2006). Eulerian vertical coordinate algorithms diagnose the dia-surface velocity component from the continuity equation. Lagrangian vertical coordinate algorithms specify the dia-surface velocity component (e.g., zero diapycnal velocity in adiabatic simulations with isopycnal coordinates). Eulerian in this context does not mean that a grid cell has a time constant vertical position. Hence, the term quasi-Eulerian is often used. This chapter develops the semi-discrete budgets of a hydrostatic ocean model and then presents quasi-Eulerian solution algorithms. Notably, as implemented in MOM4p1, the quasi-Eulerian algorithms are formulated assuming a time independent number of grid cells. That is, MOM4p1 does not allow for vanishing cell thickness. This assumption simplifies the algorithms in many ways, but in turn limits the extent to which this code can be used for simulations where water masses change in a nontrivial manner (e.g., wetting and drying is not handled in MOM4p1).

7.1 Pressure and geopotential at tracer points

We discussed the discrete pressure gradient body force appropriate for a finite difference discretization in Sections 4.2 and 4.3. We require the anomalous hydrostatic pressure in the depth based models, and the anomalous geopotential height in the pressure based models. That is, for depth based vertical coordinate models, we need a discretization of the anomalous hydrostatic pressure (equation (4.20))

$$\begin{aligned} p' &= g \int_z^0 \rho' \, \mathrm{d}z \quad s = z \\ p' &= g \int_z^\eta \rho' \, \mathrm{d}z \quad s = z^*, \sigma^{(z)}. \end{aligned} \tag{7.1}$$

For pressure based vertical coordinate models, we need a discretization of the anomalous geopotential (equation (4.25))

$$\Phi' = -(g/\rho_o) \int_{-H}^{z} \rho' \, \mathrm{d}z. \tag{7.2}$$

The vertical integrals involve some ambguity for the finite difference formulation, since the tracer point is not vertically centred within the tracer cell for the case of a vertically nonuniform grid. In

this case, we may choose to compute the pressure and geopotential at the tracer point using a more accurate vertical integration that accounts for the non-centred placement of the tracer point.

The purpose of this section is to describe two methods used for the calculation of the pressure and geopotential at the tracer grid point. Details of this discretization affect the manner used for diagnosing the pressure conversion to buoyancy work, as described in Sections 10.4 and 10.5. The MOM4p1 code provides both choices, with both producing analogous results for the surface height and bottom pressure.

7.1.1 Pressure at tracer point: energetic method

If the equation of state is linear, and both density and velocity are advected with second order centered differences, then the conversion of pressure work to buoyancy work will balance potential energy changes. This equality led Bryan (1969) to formulate the hydrostatic pressure calculation according to

$$p'_{k+1} = p'_k + g\,\mathtt{dzwt_k}\,\overline{\rho'_k}^{z}. \tag{7.3}$$

That is, anomalous hydrostatic pressure is computed given knowledge of the thicknesses `dzwt` and the density ρ'_k. In this equation, primes refer to anomalies relative to the reference Boussinesq density

$$\rho' = \rho - \rho_o \tag{7.4}$$

and

$$\overline{\rho'_k}^{z} = (\rho'_k + \rho'_{k+1})/2 \tag{7.5}$$

is the simple vertical average of density. This average is the same as a finite volume average only if the grid cell thicknesses are uniform. With stretched vertical grids, the simple average differs from the finite volume average presented in Section 7.1.1. At the ocean surface, no average is available, so we use the finite volume value for the pressure

$$p'_{k=1} = g\,\mathtt{dzwt_{k=0}}\,\rho'_{k=1}. \tag{7.6}$$

Given this surface value, we then integrate downwards according to equation (7.3) to diagnose the anomalous hydrostatic pressure at each discrete k-level.

7.1.2 Pressure at a tracer point: finite volume considerations

Although the finite volume method for computing the pressure force requires the pressure and geopotential to be computed at the bottom of the tracer cells, we may choose to use a finite volume motivated approach for computing the pressure and geopotential at the tracer point. Referring to the right hand panel in Figure 7.1, a finite volume motivated computation of hydrostatic pressure at a tracer point is given by

$$\begin{aligned} p'_{k=1} &= g\,\mathtt{dztup_{k=1}}\,\rho'_{k=1} \\ p'_{k+1} &= p'_k + g\,\mathtt{dztlo_k}\,\rho'_k + g\,\mathtt{dztup_{k+1}}\,\rho'_{k+1}. \end{aligned} \tag{7.7}$$

The pressure at $k = 1$ is the same as prescribed in the energetic method. However, for stretched vertical grid cells, the interior cells have a different discrete pressure from that computed in the energetic method. The finite volume approach is more accurate for stretched vertical grids.

7.1.3 Discrete geopotential based on energetic considerations

Following in a manner analogous to the anomalous hydrostatic pressure in Section 7.1.1, we have the discretized anomalous geopotential

$$\begin{aligned} \Phi'_{k=kbot} &= -(g/\rho_o)\,\mathtt{dzwt_{kbot}}\;\rho'_{k=kbot} \\ \Phi'_k &= \Phi'_{k+1} - (g/\rho_o)\,\mathtt{dzwt_k}\;\overline{\rho'_k}^{z}. \end{aligned} \tag{7.8}$$

Iteration starts from the bottom at $k = kbot$ using the finite volume expression, and moves upward in the column towards the surface.

7.1.4 Discrete geopotential based on finite volume considerations

Following in a manner completely analogous to the anomalous hydrostatic pressure in Section 7.1.2, we have the discretized anomalous geopotential

$$\begin{aligned} \Phi'_{k=kbot} &= -(g/\rho_o)\,\mathtt{dztlo_{kbot}}\;\rho'_{k=kbot} \\ \Phi'_k &= \Phi'_{k+1} - (g/\rho_o)\,\mathtt{dztup_{k+1}}\;\rho'_{k+1} - (g/\rho_o)\,\mathtt{dztlo_k}\;\rho'_k. \end{aligned} \tag{7.9}$$

Iteration starts from the bottom at $k = kbot$ using the finite volume expression, and moves upward in the column towards the surface.

7.2 Initialization issues

When initializing a Boussinesq model, we place a fluid with initial *in situ* density ρ^{init} onto a grid with vertical increments `dzt`. Hence, both the density and volume of the grid cells are specified. The initial mass of fluid is thus implied from this initialization method. Furthermore, by definition, the surface elevation η is zero.

For the nonBoussinesq model, we place a fluid with initial *in situ* density ρ^{init} onto a grid with vertical pressure increments `dst`. Hence, both the density and mass of the grid cells are specified. The initial volume of fluid is thus implied from this initialization method. Furthermore, by definition, the bottom pressure anomaly, `pbot_t` − `pbot0`, is zero if we choose `pbot0` as the initial bottom pressure.

The initialization methods are isomorphic. Unfortunately, when initializing the Boussinesq model, there is no guarantee that its bottom pressure anomaly will be intially zero. Likewise, there is no guarantee that the surface elevation η will be zero with the nonBoussinesq initialization. In order to ensure that such is the case, an extra step is required. We outline these considerations for the nonBoussinesq model. In this case, the issues of initialization become most apparent, since a nonzero initial η is unacceptable for climate modelling. In particular, nonzero surface height gradients affect the initial movement of sea ice, and such is undesirable.

There are three general ways to approach nonBoussinesq initialization. First, we can modify the vertical pressure increments `dst` of the grid cells to accomodate the initial density and to retain a zero surface height. This approach generally requires nontrivial horizontal deviations in the `dst` array, so that it has full grid dependence `dst(i,j,k)`. Such dependence is generally acceptable for the bottom, where partial cells introduce this three-dimensional dependence to the vertical grid increments. However, with this added dependence in the ocean interior, there is a possibility for

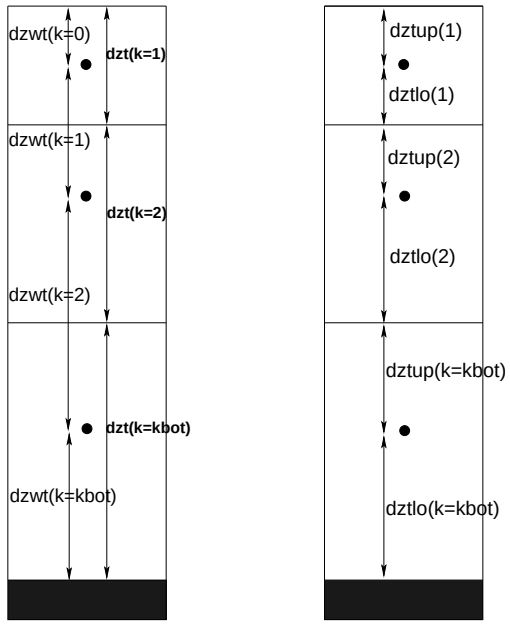

Figure 7.1: A vertical column of three tracer cells and the corresponding vertical cell dimensions. In MOM4p1, the vertical spacing is related by $\mathtt{dzt_k} = (\mathtt{dzwt_{k-1}} + \mathtt{dzwt_k})/2$. With this specification, the average tracer $\overline{T}^z = (T_k + T_{k+1})/2$ lives at the bottom of the tracer cell T_k and so is co-located with the dia-surface velocity component $\mathtt{w_bt_k}$. The right column exposes the half-distances, which measure the distance from the tracer cell point to the top and bottom faces of the tracer cell. The half-distances are used in the finite volume formulation of pressure and geopotential computed at the tracer points (Sections 7.1.2 and 7.1.4), whereas the grid spacing `dzwt` is used for the energetically based computation of pressure and geopotential computed at the tracer points (Sections 7.1.1 and 7.1.3).

introducing pressure gradient errors, depending on the magnitude of the horizontal variations. If the variations are minor, then this approach may be acceptable.

A second approach is to modify the initial density field. This approach, however, may fail after some time integration, depending on the surface forcing. That is, over time the model may be forced towards a density structure similar to the initial structure, in which case the possibility exists for losing the bottom cell in the model if the evolved bottom pressure becomes lighter than the pressure at the top of the bottom cell.

A third approach is motivated by one used with the MITgcm, and it is facilitated in the MOM4p1 code. Here, we deepen the bottom topography so that the initial mass (as set by the pressure increments) and density result in vertical columns with zero initial surface height. This approach may appear to be the least desirable, as we know the bottom topography generally more accurately than the initial density. Yet depending on details of the initial density field and the pressure increments, the changes in the bottom topography are often quite minor (see Section 37.1.1 for an example). We detail this approach in Section 7.3.3.4.

These issues of initializing the nonBoussinesq model are fundamental to how the vertical grid increments are determined for the model. So we now turn to a discussion of these increments.

7.3 Vertical dimensions of grid cells

The density weighted thickness of a grid cell is of fundamental importance in the formulation presented in this document. In particular, density weighted thickness of a tracer cell is a basic ingredient and the values on a velocity cell are diagnosed according to the minimum surrounding tracer cell values. Given these fields, most of the equations for the ocean model retain the same appearance for arbitrary vertical coordinates. The technology of generalized vertical coordinates then resides in the module specifying $\rho\,\mathrm{d}z$ (the MOM4p1 module `ocean_core/ocean_thickness` module), with extra work also needed for the pressure and grid modules.

In addition to the density weighted thicknesses, we are in need of the depth of a grid cell center, depth of the grid cell bottom, and vertical dimensions within the grid cell. Information is needed for these distances both in depth space (z-coordinate), and coordinate space (s-coordinate). These needs introduce new time dependent arrays that are updated and saved for restarts.

Figure 7.1 defines notation for the grid cell thicknesses used in MOM4p1. Here, the left figure exposes the vertical dimensions of the tracer grid cell, `dzt` and the distance between the T-cell points, `dzwt`. The right figure exposes the half-distances, which measure the distance from the T-cell point to the upper face of the cell, `dztup`, and the lower face, `dztlo`.

7.3.1 Thickness of a grid cell

The thickness of a grid cell is written

$$\mathrm{d}z = z_{,s}\,\mathrm{d}s. \tag{7.10}$$

For a tracer cell, this is written in the MOM4p1 code as

$$\mathtt{dzt} = \mathtt{dzt_dst} * \mathtt{dst}. \tag{7.11}$$

Inspection of the results from Tables 6.1 and 6.2 lead to the thicknesses given in Table 7.1, which are again applied to the tracer grid. The corresponding velocity cell thicknesses are diagnosed based on the tracer cell values.

For the finite volume approach to computing the pressure and geopotential, as discussed in Section 7.1.2, we need a method to compute the half-thicknesses. For this purpose, we assume the specific thickness factor `dzt_dst` is constant across the thickness of a tracer cell. We also assume knowledge of the half-s-thicknesses `dstlo` and `dstup`, thus leading to

$$\mathtt{dztlo} = \mathtt{dzt_dst} * \mathtt{dstlo} \tag{7.12}$$

$$\mathtt{dztup} = \mathtt{dzt_dst} * \mathtt{dstup}. \tag{7.13}$$

The full cell thickness is then recovered by setting

$$\mathtt{dzt} = \mathtt{dztlo} + \mathtt{dztup}, \tag{7.14}$$

where

$$\mathtt{dst} = \mathtt{dstlo} + \mathtt{dstup}. \tag{7.15}$$

COORD	DEFINITION	CELL THICKNESS
geopotential	z	$\mathrm{d}z$
zstar	$z^* = H\,(z-\eta)/(H+\eta)$	$\mathrm{d}z = (1+\eta/H)\mathrm{d}z^*$
z-sigma	$\sigma^{(z)} = (z-\eta)/(H+\eta)$	$\mathrm{d}z = (H+\eta)\,\mathrm{d}\sigma^{(z)}$
pressure	p	$\mathrm{d}z = -(\rho\, g)^{-1}\,\mathrm{d}p$
pstar	$p^* = p_{\mathrm{b}}^{o}\,(p-p_{\mathrm{a}})/(p_{\mathrm{b}}-p_{\mathrm{a}})$	$\mathrm{d}z = -[(p_{\mathrm{b}}-p_{\mathrm{a}})/(\rho\, g\, p_{\mathrm{b}}^{o})]\,\mathrm{d}p^*$
p-sigma	$\sigma^{(p)} = (p-p_{\mathrm{a}})/(p_{\mathrm{b}}-p_{\mathrm{a}})$	$\mathrm{d}z = -[(p_{\mathrm{b}}-p_{\mathrm{a}})/(\rho\, g)]\,\mathrm{d}\sigma^{(p)}$

Table 7.1: Table of vertical thicknesses $\mathrm{d}z$ for grid cells as determined on the tracer grid using the vertical coordinates discussed in Chapter 6. The vertical coordinate increments are specified, and the vertical thicknesses $\mathrm{d}z$ are diagnosed.

7.3.2 Vertical distance between tracer points

Through summation from the ocean surface, knowledge of the tracer cell thicknesses $\mathtt{dzt_k}$ within a vertical column provides the depth of the bottom of any tracer cell within the column. For many purposes, it is also important to know the depth where the tracer point is located. This information is obtained via vertical summation from the distance between two vertically adjacent tracer cell points. As seen in Section 7.1 when discussing the hydrostatic pressure and the geopotential, the vertical distance between tracer points is known as `dzwt` and the corresponding velocity cell vertical distance is `dzwu`.

7.3.2.1 Energetic based approach

For depth based vertical coordinates, `dzwt` is computed according to the results in Table 7.1 given the corresponding coordinate thicknesses `dswt`. For pressure based vertical coordinates using the energetic approach from Section 7.1.1, we are guided by the result (7.3) for the hydrostatic pressure computed in a depth based vertical coordinate model. In general, this expression takes the form

$$\mathrm{d}s = \overline{(s_{,z})}^{z}\,\mathrm{d}z \tag{7.16}$$

where $\overline{a}^z = (a_k + a_{k+1})/2$ is an unweighted discrete vertical average. Introducing model arrays leads to

$$\boxed{\mathtt{dzwt_k} = \left(\frac{2}{(s_{,z})_k + (s_{,z})_{k+1}}\right)\mathtt{dswt_k}.} \tag{7.17}$$

For example, with $s = p$, this relation takes the form

$$\mathtt{dzwt_k} = -\left(\frac{2}{g\,(\rho_k + \rho_{k+1})}\right)\mathtt{dswt_k}, \tag{7.18}$$

where `dswt` is known and is negative, since pressure decreases upward, whereas geopotential increases upward.

7.3.2.2 Finite volume approach

From the finite volume approach described in Section 7.3.1, we follow expressions (7.12) and (7.13) for the thickness of a grid cell to write

$$\mathtt{dzwt}_{\mathtt{k=0}} = \mathtt{dztup}_{\mathtt{k=1}} \tag{7.19}$$

$$\mathtt{dzwt}_{\mathtt{k>1}} = \mathtt{dztlo}_{\mathtt{k-1}} + \mathtt{dztup}_{\mathtt{k}} \tag{7.20}$$

$$\mathtt{dzwt}_{\mathtt{k=kbot}} = \mathtt{dztlo}_{\mathtt{k=kbot}}. \tag{7.21}$$

7.3.3 Summary of grid increments

We now summarize the previous results for the vertical coordinates z, z^*, $\sigma^{(z)}$, p, p^*, and $\sigma^{(p)}$. The notation used in mom4 is used here to allow for ready implementation in the model code.

7.3.3.1 Geopotential vertical coordinate

The geopotential vertical coordinate has the following grid dimensions

$$\begin{aligned} \mathtt{dzt_dst(i,j,k)} &= 1 \\ \mathtt{dzwt(i,j,k=0)} &= \mathtt{zt(k=1)} + \mathtt{eta_t(i,j)} \\ \mathtt{dzt(i,j,k=1)} &= \mathtt{zw(k=1)} + \mathtt{eta_t(i,j)}. \end{aligned} \tag{7.22}$$

The initial values of the depth of tracer points, `depth_zt`, remain unchanged in time. However, the thickness of the top cell is time dependent.

7.3.3.2 z^* vertical coordinate

The z^* coordinate has the grid dimensions

$$\begin{aligned} \mathtt{dzt_dst(i,j,k)} &= 1 + \mathtt{eta_t(i,j)}/\mathtt{ht(i,j)} \\ \mathtt{dst(i,j,k)} &= \mathtt{dzt(i,j,k)}|_{\tau=0} \\ \mathtt{dswt(i,j,k)} &= \mathtt{dzwt(i,j,k)}|_{\tau=0} \\ \mathtt{dzt(i,j,k)} &= \mathtt{dzt_dst(i,j,k)} * \mathtt{dst(i,j,k)}. \end{aligned} \tag{7.23}$$

For the energetically based computation of hydrostatic pressure (Section 7.1.1), the distance between tracer points is computed according to

$$\begin{aligned} \mathtt{dzwt(i,j,k=0)} &= \frac{\mathtt{dswt(i,j,k=0)}}{\mathtt{dst_dzt(i,j,k=1)}} \\ \mathtt{dzwt(i,j,k=1,kmt-1)} &= \frac{2\,\mathtt{dswt(i,j,k)}}{\mathtt{dst_dzt(i,j,k)} + \mathtt{dst_dzt(i,j,k+1)}} \\ \mathtt{dzwt(i,j,k=kmt)} &= \frac{\mathtt{dswt(i,j,k=kmt)}}{\mathtt{dst_dzt(i,j,k=kmt)}}. \end{aligned} \tag{7.24}$$

For the finite volume based computation of hydrostatic pressure (Section 7.1.2), the distance between tracer points is computed according to equations (7.19)-(7.21). Notice how the s-grid increments are constant in time, and are set by the z-grid increments at the initial model time step.

7.3.3.3 Terrain following $\sigma^{(z)}$ vertical coordinate

For the terrain following $\sigma^{(z)}$ coordinate, we proceed in a different manner than for the geopotential and z^* coordinates. Here, a dimensionless partition of the $\sigma^{(z)}$ coordinate is prescribed during initialization, and then the vertical grid dimensions deduced from knowledge of the depth field `ht`. The partitioning of $\sigma^{(z)}$ can be chosen in many ways. We choose to base this partition on the vertical grid dimensions $\mathtt{dzt(k)}$ and $\mathtt{dzw(k)}$ available in the Grid derived type. These are the *full cell* grid dimensions, which thus make `dst` and `dswt` independent of horizontal position (i, j).

$$\begin{aligned}
\mathtt{dzt_dst(i,j,k)} &= \mathtt{ht(i,j)} + \mathtt{eta_t(i,j)} \\
\mathtt{dst(i,j,k)} &= \mathtt{dzt(k)/zw(nk)} \\
\mathtt{dswt(i,j,k)} &= \mathtt{dzw(k)/zw(nk)} \\
\mathtt{dzt(i,j,k)} &= \mathtt{dzt_dst(i,j,k)} * \mathtt{dst(i,j,k)}.
\end{aligned} \tag{7.25}$$

For the energetically based computation of hydrostatic pressure (Section 7.1.1), the distance between tracer points is computed according to

$$\begin{aligned}
\mathtt{dzwt(i,j,k=0)} &= \frac{\mathtt{dswt(i,j,k=0)}}{\mathtt{dst_dzt(i,j,k=1)}} \\
\mathtt{dzwt(i,j,k=1,kmt-1)} &= \frac{2 * \mathtt{dswt(i,j,k)}}{\mathtt{dst_dzt(i,j,k)} + \mathtt{dst_dzt(i,j,k+1)}} \\
\mathtt{dzwt(i,j,k=kmt)} &= \frac{\mathtt{dswt(i,j,k=kmt)}}{\mathtt{dst_dzt(i,j,k=kmt)}}.
\end{aligned} \tag{7.26}$$

For the finite volume based computation of hydrostatic pressure (Section 7.1.2), the distance between tracer points is computed according to equations (7.19)-(7.21).

7.3.3.4 Non-terrain following pressure vertical coordinate

As described in Section 7.2, initialization of the nonBoussinesq model must take place in a manner different from the Boussinesq model. That is, specifying the vertical grid increments with pressure vertical coordinates introduces a fundamentally new consideration. Namely, the vertical grid dimensions `dzt` are a function of the initial *in situ* density ρ^{init}. However, with the present structure of MOM4p1, we only know the initial density after an initial grid structure is established. Furthermore, MOM4p1 does not allow for vanishing layers. Hence, there is a possibility that a first guess at a vertical grid layout based on the bottom topography and the initial density, will not provide for a realizable grid in a pressure model absent vanishing layers. This point necessitates a multiple step process in the initialization of the pressure based model. We clarify these points in the following discussion.

The first step of the initialization takes the initial temperature and salinity fields, and initial grid specification file, all generated using the familiar MOM4 preprocessing code that assumes geopotential vertical coordinates. From this information, we compute a vertical density profile function

$$\rho_o(k) = \frac{\sum_{i,j} \mathtt{dat}_{i,j} \mathtt{dzt}^0(i,j,k)\, \rho^{\text{init}}}{\sum_{i,j} \mathtt{dat}_{i,j} \mathtt{dzt}^0(i,j,k)}. \tag{7.27}$$

Here, the initial density ρ^{init} is assumed to live on the initial grid specified by thicknesses $\mathtt{dzt}^0(i,j,k)$ that are created just as if the model vertical coordinate were geopotential (including bottom partial cells). The model is run for a time step to allow for this function to be generated and written to a netCDF file. Then the model is rerun, now reading in this function as an input file for use in subsequent steps of the initialization.

Note that the vertical density profile function $\rho_o(k)$ takes account of the possibility for larger averaged density in the deep ocean, in which case the vertical pressure increments increase at depth even moreso than suggested by the generally larger vertical depth increments towards the deeper ocean. The utility of the density profile for specifying the pressure levels is a function of many model details. For example, in the global one degree model described in Section 37.1.1, using a reference profile proved to be detrimental to the abyssal flow in the tropics. We hypothesize that the profile produced a vertical grid spacing that was much coarser than otherwise provided with a depth basic vertical coordinate. Another possibility is there is a bug with the nontrivial $\rho_o(k)$ profile. Hence, we recommend the trivial choice

$$\rho_o(k) = \rho_o. \tag{7.28}$$

Other model configurations may find different profiles to be more useful.

We now proceed to generate the vertical grid increments $\mathtt{dst}$. As the model is pressure-based, these increments should be a function only of the vertical grid index k, with the only exception being at the bottom where partial bottom steps allow for i, j dependence

$$\mathtt{dstlo}(i,j,k) = -g\,\rho_o(k)\,\mathtt{dztlo}^0(i,j,k) \tag{7.29}$$

$$\mathtt{dstup}(i,j,k) = -g\,\rho_o(k)\,\mathtt{dztup}^0(i,j,k) \tag{7.30}$$

$$\mathtt{dst}(i,j,k) = \mathtt{dstlo}(k) + \mathtt{dstup}(k), \tag{7.31}$$

where again

$$\mathtt{dzt}^0(i,j,k) = \mathtt{dztlo}^0(i,j,k) + \mathtt{dztup}^0(i,j,k) \tag{7.32}$$

are generated by assuming the model is a geopotential model so that the i, j dependence arises just from the bottom partial cell adjustments.

Now that we have the vertical pressure increments $\mathtt{dst}(i,j,k)$, $\mathtt{dstlo}(i,j,k)$, and $\mathtt{dstup}(i,j,k)$, and the initial density ρ^{init}, we recompute the vertical depth increments so that

$$\mathtt{dztlo}^1(i,j,k) = -\frac{\mathtt{dstlo(i,j,k)}}{g\,\rho^{\text{init}}(i,j,k)} \tag{7.33}$$

$$\mathtt{dztup}^1(i,j,k) = -\frac{\mathtt{dstup(i,j,k)}}{g\,\rho^{\text{init}}(i,j,k)} \tag{7.34}$$

$$\mathtt{dzt}^1(i,j,k) = \mathtt{dztlo}(i,j,k) + \mathtt{dztup}(i,j,k). \tag{7.35}$$

The fundamental question is whether the above procedure allows for the same number of vertical grid cells to exist in a column with the pressure coordinate model as for the analog geopotential model. A general aim followed here is to include pressure coordinate models in MOM4p1 in a manner that represents an overall modest adjustment to what is commonly done for initializing geopotential models. Given this aim, we assume that both the geopotential model and pressure model have the same number of vertical grid cells within each column. That is, the $\mathtt{kmt(i,j)}$ array

computed for the geopotential model is the same as for the pressure model. This assumption is self-consistent with the same bottom topography array $\mathtt{ht(i,j)}$ *only if*

$$\sum_{k=1}^{k=kmt(i,j)} \mathtt{dzt}(i,j,k) \leq \mathtt{ht(i,j)}. \tag{7.36}$$

More stringently, we aim to allow for a nontrivial bottom cell thickness `dztmin` in the pressure model in order to regularize the numerical calculations in this cell, so that

$$\sum_{k=1}^{k=kmt(i,j)-1} \mathtt{dzt}(i,j,k) \leq \mathtt{ht(i,j)} - \mathtt{dztmin}. \tag{7.37}$$

If this condition fails, then we are unable to initialize the pressure model with the same density distribution and bottom depths as in the geopotential model. There are two options: modify the density or modify the bottom. The simplest option is to modify the bottom, and this option has been facilitated in MOM4p1. Depending on details of the initial density and `dztmin`, the modifications of the bottom are generally modest, and mostly localized to shallow ocean shelf regions. There is no general rule, and the researcher may wish to iterate somewhat to refine the choice of bottom topography for use with the pressure model. To appreciate the problem a bit more, we write the above sum as

$$\begin{aligned} \sum_{k=1}^{k=kmt(i,j)-1} \mathtt{dzt}(i,j,k) &= -\sum_{k=1}^{k=kmt(i,j)-1} \frac{\mathtt{dst(i,j,k)}}{g\,\rho^{\mathsf{init}}(i,j,k)} \\ &= \sum_{k=1}^{k=kmt(i,j)-1} \mathtt{dzt}^0(i,j,k)\,\frac{\rho_o(k)}{\rho^{\mathsf{init}}(i,j,k)}. \end{aligned} \tag{7.38}$$

Thus, if we admit regions of the ocean where density is far less than the profile $\rho_o(k)$, then the vertical column will be relatively thick. Hence, in order to maintain a zero initial surface height, as chosen in the geopotential model, we depress the bottom topography by some nonzero amount.

Assuming the bottom topography is chosen appropriately, we have the following means for computing the grid increments with the pressure vertical coordinate model. Here are the equations that summarize this step

$$\begin{aligned} \mathtt{dzt_dst(i,j,k)} &= -(\mathtt{g} * \mathtt{rho(i,j,k)})^{-1} \\ \mathtt{dswt(i,j,k=1,kmt-1)} &= -\mathtt{g} * \mathtt{rho_o(k)} * \mathtt{dzwt(i,j,k)}|_{\tau=0} \\ \mathtt{dst(i,j,k=2,kmt-1)} &= -\mathtt{g} * \mathtt{rho_o(k)} * \mathtt{dzt(i,j,k)}|_{\tau=0} \\ \mathtt{dswt(i,j,k=0)} &= -\mathtt{st(i,j,k=1)} + \mathtt{patm(i,j)} \\ \mathtt{dswt(i,j,k=kmt)} &= \mathtt{st(i,j,k=kmt)} - \mathtt{pbot(i,j)} \\ \mathtt{dst(i,j,k=1)} &= -\mathtt{sw(i,j,k=1)} + \mathtt{patm(i,j)} \\ \mathtt{dst(i,j,k=kmt)} &= \mathtt{sw(i,j,k=kmt-1)} - \mathtt{pbot(i,j)} \\ \mathtt{dzt(i,j,k)} &= \mathtt{dzt_dst(i,j,k)} * \mathtt{dst(i,j,k)}. \end{aligned} \tag{7.39}$$

For the energetically based computation of hydrostatic pressure (Section 7.1.1), the distance be-

tween tracer points is computed according to

$$\begin{aligned}
\mathtt{dzwt(i,j,k=0)} &= \frac{\mathtt{dswt(i,j,k=0)}}{\mathtt{dst_dzt(i,j,k=1)}} \\
\mathtt{dzwt(i,j,k=1,kmt-1)} &= \frac{2 * \mathtt{dswt(i,j,k)}}{\mathtt{dst_dzt(i,j,k)} + \mathtt{dst_dzt(i,j,k+1)}} \\
\mathtt{dzwt(i,j,k=kmt)} &= \frac{\mathtt{dswt(i,j,k=kmt)}}{\mathtt{dst_dzt(i,j,k=kmt)}}.
\end{aligned} \tag{7.40}$$

For the finite volume based computation of hydrostatic pressure (Section 7.1.2), the distance between tracer points is computed according to equations (7.19)-(7.21).

7.3.3.5 p^* vertical coordinate

The same initialization procedure is followed for p^* as for pressure. Following the initialization, the model employs the following equations for setting the vertical grid increments

$$\begin{aligned}
\mathtt{dzt_dst(i,j,k)} &= -\left(\frac{\mathtt{pbot(i,j)} - \mathtt{patm(i,j)}}{\mathtt{g} * \mathtt{rho(i,j,k)} * \mathtt{pbot0(i,j)}}\right) \\
\mathtt{dswt(i,j,k)} &= \mathtt{dswt(i,j,k)}|_{\tau=0} \\
\mathtt{dst(i,j,k)} &= \mathtt{dst(i,j,k)}|_{\tau=0} \\
\mathtt{dzt(i,j,k)} &= \mathtt{dzt_dst(i,j,k)} * \mathtt{dst(i,j,k)}
\end{aligned} \tag{7.41}$$

For the energetically based computation of hydrostatic pressure (Section 7.1.1), the distance between tracer points is computed according to

$$\begin{aligned}
\mathtt{dzwt(i,j,k=0)} &= \frac{\mathtt{dswt(i,j,k=0)}}{\mathtt{dst_dzt(i,j,k=1)}} \\
\mathtt{dzwt(i,j,k=1,kmt-1)} &= \frac{2 * \mathtt{dswt(i,j,k)}}{\mathtt{dst_dzt(i,j,k)} + \mathtt{dst_dzt(i,j,k+1)}} \\
\mathtt{dzwt(i,j,k=kmt)} &= \frac{\mathtt{dswt(i,j,k=kmt)}}{\mathtt{dst_dzt(i,j,k=kmt)}}.
\end{aligned} \tag{7.42}$$

For the finite volume based computation of hydrostatic pressure (Section 7.1.2), the distance between tracer points is computed according to equations (7.19)-(7.21).

7.3.3.6 Steps to initialize pressure and p^* based models

We now summarize the steps required to initialize the pressure and p^* based models.

- Determine $\mathtt{dzt}^0(i,j,k)$ as z-model, with $\sum_{k=1}^{kmt(i,j)} \mathtt{dzt}^0(i,j,k) = \mathtt{ht(i,j)}$
- Determine the density profile function $\mathtt{rho_o(k)}$ according to equation (7.27), with default $\mathtt{rho_o(k)} = \rho_o$.

- Set the pressure increments according to

$$\mathtt{dstlo}(i,j,k) = -g\,\mathtt{rho_o(k)}\,\mathtt{dztlo}^0(i,j,k) \tag{7.43}$$
$$\mathtt{dstup}(i,j,k) = -g\,\mathtt{rho_o(k)}\,\mathtt{dztup}^0(i,j,k) \tag{7.44}$$
$$\mathtt{dst}(i,j,k) = \mathtt{dstlo}(k) + \mathtt{dstup}(k), \tag{7.45}$$

- Insert the initial temperature and salinity to the grid points (i,j,k) to then determine the initial density $\rho^{\text{init}}(i,j,k)$.

- Determine the modified thickness of the grid cells according to

$$\mathtt{dztlo}^1(i,j,k) = -\frac{\mathtt{dstlo(i,j,k)}}{g\,\rho^{\text{init}}(i,j,k)} \tag{7.46}$$
$$\mathtt{dztup}^1(i,j,k) = -\frac{\mathtt{dstup(i,j,k)}}{g\,\rho^{\text{init}}(i,j,k)} \tag{7.47}$$
$$\mathtt{dzt}^1(i,j,k) = \mathtt{dztlo}(i,j,k) + \mathtt{dztup}(i,j,k). \tag{7.48}$$

- Determine if

$$\sum_{k=1}^{k=kmt(i,j)-1} \mathtt{dzt}(i,j,k) \leq \mathtt{ht(i,j)} - \mathtt{dztmin}. \tag{7.49}$$

  If so, then make no modifications to the bottom topography. If not, then deepen the bottom topography so that the following equality is satisfied

$$\mathtt{ht(i,j)}^{mod} = \sum_{k=1}^{k=kmt(i,j)-1} \mathtt{dzt}(i,j,k) + \mathtt{dztmin}. \tag{7.50}$$

- Determine the bottom cell thickness according to

$$\mathtt{dzt}(i,j,kmt) = \mathtt{ht(i,j)} - \sum_{k=1}^{k=kmt(i,j)-1} \mathtt{dzt}(i,j,k). \tag{7.51}$$

7.3.3.7 Terrain following $\sigma^{(p)}$ coordinate

For the terrain following $\sigma^{(p)}$ coordinate, we use the same dimensionless partition as for the $\sigma^{(z)}$ coordinate to initialize the grid arrangement. However, we have been unable to derive a self-consistent method to incorporate the *in situ* density into the algorithm, since to compute the bottom pressure we must know `dzt`, but to know `dzt` requires the bottom pressure. Hence, we expect there to be a large and spurious deviation in surface height just after initialization for runs with $\sigma^{(p)}$ coordinate.

During the integration, we make use of the following grid increments

$$\begin{aligned}
\mathtt{dzt_dst(i,j,k)} &= -\left(\frac{\mathtt{pbot(i,j)} - \mathtt{patm(i,j)}}{\mathtt{g} * \mathtt{rho(i,j,k)}}\right) \\
\mathtt{dswt(i,j,k)} &= -\mathtt{dzw(k)}/\mathtt{zw(nk)} \\
\mathtt{dst(i,j,k)} &= -\mathtt{dzt(k)}/\mathtt{zw(nk)} \\
\mathtt{dzt(i,j,k)} &= \mathtt{dzt_dst(i,j,k)} * \mathtt{dst(i,j,k)}
\end{aligned} \tag{7.52}$$

For the energetically based computation of hydrostatic pressure (Section 7.1.1), the distance between tracer points is computed according to

$$\begin{aligned}
\mathtt{dzwt(i,j,k=0)} &= \frac{\mathtt{dswt(i,j,k=0)}}{\mathtt{dst_dzt(i,j,k=1)}} \\
\mathtt{dzwt(i,j,k=1,kmt-1)} &= \frac{2 * \mathtt{dswt(i,j,k)}}{\mathtt{dst_dzt(i,j,k)} + \mathtt{dst_dzt(i,j,k+1)}} \\
\mathtt{dzwt(i,j,k=kmt)} &= \frac{\mathtt{dswt(i,j,k=kmt)}}{\mathtt{dst_dzt(i,j,k=kmt)}}.
\end{aligned} \tag{7.53}$$

For the finite volume based computation of hydrostatic pressure (Section 7.1.2), the distance between tracer points is computed according to equations (7.19)-(7.21).

7.3.4 Surface height diagnosed in pressure based models

For models using a pressure based vertical coordinate, the surface height η is diagnosed, whereas for depth based models it is computed prognostically (Section 7.4). To diagnose the surface height, we use the identity

$$\eta = -H + \sum \mathrm{d}z \tag{7.54}$$

given the thickness $\mathrm{d}z$ of each cell determined via Table 7.1. This is the original calculation provided in MOM4p1 for η. Another method, identical in the continuum but differing numerically due to finite precision, uses the following identity valid for the three pressure-based vertical coordinates supported in MOM4p1

$$H + \eta = \frac{p_\mathsf{b} - p_\mathsf{a}}{\rho_o\, g} - \rho_o^{-1} \int_{-H}^{\eta} \rho' \,\mathrm{d}z. \tag{7.55}$$

This alternative calculation is preferable computationally as it separates the smaller density contribution arising from density anomaly $\rho' = \rho - \rho_o$, from the larger bottom pressure contribution. This separation facilitates a more precise calculation by reducing numerical roundoff.

It is useful to note a common occurrance with pressure based models. Namely, the surface height will generally have a nonzero areal average even in the absence of mass fluxes. Such should be expected since the pressure based models conserve mass, not volume. For example, surface height can actually decrease even when mass is added to a column, so long as the column density increases by a sufficient amount. Hence, we are unable to make a general statement regarding the sign of the surface height without knowledge of both the mass per area in the column (as determined by the bottom pressure) as well as the vertical sum of the inverse density. Relatedly, the steric effect will cause the surface height to rise in regions of heating/freshing and decrease in regions of cooling/evaporation.

7.3.5 Bottom pressure diagnosed in depth based models

For models using a depth based vertical coordinate, it is necessary to diagnose the bottom pressure p_b using the following identity

$$p_\mathsf{b} = p_\mathsf{a} + g \sum \rho \,\mathrm{d}z. \tag{7.56}$$

Here, we use the *in situ* density ρ and the thickness $\mathrm{d}z$ of each cell.

7.4 Vertically integrated volume/mass budgets

The vertically integrated mass and volume budgets determine, respectively, the bottom pressure and the surface height. The purpose of this section is to derive these budgets for use with depth based and pressure based vertical coordinates.

7.4.1 Vertically integrated volume budget

The budget for the volume per unit horizontal area for a Boussinesq fluid integrated over the depth of a grid cell takes the following forms, depending on whether the cell is in the interior, the bottom, or the surface

$$\partial_t(\mathrm{d}z) = -\nabla_s \cdot (\mathrm{d}z\,\mathbf{u}) - (w^{(s)})_{s=s_{k-1}} + (w^{(s)})_{s=s_k} + \mathrm{d}z\,\mathcal{S}^{(\mathsf{V})} \tag{7.57}$$

$$\partial_t\,(\mathrm{d}z) = -\nabla_s \cdot (\mathrm{d}z\,\mathbf{u}) - (w^{(s)})_{s=s_{kbot-1}} + \mathrm{d}z\,\mathcal{S}^{(\mathsf{V})} \tag{7.58}$$

$$\partial_t\,(\mathrm{d}z) = -\nabla_s \cdot (\mathrm{d}z\,\mathbf{u}) + (w^{(s)})_{s=s_{k=1}} + q_{\mathsf{w}} + \mathrm{d}z\,\mathcal{S}^{(\mathsf{V})} \tag{7.59}$$

We obtained these equations from the mass budgets (3.166), (3.184), and (3.195), with density set to the constant Boussinesq reference value ρ_o, and with $\mathcal{S}^{(\mathsf{V})}$ a volume source (with units of inverse time). The vertical sum of these budgets leads to

$$\partial_t\,(H+\eta) = -\nabla \cdot \mathbf{U} + q_{\mathsf{w}} + \sum_k \mathrm{d}z\,\mathcal{S}^{(\mathsf{V})}, \tag{7.60}$$

where we used

$$\boxed{\sum_k \mathrm{d}z = H + \eta,} \tag{7.61}$$

which is the total thickness of the water column, and we introduced the depth integrated horizontal velocity

$$\sum_k \mathrm{d}z\,\mathbf{u} = \mathbf{U}. \tag{7.62}$$

Since H is the time independent ocean bottom, equation (7.60) provides a prognostic relation for the surface height

$$\boxed{\eta_{,t} = -\nabla \cdot \mathbf{U} + q_{\mathsf{w}} + \sum_k \mathrm{d}z\,\mathcal{S}^{(\mathsf{V})}.} \tag{7.63}$$

This is the free surface equation used for depth based vertical coordinate Boussinesq models.

7.4.2 Vertically integrated mass budget

The budget of the mass per unit horizontal area for a non-Boussinesq fluid integrated over the depth of a grid cell takes the following forms, depending on whether the cell is in the interior, the bottom, or the surface

$$\partial_t(\mathrm{d}z\,\rho) = -\nabla_s \cdot (\mathrm{d}z\,\rho\,\mathbf{u}) - (\rho\,w^{(s)})_{s=s_{k-1}} + (\rho\,w^{(s)})_{s=s_k} + \mathrm{d}z\,\rho\,\mathcal{S}^{(\mathsf{M})} \tag{7.64}$$

$$\partial_t\,(\mathrm{d}z\,\rho) = -\nabla_s \cdot (\mathrm{d}z\,\rho\,\mathbf{u}) - (\rho\,w^{(s)})_{s=s_{kbot-1}} + \mathrm{d}z\,\rho\,\mathcal{S}^{(\mathsf{M})} \tag{7.65}$$

$$\partial_t\,(\mathrm{d}z\,\rho) = -\nabla_s \cdot (\mathrm{d}z\,\rho\,\mathbf{u}) + (\rho\,w^{(s)})_{s=s_k} + \rho_{\mathsf{w}}\,q_{\mathsf{w}} + \mathrm{d}z\,\rho\,\mathcal{S}^{(\mathsf{M})}. \tag{7.66}$$

These are equations (3.166), (3.184), and (3.195). The vertical sum of these budgets lead to the vertically integrated balance of mass per area for a column of fluid

$$\partial_t \left(\sum_k \mathrm{d}z\, \rho \right) = -\nabla \cdot \left(\sum_k \mathrm{d}z\, \rho\, \mathbf{u} \right) + \rho_{\mathsf{w}}\, q_{\mathsf{w}} + \sum_k \mathrm{d}z\, \rho\, \mathcal{S}^{(\mathsf{M})}. \tag{7.67}$$

The vertical integral $\sum_k \mathrm{d}z\, \rho$ is the total mass per area in the fluid column. In a hydrostatic fluid, this mass per area is equal to the difference in pressure between the bottom and top of the column

$$\boxed{\sum_k \mathrm{d}z\, \rho = g^{-1}\, (p_{\mathsf{b}} - p_{\mathsf{a}}).} \tag{7.68}$$

Consequently, the mass budget generally takes the form

$$\begin{aligned} \partial_t (p_{\mathsf{b}} - p_{\mathsf{a}}) &= -g\, \nabla \cdot \left(\sum_k \mathrm{d}z\, \rho\, \mathbf{u} \right) + g\, \rho_{\mathsf{w}}\, q_{\mathsf{w}} + g \sum_k \mathrm{d}z\, \rho\, \mathcal{S}^{(\mathsf{M})} \\ &= -g\, \nabla \cdot \mathbf{U}^{\rho} + g\, \rho_{\mathsf{w}}\, q_{\mathsf{w}} + g \sum_k \mathrm{d}z\, \rho\, \mathcal{S}^{(\mathsf{M})} \end{aligned} \tag{7.69}$$

where

$$\mathbf{U}^{\rho} = \sum_k \mathrm{d}z\, \rho\, \mathbf{u} \tag{7.70}$$

is the vertically integrated density weighted horizontal velocity. The time tendency for the applied pressure could be provided by another component model. Without this information, it can be approximated by, for example,

$$\partial_t\, p_{\mathsf{a}} \approx \frac{p_{\mathsf{a}}(t) - p_{\mathsf{a}}(t-1)}{\Delta t}. \tag{7.71}$$

For the vertical integral of the horizontal momentum per volume, $\rho\, \mathbf{u}$, note that $z_{,s}\, \rho$ is depth independent for either choice of pressure based coordinates given in Table 6.2. In summary, for the pressure based coordinates in Table 6.2, the depth integrated mass balance (7.67) takes the form

$$\boxed{\partial_t\, (p_{\mathsf{b}} - p_{\mathsf{a}}) = -g\, \nabla \cdot \mathbf{U}^{\rho} + g\, \rho_{\mathsf{w}}\, q_{\mathsf{w}} + g \sum_k \rho\, \mathrm{d}z\, \mathcal{S}^{(\mathsf{M})}.} \tag{7.72}$$

7.4.3 Summary of the vertically integrated volume/mass budgets

In summary, the vertically integrated volume and mass budgets take on the isomorphic form

$$\boxed{\begin{aligned} \eta_{,t} &= -\nabla \cdot \mathbf{U} + q_{\mathsf{w}} + \sum_k \mathrm{d}z\, \mathcal{S}^{(\mathsf{V})} \\ g^{-1}\, \partial_t\, (p_{\mathsf{b}} - p_{\mathsf{a}}) &= -\nabla \cdot \mathbf{U}^{\rho} + \rho_{\mathsf{w}}\, q_{\mathsf{w}} + \sum_k \rho\, \mathrm{d}z\, \mathcal{S}^{(\mathsf{M})}. \end{aligned}} \tag{7.73}$$

These budgets provide prognostic relations for the surface height η in the Boussinesq case, and the bottom pressure p_{b} in the non-Boussinesq case. The tendency for the applied pressure p_{a} must be determined by another component model, or approximated via equation (7.71).

7.5 Compatibility between tracer and mass

Although we do not time step the vertically integrated tracer budget in an ocean model, it is useful to write it down for diagnostic purposes. Furthermore, it allows us to introduce a compatibility condition between tracer and mass budgets. To do so, recall the tracer budgets for the interior, bottom, and surface grid cells, given by equations (3.165), (3.183), and (3.194)

$$\begin{aligned}
\partial_t(\mathrm{d}z\,\rho\,C) &= \mathrm{d}z\,\rho\,\mathcal{S}^{(\mathsf{C})} - \nabla_s\cdot[\mathrm{d}z\,\rho\,(\mathbf{u}\,C+\mathbf{F})] \\
&\quad - [\rho\,(w^{(s)}\,C + F^{(s)})]_{s=s_{k-1}} \\
&\quad + [\rho\,(w^{(s)}\,C + F^{(s)})]_{s=s_{k}}. \\
\partial_t\,(\mathrm{d}z\,\rho\,C) &= \mathrm{d}z\,\rho\,\mathcal{S}^{(\mathsf{C})} - \nabla_s\cdot[\mathrm{d}z\,\rho\,(\mathbf{u}\,C+\mathbf{F})] \\
&\quad - \left[\rho\,(w^{(s)}\,C + F^{(s)})\right]_{s=s_{kbot-1}} \\
&\quad + Q^{(\mathsf{C})}_{(\mathsf{bot})} \\
\partial_t\,(\mathrm{d}z\,\rho\,C) &= \mathrm{d}z\,\rho\,\mathcal{S}^{(\mathsf{C})} - \nabla_s\cdot[\mathrm{d}z\,\rho\,(\mathbf{u}\,C+\mathbf{F})] \\
&\quad + \left[\rho\,(w^{(s)}\,C + F^{(s)})\right]_{s=s_{k=1}} \\
&\quad + \rho_{\mathsf{w}}\,q_{\mathsf{w}}\,C_{\mathsf{w}} - Q^{(\mathsf{turb})}_{(\mathsf{C})}.
\end{aligned}$$

Summing these budgets over a vertical column leads to

$$\begin{aligned}
\partial_t\left(\sum_k \mathrm{d}z\,\rho\,C\right) &= \sum_k \mathrm{d}z\,\rho\,\mathcal{S}^{(\mathsf{C})} - \nabla_s\cdot\left(\sum_k \mathrm{d}z\,\rho\,(\mathbf{u}\,C+\mathbf{F})\right) \\
&\quad + \left(\rho_{\mathsf{w}}\,q_{\mathsf{w}}\,C_{\mathsf{w}} - Q^{(\mathsf{turb})}_{(\mathsf{C})} + Q^{(\mathsf{bott})}_{(\mathsf{C})}\right).
\end{aligned} \tag{7.74}$$

As expected, the only contributions from vertical fluxes come from the top and bottom boundaries. Furthermore, by setting the tracer concentration to a uniform constant, all the turbulent flux terms vanish, in which case the budget reduces to the vertically integrated mass budget discussed in Section 7.4.2. This *compatiblity* between tracer and mass budgets must be carefully maintained by the discrete model equations.[1]

7.6 Diagnosing the dia-surface velocity component

The key distinction between Eulerian vertical coordinates and Lagrangian vertical coordinates is how they treat the dia-surface velocity component

$$w^{(s)} = z_{,s}\,\dot{s}. \tag{7.75}$$

[1] As discussed by Griffies et al. (2001), local conservation of an algorithm for tracer and volume/mass can readily be checked by running a model with uniform tracer concentration and blowing winds across the ocean surface. Surface height undulations will ensue, thus causing changes in volume for the grid cells. But the tracer concentration should remain uniform in the absence of surface fluxes. Changes in tracer concentration will not occur *if* the volume/mass and tracer budgets are compatible in the sense defined in this section.

The Lagrangian models prescribe it whereas Eulerian models diagnose it. The purpose of this section is develop Eulerian algorithms for diagnosing the dia-surface velocity component for the depth based and pressure based vertical coordinates of Chapter 6. As we will see, a crucial element for the utility of these algorithms is that the specific thickness $z_{,s}$ is depth independent using depth based coordinates in a Boussinesq fluid, and $\rho\, z_{,s}$ is depth independent using pressure based coordinates in a non-Boussinesq fluid.

7.6.1 Depth based vertical coordinates

Rearrange the grid cell volume budgets (7.57)-(7.59) to express the dia-surface velocity component for the top cell, interior cells, and bottom cell as

$$(w^{(s)})_{s=s_{k=1}} = \partial_t\,(\mathrm{d}z) - \mathrm{d}z\,\mathcal{S}^{(\mathsf{V})} + \nabla_s \cdot (\mathrm{d}z\,\mathbf{u}) - q_{\mathsf{w}} \tag{7.76}$$

$$(w^{(s)})_{s=s_k} = \partial_t(\mathrm{d}z) - \mathrm{d}z\,\mathcal{S}^{(\mathsf{V})} + \nabla_s \cdot (\mathrm{d}z\,\mathbf{u}) + (w^{(s)})_{s=s_{k-1}} \tag{7.77}$$

$$0 = \partial_t\,(\mathrm{d}z) - \mathrm{d}z\,\mathcal{S}^{(\mathsf{V})} + \nabla_s \cdot (\mathrm{d}z\,\mathbf{u}) + (w^{(s)})_{s=s_{kbot-1}}. \tag{7.78}$$

These equations are written from the surface to the bottom, with this order familiar from the $z-$coordinate version of MOM4p0. Equation (7.78) indicates that there is no transport through the ocean bottom. In a numerical model, this equation provides a useful diagnostic to check that dia-surface velocity components in the cells above the bottom have been diagnosed correctly. A nonzero result at the bottom signals a code bug.

We now detail how the dia-surface velocity component is diagnosed for the depth based vertical coordinates discussed in Section 6.1. To do so, we determine diagnostic relations for the time tendency $\partial_t\,(\mathrm{d}z)$ of the grid cell thickness as a function of vertical coordinate. Because $z_{,s}$ is independent of depth for these coordinates, we are able to express $\partial_t\,(\mathrm{d}z)$ as a function of $\eta_{,t}$, which in turn can be diagnosed using the vertically integrated volume budget.

7.6.1.1 Depth coordinate

For $s = z$, the only grid cell that admits a non-zero $\partial_t\,(\mathrm{d}z)$ is the surface cell, where $\partial_t\,(\mathrm{d}z) = \partial_t \eta$. Also, in MOM4p0 we assumed that there are no volume sources for $k > 1$. But this assumption is not fundamental. Indeed, volume sources throughout the column are not a problem, so long as their affects on volume conservation for the cell are properly handled in the diagnosis of the vertical velocity component. These results lead to the following expressions for the dia-surface velocity component $w^{(s)} = \dot{z} = w$

$$(w^{(s)})_{z=z_{k=1}} = \partial_t\,\eta - \mathrm{d}z\,\mathcal{S}^{(\mathsf{V})} + \nabla_z \cdot (\mathrm{d}z\,\mathbf{u}) - q_{\mathsf{w}} \tag{7.79}$$

$$(w^{(s)})_{z=z_k} = -\mathrm{d}z\,\mathcal{S}^{(\mathsf{V})} + \nabla_z \cdot (\mathrm{d}z\,\mathbf{u}) + (w^{(s)})_{z=z_{k-1}} \tag{7.80}$$

$$0 = -\mathrm{d}z\,\mathcal{S}^{(\mathsf{V})} + \nabla_z \cdot (\mathrm{d}z\,\mathbf{u}) + (w^{(s)})_{z=z_{nbot-1}}. \tag{7.81}$$

The right hand side of the surface height equation (7.63) can be used to eliminate $\eta_{,t}$ in equation (7.79), thus leading to a purely diagnostic set of equations

$$(w^{(s)})_{z=z_{k=1}} = -\mathrm{d}z\,\mathcal{S}^{(\mathsf{V})} + \nabla_z \cdot (\mathrm{d}z\,\mathbf{u}) + \sum_k \mathrm{d}z\,\mathcal{S}^{(\mathsf{V})} - \nabla \cdot \mathbf{U} \tag{7.82}$$

$$(w^{(s)})_{z=z_k} = -\mathrm{d}z\,\mathcal{S}^{(\mathsf{V})} + \nabla_z \cdot (\mathrm{d}z\,\mathbf{u}) + (w^{(s)})_{z=z_{k-1}} \tag{7.83}$$

$$0 = -\mathrm{d}z\,\mathcal{S}^{(\mathsf{V})} + \nabla_z \cdot (\mathrm{d}z\,\mathbf{u}) + (w^{(s)})_{z=z_{kbot-1}}. \tag{7.84}$$

The algorithm starts at $k = 1$ given knowledge of the right hand side terms in equation (7.82). Movement down the vertical column leads to the diagnosis of w for the full column.

7.6.1.2 Depth deviation coordinate

For $s = z - \eta$, the only grid cell that admits a non-zero $\partial_t\,(\mathrm{d}z)$ is the bottom cell where $\partial_t\,(\mathrm{d}z) = \partial_t \eta$. The dia-surface velocity component $(w^{(s)}) = \dot{s} = w - \dot{\eta}$ thus is diagnosed via

$$(w^{(s)})_{s=s_{k=1}} = -\mathrm{d}z\,\mathcal{S}^{(\mathsf{V})} + \nabla_s \cdot (\mathrm{d}z\,\mathbf{u}) - q_{\mathsf{w}} \tag{7.85}$$

$$(w^{(s)})_{s=s_k} = -\mathrm{d}z\,\mathcal{S}^{(\mathsf{V})} + \nabla_s \cdot (\mathrm{d}z\,\mathbf{u}) + (w^{(s)})_{s=s_{k-1}} \tag{7.86}$$

$$0 = \partial_t\,\eta - \mathrm{d}z\,\mathcal{S}^{(\mathsf{V})} + \nabla_s \cdot (\mathrm{d}z\,\mathbf{u}) + (w^{(s)})_{s=s_{kbot-1}}. \tag{7.87}$$

As with the depth coordinate $s = z$, we use the surface height equation (7.63) to eliminate $\eta_{,t}$ in equation (7.87) and so lead to a fully diagnostic set of equations

$$(w^{(s)})_{s=s_{k=1}} = -\mathrm{d}z\,\mathcal{S}^{(\mathsf{V})} - q_{\mathsf{w}} + \nabla_z \cdot (\mathrm{d}z\,\mathbf{u}) \tag{7.88}$$

$$(w^{(s)})_{z=z_k} = -\mathrm{d}z\,\mathcal{S}^{(\mathsf{V})} + (w^{(s)})_{z=z_{k-1}} + \nabla_z \cdot (\mathrm{d}z\,\mathbf{u}) \tag{7.89}$$

$$\begin{aligned} 0 = & -\mathrm{d}z\,\mathcal{S}^{(\mathsf{V})} + (w^{(s)})_{z=z_{kbot-1}} + \nabla_z \cdot (\mathrm{d}z\,\mathbf{u}) \\ & + q_{\mathsf{w}} + \sum_k \mathrm{d}z\,\mathcal{S}^{(\mathsf{V})} - \nabla \cdot \mathbf{U}. \end{aligned} \tag{7.90}$$

7.6.1.3 Zstar coordinate

For $s = z^* = H\,(z - \eta)/(H + \eta)$, all grid cells have time independent $\mathrm{d}s$ since the range for z^* is time independent. However, the specific thickness $z_{,s} = 1 + \eta/H$ is time dependent. The dia-surface velocity component is thus diagnosed via the equations

$$(w^{(s)})_{s=s_{k=1}} = \mathrm{d}s\,H^{-1}\,\eta_{,t} - \mathrm{d}z\,\mathcal{S}^{(\mathsf{V})} + \nabla_s \cdot (\mathrm{d}z\,\mathbf{u}) - q_{\mathsf{w}} \tag{7.91}$$

$$(w^{(s)})_{s=s_k} = \mathrm{d}s\,H^{-1}\,\eta_{,t} - \mathrm{d}z\,\mathcal{S}^{(\mathsf{V})} + \nabla_s \cdot (\mathrm{d}z\,\mathbf{u}) + (w^{(s)})_{s=s_{k-1}} \tag{7.92}$$

$$0 = \mathrm{d}s\,H^{-1}\,\eta_{,t} - \mathrm{d}z\,\mathcal{S}^{(\mathsf{V})} + \nabla_s \cdot (\mathrm{d}z\,\mathbf{u}) + (w^{(s)})_{s=s_{kbot-1}}. \tag{7.93}$$

The surface height equation (7.63) is used to eliminate $\eta_{,t}$ from each of these equations. Note that in verifying the correctness of these results, recall that $\sum_k \mathrm{d}s = H$ for $s = z^*$.

7.6.1.4 Depth-sigma coordinate

For $s = \sigma^{(z)} = (z - \eta)/(H + \eta)$, all grid cells have constant $\mathrm{d}s$ since the range for σ is time independent. However, it has a time dependent specific thickness $z_{,s} = H + \eta$. These results lead to the following expressions for the dia-surface velocity component

$$(w^{(s)})_{s=s_{k=1}} = \mathrm{d}s\, \eta_{,t} - \mathrm{d}z\, \mathcal{S}^{(\mathsf{V})} + \nabla_s \cdot (\mathrm{d}z\, \mathbf{u}) - q_{\mathsf{w}} \tag{7.94}$$

$$(w^{(s)})_{s=s_k} = \mathrm{d}s\, \eta_{,t} - \mathrm{d}z\, \mathcal{S}^{(\mathsf{V})} + \nabla_s \cdot (\mathrm{d}z\, \mathbf{u}) + (w^{(s)})_{s=s_{k-1}} \tag{7.95}$$

$$0 = \mathrm{d}s\, \eta_{,t} - \mathrm{d}z\, \mathcal{S}^{(\mathsf{V})} + \nabla_s \cdot (\mathrm{d}z\, \mathbf{u}) + (w^{(s)})_{s=s_{kbot-1}}. \tag{7.96}$$

The surface height equation (7.63) is used to eliminate $\eta_{,t}$ from each of these equations. In verifying the correctness of these results, recall that $\sum_k \mathrm{d}s = 1$ for $s = \sigma^{(z)}$.

7.6.1.5 General expression for dia-surface velocity component

In summary, for depth based vertical coordinates, the dia-surface velocity component is diagnosed via

$$\boxed{\begin{aligned} (w^{(s)})_{s=s_{k=1}} &= \partial_t\, (\mathrm{d}z) - \mathrm{d}z\, \mathcal{S}^{(\mathsf{V})} + \nabla_s \cdot (\mathrm{d}z\, \mathbf{u}) - q_{\mathsf{w}} \\ (w^{(s)})_{s=s_k} &= \partial_t (\mathrm{d}z) - \mathrm{d}z\, \mathcal{S}^{(\mathsf{V})} + \nabla_s \cdot (\mathrm{d}z\, \mathbf{u}) + (w^{(s)})_{s=s_{k-1}} \\ 0 &= \partial_t\, (\mathrm{d}z) - \mathrm{d}z\, \mathcal{S}^{(\mathsf{V})} + \nabla_s \cdot (\mathrm{d}z\, \mathbf{u}) + (w^{(s)})_{s=s_{kbot-1}} \end{aligned}} \tag{7.97}$$

where the thickness of a grid cell evolves according to

$$\boxed{\begin{aligned} &\partial_t\, (\mathrm{d}z) = \delta_{k,1}\, \eta_{,t} && s = z \\ &\partial_t\, (\mathrm{d}z) = \delta_{k,kbot}\, \eta_{,t} && s = z - \eta \\ &\partial_t\, (\mathrm{d}z) = \mathrm{d}s\, (\eta_{,t}/H) && s = H\, (z - \eta)/(H + \eta) \\ &\partial_t\, (\mathrm{d}z) = \mathrm{d}s\, \eta_{,t} && s = (z - \eta)/(H + \eta). \end{aligned}} \tag{7.98}$$

The surface height evolution

$$\boxed{\eta_{,t} = -\nabla \cdot \mathbf{U} + q_{\mathsf{w}} + \sum_k \mathrm{d}z\, \mathcal{S}^{(\mathsf{V})}} \tag{7.99}$$

embodies volume conservation for a Boussinesq fluid column. The right hand side of (7.99) is used in equations (7.98) to produce a purely diagnostic expression for the dia-surface velocity components.

7.6.2 Pressure based vertical coordinates

We now diagnose the dia-surface velocity component for pressure based vertical coordinates. For this purpose, rearrange the grid cell mass budgets (7.64)-(7.66) to express the vertical velocity component as

$$(\rho\, w^{(s)})_{s=s_{k=1}} = \partial_t\, (\mathrm{d}z\, \rho) - \mathrm{d}z\, \rho\, \mathcal{S}^{(\mathsf{M})} + \nabla_s \cdot (\mathrm{d}z\, \rho\, \mathbf{u}) - \rho_{\mathsf{w}}\, q_{\mathsf{w}} \tag{7.100}$$

$$(\rho\, w^{(s)})_{s=s_k} = \partial_t (\mathrm{d}z\, \rho) - \mathrm{d}z\, \rho\, \mathcal{S}^{(\mathsf{M})} + \nabla_s \cdot (\mathrm{d}z\, \rho\, \mathbf{u}) + (\rho\, w^{(s)})_{s=s_{k-1}} \tag{7.101}$$

$$0 = \partial_t\, (\mathrm{d}z\, \rho) - \mathrm{d}z\, \rho\, \mathcal{S}^{(\mathsf{M})} + \nabla_s \cdot (\mathrm{d}z\, \rho\, \mathbf{u}) + (\rho\, w^{(s)})_{s=s_{kbot-1}}. \tag{7.102}$$

As for the depth based vertical coordinates, we write these equations from the surface to the bottom. Equation (7.102) indicates that there is no transport through the ocean bottom. In a numerical model, this equation provides a useful diagnostic to check that velocity components in the cells above the bottom have been diagnosed correctly. A nonzero result at the bottom signals a code bug.

We proceed as for depth based vertical coordinates by determining diagnostic relations for $\partial_t (\rho \, \mathrm{d}z)$ as a function of the pressure based vertical coordinates discussed in Section 6.2. Because $\rho \, z_{,s}$ is independent of depth for these coordinates, we are able to express $\partial_t (\rho \, \mathrm{d}z)$ as a function of $\partial_t \, p_{\mathsf{a}}$ and $\partial_t \, p_{\mathsf{b}}$. The time tendency of the applied pressure is set according to other component models, or approximated as (7.71). The time tendency for the bottom pressure is set according to the vertically integrated mass budget (7.72). Finally, we note that it is the density weighted dia-surface velocity component $\rho \, w^{(s)}$ which is most naturally diagnosed in this approach. Conveniently, it is $\rho \, w^{(s)}$ that is required for the non-Boussinesq tracer and momentum budgets discussed in Sections 3.6 and 3.8.

7.6.2.1 Pressure coordinate

For $s = p$, the density weighted specific thickness is a constant for all grid cells

$$\rho \, z_{,s} = -g^{-1}, \tag{7.103}$$

but both the surface and bottom grid cells admit a non-zero $\partial_t (\rho \, \mathrm{d}z)$. At the surface[2],

$$\begin{aligned} \rho \, \mathrm{d}z &= -g^{-1} \, \mathrm{d}p \\ &= -g^{-1} \left(p_{\mathsf{a}} - p_{\text{bottom of cell } k=1} \right) \end{aligned} \tag{7.104}$$

which then leads to

$$\partial_t (\rho \, \mathrm{d}z) = -g^{-1} \, \partial_t \, p_{\mathsf{a}}. \tag{7.105}$$

That is, the top cell mass per area decreases when the applied pressure increases. This result follows since the bottom face of the top cell has a fixed pressure, but the top face is at the applied pressure p_{a}. As noted in Section 6.2, if the applied pressure becomes greater than $p_{\text{bottom of cell } k=1}$, then the top cell vanishes. For the bottom cell,

$$\begin{aligned} \rho \, \mathrm{d}z &= -g^{-1} \, \mathrm{d}p \\ &= -g^{-1} \left(p_{\text{top of cell } k=kbot} - p_{\mathsf{b}} \right), \end{aligned} \tag{7.106}$$

and so

$$\partial_t (\rho \, \mathrm{d}z) = g^{-1} \, \partial_t \, p_{\mathsf{b}}. \tag{7.107}$$

Hence, the bottom cell thickness increases as the bottom pressure increases. If the bottom pressure decreases below $p_{\text{top of cell } k=kbot}$, then the bottom cell vanishes. These results lead to the

[2]Recall that our convention in equation (6.34) is that $\mathrm{d}s < 0$ for pressure based vertical coordinates. At the surface with pressure coordinates $s = p$, the coordinate increment is $\mathrm{d}p = p_{\mathsf{a}} - p_{\text{bottom of cell } k=1}$. This increment is negative since the applied pressure is less than the pressure at the bottom interface to cell $k = 1$. For the bottom cell, $\mathrm{d}p = p_{\text{top of cell } k=kbot} - p_{\mathsf{b}}$, which is negative when the bottom pressure is greater than the pressure just above it.

following expressions for the density weighted dia-surface velocity component

$$(\rho\, w^{(s)})_{s=s_{k=1}} = \partial_t\, p_{\mathsf{a}} - \mathrm{d}s\, \mathcal{S}^{(\mathsf{M})} + \nabla_s \cdot (\mathrm{d}s\, \mathbf{u}) + g\, \rho_{\mathsf{w}}\, q_{\mathsf{w}} \tag{7.108}$$

$$(\rho\, w^{(s)})_{s=s_k} = -\mathrm{d}s\, \mathcal{S}^{(\mathsf{M})} + \nabla_s \cdot (\mathrm{d}s\, \mathbf{u}) + (\rho\, w^{(s)})_{s=s_{k-1}} \tag{7.109}$$

$$0 = -\partial_t\, p_{\mathsf{b}} - \mathrm{d}s\, \mathcal{S}^{(\mathsf{M})} + \nabla_s \cdot (\mathrm{d}z\, \mathbf{u}) + (\rho\, w^{(s)})_{s=s_{kbot-1}}. \tag{7.110}$$

As a check, a sum of these equations leads to the vertically integrated mass budget (7.72) written in pressure coordinates. These equations are converted to diagnostic expressions for the dia-surface velocity component by substituting the known time tendencies for the applied pressure $\partial_t\, p_{\mathsf{a}}$ (e.g., equation (7.71)) and the bottom pressure $\partial_t\, p_{\mathsf{b}}$ via the column integrated mass budget (7.72).

7.6.2.2 Pressure deviation coordinate

For $s = p - p_{\mathsf{a}}$, the only grid cell that admits a non-zero $\partial_t\, (\rho\, \mathrm{d}z)$ is the bottom cell. At this cell,

$$\begin{aligned} \rho\, \mathrm{d}z &= -g^{-1}\, \mathrm{d}p \\ &= -g^{-1}\, [p_{\text{top of cell } k=kbot} - (p_{\mathsf{b}} - p_{\mathsf{a}})], \end{aligned} \tag{7.111}$$

and so

$$\partial_t\, (\rho\, \mathrm{d}z) = g^{-1}\, \partial_t\, (p_{\mathsf{b}} - p_{\mathsf{a}}). \tag{7.112}$$

The right hand side can be diagnosed via the column integrated mass budget (7.72). These results lead to the following expressions for the dia-surface velocity component

$$(\rho\, w^{(s)})_{s=s_{k=1}} = -\mathrm{d}s\, \mathcal{S}^{(\mathsf{M})} + \nabla_s \cdot (\mathrm{d}s\, \mathbf{u}) + g\, \rho_{\mathsf{w}}\, q_{\mathsf{w}} \tag{7.113}$$

$$(\rho\, w^{(s)})_{s=s_k} = -\mathrm{d}s\, \mathcal{S}^{(\mathsf{M})} + \nabla_s \cdot (\mathrm{d}s\, \mathbf{u}) + (\rho\, w^{(s)})_{s=s_{k-1}} \tag{7.114}$$

$$0 = -\partial_t\, (p_{\mathsf{b}} - p_{\mathsf{a}}) - \mathrm{d}z\, \mathcal{S}^{(\mathsf{M})} + \nabla_s \cdot (\mathrm{d}s\, \mathbf{u}) + (\rho\, w^{(s)})_{s=s_{kbot-1}}. \tag{7.115}$$

As a check, the sum of these equations recovers the vertically integrated mass budget (7.72) written in pressure coordinates.

7.6.2.3 Pstar coordinate

For $s = p^*$ with

$$p^* = p_{\mathsf{b}}^o\, (p - p_{\mathsf{a}})/(p_{\mathsf{b}} - p_{\mathsf{a}}), \tag{7.116}$$

all grid cells have time independent constant $\mathrm{d}s$. We are then led to the following mass per horizontal volume of a grid cell

$$\begin{aligned} \rho\, \mathrm{d}z &= \rho\, z_{,s}\, \mathrm{d}s \\ &= -(g\, p_{\mathsf{b}}^o)^{-1}\, (p_{\mathsf{b}} - p_{\mathsf{a}})\, \mathrm{d}s. \end{aligned} \tag{7.117}$$

The time tendency

$$\partial_t\, (\rho\, \mathrm{d}z) = -\mathrm{d}s\, (g\, p_{\mathsf{b}}^o)^{-1}\, \partial_t\, (p_{\mathsf{b}} - p_{\mathsf{a}}) \tag{7.118}$$

can be diagnosed via the column integrated mass budget (7.72). We then use these results in the general expressions (7.100)-(7.102) to generate the algorithm for diagnosing the vertical velocity

components. As a check, the sum of these equations recovers the vertically integrated mass budget (7.72) written in pressure coordinates. Note that in verifying this identity, it is important to note that $\sum_k \mathrm{d}s = -p_{\mathsf{b}}^o$ for the pstar coordinate, which results from the following identities

$$\begin{aligned} p_{\mathsf{b}} - p_{\mathsf{a}} &= g \sum_k \rho \, \mathrm{d}z \\ &= g \sum_k \rho \, z_{,s} \, \mathrm{d}s \\ &= -\left(\frac{p_{\mathsf{b}} - p_{\mathsf{a}}}{p_{\mathsf{b}}^o} \right) \sum_k \mathrm{d}s, \end{aligned} \tag{7.119}$$

where we used the hydrstatic balance (7.68) for the first equality.

7.6.2.4 Pressure sigma coordinate

For $s = \sigma^{(p)} = (p - p_{\mathsf{a}})/(p_{\mathsf{b}} - p_{\mathsf{a}})$, all grid cells have time independent $\mathrm{d}s$ since the range for σ is time independent. However, this coordinate has a time dependent density weighted specific thickness, thus leading to

$$\begin{aligned} \rho \, \mathrm{d}z &= \rho \, z_{,s} \, \mathrm{d}s \\ &= -g^{-1} \, (p_{\mathsf{b}} - p_{\mathsf{a}}) \, \mathrm{d}s. \end{aligned} \tag{7.120}$$

We use these results in the general expressions (7.100)-(7.102) to generate the algorithm for diagnosing the vertical velocity components. As a check, the sum of these equations recovers the vertically integrated mass budget (7.72) written in pressure coordinates. In verifying this identity, it is important to note that $\sum_k \mathrm{d}s = -1$ for $s = \sigma^{(p)}$.

7.6.2.5 General expression for the dia-surface velocity component

In summary, for pressure based vertical coordinates, the dia-surface velocity component is diagnosed via

$$\boxed{\begin{aligned} (\rho \, w^{(s)})_{s=s_{k=1}} &= \partial_t \, (\mathrm{d}z \, \rho) - \mathrm{d}z \, \rho \, \mathcal{S}^{(\mathsf{M})} + \nabla_s \cdot (\mathrm{d}z \, \rho \, \mathbf{u}) - \rho_{\mathsf{w}} \, q_{\mathsf{w}} \\ (\rho \, w^{(s)})_{s=s_k} &= \partial_t (\mathrm{d}z \, \rho) - \mathrm{d}z \, \rho \, \mathcal{S}^{(\mathsf{M})} + \nabla_s \cdot (\mathrm{d}z \, \rho \, \mathbf{u}) + (\rho \, w^{(s)})_{s=s_{k-1}} \\ 0 &= \partial_t \, (\mathrm{d}z \, \rho) - \mathrm{d}z \, \rho \, \mathcal{S}^{(\mathsf{M})} + \nabla_s \cdot (\mathrm{d}z \, \rho \, \mathbf{u}) + (\rho \, w^{(s)})_{s=s_{kbot-1}}. \end{aligned}} \tag{7.121}$$

where the density weighted thickness of a grid cell evolves according to

$$\boxed{\begin{aligned} g \, \partial_t \, (\rho \, \mathrm{d}z) &= -\delta_{k,1} \, \partial_t \, p_{\mathsf{a}} + \delta_{k,kbot} \, \partial_t \, p_{\mathsf{b}} && s = p \\ g \, \partial_t \, (\rho \, \mathrm{d}z) &= \delta_{k,kbot} \, \partial_t \, (p_{\mathsf{b}} - p_{\mathsf{a}}) && s = p - p_{\mathsf{a}} \\ g \, \partial_t \, (\rho \, \mathrm{d}z) &= -(\mathrm{d}s / p_{\mathsf{b}}^o) \, \partial_t \, (p_{\mathsf{b}} - p_{\mathsf{a}}) && s = p_{\mathsf{b}}^o \, (p - p_{\mathsf{a}})/(p_{\mathsf{b}} - p_{\mathsf{a}}) \\ g \, \partial_t \, (\rho \, \mathrm{d}z) &= -\mathrm{d}s \, \partial_t \, (p_{\mathsf{b}} - p_{\mathsf{a}}) && s = (p - p_{\mathsf{a}})/(p_{\mathsf{b}} - p_{\mathsf{a}}) \end{aligned}} \tag{7.122}$$

and the bottom pressure evolution

$$\boxed{\partial_t \, (p_{\mathsf{b}} - p_{\mathsf{a}}) = -g \, \nabla \cdot \mathbf{U}^{\rho} + g \, \rho_{\mathsf{w}} \, q_{\mathsf{w}} + g \sum_k \rho \, \mathrm{d}z \, \mathcal{S}^{(\mathsf{M})}} \tag{7.123}$$

embodies mass conservation for a non-Boussinesq fluid column.

7.6.3 Comments about diagnosing the dia-surface velocity component

We emphasize again that a critical element in the Eulerian algorithms for diagnosing the vertical velocity components is the ability to exploit the depth independence of the specific thickness $z_{,s}$ for the depth based coordinates for a Boussinesq fluid, and the density weighted specific thickness $\rho\, z_{,s}$ for the pressure based coordinates for a non-Boussinesq fluid. These properties allow us to remove the time tendencies for surface height and pressure from the respective diagnostic relations by substituting the depth integrated budgets (7.63) for the depth based models, and (7.72) for the pressure based models. Absent the depth independence, one would be forced to consider another approach, such as the time extrapolation approach to approximate the time tendency proposed by Greatbatch and McDougall (2003) for implementing a non-Boussinesq algorithm within a Boussinesq model.

7.7 Vertically integrated horizontal momentum

We now outline the split between the fast vertically integrated dynamics from the slower depth dependent dynamics. This split forms the basis for the split-explicit method used in MOM4 to time step the momentum equation. For this purpose, we formulate the budget for the vertically integrated momentum budget.

7.7.1 Budget using contact pressures on cell boundaries

Before proceeding with a formulation directly relevant for MOM4, we note the form of the vertically integrated budget arising when we consider pressure acting on a cell as arising from the accumulation of contact stresses. For this purpose, we vertically sum the momentum budgets given by equations (3.238), (3.241) and (3.246), which leads to

$$\begin{aligned}(\partial_t + f\,\hat{\mathbf{z}}\wedge)\,\sum(\mathrm{d}z\,\rho\,\mathbf{u}) = &-\sum\Big(\hat{\mathbf{z}}\,\wedge\,(\mathrm{d}z\,\mathcal{M}\,\rho\,\mathbf{u}) + \nabla_s\cdot[\,\mathrm{d}z\,\mathbf{u}\,(\rho\,\mathbf{u})]\Big)\\ &+\sum\Big(-\nabla_s\,(p\,\mathrm{d}z) + \mathrm{d}z\,\rho\,\mathbf{F}\Big)\\ &+[\,p_{\mathrm{a}}\,\nabla\,\eta + \boldsymbol{\tau}^{\mathrm{wind}} + \rho_{\mathrm{w}}\,q_{\mathrm{w}}\,\mathbf{u}_{\mathrm{w}}\,]\\ &+[p_{\mathrm{b}}\,\nabla H - \boldsymbol{\tau}^{\mathrm{bottom}}].\end{aligned} \tag{7.124}$$

Contact pressures on the top and bottom of the grid cells cancel throughout the column, just as other vertical fluxes from momentum and friction. The remaining contact pressures are from the bottom and top of the ocean column and the vertically integrated contact pressures on the sides of the fluid column. Correspondingly, if we integrate over the horizontal extent of the ocean domain, we are left only with contact pressures acting on the solid boundaries and undulating free surface. Such is to be expected, since the full ocean domain experiences a pressure force only from its contact with other components of the earth climate system.

7.7.2 Budget using the pressure gradient body force

As discussed in Section 3.7.2, we prefer to formulate the contribution of pressure to the linear momentum balance as a body force, whereby we exploit the hydrostatic balance. Hence, to develop

the vertically integrated horizontal momentum budget, we start from the form of the budget given by equations (5.19), (5.20), and (5.21), rewritten here for the interior, bottom, and surface grid cells

$$\begin{aligned}[\partial_t + (f+\mathcal{M})\,\hat{\mathbf{z}}\wedge]\,(\mathrm{d}z\,\rho\,\mathbf{u}) = {} & \rho\,\mathrm{d}z\,\mathcal{S}^{(\mathbf{u})} - \nabla_s\cdot[\,\mathrm{d}z\,\mathbf{u}\,(\rho\,\mathbf{u})] \\ & - \mathrm{d}z\,(\nabla_s\,p + \rho\,\nabla_s\Phi) + \mathrm{d}z\,\rho\,\mathbf{F} \\ & - [\,\rho\,(w^{(s)}\,\mathbf{u} - \kappa\,\mathbf{u}_{,z})\,]_{s=s_{k-1}} \\ & + [\,\rho\,(w^{(s)}\,\mathbf{u} - \kappa\,\mathbf{u}_{,z})\,]_{s=s_k}\end{aligned} \tag{7.125}$$

$$\begin{aligned}[\partial_t + (f+\mathcal{M})\,\hat{\mathbf{z}}\wedge]\,(\mathrm{d}z\,\rho\,\mathbf{u}) = {} & \rho\,\mathrm{d}z\,\mathcal{S}^{(\mathbf{u})} - \nabla_s\cdot[\,\mathrm{d}z\,\mathbf{u}\,(\rho\,\mathbf{u})] \\ & - \mathrm{d}z\,(\nabla_s\,p + \rho\,\nabla_s\Phi) + \mathrm{d}z\,\rho\,\mathbf{F} \\ & - [\,\rho\,(w^{(s)}\,\mathbf{u} - \kappa\,\mathbf{u}_{,z})\,]_{s=s_{kbot-1}} \\ & - \boldsymbol{\tau}^{\text{bottom}}\end{aligned} \tag{7.126}$$

$$\begin{aligned}[\partial_t + (f+\mathcal{M})\,\hat{\mathbf{z}}\wedge]\,(\mathrm{d}z\,\rho\,\mathbf{u}) = {} & \rho\,\mathrm{d}z\,\mathcal{S}^{(\mathbf{u})} - \nabla_s\cdot[\,\mathrm{d}z\,\mathbf{u}\,(\rho\,\mathbf{u})] \\ & - \mathrm{d}z\,(\nabla_s\,p + \rho\,\nabla_s\Phi) + \mathrm{d}z\,\rho\,\mathbf{F} \\ & + [\,\boldsymbol{\tau}^{\text{wind}} + \rho_{\text{w}}\,q_{\text{w}}\,\mathbf{u}_{\text{w}}\,] \\ & + [\,\rho\,(w^{(s)}\,\mathbf{u} - \kappa\,\mathbf{u}_{,z})\,]_{s=s_{k=1}}.\end{aligned} \tag{7.127}$$

A vertical sum of the momentum budgets leads to

$$\begin{aligned}(\partial_t + f\,\hat{\mathbf{z}}\wedge)\,\sum(\mathrm{d}z\,\rho\,\mathbf{u}) = {} & \sum\,\rho\,\mathrm{d}z\,\mathcal{S}^{(\mathbf{u})} \\ & - \sum\Big(\hat{\mathbf{z}}\,\wedge\,(\mathrm{d}z\,\mathcal{M}\,\rho\,\mathbf{u}) + \nabla_s\cdot[\,\mathrm{d}z\,\mathbf{u}\,(\rho\,\mathbf{u})]\Big) \\ & + \sum\mathrm{d}z\,\Big(-\nabla_s\,p - \rho\,\nabla_s\,\Phi + \rho\,\mathbf{F}\Big) \\ & + \boldsymbol{\tau}^{\text{wind}} - \boldsymbol{\tau}^{\text{bottom}} + \rho_{\text{w}}\,q_{\text{w}}\,\mathbf{u}_{\text{w}}.\end{aligned} \tag{7.128}$$

Fluctuations in the surface height contribute both to fluctuations in the horizontal pressure gradient and the geopotential gradient. These fluctuations lead to fast barotropic or external gravity waves, and so they must be integrated with a small time step. In contrast, the slower baroclinic or internal motions can be integrated with a larger time step, upwards of 100 times longer depending on details of the motions. Hence, it is advantageous for ocean climate modeling to develop an algorithm that splits between the motions when time stepping the equations. Details of this split depend on whether we work with a depth based or pressure based vertical coordinate.

7.7.3 Depth based vertical coordinates

We follow the discussion in Section 4.2.1 where the pressure gradient is split according to either equation (4.18) for $s = z^*$ or $s = \sigma^{(z)}$, and equation (4.17) for $s = z$. For geopotential coordinates $s = z$ this split takes the form

$$\nabla_s\,p + \rho\nabla_s\,\Phi = \underbrace{\nabla\,(p_{\text{a}} + p_{\text{surf}})}_{\text{fast}} + \underbrace{\nabla_s\,p'_{\text{clinic}} + \rho'\,\nabla_s\,\Phi}_{\text{slow}} \tag{7.129}$$

where $p_{\text{surf}} = \rho(z=0)\, g\, \eta$, $\rho = \rho_o + \rho'$ and $p'_{\text{clinic}} = g \int_z^0 \rho' \, \mathrm{d}z$. For zstar or sigma coordinates, this split takes the form

$$\nabla_s \, p + \rho \nabla_s \, \Phi = \underbrace{\nabla \left(p_{\mathsf{a}} + \rho_0 \, g \, \eta \right)}_{\text{fast}} + \underbrace{\nabla_s \, p' + \rho' \, \nabla_s \, \Phi}_{\text{slow}} \tag{7.130}$$

where $p' = g \int_z^\eta \rho' \, \mathrm{d}z$ is the anomalous pressure field. The Boussinesq form of the vertically integrated momentum budget (7.128) thus takes the form

$$\boxed{\rho_o \left(\partial_t + f \, \hat{\mathbf{z}} \wedge \right) \sum (\mathrm{d}z \, \mathbf{u}) = \mathbf{G} - (H + \eta) \, \nabla \left(p_{\mathsf{a}} + p_{\text{surf}} \right)} \tag{7.131}$$

for $s = z$ coordinates, and similarly for $s = z^*$ and $s = \sigma^{(z)}$ coordinates. In either case, $\mathbf{G}$ is the vertical integral of the depth dependent terms on the right hand side of equation (7.128). $\mathbf{G}$ embodies all contributions that are generally evolving on the slower baroclinic time scale. This equation, along with the vertically integrated volume budget discussed in Section 7.4, form the barotropic system for the Boussinesq fluid in MOM4p1. These equations are time stepped to resolve the fast waves using a predictor-corrector or leap-frog scheme discussed in Chapter 12 of Griffies (2004) (see also Section 8.2), where $\mathbf{G}$ is held fixed over the course of the barotropic cycle. Note that the predictor-corrector is preferred due to its enhanced dissipation of small spatial scale features, which are of some concern on the B-grid due to the gravity wave null mode (Killworth et al., 1991; Griffies et al., 2001).

7.7.4 Pressure based vertical coordinates

We now follow the discussion in Section 4.2.3 where the pressure gradient is split according to equation (4.27) into a slow three dimensional term and fast two dimensional term

$$\nabla_s \, p + \rho \nabla_s \, \Phi = \underbrace{\rho \, \nabla_s \, \Phi' - (\rho'/\rho_o) \, \nabla_s \, p}_{\text{slow}} + \underbrace{(\rho/\rho_o) \, \nabla \left(p_{\mathsf{b}} + \rho_o \, \Phi_{\mathsf{b}} \right)}_{\text{fast}} . \tag{7.132}$$

where

$$\Phi' = -(g/\rho_o) \int_{-H}^{z} \rho' \, \mathrm{d}z. \tag{7.133}$$

The vertically integrated pressure gradient can be written

$$\begin{aligned} \sum \mathrm{d}z \left(\nabla_s \, p + \rho \nabla_s \, \Phi \right) &= \sum \mathrm{d}z \left[\rho \, \nabla_s \, \Phi' - (\rho'/\rho_o) \, \nabla_s \, p \right] \\ &\quad + \nabla \left(p_{\mathsf{b}} + \rho_o \, \Phi_{\mathsf{b}} \right) \sum (\rho/\rho_o) \, \mathrm{d}z \\ &= \sum \mathrm{d}z \left[\rho \, \nabla_s \, \Phi' - (\rho'/\rho_o) \, \nabla_s \, p \right] \\ &\quad + (g \, \rho_o)^{-1} \left(p_{\mathsf{b}} - p_{\mathsf{a}} \right) \nabla \left(p_{\mathsf{b}} + \rho_o \, \Phi_{\mathsf{b}} \right), \end{aligned} \tag{7.134}$$

where we used the hydrostatic balance to write

$$g \sum \rho \, \mathrm{d}z = p_{\mathsf{b}} - p_{\mathsf{a}} \tag{7.135}$$

The vertically integrated momentum budget (7.128) thus takes the form

$$\boxed{\left(\partial_t + f \, \hat{\mathbf{z}} \wedge \right) \sum (\mathrm{d}z \, \rho \, \mathbf{u}) = \mathbf{G} - (g \, \rho_o)^{-1} \left(p_{\mathsf{b}} - p_{\mathsf{a}} \right) \nabla \left(p_{\mathsf{b}} + \rho_o \, \Phi_{\mathsf{b}} \right),} \tag{7.136}$$

where $\mathbf{G}$ is the vertical integral of the depth dependent terms on the right hand side of equation (7.128), including the slow contribution to the pressure gradient force. The time stepping of equation (7.139) then proceeds as for the Boussinesq case discussed in Section 8.2. To help reduce errors in the calculation of the pressure gradient, it is useful to consider the following split of the bottom pressure

$$p_{\mathsf{b}} = p'_{\mathsf{b}} + \rho_o \, g \, H, \tag{7.137}$$

so that the vertically integrated mass and momentum budgets take the form

$$\partial_t \left(p'_{\mathsf{b}} - p_{\mathsf{a}} \right) = -g \, \nabla \cdot \mathbf{U}^{\rho} + g \, \rho_{\mathsf{w}} \, q_{\mathsf{w}} + g \sum_k \rho \, \mathrm{d}z \, \mathcal{S}^{(\mathsf{M})} \tag{7.138}$$

$$\left(\partial_t + f \, \hat{\mathbf{z}} \wedge \right) \mathbf{U}^{\rho} = \mathbf{G} - \left(g \, \rho_o \right)^{-1} \left(p_{\mathsf{b}} - p_{\mathsf{a}} \right) \nabla \, p'_{\mathsf{b}}. \tag{7.139}$$

The advantage of this formulation is that we remove the time independent bottom geopotential $\rho_o \, g \, H$ from the pressure gradient contribution to the vertically integrated velocity. As this contribution is huge, its removal enhances the numerical accuracy of the resulting pressure gradient.

CHAPTER

EIGHT

Time stepping schemes

The purpose of this chapter is to detail various issues of time stepping the discrete equations of MOM4p1. It is written in two main parts, with the first part focusing on details of the scheme inherited from MOM4.0, and successfully used for climate modelling. The second part revisits the MOM4.0 scheme, and proposes some alternatives that are presently under investigation in MOM4p1. The motivation for revisiting the MOM4.0 schemes is that they show problems when used with radiating open boundary conditions. Martin Schmidt led the studies into these alternative time stepping schemes, with further discussion in the appendix to Herzfeld et al. (2010).

8.1 Split between fast and slow motions

An algorithm of practical utility for climate modeling must split the fast and slow dynamics so that the slow dynamics can be updated with a much longer time step than the fast dynamics. These algorithms are known as split-explicit methods. Alternatives exist whereby the fast dynamics are time stepped implicitly and so may use the same time step as the slow dynamics. We prefer split-explicit methods since they are more efficient on parallel computers and arguably more straightforward (Griffies et al., 2001).

For a hydrostatic fluid, the fast motions can be approximated by the vertically integrated dynamics of Section 7.7 and the vertically integrated mass or volume budgets of Section 7.4. The remainder constitutes an approximation to the slower dynamics. Motions constituting the fast dynamics are embodied by the *barotropic* or *external* mode, and the slower motions are embodied by advection as well as the *baroclinic* or *internal* mode. Given the fundamental nature of the mass conserving non-Boussinesq flow, we formulate the split between the fast and slow modes using density weighting. For the Boussinesq flow, the density weighting reduces to an extra ρ_o factor that trivially cancels.

Following the discussion in Section 12.3.5 of Griffies (2004), we consider the following split of

the velocity

$$\begin{aligned}\mathbf{u} &= \underbrace{\mathbf{u} - \frac{\sum_k \rho\,\mathrm{d}z\,\mathbf{u}}{\sum_k \rho\,\mathrm{d}z}}_{\text{slow}} + \underbrace{\frac{\sum_k \rho\,\mathrm{d}z\,\mathbf{u}}{\sum_k \rho\,\mathrm{d}z}}_{\text{fast}} \\ &\equiv \hat{\mathbf{u}} + \overline{\mathbf{u}}^z.\end{aligned} \tag{8.1}$$

The fast barotropic velocity

$$\overline{\mathbf{u}}^z = \frac{\mathbf{U}^\rho}{\sum_k \rho\,\mathrm{d}z} \tag{8.2}$$

is updated according to the vertically integrated momentum equation of Section 7.7. The slow baroclinic velocity $\hat{\mathbf{u}}$ has zero density weighted vertical sum, and so its update is independent of any depth independent forcing, such as fast fluctuations in the surface height associated with external gravity waves. Therefore, we choose to update the slow dynamics using all pieces of the momentum equation forcing, except contributions from the rapid pressure and geopotential fluctuations. This update produces a velocity $\mathbf{u}'$ that is related to the baroclinic velocity via

$$\hat{\mathbf{u}} = \mathbf{u}' - \frac{\sum_k \rho\,\mathrm{d}z\,\mathbf{u}'}{\sum_k \rho\,\mathrm{d}z}. \tag{8.3}$$

A similar relation was discussed in Section 12.4.2 of Griffies (2004). For global climate simulations, the time step available for the update of the slow dynamics is much larger (50 to 100 times larger) than the fast dynamics. It is this large time split, and the attendant improved model efficiency, that motivate the added complication arising from splitting the modes. Completing the updates of $\mathbf{u}'$ and $\mathbf{U}^\rho$ allows for an update of the full horizontal velocity via

$$\mathbf{u} = \left(\mathbf{u}' - \frac{\sum_k \rho\,\mathrm{d}z\,\mathbf{u}'}{\sum_k \rho\,\mathrm{d}z}\right) + \frac{\mathbf{U}^\rho}{\sum_k \rho\,\mathrm{d}z}. \tag{8.4}$$

8.2 Time stepping the model equations as in MOM4.0

We present here some details of the time stepping schemes available in MOM4p1. Much of this section is taken from the paper Griffies et al. (2005) that documents two ocean climate models developed at GFDL; the OM3.0 and OM3.1 models. Time stepping in OM3.0 is based on the standard MOM approach originating from the work of Bryan (1969), and detailed for an explicit free surface by Killworth et al. (1991) and Griffies et al. (2001). An alternative was developed for OM3.1.

The main motivation for developing an alternative was to address tracer non-conservation associated with time filtering used to suppress the leap frog computational mode appearing in the standard method. The proposed *time staggered* method has much in common with that used by Hallberg (1997) for his isopycnal model, as well as by Marshall et al. (1997) and Campin et al. (2004) for their hydrostatic and non-hydrostatic z-coordinate models.

The purpose of this section is to detail features of the time stepping schemes employed in OM3.0 and OM3.1. Further details are provided in Chapter 12 of Griffies (2004). We also refer the reader to the pedagogical treatments of time stepping given by Mesinger and Arakawa (1976), Haltiner and Williams (1980), and Durran (1999). For simplicity, we focus here on the Boussinesq system assuming z-coordinates for the vertical. The more general case of arbitrary vertical coordinates with Boussinesq or nonBoussinesq equations follows trivially from the discussions here.

8.2.1 The standard scheme used in OM3.0

We start by describing the standard approach used in MOM for time stepping tracers and baroclinic velocity. For the thickness weighted tracer equation, this update takes the form

$$\frac{(h\,T)^{\tau+1} - (\overline{h}\,\overline{T})^{\tau-1}}{2\,\Delta\tau_{\text{leap}}} = -\nabla_z \cdot \left[\,(h\,\mathbf{u})^{\tau}\,T^{\tau,\tau-1} + h^{\tau}\,\mathbf{F}^{\tau-1}\,\right] - \delta_k\left[\,w^{\tau}\,T^{\tau,\tau-1} + F_z^{\tau+1}\,\right]. \tag{8.5}$$

Here, h is the time dependent thickness of a tracer cell and T is the associated tracer concentration. Horizontal and vertical advection velocity components are written $(\mathbf{u}, w)$, and $(\mathbf{F}, F_z)$ are the horizontal and vertical SGS flux components. The horizontal gradient operator is written ∇_z, and δ_k is the vertical finite difference operator acting across a discrete level k. Prognostic fields are updated in time increments of $\Delta\tau_{\text{leap}}$. The thickness of a tracer cell is updated analogously to the tracer, as required to maintain compatiblity between volume and tracer evolution (see Section (Griffies et al., 2001).

The time tendency in equation (8.5) has been aproximated with a centred in time discrete operator. Skipping the central time step τ introduces a spurious computational mode, where even and odd steps decouple. We choose time filtering to suppress the associated instability, with $\overline{h}$ and $\overline{T}$ denoting the time filtered thickness and tracer concentration. Absent time filtering, the discrete time tendency has a second order global truncation error, whereas time filtering degrades the truncation error to first order (see Section 2.3.5 of Durran (1999)). We comment further on time filtering in the subsequent discussion, as it is central to why we considered alternative time stepping schemes.

Global ocean models generally employ anisotropic grids, with significantly more refined vertical spacing than horizontal. When admitting realistically fast vertical mixing processes, parameterized by F_z, a time implicit method is used to overcome the stringent time step constraints of an explicit approach. Hence, F_z is evaluated at the future time $\tau + \Delta\tau_{\text{leap}}$. In contrast, coarser grid spacing in the horizontal generally allows for an explicit implementation of the horizontal SGS fluxes. Due to the dissipative nature of SGS fluxes, stability considerations require them to be evaluated at the lagged time $\tau - \Delta\tau_{\text{leap}}$, with evaluation at the central time τ numerically unstable. That is, the horizontal SGS fluxes are implemented with a forward time step of size $2\,\Delta\tau_{\text{leap}}$.

In contrast to dissipative terms, numerical stability dictates that tracer concentration in the advection operator be evaluated at the central time τ *if* using central spatial differencing. As reviewed by Griffies et al. (2000a), this approach has been common in z-models for decades. This form of the time stepping gives rise to the commonly referred name *leap frog* applied to the standard time stepping used in MOM. However, it is important to note that leap frog in the tracer equation is used only for advection, and only for central spatial discretizations of advection. Dissipative terms are implemented with either a forward or an implicit time step as described above.

We found the dispersive errors from central differenced tracer advection to be unacceptable, due to the introduction of spurious tracer extrema and the large levels of spurious dianeutral mixing when convective adjustment acts on dispersion errors (Griffies et al., 2000b). We chose the third order upwind biased scheme to address these issues. As reviewed in Durran (1999), upwind biasing introduces a damping or dissipative element to numerical advection. Consequently, upwind biased fluxes *must* be evaluated at the lagged time $\tau - \Delta\tau_{\text{leap}}$ just like the dissipative horizontal SGS fluxes. A similar situation arises when implementing the Quicker advection scheme, in which one separates a dissipative portion evaluated at the lagged time step from a non-dissipative piece

evaluated at τ (Holland et al., 1998; Pacanowski and Griffies, 1999). This is the origin of the two time labels placed on the tracer concentration for the advective flux in equation (8.5).

For the Sweby advection scheme, the split into dissipative and non-dissipative terms is not possible. The full advective flux is thus evaluated at the lagged time step. This result may suggest increased levels of dissipation using Sweby relative to Quicker. Indeed, this is the case in regions where dissipation is welcomed, such as near river mouths where Quicker was found to introduce unacceptable tracer extrema. In other regions of the simulation, we have seen negligible differences between the two advection schemes.

An update of the thickness weighted baroclinic velocity using the standard time stepping scheme in MOM takes the form

$$\begin{aligned}\frac{h^{\tau+1}\,\mathbf{u}^{\tau+1} - \overline{h}^{\tau-1}\,\overline{\mathbf{u}}^{\tau-1}}{2\,\Delta\tau} = &- \mathcal{M}^{\tau}\,\hat{\mathbf{z}} \times h^{\tau}\,\mathbf{u}^{\tau} \\ &+ (w^{\tau}\,\mathbf{u}^{\tau})_k - (w^{\tau}\,\mathbf{u}^{\tau})_{k-1} \\ &- \nabla_z \cdot (h^{\tau}\,\mathbf{u}^{\tau}\,\mathbf{u}^{\tau}) \\ &- h^{\tau}\,(f\,\hat{\mathbf{z}} \times \mathbf{u})_{\text{trapezoidal}} \\ &- h^{\tau}\,\nabla_z\,(p^{\tau}/\rho_o) \\ &+ h^{\tau}\,(\mathbf{F}^{\mathbf{u}})^{(\tau-1,\tau+1)}.\end{aligned} \tag{8.6}$$

As for the tracer update, time filtering is applied to the lagged values of velocity and velocity cell thickness to suppress time splitting. Central differences are used to spatially discretize velocity self-advection, thus necessitating its evaluation at the central time step. Pressure is temporally evaluated likewise. The friction operator $(\mathbf{F}^{\mathbf{u}})^{(\tau-1,\tau+1)}$ arises from horizontal and vertical fluid deformations. Analogous to the treatment of tracer SGS fluxes, horizontal deformations are evaluated at $\tau - \Delta\tau_{\text{leap}}$ (forward time step) and vertical deformations at $\tau + \Delta\tau_{\text{leap}}$ (implicit time step).

Inertial energy is realistic in the climate model since it includes a diurnal cycle of solar insolation, and the atmosphere and sea ice fields passed to the ocean (wind stress, fresh water, turbulent and radiative fluxes)[1] are updated every two hours. Inertial energy has important contributions to the mixing coefficients determined by the model's boundary layer scheme.

The model's baroclinic time step is smaller than that needed to resolve inertial oscillations (e.g., Section 12.8.3 of Griffies (2004)). We nonetheless encountered an inertial-like instability in the climate model's Arctic sector when implementing the Coriolis force explicitly in time (see Chapter 11 for a discussion of a discrete implementation of the Coriolis Force). This instability is presumably related to the coupling between the ocean and sea ice, although the precise mechanism remains under investigation. The climate model remained stable, however, when implementing the ocean's Coriolis force with a trapezoidal or semi-implicit method (Section 11.3). Hence, this is the method employed in both OM3.0 and OM3.1.

8.2.2 Problems related to tracer conservation

Consider now the discrete time tracer equation in the abbreviated form

$$(h\,T)^{\tau+\Delta\tau_{\text{leap}}} = (\overline{h}\,\overline{T})^{\tau-\Delta\tau_{\text{leap}}} + 2\,\Delta\tau\,G, \tag{8.7}$$

[1] As recommended by Pacanowski (1987), wind stress applied to the ocean surface is computed using the relative velocity between the atmospheric winds and the ocean currents.

where G symbolizes the advective and diffusive terms as well as boundary fluxes (we ignore source/sink terms for brevity). Thickness at the lagged time step results from a time average as described in Griffies et al. (2001), whereas time filtering of tracer concentration is taken in the form suggested by Robert (1966) and Asselin (1972) (see also Section 2.3.5 of Durran (1999)).[2] Integrating equation (8.7) over the model domain leads to the balance of total tracer content in the model. Total tracer at time $\tau + \Delta\tau_{\text{leap}}$ is determined by the input of tracer through boundaries during the $2\,\Delta\tau_{\text{leap}}$ time step, plus the volume integrated product of the time filtered thickness and tracer concentration, $\overline{h}\,\overline{T}$, at the lagged time $\tau - \Delta\tau_{\text{leap}}$. Notably, because of time filtering, the model's total tracer changes even in the case of zero boundary fluxes.

The magnitude of tracer change associated with time filtering can be negligible for many purposes, as discussed in Griffies et al. (2001). However, we found the changes unacceptable when developing ecosystem models, where precise conservation is desired. Additionally, filtering contributed to a globally averaged heat non-conservation in the climate model on the order of $\pm 0.03\,\text{W}\,\text{m}^{-2}$. This non-conservative heat flux is a few percent of the surface insolation change expected from doubling greenhouse gas concentrations in the atmosphere. It is therefore of concern for our climate change simulations. Consequently, alternative approaches were investigated.

8.2.3 The time staggered scheme used in OM3.1

The alternative scheme we employ in OM3.1 discretizes the time derivative with a forward time step. That is, it does not skip any time levels. Additionally, it staggers tracer and velocity fields by one-half time step in a manner analogous to spatial staggering on Arakawa grids. We therefore refer to this method as a *time staggered scheme*.

Forward time stepping does not admit time splitting, and so no time filters are needed. The alternative scheme therefore ensures tracer is conserved, which is our primary motivation for moving away from the standard method involving the leap frog. There are other consequences of changing the time tendency discretization, and the purpose of this section is to expose these issues.

A time staggered update of thickness weighted tracer is given by

$$\frac{(h\,T)^{\tau+1/2} - (h\,T)^{\tau-1/2}}{\Delta\tau_{\text{stag}}} = -\nabla_z \cdot \left[\, (h\,\mathbf{u})^{\tau}\, T^{\tau-1/2} + h^{\tau}\, \mathbf{F}^{\tau-1/2} \,\right] - \delta_k \left[\, w^{\tau}\, T^{\tau-1/2} + F_z^{\tau+1/2} \,\right]. \tag{8.8}$$

The two equations (8.5) and (8.8) become identical when the following holds:

- time steps are related by $\Delta\tau_{\text{stag}} = 2\,\Delta\tau_{\text{leap}}$,
- time filtering in the standard method is not used, and
- tracer advection employs an upwind biased scheme.

In effect, the time staggered method stays on just one of the two leap frog branches. This is the fundamental reason that the two methods should be expected, for many purposes, to yield similar solutions.

[2] We chose filtering for tracer over the alternative of periodically using a forward or backward time step, which was the method used by Cox (1984). The use of a periodic forward or backward time step introduces an unphysical periodicity to the simulation, and in particular was found by Marotzke (1991) to interact in unphysical ways with convective adjustment.

We note the following points to keep in mind when transitioning to the staggered approach from the standard leap-frog.

- Centred spatial differencing of advection is unstable with a forward time step. Hence, for tracer advection we *must* employ an upwind biased advection scheme when using the staggered approach. For our purposes with global ocean climate modelling, such advection schemes are motivated to resolve problems with other schemes. Nonetheless, this consequence of changing the time stepping scheme may be unacceptable for certain applications. An alternative method is to retain the ability to discretize advection with centred spatial differences, but to alter the temporal evaluation of the advection operator according to Adams-Bashforth methods (Durran, 1999), or other schemes. In particular, we chose a temporally third order accurate Adams-Bashforth method for velocity self-advection, thus maintaining the traditional centred spatial differences of this operator. The third order Adams-Bashforth method requires the advection operator at time steps τ, $\tau - 1$, and $\tau - 2$, thus increasing memory requirements.

- When choosing a forward time step for the tendency, the Coriolis force *must* be computed using an implicit or semi-implicit approach, such as that described in Chapter 11. A time explicit approach is numerically unstable. In contrast, the standard approach with the leap frog allows for an explicit leap frog time stepping of the Coriolis force, as well as the semi-implicit or implicit.

- A leap frog discretization of the time tendency updates the ocean state by $\Delta\tau_{\text{leap}}$ through taking a $2\,\Delta\tau_{\text{leap}}$ step for the discrete time tendency. Consequently, gravity waves and dissipative operators (i.e., diffusion, friction, and upwind biased advection) are time step constrained based on $2\,\Delta\tau_{\text{leap}}$. In constrast, the staggered scheme updates the ocean state by $\Delta\tau_{\text{stag}}$ *and* it employs $\Delta\tau_{\text{stag}}$ to compute tendencies. It is therefore time step constrained based on a $\Delta\tau_{\text{stag}}$ time step. Hence, the staggered time step $\Delta\tau_{\text{stag}}$ can generally be twice that of the leap frog $\Delta\tau_{\text{leap}}$

  $$\Delta\tau_{\text{stag}} = 2\,\Delta\tau_{\text{leap}}. \tag{8.9}$$

  The computational cost of OM3.1 with the staggered scheme is therefore one-half that of OM3.0 using the standard scheme. There can be little argument that such an improvement in efficiency is of great use for ocean modelling.

8.2.4 Sensitivity to the time stepping scheme

During the bulk of our development, the ocean model employed the standard time stepping scheme for tracer, baroclinic, and barotropic equations. Upon developing the staggered time stepping scheme for the tracer and baroclinic equations, we became convinced that the modified scheme has utility for our climate modelling applications. The question arose whether switching time stepping schemes would require retuning of the physical parameterizations.

Tests were run with the ocean and ice models using an annually repeating atmospheric forcing with daily synoptic variability, again repeating annually. Runs using the staggered scheme had a two hour time step for both tracer and baroclinic momentum, and a predictor-corrector scheme

(e.g., Killworth et al., 1991; Griffies, 2004) for the barotropic equations with a 90s time step.[3] The comparison was made to the standard time stepping scheme using one hour time steps for the tracer and baroclinic equations, and (3600/64)s for the leap frog barotropic equations.

Analysis of these solutions after 10 years revealed that regions with relatively high frequency temporal variability, such as the equatorial wave guide, exhibit the most differences instantanously. Figure 8.1 illustrates the situation along the equator in the East Pacific. The standard simulation exhibits substantial time splitting, even with a nontrivial level of time filtering from a Robert-Asselin time filter. Moving just five degrees north of the equator, however, reveals that the simulation has much less relative variability, and a correspondingly negligible amount of time splitting. Even though the simulation along the equator showed substantial time splitting, over longer periods of time, the large scale patterns and annual cycles showed negligible differences between time stepping schemes. Indeed, time averaging, even over just a day, seems sufficient to smooth over most of the instantaneous differences.

Tests were then run with the GFDL coupled climate models CM2.0 (using OM3.0 as the ocean component) and CM2.1 (using OM3.1). Instantaneous differences were much larger, as expected due to the nontrivial natural variability in the coupled system with a freely evolving atmospheric component. Nonetheless, differences for large scale patterns and seasonal or longer time averages were within levels expected from the model's natural variability.

8.2.5 Dissipative aspects of the predictor-corrector

The purpose of this section is to expose the dissipative aspects of the predictor-corrector scheme available for use in the barotropic equations in MOM4p1. A similar treatment is given in Section 12.8.1 of Griffies (2004).

In two space dimensions, the predictor-corrector equations for an update of the surface height and vertically integrated horizontal velocity in a Boussinesq model are

$$\frac{\eta^* - \eta^n}{\Delta t} = -\gamma \, \nabla \cdot \mathbf{U}^n \tag{8.10}$$

$$\frac{\mathbf{U}^{n+1} - \mathbf{U}^n}{\Delta t} = -c^2 \, \nabla \eta^* \tag{8.11}$$

$$\frac{\eta^{n+1} - \eta^n}{\Delta t} = -\nabla \cdot \mathbf{U}^{n+1}, \tag{8.12}$$

where n symbolizes the barotropic time step. For brevity we dropped the fresh water and source terms appearing in the free surface equation (7.63), and we assumed an unforced linear shallow water system with squared wave speed $c^2 = g\,H$. Setting the dimensionless dissipation parameter $\gamma \geq 0$ to zero recovers a *forward-backward* scheme discussed by Killworth et al. (1991). Keeping $\gamma > 0$ was useful in our simulations and was motivated by similar experiences in the Hallberg Isopycnal Model (Hallberg, 1997).

[3]We found the predictor-corrector to be suitable for the barotropic equations due to our ability to increase the barotropic time step beyond that of the leap frog. Additionally, it preferentially dissipates grid scale features, which are commonly found when discretizing gravity waves on a B-grid (Killworth et al., 1991; Griffies et al., 2001). We present an analysis of the dissipative aspects in Section 8.2.5.

Eliminating the predicted surface height η^* leads to

$$\frac{\mathbf{U}^{n+1} - \mathbf{U}^n}{\Delta t} = -c^2 \, \nabla \eta^n + \gamma \, c^2 \, \Delta t \, \nabla \left[\nabla \cdot \mathbf{U}^n \right] \tag{8.13}$$

$$\frac{\eta^{n+1} - \eta^n}{\Delta t} = -\nabla \cdot \mathbf{U}^{n+1}. \tag{8.14}$$

To directly see how the surface height evolves, eliminate $\mathbf{U}$ to find

$$\frac{\eta^{n+1} - 2\,\eta^n + \eta^{n-1}}{(\Delta t)^2} = (c\,\nabla)^2 \, \eta^n + \gamma \, (c\,\nabla)^2 \, \left(\eta^n - \eta^{n-1} \right). \tag{8.15}$$

Taking the limit $\Delta t \to 0$, yet with $\gamma \, \Delta t$ constant, leads to a dissipative wave equation

$$\left(\partial_{tt} - c^2 \, \nabla^2 \right) \eta = \left(\gamma \, \Delta t \right) \left(c \, \nabla \right)^2 \partial_t \, \eta. \tag{8.16}$$

A single spatial Fourier mode with wavenumber amplitude κ thus satisfies

$$\left(\mathrm{d}^2/\mathrm{d}t^2 + \gamma \, \Delta t \, (c\,\kappa)^2 \, \mathrm{d}/\mathrm{d}t + (c\,\kappa)^2 \right) \, \eta = 0. \tag{8.17}$$

This is the equation for a damped harmonic oscillator with inverse e-folding time $(1/2) \, \gamma \, \Delta t \, (c\,\kappa)^2$. With $\gamma > 0$, external gravity waves are selectively dissipated in regions where the surface height is changing in time, and where the spatial scales are small. Faster waves are damped more readily than slower waves. These properties are useful when aiming to suppress the B-grid computational null mode discussed in Killworth et al. (1991) and Griffies et al. (2001).

8.3 Surface height and bottom pressure smoothing

As discussed by Mesinger (1973), Killworth et al. (1991), Pacanowski and Griffies (1999), Griffies et al. (2001), and Section 12.9 of Griffies (2004), there is a ubiquitous problem with B-grid models due to a null mode present when discretizing inviscid gravity waves. This mode manifests in the velocity field when using a relatively small viscosity. Additionally, it manifests in the surface height or bottom pressure, especially in coarsely represented enclosed or semi-enclosed embayments where waves tend to resonate rather than to propagate. The pattern is stationary[4] and appears as a plus-minus pattern; i.e., as a checkerboard. As there is generally no dissipation in the surface height budget

$$\eta_{,t} = \nabla \cdot \mathbf{U} + q_{\mathrm{w}}, \tag{8.18}$$

suppression of the null mode requires some form of artificial dissipation. An anlogous situation exists with the bottom pressure equation in a pressure based vertical coordinate model.

Various methods have been described in the literature (e.g., Killworth et al., 1991; Griffies et al., 2001) to address this problem. The following constraints guide how we specify the filter.

- For the Boussinesq fluid, the tracer and surface height budgets must remain compatible in the sense defined in Section 7.5. Hence, if a filter is added to the surface height equation, one must correspondingly be added to the tracer equation. Likewise, the non-Boussinesq tracer equation must have a filter added if the bottom pressure equation has a filter.

[4]Hence the term "null," thus indicating it has a zero eigenvalue.

- The filter should be zero in the case that the surface height is locally a constant, or if the bottom pressure remains locally the same as the reference bottom pressure.

The following filter for the surface height in a depth based vertical coordinate model has been found suitable for suppressing noise[5] in the model of Griffies et al. (2004), and a variant on this form sufficient for geopotential vertical coordinates was described in Section 12.9 of Griffies (2004)

$$\partial_t \, \eta = [\partial_t \, \eta]_{\text{no filter}} + \nabla \cdot (A \nabla \eta^*) \; \delta_{\nabla \, \eta} \tag{8.19}$$

$$\partial_t \, (\texttt{dzt} \, T) = [\partial_t \, (\texttt{dzt} \, T)]_{\text{no filter}} + \delta_{k,1} \, \nabla \cdot [A \, \nabla \, (\eta^* \, T)] \; \delta_{\nabla \, \eta}. \tag{8.20}$$

In these equations, $A > 0$ is a diffusivity, $\delta_{\nabla \, \eta}$ vanishes if the surface height is locally constant, and $\delta_{k,1}$ vanishes for all but the surface grid cell at $k = 1$. The surface height η^* is defined by

$$\eta^* = \eta + |\eta_{\text{min}}| + \eta_{\text{off}} \tag{8.21}$$

where η_{min} is the global minimum of the surface height, and η_{off} is a nonzero offset. The use of η^* rather than η does not alter the filter acting on the surface height, since $\nabla \, \eta^* = \nabla \, \eta$. However, η^* is important for the tracer, since it ensures that $\eta^* \, T$ has the same sign as T. If we instead diffused $\eta \, T$, regions where $\eta < 0$ could lead to negative diffusion, which results in tracer extrema and potential instabilities. The alternative $\delta_{k,1} \, \nabla \cdot [A \, \nabla \, (\texttt{dzt} \, T)]$ is not desirable for z^* and σ vertical coordinates, in which case the bottom topography potentially adds a nontrivial level of smoothing even when the surface height is a uniform constant.

Global conservation of volume and tracer is ensured by using no-flux conditions at the side boundaries. Local conservation is ensured since the tracer and volume equations are compatible, as evidenced by setting the tracer concentration to unity in the tracer equation which, upon vertical integration, recovers the surface height equation (see Section 7.5). Note that a more conventional treatment of the filter in the tracer equation is given by the convergence of the thickness weighted flux $-\eta \, A \, \nabla \, T$. However, $\nabla \cdot (\eta \, A \, \nabla \, T)$ is not compatible with the filter applied to the surface height, and so this alternative approach will lead to local non-conservation.

For pressure based vertical coordinates, we use the following filter

$$\partial_t \, p_{\text{b}} = [\partial_t \, p_{\text{b}}]_{\text{no filter}} + \nabla \cdot (A \nabla \, p_{\text{b}}^*) \, \delta_{\nabla \, p_{\text{b}}^*} \tag{8.22}$$

$$\partial_t \, (\rho \, \texttt{dzt} \, T) = [\partial_t \, (\rho \, \texttt{dzt} \, T)]_{\text{no filter}} + \delta_{k,kb} \, \nabla \cdot [A \, \nabla \, (g^{-1} \, p_{\text{b}}^* \, T)] \, \delta_{\nabla \, p_{\text{b}}^*}, \tag{8.23}$$

where $\delta_{\nabla \, p_{\text{b}}^*}$ vanishes where $\nabla \, p_{\text{b}}^*$ vanishes. The modified bottom pressure $p_{\text{b}}^* > 0$ is defined by

$$p_{\text{b}}^* = p_{\text{b}} - p_{\text{b}}^o + |\text{min}(p_{\text{b}} - p_{\text{b}}^o)| + p_{\text{b}}^{\text{off}}, \tag{8.24}$$

where $p_{\text{b}}^{\text{off}}$ is a nonzero offset pressure. The positive pressure p_{b}^* is defined in a manner analogous to the definition of η^* given by equation (8.21). Note that subtracting out the reference bottom pressure p_{b}^o is useful prior to performing the Laplacian operations. Doing so ensures that the filter does not overly smooth the bottom pressure in regions where its undulations arise from variations

[5]For added scale selectivity, it is sometimes useful to employ a biharmonic operator instead of a Laplacian. However, much care should be exercised when using the biharmonic, as it is not positive definite and so can lead to negative tracer concentrations. Therefore, the biharmonic, although present in the MOM4p1 code, is *not recommended* for general use.

in the bottom topography. Such variations are physical, and do not reflect a problem with the B-grid and so should not be filtered. The term $g^{-1}\, p_{\mathsf{b}}^{*}$ appearing in the tracer equation acts like an effective mass per area

$$(\rho\, \mathtt{dzt})^{\mathsf{eff}} \equiv g^{-1}\, p_{\mathsf{b}}^{*}, \tag{8.25}$$

which is positive since $p_{\mathsf{b}}^{*} > 0$. That is, the filter on the bottom pressure equation acts like a mass source in the bottom cell. Hence, tracer must be rearranged in the bottom cell in order to maintain compatibility (see Section 7.5). This filter satisfies the global and local conservation constraints, while adding a level of filtering needed to smooth the bottom pressure.

8.4 Introduction to time stepping in MOM4p1

For the remainder of this chapter, we step back from the OM3 simulations and revisit some of the basic algorithmic details of the time stepping schemes used in MOM4p1. Before doing so, let us summarize advantages of the staggered time stepping scheme employed by MOM4p0. For climate modelling, this scheme has proven to be a great improvement over the traditional leap-frog based methods found in earlier GFDL ocean codes, as well as many other ocean circulation models (Griffies et al. (2000a)). The improvements include the following.

- There is no need to employ explicit time filters (e.g., Robert-Asselin filter) with the staggered scheme, thus enhancing temporal accuracy over the time filtered leap-frog scheme.

- The time staggered scheme conserves seawater mass and tracer mass to within numerical roundoff, whereas the leap-frog based methods, due to the use of explicit time filtering, fail to conserve.

- The time staggered scheme updates the state of the ocean one time step by employing tendencies based on that one time step. In contrast, leap-frog based schemes update the state over one time step by using tendencies based on two time steps. Hence, the leap-frog based schemes have a CFL stability constraint based on the two time step tendencies, and so can be run at only one-half the time step of the staggered scheme. Thus, the staggered scheme is generally one half the computational cost of the leap-frog based schemes.

The purpose of the following sections of this chapter is to expose salient points regarding the time stepping algorithm that have been raised when developing the radiating open boundary condition.

8.5 Basics of staggered time stepping in MOM4p1

Fundamental to the time staggered method is the need to provide a surface height η at integer time steps $\eta(\tau)$ as well as half integer time steps $\eta(\tau + \Delta\tau/2)$. The surface height at integer time steps is needed to couple to velocity variables, which are placed on integer time steps, whereas half integer time steps provide a surface height for tracers. In addition, due to the split between barotropic and baroclinic modes, the surface height is updated over the small barotropic time steps

$\eta^{(b)}(\tau, t_n)$, where a raised (b) denotes a field evaluated on the small barotropic time step. The first time label τ designates which baroclinic branch the cycle started, and

$$t_n = \tau + n\,\Delta\,t \tag{8.26}$$

is the barotropic time step. The relation between the large time step $\Delta\tau$ and small time step Δt is given by

$$2\,\Delta\tau = N\,\Delta t. \tag{8.27}$$

The barotropic time stepping procedes from the intitial barotropic time $t_0 = \tau$ to the final time $t_N = \tau + 2\,\Delta\tau$. The integer N is a function of the split between barotropic and baroclinic gravity waves, which can be on the order of 100 in a global model. Deducing the connection between $\eta(\tau)$, $\eta(\tau + \Delta\tau/2)$, and $\eta^{(b)}(\tau, t_n)$ is a focus of these notes. Correspondingly, we require a connection between the barotropic time cycled vertically integrated velocity $\mathbf{U}^{(b)}$ and $\mathbf{U}(\tau)$.

The barotropic cycle integrates over time $2\,\Delta\tau$ for every $\Delta\tau$ update of the baroclinic system. Why the doubling of the time integration? This method is based on experience with split-explicit time stepping schemes, where we have found it important to provide sufficient time averaging to damp instabilities arising from the incomplete split between the fast and slow motions available with a vertical integration. Longer time averaging is possible, though less convenient algorithmically, less accurate, and more expensive.

A fundamental constraint of any time stepping scheme is that the tracer and volume equations must remain compatible with one another. Compatibility means that the tracer concentration equation reduces to the volume conservation equation when setting the tracer concentration to a constant. Without compatibility, tracer and volume conservation are lost, and the algorithm is of little use for ocean climate modelling.

After completing the barotropic cycle, which extends from $t_0 = \tau$ to $t_N = \tau + 2\,\Delta\tau$, we aim to have a prescription for updating the vertically integrated velocity $\mathbf{U}(\tau + \Delta\tau)$, the free surface height $\eta(\tau + \Delta\tau/2)$, as well as $\eta(\tau + \Delta\tau)$.

8.6 Predictor-corrector for the barotropic system

The preferred barotropic time stepping algorithm is the predictor-corrector scheme. The first step in the algorithm "predicts" the surface height via

$$\frac{\eta^{(*)}(\tau, t_{n+1}) - \eta^{(\mathsf{b})}(\tau, t_n)}{\gamma\,\Delta t} = -\nabla \cdot \mathbf{U}^{(\mathsf{b})}(\tau, t_n) + \mathcal{E}, \tag{8.28}$$

where $\mathcal{E}$ is the fresh water forcing or volume source, both of which are held constant over the course of the barotropic cycle. We expose the time labels on these fields in later discussions. The raised $(*)$ denotes an intermediate value of the surface height. This is the "predicted" value, to be later "corrected." The nondimensional parameter $0 \leq \gamma$ acts to dissipate the small scales of motion (see Section 12.8 of Griffies (2004)). Setting $\gamma = 0$ recovers a second order accurate forward-backward scheme, in which case the predictor step (8.28) is eliminated. Larger values of γ reduce the order of accuracy, yet provide effective damping. However, as shown in Section 12.8 of Griffies (2004), values of γ larger than $1/4$ can compromise the scheme's stability. The value $\gamma = 1/5$ has been found useful for many purposes.

The predicted surface height $\eta^{(*)}(\tau, t_{n+1})$ is used to compute the surface pressure via

$$\rho_o \, \tilde{p}_{\mathsf{s}}^{(*)}(\tau, t_{n+1}) = g \, \eta^{(*)}(\tau, t_{n+1}) \, \rho_{k=1}^{(\tau+1/2)} \tag{8.29}$$

where the applied pressure p_{a} has been dropped for brevity but can be trivially added. The surface pressure is used to update the vertically integrated velocity

$$\begin{aligned} \frac{\mathbf{U}^{(\mathsf{b})}(\tau, t_{n+1}) - \mathbf{U}^{(\mathsf{b})}(\tau, t_n)}{\Delta t} = \Bigg[& -f \, \hat{\mathbf{z}} \wedge \frac{\mathbf{U}^{(\mathsf{b})}(\tau, t_n) + \mathbf{U}^{(\mathsf{b})}(\tau, t_{n+1})}{2} \\ & - D(\tau) \, \nabla_z \, \tilde{p}_{\mathsf{s}}^{(*)}(\tau, t_{n+1}) + \mathbf{G}(\tau) \Bigg] . \end{aligned} \tag{8.30}$$

For the vertically integrated transport, the Coriolis force is evaluated using the Crank-Nicholson semi-implicit time scheme in equation (8.30). Inverting provides an explicit update of the vertically integrated transport

$$U^{(\mathsf{b})}(\tau, t_{n+1}) = [1 + (f \, \Delta t/2)^2]^{-1} \, [U^{(\#)}(\tau, t_{n+1}) + (f \, \Delta t/2) \, V^{(\#)}(\tau, t_{n+1})] \tag{8.31}$$

$$V^{(\mathsf{b})}(\tau, t_{n+1}) = [1 + (f \, \Delta t/2)^2]^{-1} \, [V^{(\#)}(\tau, t_{n+1}) - (f \, \Delta t/2) \, U^{(\#)}(\tau, t_{n+1})] \tag{8.32}$$

where $\mathbf{U}^{(\#)}(\tau, t_{n+1})$ is updated just with the time-explicit tendencies

$$\frac{U^{(\#)}(\tau, t_{n+1}) - U^{(\mathsf{b})}(\tau, t_n)}{\Delta t} = (f/2) \, V^{(\mathsf{b})}(\tau, t_n) - D(\tau) \, \partial_x \, \tilde{p}_{\mathsf{s}}^{(*)}(\tau, t_{n+1}) + G^x(\tau) \tag{8.33}$$

$$\frac{V^{(\#)}(\tau, t_{n+1}) - V^{(\mathsf{b})}(\tau, t_n)}{\Delta t} = -(f/2) \, U^{(\mathsf{b})}(\tau, t_n) - D(\tau) \, \partial_y \, \tilde{p}_{\mathsf{s}}^{(*)}(\tau, t_{n+1}) + G^y(\tau). \tag{8.34}$$

The "corrector" part of the scheme steps the surface height using the updated transport

$$\frac{\eta^{(\mathsf{b})}(\tau, t_{n+1}) - \eta^{(\mathsf{b})}(\tau, t_n)}{\Delta t} = -\nabla \cdot \mathbf{U}^{(\mathsf{b})}(\tau, t_{n+1}) + \mathcal{E}. \tag{8.35}$$

Note that $\eta^{(\mathsf{b})}(\tau, t_{n+1})$ is used rather than the predicted height $\eta^{(*)}(\tau, t_{n+1})$, since $\eta^{(*)}(\tau, t_{n+1})$ is computed with the altered time step $\gamma \, \Delta t$. Temporal dissipation is localized to the predictor portion of the time stepping, with the corrector part hidden from this dissipation. Because of the predictor step, the convergence of the vertically integrated transport is computed twice in the predictor-corrector scheme, thus increasing the cost relative to a forward-backward approach where $\gamma = 0$. The payoff is an extra parameter that can be used to tune the level of dissipation. Additionally, there is added stability towards representing gravity waves so that Δt can be longer than when using the leap-frog method.

Let us detail how the barotropic steps accumulate over the course of a particular barotropic cycle. For this purpose, write out the first and second corrector steps (8.35) for the surface height

$$\frac{\eta^{(\mathsf{b})}(\tau, t_{n=1}) - \eta^{(\mathsf{b})}(\tau, t_{n=0})}{\Delta t} = F(t_{n=1}) \tag{8.36}$$

$$\frac{\eta^{(\mathsf{b})}(\tau, t_{n=2}) - \eta^{(\mathsf{b})}(\tau, t_{n=1})}{\Delta t} = F(t_{n=2}), \tag{8.37}$$

where the right-hand side of equation (8.35) is abbreviated as F. Adding these two equations leads to

$$\frac{\eta^{(\mathsf{b})}(\tau, t_{n=2}) - \eta^{(\mathsf{b})}(\tau, t_{n=0})}{\Delta t} = F(t_{n=1}) + F(t_{n=2}), \tag{8.38}$$

where the intermediate value $\eta^{(\mathsf{b})}(\tau, t_{n=1})$ has identically cancelled. This result easily generalizes, so that

$$\frac{\eta^{(\mathsf{b})}(\tau, t_{n=N}) - \eta^{(\mathsf{b})}(\tau, t_{n=0})}{N\,\Delta t} = \frac{1}{N} \sum_{n=1}^{N} F(t_n). \tag{8.39}$$

This result does not hold for a leap-frog algorithm, since the intermediate values of the surface height do not generally cancel completely, as they do here for the predictor-corrector.

8.7 The Griffies (2004) scheme

The only piece of the forcing $F(t_n)$ that changes during the barotropic cycle is the convergence of the vertically integrated velocity. The result (8.39) then suggests that the time averaged vertically integrated velocity should be given back to the baroclinic part of the model upon completion of the barotropic cycle. To have this velocity centered on the integer time step $\tau + \Delta\tau$, it is necessary to run the barotropic cycle to $\tau + 2\,\Delta\tau$. Hence, upon reaching the last barotropic time step

$$t_{n=N} = \tau + 2\Delta\tau, \tag{8.40}$$

the vertically integrated velocity is time averaged,

$$\tilde{\mathbf{U}} = \frac{1}{N} \sum_{n=1}^{N} \mathbf{U}^{(\mathsf{b})}(\tau, t_n). \tag{8.41}$$

To produce the updated vertically integrated velocity at baroclinic time $\tau + \Delta\tau$, the vertically integrated velocity $\mathbf{U}(\tau + \Delta\tau)$ is identified with this time averaged value,

$$\mathbf{U}(\tau + \Delta\tau) \equiv \tilde{\mathbf{U}}. \tag{8.42}$$

The surface height is needed at the integer time steps in order to specify the thickness of the velocity cells. There are two options for updating the surface height to time step $\tau + \Delta\tau$. First, we could take the instantaneous value from the barotropic portion of the cycle

$$\eta(\tau + \Delta\tau) \equiv \eta^{(\mathsf{b})}(\tau, t_{n=N/2}). \tag{8.43}$$

This approach has not been tried, since it likely leads to a meta-stable algorithm due to the absence of time averaging, depending on the predictor-corrector dissipation parameter γ. In contrast, extensive experience indicates that added stability is realized by using the time averaged surface height

$$\eta(\tau + \Delta\tau) = \frac{1}{N+1} \sum_{n=0}^{N} \eta^{(\mathsf{b})}(\tau, t_n). \tag{8.44}$$

Notably, tracer and volume conservation is not compromised by this specification since it is only used to define the surface height carried by the velocity cells. However, the surface height at half integer timesteps needed for the tracer equation is diagnosed using equation (8.41),

$$\frac{\eta(\tau + \Delta\tau/2) - \eta(\tau - \Delta\tau/2)}{\Delta\tau} = -\nabla \cdot \mathbf{U}(\tau) + q_{\mathsf{w}}(\tau) + \mathcal{S}^{(\eta)}(\tau). \tag{8.45}$$

As described in Section 8.8, this approach may cause divergence of sea level at integer and half integer time steps.

8.8 Algorithms motivated from predictor-corrector

The previous algorithm makes a distinction between how the integer and half-integer surface heights are updated. This distinction exposes the algorithm to possible time splitting between these surface heights. The splitting has been found to be unacceptable for models with radiating open boundary conditions, whereas other boundary conditions have shown no problem. Given the interest in radiating boundary conditions, we consider here an alternative approach which is motivated from details of the barotropic predictor-corrector method. It will turn out that the schemes developed here are not algorithmically closed. However, approximations are considered in 8.9.2 to close the algorithms.

8.8.1 Barotropic time stepping and surface height on integer time steps

The predictor step in the predictor-corrector algorithm updates the surface height according to

$$\eta^{(b)}(\tau, t_{n+1}) - \eta^{(b)}(\tau, t_n) = \Delta t \, F(t_{n+1}). \tag{8.46}$$

We now expose the time labels on all terms appearing in the forcing, whereby we set volume sources

$$F(t_{n+1}) = -\nabla \cdot \mathbf{U}^{(b)}(\tau, t_{n+1}) + q_{\mathsf{w}}(\tau + \Delta\tau/2) + \mathcal{S}^{(\eta)}(\tau + \Delta\tau/2). \tag{8.47}$$

Only the convergence of the vertically integrated velocity $\mathbf{U}^{(b)}(\tau, t_{n+1})$ changes on each barotropic time step, whereas the water forcing $q_{\mathsf{w}}(\tau + \Delta\tau/2)$ and source $\mathcal{S}^{(\eta)}(\tau + \Delta\tau/2)$ are held fixed.

To begin the barotropic integration of the surface height, it is necessary to prescribe an initial condition. We choose to set

$$\eta^{(b)}(\tau, t_0) = \eta(\tau) \tag{8.48}$$

for the surface height, and

$$\mathbf{U}^{(b)}(\tau, t_0) = \mathbf{U}(\tau) \tag{8.49}$$

for the vertically integrated velocity. This choice of the starting point is essential for η, but different approximations are possible for the vertically integrated velocity. Here, $\eta(\tau)$ and $\mathbf{U}(\tau)$ are centred at an integer baroclinic time step, which again is the time step where the velocity field is centred using the MOM4p1 time staggered method. These two prescriptions lead us to ask how to compute the updated surface height $\eta(\tau + \Delta\tau)$ and vertically integrated velocity $\mathbf{U}(\tau + \Delta\tau)$. Experience with various versions of the split-explicit time stepping in MOM motivates us to take for the surface height a time average over the full suite of barotropic surface heights according to

$$\boxed{\eta(\tau + \Delta\tau) = \frac{1}{N+1} \sum_{n=0}^{N} \eta^{(b)}(\tau, t_n).} \tag{8.50}$$

We choose this simple form of time filtering, in which all terms within the barotropic time stepping contribute equally. Although more sophisticated time filters are available, this one has been found suitable for our purposes. Without time filtering, the algorithm can be very unstable and thus is unsuitable for large scale modelling. As shown below, this time averaging for the surface height motivates a different form for the time averaging of the vertically integrated velocity field.

8.8.2 Surface height on half-integer time steps

The fundamental prescription (8.50) for the integer time step surface height is readily extended to the half-integer surface height by setting

$$\boxed{\eta(\tau + \Delta\tau/2) \equiv \frac{\eta(\tau) + \eta(\tau + \Delta\tau)}{2}.} \tag{8.51}$$

This prescription couples the integer and half-integer time steps, and ensures that both are determined by time averages over the barotropic cycle. The question then arises how to make this prescription compatible with the time stepping for the tracer concentration. Compatibility is required for conservation of volume and tracer, and so is of fundamental importance. Compatibility is also needed with the baroclinic velocity scheme, but keeping in mind the uncertainties of wind stress parameterisation, minor approximation should be possible. Addressing these issues forms the remainder of this section.

To proceed, we first deduce the time stepping algorithm for the integer time steps which is implied from the barotropic time stepping (8.46) and the time average (8.50). For this purpose, start by using the initial condition (8.48) in the time average (8.50) to find

$$\eta(\tau + \Delta\tau) = \frac{1}{N+1} \sum_{n=0}^{N} \eta^{(b)}(\tau, t_n) \tag{8.52}$$

$$= \frac{\eta(\tau)}{N+1} + \frac{1}{N+1} \sum_{n=1}^{N} \eta^{(b)}(\tau, t_n). \tag{8.53}$$

Iterating the barotropic time stepping equation (8.46) and using the initial condition (8.48) renders

$$\eta^{(b)}(\tau, t_n) = \eta(\tau) + \Delta t \sum_{i=1}^{n} F(t_i). \tag{8.54}$$

Substitution of this result into equation (8.53) then leads to

$$\eta(\tau + \Delta\tau) - \eta(\tau) = \frac{\Delta t}{N+1} \sum_{n=1}^{N} \sum_{i=1}^{n} F(t_i). \tag{8.55}$$

The double sum on the right hand side arises from the need to ensure that over the course of the barotropic cycle, changes in volume correspond to changes in forcing; in particular, with changes in the convergence of the depth integrated transport. To facilitate computing the double sum within the barotropic time stepping scheme, we employ the following identity to reduce the double sum to a single sum

$$\boxed{\sum_{n=1}^{N} \sum_{i=1}^{n} F(t_i) = \sum_{n=1}^{N} (N - n + 1)\, F(t_i),} \tag{8.56}$$

which can be readily verified by induction.

The sum (8.56) does not represent a straightforward time average. It does, nonetheless, motivate defining a "modified average" forcing that is implied by the barotropic cycle running from

$t_{n=0} = \tau$ to $t_N = \tau + 2\,\Delta\tau$. In particular, the relation $2\,\Delta\tau = N\,\Delta t$ between baroclinic and barotropic time steps motivates the following definition for the averaged forcing

$$\boxed{\begin{aligned}\overline{F} &\equiv \frac{2}{N\,(N+1)} \sum_{n=1}^{N} \sum_{i=1}^{n} F(t_i), \\ &\equiv \frac{2}{N\,(N+1)} \sum_{n=1}^{N} (N-n+1)\,F(t_i),\end{aligned}} \tag{8.57}$$

which renders

$$\frac{\eta(\tau+\Delta\tau)-\eta(\tau)}{\Delta\tau} = \overline{F}. \tag{8.58}$$

Note that the average operator (8.57) reduces to the trivial result $\overline{F} = F$ in the special case when each of the barotropic time steps see a constant forcing $F(t_i) \equiv F$. That is,

$$\sum_{n=1}^{N} \sum_{i=1}^{n} F(t_i) = F \sum_{n=1}^{N} n \tag{8.59}$$

$$= F\,(N/2)\,(N+1), \tag{8.60}$$

where the last step used a common summation identity. This special case supports our definition of the averaging operator, and furthermore checks the integrity of the manipulations. In particular, since the fresh water and volume source are assumed to be constant over the barotropic time steps, we have

$$\overline{F} = \frac{2}{N\,(N+1)} \sum_{n=1}^{N} \sum_{i=1}^{n} F(t_i) \tag{8.61}$$

$$= -\frac{2}{N(N+1)} \sum_{n=1}^{N} \sum_{i=1}^{n} \nabla\cdot\mathbf{U}^{(b)}(\tau,t_i) + q_{\mathsf{w}}(\tau+\Delta\tau/2) + \mathcal{S}^{(\eta)}(\tau+\Delta\tau/2) \tag{8.62}$$

which leads to

$$\boxed{\frac{\eta(\tau+\Delta\tau)-\eta(\tau)}{\Delta\tau} = -\nabla\cdot\overline{\mathbf{U}} + q_{\mathsf{w}}(\tau+\Delta\tau/2) + \mathcal{S}^{(\eta)}(\tau+\Delta\tau/2).} \tag{8.63}$$

So far, we have avoided placing a time label on the modified average operator. In particular, the question arises how the averaged vertically integrated velocity

$$\overline{\mathbf{U}} = \frac{2}{N(N+1)} \sum_{n=1}^{N} \sum_{i=1}^{n} \mathbf{U}^{(b)}(\tau,t_i) \tag{8.64}$$

is related to the updated velocity $\mathbf{U}(\tau+\Delta\tau)$ or $\mathbf{U}(\tau+\Delta\tau/2)$. Absent the second summation, the resulting average would be closely centred on the time step $\tau+\Delta\tau$, but the barycenter of the double sum is at $\tau+\Delta\tau/2$. We now discuss algorithms based on both approximations.

8.8.3 Method A: $\mathbf{U}(\tau + \Delta\tau) = \overline{\mathbf{U}}$

In this method, we consider $\mathbf{U}(\tau + \Delta\tau) = \overline{\mathbf{U}}$, so that

$$\mathbf{U}(\tau + \Delta\tau) = \frac{2}{N(N+1)} \sum_{n=1}^{N} \sum_{i=1}^{n} \mathbf{U}^{(b)}(\tau, t_i). \tag{8.65}$$

Given this assumed time labelling of $\overline{\mathbf{U}}$, we are able to update the three dimensional velocity to the new time step $\tau + \Delta\tau$ after the baroclinic velocity is updated. The prescription (8.65) implies that the integer time step surface height, which is computed as the time average in equation (8.50), also satisfies the following time tendency equation

$$\frac{\eta(\tau + \Delta\tau) - \eta(\tau)}{\Delta\tau} = -\nabla \cdot \mathbf{U}(\tau + \Delta\tau) + q_{\mathsf{w}}(\tau + \Delta\tau/2) + \mathcal{S}^{(\eta)}(\tau + \Delta\tau/2). \tag{8.66}$$

The definition (8.51) of the half-integer time step surface height then implies that it satisfies the tendency equation

$$\frac{\eta(\tau + \Delta\tau/2) - \eta(\tau - \Delta\tau/2)}{\Delta\tau} = -\nabla \cdot \mathbf{U}(\tau + \Delta\tau/2) + q_{\mathsf{w}}(\tau) + \mathcal{S}^{(\eta)}(\tau), \tag{8.67}$$

where

$$\mathbf{U}(\tau + \Delta\tau/2) = \frac{\mathbf{U}(\tau) + \mathbf{U}(\tau + \Delta\tau)}{2} \tag{8.68}$$

$$q_{\mathsf{w}}(\tau) = \frac{q_{\mathsf{w}}(\tau + \Delta\tau/2) + q_{\mathsf{w}}(\tau - \Delta\tau/2)}{2} \tag{8.69}$$

$$\mathcal{S}^{(\eta)}(\tau) = \frac{\mathcal{S}^{(\eta)}(\tau + \Delta\tau/2) + \mathcal{S}^{(\eta)}(\tau - \Delta\tau/2)}{2}. \tag{8.70}$$

8.8.3.1 Compatibile tracer concentration

For the surface height on half integer time steps, we must maintain compatibility with tracer concentration fields, which are also centered on half-integer time steps. Compatibility means that time stepping the surface height must take the identical form to time stepping tracer concentration, so that the two equations agree in the special case of a constant tracer concentration. Without such compatibility, tracer and volume are not conserved by the discrete model. This point was emphasized by Griffies et al. (2001) in the context of the leap-frog based algorithm exclusively used in earlier versions of MOM.

Compatibility implies that the tracer concentration must be forced with the water source (8.69), the volume source (8.70), and, because of equation (8.67), with the half-integer advection velocity. Given these considerations, a compatible staggered time discretization of thickness weighted tracer, absent subgrid scale processes, takes the form (note the shorthand used for the time labels)

$$\frac{h^{\tau+1/2}\, C^{\tau+1/2} - h^{\tau-1/2}\, C^{\tau-1/2}}{\Delta\tau} = -\nabla_s \cdot [(h\,\mathbf{u})^{\tau+1/2}\, C^{\tau-1/2}] \tag{8.71}$$

$$+ [w^{\tau+1/2}\, C^{\tau-1/2}]_k - [w^{\tau+1/2}\, C^{\tau-1/2}]_{k-1}, \tag{8.72}$$

where the thickness weighted advection velocity on half-integer time steps is given by

$$(h\,\mathbf{u})^{\tau+1/2} = \frac{(h\,\mathbf{u})^{\tau+1} + (h\,\mathbf{u})^{\tau}}{2}. \tag{8.73}$$

8.8.3.2 Why this scheme is not closed

This algorithm is not closed, and so is not practical. The reason is that the compatible tracer equation (8.72) requires the thickness weighted advection velocity $(h\,\mathbf{u})^{\tau+1/2}$. However, this velocity requires the updated thickness weighted velocity $(h\,\mathbf{u})^{\tau+1}$, but the velocity at time $\mathbf{u}^{\tau+1}$ is not known until the momentum is updated.

8.8.4 Method B: $\mathbf{U}(\tau+\Delta\tau/2)=\overline{\mathbf{U}}$

Since the barycenter of the double sum (8.56) is $\tau+\Delta\tau/2$, it is reasonable to prescribe $\mathbf{U}(\tau+\Delta\tau/2)=\overline{\mathbf{U}}$, so that

$$\mathbf{U}(\tau+\Delta\tau/2)=\frac{2}{N(N+1)}\sum_{n=1}^{N}\sum_{i=1}^{n}\mathbf{U}^{(b)}(\tau,t_i). \tag{8.74}$$

The prescription (8.65) implies that the integer time step surface height, which is computed as the time average in equation (8.50), also satisfies the following time tendency equation

$$\frac{\eta(\tau+\Delta\tau)-\eta(\tau)}{\Delta\tau}=-\nabla\cdot\mathbf{U}(\tau+\Delta\tau/2)+q_{\mathsf{w}}(\tau+\Delta\tau/2)+\mathcal{S}^{(\eta)}(\tau+\Delta\tau/2). \tag{8.75}$$

The definition (8.51) of the half-integer time step surface height then implies

$$\frac{\eta(\tau+\Delta\tau/2)-\eta(\tau-\Delta\tau/2)}{\Delta\tau}=-\nabla\cdot\mathbf{U}(\tau)+q_{\mathsf{w}}(\tau)+\mathcal{S}^{(\eta)}(\tau), \tag{8.76}$$

where

$$\mathbf{U}(\tau)=\frac{\mathbf{U}(\tau+\Delta\tau/2)+\mathbf{U}(\tau-\Delta\tau/2)}{2} \tag{8.77}$$

$$q_{\mathsf{w}}(\tau)=\frac{q_{\mathsf{w}}(\tau+\Delta\tau/2)+q_{\mathsf{w}}(\tau-\Delta\tau/2)}{2} \tag{8.78}$$

$$\mathcal{S}^{(\eta)}(\tau)=\frac{\mathcal{S}^{(\eta)}(\tau+\Delta\tau/2)+\mathcal{S}^{(\eta)}(\tau-\Delta\tau/2)}{2}. \tag{8.79}$$

8.8.4.1 Compatibile tracer concentration

Compatibility implies that in contrast to Section 8.8.3.1, the tracer concentration must be forced with the water source (8.78), the volume source (8.79), and, because of Equation (8.76) with the integer advection velocity. The compatible staggered time discretization of thickness weighted tracer, absent subgrid scale processes, takes the form

$$\frac{h^{\tau+1/2}\,C^{\tau+1/2}-h^{\tau-1/2}\,C^{\tau-1/2}}{\Delta\tau}=-\nabla_s\cdot\left[(h\,\mathbf{u})^{\tau}\,C^{\tau-1/2}\right] \tag{8.80}$$

$$+\left[w^{\tau}\,C^{\tau-1/2}\right]_k-\left[w^{\tau}\,C^{\tau-1/2}\right]_{k-1}, \tag{8.81}$$

where the thickness weighted advection velocity on integer time steps is given by

$$(h\,\mathbf{u})^{\tau}=\frac{(h\,\mathbf{u})^{\tau+1/2}+(h\,\mathbf{u})^{\tau-1/2}}{2}. \tag{8.82}$$

8.8.4.2 Why this scheme is not closed

This scheme is not closed algorithmically. That is, the velocity scheme cannot be completed after the barotropic sequence is ready, because $\mathbf{U}(\tau + \Delta\tau)$ is still unknown. The compatible tracer equation (8.81) requires also the thickness weighted advection velocity $(h\,\mathbf{u})^{\tau+1/2}$, which itself requires the updated thickness weighted velocity $(h\,\mathbf{u})^{\tau+1}$. The velocity at time $\mathbf{u}^{\tau+1}$, however, is not known until the momentum is updated which in turn requres the barotropic scheme to be completed. Yet the momentum is updated only after the tracer is updated. The repeated mapping between integer to half integer steps would reduce accuracy. A significant rearrangement of the baroclinic and tracer equation may facilitate the use of this algorithm. However, many attempts have failed.

8.9 Algorithms enforcing compatibility

We present three methods for time stepping the equations in MOM4p1. Method I is that one discussed in Section 8.7 based on Griffies (2004) and Griffies et al. (2005). Method III is a modification to Method I, and Method II is a closed algorithm based on the barotropic predictor-corrector from Section 8.8. Methods II and III each aim to provide a closed and compatible scheme that maintains stability with the radiating open boundary condition. Methods I and II are implemented in MOM4p1, with Method III remaining untested.

8.9.1 Method I: Griffies (2004)

We first summarize the method of Griffies (2004) and Griffies et al. (2005), as described in Section 8.7. To produce an algorithm that maintains compatibility with tracer concentration, and is algorithmically closed, we take the philosophy here that the fundamental fields are those which live on the baroclinic time steps (including baroclinic velocity and tracer fields). The barotropic fields are coupled to the baroclinic and tracer fields, but details of the barotropic algorithm do not dictate details of the baroclinic and tracer algorithm. In particular, details of whether we use a barotropic leap-frog or predictor-corrector are unimportant, nor are details of the initial values used for the surface height and vertically integrated velocity (so long as the initial values are reasonable). This philosophy is in contrast to that taken in Section 8.8, and further described in Method III below, where the barotropic predictor-corrector motivated details of the baroclinic and tracer updates.

The main steps of this scheme prescribe an updated vertically integrated velocity and updated surface height, both as time averages over the barotropic time steps

$$\boxed{\mathbf{U}(\tau + \Delta\tau) = \frac{1}{N} \sum_{n=1}^{N} \mathbf{U}^{(\mathsf{b})}(\tau, t_n)} \tag{8.83}$$

$$\boxed{\eta(\tau + \Delta\tau) = \frac{1}{N+1} \sum_{n=0}^{N} \eta^{(\mathsf{b})}(\tau, t_n).} \tag{8.84}$$

The half-integer time step surface height is driven by the convergence of the time averaged verti-

cally integrated velocity, as well as surface boundary fluxes and interior volume sources

$$\boxed{\frac{\eta(\tau+\Delta\tau/2)-\eta(\tau-\Delta\tau/2)}{\Delta\tau} = -\nabla\cdot\mathbf{U}(\tau)+q_{\mathsf{w}}(\tau)+\mathcal{S}^{(\eta)}(\tau).} \tag{8.85}$$

The compatible evolution equation for the tracer concentration follows from the update to the half-integer surface height

$$\frac{h^{\tau+1/2}\,C^{\tau+1/2}-h^{\tau-1/2}\,C^{\tau-1/2}}{\Delta\tau} = -\nabla_s\cdot\left[(h\,\mathbf{u})^{\tau}\,C^{\tau-1/2}\right] \tag{8.86}$$

$$+\left[w^{\tau}\,C^{\tau-1/2}\right]_k-\left[w^{\tau}\,C^{\tau-1/2}\right]_{k-1}. \tag{8.87}$$

There is a distinction in this method between $\eta(\tau+\Delta\tau)$, which is based on a time average, and $\eta(\tau+\Delta\tau/2)$, which is based on a baroclinic forward time step. This dichotomy has been found to allow splitting between the surface heights when using radiating open boundary conditions.

8.9.2 Method II: Algorithm based on barotropic predictor-corrector

We were led to the non-closed algorithms in Section 8.8 by aiming to treat the barotropic system in a systematic manner, and by prescribing the use of a particular form of time averaging for the surface height. Alternative methods can be found by altering the form of the time average, or by jettisoning time averaged operators altogether. However, we are not in favour of jettisoning the time average, as past explorations of this approach have led to unacceptably unstable schemes. Instead, we consider approximations described in the following that close the algorithm.

To start, we follow the scheme proposed in Section 8.8.4, in which the integer time step surface height is updated via a time average as in equation (8.84)

$$\boxed{\eta(\tau+\Delta\tau)=\frac{1}{N+1}\sum_{n=0}^{N}\eta^{(\mathsf{b})}(\tau,t_n),} \tag{8.88}$$

and the half-integer time step surface height is also a time average via

$$\boxed{\eta(\tau+\Delta\tau/2)\equiv\frac{\eta(\tau)+\eta(\tau+\Delta\tau)}{2}.} \tag{8.89}$$

Following the details of the barotropic predictor-corrector, we are led to the updated vertically integrated velocity via the sum in equation (8.74) and using the barycenter for the time step placement as in Section 8.8.4

$$\boxed{\begin{aligned}\mathbf{U}(\tau+\Delta\tau/2) &= \frac{2}{N(N+1)}\sum_{n=1}^{N}\sum_{i=1}^{n}\mathbf{U}^{(b)}(\tau,t_i)\\ &= \frac{2}{N(N+1)}\sum_{n=1}^{N}(N-n+1)\,\mathbf{U}^{(b)}(\tau,t_i).\end{aligned}} \tag{8.90}$$

As described in Section 8.8.2, this sum arises from the need to maintain consistency with volume fluxes passing across the radiating open boundaries, and thus for providing a stable scheme with radiating open boundaries.

As noted in Section 8.8.4, the prescription (8.90) does not lead to a closed algorithm, since we need to know the updated velocity $\mathbf{U}(\tau + \Delta\tau)$ at the end of the barotropic cycle in order to update the three dimensional velocity field $\mathbf{u}(\tau + \Delta\tau)$. The following approximation which closes the algorithm has also been found to lead to a stable scheme with radiating open boundaries

$$\mathbf{U}(\tau + \Delta\tau) \approx \mathbf{U}(\tau + \Delta\tau/2). \tag{8.91}$$

The half-integer time step surface height, which is defined by the time average (8.89), also satisfies the time tendency equation

$$\frac{\eta(\tau + \Delta\tau/2) - \eta(\tau - \Delta\tau/2)}{\Delta\tau} = -\nabla \cdot \mathbf{U}(\tau) + q_{\mathsf{w}}(\tau) + S^{(\eta)}(\tau). \tag{8.92}$$

It follows that the compatible tracer equation is given by

$$\frac{h^{\tau+1/2}\, C^{\tau+1/2} - h^{\tau-1/2}\, C^{\tau-1/2}}{\Delta\tau} = -\nabla_s \cdot [(h\,\mathbf{u})^{\tau}\, C^{\tau-1/2}] \tag{8.93}$$

$$+ [w^{\tau}\, C^{\tau-1/2}]_k - [w^{\tau}\, C^{\tau-1/2}]_{k-1}. \tag{8.94}$$

The discrete tracer equation thus takes the same form as in Methods I and III.

8.9.3 Method III: Modified Griffies (2004)

To possibly resolve the problem of splitting between the integer and half-integer time steps encountered with Method I in radiating open boundary problems, we consider here an alternative approach, whereby the integer time step surface height is prescribed as the time average of the half-integer time step surface height

$$2\,\eta(\tau + \Delta\tau) = \eta(\tau + \Delta\tau/2) + \eta(\tau + 3\Delta\tau/2). \tag{8.95}$$

That is, the integer time step surface height is no longer based on a time average, but instead evolves according to

$$\frac{\eta(\tau + \Delta\tau) - \eta(\tau)}{\Delta\tau} = -\nabla \cdot \mathbf{U}(\tau + \Delta\tau/2) + q_{\mathsf{w}}(\tau + \Delta\tau/2) + S^{(\eta)}(\tau + \Delta\tau/2), \tag{8.96}$$

where

$$2\,\mathbf{U}(\tau + \Delta\tau/2) = \mathbf{U}(\tau + \Delta\tau) + \mathbf{U}(\tau) \tag{8.97}$$

$$2\,q_{\mathsf{w}}(\tau + \Delta\tau/2) = q_{\mathsf{w}}(\tau + \Delta\tau) + q_{\mathsf{w}}(\tau) \tag{8.98}$$

$$2\,S^{(\eta)}(\tau + \Delta\tau/2) = S^{(\eta)}(\tau + \Delta\tau) + S^{(\eta)}(\tau). \tag{8.99}$$

The problem with this prescription is that it is not closed, since the surface boundary condition module only provides information about the surface forcing at the present time step. Likewise, we do not know the updated volume source. Hence, to close the algorithm we make the following approximation

$$q_{\mathsf{w}}(\tau + \Delta\tau/2) \approx q_{\mathsf{w}}(\tau) \tag{8.100}$$

$$S^{(\eta)}(\tau + \Delta\tau/2) \approx S^{(\eta)}(\tau), \tag{8.101}$$

which amounts to saying that the boundary forcing and volume source term remain constant over the course of a baroclinic time step; i.e., we cannot obtain information at higher frequency for these fields. Hence, we are led to the following update for the integer time step surface height

$$\boxed{\frac{\eta(\tau+\Delta\tau)-\eta(\tau)}{\Delta\tau} = -\nabla\cdot\mathbf{U}(\tau+\Delta\tau/2) + q_{\mathsf{w}}(\tau) + S^{(\eta)}(\tau).} \tag{8.102}$$

Although of some interest, this scheme has not yet been coded in MOM4p1. It thus remains untested.

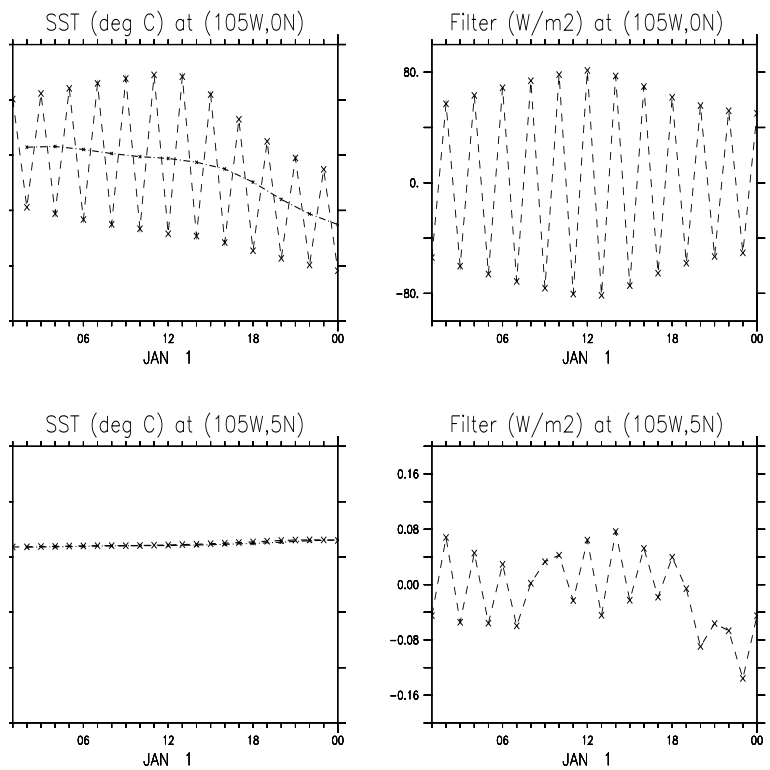

Figure 8.1: Upper left panel: Instantaneous sea surface temperature over January 1 at $(105°W, 0°N)$ as realized in a simulation using the standard time stepping scheme with an hour tracer time step (noisy time series) and the staggered scheme with a two hour tracer time step (smooth time series). Upper right panel: Surface heating applied at $(105°W, 0°N)$ from the Robert-Asselin time filter used to damp the leap frog splitting. Lower left panel: Instantaneous sea surface temperature over a single day at $(105°W, 5°N)$ as realized in a simulation using the standard scheme with an hour tracer time step and the staggered scheme with a two hour tracer time step. Note the width of the temperature range is set the same as at the equator. In general, the agreement of the solution off the equator, where the leap frog splitting is minimal, is far greater than on the equator. Lower right panel: Surface heating applied at $(105°W, 5°N)$ from the Robert-Asselin filter. Note the much smaller magnitude relative to the values on the equator.

CHAPTER

NINE

Equation of state and related quantities

The purpose of this chapter is to present some features of the equation of state used in MOM4p1, with the discussion here an extension of that given in Griffies et al. (2004). The realistic equation of state used in MOM4.1 is based on an early version of that documented in Jackett et al. (2006).

9.1 Introduction

It is important that the equation of state be accurate over the range of temperature, salinity, and pressure values occurring in ocean simulations. Reasons for needing such accuracy include the following.

- Density is needed to compute the hydrostatic pressure, whose horizontal gradients drive ocean currents in the primitive equations.

- The locally referenced vertical derivative of density determines the static stability of a vertical fluid column. This stability determines conditions for convective instability and is used to compute Richardson numbers necessary for mixing for such schemes as Pacanowski and Philander (1981), Chen et al. (1994), Large et al. (1994), and Simmons et al. (2004).

- The locally referenced derivatives with respect to potential temperature and salinity

$$\rho_{,\theta} = \left(\frac{\partial \rho}{\partial \theta}\right)_{p,s} \tag{9.1}$$

$$\rho_{,s} = \left(\frac{\partial \rho}{\partial s}\right)_{p,\theta} \tag{9.2}$$

  are important for computing both the vertical stratification, and to compute the neutral slopes used for sub-grid-scale tracer transport as in Griffies et al. (1998); Griffies (1998).

- The following combination of second derivatives is used to diagnose the potential for cabbel-

ing to occur in the ocean McDougall (1987)

$$\begin{aligned} \mathcal{C} &= \frac{\partial \alpha}{\partial \theta} + 2 \frac{\alpha}{\beta} \frac{\partial \alpha}{\partial S} - \left(\frac{\alpha}{\beta}\right)^2 \frac{\partial \beta}{\partial S} \\ &= -\rho^{-1} \left[\rho_{,\theta\theta} - 2\, \rho_{,\theta S} \left(\frac{\rho_{,\theta}}{\rho_{,S}}\right) + \rho_{,SS} \left(\frac{\rho_{,\theta}}{\rho_{,S}}\right)^2 \right]. \end{aligned} \tag{9.3}$$

- The following combination of second derivatives is used to diagnose the potential for thermobaricity and halobaricity to occur in the ocean McDougall (1987)

$$\begin{aligned} \mathcal{T} &= \beta\, \partial_p \left(\frac{\alpha}{\beta}\right) \\ &= \frac{\partial \alpha}{\partial p} - \frac{\alpha}{\beta} \frac{\partial \beta}{\partial p} \\ &= -\rho^{-1} \left[\rho_{,\theta p} - \rho_{,pS} \left(\frac{\rho_{,\theta}}{\rho_{,S}}\right) \right]. \end{aligned} \tag{9.4}$$

  Note that the name *thermobaricity* is generally used for this parameter, and we evaluate it as given here. However, there are actually contributions from both halobaricity (dependency of haline contraction coefficient on the pressure) and thermobaricity (dependency of thermal expansion coefficient on the pressure). But the thermal piece is generally far larger McDougall (1987).

In early versions of MOM, density was computed according to the Bryan and Cox (1972) cubic polynomial approximation to the UNESCO equation of state (Gill (1982)). That approach was quite useful for certain problems. Unfortunately, it has limitations that are no longer acceptable for global climate modeling. First, the polynomials are fit at discrete depth levels. The use of partial cells makes this approach cumbersome since with partial cells it is necessary to generally compute density at arbitrary depths. Second, the cubic approximation is inaccurate for many regimes of ocean climate modeling, such as wide ranges in salinity associated with rivers and sea ice. For these two reasons, a more accurate method is desired.

Two equations of state (EOS) are currently available in MOM4 for computing density. The first is a linear equation of state whereby density is a linear function of potential temperature and salinity. This EOS is relevant only for idealized simulations with the Boussinesq approximation. The second EOS is that proposed by Jackett et al. (2006). As they argue, their EOS is more accurate than the UNESCO EOS due to the use of more accurate empirical data as reported in Feistel (1993), Feistel and Hagen (1995), and Feistel (2003). Such equations of state are now standard in ocean climate modeling.

9.2 Linear equation of state

The default linear equation of state in MOM4 assumes that density is a linear function of potential temperature and salinity. There is no pressure dependence. Due to the absence of pressure effects, the linear equation of state leads to a density that is more precisely thought of as a potential density. The form used for this equation of state is

$$\rho(\mathbf{x}, t) = \rho_0 - \tilde{\alpha}\, \theta(\mathbf{x}, t) + \tilde{\beta}\, s(\mathbf{x}, t). \tag{9.5}$$

The default settings are

$$\tilde{\alpha} = 0.255\,\mathrm{kg/m^3/^\circ K} \tag{9.6}$$
$$\tilde{\beta} = 0 \tag{9.7}$$
$$\rho_0 = 1035\,\mathrm{kg/m^3}. \tag{9.8}$$

Hence, the density partial derivatives are given by

$$\rho_{,\theta} = -\tilde{\alpha} \tag{9.9}$$
$$\rho_{,s} = \tilde{\beta}. \tag{9.10}$$

The cabbeling and thermobaric parameters vanish for this linear equation of state.

9.3 Jackett et al. equation of state

Feistel (1993), Feistel and Hagen (1995), and Feistel (2003) studied the equilibrium thermodynamics of seawater and produced a more accurate EOS than UNESCO by using more recent empirical data. McDougall et al. (2003) produced a fit to Feistel and Hagen (1995) to render an expression convenient for use in ocean models, and Jackett et al. (2006) updated this equation of state based on Feistel (2003). MOM4.0 has the McDougall et al. (2003) equation of state, with MOM4p1 moving to the updates provided by Jackett et al. (2006) version. Either EOS is highly recommended for purposes of realistic ocean climate simulations, where accuracy over a wide range temperature, salinity, and pressure is crucial. The following equation has been fit over the range

$$0\mathrm{psu} \le s \le 40\mathrm{psu} \tag{9.11}$$
$$-3^\circ\mathrm{C} \le \theta \le 40^\circ\mathrm{C} \tag{9.12}$$
$$0\mathrm{db} \le p \le 8000\mathrm{db}. \tag{9.13}$$

The EOS has 25 terms. Its general form is motivated by that of Wright (1997). Appendix A to Jackett et al. (2006) provides the following equation for *in situ* density ρ written in terms of pressure, salinity, and potential temperature

$$\rho(s,\theta,p) = \frac{P_n(s,\theta,p)}{P_d(s,\theta,p)}, \tag{9.14}$$

where p is the guage pressure in units of decibars, θ is the potential temperature referenced to zero pressure in units of $Celsius$, and s is salinity in psu. Note the conversion between mks pressure and decibars is given by

$$10^{-4}\,\mathrm{db} = 1\,\mathrm{Pa}. \tag{9.15}$$

The *gauge pressure* is given by

$$p = P_{absolute} - 10.1325\mathrm{dbars} \tag{9.16}$$

where the absolute pressure is the *in situ* pressure measured in the ocean. Salinity is measured in practical salinity units (psu), consistent with modern oceanographic measurements. As emphasized in Jackett et al. (2006), this salinity is distinct from the salt concentration in parts per thousand. To a good approximation, a constant factor distinguishes the two

$$s(ppt) = 1.004867\, s(psu) \tag{9.17}$$

The salinity variable in MOM4 is interpreted as psu salinity, since this facilitates a more direct comparison with observations. Notably, to perform salt budgets for diagnostic purposes, it is necessary to multiply by 1.004867 to generate salt budgets in terms of mass of salt. A check value for this equation is $\rho = 1033.213387\,\mathrm{kg.\,m^{-3}}$ with $s = 35$psu, $\theta = 20^\circ C$, and $p = 2000$db $= 2 \times 10^7$Pa. The polynomial functions P_n and P_d are given by

$$\begin{aligned} P_n &= a_o + a_1\,\theta + a_2\,\theta^2 + a_3\,\theta^3 + a_4\,s + a_5\,s\,\theta + a_6\,s^2 \\ &\quad + a_7\,p + a_8\,p\,\theta^2 + a_9 p\,s + a_{10}\,p^2 + a_{11}\,p^2\,\theta^2 \end{aligned} \tag{9.18}$$

$$\begin{aligned} P_d &= b_o + b_1\,\theta + b_2\,\theta^2 + b_3\,\theta^3 + b_4\,\theta^4 + b_5\,s + b_6\,s\,\theta + b_7\,s\,\theta^3 + b_8\,s^{3/2} + b_9\,s^{3/2}\,\theta^2 \\ &\quad + b_{10}\,p + b_{11}\,p^2\,\theta^3 + b_{12}\,p^3\,\theta. \end{aligned} \tag{9.19}$$

The coefficients a_n and b_n are tabulated in Table A2 Jackett et al. (2006). Rearrangement in order to reduce multiplications leads to

$$\begin{aligned} P_n &= a_o + \theta\,(a_1 + \theta\,(a_2 + a_3\,\theta)) + s\,(a_4 + a_5\,\theta + a_6\,s) \\ &\quad + p\,(a_7 + a_8\,\theta^2 + a_9\,s + p\,(a_{10} + a_{11}\,\theta^2)) \end{aligned} \tag{9.20}$$

$$\begin{aligned} P_d &= b_o + \theta\,(b_1 + \theta\,(b_2 + \theta\,(b_3 + \theta\,b_4))) + s\,(b_5 + \theta\,(b_6 + b_7\,\theta^2) + s^{1/2}\,(b_8 + b_9\,\theta^2)) \\ &\quad + p\,(b_{10} + p\,\theta\,(b_{11}\,\theta^2 + b_{12}\,p)). \end{aligned} \tag{9.21}$$

The first order partial derivatives of density are

$$\left(\frac{\partial\rho}{\partial\theta}\right)_{s,p} = \rho\left(\frac{1}{P_n}\left(\frac{\partial P_n}{\partial\theta}\right)_{s,p} - \frac{1}{P_d}\left(\frac{\partial P_d}{\partial\theta}\right)_{s,p}\right) \tag{9.22}$$

$$\left(\frac{\partial\rho}{\partial s}\right)_{\theta,p} = \rho\left(\frac{1}{P_n}\left(\frac{\partial P_n}{\partial s}\right)_{\theta,p} - \frac{1}{P_d}\left(\frac{\partial P_d}{\partial s}\right)_{\theta,p}\right) \tag{9.23}$$

$$\left(\frac{\partial\rho}{\partial p}\right)_{\theta,s} = \rho\left(\frac{1}{P_n}\left(\frac{\partial P_n}{\partial p}\right)_{\theta,s} - \frac{1}{P_d}\left(\frac{\partial P_d}{\partial p}\right)_{\theta,s}\right). \tag{9.24}$$

Since divisions are computationally more expensive than multiplications, we find it useful to rearrange these results to

$$\left(\frac{\partial\rho}{\partial\theta}\right)_{s,p} = (P_d)^{-1}\left[\left(\frac{\partial P_n}{\partial\theta}\right)_{s,p} - \rho\left(\frac{\partial P_d}{\partial\theta}\right)_{s,p}\right] \tag{9.25}$$

$$\left(\frac{\partial\rho}{\partial s}\right)_{\theta,p} = (P_d)^{-1}\left[\left(\frac{\partial P_n}{\partial s}\right)_{\theta,p} - \rho\left(\frac{\partial P_d}{\partial s}\right)_{\theta,p}\right] \tag{9.26}$$

$$\left(\frac{\partial\rho}{\partial p}\right)_{\theta,s} = (P_d)^{-1}\left[\left(\frac{\partial P_n}{\partial p}\right)_{\theta,s} - \rho\left(\frac{\partial P_d}{\partial p}\right)_{\theta,s}\right] \tag{9.27}$$

where $(P_d)^{-1}$ can be saved in a temporary array, thus reducing the number of divisions.[1]

The second order density partial derivatives are

$$\left(\frac{\partial^2 \rho}{\partial \theta^2}\right)_{s,p} = (P_d)^{-1} \left[\frac{\partial^2 P_n}{\partial \theta^2} - 2\,\frac{\partial \rho}{\partial \theta}\frac{\partial P_d}{\partial \theta} - \rho\,\frac{\partial^2 P_d}{\partial \theta^2}\right] \tag{9.28}$$

$$\left(\frac{\partial^2 \rho}{\partial s^2}\right)_{\theta,p} = (P_d)^{-1} \left[\frac{\partial^2 P_n}{\partial s^2} - 2\,\frac{\partial \rho}{\partial s}\frac{\partial P_d}{\partial s} - \rho\,\frac{\partial^2 P_d}{\partial s^2}\right] \tag{9.29}$$

$$\left(\frac{\partial^2 \rho}{\partial s\,\partial \theta}\right) = (P_d)^{-1} \left[\frac{\partial^2 P_n}{\partial s\,\partial \theta} - \frac{\partial \rho}{\partial s}\frac{\partial P_d}{\partial \theta} - \frac{\partial \rho}{\partial \theta}\frac{\partial P_d}{\partial s} - \rho\,\frac{\partial^2 P_d}{\partial s\,\partial \theta}\right] \tag{9.30}$$

$$\left(\frac{\partial^2 \rho}{\partial s\,\partial p}\right) = (P_d)^{-1} \left[\frac{\partial^2 P_n}{\partial s\,\partial p} - \frac{\partial \rho}{\partial p}\frac{\partial P_d}{\partial s} - \frac{\partial \rho}{\partial s}\frac{\partial P_d}{\partial p} - \rho\,\frac{\partial^2 P_d}{\partial s\,\partial p}\right] \tag{9.31}$$

$$\left(\frac{\partial^2 \rho}{\partial \theta\,\partial p}\right) = (P_d)^{-1} \left[\frac{\partial^2 P_n}{\partial \theta\,\partial p} - \frac{\partial \rho}{\partial p}\frac{\partial P_d}{\partial \theta} - \frac{\partial \rho}{\partial \theta}\frac{\partial P_d}{\partial p} - \rho\,\frac{\partial^2 P_d}{\partial \theta\,\partial p}\right]. \tag{9.32}$$

The first order partial derivatives of the equation of state functions are given by

$$\left(\frac{\partial P_n}{\partial \theta}\right)_{s,p} = a_1 + 2\,a_2\,\theta + 3\,a_3\,\theta^2 + a_5\,s + 2\,a_8\,p\,\theta + 2\,a_{11}\,p^2\,\theta \tag{9.33}$$

$$\left(\frac{\partial P_n}{\partial s}\right)_{\theta,p} = a_4 + a_5\,\theta + 2\,a_6\,s + a_9\,p \tag{9.34}$$

$$\left(\frac{\partial P_n}{\partial p}\right)_{\theta,s} = a_7 + a_8\,\theta^2 + a_9\,s + 2\,a_{10}\,p + 2\,a_{11}\,p\,\theta^2 \tag{9.35}$$

$$\left(\frac{\partial P_d}{\partial \theta}\right)_{s,p} = b_1 + 2\,b_2\,\theta + 3\,b_3\,\theta^2 + 4\,b_4\,\theta^3 + b_6\,s + 3\,b_7\,s\,\theta^2 + 2\,b_9\,s^{3/2}\,\theta + 3\,b_{11}\,p^2\,\theta^2 + b_{12}\,p^3 \tag{9.36}$$

$$\left(\frac{\partial P_d}{\partial s}\right)_{\theta,p} = b_5 + b_6\,\theta + b_7\,\theta^3 + (3/2)\,b_8\,s^{1/2} + (3/2)\,b_9\,s^{1/2}\,\theta^2 \tag{9.37}$$

$$\left(\frac{\partial P_d}{\partial p}\right)_{\theta,s} = b_{10} + 2\,b_{11}\,p\,\theta^3 + 3\,b_{12}\,p^2\,\theta \tag{9.38}$$

[1] We thank Trevor McDougall for pointing out this simplification.

with rearrangement leading to

$$\left(\frac{\partial P_n}{\partial \theta}\right)_{s,p} = a_1 + \theta\,(2\,a_2 + 3\,a_3\,\theta) + a_5\,s + 2\,p\,\theta\,(a_8 + a_{11}\,p) \tag{9.39}$$

$$\left(\frac{\partial P_n}{\partial s}\right)_{\theta,p} = a_4 + a_5\,\theta + 2\,a_6\,s + a_9\,p \tag{9.40}$$

$$\left(\frac{\partial P_n}{\partial p}\right)_{\theta,s} = a_7 + a_8\,\theta^2 + a_9\,s + 2\,a_{10}\,p + 2\,a_{11}\,p\,\theta^2 \tag{9.41}$$

$$\left(\frac{\partial P_d}{\partial \theta}\right)_{s,p} = b_1 + \theta\,(2\,b_2 + \theta\,(3\,b_3 + 4\,b_4\,\theta)) + s\,(b_6 + \theta\,(3\,b_7\,\theta + 2\,b_9\,s^{1/2})) + p^2\,(3\,b_{11}\,\theta^2 + b_{12}\,p) \tag{9.42}$$

$$\left(\frac{\partial P_d}{\partial s}\right)_{\theta,p} = b_5 + \theta\,(b_6 + b_7\,\theta^2) + (3/2)\,s^{1/2}\,(b_8 + b_9\,\theta^2) \tag{9.43}$$

$$\left(\frac{\partial P_d}{\partial p}\right)_{\theta,s} = b_{10} + 2\,b_{11}\,p\,\theta^3 + 3\,b_{12}\,p^2\,\theta. \tag{9.44}$$

The second order partial derivatives of the equation of state functions are given by

$$\frac{\partial^2 P_n}{\partial \theta^2} = 2\,a_2 + 6\,a_3\,\theta + 2\,a_8\,p + 2\,a_{11}\,p^2 \tag{9.45}$$

$$\frac{\partial^2 P_n}{\partial s^2} = 2\,a_6 \tag{9.46}$$

$$\frac{\partial^2 P_n}{\partial s\,\partial \theta} = a_5 \tag{9.47}$$

$$\frac{\partial^2 P_n}{\partial s\,\partial p} = a_9 \tag{9.48}$$

$$\frac{\partial^2 P_n}{\partial \theta\,\partial p} = 2\,a_8\,\theta + 4a_{11}\,p\,\theta \tag{9.49}$$

$$\frac{\partial^2 P_d}{\partial \theta^2} = 2\,b_2 + 6\,b_3\,\theta + 12\,b_4\,\theta^2 + 6\,b_7\,s\,\theta + 2\,b_9\,s^{3/2} + 6\,b_{11}\,p^2\,\theta \tag{9.50}$$

$$\frac{\partial^2 P_d}{\partial s^2} = (3/4)\,b_8\,s^{-1/2} + (3/4)\,b_9\,s^{-1/2}\,\theta^2 \tag{9.51}$$

$$\frac{\partial^2 P_d}{\partial s\,\partial \theta} = b_6 + 3\,b_7\,\theta^2 + 3\,b_9\,s^{1/2}\,\theta \tag{9.52}$$

$$\frac{\partial^2 P_d}{\partial s\,\partial p} = 0 \tag{9.53}$$

$$\frac{\partial^2 P_d}{\partial \theta\,\partial p} = 6\,b_{11}\,p\,\theta^2 + 3\,b_{12}\,p^2. \tag{9.54}$$

CHAPTER
TEN

Mechanical energy budgets and conversions

The purpose of this chapter is to discuss energetic balances. Here are the assumptions made for the manipulations of this chapter.

- Choosing to maintain the integrity of certain energetic balances on the B-grid lattice prescribes the form of the discrete advection velocity components located on the sides of tracer cells.
- Second order finite differenced advective fluxes are used for momentum. Tracer fluxes can remain arbitrarily discretized.
- We choose a finite difference computation of the pressure gradient force, as described in Sections 4.1, 4.2, and 4.3. The finite volume method for computing the pressure force, as described in Section 3.7.1, does not lend itself to the results of this chapter.
- Details of the time stepping scheme play a role in determining the form of the energy diagnostics.
- Energy balance diagnostics are important for checking the integrity of certain finite difference algorithms. Consequently, it is useful to provide a careful suite of energy diagnostics for algorithm development purposes.

10.1 Energetic conversions in the continuum

In the continuum, the horizontal momentum equation for a shallow ocean fluid is given by (see chapter 4 of Griffies, 2004)

$$(\rho\,\mathbf{u})_{,t} + \nabla\cdot(\rho\,\mathbf{v}\,\mathbf{u}) + (f+\mathcal{M})\,(\hat{\mathbf{z}}\wedge\rho\,\mathbf{u}) = -\nabla_z p + \rho\,\mathbf{F} \tag{10.1}$$

for the non-Boussinesq case, and

$$(\mathbf{u})_{,t} + \nabla\cdot(\mathbf{v}\,\mathbf{u}) + (f+\mathcal{M})\,(\hat{\mathbf{z}}\wedge\,\mathbf{u}) = -\nabla_z(p/\rho_o) + \mathbf{F} \tag{10.2}$$

for the Boussinesq case. The evolution of horizontal kinetic energy can be found by taking the scalar product of horizontal velocity $\mathbf{u}$ with the momentum equation. When globally integrating the

kinetic energy evolution, the forcing terms can be transformed into terms that highlight physically interesting processes. These manipulations identify *conversions* between one form of energy and another. The form of these conversions can be deduced from the momentum equations, boundary conditions, mass or volume conservation, and integration by parts. Maintaining an analog of these energetic conversions on the discrete lattice has been found to be very useful in the development of ocean model algorithms. The reason is that these conversions provide the modeler with a powerful set of diagnostics to test the integrity of the numerics.

There are three forms of energy conversion of interest in MOM4. The first involves the pressure gradient term, the second involves the advection term, and the third involves friction. We address only the inviscid terms in this chapter. Part 5 of Griffies (2004) describes how friction dissipates kinetic energy in both the continuous case and for a particular friction algorithm available in MOM4.

10.1.1 Pressure work conversions in Boussinesq fluids

Let us first examine how pressure work is converted to other processes in Boussinesq fluids. For this purpose, consider the following identities found using z for the vertical coordinate

$$\begin{aligned}
\int \mathrm{d}V\, \mathbf{u} \cdot \nabla\, p &= \int \mathrm{d}V\, (\mathbf{v} \cdot \nabla p - w\, p_{,z}) \\
&= \int \mathrm{d}V\, [\nabla \cdot (\mathbf{v}\, p) - w\, p_{,z}] \\
&= \int \mathrm{d}A_{(\hat{\mathbf{n}})}\, p\, (\hat{\mathbf{n}} \cdot \mathbf{v}) + g \int \mathrm{d}V\, w\, \rho \\
&= \int \mathrm{d}A_{(\hat{\mathbf{n}})}\, p\, (\hat{\mathbf{n}} \cdot \mathbf{v}) + \int \mathrm{d}V\, \rho\, \mathrm{d}\Phi/\mathrm{d}t
\end{aligned} \tag{10.3}$$

where $\mathrm{d}V = \mathrm{d}x\, \mathrm{d}y\, \mathrm{d}z$ is the volume element and $\mathrm{d}\Phi/\mathrm{d}t$ is the material time derivative of the geopotential $\Phi = g\, z$. To reach these results required volume conservation for a parcel in the form of the constraint $\nabla \cdot \mathbf{v} = 0$, the hydrostatic relation $p_{,z} = -\rho\, g$, and the definitions

$$\begin{aligned}
g\, w &= g\, \mathrm{d}z/\mathrm{d}t \\
&= \mathrm{d}\Phi/\mathrm{d}t.
\end{aligned} \tag{10.4}$$

Assuming no-normal flow at the solid boundaries leaves only the surface boundary at $z = \eta$ for the surface integral. The surface kinematic boundary condition, and volume conservation, lead to[1]

$$\mathrm{d}A_{(\hat{\mathbf{n}})}\, \hat{\mathbf{n}} \cdot \mathbf{v} = -\mathrm{d}x\, \mathrm{d}y\, \nabla \cdot \mathbf{U}, \tag{10.5}$$

and so

$$\int \mathrm{d}V\, \mathbf{u} \cdot \nabla p = -\int_{z=\eta} \mathrm{d}x\, \mathrm{d}y\, p_{\mathrm{a}}\, \nabla \cdot \mathbf{U} + \int \mathrm{d}V\, \rho\, \mathrm{d}\Phi/\mathrm{d}t. \tag{10.6}$$

In a rigid lid model, the first term vanishes. For the free surface model it represents the work done by atmospheric pressure on the depth integrated flow. The second term is the volume integrated work done by vertical currents against the buoyancy force. In generalized vertical coordinates, the buoyancy term takes the form

$$\begin{aligned}
\mathrm{d}\Phi/\mathrm{d}t &= (\partial_t + \mathbf{u} \cdot \nabla_s + w^{(s)}\, \partial_z)\, \Phi \\
&= (\partial_t + \mathbf{u} \cdot \nabla_s)\, \Phi + g\, w^{(s)},
\end{aligned} \tag{10.7}$$

[1] See Section 3.4 of Griffies (2004) for derivation.

where equation (6.72) of Griffies (2004) was used to express the material time derivative in general vertical coordinates. Hence, the pressure conversion becomes

$$\int \mathrm{d}V\, \mathbf{u} \cdot \nabla p = -\int\limits_{z=\eta} \mathrm{d}x\, \mathrm{d}y\, p\, \nabla \cdot \mathbf{U} + \int \mathrm{d}V\, \rho\, [\, (\partial_t + \mathbf{u} \cdot \nabla_s)\, \Phi + g\, w^{(s)}\,]. \tag{10.8}$$

Buoyancy contributions now comprise three terms instead of the one found with z-coordinates. This result reflects the non-orthogonal nature of generalized vertical coordinates.

10.1.2 Pressure work conversions in non-Boussinesq fluids

For non-Boussinesq flows, pressure conversion takes the form

$$\int \mathrm{d}V\, \mathbf{u} \cdot \nabla p = \int\limits_{z=\eta} p\, \hat{\mathbf{n}} \cdot \mathbf{v} + \int \mathrm{d}V\, (\rho\, \mathrm{d}\Phi/\mathrm{d}t - p\, \nabla \cdot \mathbf{v}). \tag{10.9}$$

The $p\, \nabla \cdot \mathbf{v}$ term represents pressure work on the changing volume of fluid parcels found in the compressible non-Boussinesq fluid. The boundary condition

$$\mathrm{d}A_{(\hat{\mathbf{n}})}\, \hat{\mathbf{n}} \cdot \mathbf{v} = \mathrm{d}x\, \mathrm{d}y\, (\eta_{,t} - \rho_{\mathsf{w}}\, q_{\mathsf{w}}/\rho) \tag{10.10}$$

is discussed in Section 3.4.3 of Griffies (2004). The generalized vertical coordinate form of equation (10.9) follows similarly to the Boussinesq case, where extra terms arise from expanding the material time derivative.

10.1.3 Boussinesq kinetic energy advection conversion

Just as for the pressure gradient term, the scalar product of the horizontal velocity and the advection of momentum can be converted into alternative forms. To see this conversion in the continuum, write the advection of horizontal velocity in the Boussinesq fluid as

$$\mathbf{A} \equiv -\nabla \cdot (\mathbf{v}\, \mathbf{u}) - \mathcal{M}\, \hat{\mathbf{z}} \wedge \mathbf{v}. \tag{10.11}$$

The scalar product of $\mathbf{A}$ with the horizontal currents leads to

$$\begin{aligned} \mathbf{u} \cdot \mathbf{A} &= -\mathbf{u} \cdot \nabla \cdot (\mathbf{v}\, \mathbf{u}) \\ &= -\nabla \cdot (\mathbf{v}\, \mathcal{K}), \end{aligned} \tag{10.12}$$

where $\mathcal{K} = \mathbf{u} \cdot \mathbf{u}/2$ is the horizontal kinetic energy per mass. Integrating over the volume of the domain, and using the surface and solid wall boundary conditions, leads to

$$\begin{aligned} \mathcal{A} &\equiv \int \mathrm{d}V\, \mathbf{u} \cdot \mathbf{A} \\ &= \int\limits_{z=\eta} \mathrm{d}x\, \mathrm{d}y\, \mathcal{K}\, \nabla \cdot \mathbf{U}. \end{aligned} \tag{10.13}$$

Consequently, the global integral of kinetic energy advection reduces to a boundary term, which vanishes in the rigid lid model but remains nontrivial in a free surface model.

10.1.4 Non-Boussinesq kinetic energy advection conversion

For the non-Boussinesq fluid, we consider

$$\mathbf{A} \equiv -\nabla \cdot (\rho \, \mathbf{v} \, \mathbf{u}) - \mathcal{M} \, \hat{\mathbf{z}} \wedge \rho \, \mathbf{v}. \tag{10.14}$$

The scalar product of $\mathbf{A}$ with the horizontal currents leads to

$$\begin{aligned} \mathbf{u} \cdot \mathbf{A} &= -\mathbf{u} \cdot \nabla \cdot (\rho \, \mathbf{v} \, \mathbf{u}) \\ &= -\nabla \cdot (\mathbf{v} \, \mathcal{K}) - \mathcal{K} \, \nabla \cdot (\rho \, \mathbf{v}), \end{aligned} \tag{10.15}$$

and integrating over the volume of the domain yields

$$\begin{aligned} \mathcal{A} &\equiv \int \mathrm{d}V \, \mathbf{u} \cdot \mathbf{A} \\ &= -\int_{z=\eta} \mathrm{d}\, A_{(\hat{\mathbf{n}})} \, \mathcal{K} \, \rho \, \hat{\mathbf{n}} \cdot \mathbf{v} - \int \mathrm{d}V \, \mathcal{K} \, \nabla \cdot (\rho \, \mathbf{v}) \\ &= -\int_{z=\eta} \mathrm{d}x \, \mathrm{d}y \, \mathcal{K} \, (\rho \, \eta_{,t} - \rho_{\mathsf{w}} \, q_{\mathsf{w}}) - \int \mathrm{d}V \, \mathcal{K} \, \nabla \cdot (\rho \, \mathbf{v}), \end{aligned} \tag{10.16}$$

where we used the surface boundary condition (10.10) for the last step.

10.2 Conservation, consistency, and accuracy

Accuracy is often a primary consideration for numerical methods. Additionally, ease of analysis and interpretation are also important. The presence of discrete analogs to continuous conservation properties assists in the interpretation of the numerical simulation. Unfortunately, conservation and accuracy are often incompatible.

Traditionally, climate modelers have chosen conservation properties over accuracy. For example, conservation of scalar properties are essential to ensure that heat and salt are conserved over the course of a long climate integration. Another property that certain models claim is conservation of mechanical energy. This claim, however, is unfounded for the space-time discrete equations in all models discussed in Griffies et al. (2000a). All ocean climate models break kinetic energy conservation when discretizing in time. This point is explained below in the discussion of equation (10.17).

What is often meant by energy conservation statements is the more qualified property whereby certain spatially discrete terms are discretized so they do not alter global kinetic energy in the absence of boundary forcing. Deriving energetically consistent numerical schemes requires some care. In particular, ensuring that pressure work transfers into vertical buoyancy work in the Boussinesq model necessitates a particular form for the discrete advection velocity. We discuss this point in Section 10.4.

When considering energetic issues using alternative time stepping schemes, one often encounters the situation where certain terms, such as advection and pressure gradients, are evaluated at staggered time steps. Indeed, the preferred method discussed in Chapter 12 of Griffies (2004) staggers the velocity and tracer one-half time step relative to one another. Hence, pressure gradients, whose temporal placement is set by density, is off-set in time from momentum

advection, the Coriolis force, and friction. These details are important when interpreting energetic consistency of a space-time discrete model. Often the more sophisticated the time stepping scheme (e.g., the three-time level Adams-Bashforth method discussed in Chapter 12 of Griffies (2004)), the more difficult it is to maintain energetic consistency.

Energetic consistency is necessary but not sufficient for ensuring the discrete system conserves mechanical energy in the unforced inviscid limit. For example, time stepping according to the leap-frog method, which possesses useful energy consistency properties, precludes mechanical energy conservation. The Robert-Asselin time filter breaks energy conservation in a manner analogous to its corruption of global tracer conservation (Section 12.5.4 of Griffies (2004)). Furthermore, even without time filtering, the continuum identity

$$2\,\mathbf{u}\cdot\partial_t\,\mathbf{u} = \partial_t\,(\mathbf{u}\cdot\mathbf{u}) \tag{10.17}$$

is generally not satisfied by discrete time stepping schemes. As noted on page 158 of Durran (1999), trapezoidal time differencing allows for this property. Other schemes commonly used do not. As trapezoidal time differencing is semi-implicit and not readily implemented for the primitive equations, it is not considered in the following.

10.3 Thickness weighted volume and mass budgets

We make use of the thickness weighted volume budgets for the Boussinesq fluid when deriving the discrete energetic balances. The volume budgets are given by equations (7.76), (7.77), and (7.78). We expose them here for completeness

$$(w^{(s)})_{s=s_{k=1}} = \partial_t\,(\mathrm{d}z) - \mathrm{d}z\,\mathcal{S}^{(\mathsf{V})} + \nabla_s\cdot(\mathrm{d}z\,\mathbf{u}) - q_{\mathsf{w}} \tag{10.18}$$

$$(w^{(s)})_{s=s_k} = \partial_t(\mathrm{d}z) - \mathrm{d}z\,\mathcal{S}^{(\mathsf{V})} + \nabla_s\cdot(\mathrm{d}z\,\mathbf{u}) + (w^{(s)})_{s=s_{k-1}} \tag{10.19}$$

$$0 = \partial_t\,(\mathrm{d}z) - \mathrm{d}z\,\mathcal{S}^{(\mathsf{V})} + \nabla_s\cdot(\mathrm{d}z\,\mathbf{u}) + (w^{(s)})_{s=s_{kbot-1}}. \tag{10.20}$$

We also make use of the thickness weighted mass budgets for the non-Boussinesq case, given by equations (7.100), (7.101), and (7.102). We expose them here for completeness

$$(\rho\,w^{(s)})_{s=s_{k=1}} = \partial_t\,(\mathrm{d}z\;\rho) - \rho\,\mathrm{d}z\;\mathcal{S}^{(\mathsf{M})} + \nabla_s\cdot(\mathrm{d}z\;\rho\,\mathbf{u}) - \rho_{\mathsf{w}}\,q_{\mathsf{w}} \tag{10.21}$$

$$(\rho\,w^{(s)})_{s=s_k} = \partial_t(\mathrm{d}z\;\rho) - \rho\,\mathrm{d}z\;\mathcal{S}^{(\mathsf{M})} + \nabla_s\cdot(\mathrm{d}z\;\rho\,\mathbf{u}) + (\rho\,w^{(s)})_{s=s_{k-1}} \tag{10.22}$$

$$0 = \partial_t\,(\mathrm{d}z\;\rho) - \rho\,\mathrm{d}z\;\mathcal{S}^{(\mathsf{M})} + \nabla_s\cdot(\mathrm{d}z\;\rho\,\mathbf{u}) + (\rho\,w^{(s)})_{s=s_{kbot-1}}. \tag{10.23}$$

As described in Section 7.6.1, depth based vertical coordinates used in MOM4p1 (Section 6.1) allow for the time derivative $\partial_t\,(\mathrm{d}z)$ to be diagnosed from the vertically integrated volume budget. Likewise, the pressure based vertical coordinates (Section 6.2) allow for the time derivative $\partial_t\,(\rho\,\mathrm{d}z)$ to be diagnosed from the vertically integrated mass budget. These two properties are important to ensure the utility of the Eulerian algorithms employed by MOM4p1.

10.4 Discrete Boussinesq pressure work conversions

We now consider manipulations of the globally integrated discrete B-grid representation of $\mathbf{u}\cdot\nabla_z\,p$ for the Boussinesq case. In this section, discrete grid labels are exposed when needed, with many

labels suppressed to reduce clutter. The material in this Section is based on a similar z-coordinate discussion given in Griffies et al. (2004).

Consider the domain integrated scalar product of

$$\begin{aligned} \mathbf{u} \cdot \nabla_z \, p &= \mathbf{u} \cdot (\nabla_s \, p + \rho \nabla_s \, \Phi) \\ &= \mathbf{u} \cdot \nabla \, (p_{\mathsf{a}} + p_{\mathsf{surf}}) + \mathbf{u} \cdot (\nabla_s \, p' + \rho' \, \nabla_s \, \Phi). \end{aligned} \tag{10.24}$$

To reach this result we use equation (4.18) with $s = z^*$ or $s = \sigma^{(z)}$, in which case

$$p_{\mathsf{surf}} = g \, \rho_o \, \eta \qquad \text{when } s = z^* \text{ or } s = \sigma^{(z)} \tag{10.25}$$

is the rapidly fluctuating surface pressure term, and

$$p' = g \int_z^{\eta} \rho' \, \mathrm{d}z \qquad \text{when } s = z^* \text{ or } s = \sigma^{(z)} \tag{10.26}$$

is the slower fluctuating pressure anomaly where $\rho' = \rho - \rho_0$. When $s = z$ is the vertical coordinate, equation (4.17) is used, in which case

$$p_{\mathsf{surf}} = g \, \rho_{\mathsf{surf}} \, \eta \qquad \text{when } s = z \tag{10.27}$$

and

$$p' = g \int_z^{0} \rho' \, \mathrm{d}z \qquad \text{when } s = z. \tag{10.28}$$

On the discrete lattice we consider

$$- \int \mathrm{d}V \; \mathbf{u} \cdot \nabla_z \, p \rightarrow \mathcal{P}, \tag{10.29}$$

where

$$\begin{aligned} \mathcal{P} \equiv & - \sum_{i,j,k} dvu \, u \; FDX_NT(FAY(p_{\mathsf{a}} + p_{\mathsf{surf}})) \\ & - \sum_{i,j,k} dvu \, v \; FDY_ET(FAX(p_{\mathsf{a}} + p_{\mathsf{surf}})) \\ & - \sum_{i,j,k} dvu \; [\, u \; FDX_NT(FAY(p')) + v \; FDY_ET(FAX(p'))\,] \\ & - \sum_{i,j,k} dvu \; [\, u \; FAY(FAX(\rho') \, \delta_i \Phi)/\mathtt{dxu} + v \; FAX(FAY(\rho') \, \delta_j \Phi)/\mathtt{dyu}\,] \end{aligned} \tag{10.30}$$

with

$$dvu = \mathtt{dau} \; \mathtt{dzu} \tag{10.31}$$

the U-cell volume. MOM4 employs the following discrete forward derivative operators

$$FDX_NT(a) = \frac{a_{i+1} - a_i}{\mathtt{dxu}} \tag{10.32}$$

$$FDY_ET(a) = \frac{a_{j+1} - a_j}{\mathtt{dyu}}, \tag{10.33}$$

where the derivatives live on the east and north faces, respectively, of a tracer cell. The operators $\delta_i a$ and $\delta_j a$ compute the forward difference

$$\delta_i a = a_{i+1} - a_i \tag{10.34}$$
$$\delta_j a = a_{j+1} - a_j \tag{10.35}$$

of a discrete field. MOM4 also employs the following forward averaging operators

$$FAX(a) = \frac{a_{i+1} + a_i}{2} \tag{10.36}$$
$$FAY(a) = \frac{a_{j+1} + a_j}{2}. \tag{10.37}$$

The first group of terms in equation (10.30) arises from applied pressure and surface geopotential acting on the vertically integrated velocity. The second represents the constant s lateral pressure gradient taken between cells living on the same discrete k-level. The third arises from the use of generalized vertical coordinates, where the depth of a k-level is generally a function of horizontal position.

10.4.1 The vertically integrated term $\mathcal{P}_1$

The first term in equation (10.30) can be vertically integrated to yield

$$\begin{aligned}\mathcal{P}_1 \equiv & -\sum_{i,j,k} \mathrm{dau}\ \mathrm{dzu}\ u\ FDX_NT(FAY(p_{\mathsf{a}} + p_{\mathsf{surf}})) \\ & - \sum_{i,j,k} \mathrm{dau}\ \mathrm{dzu}\ v\ FDY_ET(FAX(p_{\mathsf{a}} + p_{\mathsf{surf}})) \\ = & -\sum_{i,j} \mathrm{dau}\ U\ FDX_NT(FAY(p_{\mathsf{a}} + p_{\mathsf{surf}})) \\ & - \sum_{i,j} \mathrm{dau}\ V\ FDY_ET(FAX(p_{\mathsf{a}} + p_{\mathsf{surf}}))\end{aligned} \tag{10.38}$$

where

$$(U, V) = \sum_k \mathrm{dzu}\,(u, v) \tag{10.39}$$

is the vertically integrated horizontal velocity field. The $\mathcal{P}_1$ term represents the effects of applied pressure and geopotential working on moving vertical columns of fluid.

10.4.2 Advection velocity components for tracers

Focus on the zonal piece of the second term, where

$$\begin{aligned}\mathcal{P}_{2x} \equiv & -\sum_{i,j,k} \mathrm{dau}\ \mathrm{dzu}\ u\ FDX_NT(FAY(p')) \\ = & -\frac{1}{2}\sum \mathrm{dyu}\ \mathrm{dzu}\ u\ \delta_i(p'_j + p'_{j+1}) \\ = & -\sum BAY(\mathrm{dyu}\ \mathrm{dzu}\ u)\ \delta_i p'_j.\end{aligned} \tag{10.40}$$

The boundary terms were dropped since they vanish for either periodic or solid wall conditions. We also introduced the backward meridional average operator

$$BAY(a) = \frac{a_j + a_{j-1}}{2}. \tag{10.41}$$

Now *define* the zonal thickness weighted advective transport velocity on the eastern face of a tracer cell as

$$\boxed{\mathtt{uh_et}_{i,j,k} = \frac{BAY(\mathtt{dyu\ dzu}\ u)}{\mathtt{dyte}_{i,j}},} \tag{10.42}$$

where $\mathtt{dyte}_{i,j}$ is the meridional width of the tracer cell's east side (see Figure 10.2 for definitions of grid distances). Doing so leads to

$$\begin{aligned} \mathcal{P}_{2x} &= -\sum \delta_i p' \ (\mathtt{dyte\ uh_et}) \\ &= \sum p' \ \delta_i \ (\mathtt{dyte\ uh_et}) \\ &= \sum p' \ \mathtt{dat}\ BDX_ET(\mathtt{uh_et}), \end{aligned} \tag{10.43}$$

where boundary terms vanish, and

$$BDX_ET(a) = \frac{a_{i,j}\,\mathtt{dyte}_{i,j} - a_{i-1,j}\,\mathtt{dyte}_{i-1,j}}{\mathtt{dat}_{i,j}} \tag{10.44}$$

is a backwards finite difference operator for fields defined on the east face of tracer cells. Similar manipulations with the meridional term $v\,\partial_y p'$ leads to

$$\mathcal{P}_2 = \sum_{i,j,k} p' \ \mathtt{dat}\ (BDX_ET(\mathtt{uh_et}) + BDY_NT(\mathtt{vh_nt})), \tag{10.45}$$

with

$$\boxed{\mathtt{vh_nt}_{i,j,k} = \frac{BAX(\mathtt{dxu\ dzu}\ v)}{\mathtt{dxtn}_{i,j}}} \tag{10.46}$$

the meridional tracer advective velocity on the north face of the tracer cell. Finally,

$$BDY_NT(a) = \frac{a_{i,j}\,\mathtt{dxtn}_{i,j} - a_{i,j-1}\,\mathtt{dxtn}_{i,j-1}}{\mathtt{dat}_{i,j}} \tag{10.47}$$

is a backwards finite difference operator for fields defined on the north face of tracer cells.

The horizontal velocity components uh_et and vh_nt are defined at the sides of the tracer cells. They are the discrete representation of the thickness weighted advective velocity components that transport tracer and volume through the east and north cell faces. When fluid volume converges horizontally to a tracer cell, there is a corresponding dia-surface velocity component and a generally nonzero time tendency for the cell thickness. The thickness weighted volume budgets given by equations (10.18), (10.19), and (10.20) describe these effects.

Given that the advective velocity components uh_et and vh_nt are defined at the sides of the tracer cells, we are led to define a dia-surface velocity component $\mathtt{w_bt}_k$ at the bottom of the cell. It can generally be written by the discrete form of equation (10.19)

$$\boxed{\begin{aligned} \mathtt{w_bt}_k =& \partial_t\,(\mathtt{dzt_k}) - \mathtt{dzt_k}\,\mathcal{S}^{(\mathsf{V})} \\ &+\ BDX_ET(\mathtt{uh_et}_k) + BDY_NT(\mathtt{vh_nt}_k) + \mathtt{w_bt}_{k-1}. \end{aligned}} \tag{10.48}$$

Again, the time tendency on tracer cell thickness $\mathtt{dzt_k}$ is known in MOM4p1 from information about the vertically integrated volume budget (Section 7.6.1.5). So this expression is indeed a diagnostic expression for $\mathtt{w_bt}_k$, evaluated from the surface down to the bottom. At the ocean surface, the dia-surface velocity component is determined by the input of water to the system

$$\boxed{\mathtt{w_bt}_{k=0} = -q_{\mathtt{w}}.} \tag{10.49}$$

The minus sign is a convention, where positive w represents upward transport whereas positive $q_{\mathtt{w}}$ represents downward transport of fresh water through the ocean surface into the ocean domain. Note that in general, water can enter the ocean domain at any depth through the source term $\mathcal{S}^{(\mathsf{V})}$. At the ocean bottom, we are ensured of a proper discretization so long as

$$\boxed{\mathtt{w_bt}_{k=kbot} = 0} \tag{10.50}$$

is diagnosed. This statement is valid on the B-grid since the ocean bottom on tracer cells is flat. It has proven to be a very useful diagnostic to verify the integrity of the volume conservation discretization throughout a vertical column.

10.4.3 Completing the manipulations for $\mathcal{P}_2$

Substituting expression (10.48) for the vertical advective velocity component into equation (10.45) leads to

$$\mathcal{P}_2 = \sum_{i,j,k} p'_k \, \mathtt{dat} \, (\mathtt{w_bt}_k - \mathtt{w_bt}_{k-1} - \partial_t \, \mathtt{dzt_k} + \mathtt{dzt_k} \, \mathcal{S}^{(\mathsf{V})}). \tag{10.51}$$

Now move the vertical difference operator from the dia-surface velocity to the hydrostatic pressure via the following identity

$$\sum_{k=1}^{kbot} p'_k \, \mathtt{dat} \, (\mathtt{w_bt}_k - \mathtt{w_bt}_{k-1}) = -p'_{k=1} \, \mathtt{w_bt}_{k=0} \, \mathtt{dat} - \sum_{k=1}^{kbot} \mathtt{dat} \, \mathtt{w_bt}_k \, (p'_{k+1} - p'_k), \tag{10.52}$$

where we used the lower boundary condition $p'_{kbot+1} \, \mathtt{w_bt}_{kbot} = 0$ to reach this result. The next step requires us to specify how the hydrostatic pressure is computed. There are two ways, described in Sections 7.1.1 and 7.1.2.

10.4.3.1 Energetic approach

Section 7.1.1 noted that the older energetically based method specifies the hydrostatic pressure at the tracer point depth (Figure 10.1) according to

$$\begin{aligned} p'_{k=1} &= g \, \mathtt{dztup_{k=1}} \, \rho'_{k=1} && k = 1 \\ p'_{k+1} &= p'_k + g \, \mathtt{dzwt_k} \, \overline{\rho'_k}^{z} && k > 1, \end{aligned} \tag{10.53}$$

where

$$\overline{\rho'_k}^{z} = (\rho'_k + \rho'_{k+1})/2 \tag{10.54}$$

is the algebraically averaged density over the region between two tracer points T_k and T_{k+1}, and $\mathtt{dzwt_k}$ is the vertical distance between the tracer points (Section 7.3). Substituting this result into equation (10.52) renders

$$\sum_{k=1}^{kbot} p'_k \, \mathtt{dat} \, (\mathtt{w_bt}_k - \mathtt{w_bt}_{k-1}) = -p'_{k=1} \, \mathtt{w_bt}_{k=0} \, \mathtt{dat} - g \sum_{k=1}^{kbot} \mathtt{dat} \, \mathtt{dzwt_k} \, \mathtt{w_bt}_k \, \overline{\rho'_k}^{z}. \tag{10.55}$$

This result then leads to

$$\boxed{\begin{aligned} \mathcal{P}_2 = & - g \sum_{i,j,k} \mathtt{dat} \, \mathtt{dzwt_k} \, \mathtt{w_bt}_k \, \overline{\rho'_k}^{z} \\ & - \sum_{i,j} \mathtt{dat} \, p'_{k=1} \, \mathtt{w_bt}_{k=0} - \sum_{i,j,k} \mathtt{dat} \, p'_k \, [\, \partial_t \, \mathtt{dzt_k} - \mathtt{dzt_k} \, \mathcal{S}^{(\mathsf{V})} \,]. \end{aligned}} \tag{10.56}$$

10.4.3.2 Finite volume approach

Section 7.1.2 noted that a finite volume based method specifies the hydrostatic pressure at the tracer point depth according to

$$\begin{aligned} p'_{k=1} &= g \, \mathtt{dztup_{k=1}} \, \rho'_{k=1} \\ p'_{k+1} &= p'_k + g \, \mathtt{dztlo_k} \, \rho'_k + g \, \mathtt{dztup_{k+1}} \, \rho'_{k+1}. \end{aligned} \tag{10.57}$$

Substituting this result into equation (10.52) renders

$$\begin{aligned} \sum_{k=1}^{kbot} p'_k \, \mathtt{dat} \, (\mathtt{w_bt}_k - \mathtt{w_bt}_{k-1}) = & -p'_{k=1} \, \mathtt{w_bt}_{k=0} \, \mathtt{dat} \\ & - g \sum_{k=1}^{kbot} \mathtt{dat} \, \mathtt{w_bt}_k \, (\mathtt{dztlo_k} \, \rho'_k + g \, \mathtt{dztup_{k+1}} \, \rho'_{k+1}). \end{aligned} \tag{10.58}$$

This result then leads to

$$\boxed{\begin{aligned} \mathcal{P}_2 = & - g \sum_{i,j,k} \mathtt{dat} \, \mathtt{w_bt}_k \, (\mathtt{dztlo_k} \, \rho'_k + g \, \mathtt{dztup_{k+1}} \, \rho'_{k+1}) \\ & - \sum_{i,j} \mathtt{dat} \, p'_{k=1} \, \mathtt{w_bt}_{k=0} - \sum_{i,j,k} \mathtt{dat} \, p'_k \, [\, \partial_t \, \mathtt{dzt_k} - \mathtt{dzt_k} \, \mathcal{S}^{(\mathsf{V})} \,]. \end{aligned}} \tag{10.59}$$

10.4.4 The geopotential gradient term $\mathcal{P}_3$

Now consider the zonal piece of the geopotential gradient from equation (10.30)

$$\mathcal{P}_{3x} = - \sum_{i,j,k} \mathtt{dxu} \, \mathtt{dyu} \, \mathtt{dzu} \; u \, FAY(FAX(\rho') \, \delta_i \Phi)/\mathtt{dxu}. \tag{10.60}$$

Transferring the forward average FAY to a backward average BAY leads to

$$\mathcal{P}_{3x} = - \sum BAY(\mathtt{dyu} \, \mathtt{dzu} \; u) \, FAX(\rho') \, \delta_i \Phi, \tag{10.61}$$

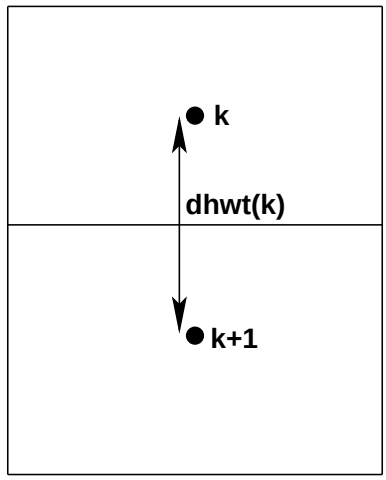

Figure 10.1: Schematic of the vertical grid cell arrangment used for computing the hydrostatic pressure at a depth $k+1$ in terms of the pressure at depth k using the equation $p'_{k+1} = p'_k + g\,\mathtt{dzwt_k}\,\overline{\rho'_k}^z$. The vertical average of density is meant to account for the part of density within each of the two adjacent cells. The factor of $1/2$ used in the average operator yields an approximate average when vertical cells are non-uniform. Yet the $1/2$ factor is used for all vertical grid spacing since it renders a simple conversion of discrete pressure work to discrete gravity work.

where boundary terms vanish. Introducing the zonal thickness weighted advective transport velocity (10.42) yields

$$\mathcal{P}_{3x} = -\sum \mathtt{dyte}\,\mathtt{uh_et}\,FAX(\rho')\,\delta_i\Phi. \tag{10.62}$$

Moving the difference operator $\delta_i\Phi = \Phi_{i+1} - \Phi_i$ from the geopotential to the remaining terms gives

$$\begin{aligned}\mathcal{P}_{3x} &= \sum \Phi\,\delta_i(\mathtt{dyte}\,FAX(\rho')\,\mathtt{uh_et}) \\ &= \sum \Phi\,\mathtt{dat}\,BDX_ET(FAX(\rho')\,\mathtt{uh_et}),\end{aligned} \tag{10.63}$$

where boundary terms vanish. Similar manipulations with the meridional piece of $\mathcal{P}_3$ lead to

$$\boxed{\mathcal{P}_3 = \sum \Phi\,\mathtt{dat}\,[BDX_ET(FAX(\rho')\,\mathtt{uh_et}) + BDY_NT(FAY(\rho')\,\mathtt{vh_nt})]} \tag{10.64}$$

10.4.5 Summary for the Boussinesq pressure conversion

In summary, for the older energetically based method for computing hydrostatic pressure, the projection of the horizontal velocity onto the downgradient pressure field is given by

$$\boxed{\begin{aligned}\mathcal{P} = &-\sum_{i,j} \mathtt{dau}\, U \;\; FDX_NT(FAY(p_{\mathsf{a}} + p_{\mathsf{surf}})) \\ &- \sum_{i,j} \mathtt{dau}\, V \;\; FDY_ET(FAX(p_{\mathsf{a}} + p_{\mathsf{surf}})) \\ &- \sum_{i,j} \mathtt{dat}\; p'_{k=1}\; \mathtt{w_bt}_{k=0} \\ &- g \sum_{i,j,k} \mathtt{dat}\; \mathtt{dzwt_k}\; \mathtt{w_bt}_k\; \overline{\rho'_k}^{z} \\ &- \sum_{i,j,k} \mathtt{dat}\; p'_k\; [\,\partial_t\, \mathtt{dzt_k} - \mathtt{dzt_k}\; \mathcal{S}^{(\mathsf{V})}\,] \\ &+ \sum_{i,j,k} \Phi\; \mathtt{dat}\; [BDX_ET(FAX(\rho')\, \mathtt{uh_et}) + BDY_NT(FAY(\rho')\, \mathtt{vh_nt})].\end{aligned}} \tag{10.65}$$

Within the MOM4 energy analysis diagnostic, the code computes the left hand side of equation (10.65) and compares to the right hand side. Differences are due to coding errors. This diagnostic is very effective because it involves advective velocities on the tracer cells, both tracer and velocity cell distances, the calculation of pressure, and details of partial steps. Each require precise discretization in order to ensure an energy conversion error at the roundoff level. In a similar manner, for the finite volume approach to computing hydrostatic pressure, we have the projection of the horizontal velocity onto the downgradient pressure field is given by

$$\boxed{\begin{aligned}\mathcal{P} = &-\sum_{i,j} \mathtt{dau}\, U \;\; FDX_NT(FAY(p_{\mathsf{a}} + p_{\mathsf{surf}})) \\ &- \sum_{i,j} \mathtt{dau}\, V \;\; FDY_ET(FAX(p_{\mathsf{a}} + p_{\mathsf{surf}})) \\ &- \sum_{i,j} \mathtt{dat}\; p'_{k=1}\; \mathtt{w_bt}_{k=0} \\ &- g \sum_{i,j,k} \mathtt{dat}\; \mathtt{w_bt}_k\; (\mathtt{dztlo_k}\; \rho'_k + g\, \mathtt{dztup_{k+1}}\; \rho'_{k+1}) \\ &- \sum_{i,j,k} \mathtt{dat}\; p'_k\; [\,\partial_t\, \mathtt{dzt_k} - \mathtt{dzt_k}\; \mathcal{S}^{(\mathsf{V})}\,] \\ &+ \sum_{i,j,k} \Phi\; \mathtt{dat}\; [BDX_ET(FAX(\rho')\, \mathtt{uh_et}) + BDY_NT(FAY(\rho')\, \mathtt{vh_nt})].\end{aligned}} \tag{10.66}$$

10.5 Discrete non-Boussinesq pressure work conversions

Now consider manipulations of the globally integrated discrete B-grid representation of $\mathbf{u} \cdot \nabla_z\, p$ for the non-Boussinesq case. Here, we are concerned with the domain integrated scalar product

$$\begin{aligned}\mathbf{u} \cdot \nabla_z\, p &= \mathbf{u} \cdot (\nabla_s\, p + \rho \nabla_s\, \Phi) \\ &= (\rho/\rho_o)\, \mathbf{u} \cdot \nabla\, (p_{\mathsf{b}} + \rho_o\, \Phi_{\mathsf{b}}) + \mathbf{u} \cdot [-(\rho'/\rho_o)\, \nabla_s\, p + \rho\, \nabla_s\, \Phi'],\end{aligned} \tag{10.67}$$

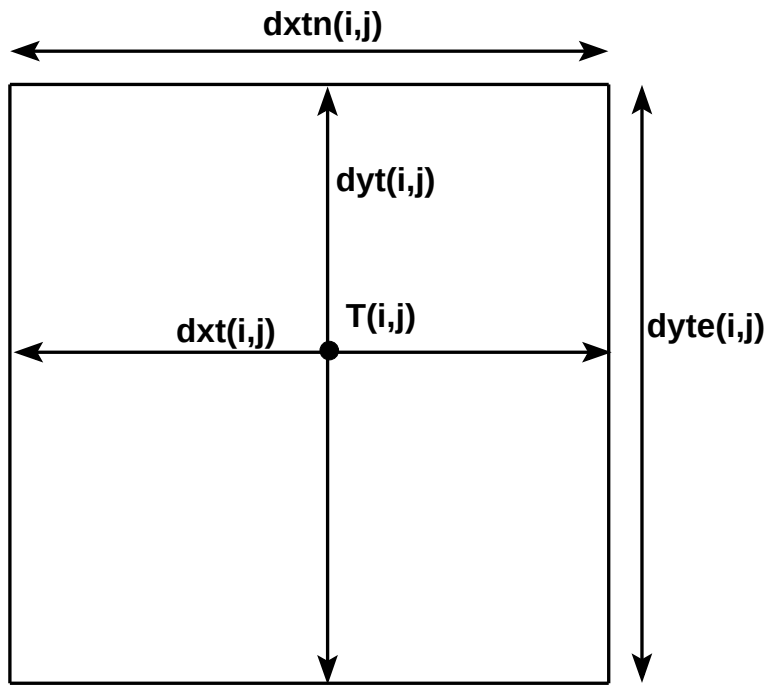

Figure 10.2: Time independent horizontal grid distances (meters) used for the tracer cell $T_{i,j}$ in MOM4. $dxt_{i,j}$ and $dyt_{i,j}$ are the grid distances of the tracer cell in the generalized zonal and meridional directions, and $\mathtt{dat}_{i,j} = dxt_{i,j}\, dyt_{i,j}$ is the area of the cell. The grid distance $\mathtt{dxtn}_{i,j}$ is the zonal width of the north face of a tracer cell, and $\mathtt{dyte}_{i,j}$ is the meridional width of the east face. Note that the tracer point $T_{i,j}$ is not generally at the center of the tracer cell. Distances are functions of both i and j due to the use of generalized orthogonal coordinates.

where equation (4.27) was used for the pressure gradient as implemented in pressure based vertical coordinate models. In order to maintain a clean analog to the Boussinesq case, we were led in Section 4.3.2 to introduce the discrete representations of the pressure gradient so that

$$-\int \mathrm{d}V\ \mathbf{u}\cdot\nabla_z\, p \rightarrow \mathcal{P} \tag{10.68}$$

becomes in the discrete case

$$\begin{aligned}
\rho_o\,\mathcal{P} \equiv &-\sum_{i,j,k} \mathtt{dau}\,\mathtt{rhodzu}\, u\, FDX_NT(FAY(p_{\mathsf{b}} + \rho_o\,\Phi_{\mathsf{b}})) \\
&-\sum_{i,j,k} \mathtt{dau}\,\mathtt{rhodzu}\, v\, FDY_ET(FAX(p_{\mathsf{b}} + \rho_o\,\Phi_{\mathsf{b}})) \\
&+\sum_{i,j,k} \mathtt{dau}\,\mathtt{dzu}\ u\ FAY(FAX(\rho')\,\delta_i p)/\mathtt{dxu} \\
&+\sum_{i,j,k} \mathtt{dau}\,\mathtt{dzu}\ v\ FAX(FAY(\rho')\,\delta_j p)/\mathtt{dyu} \\
&-\sum_{i,j,k} \mathtt{dau}\,\mathtt{rhodzu}\ [\,u\, FDX_NT(FAY(\Phi')) + v\, FDY_ET(FAX(\Phi'))].
\end{aligned} \tag{10.69}$$

We now consider these terms individually.

10.5.1 The vertically integrated term $\mathcal{P}_1$

The first term in equation (10.69) can be vertically integrated as

$$\boxed{\begin{aligned}\mathcal{P}_1 \equiv & -\sum_{i,j,k} \mathtt{dau}\ \mathtt{rhodzu}\, u\ FDX_NT(FAY(p_\mathsf{b}/\rho_o + \Phi_\mathsf{b})) \\ & -\sum_{i,j,k} \mathtt{dau}\ \mathtt{rhodzu}\, v\ FDY_ET(FAX(p_\mathsf{b}/\rho_o + \Phi_\mathsf{b})) \\ = & -\sum_{i,j} \mathtt{dau}\ U^\rho\ FDX_NT(FAY(p_\mathsf{b}/\rho_o + \Phi_\mathsf{b})) \\ & -\sum_{i,j} \mathtt{dau}\ V^\rho\ FDY_ET(FAX(p_\mathsf{b}/\rho_o + \Phi_\mathsf{b}))\end{aligned}} \tag{10.70}$$

where

$$(U^\rho, V^\rho) = \sum_k \mathtt{rhodzu}\,(u, v) \tag{10.71}$$

is the vertically integrated density weighted horizontal velocity field. The $\mathcal{P}_1$ term represents the effects of applied pressure and geopotential working on moving vertical columns of fluid.

10.5.2 Defining the advection velocities

To motivate the definition of the advection velocity for the non-Boussinesq case, we focus on the zonal part of the geopotential term

$$\begin{aligned}\mathcal{P}_{3x} &\equiv -\sum_{i,j,k} \mathtt{dau}\ \mathtt{rhodzu}\ u\, FDX_NT(FAY(\Phi')) \\ &= -\frac{1}{2}\sum \mathtt{dyu}\ \mathtt{rhodzu}\ u\ \delta_i(\Phi'_j + \Phi'_{j+1}) \\ &= -\sum BAY(\mathtt{dyu}\ \mathtt{rhodzu}\ u)\ \delta_i \Phi'_j.\end{aligned} \tag{10.72}$$

The boundary terms were dropped since they vanish for either periodic or solid wall conditions. Now *define* the zonal thickness weighted and density weighted advective transport velocity on the eastern face of a tracer cell

$$\boxed{\mathtt{uhrho_et}_{i,j,k} = \frac{BAY(\mathtt{dyu}\ \mathtt{rhodzu}\ u)}{\mathtt{dyte}_{i,j}}.} \tag{10.73}$$

This definition of the non-Boussinesq advection velocity component leads to

$$\begin{aligned}\mathcal{P}_{3x} &= -\sum \delta_i \Phi'\ (\mathtt{dyte}\ \mathtt{uhrho_et}) \\ &= \sum \Phi'\ \delta_i\,(\mathtt{dyte}\ \mathtt{uhrho_et}) \\ &= \sum \Phi'\ \mathtt{dat}\ BDX_ET(\mathtt{uhrho_et}),\end{aligned} \tag{10.74}$$

where boundary terms vanish. Similar manipulations with the meridional term $v\,\partial_y p$, and reintroducing the two-dimensional pieces, leads to

$$\mathcal{P}_3 = \sum \Phi' \; \mathtt{dat} \; (BDX_ET(\mathtt{uhrho_et}) + BDY_NT(\mathtt{vhrho_nt})), \tag{10.75}$$

with

$$\boxed{\mathtt{vhrho_nt}_{i,j,k} = \frac{BAX(\mathtt{dxu\ rhodzu}\ v)}{\mathtt{dxtn}_{i,j}}} \tag{10.76}$$

the meridional density and thickness weighted advective tracer velocity on the north face of the tracer cell.

As for the Boussinesq case, the horizontal advective velocities uhrho_et and vhrho_nt are defined at the sides of the tracer cells. They are the discrete representation of the thickness and density weighted advective velocity transporting tracer and volume through the east and north cell faces. When mass converges horizontally to a tracer cell, there is a corresponding dia-surface velocity component and a generally nonzero time tendency for the cell thickness. The thickness weighted mass budgets given by equations (10.21), (10.22), and (10.23) describe these effects.

Given that the advective velocities uhrho_et and vhrho_nt are defined at the sides of the tracer cells, we are led to define a density weighted dia-surface velocity component $\mathtt{wrho_bt}_k$ at the bottom of the cell. It is determined by the discrete form of equation (10.22)

$$\boxed{\begin{aligned}\mathtt{wrho_bt}_k =& \partial_t(\mathtt{rhodzt})_k - \mathtt{rhodzt}\ \mathcal{S}^{(\mathsf{M})} \\ &+\ BDX_ET(\mathtt{uhrho_et}_k) + BDY_NT(\mathtt{vhrho_nt}_k) + \mathtt{wrho_bt}_{k-1}.\end{aligned}} \tag{10.77}$$

As for the velocity cells, we use vertical coordinates so that the tracer cells maintain

$$\boxed{\rho\ dzt = (\rho\ z_{,s})_{(t)}\ dst} \tag{10.78}$$

where $(\rho\, z_{,s})_{(t)}$ is depth independent. The time tendency on density weighted tracer cell thickness $(\mathtt{rhodzt})_k$ is known in MOM4p1 from information about the vertically integrated mass budget (Section 7.4.2). So equation (10.77) is indeed a diagnostic expression for $\mathtt{wrho_bt}_k$, evaluated from the surface down to the bottom. At the ocean surface, the dia-surface velocity component is determined by the input of fresh water to the system

$$\boxed{\mathtt{wrho_bt}_{k=0} = -\rho_{\mathsf{w}}\ q_{\mathsf{w}}.} \tag{10.79}$$

At the ocean bottom, we are ensured of a proper discretization so long as

$$\boxed{\mathtt{wrho_bt}_{k=kbot} = 0} \tag{10.80}$$

is diagnosed.

10.5.3 Completing the manipulations for $\mathcal{P}_3$

Substituting expression (10.77) for the vertical advective velocity component into equation (10.75) leads to

$$\mathcal{P}_3 = \sum \Phi'_k \; \mathtt{dat} \; (\mathtt{wrho_bt}_k - \mathtt{wrho_bt}_{k-1} - \partial_t\,(\mathtt{rhodzt})_k + \mathtt{rhodzt_k}\ \mathcal{S}^{(\mathsf{M})}). \tag{10.81}$$

Now move the vertical difference operator from the dia-surface velocity to the hydrostatic pressure via the following identity

$$\begin{aligned}\sum_{k=1}^{kbot} \Phi'_k \, \mathtt{dat} \, (\mathtt{wrho_bt}_k - \mathtt{wrho_bt}_{k-1}) = & - \mathtt{dat} \, \Phi'_{k=1} \, \mathtt{wrho_bt}_{k=0} \\ & + \sum_{k=1}^{kbot} \mathtt{dat} \, \mathtt{wrho_bt}_k \, (\Phi'_k - \Phi'_{k+1}),\end{aligned} \tag{10.82}$$

where we used the lower boundary condition $\Phi'_{kbot+1} \, \mathtt{wrho_bt}_{kbot} = 0$ to reach this result. The next step requires us to specify how the anomalous geopotential height is computed. There are two ways, described in Sections 7.1.3 and 7.1.4.

10.5.3.1 Energetic approach

In Section 7.1.3, we noted that the older energetically based method specifies the anomalous geopotential height at the tracer point depth (Figure 10.1) according to

$$\Phi'_k = \Phi'_{k+1} - (g/\rho_o) \, \mathtt{dzwt_k} \, \overline{\rho'_k}^z. \tag{10.83}$$

In contrast to the hydrostatic pressure calculation (10.53), the geopotential calculation procedes from the bottom upwards. Substituting equation (10.83) into equation (10.82) renders

$$\begin{aligned}\sum_{k=1}^{kbot} \Phi'_k \, \mathtt{dat} \, (\mathtt{wrho_bt}_k - \mathtt{wrho_bt}_{k-1}) = & - \Phi'_{k=1} \, \mathtt{wrho_bt}_{k=0} \, \mathtt{dat} \\ & -(g/\rho_o) \sum_{k=1}^{kbot} \mathtt{dat} \, \mathtt{dzwt_k} \, \mathtt{wrho_bt}_k \, \overline{\rho'_k}^z,\end{aligned} \tag{10.84}$$

which then leads to

$$\boxed{\begin{aligned}\mathcal{P}_3 = & - (g/\rho_o) \sum_{i,j,k} \mathtt{dat} \, \mathtt{dzwt_k} \, \mathtt{wrho_bt}_k \, \overline{\rho'_k}^z \\ & - \sum_{i,j} \mathtt{dat} \, \Phi'_{k=1} \, \mathtt{wrho_bt}_{k=0} \\ & + \sum_{i,j,k} \mathtt{dat} \, \Phi' \, [\, (\mathtt{rhodzt})_k \, \mathcal{S}^{(\mathsf{M})} - \partial_t \, (\mathtt{rhodzt})_k \,]\end{aligned}} \tag{10.85}$$

10.5.3.2 Finite volume approach

Section 7.1.4 noted that the finite volume based method specifies the anomalous geopotential height at the tracer point depth (Figure 10.1) according to

$$\begin{aligned}\Phi'_{k=kbot} &= -(g/\rho_o) \, \mathtt{dztlo_{kbot}} \, \rho'_{k=kbot} \\ \Phi'_k &= \Phi'_{k+1} - (g/\rho_o) \, \mathtt{dztup_{k+1}} \, \rho'_{k+1} - (g/\rho_o) \, \mathtt{dztlo_k} \, \rho'_k.\end{aligned} \tag{10.86}$$

Substituting equation (10.86) into equation (10.82) renders

$$\begin{aligned}\sum_{k=1}^{kbot} \Phi'_k \, \mathtt{dat} \, (\mathtt{wrho_bt}_k - \mathtt{wrho_bt}_{k-1}) = & - \Phi'_{k=1} \, \mathtt{wrho_bt}_{k=0} \, \mathtt{dat} \\ & - (g/\rho_o) \sum_{k=1}^{kbot} \mathtt{dat} \, \mathtt{wrho_bt}_k \, (\mathtt{dztup}_{\mathtt{k}+1} \, \rho'_{k+1} + \mathtt{dztlo}_{\mathtt{k}} \, \rho'_k),\end{aligned} \tag{10.87}$$

which then leads to

$$\boxed{\begin{aligned}\mathcal{P}_3 = & - (g/\rho_o) \sum_{i,j,k} \mathtt{dat} \, \mathtt{wrho_bt}_k \, (\mathtt{dztup}_{\mathtt{k}+1} \, \rho'_{k+1} + \mathtt{dztlo}_{\mathtt{k}} \, \rho'_k) \\ & - \sum_{i,j} \mathtt{dat} \, \Phi'_{k=1} \, \mathtt{wrho_bt}_{k=0} \\ & + \sum_{i,j,k} \mathtt{dat} \, \Phi' \, [\, (\mathtt{rhodzt})_k \, \mathcal{S}^{(\mathsf{M})} - \partial_t \, (\mathtt{rhodzt})_k \,].\end{aligned}} \tag{10.88}$$

10.5.4 The pressure gradient term $\mathcal{P}_2$

Now consider the zonal piece of the geopotential gradient from equation (10.69)

$$\rho_o \, \mathcal{P}_{2x} = \sum_{i,j,k} \mathtt{dxu} \, \mathtt{dyu} \, \mathtt{dzu} \; u \; FAY(FAX(\rho') \, \delta_i p)/\mathtt{dxu} \tag{10.89}$$

Transferring the forward average FAY to a backward average BAY leads to

$$\rho_o \, \mathcal{P}_{2x} = - \sum BAY(\mathtt{dyu} \, \mathtt{dzu} \; u) \, FAX(\rho') \, \delta_i p, \tag{10.90}$$

where boundary terms vanish. Further manipulations, analogous to the Boussinesq case in Section 10.4.4, do not appear possible since the density weighted advection velocity will not appear. Instead, the ρ' weighted velocity appears, and this is not relevant. So we simply write this term in its unmanipulated form

$$\boxed{\begin{aligned}\mathcal{P}_2 = & \; \rho_o^{-1} \sum_{i,j,k} \mathtt{dau} \, \mathtt{dzu} \; u \; FAY(FAX(\rho') \, \delta_i p)/\mathtt{dxu} \\ & + \; \rho_o^{-1} \sum_{i,j,k} \mathtt{dau} \, \mathtt{dzu} \; v \; FAX(FAY(\rho') \, \delta_j p)/\mathtt{dyu}.\end{aligned}} \tag{10.91}$$

10.5.5 Summary for the non-Boussinesq pressure conversion

In summary, for the older energetically based method for computing the anomalous geopotential, the projection of the horizontal velocity onto the downgradient pressure field in the non-Boussinesq

case is given by

$$
\begin{aligned}
\mathcal{P} = & -\sum_{i,j} \mathtt{dau}\, U^{\rho}\ FDX_NT(FAY(p_{\mathsf{b}}/\rho_o + \Phi_{\mathsf{b}})) \\
& - \sum_{i,j} \mathtt{dau}\ \ V^{\rho}\ FDY_ET(FAX(p_{\mathsf{b}}/\rho_o + \Phi_{\mathsf{b}})) \\
& - \sum_{i,j} \mathtt{dat}\ \Phi'_{k=1}\ \mathtt{wrho_bt}_{k=0} \\
& - (g/\rho_o) \sum_{i,j,k} \mathtt{dat}\ \mathtt{dzwt_k}\ \mathtt{wrho_bt}_k\ \overline{\rho'_k}^{z} \\
& - \sum_{i,j,k} \mathtt{dat}\ \Phi'_k\ [\,\partial_t\,(\mathtt{rhodzt})_k - \rho\,\mathtt{dzt_k}\ \mathcal{S}^{(\mathsf{M})}\,] \\
& + \rho_o^{-1} \sum_{i,j,k} \mathtt{dau}\,\mathtt{dzu}\ u\ FAY(FAX(\rho')\,\delta_i p)/\mathtt{dxu} \\
& + \rho_o^{-1} \sum_{i,j,k} \mathtt{dau}\,\mathtt{dzu}\ v\ FAX(FAY(\rho')\,\delta_j p)/\mathtt{dyu}.
\end{aligned}
\tag{10.92}
$$

In a similar manner, for the finite volume approach to computing anomalous geopotential height, the projection of the horizontal velocity onto the downgradient pressure field is given by

$$
\begin{aligned}
\mathcal{P} = & -\sum_{i,j} \mathtt{dau}\, U^{\rho}\ FDX_NT(FAY(p_{\mathsf{b}}/\rho_o + \Phi_{\mathsf{b}})) \\
& - \sum_{i,j} \mathtt{dau}\ \ V^{\rho}\ FDY_ET(FAX(p_{\mathsf{b}}/\rho_o + \Phi_{\mathsf{b}})) \\
& - \sum_{i,j} \mathtt{dat}\ \Phi'_{k=1}\ \mathtt{wrho_bt}_{k=0} \\
& - (g/\rho_o) \sum_{i,j,k} \mathtt{dat}\ \mathtt{wrho_bt}_k\,(\mathtt{dztup_{k+1}}\ \rho'_{k+1} + \mathtt{dztlo_k}\ \rho'_k) \\
& - \sum_{i,j,k} \mathtt{dat}\ \Phi'_k\ [\,\partial_t\,(\mathtt{rhodzt})_k - \mathtt{rhodzt_k}\ \mathcal{S}^{(\mathsf{M})}\,] \\
& + \rho_o^{-1} \sum_{i,j,k} \mathtt{dau}\,\mathtt{dzu}\ u\ FAY(FAX(\rho')\,\delta_i p)/\mathtt{dxu} \\
& + \rho_o^{-1} \sum_{i,j,k} \mathtt{dau}\,\mathtt{dzu}\ v\ FAX(FAY(\rho')\,\delta_j p)/\mathtt{dyu}.
\end{aligned}
\tag{10.93}
$$

10.6 Discrete Boussinesq kinetic energy advection

We now consider how kinetic energy is advected in the discrete case. For this purpose, we assume that momentum advection is evaluated at a single time step, as is the case for a leap-frog version of MOM4. But for the preferred staggered scheme, momentum advection is implemented according to a third order Adams-Bashforth (chapter 12 of Griffies, 2004). In this case, the following results are understood to be relevant when we take the scalar product of the horizontal velocity with one of the three Adams-Bashforth terms contributing to the advection tendency. Even though the conversion properties are compromised, the utility of the kinetic energy conversion diagnostic remains. A second assumption made here is that velocity advection is discretized using second

order centered advection. The following is a generalization of material presented in Griffies et al. (2004).

10.6.1 Coriolis force

We first verify that the scalar product of horizontal velocity and the advection metric term trivially vanishes at each grid point on the B-grid. Written as in the numerical model, keeping only grid labels of relevance, we have

$$\mathbf{u} \cdot \mathcal{M}\left(\hat{\mathbf{z}} \wedge \mathbf{v}\right) \rightarrow \sum_{n=1}^{2} u_n \, u_{3-n} \left(u_1 \, dh1dy - u_2 \, dh2dx\right) = 0. \tag{10.94}$$

In this equation,

$$dh1dy = \partial_y \ln dx \tag{10.95}$$

$$dh2dx = \partial_x \ln dy \tag{10.96}$$

are the model arrays carrying information about the partial derivatives of the grid spacing in the two orthogonal directions. The sum in equation (10.94) vanishes trivially at each grid point upon writing out the two terms. Similar manipulations are appropriate for the Coriolis force, so long as the Coriolis force is evaluated explicitly in time. When semi-implicit time stepping is used, the cancellation is broken.

10.6.2 Horizontal convergence

Next consider the scalar product of the horizontal convergence term with the horizontal velocity $\mathbf{u}$, and integrate over the full ocean

$$\begin{aligned} \mathcal{A}_{horz} = & - \sum_{i,j,k} \mathrm{dau}\ \mathbf{u} \cdot BDX_EU(\mathrm{uh_eu} * FAX(\mathbf{u})) \\ & - \sum_{i,j,k} \mathrm{dau}\ \mathbf{u} \cdot BDY_NU(\mathrm{vh_nu} * FAY(\mathbf{u})). \end{aligned} \tag{10.97}$$

Note the use of thickness weighted advection velocity components uh_eu and vh_nu provides for the vertical grid increment dzu needed for the discrete volume integral. The forward averaging operators FAX and FAY are the unweighted averages used to estimate velocity on the velocity cell faces. They are used to define the centered difference advective fluxes of velocity. MOM4 also uses the backward derivative operators

$$BDX_EU(a) = \frac{\mathrm{dyue}_{i,j}\, a_i - \mathrm{dyue}_{i-1,j}\, a_{i-1}}{\mathrm{dau}_{i,j}} \tag{10.98}$$

$$BDY_NU(a) = \frac{\mathrm{dxue}_{i,j}\, a_j - \mathrm{dxue}_{i,j-1}\, a_{j-1}}{\mathrm{dau}_{i,j}}. \tag{10.99}$$

These backward derivative operators act on fields defined at the east and north face of velocity cells, respectively (see Figure 10.3 for definitions of grid distances).

10.6.3 Diagnosing the vertical transport for U-cells

Thickness weighted horizontal advective velocities uh_eu and vh_nu are defined in MOM4 by remapping the horizontal advective velocities uh_et and vh_nt, defined in Section 10.4.2, onto the velocity cell faces. The satisfy continuity via a U-grid version of the T-grid result (10.48)

$$\boxed{\begin{aligned}\mathtt{w_bu}_k &= \partial_t\left(\mathtt{dzu_k}\right) - \mathtt{dzu_k}\,\mathcal{S}^{(\mathsf{V})} \\ &\quad + \; BDX_EU(\mathtt{uh_eu}_k) + BDY_NU(\mathtt{vh_nu}_k) + \mathtt{w_bu}_{k-1},\end{aligned}} \tag{10.100}$$

where the volume source $\mathcal{S}^{(\mathsf{V})}$ and tendency $\partial_t\left(\mathtt{dzu_k}\right)$ have been mapped from their counterparts on the tracer grid. In this equation, w_bu is the dia-surface advective velocity component defined at the bottom face of a velocity cell.

To diagnose the vertical transport w_bu, we need to start at either the bottom or top of the ocean column, given a boundary condition. On the B-grid, the bottom of the bottom-most U-cell does not live on the ocean bottom, unless the ocean bottom is flat. Hence, a nontrivial mass or volume transport generally occurs through the bottom of a velocity cell column. That is, in general

$$\mathtt{w_bu}_{k=kbot} \neq 0, \tag{10.101}$$

which contrasts with the case on the T-cells (equations (10.50) and (10.80)).

A thorough discussion of this issue is provided in Section 22.3.3.2 of the MOM3 Manual (Pacanowski and Griffies, 1999). For present purposes, we note that it is sufficient to start the integration at the ocean surface and integrate downwards, just as for the tracer cells. Equivalently, we can use the remapping operator in MOM to map $\mathtt{w_bt}_k$ to $\mathtt{w_bu}_k$. Either way, the continuity equation (10.100) is maintained.

10.6.4 Discrete integration by parts on horizontal convergence

We now perform the discrete analog of integration by parts. For this purpose, expand the backwards derivative and average operators on the zonal flux terms, dropping the j, k labels for brevity

$$\begin{aligned}
&2\sum_i \mathtt{dau}\,\mathbf{u}_i \cdot BDX_EU(\mathtt{uh_eu}\; FAX(\mathbf{u})) = \\
&\sum \mathbf{u}_i \cdot [\mathtt{dyue}_i\; \mathtt{uh_eu}_i\; \mathbf{u}_{i+1} + \mathtt{dyue}_i\; \mathtt{uh_eu}_i\; \mathbf{u}_i \\
&-\mathtt{dyue}_{i-1}\; \mathtt{uh_eu}_{i-1}\; \mathbf{u}_i - \mathtt{dyue}_{i-1}\; \mathtt{uh_eu}_{i-1}\; \mathbf{u}_{i-1}] \\
&= \sum \mathbf{u}_i \cdot \mathbf{u}_i \left(\mathtt{dyue}_i\; \mathtt{uh_eu}_i - \mathtt{dyue}_{i-1}\; \mathtt{uh_eu}_{i-1}\right) \\
&+ \sum \mathbf{u}_i \cdot \left(\mathtt{dyue}_i\; \mathtt{uh_eu}_i\; \mathbf{u}_{i+1} - \mathtt{dyue}_{i-1}\; \mathtt{uh_eu}_{i-1}\; \mathbf{u}_{i-1}\right).
\end{aligned} \tag{10.102}$$

Focus now on the second group of terms, where shifting sum labels leads to

$$\begin{aligned}
&\sum_{i=1}^{nx} \mathbf{u}_i \cdot \mathbf{u}_{i+1}\; \mathtt{dyue}_i\; \mathtt{uh_eu}_i - \sum_{i=1}^{nx} \mathbf{u}_i \cdot \mathbf{u}_{i-1}\; \mathtt{dyue}_{i-1}\; \mathtt{uh_eu}_{i-1} = \\
&\sum_{i=2}^{nx+1} \mathbf{u}_{i-1} \cdot \mathbf{u}_i\; \mathtt{dyue}_{i-1}\; \mathtt{uh_eu}_{i-1} - \sum_{i=1}^{nx} \mathbf{u}_i \cdot \mathbf{u}_{i-1}\; \mathtt{dyue}_{i-1}\; \mathtt{uh_eu}_{i-1} \\
&= \mathbf{u}_{nx} \cdot \mathbf{u}_{nx+1}\; \mathtt{dyue}_{nx}\; \mathtt{uh_eu}_{nx} - \mathbf{u}_1 \cdot \mathbf{u}_0\; \mathtt{dyue}_0\; \mathtt{uh_eu}_0.
\end{aligned} \tag{10.103}$$

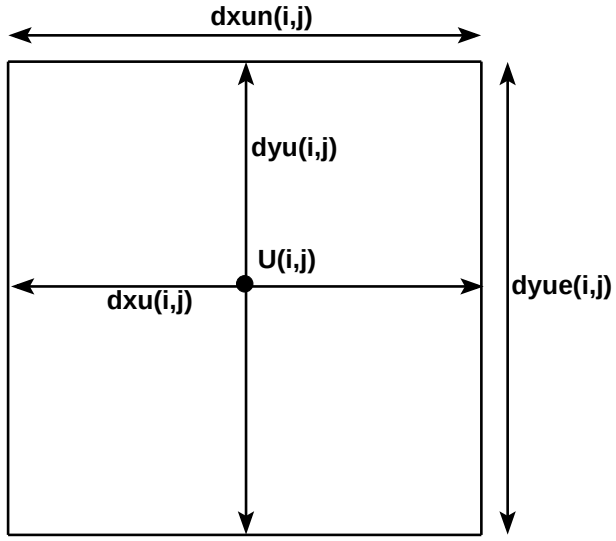

Figure 10.3: Time independent horizontal grid distances (meters) used for the velocity cell $U_{i,j}$ in MOM4. $\mathtt{dxu}_{i,j}$ and $\mathtt{dyu}_{i,j}$ are the grid distances of the velocity cell in the generalized zonal and meridional directions, and $\mathtt{dau}_{i,j} = \mathtt{dxu}_{i,j}\,\mathtt{dyu}_{i,j}$ is the area of the cell. The grid distance $\mathtt{dxue}_{i,j}$ is the zonal width of the north face of a velocity cell, and $\mathtt{dyue}_{i,j}$ is the meridional width of the east face. Note that the velocity point $U_{i,j}$ is not generally at the center of the velocity cell. Distances are functions of both i and j due to the use of generalized orthogonal coordinates.

This result vanishes for either solid wall or periodic boundary conditions. Similar manipulations apply for the meridional term, thus leading to

$$\begin{aligned}\mathcal{A}_{horz} &= -\sum \mathcal{K}\,\left(\mathtt{dyue}_i\ \mathtt{uh_eu}_i - \mathtt{dyue}_{i-1}\ \mathtt{uh_eu}_{i-1}\right)\\ &\quad - \sum \mathcal{K}\,\left(\mathtt{dxue}_j\ \mathtt{vh_nu}_j - \mathtt{dxue}_{j-1}\ \mathtt{vh_nu}_{j-1}\right)\\ &= -\sum \mathtt{dau}\ \mathcal{K}\ \left[BDX_EU(\mathtt{uh_eu}) + BDY_NU(\mathtt{vh_nu})\right],\end{aligned} \tag{10.104}$$

where

$$\mathcal{K}_{i,j,k} = \frac{1}{2}\,\mathbf{u}_{i,j,k}\cdot\mathbf{u}_{i,j,k} \tag{10.105}$$

is the discrete kinetic energy per mass.

10.6.5 Discrete integration by parts on vertical convergence

Now focus on the vertical advection term, which takes the form

$$\begin{aligned}
2\,\mathcal{A}_{vert} &= \sum_{k=1}^{kbot} \mathtt{dau}\ \mathbf{u}_k \cdot \left[-\mathtt{w_bu}_{k-1}\ (\mathbf{u}_{k-1}+\mathbf{u}_k) + \mathtt{w_bu}_k\ (\mathbf{u}_k+\mathbf{u}_{k+1})\right] \\
&= \sum_{k=1}^{kbot} \mathtt{dau}\ \mathbf{u}_k \cdot \mathbf{u}_k\ (\mathtt{w_bu}_k - \mathtt{w_bu}_{k-1}) \\
&\quad + \sum_{k=1}^{kbot} \mathtt{dau}\ (\mathtt{w_bu}_k\ \mathbf{u}_{k+1}\cdot\mathbf{u}_k - \mathtt{w_bu}_{k-1}\ \mathbf{u}_k\cdot\mathbf{u}_{k-1}) \\
&= 2\sum_{k=1}^{kbot} \mathtt{dau}\ \mathcal{K}_k\ (\mathtt{w_bu}_k - \mathtt{w_bu}_{k-1}) \\
&\quad - \sum \mathtt{dau}\ \mathtt{w_bu}_0\ (\mathbf{u}_0\cdot\mathbf{u}_1) + \sum \mathtt{dau}\ \mathtt{w_bu}_{kbot}\ (\mathbf{u}_{kbot+1}\cdot\mathbf{u}_{kbot}).
\end{aligned} \tag{10.106}$$

The horizontal velocity at $k = kbot + 1$ vanishes

$$\mathbf{u}_{kbot+1} = 0, \tag{10.107}$$

since $k = kbot + 1$ is interpreted as part of the solid earth. In contrast,

$$\mathbf{u}_{k=0} = \mathbf{u}_w \tag{10.108}$$

is the horizontal velocity of the fresh water. This velocity is often set equal to the surface ocean velocity $\mathbf{u}_w = \mathbf{u}_1$, yet MOM4 retains the option of providing a different value. This result then leads to

$$2\,\mathcal{A}_{vert} = 2\sum_{k=1}^{kbot} \mathtt{dau}\ \mathcal{K}_k\ (\mathtt{w_bu}_k - \mathtt{w_bu}_{k-1}) - \sum_{i,j} \mathtt{dau}\ \mathtt{w_bu}_0\ (\mathbf{u}_1\cdot\mathbf{u}_w). \tag{10.109}$$

10.6.6 Final result

Combining the results for $\mathcal{A}_{horz}$ and $\mathcal{A}_{vert}$ renders

$$\boxed{\begin{aligned}
\mathcal{A}_{horz} + \mathcal{A}_{vert} &= -(1/2)\sum \mathtt{dau}\ \mathtt{w_bu}_0\ (\mathbf{u}_1\cdot\mathbf{u}_w) \\
&\quad - \sum_{k=1}^{nk} \mathtt{dau}\ \mathcal{K}\ [BDX_EU(\mathtt{uh_eu}) + BDY_NU(\mathtt{vh_nu})] \\
&\quad - \sum_{k=1}^{nk} \mathtt{dau}\ \mathcal{K}\ (\mathtt{w_bu}_{k-1} - \mathtt{w_bu}_k) \\
&= -(1/2)\sum \mathtt{dau}\ \mathtt{w_bu}_0\ (\mathbf{u}_1\cdot\mathbf{u}_w) \\
&\quad + \sum_{i,j,k} \mathtt{dau}\ \mathcal{K}\ [\,\partial_t\,(\mathtt{dzu_k}) - \mathtt{dzu_k}\,\mathcal{S}^{(\mathsf{V})}\,],
\end{aligned}} \tag{10.110}$$

where we applied volume conservation over each U-cell as given by equation (10.100).

10.7 Discrete non-Boussinesq kinetic energy advection

Building on the results from Section 10.6, we now consider the conversion of kinetic energy advection in the discret non-Boussinesq discete. For this purpose, consider

$$\begin{aligned}\mathcal{A}_{horz} = &- \sum_{i,j,k} \mathtt{dau}\ \mathtt{dzu}\ \mathbf{u} \cdot BDX_EU(\mathtt{uhrho_eu} * FAX(\mathbf{u}))/\mathtt{dzu} \\ &- \sum_{i,j,k} \mathtt{dau}\ \mathtt{dzu}\ \mathbf{u} \cdot BDY_NU(\mathtt{vhrho_nu} * FAY(\mathbf{u}))/\mathtt{dzu}.\end{aligned} \tag{10.111}$$

Thickness weighted and density weighted horizontal advective velocities uhrho_eu and vhrho_nu are defined in MOM4 by remapping the horizontal advective velocities uhrho_et and vhrho_nt, defined by equations (10.73) and (10.76), onto the velocity cell faces. These horizontal transports satisfy continuity via a U-grid version of the T-grid result (10.77)

$$\boxed{\begin{aligned}\mathtt{wrho_bu_k} =& \partial_t(\mathtt{rho_dzu})_k - \mathtt{rho_dzu}\ \mathcal{S}^{(\mathsf{M})} \\ &+ BDX_EU(\mathtt{uhrho_eu_k}) + BDY_NU(\mathtt{vhrho_nu_k}) + \mathtt{wrho_bu_{k-1}}.\end{aligned}} \tag{10.112}$$

where the mass source has been mapped from the tracer to the velocity grid. In this equation, wrho_bu is the density weighted dia-surface advective velocity component defined at the bottom face of a velocity cell. As in the Boussinesq case discussed in Section 10.6, this vertical transport is diagnosed using the continuity equation, or equivalently via the MOM remap operator.

In general, results for the Boussinesq case transparently generalize to the non-Boussinesq case, which allows us to write by inspection

$$\boxed{\begin{aligned}\mathcal{A} =& -(1/2) \sum \mathtt{dau}\ \mathtt{wrho_bu_0}\ (\mathbf{u}_1 \cdot \mathbf{u}_w) \\ &- \sum_{k=1}^{nk} \mathtt{dau}\ \mathcal{K}\ [BDX_EU(\mathtt{uhrho_eu}) + BDY_NU(\mathtt{vhrho_nu})] \\ &- \sum_{k=1}^{nk} \mathtt{dau}\ \mathcal{K}\ (\mathtt{wrho_bu_{k-1}} - \mathtt{wrho_bu_k}) \\ =& -(1/2) \sum \mathtt{dau}\ \mathtt{wrho_bu_0}\ (\mathbf{u}_1 \cdot \mathbf{u}_w) \\ &+ \sum_{i,j,k} \mathtt{dau}\ \mathcal{K}\ [\,\partial_t\,(\mathtt{rho_dzu_k}) - \mathtt{rho_dzu_k}\ \mathcal{S}^{(\mathsf{M})}\,].\end{aligned}} \tag{10.113}$$

CHAPTER
ELEVEN

Temporal treatment of the Coriolis force

The purpose of this chapter is to present the two methods used in MOM4 for temporally discretizing the Coriolis force. Much of this material was presented in the MOM4 Guide of Griffies et al. (2004). It is useful to repeat this material, however, in the context of the density and thickness weighting used in MOM4p1 as well as the preferred forward time step for the tendencies (Section 8.5) rather than the older leap frog (Section 8.2).

11.1 Inertial oscillations

The inviscid horizontal momentum equation in the absence of pressure is given by

$$(\mathrm{d}/\mathrm{d}t + f\,\hat{\mathbf{z}}\wedge)\,\mathbf{u} = 0, \tag{11.1}$$

which is equivalent to the second order free oscillator equation

$$(\mathrm{d}^2/\mathrm{d}t^2 + f^2)\,\mathbf{u} = 0. \tag{11.2}$$

Here, $\mathrm{d}/\mathrm{d}t$ is the material time derivative relevant for Lagrangian observers. Motions which satisfy this equation are termed *inertial oscillations* and they have period given by

$$T_{\text{inertial}} = \frac{2\,\pi}{f} = \frac{11.97}{\sin\phi}\,\text{hour} \tag{11.3}$$

where $\Omega = 7.292 \times 10^{-5}\mathrm{s}^{-1}$ is the earth's angular speed. The period of inertial oscillations is smallest at the North pole where $\phi = \pi/2$ and $T_{\text{smallest}} \approx 12\,\text{hour}$.

An explicit temporal discretization of the inertial oscillation equation (11.1) will be unstable if the time step is longer than some fraction of the inertial period, where the fraction depends on details of the time stepping. Coarse resolution models (models with resolutions on the order of 4-5 degrees) may find this time step constraint is the most stringent of the model's baroclinic momentum processes. To get around this limitation, a semi-implicit temporal treatment has been traditionally considered, as in Bryan (1969).

Additional issues with coupling to sea ice may warrant an implicit treatment even for ocean models run with a momentum time step that well resolves the inertial period. In these cases,

temporal details of ocean-ice coupling have been found to cause enhanced energy at the inertial period. Semi-implicit time stepping of the Coriolis force may assist in damping this energy.

It is for these reasons that MOM4 provides an option to time step the Coriolis force either explicitly or semi-implicitly in the baroclinic portion of the model. The namelist parameter *acor* sets the level of implicitness, as described in Section 11.5.2.

11.2 Explicit temporal discretization with leap frog

Consider now just the linear part of the inertial oscillation equation, where advection is dropped

$$(\partial_t + f\,\hat{\mathbf{z}}\wedge)\,\mathbf{u} = 0. \tag{11.4}$$

Following the time integration discussions in O'Brien (1986) and Bryan (1991) (see also Section 2.3 of Durran (1999)), introduce the complex velocity

$$w = u + i\,v \tag{11.5}$$

where $i = \sqrt{-1}$ and w should not be confused with the vertical velocity component. In terms of w, equation (11.4) takes the form

$$\partial_t\, w = -i\,f\,w \tag{11.6}$$

which has an oscillatory solution

$$w = w_o\, e^{ift} \tag{11.7}$$

with period

$$T_{\text{inertial}} = 2\,\pi/f. \tag{11.8}$$

Time discretizing equation (11.6) with a centered leap-frog scheme leads to

$$w(\tau + \Delta\tau) = w(\tau - \Delta\tau) - i\lambda\, w(\tau) \tag{11.9}$$

with

$$\lambda = 2\,f\,\Delta\tau \tag{11.10}$$

a dimensionless number. We can write the finite difference solution in terms of an amplification factor

$$w(\tau + \Delta\tau) = G\,w(\tau). \tag{11.11}$$

Substituting this *ansatz* into equation (11.9) leads to the quadratic equation

$$G^2 + i\,\lambda\,G - 1 = 0 \tag{11.12}$$

whose solution is

$$G = \frac{-i\,\lambda \pm \sqrt{-\lambda^2 + 4}}{2}. \tag{11.13}$$

If

$$\lambda/2 = f\,\Delta\tau < 1, \tag{11.14}$$

then $|G| = 1$, which means the two finite difference solutions are neutral and stable. One root is an unphysical mode, known as the leap-frog *computational mode*, and the other corresponds to

the physical solution. If $\lambda > 2$ then $|G| > 1$ which means both roots are unstable. Hence, stability requires a time step satisfying

$$\Delta\tau < f^{-1}. \tag{11.15}$$

That is,

$$\frac{T_{\text{inertial}}}{\Delta\tau} = \frac{2\,\pi}{f\,\Delta\tau} > 2\,\pi, \tag{11.16}$$

meaning the leap-frog scheme remains stable if there are at least $2\,\pi$ time steps per inertial period. At the North Pole, this constraint means

$$\Delta\tau < 1.9\,\text{hours}. \tag{11.17}$$

For the baroclinic part of the model algorithm, $\Delta\tau < 1.9$ hours can be the limiting time step for coarse resolution global models, thus motivating an alternative approach discussed in Section 11.3.

11.3 Semi-implicit time discretization with leap frog

To overcome the time-step constraint (11.17) on the baroclinic time step, we now consider a semi-implicit time stepping scheme within the leap-frog portion of the baroclinic algorithm. As with any implicit approach, stability can be enhanced relative to explicit schemes. The price to pay is dissipation of the inertial motions. See section 2.3 of Durran (1999) for discussion.

A semi-implicit treatment of the Coriolis force, within a leap-frog scheme, leads to

$$w(\tau+\Delta\tau) - w(\tau-\Delta\tau) = -i\,\lambda\,[(1-\gamma)\,w(\tau-\Delta\tau) + \gamma\,w(\tau+\Delta\tau)] \tag{11.18}$$

where $0 \leq \gamma \leq 1$ is a dimensionless number whose value is set according to stability considerations. We can write $w(\tau+\Delta\tau) = G\,w(\tau-\Delta\tau)$, with the semi-implicit scheme yielding the amplification factor

$$G = \frac{1 - i\,\lambda\,(1-\gamma)}{1 + i\,\lambda\,\gamma}. \tag{11.19}$$

The squared modulus $|G|^2$ is used to determine conditions for stability

$$|G|^2 = \frac{[1-\gamma\,\lambda^2\,(1-\gamma)]^2 + \lambda^2}{[1+(\gamma\,\lambda)^2]^2}. \tag{11.20}$$

For $\gamma = 0$, $|G| > 1$ which leads to an unstable scheme. For $\gamma = 1/2$, $|G| = 1$ and so the scheme is neutral. With $1/2 < \gamma \leq 1$, $|G| < 1$, and so the scheme is unconditionally stable. Hence, we arrive at the stability range for the semi-implicit parameter

$$1/2 \leq \gamma \leq 1, \tag{11.21}$$

with $\gamma = 1$ yielding the most stable scheme. Section 2.3.2 of Durran (1999) details the impact on the phase and amplitude of inertial waves depending on the value of γ. That analysis shows that $\gamma = 1/2$ is the most accurate, with zero amplitude error and favorable phase errors relative to other methods.

11.4 Semi-implicit time discretization with forward step

As discussed in Section 12.8.3 of Griffies (2004) (see also page 51 of Durran (1999)), the Coriolis force with a forward time step is unstable, and so an alternative must be considered. We apply here the semi-implicit approach from Section 11.3 with a forward time step rather than the leap frog. Here, we consider

$$w(\tau + \Delta\tau) - w(\tau) = -i\,\Lambda\,[(1-\gamma)\,w(\tau) + \gamma\,w(\tau + \Delta\tau)] \tag{11.22}$$

where again $0 \leq \gamma \leq 1$ is a dimensionless number whose value is set according to stability considerations. The dimensionless parameter Λ is given by

$$\Lambda = f\,\Delta\tau. \tag{11.23}$$

Note the factor of 2 needed for the leap frog scheme (equation (11.10)) is now absent for the forward scheme. All of the analysis in Section 11.3 follows through, with the factor of 2 the only distinction.

11.5 As implemented in MOM4

Both an explicit and semi-implicit treatment of the Coriolis force in the baroclinic equations are available in MOM4 when using leap frog tendencies, with the semi-implicit treatment required when using the forward tendencies. For both cases, the semi-implicit piece is handled at the end of a baroclinic time step, even after the implicit treatment of vertical mixing. The logic used in the code can be a bit confusing, so it is useful to expose some details here.

11.5.1 Algorithm in the code

Let us separate that portion of the Coriolis force proportional to γ from the portion independent of γ in order to ease coding for the case with a fully explicit Coriolis force. We also expose the thickness and density weighting used in MOM4p1. Since velocity is updated first as the density and thickness weighted velocity, it is useful to introduce a shorthand

$$\widetilde{\mathbf{u}} \equiv (\rho\,\mathrm{d}z)\,\mathbf{u}. \tag{11.24}$$

We consider now three cases for handling the Coriolis force.

- An explicit treatment of the Coriolis force with the leap frog takes the form

$$-f\,\hat{\mathbf{z}} \wedge \widetilde{\mathbf{u}} \rightarrow -f\,\hat{\mathbf{z}} \wedge \widetilde{\mathbf{u}}(\tau), \tag{11.25}$$

- whereas a semi-implicit Coriolis force with the leap frog is

$$\begin{aligned} -f\,\hat{\mathbf{z}} \wedge \widetilde{\mathbf{u}} &\rightarrow -f\,\hat{\mathbf{z}} \wedge [(1-\gamma)\,\widetilde{\mathbf{u}}(\tau - \Delta\tau) + \gamma\,\widetilde{\mathbf{u}}(\tau + \Delta\tau)] \\ &= -f\,\hat{\mathbf{z}} \wedge \widetilde{\mathbf{u}}(\tau - \Delta\tau) - f\,\gamma\,\hat{\mathbf{z}} \wedge [\,\widetilde{\mathbf{u}}(\tau + \Delta\tau) - \widetilde{\mathbf{u}}(\tau - \Delta\tau)\,], \end{aligned} \tag{11.26}$$

- and a semi-implicit Coriolis force with a forward time step is

$$\begin{aligned} -f\,\hat{\mathbf{z}} \wedge \widetilde{\mathbf{u}} &\rightarrow -f\,\hat{\mathbf{z}} \wedge [\,(1-\gamma)\,\widetilde{\mathbf{u}}(\tau) + \gamma\,\widetilde{\mathbf{u}}(\tau+\Delta\tau)\,] \\ &= -f\,\hat{\mathbf{z}} \wedge \widetilde{\mathbf{u}}(\tau) - f\,\gamma\,\hat{\mathbf{z}} \wedge [\,\widetilde{\mathbf{u}}(\tau+\Delta\tau) - \widetilde{\mathbf{u}}(\tau)\,]. \end{aligned} \tag{11.27}$$

We now consider the remaining terms in the equations of motion. As stated earlier, when treating the Coriolis force with an implicit piece (i.e., with $\gamma > 0$), this is handled last. We write those accelerations independent of γ in the form

$$\delta_\tau\,\widetilde{\mathbf{u}}^* = \mathbf{F} \tag{11.28}$$

where $\mathbf{F}$ includes the thickness weighted and density weighted accelerations from velocity self-advection, the horizontal pressure gradient force, friction force (both explicit and implicit), as well as that piece of the Coriolis force independent of γ. If the Coriolis force is computed explicitly, then $\mathbf{F}$ is the full time tendency for the baroclinic velocity. For the semi-implicit treatment, we require those contributions proportional to γ. For the leap frog, this leads to

$$\widetilde{\mathbf{u}}(\tau+\Delta\tau) = \widetilde{\mathbf{u}}(\tau-\Delta\tau) + 2\,\Delta\tau\,\delta_\tau\widetilde{\mathbf{u}}^* - \lambda\,\gamma\,\hat{\mathbf{z}} \wedge [\,\widetilde{\mathbf{u}}(\tau+\Delta\tau) - \widetilde{\mathbf{u}}(\tau-\Delta\tau)\,] \tag{11.29}$$

where again $\lambda = 2\,f\,\Delta\tau$. Writing out the components leads to

$$\widetilde{u}(\tau+\Delta\tau) = \widetilde{u}(\tau-\Delta\tau) + 2\,\Delta\tau\,\delta_\tau\widetilde{\mathbf{u}}^* + \lambda\,\gamma\,[\,\widetilde{v}(\tau+\Delta\tau) - \widetilde{v}(\tau-\Delta\tau)\,] \tag{11.30}$$

$$\widetilde{v}(\tau+\Delta\tau) = \widetilde{v}(\tau-\Delta\tau) + 2\,\Delta\tau\,\delta_\tau\widetilde{v}^* - \lambda\,\gamma\,[\,\widetilde{u}(\tau+\Delta\tau) - \widetilde{u}(\tau-\Delta\tau)], \tag{11.31}$$

and solving for $\widetilde{\mathbf{u}}(\tau+\Delta\tau)$ renders

$$\widetilde{u}(\tau+\Delta\tau) = \widetilde{u}(\tau-\Delta\tau) + 2\,\Delta\tau\,\left(\frac{\delta_\tau\widetilde{u}^* + \lambda\,\delta_\tau\widetilde{v}^*}{1+(\lambda\,\gamma)^2}\right) \tag{11.32}$$

$$\widetilde{v}(\tau+\Delta\tau) = \widetilde{v}(\tau-\Delta\tau) + 2\,\Delta\tau\,\left(\frac{\delta_\tau\widetilde{u}^* - \lambda\,\delta_\tau\widetilde{u}^*}{1+(\lambda\,\gamma)^2}\right). \tag{11.33}$$

The forward time stepping scheme is handled analogously, which leads to the update for the two components

$$\widetilde{u}(\tau+\Delta\tau) = \widetilde{u}(\tau) + \Delta\tau\,\left(\frac{\delta_\tau\widetilde{u}^* + \Lambda\,\delta_\tau\widetilde{v}^*}{1+(\Lambda\,\gamma)^2}\right) \tag{11.34}$$

$$\widetilde{v}(\tau+\Delta\tau) = \widetilde{v}(\tau) + \Delta\tau\,\left(\frac{\delta_\tau\widetilde{u}^* - \Lambda\,\delta_\tau\widetilde{u}^*}{1+(\Lambda\,\gamma)^2}\right), \tag{11.35}$$

where again $\Lambda = f\,\Delta\tau$.

11.5.2 Namelist parameters

In the code,

$$\Delta\tau = \text{dtuv} \tag{11.36}$$

is the baroclinic time step, and

$$\gamma = \text{acor} \tag{11.37}$$

is a namelist parameter setting the level of implicit treatment for the Coriolis force. The method for discretizing the Coriolis force in the baroclinic part of the model is set according to the value of acor, with

$$\text{acor} = 0 \Rightarrow \text{explicit Coriolis: only stable for leap frog} \tag{11.38}$$

$$1/2 \leq \text{acor} \leq 1 \Rightarrow \text{semi-implicit Coriolis: required if using forward step.} \tag{11.39}$$

The vertically integrated part of the model algorithm typically uses a time step much smaller than f^{-1}. Hence, it is not necessary to discretize the Coriolis force semi-implicitly when time stepping the vertically integrated equations with a leap frog algorithm. However, when using the predictor-corrector described in Section 12.7 of Griffies (2004), $1/2 \leq \gamma \leq 1$ is required for stability, and we choose $\gamma = 1/2$.

11.5.3 Energy analysis

In the continuum, the Coriolis force does no work on a fluid parcel since it is always directed orthogonal to the flow direction

$$\mathbf{v} \cdot f\,\hat{\mathbf{z}} \wedge \mathbf{u} = 0. \tag{11.40}$$

This property is respected on the B-grid when we discretize the Coriolis force explicitly in time

$$\mathbf{v}(\tau) \cdot f\,\hat{\mathbf{z}} \wedge \mathbf{u}(\tau) = 0. \tag{11.41}$$

However, the semi-implicit treatment does not respect this property since in general the product

$$\mathbf{v}(\tau) \cdot f\,\hat{\mathbf{z}} \wedge [(1-\gamma)\,\mathbf{u}(\tau - \Delta\tau) + \gamma\,\mathbf{u}(\tau + \Delta\tau)] \tag{11.42}$$

does not vanish unless the flow is in time independent steady state.

CHAPTER
TWELV

Open boundary conditions

The purpose of this chapter is to present the method used in MOM4p1 for prescribing open boundary conditions (OBCs), with further documentation with examples presented by Herzfeld et al. (2010). If there is one point to take from this chapter, it is the following.

> The numerical schemes for OBCs are very much dependent on details of the model setup. Hence, MOM4p1 is provided with many options.

This chapter was written by Michael Herzfeld, Martin Schmidt, and Stephen Griffies. The algorithm and code developers for the MOM4p1 OBC are

`Mike.Herzfeld@csiro.au`
`Martin.Schmidt@io-warnemuende.de`
`Zhi.Liang@noaa.gov`
`Matthew.Harrison@noaa.gov`

Please email them directly for queries about the documentation or the OBC code.

12.1 Introduction

Numerical circulation models of marginal seas with biological, chemical and sediment dynamic components require a high model resolution and involve a large number of variables. Working with regional models is one method to meet this challenge with a reasonable amount of computer resource consumption. Mostly, the exchange of mass, heat, momentum and dissolved or suspended matter with the outer ocean is important. At the model boundary an open boundary condition (OBC) must apply, which permits flux out of - and into the model area.

This chapter describes the numerical schemes implemented for this purpose in MOM4p1. They are described in detail in the corresponding literature. It seems, that an universal open boundary condition suitable for all kinds of regional models does not exist. Hence, we have chosen to implement several schemes, which can be selected and modified by namelist parameters.

Open boundary conditions for a regional model is a complex problem. To be more specific, consider a large model ocean, subdivided by a virtual boundary into a western and an eastern

sub-basin. Wind forcing, heat flux or fresh water flux in the eastern subbasin drives elevation of the sea surface, currents and changes in the density field as well. The information on such events in the eastern part is transmitted to the west by waves, at large time scales also by advection. If the virtual boundary is replaced with the open western boundary of a regional submodel of the eastern subbasin, the results of the regional submodel and those of the larger model must be the same. Hence, waves generated in the eastern subbasin must be able to pass an open boundary without reflection and refraction, just as if it was not there. In the same manner, processes forced in the western subbasin influence the eastern part by waves too. If this is of importance for the eastern model part, the western open boundary condition must generate these waves.

Hence, the required boundary condition is solution of the hydrodynamic equations at the boundary itself and is basically unknown. Simplifying assumptions on the nature of the flow near the boundary are needed to close the numerical schemes at the boundary. For ocean models many different methods are known. Here we confine ourselves to methods, which combine a radiation condition, to facilitate outward directed wave propagation through open boundaries in combination with relaxation to prescribed values of ocean variables, to simulate the influences from outside the model domain. Relaxation of boundary values helps also to eliminate numerical errors of the boundary scheme and to prevent the model from divergence by the accumulation of numerical errors over longer model integration time.

12.2 Types of open boundary conditions

The purpose of this section is to describe the sorts of boundary conditions implemented in MOM4p1. For realistic applications the numerical solution near a boundary is always a superposition of outgoing and incoming waves, which cannot be separated. Applying the radiation condition and relaxation of boundary values to this complex variables, turns OBC into a mathematically ill-posed problem and there is no universally perfect scheme for open boundary conditions. Hence, often the OBC configuration must be established by trial and error on a case by case basis. So what may work fine in one application may not work if one alters the bathymetry, geography, forcing, subgrid scale parameterizations, or numerical implementation of the OBC.

12.2.1 Open boundaries in the ARAKAWA B-grid

Because MOM4p1 uses the ARAKAWA B-grid, tracers and sea level points are the outmost points, where the numerical scheme has to be closed by an open boundary condition. Velocity points are within the model domain. At points adjacent to the boundary the non-linear advective terms and diffusion terms are undefined. To close the numerical scheme for these terms, velocity points beyond the boundaries are defined by appropriate extrapolation. The remaining terms in the momentum equations can be calculated using pre-existing fields. This formulation of the open boundary conforms to a stencil originally proposed by Stevens (1990),Stevens (1991). This approach effectively limits any error introduced by the OBC to the two non-linear terms, thus preventing any error associated with the OBC from rapidly propagating into the interior via the Coriolis terms.

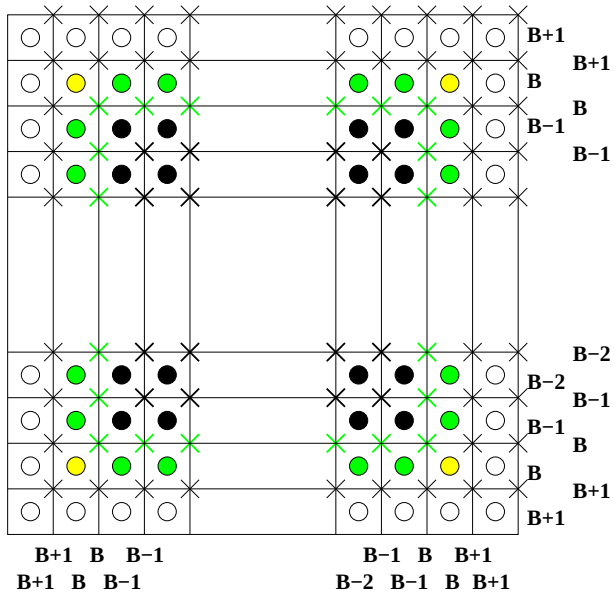

Figure 12.1: Open boundary conditions in the Arakawa B-grid. Circles mark tracer points, crosses velocity points. Open boundary conditions apply at green points.

12.2.1.1 Notation

Boundary points are marked with a capital B. The first points beyond the boundary outside the model domain is $B+1$, the first internal point in the model domain is $B-1$. See also Figure 12.1!

12.2.1.2 Boundary conditions for the sea level

The boundary conditions presented here refer to circulation models which use explicit solvers for the sea surface height where the variablity of the sea level is governed by waves. Hence, the boundary condition for the sea level is based on the wave like properties of the solution and has the form of a radiation condition for outgoing waves. Boundary conditions for the sea level apply at points marked with green circles in Figure figure:grid.

12.2.1.3 Boundary conditions for tracers

The tracer propagation is described by an advection-diffusion equation, which does not have a wave like solution itself. However, the underlying velocity field may be wave like. Hence, especially vertical tracer advection, which is not well defined near an open boundary, can be approximated by a radiation condition. The boundary condition used here combines a radiation condition, approximations for horizontal advection and relaxation towards prescribed data. Boundary conditions for the tracers apply at points marked with green circles in Figure 12.1.

12.2.1.4 Boundary conditions for velocity

Boundary conditions for velocity vectors apply at points marked with a green cross in Figure figure:grid. At these points horizontal and vertical velocity advection is set to zero. An exception is the metric term, which is well defined. Removing it implies horizontal inhomogeneity in the flow fields, which show up especially in nearly uniform flow.

To get a well defined friction operator, velocity beyond the boundary must be defined too. This is done with a no gradient condition. This condition applies at points marked with a this black cross in Figure 12.1.

For some application it may help, to take vertical advection of tracers at boundary points into consideration. A no gradient condition for the tangential velocity enhances $\pm$-structures, which are typical for the Arakawa B-grid, and couples such structures into the tracer equations. Hence, the tangential velocity at points beyond the boundary should be set to the value of the second interiour point, which prevents infiltration of $\pm$-structures from the velocity field into the tracer fields from the OBC.

12.2.2 Sommerfeld radiation condition

Most open boundary conditions are based on the Sommerfeld radiation condition (Sommerfeld, 1949). This kind of boundary condition was originally derived for the theory of electromagnetic waves to remove incoming waves from the far field solution for an oscillating dipole antenna. The Sommerfeld radiation condition takes the form:

$$\eta_{,t} = -c\,\eta_{,x} \qquad \text{at } x = x_{\mathsf{B}}. \tag{12.1}$$

In this equation, $\eta(x,t)$ is the space-time dependent free surface height, c is the wave phase speed determined via a method discussed in Section 12.3, $x = x_{\mathsf{B}}$ is the spatial position of the open boundary in question. Finally, we use the shorthand notation

$$\begin{aligned} \eta_{,t} &= \frac{\partial \eta}{\partial t} \\ \eta_{,x} &= \frac{\partial \eta}{\partial x} \end{aligned} \tag{12.2}$$

to denote partial derivatives. The performance of OBC's based on the Sommerfeld condition (12.1) has been extensively assessed in the literature (see, for example Chapman, 1985; Roed and Cooper, 1987; Tang and Grimshaw, 1996; Palma and Matano, 1998, 2001). Unfortunately, OBC's based on the Sommerfeld condition often exhibit inaccuracies. The key reason is that the model solution is a superposition of several waves which have different phase speeds and which are dispersive (in contrast to the linear electromagnetic waves that Sommerfeld was concerned). However, the Sommerfeld condition is based on just a single wave condition. The OBC behaviour in practice is thus very sensitive to how the phase speed in equation (12.1) is determined.

We can classify the boundary conditions as *passive*, in which case the OBC is determined solely from information within the computational domain, or *active*, so that data is prescribed from an external source. Since the behaviour of the model interior is rarely consistent with data prescribed at the boundary, the model may become prone to errors due to under-specification (not enough information describing external processes is provided) or over-specification (OBC information is incompatible with interior equations). Marchesiello and Shchepetkin (2001) provide a

thorough discussion of the active versus passive boundaries, and over versus under-specification of data.

To alleviate problems with over-specification, an active boundary condition may be rendered partially passive by coupling to a radiation condition. This approach was used by Blumberg and Kantha (1985). Here, relaxation towards externally prescribed data is performed with an associated relaxation timescale, so that

$$\eta_{,t} = -c\,\eta_{,x} - (\eta - \eta_o)/\tau_f. \tag{12.3}$$

Here, η_o is the prescribed data for the surface height, and τ_f is a timescale. Even with this prescription for the OBC, the behaviour of the simulation can be sensitive to the choice of radiation condition and relaxation timescale used.

Likewise a fresh water flux may be added, but its influence will most probably disappear behind the relaxation term.

12.2.3 Clamped boundary conditions

A simple boundary condition is the clamped boundary condition, i.e., sea level or tracers are kept at a fixed value. For the sea level no physical justification is given for using this condition. It is motivated solely from the fact that it keeps the numerical scheme stable. For salinity and temperature it may be a reasonable approximation. The clamped condition requires the user to supply a single time and space independent value to be imposed on the boundary. This type of condition corresponds to a zero phase speed, $c = 0$, in the Sommerfeld radiation condition (12.1). It creates many reflections at the boundary, which can be undesirable.

In a modified form time and space dependent values for the sea level or tracers may be prescribed. Keeping in mind, that most ocean flow is geostropically balanced, this defines the baroclinic and barotropic geostrophic transport through the boundary. This may be desired, but implies also the possibility of unwanted numerical effects, which may corrupt the numerical solution in the model domain.

12.2.4 No gradient boundary conditions

This condition imposes a smooth solution near the boundary. The no-gradient OBC assumes that there does not exist a gradient of a variable across the open boundary. It is sometimes referred to as a *Neumann* boundary condition. This condition corresponds to setting the phase speed to infinity in the Sommerfeld radiation condition (12.1). It is specified by setting the value at the open boundary equal to the value immediately adjacent to the open boundary in the model interior, so that

$$\eta(t+1, x_B) = \eta(t+1, x_{B-1}). \tag{12.4}$$

In this equation, $t+1$ is the updated time step, x_B signifies the spatial position of the open boundary, with $\eta(t+1, x_B)$ is the surface height at that boundary. As shown in Figure 12.1 x_{B-1} signifies the spatial position of the nearest point interior from the open boundary, with the sign determined by the relative position of the open boundary.

For velocity a no gradient boundary condition applies across the boundary, to get a defined viscosity operator

$$u(t+1, x_{B+1}) = u(t+1, x_B). \tag{12.5}$$

12.2.5 Interior cell no gradient boundary conditions

This condition is similar to the no-gradient boundary condition (12.4). However, instead of using the value at the nearest interior grid cell, the boundary is set to the value at the next nearest interior $(B-2)$ cell (i.e., two grid points away from the boundary)

$$\eta(t+1, x_B) = \eta(t+1, x_{B-2}). \tag{12.6}$$

For the tangetial velocity a no gradient boundary condition across the boundary is used to get a defined viscosity operator

$$u(t+1, x_{B+1}) = u(t+1, x_{B-1}). \tag{12.7}$$

12.2.6 Enhanced friction and diffusion near the boundary

This method increases the dissipation from tracer diffusion and momentum friction in regions near the open boundary. This approach acts to dissipate spurious reflections at the boundary. It also may be useful to remove artificial currents near the boundary, which may grow to be large in some cases. However, this approach has the detrimental effect of slowing cross boundary transport.

12.3 Implementation of sea level radiation conditions

In this section, we discuss various radiation conditions that are used to specify the phase speed. We also discuss how to specify the tracers across the open boundary.

12.3.1 Sign convention for the phase speed

The phase speed is a vector quantity. Here it is always directed perpendicularly to the model boundary and notation can simplified considerably by considering the projection of the phase speed onto the normal vector of the model boundary. The sign of the phase speed is positive for eastward or northward travelling waves and negative for westward or southward directed waves. However, the quantity of interest is the projection of the phase speed onto the boundary normal vector. In all radiation conditions given below, phase speed means this projection, which is positive for outgoing waves and negative for incoming waves.

12.3.2 Gravity wave radiation condition for the phase speed

This formulation computes a phase speed relevant for a flat bottom barotropic shallow water configuration, so that

$$c = \sqrt{g\, D_B}, \tag{12.8}$$

where g is the acceleration from gravity, and D_B is the depth at the boundary (Chapman, 1985)). Hence, in this approximation it is assumed, that processes near the boundary are always governed by outgoing waves. The OBC is implemented in an implicit form, so that

$$\eta(t+1, x_B) = \frac{\eta(t, x_B) + \mu\, \eta(t+1, x_{B-1})}{1+\mu}, \tag{12.9}$$

where

$$\mu = c\,\frac{\Delta t}{\Delta x}, \tag{12.10}$$

where Δx is the horizontal grid spacing. That is, equation (12.9) is the implicit solution to equation (12.1) using c as the gravity wave speed.

Note: phase speed is always positive for gravity wave radiation, implying that waves are always outgoing. This means that outgoing relaxation ,τ_{out}, is always used when relaxing to data (see Section 12.3.9.3).

12.3.3 Orlanski radiation condition for the phase speed

We aim to account for the most important part of the wave spectrum. There are various means for doing so, with the Orlanski radiation condition (Orlanski, 1976) one of the most common. Here, the the phase speed of disturbances approaching the boundary is diagnosed at every time-step from the distribution of the interior values of the surface height near the boundary, so that

$$\vec{c} = -\eta_{,t}/\eta_{,x}. \tag{12.11}$$

The Orlanski radiation condition theoretically has a zero reflection coefficient. This property is desired to reduce spurious reflected waves at the open boundary. Unfortunately, in practice reflections occur due to inaccuracies in the phase speed computation.

The form employed by MOM4p1 is the implicit formulation based on (Chapman, 1985)

$$\eta(t+1, x_B) = \frac{(1-\mu)\,\eta(t-1, x_B) + 2\,\mu\,\eta(t, x_{B-1})}{1+\mu}. \tag{12.12}$$

Here, the dimensionless parameter μ is set according to

$$\mu = \begin{cases} 1 & \text{if} \quad C \geq 1 \\ C & \text{if} \quad 0 < C < 1 \\ 0 & \text{if} \quad C \leq 0, \end{cases} \tag{12.13}$$

where

$$C = \frac{\eta(t-1, x_{B-1}) - \eta(t+1, x_{B-1})}{\eta(t+1, x_{B-1}) + \eta(t-1, x_{B-1}) - 2\eta(t, x_{B-2})}. \tag{12.14}$$

12.3.4 Camerlengo and O'Brien radiation condition

Camerlengo and O'Brien (1980) suggested a modified form of the Orlanski radiation condition, where only the extreme values of the phase speed, zero or h/t, so that;

$$\eta(t+1, x_B) = \begin{cases} \eta(t, x_{B-1}) & \text{if} \quad C > 0 \\ \eta(t-1, x_B) & \text{if} \quad C \leq 0, \end{cases} \tag{12.15}$$

with C given by equation (12.14).

12.3.5 Radiation condition after Miller & Thorpe

The Orlanski scheme is modified here so that time differences are evaluated using a forward scheme and space differences with an upwind scheme (see equation 15 in Miller and Thorpe, 1981)

$$\eta(t+1, x_B) = \eta(t, x_B) - \mu\left(\eta(t, x_B) - \eta(t, x_{B-1})\right). \tag{12.16}$$

In this case, the dimensionless coefficient

$$\mu = \mu_1 + \mu_2 + \mu_3, \tag{12.17}$$

with

$$\mu_1 = \frac{\eta(t+1, x_{B-1}) - \eta(t, x_{B-1})}{\eta(t, x_{B-2}) - \eta(t, x_{B-1})} \tag{12.18}$$

$$\mu_2 = \frac{\eta(t, x_B) - \eta(t-1, x_B)}{\eta(t-1, x_{B-1}) - \eta(t-1, x_B)} \tag{12.19}$$

$$\mu_3 = \frac{\eta(t, x_{B-1}) - \eta(t-1, x_{B-1})}{\eta(t-1, x_{B-2}) - \eta(t-1, x_{B-1})}. \tag{12.20}$$

The scheme is implemented in an explicit temporal form.

12.3.6 Raymond and Kuo radiation condition

This radiation condition was introduced by Raymond and Kuo (1984) and used in adaptive form by Marchesiello et al. (2001). This scheme calculates the phase velocity for multidimensional flows using a projection of each coordinate direction, i.e. not just the normal component. The scheme is implemented in implicit form. The Sommerfeld radiation condition takes the form:

$$\eta_{,t} = -c_x\,\eta_{,x} - c_y\,\eta_{,y} \tag{12.21}$$

where x and y are directions normal and tangential to the boundary respectively. The phase speeds c_x and c_y are projections given by:

$$c_x = -\eta_{,t}\frac{\eta_{,x}}{\eta_{,x}^2 + \eta_{,y}^2}, \tag{12.22}$$

$$c_y = -\eta_{,t}\frac{\eta_{,y}}{\eta_{,x}^2 + \eta_{,y}^2}. \tag{12.23}$$

This is discretised following Marchesiello et al (2001);

$$\eta(t+1, x_B, y_B) = \frac{1}{1+r_x} \left\{ \begin{array}{l} \eta(t, x_B, y_B) + r_x\eta(t+1, x_{B-1}, y_B) - r_y\left(\eta(t, x_B, y_B) - \eta(t, x_B, y_{B-1})\right)\ r_y > 0, \\ \eta(t, x_B, y_B) + r_x\eta(t+1, x_{B-1}, y_B) - r_y\left(\eta(t, x_B, y_{B+1}) - \eta(t, x_B, y_B)\right)\ r_y < 0. \end{array} \right. \tag{12.24}$$

where:

$$r_x = -\frac{\Delta\eta_t \Delta\eta_x}{\Delta\eta_x^2 + \Delta\eta_y^2}$$

$$r_y = -\frac{\Delta\eta_t \Delta\eta_y}{\Delta\eta_x^2 + \Delta\eta_y^2} \tag{12.25}$$

$$\Delta\eta_t = \eta(t+1, x_{B-1}, y_B) - \eta(t, x_{B-1}, y_B) \tag{12.26}$$

$$\Delta\eta_x = \eta(t+1, x_{B-1}, y_B) - \eta(t+1, x_{B-2}, y_B) \tag{12.27}$$

$$\Delta\eta_y = \begin{cases} \eta(t, x_{B-1}, y_B) - \eta(t, x_{B-1}, y_{B-1}) & \text{if } D > 0, \\ \eta(t, x_{B-1}, y_{B+1}) - \eta(t, x_{B-1}, y_B) & \text{if } D < 0 \end{cases}$$

$$D = \Delta\eta_t \left(\eta(t, x_{B-1}, y_{B+1}) - \eta(t+1, x_{B-1}, y_{B-1})\right) \tag{12.28}$$

The adaptive for relaxation takes on a form similar to Equation (12.3),

$$\eta_{,t} = -c_x\, \eta_{,x} - c_y\, \eta_{,y} - (\eta - \eta_o)/\tau_f. \tag{12.29}$$

where $\tau_f = \tau_{out}$ if $c_x > 0$ and $\tau_f = \tau_{in}$ with $c_x = c_y = 0$ if $c_x < 0$. The relaxation time scale $\tau_{out} \gg \tau_{in}$ such that during outward phase propagation a weak relaxation exists to avoid boundary values drifting excessively but also preventing problems of over-specification, while during inward phase propagation stronger relaxation is applied that avoids shock issues.

12.3.7 The IOW-radiation condition

As for the gravity wave radiation condition an implicite scheme is used,

$$\eta(t+1, x_B) = \frac{\eta(t, x_B) + \mu\, \eta(t+1, x_{B-1})}{1+\mu}, \tag{12.30}$$

where

$$\mu = C\, \frac{\Delta t}{\Delta x}. \tag{12.31}$$

The spatial and time derivative of η are

$$\Delta\eta_{,x} = \frac{\eta(t+1, x_{B-1}) - \eta(t+1, x_{B-2})}{\Delta x}, \tag{12.32}$$

$$\Delta\eta_{,t} = \frac{\eta(t_s, x_{B-1}) - \eta(t+1, x_{B-1})}{\Delta t}. \tag{12.33}$$

If the predictor-corrector scheme is used, the phase speed is calculated twice. In this case $\eta(t_s)$ denotes η at the starting time step of this scheme. In the predictor step Δt is the reduced time step $\Delta t = \gamma dt$. For the leapfrog scheme $t_s = t - 1$ and $\Delta t = 2dt$.

To ensure a well defined phase speed for small horizontal gradients this case is treated separately,

$$C(t+1) = \begin{cases} C^*(t+1) & \text{if} \quad \Delta\eta^x > a, \\ 0.99\, \widetilde{C}(t) & \text{if} \quad \Delta\eta^x \leq a, \end{cases} \tag{12.34}$$

where $\Delta\eta^x = |\eta(t+1, x_{B-1}) - \eta(t+1, x_{B-2})|$ and a is a small length, typically 10^{-8} m. $\widetilde{C}$ is the time smoothed phase speed from the previous time step. The scheme allows to control the minium and

maximum value of the phase speed. For incoming waves, negative phase speed, positive values (or zero) are assumed,

$$C^*(t+1) = \begin{cases} C_{inc} & \text{if} \quad C^+ < 0, \\ C_{min} & \text{if} \quad C^+ < C_{min}, \\ C^+ & \text{if} \quad C_{max} > C^+ > C_{min}, \\ C_{max} & \text{if} \quad C^+ > C_{max}. \end{cases} \tag{12.35}$$

$C^+(t+1)$ is calculated from the derivatives of η,

$$C^+(t+1) = \frac{\Delta\eta_{,t}}{\Delta\eta_{,x}}. \tag{12.36}$$

C_{max}, C_{min} and C_{inc} are defined in terms of the gravity wave speed,

$$C_{max} = c_{max}\sqrt{g\,D_B} \tag{12.37}$$

$$C_{min} = c_{min}\sqrt{g\,D_B} \tag{12.38}$$

$$C_{inc} = c_{inc}\sqrt{g\,D_B}. \tag{12.39}$$

The factors c_{max}, c_{min} and c_{inc} can be modified via the namelist.

Relaxation is done as described in Section 12.3.9.

12.3.8 Phase speed smoothing

The diagnosed phase speed may be very noisy with altering sign every time step. A time smoother

$$\widetilde{C}(t+1) = F\,\widetilde{C}(t) + (1-F)\,C(t+1), \tag{12.40}$$

helps to reduce numerical noise. The default value is $F = 0.7$. The application of the smoother requires to save $\widetilde{C}$ in a restart file, to ensure reproducibility across model restarts.

12.3.9 Relaxation to data

12.3.9.1 Relaxation towards prescribed profiles

The radiation conditions may be coupled to prescribed data as described by Equation (12.3). This approach is implemented implicitly as

$$\eta(t+1, x_B) = \frac{\widetilde{\eta}(t+1, x_B) + \eta_o \frac{\Delta t}{\tau_f}}{1 + \frac{\Delta t}{\tau_f}}, \tag{12.41}$$

where $\widetilde{\eta}(t+1, x_B)$ is the solution on the boundary derived from the radiation conditions. τ_f is the time scale for the relaxation process.

The relaxation may occur a given number of cells into the interior, in which case $\widetilde{\eta}(t+\Delta t, x_B)$ is the interior solution to the continuity equation.

12.3.9.2 Relaxation of the sea level average - conservation of geostrophic currents

If the model area is a semi-enclosed sea, which is connected to the ocean by a narrow channel, the open boundary may be placed within this channel. By prescribing the sea level profile across the channel, one defines also the geostrophic volume transport through this channel. In this case the incertitude of the OBC may dominate the volume budget of the model. To overcome this serious shortcoming, an alternative relaxation scheme may be used, which prescribes only the average sea level at the boundary. Doing so, the geostropic transport defined by the cross channel sea level gradient is not affected by the relaxation. Only the ageostropic flow may react to the prescribed sea level variation, geostrophic adjustment happens through the internal model dynamics. The scheme works explicitly,

$$\eta(t+1, x_B) = \widetilde{\eta}(t+1, x_B) + \frac{\Delta t}{\tau_f}\left(\eta_o - \langle\widetilde{\eta}(t+1, x_B)\rangle\right) \tag{12.42}$$

$\langle\widetilde{\eta}(t+1, x_B)\rangle$ is sea level averaged over the boundary.

12.3.9.3 Variable relaxation for incoming and outgoing waves

Likewise, the value of τ_f may be different for prevailing incoming or outgoing waves,

$$\tau_f^{-1} = r\,\tau_{out}^{-1} + (1-r)\,\tau_{in}^{-1}, \tag{12.43}$$

$$r(t) = \frac{\widetilde{C}(t)}{C_{max}}. \tag{12.44}$$

12.4 OBC for tracers

12.4.1 Reduced tracer equations at open boundaries

The tracer equations in MOM4p1 are strongly linked with the sea level equation and tracers and sea level are treated consistently. Because the radiation condition for the sea level is a rough approximation, a similar consistency cannot be achieved for boundary points. Hence, the tracer equations at the boundaries are simplified.

To avoid double coding, the normal code should be used at boundaries as far as possible. Tracers are updated as

$$T(t+1)\rho(t+1)h(t+1) = T(t)\rho(t)h(t) + \Delta t\delta(h(t)\rho(t)T(t)) \tag{12.45}$$

The time tendency of the vertically integrated tracer in the grid cell $\delta(\rho T)$ is the combined time tendency of tracer concentration, density and cell thickness. It consists of an advective and diffusive contribution and eventually of source terms from radiation and special convective schemes (kpp). We rewrite these terms in such a manner, that for a constant tracer the sea level equation is retained. Especially for a uniform tracer $T = 1$, $\delta(h\rho T)$ must be the time tendency of the cell thickness, $\delta(h\rho)$, i.e. $\delta(h\rho 1) \rightarrow \delta(h\rho) = \frac{\Delta h\rho}{\Delta t}$.

$$\begin{aligned}
\delta(h\rho T)_k &= -(\nabla_s \cdot h\rho(\mathbf{u}T + \mathbf{F}))_k - (\rho(wT + F^{(s)}))_{k-1} + (\rho(wT + F^{(s)}))_k + (h\rho S^T)_k \\
\delta(h\rho)_k &= -(\nabla_s \cdot h\rho\mathbf{u})_k - (\rho w)_{k-1} + (\rho w)_k + (h\rho S^M)_k
\end{aligned} \tag{12.46}$$

Advection is rewritten to separate the different contributions to the time tendency,

$$\begin{aligned} Adv(T)_k &= -(\nabla_s \cdot h\rho\mathbf{u}T)_k - (\rho wT)_{k-1} + (\rho wT)_k \\ &= -(T\nabla_s \cdot h\rho\mathbf{u})_k - (\rho wT)_{k-1} + (\rho wT)_k - (h\rho\mathbf{u} \cdot \nabla_s T)_k. \end{aligned} \tag{12.47}$$

Applying approximations for open boundaries, the first three terms have to be kept consistent with the equation for the level thickness. The level thickness is calculated from approximations only and it is appropriate to express the convergence of the flow in terms of the level thickness time tendency. With of

$$-(\nabla_s \cdot h\rho\mathbf{u})_k = \delta(h\rho)_k + (\rho w)_{k-1} - (\rho w)_k - (h\rho S^M)_k \tag{12.48}$$

this renders to

$$\begin{aligned} \delta(h\rho T)_k &= \delta(h\rho)_k T_k + (h\rho(S^T - S^M T))_k + SGS \\ &\quad -(h\rho\mathbf{u} \cdot \nabla_s T)_k - (\rho wT)_{k-1} + (\rho wT)_k + ((\rho w)_{k-1} - (\rho w)_k)T_k. \end{aligned} \tag{12.49}$$

i.e., which ensures consistency between tracers and layer thickness for a uniform tracer. Also the approximation of zero vertical advection and horizontal advection with an upwind scheme is consistent with the thickness equation for cells of constant thickness. Diffusion and source terms apply unchanged and will not be specified here.

For surface cells the vertical advection at the surface is expressed in terms of sea level variation, fresh water flux and turbulent tracer flux,

$$\begin{aligned} \delta(h\rho T)_1 &= (\delta(h\rho)_1 T_1 + \rho_w q_w (T_w - T_1) + (h\rho(S^T - S^M T))_1 - Q_T^{turb} + SGS \\ &\quad -(h\rho\mathbf{u} \cdot \nabla_s T)_1 + (\rho wT)_1 - (\rho w)_1 T_1. \end{aligned} \tag{12.50}$$

With this approximation the tracer concentration remains unchanged, if only the sea surface height is undulating. If currents are zero, but fresh water flux and diffusion are present, a horizontally uniform tracer distribution will not be disturbed near an open boundary. The consistency between sea level equation and tracer equation is not broken, if approximations for the horizontal advection term are made, or if radiation terms are added. Those terms vanish for horizontally uniform tracers especially for $T = 1$ and the sea level time tendency is trivially retained.

Because vertical velocity is not well defined it is left out of consideration. It is replaced by a radiation term, which accounts for the propagation of wave like undulations of internal interfaces from baroclinic waves.

$$\begin{aligned} \delta(h\rho T)_k &= \delta(h\rho)_k T_k + (h\rho(S^T - S^M T))_k + SGS \\ &\quad -(h\rho\mathbf{u} \cdot \nabla_s T)_k + c\rho h \frac{\partial T_k}{\partial x} + \rho h \frac{T^{ref} - T_k}{\tau_f} \end{aligned} \tag{12.51}$$

$$\begin{aligned} \delta(h\rho T)_1 &\approx (\delta(h\rho)_1 T_1 + \rho_w q_w (T_w - T_1) + (h\rho(S^T - S^M T))_1 - Q_T^{turb} + SGS \\ &\quad -(h\rho\mathbf{u} \cdot \nabla_s T)_1 + c\rho h \frac{\partial T_1}{\partial x} + \rho h \frac{T^{ref} - T_1}{\tau_f}. \end{aligned} \tag{12.52}$$

Implementation of the radiation condition and of the relaxation towards prescribed data is documented below. Diagnostics of the phase speed is based on the tracer concentration, because the total tracer contend may undulate rapidly from the barotropic mode in the cell thickness variability.

12.4.2 Upstream advection of tracers near the boundary

For advection across the open boundary, an upstream scheme with

$$T(x_{B+1}) = T(x_B) \tag{12.53}$$

means that the incoming tracer has the same concentration as the tracer at the boundary point. This approximation may give poor results for long model runs and can cause model drifts.

After running a *passive* boundary over a long period, the tracer near the boundary will be determined completely by processes in the model domain. As an example consider a marginal sea with a strong fresh water surplus. There will be an estuarine circulation with a more or less permanent outflow of brackish water in a surface layer and inflow near the bottom. However, the salinity of the inflowing water will be reduced as well after some time by vertical mixing processes. The model results will suffer from underestimated stratification. To overcome this problem, information on the tracer concentration in the adjacent sea must be provided for the model. The simple approximation

$$T(x_{B+1}) = T(x_0) \tag{12.54}$$

where T_0 may stem from a database, improves the performance of the diffusion and the advection operators, which in turn may invoke wave like processes spreading from the boundary into the model. Using an upstream formulation for the tracer gradient in the advective term, this can switch on an inflow through the open boundary. However, waves of a small amplitude but with a high phase speed may disturb this scheme. Thus, the tracer source term $\mathcal{S}_T$ can be used for a controlled restoring to prescribed boundary values. The upstream advection condition is discretized as:

$$\begin{aligned} T(t+1, x_B) &= T(t, x_B) \\ &\quad + \frac{\Delta t}{\Delta x}\left[(u_n - |u_n|)\left(T(t, x_{B-1}) - T(t, x_B)\right) + (u_n + |u_n|)\left(T(t, x_B) - T(t, x_0)\right)\right] \end{aligned} \tag{12.55}$$

where u_n is the velocity normal to the boundary times density and the cell height, $T(x_B)$ is the tracer on the boundary, $T(x_{B-1})$ is the tracer one cell into the interior and $T(x_0)$ is a tracer value that must be supplied externally.

12.4.3 Relaxation towards external data

If external data are prescribed boundary values may be relaxed towards there data as

$$T(t+1, x_B) = \left(T_0 - T(t, x_B)\right)\frac{\Delta t}{\tau_f}. \tag{12.56}$$

The relaxation time τ_f depends on the flow direction near the boundary. If the sum of advection velocity and phase speed at the boundary is directed inwards, one has $\tau_f = \tau_f^{in}$ and $\tau_f = \tau_f^{out}$ otherwise. τ_f^{in} and τ_f^{out} can be specified in the namelist for each tracer and boundary separately.

12.4.4 Flow relaxation scheme of Martinsen and Engedahl

The flow relaxation scheme of Martinsen and Engedahl (1987) has been included to relax boundary data to interior data. This is accomplished over a region NN cells wide (typically NN=10) where the tracer variables are updated according to:

$$T = \alpha_i T_B + (1 - \alpha_i) T_{B\pm i} \tag{12.57}$$

where T_B is the boundary specified value, $T_{B\pm i}$ are the interior variable values and α_i is a relaxation parameter given by:

$$\alpha_i T_B = 1 - \tanh \frac{i-1}{2} \quad i = 1, 2, ..NN \tag{12.58}$$

Note that the flow relaxation scheme is used in conjunction with another boundary condition and T_B may be obtained from the `FILEIN` or `NOGRAD` condition; whatever is specified on the boundary is relaxed to the model integrated values over NN cells. The flow relaxation scheme is only implemented if `UPSTRM` is included in the tracer obc. If T_B is equal to zero (clamped boundary condition) then this flow relaxation scheme acts as a sponge type condition. An example of the flow relaxation scheme implementation in the namelist is given below:

```
obc_flow_relax(:,1) = 10, 1, 1
obc_flow_relax(:,2) = 10, 1, 1
```

12.4.5 Radiation conditions

If the velocity field near the boundary is wave like, vertical advection may result in a wave like tracer motion. Hence, a radiation condition may improve the numerical scheme at the boundary.

The radiation condition for tracers is applied implicitly,

$$T(t+1, x_B) = \frac{T(t, x_B) + \mu\, T(t+1, x_{B-1})}{1+\mu}, \tag{12.59}$$

where

$$\mu = C\,\frac{\Delta t}{\Delta x}. \tag{12.60}$$

The phase speed C is set to zero for incoming waves and is limited by C_{max},

$$\mu = \begin{cases} 0 & \text{if} \quad C^* < 0, \\ C^* & \text{if} \quad 0 < C^* < C_{max}, \\ C_{max} & \text{if} \quad C^* > C_{max}. \end{cases} \tag{12.61}$$

C^* is calculated either bei the Orlanski scheme,

$$C^* = \frac{\Delta x}{\Delta t} \frac{T(t-1, x_{B-1}) - T(t+1, x_{B-1})}{T(t+1, x_{B-1}) + T(t-1, x_{B-1}) - 2T(t, x_{B-2})}, \tag{12.62}$$

or by used in MOM-31 (IOW).

$$C^* = \frac{\Delta x}{\Delta t} \frac{T(t-1, x_{B-1}) - T(t+1, x_{B-1})}{T(t, x_{B-1}) - T(t, x_{B-2})}. \tag{12.63}$$

For the time staggered scheme the index $t-1$ points to the same filed as t. The maximum phase speed, C_{max}, is given by the CFL-criterion,

$$C_{max} = \frac{\Delta x}{\Delta t}. \tag{12.64}$$

12.4.6 Vertical mixing and viscosity co-efficients

Vertical mixing at boundary points my be enabled or diabled. However, the mixing co-efficients at these points are used to define viscosity at adjacent velocity points. The namelist parameter `obc_mix` specifies, how the mixing coefficient at boundary points is defined. Options are `NOTHIN`, `NOGRAD`, `INGRAD` and `CLAMPD`, `obc_mix=NOGRAD` is the default.

12.4.7 Enhanced horizontal mixing and viscosity co-efficients

To damp unwanted numerically generated flow patterns near open boundaries viscosity and diffusivity may be enhanced within a stripe near the boundary.

12.5 The namelist obc_nml

MOM4p1 requires that two components of velocity be prescribed on each open boundary (normal and tangential velocities to the boundary) for both the 3D and 2D modes. Surface elevation and the values of any tracers present are also required. Here are the flags that specify the various fields:

- Normal velocity: `obc_nor`
- Tangential velocity: `obc_tan`
- Sea level elevation: `obc_eta`
- Tracers: `obc_tra(:)`.

The OBC specification is determined via text strings as listed in Table 12.1, where the variables these conditions may be applied to are listed as `un` = normal velocity, `ut` = tangential velocity, η = surface elevation, and `T` = tracers. The condition specified for velocities is used for both the 2D and 3D modes. Note that the text identifier strings have have been truncated to the same length while attempting to describe the OBC condition to accommodate neat alignment in the namelist.

An example of open boundary specification for a domain containing three open boundaries and two tracers is given below:

```
nobc = 3
direction  ='west',   'south', 'north'
is = 2,  2,  2
ie = 2,  10,  10
js = 2,  2,  20
je = 20,  2,  20
obc_nor ='NOGRAD',    'NOGRAD',   'NOGRAD'
```

CONDITION NAME	TEXT IDENTIFIER	APPLICABLE VARIABLES
Relaxation to data	FILEIN	η, T
Relaxation of mean	MEANIN	η
Clamped	CLAMPD	u_n, u_t, η
No-gradient	NOGRAD	u_n, u_t, η, T
Interior-gradient	INGRAD	u_n, u_t
Linear extrapolation	LINEAR	u_n, u_t
Gravity wave radiation	GRAVTY	η
Orlanski	ORLANS	η, T
Camerlengo and O-Brien	CAMOBR	η
Miller and Thorpe	MILLER	η
Raymond and Kuo	RAYMND	η
Schmidt	MARTIN	η, T
Upstream advection	UPSTRM	T

Table 12.1: Namelist settings for the OBC specification.

```
obc_tan ='INGRAD',    'INGRAD',   'INGRAD'
obc_eta ='GRAVTY',    'FILEIN',   'MEANIN|ORLANS'
obc_tra(:,1) ='UPSTRM|FILEIN', 'UPSTRM|FILEIN','UPSTRM|FILEIN'
obc_tra(:,1) ='NOGRAD', 'NOGRAD','UPSTRM|NOGRAD'
```

Note that by 'or-ing' two conditions together then these two conditions will be invoked sequentially (order is not important). Hence the condition `UPSTRM|FILEIN` will invoke an upstream advection condition, using data from file when flow is into the domain. The condition `UPSTRM|NOGRAD` will invoke an upstream advection condition, using the value one cell into the domain when flow is into the domain. A wave-like contribution to the OBC can also be added for tracers, e.g. invoked by `UPSTRM|FILEIN|ORLANS`. This wave-like contribution is added implicitly.

If partially passive conditions are to be used for elevation, then the FILEIN or MEANIN condition is 'or-ed' with the desired radiation condition, e.g. using the Orlanski partially passive condition with data prescribed from file use `FILEIN|ORLANS`. Note that in-going and out-coming relaxation timescales are also required to be prescribed for these partially passive conditions.

Some compilers do not like the colon (:) syntax in field specifications. In this case each element must be specified separately.

12.6 Topography generation - Preparation of boundary data

12.6.1 Topography generation with open boundaries

Open boundary conditions require modifications of the topography near the boundary. Gradients of the depth normal to the boundary should be zero to avoid large vertical velocity in the boundary area. Because vertical velocity usually is set to zero at boundary points, this approximation is less serious, if vertical velocity is zero anyway.

The grid and topography generator *ocean_grid_generator* closes all model boundaries, if the model is neither cyclic or global. This has to be modified for open boundaries. Hence, open

boundaries need to be specified in this early stage of model preparation. This ensures, that initial fields and boundary values, which may use the information in the grid specification file *grid_spec.nc*, are fully consistent with the topography used during model run time. For this purpose, the ocean grid generator *ocean_grid_generator* is able to read those parts of the namelist *obc_nml*, which define the open boundaries geographically. Here is an example:

```
\&obc_nml
  nobc                = 3
  direction           = 'north', 'south', 'west',
  is                  =       2,       2,     2,
  ie                  =      39,      63,     2,
  js                  =      74,       2,     2,
  je                  =      74,       2,    74,
  name                = 'northern', 'southern', 'western'
```

It is not recommended, to define the boundary conditions at outmost model points.

12.6.2 Preparation of input data files

Having the *grid_spec.nc* file ready, one may proceed with preparing obc input data files. The grid of input data files should match exactly the size of the open boundary. However, it is also possible, that the grid of the input files may cover a larger area. In this case, those start and end index of the model grid, which matches the first and the last index in the input file, must be specified in the namelist *obc_nml* (but not for *ocean_grid_generator*). The default is, that the input data files match the size of the boundary exactly. In the example below, the input files for sea level and tracers have the same size as the model itself, 75×65. They may be either preprocessed as decribed below, or used directly with help of namelist specifications:

```
\&obc_nml
  nobc                = 3
  direction           = 'north', 'south', 'west',
  is                  =       2,       2,     2,
  ie                  =      39,      63,     2,
  js                  =      74,       2,     2,
  je                  =      74,       2,    74,
  name                = 'northern', 'southern', 'western'
  iers                  =     1,       1,     2,
  iere                  =    65,      65,     2,
  jers                  =     2,       2,     1,
  jere                  =     2,       2,    75,
  itrs                  =     1,       1,     2,
  itre                  =    65,      65,     2,
  jtrs                  =    74,       2,     1,
  jtre                  =    74,       2,    75,
```

It is supposed, that some data suitable for OBC are ready in netcdf-format. There are many tools to process such files, here *ferret* is used. Alternatives may be *grads* and possibly *matlab* in

combination with the *netcdf toolbox*. *Ferret* is available from `http://ferret.wrc.noaa.gov/Ferret`. It is recommended to use *Ferret 6* or a later version, because previous versious do not permit full access to all netcdf attributes. However, as long as the file are not to large, some fine tuning in the file structure could also be done with a combination of the programs *ncdump*, a good editor, which can handle large files and *ncgen*. *ncdump* and *ncgen* come with the netcdf library. Also the *nco-tools* are of great help.

Examples for *ferret* scripts are given below. For details of the syntax visit `http://ferret.wrc.noaa.gov/Ferret`.

The following directory structure is assumed:

```
preprocessing/grid_spec.nc
preprocessing/OBCDATA
preprocessing/OBCDATA/1999/your_input.dta.nc
preprocessing/OBCDATA/2000/your_input.dta.nc
...
```

The working directory is for example

```
preprocessing/OBC/2000/
```

Then the following ferret commands should sufficient to generate the input file for the sea level at a northern boundary at j=74:

```
SET MEMORY/SIZE=30
use "../../grid_spec.nc"
use "../OBCDATA/2000/your_input.dta.nc"
! the input file has units "cm", mom4 needs "m"
let/units=m/title=eta_t eta_t = eta[d=3,gx=wet[d=1,j=74]]/100
can axis/modulo ‘eta_t,return=xaxis‘
! add a calendar
SET AXIS/CALENDAR=JULIAN ‘eta_t,return=taxis‘
save/clobber/file=obc_trop_north.dta.nc/2:39 eta_t
```

It may happen, that the model landmask differs from the land mask in the input data. In this case one may have land information from the input file at ocean points in the OBC input file, which would let the model crash. In this case ferret functions could be used to fill these values with ocean data. Suitable tools are the *@fnr* transformation or the new external function *fill_xy* which is in the latest *Ferret 6* release.

For depth dependent data as temperature and salinity more care is needed to avoid gaps in the input data near the bottom. Most likely, topography representation in the model differes from topography representation in the input data. So two things or needed, to organise the input data

- a mask, to define ocean points in your model
- an input data set, which covers all model ocean points with ocean data.

The mask can be derived from the *grid_spec.nc* file:

```
SET MEMORY/SIZE=30
use "../../grid_spec.nc"
let mask_t=if k[gz=zb] le NUM_LEVELS then 1 else (-1)/0
save/clobber/file=tempfile.nc mask_t
```

For velocity data *NUM_LEVELS_C* can be used in the same manner.

Extrapolation into the bottom should be mostly sufficient, to extend the input data, so that all model ocean points are covered with input ocean data later:

```
use "../OBCDATA/2000/your_input.dta.nc"
let temp_n = temp[k=@fnr:5]            ! 5 should sufficient
let salt_n = salinity[k=@fnr:5]
save/append/file=tempfile.nc temp_n, salt_n
```

The names of variables in the input file may be different. Saving into a temporary file is not needed in any case, but it helps to avoid problems from ambiguous indecees in variables with different coordinate definitions.

Now use *tempfile.nc* as new input file:

```
can data/all
can/var/all
!_____________________________________________________________________
SET MEMORY/SIZE=55
use tempfile.nc
let/unit=Celsius/title=temperature temp = temp_n[g=mask_t]*mask_t[j=74]
let/unit=PSU/title=salinity        salt =  salt_n[g=mask_t]*mask_t[j=74]
save/clobber/file=obc_clin_north.dta.nc/2:39 temp, salt
```

Multiplying with the mask ensures, that only model ocean points contain tracer information. The grid information is implicitely in *mask_t*. Do not specify the range of the grid index for writing *tempfile.nc*. This may disturb the horizontal interpolation.

12.6.3 Consistency of input data and model configuration

12.6.3.1 The sea level in external data and the model zero level

The models zero motion sea level is the average of the initial sea level. This value needs to be consistent with boundary sea level data. If boundary and initial data come from a larger model, this should be the trivially the case. Otherwise some adjustment is needed, because because even small artificial gradients between boundaries and the model interiour may drive large currents, which would rapidly corrupt the initial stratification. This requires an initial run, with advection of tracers switched off. This can be done with the options *zero_tracer_advect_horz* and *zero_tracer_advect_vert* enabled in *ocean_tracer_advect_nml*. The resulting model sea level should be a reasonable choice for model initialisation. Eventually the procedure could be repeated.

12.6.3.2 The sea level and the problem of air pressure

Air pressure gradients are part of geostrophic balance of current systems. If the air pressure gradients vary only slowly, a corresponding negative sea level gradient develops, which may compensate its influence, so that the currents calculated with and without air pressure are approximately the same. This is the reason, why air pressure is often ommited in circulation models.

The sea level however may differ considerably in both cases. This has to be taken into account, if sea level data are prescribed at open boundaries. MOM-4 permits the input of sea level air pressure, which is added to the sea level elevation. Hence, after geostrophic adjustment air pressure gradients and sea level gradients partially balance each other.

CHAPTER
THIRTEEN

Tidal forcing from the moon and sun

The purpose of this chapter is to describe the formulation of lunar and solar tidal forcing implemented in MOM4. This chapter was written by Harper Simmons (hsimmons@iarc.uaf.edu) with some additions and edits by Stephen.Griffies@noaa.gov.

13.1 Tidal consituents and tidal forcing

As formulated by Marchuk and Kagan (1989), tidal forcing appears in the momentum equations as a depth independent acceleration. Consequently, tide dynamics can be isolated in the vertically integrated momentum budget. As shown in Section 7.7.3, the equation for the vertically integrated transport $\mathbf{U}$ in a Boussinesq version of MOM4p1 takes the form (equation (7.131))

$$\rho_o \left(\partial_t + f\,\hat{\mathbf{z}}\wedge\right) \sum(\mathrm{d}z\,\mathbf{u}) = \mathbf{G} - (H+\eta)\,\nabla\left(p_{\mathrm{a}} + p_{\mathrm{surf}}\right). \tag{13.1}$$

In this equation, $\mathbf{G}$ is the vertically integrated forcing arising from baroclinic effects, p_s is the pressure associated with undulations of the surface height, p_a is the applied pressure from the atmosphere and sea ice, H is the depth of the ocean, and η is the surface height deviation from a resting state with $z = 0$. Our goal is to modify this equation to account for gravitational forcing that give rise to ocean tides.

Tidal forcing arising from the eight primary constituents (M2, S2, N2, K2, K1, O1, P1, Q1) (see Gill (1982)) can be added to the forcing for $\mathbf{U}$ in MOM4p1. The formulation follows Marchuk and Kagan (1989), by considering a tide generating potential ($g\eta_{\mathrm{eq}}$) with corrections due to both the earth tide ($1+k-h$) and self-attraction and loading (α). In this approach, the depth independent pressure gradient acceleration is modified to the form

$$\rho_o^{-1}\,\nabla\left(p_s + p_a\right) \rightarrow \rho_o^{-1}\,\nabla(p_s + p_a) + g\,\nabla\left[(1-\alpha)\eta - (1+k-h)\eta_{\mathrm{eq}}\right]. \tag{13.2}$$

The term η_{eq} is known as the *equilibrium tide*, and it arises from the astronomically derived gravity producing forces. It is modified by several factors. The Love numbers, k and h, named for the physicist A.L. Love, account for the reduction of the ocean tide because of the deformation of the solid earth by tidal forces. The Love numbers are frequency dependent, with $1+k-h$ generally close to 0.7 (Wahr (1998)).

The term α in equation (13.2) accounts for a modification of the ocean's tidal response as a result of self-attraction and loading (SAL) (Hendershott (1972)). Self attraction is the modification of the tidal potential as a result of the redistribution of the earth and ocean due to the equilibrium tidal forcing. Loading refers to the depression of the earth's crust by the mounding of tides. Calculation of the SAL term requires an extremely cumbersome integration over the earth surface, rendering equation (13.2) an integro-differential equation (Ray (1998)).

Instead of solving the integro-differential form of equation (13.2), MOM4 uses the scalar approximation to SAL. We feel this is justified since our purpose in introducing tidal forcing is to study the *effects* of tides on the general circulation, not the details of the tides themselves. The conjecture is that precise calculation of the SAL term is not needed for to understand tidal effects on the general circulation. For the scalar approximation, α is usually set between $0.940 - 0.953$. MOM4 uses $\alpha = 0.948$. Limitations of the scalar approximation to SAL are discussed by Ray (1998), who concluded that the scalar approximation introduces phase errors of up to 30° and amplitude errors of 10% into a global scale tidal simulation.

13.2 Formulation in nonBoussinesq models

The horizontal acceleration from pressure gradients is given by the two terms (see Section 7.7.4, where we drop here the tilde notation used in that section)

$$\rho^{-1}\,(\nabla_z\, p)_{\text{without tidal forcing}} = \rho^{-1}\,\nabla_s\, p + \nabla_s\,\Phi. \tag{13.3}$$

In this equation, p is the hydrostatic pressure at a grid point, Φ is the geopotential at this point, and s is the generalized vertical coordinate. The ρ^{-1} factor is set to ρ_o^{-1} for Boussinesq models, but remains nontrivial for nonBoussinesq, pressure-based vertical coordinates in MOM4p1. As noted in Section 13.1, gravitational forces giving rise to ocean tides can be incorporated into MOM4p1 by adding a depth independent acceleration throughout the water column. Following the approach used for the Boussinesq case, we add to the nonBoussinesq pressure gradient a modification to the geopotential due to tidal acceleration

$$\rho^{-1}\,(\nabla_z\, p)_{\text{with tidal forcing}} = \rho^{-1}\,\nabla_s\, p + \nabla_s\,\Phi + g\,\nabla\left[(1-\alpha)\eta - (1+k-h)\eta_{\text{eq}}\right], \tag{13.4}$$

where the tidal term is taken from equation (13.2). Inserting this modified acceleration into the vertically integrated momentum equation (7.139) yields

$$(\partial_t + f\,\hat{\mathbf{z}}\wedge)\,\sum(\mathrm{d}z\,\rho\,\mathbf{u}) = \mathbf{G} - \frac{p_{\text{b}} - p_{\text{a}}}{g\,\rho_o}\,\nabla\,(p_{\text{b}} + \rho_o\,\Phi_{\text{b}} + g\,\rho_o\,h_{\text{tide}}), \tag{13.5}$$

where

$$h_{\text{tide}} = (1-\alpha)\eta - (1+k-h)\eta_{\text{eq}} \tag{13.6}$$

is shorthand for the tidal term, p_{b} is the pressure at the ocean bottom, and $\Phi_{\text{b}} = -g\,H$ is the geopotential at the bottom.

13.3 Implementation in MOM4

The equilibrium tide is written for the nth diurnal tidal constituent as

$$\eta_{eq,n} = H_n \sin 2\phi \cos(\omega_n t + \lambda), \tag{13.7}$$

constit	name	origin	ω (1/day)	$1+k-h$	a (m)
1	K_1	Luni-solar declinational	0.7292117	0.736	0.141565
2	O_1	Principal lunar declinational	0.6759774	0.695	0.100661
3	P_1	Principal solar declinational	0.7252295	0.706	0.046848
4	Q_1	Larger lunar elliptic	0.6495854	0.695	0.019273
5	M_2	Principal lunar	1.405189	0.693	0.242334
6	S_2	Principal solar	1.454441	0.693	0.112743
7	N_2	Largerl lunar elliptic	1.378797	0.693	0.046397
8	K_2	Luni-solar declinational	1.458423	0.693	0.030684

Table 13.1: Frequencies, Love numbers, and amplitude functions for the eight principle constituents of tidal forcing available in MOM4.

and for the nth semi-diurnal constituent as

$$\eta_{eq,n} = H_n \cos^2\phi \cos(\omega_n t + 2\lambda), \tag{13.8}$$

where ϕ is latitude and λ is longitude. Recognizing that equations (13.7) and (13.8) require the evaluation of trigonometric functions at every grid point and every time-step, tidal forcing is introduced into MOM4 in the following mathematically equivalent form. Making use of the identity

$$\cos(A+B) = \cos(A)\ \cos(B) - \sin(A)\ \sin(B), \tag{13.9}$$

we can write the eight tidal forcing constituents as

$$\begin{aligned}\eta_{\mathrm{eq}} = \Sigma_{n=1}^{4} \Big[\beta_n \quad a_n \quad \cos^2\phi\,[\cos(\omega_n \quad t)\cos 2\lambda - \sin(\omega_n \quad t)\sin 2\lambda] + \\ \beta_{n+4} a_{n+4} \sin 2\phi\,[\cos(\omega_{n+4} t)\cos 2\lambda - \sin(\omega_{n+4} t)\sin 2\lambda]\ \Big],\end{aligned} \tag{13.10}$$

which allows all the trigonometric functions of ϕ and λ to be precomputed. Note that we have written $\beta_n = 1 + k_n - h_n$. The frequencies (ω_n), amplitudes (a_n) and Love numbers are listed in Table 13.1.

PART III
Subgrid scale parameterizations

The purpose of this part of the manual is to describe certain of the subgrid scale (SGS) parameterizations used in MOM4p1. This discussion is by no means complete.

CHAPTER
FOURTEEN

Mixing related to tidal energy dissipation

The purpose of this chapter is to summarize the MOM4 implementation of the dianeutral parameterization of Simmons et al. (2004) and Lee et al. (2006). Both schemes are available in MOM4p1. These schemes provide a physically based replacement for the vertical tracer diffusivity of Bryan and Lewis (1979).

Throughout this chapter, we assume that the mixing of interest occurs with a unit Prandtl number[1], thus enhancing both the dianeutral tracer diffusivity and momentum viscosity by equal amounts. This issue was not discussed in the work of Simmons et al. (2004).

Hyun-Chul Lee and Harper Simmons provided valuable comments and suggestions for this chapter.

14.1 Formulation

Dianeutral mixing of tracer and momentum arises when energy dissipates at the small scales. There are two sources of energy dissipation considered here:

- breaking internal gravity waves, where the gravity wave energy source is from barotropic tidal energy scattered into internal tidal energy occuring when tides interact with rough bottom topography,
- frictional bottom drag as tides encounter continental shelves (whose depths are generally 500m or less).

To resolve both of these dissipation processes explicitly in a numerical model requires grid resolution no coarser than meters in the vertical (throughout the water column), and 1-10 kilometers in the horizontal. This very fine resolution is not generally accessible to global climate models, in which case it is necessary to consider a parameterization.

Bottom drag is typically parameterized as

$$D_{\text{bottom drag}} = C_D \, \mathbf{u} \, |\mathbf{u}|, \tag{14.1}$$

[1]The Prandlt number is the ratio of viscosity to diffusivity.

where C_D is a dimensionless drag coefficient taken as 2.4×10^{-3} by Lee et al. (2006). As discussed by Lee et al. (2006), the velocity dominating this drag is associated with energy input to the ocean via the barotropic tides as they encounter continental shelves and other shallow ocean regions. The energy dissipation (W m^{-2}) associated with this bottom drag is given by

$$E_{\text{bottom drag}} = C_D \, \rho_o \, \langle \mathbf{u}^2 \rangle \, |\mathbf{u}| \tag{14.2}$$

where the angle bracket symbolizes a time or ensemble average. This energy dissipation represents energy taken out of the barotropic tide and into small scale dissipation within the ocean bottom boundary layer. We assume that the dissipated energy due to bottom drag contributes to enhanced dianeutral mixing locally, with a form for the dianeutral diffusivity described in Section 14.3.

A wave drag associated with breaking internal gravity waves is written by Jayne and St.Laurent (2001) as

$$D_{\text{wave drag}} = (1/2) \, N_b \, \kappa \, h^2 \, \mathbf{u}, \tag{14.3}$$

where N_b is the buoyancy frequency at the ocean bottom, and (κ, h) are wavenumber and amplitude scales for the topography. The product κh^2 has dimensions of length and thus defines a *roughness length*

$$L_{\text{rough}} = \kappa \, h^2 \tag{14.4}$$

to be specified according to statistics of the observed ocean bottom topography.

The energy dissipation (W m^{-2}) associated with breaking internal gravity waves is given by

$$E_{\text{wave drag}} = (\rho_o/2) \, N_b \, L_{\text{rough}} \, \langle \mathbf{u}^2 \rangle. \tag{14.5}$$

In the Jayne and St.Laurent (2001) paper, they emphasize that κ, which sets the roughness length through $L_{\text{rough}} = \kappa h^2$, is used as a tuning parameter, with the tide model tuned to give sea level values agreeing with observations. Then, the energy dissipation can be diagnosed from the tide model. As with the bottom drag, the wave drag energy dissipation represents energy taken out of the barotropic tides, with the energy here transferred into the baroclinic tides. Some of the energy transferred into the baroclinic tides dissipates locally due to local wave breaking, and this then leads to enhanced dianeutral mixing locally. The remaining baroclinic energy propogates away (i.e., it is nonlocal). The ratio of local to nonlocal energy is not well known, and is the focus of research.

14.2 Mixing from internal wave breaking

When mechanical energy is dissipated, it is associated with dianeutral mixing. The relation between energy dissipation and mixing is not known precisely, though some empirical formulations have proven useful.

14.2.1 Simmons etal (2004) scheme

For energy dissipation due to breaking internal gravity waves, we follow Simmons et al. (2004), who compute a tracer diffusivity[2]

$$\kappa_{\text{waves}} = \kappa_0 + \frac{q\,\Gamma\,E_{\text{waves}}(x,y)\,F(z)}{\rho\,N^2}, \tag{14.6}$$

where $E_{\text{wave drag}}$ is the wave energy flux from scattered barotropic to baroclinic waves, given by equation (14.5). Vertical stratification

$$\rho\,N^2 = -g\,\rho_{,z} \tag{14.7}$$

acts to suppress vertical mixing, hence its presence in the denominator of equation (14.6). The energy flux in equation (14.5) is evaluated as follows.

- N_b is computed from the model's evolving buoyancy frequency at the top face of the bottom-most tracer cell (the frequency at the bottom face of the bottom-most cell is zero, by definition).
- The effective roughness length $L_{\text{rough}} = \kappa\,h^2$ requires an algorithm to compute h from the best of the observed bottom topography, and tide model to tune κ. However, in practice what can be done is to take h given some variance of topography within a grid cell, and then tune $E_{\text{wave drag}}$ to be roughly 1TW in ocean deeper than 1000m, with κ as the tuning paramter.

The dimensionless parameter Γ in equation (14.6) measures the efficiency that wave energy dissipation translates into dianeutral mixing. It is often chosen as

$$\Gamma = 0.2 \tag{14.8}$$

based on Osborn (1980). However, in regions of very weak stratification, the mixing efficiency tends to zero according to

$$\Gamma = 0.2\left(\frac{N^2}{N^2+\Omega^2}\right) \tag{14.9}$$

where

$$\begin{aligned}\Omega &= \left(\frac{2\pi + 2\pi/365.24}{86400\text{s}}\right)\\ &= \left(\frac{\pi}{43082}\right)\text{s}^{-1}\\ &= 7.2921\times 10^{-5}\text{s}^{-1}.\end{aligned} \tag{14.10}$$

is the angular rotation rate of the earth about its axis and about the sun. This modified mixing efficiency reduces the regions where spuriously large values of diffusivity may occur, especially next to the bottom, where low values of N^2 may appear. There is little physical reason to believe the huge diffusivities diagnosed from regions with $N^2 < \Omega^2$.

[2] As stated at the start of this chapter, we assume a unit Prandtl number. This assumption means the vertical viscosity is enhanced along with the diffusivity when considering internal wave breaking. Simmons et al. (2004) do not discuss vertical viscosity in their study.

Another dimensionless parameter, q, is used to measure the amount of energy dissipated locally, and thus contributes to local dianeutral mixing. Simmons et al. (2004) chose

$$q = 1/3 \tag{14.11}$$

based on the work of St.Laurent et al. (2002). The remaining 2/3 of the energy propagates away. This nonlocal dissipation of internal tidal energy, as well as the dissipation of internal energy from other sources (e.g., wind energy), are accounted for in an *ad hoc* manner via the background diffusivity κ_0 (and viscosity). A value within the range

$$\kappa_0 = (0.1 - 0.2) \times 10^{-4}\,\mathrm{m}^2\,\mathrm{s}^{-1} \tag{14.12}$$

is recommended based on the measurements of Ledwell et al. (1993). Note that this value does not account for mixing in a planetary boundary layer, such as that discussed by Large et al. (1994).

Setting $q = 1/3$ globally is strictly incorrect. The actual value is related to the modal content of the excited internal tide, which is related to the roughness spectrum of topography. The redder the mode/roughness spectrum, the lower q. For example, Hawaii has been modelled as a knife-edge by (St.Laurent et al., 2003). This topography excites predominantly low modes, and these modes are stable, propogate quickly, and have long interaction times. That is, they propagate to the far field. Klymak et al. (2005) argue that $q = 0.1$ for Hawaii from the Hawaiian Ocean Mixing Experiment (HOME) data. For the mid-Atlantic ridge, the use of $q = 1/3$, as in Simmons et al. (2004), may be more suitable.

The bottom intensified vertical profile, or *deposition function*, $F(z)$ is taken as

$$\begin{aligned} F &= \frac{e^{-(D-h)/\zeta}}{\zeta\left(1 - e^{-D/\zeta}\right)} \\ &= \frac{e^{h/\zeta}}{\zeta\left(e^{D/\zeta} - 1\right)}. \end{aligned} \tag{14.13}$$

In this expression,

$$D = H + \eta \tag{14.14}$$

is the time dependent thickness of water between the free surface at $z = \eta$ and the ocean bottom at $z = -H$, and

$$h = -z + \eta \tag{14.15}$$

is the time dependent distance from the free surface to a point within the water column.[3] The chosen form of the deposition function is motivated by the microstructure measurements of St.Laurent et al. (2001) in the abyssal Brazil Basin, and the continental slope measurements of Moum et al. (2002). This profile respects the observation that mixing from breaking internal gravity waves, generated by scattered barotropic tidal energy, is exponentially trapped within a distance ζ from the bottom. An *ad hoc* decay scale of

$$\zeta = 500\,\mathrm{m} \tag{14.16}$$

is suggested by Simmons et al. (2004) for use with internal gravity wave breaking in the abyssal ocean.

[3]We emphasize that with a free surface, D and h are generally time dependent. Furthermore, with general vertical coordinates, h is time dependent for all grid cells.

14.2.2 Some considerations for testing the implementation

We present some comments and details regarding the implementation and testing of the Simmons et al. (2004) scheme.

14.2.2.1 Regularization of the diffusivity

The diffusivities resulting from this parameterization can reach levels upwards of the maximum around $20 \times 10^{-4}\,\mathrm{m}^2\,\mathrm{s}^{-1}$ seen in the Polzin et al. (1997) results. Due to numerical resolution issues, the scheme can in practice produce values larger as well. We need to consider the physical relevance of these large values. The following lists some options that the modeller may wish to exercise.

- We may simply choose to limit the diffusivity to be no larger than a maximum value, defaulted to $50 \times 10^{-4}\,\mathrm{m}^2\,\mathrm{s}^{-1}$ in MOM4p1.
- Based on observations, the mechanical energy input from wave drag (equation (14.5)) should not exceed roughly $0.1\,\mathrm{W\,m}^{-2}$ at a grid point (Bob Hallberg, personal communication 2008). Depending on details of the bottom roughness and tide velocity amplitude, a typical model implementation may easily exceed this bound. Hence, it may be necessary to cap the mechanical energy input to be no larger than a set bound.
- Use of the stratification dependent mixing efficiency (14.9) provides a physically based means to regularize the regions where N^2 can get extremely small.

14.2.2.2 Use of the scheme for all depths

Simmons et al. (2004) do not apply their scheme in waters with ocean bottom shallower than 1000m, whereas Jayne (2008) applies the scheme for all depths. MOM4 maintains a namelist that allows for setting a cutoff depth. For the continental shelves, the scheme of Lee et al. (2006) described in Section 14.3 dominates. Hence, in principle, there is nothing wrong with using the Simmons et al. (2004) scheme all the way to shallow waters. So one may wish to naively use $q = 1/3$ without a 1000m depth cutoff. Likewise, $\zeta = 500$m globally may be a reasonable choice. The structure function will do the right thing and integrate to unity, whether or not the ocean depth H is greater or less than ζ.

14.2.2.3 Energetic balances

One of the main reasons to formulate diffusivites based on energy input is that energy is exchanged in a conservative manner. This conservation then leads to self-consistency tests for the model implementation. In particular, the work done against stratification by dianeutral diffusion is given by

$$\mathcal{P} \equiv \int \mathrm{d}V\, \kappa_{\mathrm{dianeutral}}\, \rho\, N^2. \tag{14.17}$$

Use of equation (14.6) for the diffusivity with a constant mixing efficiency $\Gamma = 0.2$ yields

$$\begin{aligned} \mathcal{P} &= \int \mathrm{d}V \, (\kappa_{\text{wave drag}} - \kappa_0) \, \rho \, N^2 \\ &= q \, \Gamma \int \mathrm{d}x \, \mathrm{d}y \, E_{\text{wave drag}}(x, y) \end{aligned} \tag{14.18}$$

assuming $q \, \Gamma$ constant. Note that to reach this result, we set $\int F(z) \, \mathrm{d}z = 1$, which is a constraint that should be maintained by the model implementation. Equation (14.18) says that the energy deposited in the ocean interior that works against stratification originates from that scattered from the ocean bottom. For the general case of $q \, \Gamma$ spatially dependent, we have the balance

$$\begin{aligned} \mathcal{P} &= \int \mathrm{d}V \, (\kappa_{\text{wave drag}} - \kappa_0) \, \rho \, N^2 \\ &= \int \mathrm{d}x \, \mathrm{d}y \, \mathrm{d}z \, q \, \Gamma \, E_{\text{wave drag}}(x, y) \, F(z), \end{aligned} \tag{14.19}$$

which again is a statement of energy conservation between wave dissipation and mixing of density.

Although equation (14.19) is a trivial identity following from the definition of the closure, it is not trivial to maintain in the ocean model. The main reason is that we work with diffusivities when integrating the equations of an ocean model, and these diffusivities are often subjected to basic numerical consistency criteria, such as the following.

- We may wish to have the diffusivities monotonically decay upwards in the column. Given the N^{-2} dependence, this behaviour is not necessarily the case. Without a monotonic constraint, the simulation can be subject to spurious instabilities in which intermediate depths destratify, then producing larger diffusivities, and further reducing the stratification. Jayne (2008) discovered this behaviour in his simulations.

- The diffusivities should be bounded by a reasonable number, such as $50 - 100 \, \mathrm{cm}^2 \, \mathrm{sec}^{-1}$.

Imposing constraints such as these on the diffusivity corrupts the identity (14.18). In general, they remove energy from the interior, so that in practice $\int \mathrm{d}V \, (\kappa_{\text{wave drag}} - \kappa_0) \, \rho \, N^2 < \int \mathrm{d}x \, \mathrm{d}y \, \mathrm{d}z \, q \, \Gamma \, E_{\text{wave drag}}(x, y)$.

14.2.2.4 Further comments

Here are some further points to consider when setting some of the namelists for this scheme.

- One means to ensure that the diffusivities are within a reasonable bound, without capping them after their computation, is to artificially restrict the stratification used in the calculation to be no less than a certain number. Simmons et al. (2004) chose the floor value $N^2 \geq 10^{-8} \, \mathrm{s}^{-2}$. There is a great deal of sensitivity to the floor value used. GFDL practice is to keep the floor value quite low so that $N^2_{\text{min}} < \Omega^2$.

- If the maximum diffusivity realized by the scheme is allowed to be very large, say much greater than as $1000 \, \mathrm{cm}^2 \, \mathrm{sec}^{-1}$, then the near bottom stratification can become very small. In this case, $E_{\text{wave drag}}$ can dip below the canonical 1TW value. This process resembles a negative feedback in some manner, though it has not been explored extensively.

14.3 Dianeutral diffusivities from bottom drag

The Lee et al. (2006) scheme does not consider energetic arguments for determining the diffusivity associated with barotropic tides dissipated by the bottom boundary layer. Instead, they follow the ideas of Munk and Anderson (1948), whereby a dianeutral diffusivity is given by

$$\kappa_{\text{drag}} = \kappa_{max} \left(1 + \sigma \, \mathrm{Ri}\right)^{-p}, \tag{14.20}$$

where the dimensionless parameters σ and p have the default values

$$\sigma = 3 \tag{14.21}$$

$$p = 1/4. \tag{14.22}$$

The Richardson number is given by

$$\mathrm{Ri} = \frac{N^2}{|\partial_z \, \mathbf{u}|^2}. \tag{14.23}$$

Small Richardson numbers give larger vertical diffusivities, with the maximum diffusivity set by κ_{max}. Following Lee et al. (2006), we set the default for the maximum diffusivity arising from bottom drag dissipation as

$$\kappa_{max} = 5 \times 10^{-3} \, \mathrm{m}^2 \, \mathrm{s}^{-1}. \tag{14.24}$$

Since we do not generally resolve the bottom boundary layer in global models, we must approximate the vertical shear to compute the Richardson number, and here we use the form

$$2 \, |\partial_z \, \mathbf{u}|^2 = \left(\frac{A}{D - h} \right)^2, \tag{14.25}$$

with the scaled tidal speed A given by

$$A = U_{\text{tide}} \, \sqrt{Cd} / \kappa_{\text{von Karman}}. \tag{14.26}$$

Here, Cd is the bottom drag coefficient, taken as 2.4×10^{-3} by Lee et al. (2006),

$$\kappa_{\text{von Karman}} = 0.41 \tag{14.27}$$

is the von Karman constant, and U_{tide} is the tidal speed taken from a barotropic tidal model. These speeds are largest in the shallow regions.

CHAPTER
FIFTEEN

Calculation of buoyancy forcing

This chapter documents the conventions used for computing the buoyancy forcing. This forcing is fundamental to some of the MOM4p1 mixed layer schemes, such as the KPP scheme of Large et al. (1994) and the scheme of Chen et al. (1994). For the KPP scheme, Martin Schmidt noted that the MOM4.0 code computed the contribution from fresh water with an incorrect sign. Hence, adding fresh water reduced the buoyancy forcing in the KPP scheme, thus altering the mixing coefficients produced by the scheme. The effects of this bug are enhanced in the high latitudes, where fresh water has more of an effect on buoyancy than at lower latitudes.

15.1 Fundamentals

Buoyancy is defined here as

$$B = -g\,\rho, \tag{15.1}$$

where g is the gravitational acceleration and ρ is the *in situ* density. Buoyancy as defined is minus the weight per volume of a fluid parcel.[1] The minus sign is motivated by noting that as B increases, a water parcel tends to rise to a higher level in the water column; that is, it is more *buoyant*.

Forcing at the ocean surface that affects the density of a parcel thus affects the buoyancy. For example, surface heating increases the buoyancy since it reduces density, as does the introduction of fresh water. In contrast, cooling increases density and so reduces buoyancy, as does evaporation. If the buoyancy forcing succeeds in making a surface water parcel denser than deeper parcels, vertical convective motions will occur. Such processes constitute a critical aspect of the World Ocean's thermohaline circulation.

As MOM4p1 is a hydrostatic model, the vertical motions associated with convection are filtered out from the resolved dynamical equations. These motions must therefore be parameterized. There are two general manners for parameterizing convection. First, there are *convective adjustment* schemes, whereby adiabatic comparisons of vertically adjacent water parcels determine whether to perform some form of adjustment. This adjustment amounts to a form of mixing between the two parcels, with full mixing one end of the spectrum, and swapping of water parcels the other end. The MOM4p1 code defaults its convective adjustment scheme to that from Rahmstorf (1993), with the older scheme of Cox (1984) an option retained for legacy purposes. The second

[1] In most treatments, buoyancy is defined as $-g\,\rho/\rho_o$, which gives buoyancy the units of acceleration.

parameterization of vertical convection is handled via a mixed layer scheme, such as Pacanowski and Philander (1981), Chen et al. (1994), and Large et al. (1994). Here, mixing coefficients are enhanced in regions of negative buoyancy forcing. Additionally, the KPP scheme establishes a level of nonlocal penetrative mixing that is a function of the buoyancy forcing.

In order to compute the level of mixing from KPP or Chen due to buoyancy forcing, it is necessary to be precise about what is the buoyancy forcing. For this purpose, focus on the evolution of temperature and salinity in the top model grid cell, with effects from surface boundary conditions of focus. The tracer and mass budget for a surface model grid cell was derived in Section 3.6.7, in which case we have (again, dropping all terms except those from surface buoyancy forcing)

$$\partial_t \left(\rho \, \mathrm{d}z \, \theta\right) = Q_w \, \theta_w - Q_\theta / C_p \tag{15.2}$$

$$\partial_t \left(\rho \, \mathrm{d}z \, S\right) = Q_w \, S_w - Q_S \tag{15.3}$$

$$\partial_t \left(\rho \, \mathrm{d}z\right) = Q_w. \tag{15.4}$$

In these equations,

- θ is the potential temperature;
- S is the salinity;
- Q_w is the mass flux ($\mathrm{kg\,m^{-2}\,sec^{-1}}$) of water crossing the ocean surface, with $Q_w > 0$ for water entering the ocean (as when precipitation exceeds evaporation);
- $\rho \, \mathrm{d}z$ is the mass per horizontal area of seawater in the grid cell;
- θ_w is the temperature of water crossing the ocean surface;
- S_w is the salinity of water crossing the ocean surface;
- Q_S is the turbulent flux of salt ($\mathrm{kg\,m^{-2}\,sec^{-1}}$) that leaves the ocean through the ocean surface;
- Q_θ is the turbulent and radiative heat flux ($\mathrm{W\,m^{-2}}$) leaving the ocean ($Q_\theta > 0$ for heat leaving the ocean surface as when cooling);
- C_p is the seawater heat capacity at constant pressure ($\mathrm{J\,kg^{-1}\,{}^\circ C^{-1}}$).
- We note that in some formulations, the products $Q_w \, \theta_w$ and $Q_w \, S_w$ are specified from component models, such as sea ice and land models. For example, if the heat flux with respect to $0^\circ C$ (in units of Watts per square metre) of liquid river runoff $\mathcal{H}_w^\theta$ is given to the ocean from the land model, then to compute the buoyancy forcing we make use of the identity

$$Q_w \, \theta_w = \frac{\mathcal{H}^\theta_{\text{liquid runoff}}}{C_p^{\text{liquid runoff}}}, \tag{15.5}$$

with $C_p^{\text{liquid runoff}}$ the heat capacity of the water coming in from the river runoff. Likewise, if the heat associated with frozen runoff (e.g., calving land ice) is provided by the land model, then we have

$$Q_w \, \theta_w = \frac{\mathcal{H}^\theta_{\text{solid runoff}}}{C_p^{\text{solid runoff}}}, \tag{15.6}$$

with $C_p^{\text{solid runoff}}$ the heat capacity of the solid runoff. These two heat capacities are typically provided by the component model (i.e., the land model) used to compute the runoff fields. Similar considerations hold for transfer of water betwen sea ice models and the ocean.

The turbulent mass flux of salt Q_S (kg m^{-2} sec^{-1}) is positive for salt leaving the ocean surface. There is transport of salt across the ocean surface when sea ice forms and melts, due to the nonzero salt content in sea ice. Otherwise, the surface salt flux is generally zero for the large scale ocean. For ocean models, however, it can be nonzero when formulating the surface boundary in terms of virtual salt fluxes rather than real water fluxes (Huang, 1993; Griffies et al., 2001). This formulation is not recommended, as it is distinctly unphysical and unnatural when using an explicit free surface or bottom pressure solver as in MOM4.

The heat flux Q_θ (W m^{-2}) is positive for heat leaving the ocean. This flux is comprised of the following contributions (see page 34 of Gill, 1982)

$$Q_\theta = Q_{long} + L\,E + Q_{sens} - Q_{short}, \tag{15.7}$$

where Q_{short} is the shortwave radiative heat entering the ocean, Q_{long} is the longwave radiation leaving the ocean in the form of the $\sigma\,T^4$ Stefan-Boltzmann Law, L is the latent heat of vaporization of water

$$L = 2.5 \times 10^6\,\text{J kg}^{-1} \tag{15.8}$$

with E the mass flux (kg m^{-2} sec^{-1}) of water leaving the ocean due to evaporation, and Q_{sens} is the sensible heat transfer proportional to the difference between atmosphere and ocean temperatures.

When considering time changes in buoyancy (15.1), we are concerned with the constant pressure changes, since buoyancy is used for comparing two water parcels to check for vertical stability. Hence, the time tendency of buoyancy $B = -g\,\rho$ is given by

$$-\,g^{-1}\,B_{,t} = \rho_{,\theta}\,\theta_{,t} + \rho_{,S}\,S_{,t} \tag{15.9}$$

where

$$\rho_{,\theta} = \left(\frac{\partial \rho}{\partial \theta}\right)_{S,p} \tag{15.10}$$

$$\rho_{,S} = \left(\frac{\partial \rho}{\partial S}\right)_{\theta,p} \tag{15.11}$$

are the partial derivatives of density with respect to potential temperature and salinity, respectively, each with pressure held constant. We wish to form an evolution equation for buoyancy at the ocean surface due to the effects of surface forcing. For this purpose, multiply the temperature equation (15.2) by $\rho_{,\theta}$ and add to the surface salinity equation (15.3) multiplied by $\rho_{,S}$

$$\rho_{,\theta}\,(\rho\,\mathrm{dz}\,\theta)_{,t} + \rho_{,S}\,(\rho\,\mathrm{dz}\,S)_{,t} = Q_w\,(\theta\,\rho_{,\theta} + S\,\rho_{,S}) - g^{-1}\,\rho\,\mathrm{dz}\,B_{,t} \tag{15.12}$$

where we used the mass budget (15.4) and introduced the buoyancy tendency according to equation (15.9). We thus have the expression for the time tendency of the surface ocean buoyancy

$$g^{-1}\,\rho\,\mathrm{dz}\,B_{,t} = Q_w\,(\theta\,\rho_{,\theta} + S\,\rho_{,S}) - \rho_{,\theta}\,(\rho\,\mathrm{dz}\,\theta)_{,t} - \rho_{,S}\,(\rho\,\mathrm{dz}\,S)_{,t} \tag{15.13}$$

$$= Q_w\,(\theta\,\rho_{,\theta} + S\,\rho_{,S}) - \rho_{,\theta}\,(Q_w\,\theta_w - Q_\theta/C_p) - \rho_{,S}\,(Q_w\,S_w - Q_S) \tag{15.14}$$

$$= \rho_{,\theta}\,Q_w\,(\theta - \theta_w) + \rho_{,S}\,Q_w\,(S - S_w) + \rho_{,\theta}\,Q_\theta/C_p + \rho_{,S}\,Q_S, \tag{15.15}$$

where we used the surface temperature and salt budgets (15.2) and (15.3). Again, the temperature and salinity appearing on the right hand side are those of the surface ocean cell. We now introduce the thermal expansion and saline contraction coefficients

$$\alpha = -\left(\frac{\partial \ln \rho}{\partial \theta}\right)_{S,p} \tag{15.16}$$

$$\beta = \left(\frac{\partial \ln \rho}{\partial S}\right)_{\theta,p} \tag{15.17}$$

with each of these coefficients positive for most applicable ranges of seawater (see Table A3.1 of Gill, 1982), with the exception of very fresh and cold waters, where α can become negative. The buoyancy equation thus takes the form

$$\mathrm{d}z\, B_{,t} = -g\,\alpha\,\left[Q_w\,(\theta - \theta_w) + Q_\theta/C_p\right] + g\,\beta\,\left[Q_w\,(S - S_w) + Q_S\right]. \tag{15.18}$$

For future comparison to the Large et al. (1994) formulation in their Appendix A, we write

$$\mathrm{d}z\, B_{,t} = B_f \tag{15.19}$$

where B_f is the *buoyancy forcing* of Large et al. (1994) with units of $\mathrm{kg\,m^{-1}\,s^{-3}}$.

We are now in a position to provide physical interpretations of the buoyancy tendency in equation (15.18). First, as water is added to the ocean ($Q_w > 0$) with temperature less than that of the ocean surface temperature ($\theta - \theta_w > 0$), the buoyancy is decreased due to the introduction of the cooler fresh water. In most applications, the water crossing the ocean surface is assumed to be at the ocean surface temperature, in which case $g\,\alpha\,Q_w\,(\theta - \theta_w) = 0$ and so does not contribute to buoyancy changes. Second, as water is added to the ocean with salinity less than that of the ocean surface salinity ($S - S_w > 0$), the buoyancy is increased due to the introduction of fresher water. In most applications, the water crossing the ocean surface is assumed to have zero salinity, in which case $g\,\beta\,Q_w\,S$ represents a positive buoyancy forcing when fresh water is added to the ocean. Third, as heat leaves the ocean ($Q_\theta > 0$), buoyancy is decreased due to the cooling, whereas when salt leaves the ocean ($Q_S > 0$), buoyancy is increased due to the freshening.

Equation (15.18) provides the mathematical basis for determining how buoyancy is affected in the ocean surface due to water and heat transfers between the ocean and other components of the climate system. The four processes identified in this equation act on the ocean surface, with some regions feeling the effects from fresh water more than heat, such as in the high latitudes where α is small and Arctic rivers and sea ice forcing are nontrivial sources of buoyancy forcing, whereas other regions are dominated by heat fluxes. The calculation of these buoyancy forces is an important part of the mixing parameterization of KPP and Chen, as the buoyancy forcing is used in these schemes to determine details of the mixing coefficients and nonlocal transfer.

15.2 The formulation as in Large et al. (1994)

To help understand the KPP code in MOM4p1, it is useful to revisit the formulation of Appendix A in Large et al. (1994). The notation is quite different from the above formulation, so it is useful to redefine symbols in this section for clarity. Large et al. (1994) introduce the turbulent buoyancy flux at the ocean surface (equation (A3b))

$$-\overline{w\,b_o} = g\,\rho_{,\theta}\,\overline{w\,\theta} + \rho_{,S}\,\overline{w\,S}, \tag{15.20}$$

where w is positive upwards, and $-\overline{w\,b_o} > 0$ implies an increase in buoyancy forcing on the ocean surface. Now introduce

$$\alpha^L = -\left(\frac{\partial \rho}{\partial \theta}\right)_{S,p} \tag{15.21}$$

$$\beta^L = \left(\frac{\partial \rho}{\partial S}\right)_{\theta,p} \tag{15.22}$$

as shorthand, with both α^L and β^L positive numbers (Table A3.1 in Gill, 1982), and write the turbulent temperature and salinity fluxes at the ocean surface as (equations (A2c) and (A2d))

$$\overline{w\,\theta} = -\left(\frac{Q_t}{\rho(0)\,C_p}\right) \tag{15.23}$$

$$\overline{w\,S} = \frac{Q_w\,S(0)}{\rho_w} + \frac{F_s\,(S(0) - S_I)}{\rho_I}, \tag{15.24}$$

with

- Q_t (W m^{-2}) the turbulent heat flux with $Q_t > 0$ heating the ocean (radiative heating is handled separately);
- Q_w (kg m^{-2} s^{-1}) the mass flux of water, with $Q_w > 0$ for water entering the ocean;
- F_s (kg m^{-2} s^{-1}) the mass flux of water due to melting sea ice, with $F_s > 0$ for sea ice melt water entering the ocean;
- $S(0)$ the salinity of the ocean surface grid cell with density $\rho(0)$;
- S_I the salinity of the sea ice with density ρ_I;
- ρ_w the density of fresh water.

Inserting these fluxes into the buoyancy flux leads to

$$-\overline{w\,b_o} = \frac{g\,\alpha^L\,Q_t}{\rho(0)\,C_p} + \frac{\beta^L\,Q_w\,S(0)}{\rho_w} + \frac{\beta^L\,F_s\,(S(0) - S_I)}{\rho_I}. \tag{15.25}$$

Note that Large et al. (1994) assume the temperature of water passed across the ocean surface is the same as the sea surface temperature, thus eliminating the $Q_w\,(\theta - \theta_w)$ term appearing in the buoyancy equation (15.18). They also assume the salinity of water in the evaporation and precipitation to be zero, yet allow for a nonzero salinity of the sea ice.

15.3 Buoyancy forcing for KPP in MOM

In the KPP scheme of MOM, we compute an array `Bo` defined by

$$\texttt{Bo} = g\,\alpha^L\,\texttt{wsfc(temp)} - g\,\beta^L\,\texttt{wsfc(salt)} + g\,\texttt{frazil}/(\rho_o\,C_p\,\Delta t), \tag{15.26}$$

with ρ_o the constant Boussinesq density, Δt the model time step, `frazil` the heating of seawater (in Joules) due to frazil formation, and `wsfc` kinematic fluxes given by

$$\texttt{wsfc}(\texttt{temp}) = \texttt{stf}(\texttt{temp}) - \texttt{pme}\,(T(k=1) - Tpme) - \texttt{river}\,(T(k=1) - Triver) \tag{15.27}$$

$$\texttt{wsfc}(\texttt{salt}) = \texttt{stf}(\texttt{salt}) - \texttt{pme}\,(S(k=1) - Spme) - \texttt{river}\,(S(k=1) - Sriver). \tag{15.28}$$

In MOM, the flux array `stf` is positive for tracer entering the ocean. The array `Bo` thus corresponds to the buoyancy forcing B_f defined by equation (15.19). It includes the radiative and turbulent heating, as well as the forcing from water and salt fluxes.

15.4 Bug in MOM4.0

Martin Schmidt noted that the signs in front of the water terms in equations (15.27) and (15.28) are wrong in MOM4.0 (they were mistakenly set to plus rather than minus). The MOM4p1 code has corrected the error. Users of the MOM4.0 code may wish to test the sensitivity of their simulations, especially if their domain includes high latitudes with sea ice.

CHAPTER
SIXTEEN

Neutral physics and boundary layers

As noted by Griffies (2004) and Ferrari et al. (2008), the treatment of neutral physics in boundary regions is traditionally *ad hoc* and largely determined by numerical considerations. Griffies (2004) summarizes the methods used in MOM4p0, which are perhaps the most physically based of the methods employed in the IPCC AR4 ocean climate models (e.g., Griffies et al. (2005)). Nonetheless, Gnanadesikan et al. (2006b) note that there remain arbitrary choices within the MOM4p0 methods that have nontrivial influences on the climate in a coupled climate model. Hence, there is motivation to seek a method that is more physically based and involves less *ad hoc* parameter inputs. The methods of Ferrari et al. (2008) are promising from this perspective, as are those of Ferrari et al. (2009).

16.1 Notes on implementation as of June 2008

The bulk of these notes were written in 2005, when the Ferrari et al. (2008) paper was a preprint. When released in December 2007, the module that resulted was called

`mom4/ocean_param/mixing/ocean_nphysics_mom4p1_mod`,

to distinguish the code from the standard neutral physics in MOM4.0. The original MOM4p1 implementation of Ferrari et al. (2008) was buggy, and resulted in unphysical simulation features. Because the bulk of the concerns raised by Ferrari et al. (2008) had already been addressed with the `ocean_nphysics_mom4p0_mod` module (now called `ocean_nphysicsA_mod`), there was little motivation to remedy the bugs in `ocean_nphysics_mom4p1_mod`.

During development of `ocean_nphysicsC_mod` in June 2008, we revisited the problems with the MOM4p1 implementation of Ferrari et al. (2008).[1] At this point, it was decided that the generality provided by the transition region (see Section 16.2 and Figure 16.2) was not critical, nor was it worth the added code complexity. Hence, the `ocean_nphysicsB_mod` module represents a stripped-down version of the Ferrari et al. (2008) scheme, in which (1) there is no quadratic transition region, and (2) only the surface boundary layer is considered. As a result, `ocean_nphysicsB_mod` is very similar to `ocean_nphysicsA_mod`.

[1] The `ocean_nphysicsC_mod` module implements the methods of Ferrari et al. (2009). It is a research module whose general use is strongly discouraged.

Given the simplifications present in `ocean_nphysicsB_mod`, we still feel it useful to present a discussion of the Ferrari et al. (2008) scheme as it was originally intended to be implemented in MOM4p1. Such remains the purpose of this chapter.

16.2 Regions affecting neutral physics

Ferrari et al. (2008) identify five distinct regions in the vertical where treatment of the neutral physics parameterization is distinct. Figure 16.1 illustrates the three regions in the upper ocean, with the reflection of this treatment relevant for the bottom. The `nphysicB` treatment of neutral physics considers all of these regions. The purpose of this section is to describe these regions and how they are computed in MOM4p1.

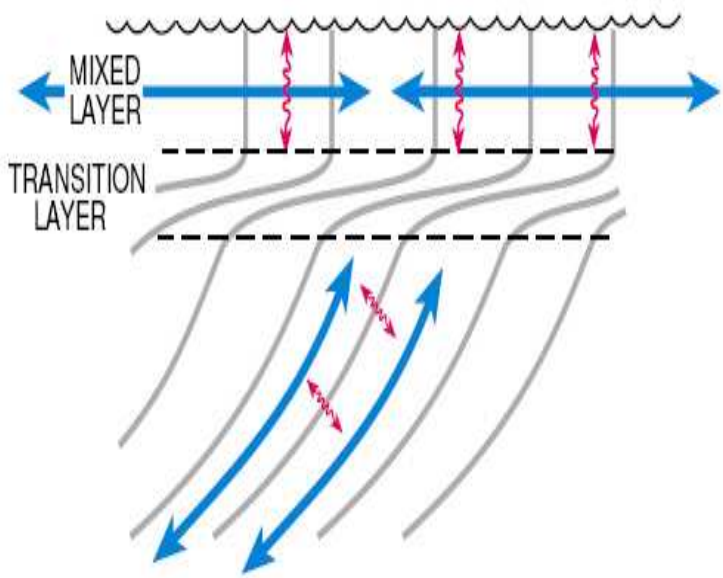

Figure 16.1: Surface region of the ocean as discussed by Ferrari et al. (2008) (this figure is taken from their preprint). Isopycnals are drawn here, along with directions whereby tracer transport dominates.

We will make much use in the following of the vertical distance from the ocean free surface to a depth $z < 0$:

$$\begin{aligned} h &= \text{ thickness of water between free surface and depth } z < 0 \\ &= -z + \eta, \end{aligned} \tag{16.1}$$

where $z = \eta$ is the time dependent free surface height. In particular, the MOM4p1 code denotes the thickness between the free surface and the bottom of a tracer cell as `depth_zwt`, and the distance to the tracer cell point as `depth_zt`. These arrays are functions of the horizontal grid cell labelled by i, j and the vertical cell labelled by k, where k increases downward. These thickness arrays are evaluated for all vertical coordinate choices in MOM4p1.[2]

[2] As MOM4p1 employes a suite of possible vertical coordinates, it is important that the code carry arrays that are zero

It is convenient in the following to consider the streamfunction's vertical dependence as a dependence on h rather than z. Note, however, that it is important to keep in mind the sign change in the vertical derivative operator

$$\partial_z = -\partial_h. \tag{16.2}$$

16.2.1 Upper turbulent boundary layer

The near ocean surface is dominated by three dimensional nonhydrostatic turbulent processes. The distance from the free ocean surface to the base of the turbulent zone is written

$$h_{\text{surf}} = \text{ surface turbulent layer thickness}, \tag{16.3}$$

and the thickness region

$$0 \leq h \leq h_{\text{surf}} \text{ surface turbulent boundary layer} \tag{16.4}$$

defines the surface turbulent boundary layer (see Figure 16.2). The boundary layer thickness h_{surf} is determined in a hydrostatic model by a boundary layer parameterization scheme such as KPP (Large et al., 1994). The boundary layer scheme parameterizes vertical mixing processes. When the mixing is strong, such as occurs with intense momentum forcing and/or buoyancy loss, the upper ocean destabilizes and results in vertical isopycnals as shown in Figure 16.1. The turbulent boundary layer thickness can be thin (order tens of metres) during daytime warming in the tropics which stabilizes the ocean, or thick (order a few hundred to few thousand metres) for late winter deep convection in regions of large buoyancy loss such as the Labrador Sea and Weddell Sea (Marshall and Schott, 1999).

Mesoscale eddies that penetrate to the ocean surface feel the geometric effect from the surface boundary. Treguier et al. (1997) discussed this point in the context of ocean mesoscale eddy parameterizations, and Held and Schneider (1999) described similar issues for synoptic atmospheric variability. Following suggestions in these papers, Ferrari et al. (2008) propose that the lateral diffusive effects from the mesoscale eddies should be parameterized by downgradient *horizontal* tracer diffusion within the surface turbulent boundary layer, rather than neutral diffusion considered in the ocean interior. Indeed, neutral diffusion in a region of vertical isopycnals will compete with, and perhaps dominate over, the turbulent parameterizations from KPP or other diabatic schemes. Hence, it is not sensible to continue retaining neutral diffusion in the surface boundary layer. In a similar manner, subgrid scale advective effects should be parameterized by an eddy induced velocity that has zero vertical shear within the surface boundary layer. More vertical structure for the eddy induced velocity is unwarranted in a region of weak or zero vertical stratification. Equivalently, the quasi-Stokes streamfunction (McDougall and McIntosh, 2001; Griffies, 2004) used to compute the eddy induced velocity is linearly tapered to zero as the ocean surface is approached. Finally, the diffusivity used to parameterize lateral diffusive and advective processes is taken from the diffusivity computed in the ocean interior.

16.2.2 Transition between surface boundary layer and interior

Beneath the surface turbulent layer lies a transition region of enhanced stratification. Notably, this transition region is generally *not* represented in coarse resolution models, and it remains a topic of

at the ocean free surface, rather than at the rigid lid surface defined by $z = 0$, in order to measure the time dependent thickness of the water column from the free surface to a grid cell.

research with nonhydrostatic models to further explore the physics active in this region (R. Ferrari 2005 personal communication), and in particular how to parameterie the thickness of this layer.

Mesoscale eddies sporadically penetrate the transition region and interact with processes in the turbulent surface layer. Tracer transport from mesoscale eddies is modified by these interactions in manners that remain a topic of research. Even so, because of this modification, we are motivated to alter the treatment of neutral physics in this region using some basic ideas from Ferrari et al. (2008), who were the first to emphasize the importance of the transition region for mesoscale eddy parameterization schemes.

The thickness of the surface transition region is denoted by

$$D_{\text{surf}} = \text{ surface transition layer thickness,} \tag{16.5}$$

and the transition region is defined for thickness ranges

$$h_{\text{surf}} \leq h \leq h_{\text{surf}} + D_{\text{surf}} \text{ surface transition region.} \tag{16.6}$$

Scaling arguments provided by Large et al. (1997), Smith and Vallis (2002), and Griffies (2004) were used by Ferrari et al. (2008) to provide an approximation to the thickness D_{surf}. We describe these arguments now.

If the tracer cell labelled by integer k is beneath the surface turbulent layer, we compute the absolute value of the neutral slope S_k and multiply it by the Rossby radius R_{rossby} (details of how MOM4p1 computes the Rossby radius are give in Section 16.7). As discussed by Large et al. (1997), Smith and Vallis (2002), and Griffies (2004), this product is representative of the vertical excursion of a typical mesoscale eddy. The first ocean model depth, denoted by $k = k^{(+)}$, that is just deeper than $h_{\text{surf}} + R_{\text{rossby}}\, S_{k^{(+)}}$ defines the transition layer thickness D_{surf}, so that

$$D_{\text{surf}} \approx R_{\text{rossby}}\, S_{k^{(+)}}. \tag{16.7}$$

Again, mesoscale eddies deeper than $h_{\text{surf}} + D_{\text{surf}}$ are thought, on average, to never reach the surface turbulent layer, whereas eddies shallower typically do reach this layer and so their transport effects are modified relative to the interior. In the subsequent discussion, the depth level $k^{(+)}$, and the quasi-Stokes streamfunction at this depth, play important roles in determining the strength of the neutral physics fluxes in the region shallower than $h_{\text{surf}} + D_{\text{surf}}$.

16.2.3 Ocean interior

Motivated from the above discussion, the ocean interior is defined for present purposes as regions where mesoscale eddies do not reach into the surface turbulent layer or to the bottom turbulent layer. That is, the ocean interior is defined for water column thicknesses satisfying

$$h_{\text{surf}} + D_{\text{surf}} \leq h \leq H_{\text{bott}} - (h_{\text{bott}} + D_{\text{bott}}). \tag{16.8}$$

In this expression, H_{bott} is the total water column thickness from the free surface at $z = \eta$ to the ocean bottom topography at $z = -H$

$$H_{\text{bott}} = \eta + H. \tag{16.9}$$

The bottom transition layer and bottom turbulent boundary layer are discussed in Sections 16.2.4 and 16.2.5. In the ocean interior, mesoscale eddy parameterizations used in MOM4p1 act without boundary layer modification. We provide more discussion of these parameterizations in Sections 16.3 and 16.6.

16.2.4 Transition between the interior and bottom boundary layer

As eddies interact with the bottom boundary layer, their tracer transport effects are modified relative to their effects in the interior. We note that the local normal at the bottom grid cell in MOM4 is treated as normal to the generalized vertical coordinate. Hence, the treatment of the bottom transition layer remains analogous kinematically to the surface.

The bottom transition thickness

$$D_{\text{bott}} = \text{ bottom transition layer thickness} \tag{16.10}$$

is used to define the bottom transition layer, whose thickness h satisfies

$$H_{\text{bott}} - (h_{\text{bott}} + D_{\text{bott}}) \leq h \leq H_{\text{bott}} - h_{\text{bott}}, \tag{16.11}$$

where h_{bott} is the bottom boundary layer thickness discussed in Section 16.2.5. We have two choices in MOM4p1 for determining D_{bott}: (1) an algorithm analogous to that used to compute D_{surf}, (2) specify D_{bott} according to a constant namelist value, similar to how h_{bott} is presently set in the absence of a prognostic bottom boundar layer scheme. Modification of the neutral physics transport from the interior through the bottom transition layer is directly analogous to the surface transition layer.

16.2.5 Bottom turbulent boundary layer

Topography orients tracer transport near the ocean bottom, and considerations analogous to the ocean surface turbulent layer arise in this region. That is, lateral diffusive processes are oriented according to the topography, and eddy-induced velocities have zero vertical shear in this region.

Thickness of the bottom turbulent layer,

$$h_{\text{bott}} = \text{ bottom turbulent layer thickness}, \tag{16.12}$$

is sometimes specified via a namelist parameter often taken to be roughly 50m. Alternatively, using the methods discussed in Chapter 19, we can compute a space-time dependent bottom boundary layer thickness. In general, this thickness is used to specify a bottom boundary layer region where the column thickness satisfies

$$H_{\text{bott}} - h_{\text{bott}} \leq h \leq H_{\text{bott}}. \tag{16.13}$$

16.2.6 Comments on the treatment in MOM4p0

The treatment of neutral physics in MOM4p0 is detailed in Griffies (2004) and Griffies et al. (2005). This treatment failed to consider the two transition regions described above. Instead, the depth

$$D_{\text{mom4p0}} = \max(h_{\text{surf}}, D_1, D_2) \tag{16.14}$$

is used to define a surface region over which the neutral diffusive fluxes are tapered to horizontal downgradient fluxes, and the eddy induced velocity has zero vertical shear with strength determined by that at the base of the boundary layer. Here, D_1 is defined just according to the surface transition depth D_{surf} (equation (16.7)) used in `nphysicsB`. In contrast, D_2 is the depth

below which the neutral slope becomes less than some specified maximum value S_{max}. That is, D_2 is determined by the stratification whereas D_1 is determined by both the stratification and the Rossby radius. There is no bottom boundary layer considered for the neutral physics scheme in `nphysicsA`, though in practice neutral fluxes were reduced to downgradient *horizontal* diffusion next to the bottom and sides, according to the suggestions from Gerdes et al. (1991).

An unsatisfying element of the `nphysicsA` method is the introduction of the depth D_2, since this depth is determined by an *ad hoc* maximum slope S_{max}.[3] D_1 is generally larger or smaller than D_2 depending on the arbitrary choice of the maximum slope. That is, when S_{max} is small, then D_1 tends to be smaller than D_2. When S_{max} is large, then D_1 tends to be larger than D_2, in which case the boundary layer depth approaches that found in the `nphysicsB` scheme, absent the transition layer thickness. Sensitivity of a coupled climate model simulation to the value of the maximum slope parameter is documented in Gnanadesikan et al. (2006b).

Without the extra depth D_2 used to determine D_{mom4p0}, such as when S_{max} is large enough, then the `nphysicsA` method becomes similar to that used in `nphysicsB`. However, as discussed below, the Ferrari et al. (2008) transition region used in `nphysicsB` ensures that the eddy induced velocity linearly interpolates from the boundary layer values to the interior values. As `nphysicsA` does not consider this transition region, the eddy induced velocity does not possess this interpolation behaviour, and instead exhibits a jump at the boundary layer base. This jump is non-physical and can potentially cause unsatisfying numerical and physical effects in the simulation.

16.3 Quasi-Stokes streamfunction

.

As discussed in Griffies (1998), McDougall and McIntosh (2001), and Griffies (2004), the introduction of a divergence-free eddy induced velocity $\mathbf{v}^*$ is more conveniently formulated and numerically implemented in terms of its vector streamfunction $\boldsymbol{\Psi}$, where

$$\mathbf{v}^* = \nabla \wedge \boldsymbol{\Psi}. \tag{16.15}$$

McDougall and McIntosh (2001) motivate the name *quasi-Stokes streamfunction* for $\boldsymbol{\Psi}$. Following the discussion in Section 9.2.2 of Griffies (2004), we identify the skew tracer flux associated with the quasi-Stokes streamfunction

$$F = -\nabla C \wedge \boldsymbol{\Psi}. \tag{16.16}$$

In component form, using the summation convention, this flux can be written

$$\begin{aligned} F^m &= -\epsilon^{mnp}\, C_{,n}\, \Upsilon_p \\ &= -A^{mn}\, C_{,n} \end{aligned} \tag{16.17}$$

[3] Additionally, one of the slope tapering schemes proposed by Gerdes et al. (1991) (a quadratic tapering scheme) or Danabasoglu and McWilliams (1995) (an exponential tapering scheme) is used to taper the neutral diffusive fluxes to horizontal in the depths shallower than D_{mom4p0}. Sensitivity of the simulation to the transition from neutral diffusion to horizontal diffusion has generally been found to be far less than sensitivity to the treatment of the eddy induced skew transport.

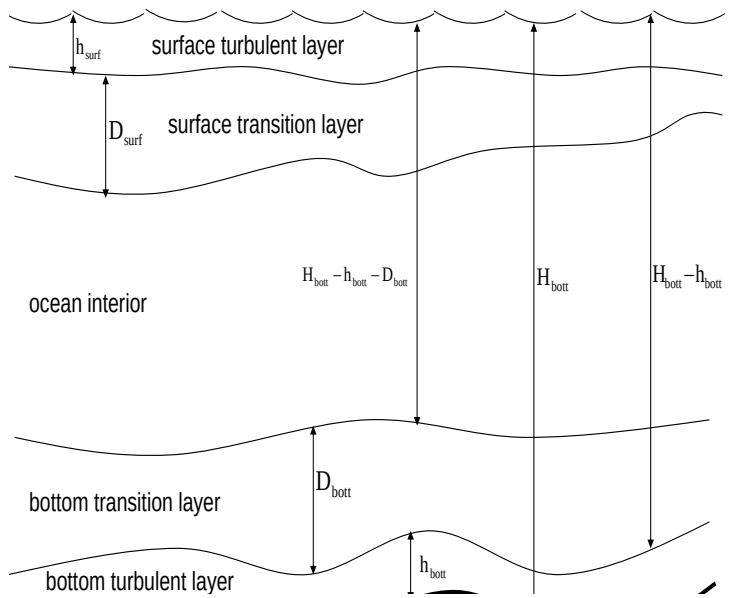

Figure 16.2: Summary of the regions for treating the neutral physics parameterizations, according to the notions described in Ferrari et al. (2008).

where the skew-symmetric tensor A^{mn} represents a reorganization of the vector streamfunction

$$\begin{aligned} A^{mn} &= \epsilon^{mnp}\,\Upsilon_p \\ &= \begin{pmatrix} 0 & \Psi_3 & -\Psi_2 \\ -\Psi_3 & 0 & \Psi_1 \\ \Psi_2 & -\Psi_1 & 0 \end{pmatrix}, \end{aligned} \tag{16.18}$$

and ϵ^{mnp} is the totally antisymmetric Levi-Civita tensor. It is sufficient to work with the *vertical gauge* described in Section 9.2.2 of Griffies (2004), whereby only the horizontal components of $\boldsymbol{\Psi}$ are non-zero

$$\Psi_3 = 0. \tag{16.19}$$

In the remainder of this section, we detail the form that the quasi-Stokes streamfunction takes within the regions identified in Section 16.2. This discussion follows Ferrari et al. (2008). In Section 16.4, we specialize the results to the quasi-Stokes streamfunction prescribed by the parameterization of Gent and McWilliams (1990) and Gent et al. (1995)

16.3.1 Surface turbulent boundary layer

For the upper surface turbulent boundary layer discussed in Section 16.2.1, we assume the eddy induced velocity has zero vertical shear, which means that the streamfunction is a linear function of water column thickness within this region. Because the streamfunction has the kinematic

interpretation of a horizontal transport between a given depth range set by the mean depths of isopycnals (see for example Sections 9.3.5 and 9.5.2 of Griffies (2004) as well as McDougall and McIntosh (2001)), the quasi-Stokes streamfunction vanishes at the ocean surface. Hence, the linear thickness dependence of $\mathbf{\Psi}$ within the surface turbulent region takes the form

$$\mathbf{\Psi}_{\text{surf}} = \left(\frac{h}{h_{\text{surf}}}\right) \mathbf{\Phi}_{\text{surf}}(x, y, t) \quad \text{for } 0 \leq h \leq h_{\text{surf}}. \tag{16.20}$$

The streamfunction $\mathbf{\Phi}_{\text{surf}}$ is determined by matching conditions across the transition region into the ocean interior. Note that this form for the streamfunction assumes a nonzero surface boundary layer thickness.

16.3.2 Surface transition region

To ensure that the eddy induced velocity is smoothly interpolated from the interior into the surface turbulent boundary layer, it is necessary for the quasi-Stokes streamfunction to satisfy the following boundary conditions

$$\mathbf{\Psi}_{\text{surf-trans}} = \begin{cases} \mathbf{\Psi}_{\text{surf}} & h = h_{\text{surf}} \\ \mathbf{\Psi}_{\text{interior}} & h = h_{\text{surf}} + D_{\text{surf}}, \end{cases} \tag{16.21}$$

and for its vertical derivative to satisfy

$$\partial_h \mathbf{\Psi}_{\text{surf-trans}} = \partial_h \mathbf{\Psi}_{\text{interior}} \qquad h = h_{\text{surf}} + D_{\text{surf}}. \tag{16.22}$$

Matching first at the bottom of the surface turbulent boundary layer, where $h = h_{\text{surf}}$ and where we insist on continuity of the streamfunction, leads us to take the surface transition region streamfunction in the form

$$\mathbf{\Psi}_{\text{surf-trans}} = \left(\frac{h - h_{\text{surf}}}{D_{\text{surf}}}\right)^2 \mathbf{\Phi}_{\text{surf-trans}} + \left(\frac{h}{h_{\text{surf}}}\right)^2 \mathbf{\Phi}_{\text{surf}}. \tag{16.23}$$

The quadratic depth dependence is *chosen* to provide a linear interpolation of the eddy induced velocity from the interior to the surface turbulent boundary layer.

Matching now at the bottom of the surface transition layer, where $h = h_{\text{surf}} + D_{\text{surf}}$ and we insist on continuity of the streamfunction *and* its vertical derivative, leads to

$$\mathbf{\Phi}_{\text{surf}} = \left(\frac{h_{\text{surf}}}{h_{\text{surf}} + D_{\text{surf}}}\right) \left(\mathbf{\Psi}^{(+)}_{\text{interior}} - \frac{D_{\text{surf}}}{2} \partial_h \mathbf{\Psi}^{(+)}_{\text{interior}}\right) \tag{16.24}$$

$$\mathbf{\Phi}_{\text{surf-trans}} = -\left(\frac{D_{\text{surf}}}{h_{\text{surf}}}\right) \left(\mathbf{\Psi}^{(+)}_{\text{interior}} - \frac{h_{\text{surf}} + D_{\text{surf}}}{2} \partial_h \mathbf{\Psi}^{(+)}_{\text{interior}}\right), \tag{16.25}$$

where again $\partial_h = -\partial_z$, and where

$$\mathbf{\Psi}^{(+)}_{\text{interior}} = \mathbf{\Psi}_{\text{interior}}(h = h_{\text{surf}} + D_{\text{surf}}) \tag{16.26}$$

is the interior streamfunction at the top of the interior region; i.e., base of the surface transition layer, and $\partial_h \mathbf{\Psi}^{(+)}_{\text{interior}}$ is its derivative. As a check on the manipulations, note that as the transition layer thickness vanishes, the streamfunctions reduce to $\mathbf{\Phi}_{\text{surf}} = \mathbf{\Psi}^{(+)}_{\text{interior}}$ and $\mathbf{\Phi}_{\text{surf-trans}} = 0$. In order for this limit to be well defined for the quasi-Stokes streamfunction $\mathbf{\Phi}_{\text{surf-trans}}$, we add a positive number $\epsilon = 10^{-20}$ to D_{surf} in the denominator of the first term on the right side of equation (16.23).

16.3.3 Bottom transition region

Just as for the surface transition region, the eddy induced velocity is smoothly interpolated from the interior into the bottom turbulent boundary layer so long as the quasi-Stokes streamfunction satisfies

$$\mathbf{\Psi}_{\text{bott-trans}} = \begin{cases} \mathbf{\Psi}_{\text{bott}} & h = H^*_{\text{bott}} \\ \mathbf{\Psi}_{\text{interior}} & h = H^*_{\text{bott}} - D_{\text{bott}}, \end{cases} \tag{16.27}$$

and its vertical derivative satisfies

$$\partial_h \mathbf{\Psi}_{\text{bott-trans}} = \partial_h \mathbf{\Psi}_{\text{interior}} \qquad h = H^*_{\text{bott}} - D_{\text{bott}}, \tag{16.28}$$

where

$$H^*_{\text{bott}} = H_{\text{bott}} - h_{\text{bott}} \tag{16.29}$$

is a useful shorthand.

Matching first at the top of the bottom turbulent boundary layer, where $h = H^*_{\text{bott}}$ and where we insist on continuity of the streamfunction, leads us to take the bottom transition region streamfunction in the form

$$\mathbf{\Psi}_{\text{bott-trans}} = \left(\frac{H^*_{\text{bott}} - h}{D_{\text{bott}}}\right)^2 \mathbf{\Phi}_{\text{bott-trans}} + \left(\frac{H_{\text{bott}} - h}{h_{\text{bott}}}\right)^2 \mathbf{\Phi}_{\text{bott}}. \tag{16.30}$$

As for the surface, the quadratic depth dependence is *chosen* to provide a linear interpolation of the eddy induced velocity from the interior to the bottom turbulent boundary layer.

Matching now at the top of the bottom transition region, where $h = H^*_{\text{bott}} - D_{\text{bott}}$ and we insist on continuity of the streamfunction *and* its vertical derivative, leads to

$$\mathbf{\Phi}_{\text{bott}} = \left(\frac{h_{\text{bott}}}{h_{\text{bott}} + D_{\text{bott}}}\right) \left(\mathbf{\Psi}^{(-)}_{\text{interior}} + \frac{D_{\text{bott}}}{2}\, \partial_h \mathbf{\Psi}^{(-)}_{\text{interior}}\right) \tag{16.31}$$

$$\mathbf{\Phi}_{\text{bott-trans}} = -\left(\frac{D_{\text{bott}}}{h_{\text{bott}}}\right) \left(\mathbf{\Psi}^{(-)}_{\text{interior}} + \frac{h_{\text{bott}} + D_{\text{bott}}}{2}\, \partial_h \mathbf{\Psi}^{(-)}_{\text{interior}}\right), \tag{16.32}$$

where

$$\mathbf{\Psi}^{(-)}_{\text{interior}} = \mathbf{\Psi}_{\text{interior}}(h = H^*_{\text{bott}} - D_{\text{bott}}) \tag{16.33}$$

is the interior streamfunction at the bottom of the interior region (i.e., top of the bottom transition layer).

16.3.4 Bottom turbulent boundary layer

Just as for the surface, the quasi-Stokes stremfunction vanishes at the ocean bottom, and we assume it has a linear thickness dependence within the bottom turbulent boundary layer, thus leading to

$$\mathbf{\Psi}_{\text{bott}} = \left(\frac{H_{\text{bott}} - h}{h_{\text{bott}}}\right) \mathbf{\Phi}_{\text{bott}} \quad \text{for } H_{\text{bott}} - h_{\text{bott}} \le h \le H_{\text{bott}}. \tag{16.34}$$

The streamfunction $\mathbf{\Phi}_{\text{bott}}$ (equation (16.31)) was determined by matching across the bottom transition region.

16.3.5 Summary of the streamfunction algorithm

Based on the previous derivation, the quasi-Stokes streamfunction $\mathbf{\Psi}$ can be written in the form

$$\begin{aligned}\mathbf{\Psi} = &\mathcal{H}_{\text{surf}} \left(\frac{h}{h_{\text{surf}}}\right) \mathbf{\Phi}_{\text{surf}} \\ &+ \mathcal{H}_{\text{surf-trans}} \left[\left(\frac{h - h_{\text{surf}}}{D_{\text{surf}}}\right)^2 \mathbf{\Phi}_{\text{surf-trans}} + \left(\frac{h}{h_{\text{surf}}}\right)^2 \mathbf{\Phi}_{\text{surf}}\right] \\ &+ \mathcal{H}_{\text{interior}} \mathbf{\Psi}_{\text{interior}} \\ &+ \mathcal{H}_{\text{bott-trans}} \left[\left(\frac{H^*_{\text{bott}} - h}{D_{\text{bott}}}\right)^2 \mathbf{\Phi}_{\text{bott-trans}} + \left(\frac{H_{\text{bott}} - h}{h_{\text{bott}}}\right)^2 \mathbf{\Phi}_{\text{bott}}\right] \\ &+ \mathcal{H}_{\text{bott}} \left(\frac{H_{\text{bott}} - h}{h_{\text{bott}}}\right) \mathbf{\Phi}_{\text{bott}}.\end{aligned} \tag{16.35}$$

Here, the on-off functions $\mathcal{H}$ are unity in the labelled region, and zero outside. The regional streamfunctions are given by

$$\mathbf{\Phi}_{\text{surf}} = \left(\frac{h_{\text{surf}}}{h_{\text{surf}} + D_{\text{surf}}}\right) \left(\mathbf{\Psi}^{(+)}_{\text{interior}} + \frac{D_{\text{surf}}}{2} \partial_z \mathbf{\Psi}^{(+)}_{\text{interior}}\right) \tag{16.36}$$

$$\mathbf{\Phi}_{\text{surf-trans}} = -\left(\frac{D_{\text{surf}}}{h_{\text{surf}}}\right) \left(\mathbf{\Psi}^{(+)}_{\text{interior}} + \frac{h_{\text{surf}} + D_{\text{surf}}}{2} \partial_z \mathbf{\Psi}^{(+)}_{\text{interior}}\right) \tag{16.37}$$

$$\mathbf{\Phi}_{\text{bott-trans}} = -\left(\frac{D_{\text{bott}}}{h_{\text{bott}}}\right) \left(\mathbf{\Psi}^{(-)}_{\text{interior}} - \frac{h_{\text{bott}} + D_{\text{bott}}}{2} \partial_z \mathbf{\Psi}^{(-)}_{\text{interior}}\right) \tag{16.38}$$

$$\mathbf{\Phi}_{\text{bott}} = \left(\frac{h_{\text{bott}}}{h_{\text{bott}} + D_{\text{bott}}}\right) \left(\mathbf{\Psi}^{(-)}_{\text{interior}} - \frac{D_{\text{bott}}}{2} \partial_z \mathbf{\Psi}^{(-)}_{\text{interior}}\right), \tag{16.39}$$

where

$$\mathbf{\Psi}^{(+)}_{\text{interior}} = \mathbf{\Psi}_{\text{interior}}(h = h_{\text{surf}} + D_{\text{surf}}) \tag{16.40}$$

$$\mathbf{\Psi}^{(-)}_{\text{interior}} = \mathbf{\Psi}_{\text{interior}}(h = H_{\text{bott}} - h_{\text{bott}} - D_{\text{bott}}) \tag{16.41}$$

are the interior streamfunctions evaluated at the transition region boundaries (see Figure 16.2).

There are two main subroutines in `nphysicsB` used to compute this streamfunction.

- `neutral_blayer`: This routine computes properties of the various boundary and transition regions. It is a tedious calculation due to the multiple regions that must be characterized.
  - Thicknesses: h_{surf}, D_{surf}, h_{bott}, D_{bott}; each are a function of (i, j, triad), where "triad" refers to the four triads surrounding each grid point.
  - Streamfunctions: $\mathbf{\Phi}_{\text{surf}}$, $\mathbf{\Phi}_{\text{surf-trans}}$, $\mathbf{\Phi}_{\text{bott-trans}}$, and $\mathbf{\Phi}_{\text{bott}}$; each are a function of (i, j, triad).
  - Quasi-Stokes streamfunction accumulated over the boundary regions. This streamfunction is zero in the interior, and nonzero within the boundary layers. It is a function of (i, j, k).

- `fz_terms`, `fx_flux`, `fy_flux`, and `fz_flux`: These routines compute the flux components for the neutral physics parameterization, including the interior quasi-Stokes streamfunction $\mathbf{\Psi}_{\text{interior}}$. These fluxes are computed using information from the `neutral_blayer` routine. As detailed in Griffies (2004), the fluxes for each (i, j, k) point are the grid weighted sum of the four triads surrounding each point.

16.4 Specializing the quasi-Stokes streamfunction

We discuss here some specific forms for the quasi-Stokes streamfunction.

16.4.1 GM90 streamfunction

The quasi-Stokes streamfunction for the parameterization of Gent and McWilliams (1990) and Gent et al. (1995) is given by

$$\begin{aligned} \mathbf{\Psi}_{\text{interior}} &= \hat{\mathbf{z}} \wedge A_{\text{gm}}\, \mathbf{S} \\ &= A_{\text{gm}}\, (-S_y\, \hat{\mathbf{x}} + S_x\, \hat{\mathbf{y}}), \end{aligned} \tag{16.42}$$

which is equivalent to a skew-symmetric tensor (Section 13.5 of Griffies (2004))

$$\mathbf{A} = A_{\text{gm}} \begin{pmatrix} 0 & 0 & -S_x \\ 0 & 0 & -S_y \\ S_x & S_y & 0 \end{pmatrix}. \tag{16.43}$$

In these equations, $\mathbf{S} = (S_x, S_y, 0)$ is the neutral slope vector computed as

$$\mathbf{S} = -\left(\frac{\rho_{,s}\, \nabla_z\, s + \rho_{,\theta}\, \nabla_z\, \theta}{\rho_{,s}\, s_{,z} + \rho_{,\theta}\, \theta_{,z}} \right). \tag{16.44}$$

The diffusivity A_{gm} can be computed one of many ways, with options described in Section 14.4 of Griffies (2004). In principle, the `nphysicsB` implementation of the quasi-Stokes streamfunction (16.42) can be generalized to other streamfunctions motivated by other theoretical arguments.

16.4.2 Streamfunction in completely unstratified regions

For regions that are completely unstratified in the vertical, such as in regions of strong surface buoyancy forcing and/or in shallow shelf regions, we specify the following quadratic dependence for the quasi-Stokes streamfunction, with zero values at the top and bottom boundaries

$$\mathbf{\Psi}(h) = \left(\frac{4\, h\, (H - h)}{H^2} \right) \mathbf{\Psi}_{\text{max}}, \tag{16.45}$$

where H is the thickness of the fully turbulent column, and

$$h = \eta - z \tag{16.46}$$

is the thickness of the fluid between depth z and the surface at $z = \eta$.

Two methods are available to determine the maximum absolute value of the streamfunction $\mathbf{\Psi}_{\mathsf{max}}$. The first sets $\mathbf{\Psi}_{\mathsf{max}}$ according to a namelist specified maximum slope parameter, with 1/100 a typical value. The problem with this specification is that it will provide a nontrivial streamfunction in regions where both the vertical and horizontal density stratification are small. In contrast, one may expect the streamfunction in an eddying model to remain quite small in such regions, due to the absence of horizontal density gradients. This observation motivates an alternative, whereby the streamfunction is set according to the vertical average of the diffusivity times the horizontal density gradient[4]

$$\mathbf{\Psi}_{\mathsf{max}} = -\hat{\mathbf{z}} \wedge \frac{\overline{A_{\mathsf{gm}} \nabla_z \rho}^{(z)}}{\rho^o_{,z}}, \tag{16.47}$$

where $\rho^o_{,z}$ is a constant reference vertical density derivative,

$$\overline{A_{\mathsf{gm}} \nabla_z \rho}^{(z)} = \frac{\sum_{k=1}^{\mathsf{kbot}} \mathrm{rho_dzt}\, A_{\mathsf{gm}} \nabla_z \rho}{\sum_{k=1}^{\mathsf{kbot}} \mathrm{rho_dzt}} \tag{16.48}$$

is the vertically averaged diffusivity times the horizontal density gradient, averaged over the depth of the vertically unstratified region. So that we are computing the horizontal stratification, rather than the horizontal gradient of the *in situ* density, we compute the horizontal density gradient according to

$$\nabla_z \rho = \rho_{,\theta} \nabla_z \theta + \rho_{,S} \nabla_z S, \tag{16.49}$$

with θ the potential or conservative temperature, S the salinity, and $\rho_{,\theta}$ and $\rho_{,S}$ the density expansion coefficients whose values are determined by the temperature, salinity, and pressure at a common point for each vertical level. The streamfunction (16.47) corresponds to the following anti-symmetric transport tensor

$$A^{mn} = \left(\frac{1}{-\rho^o_{,z}}\right) \begin{pmatrix} 0 & 0 & -\overline{A_{\mathsf{gm}}\, \rho_{,x}}^{(z)} \\ 0 & 0 & -\overline{A_{\mathsf{gm}}\, \rho_{,y}}^{(z)} \\ \overline{A_{\mathsf{gm}}\, \rho_{,x}}^{(z)} & \overline{A_{\mathsf{gm}}\, \rho_{,y}}^{(z)} & 0 \end{pmatrix}. \tag{16.50}$$

16.4.3 Local N^2 dependent diffusivity

Ferreira et al. (2005) and Ferreira and Marshall (2006) argue for the relevance of a local N^2 dependence to the diffusivity used to compute the quasi-Stokes streamfunction. That is,

$$A_{\mathsf{gm}} = A^{2d}_{\mathsf{gm}} \left(N/N_o\right)^2 \tag{16.51}$$

where A^{2d}_{gm} can be any two-dimensional diffusivity, N is the buoyancy frequency, and N_o is a reference buoyancy frequency. This choice for the diffusivity greatly simplifies the quasi-Stokes streamfunction, which now takes the form

$$\begin{aligned} \mathbf{\Psi} &= \hat{\mathbf{z}} \wedge A_{\mathsf{gm}} \mathbf{S} \\ &= -\hat{\mathbf{z}} \wedge A^{2d}_{\mathsf{gm}} \frac{\nabla_z \rho}{\rho^o_{,z}}, \end{aligned} \tag{16.52}$$

[4]This streamfunction has a form analogous to that considered with the TEM approach in Section 17.1. It is also similar to that employed with the submesoscale parameterization of Chapter 18.

which corresponds to the anti-symmetric tensor

$$A^{mn} = \left(\frac{A^{2d}_{\mathsf{gm}}}{-\rho^o_{,z}} \right) \begin{pmatrix} 0 & 0 & -\rho_{,x} \\ 0 & 0 & -\rho_{,y} \\ \rho_{,x} & \rho_{,y} & 0 \end{pmatrix} . \tag{16.53}$$

In these expressions, $\rho^o_{,z}$ is a reference vertical density stratification corresponding to the reference buoyancy frequency N_o.

Numerical treatment of vertically unstratified regions becomes trivial with this streamfunction, since it is only the horizontal stratification which is required and there are no divisions by small numbers. We have implemented this streamfunction in MOM4p1 using the namelist option `agm_local_n2`.

16.5 Discussion of some details

During the development of the algorithm described in this chapter, tests were run with an idealized sector model forced with temperature restoring at the surface. This forcing produced deep convection at the poleward end of the domain, thus ensuring a deep mixed layer in this region. There was no seasonal nor diurnal cycle, and thus no active mixed layer processes other than deep convection driven by buoyancy forcing. This test problem exposed many sensitivities that helped to guide the development of neutral physics within the boundary layer. Notably, much of this sensitivity is removed in realistic simulations possessing an active mixed layer. The purpose of this section is to summarize some of the issues and methods used to address the issues.

16.5.1 Step-like features in the upper ocean

The presence of a nontrivial quasi-Stokes streamfunction within the upper ocean can lead to step-like features in the density field. These steps resulted in (or were the result of) large neutral slopes mixed with small slopes. To overcome this difficulty, it is useful to compute the turbulent boundary layer depth according to the parameterized mixed layer physics *plus* any region beneath this "mixed layer" that has huge neutral slopes. For idealized simulations, an objective specification of the surface turbulent boundary layer must be based on the neutral slopes.

16.5.2 Handling the triads of slopes

The scheme of Griffies et al. (1998) employs four triad slopes for each of the two horizontal directions at each tracer point. One may be motivated to then produce a corresponding set of streamfunctions and boundary layer regions for each triad. Doing so introduces a tremendous level of added computation, which is arguably unwarranted. Alternatively, the method chosen in MOM4p1 is to determine the boundary layer regions based on the maximum absolute slope from amongst the triad slopes occurring at each tracer point. Additionally, we smoothed the resulting region thicknesses and corresponding streamfunctions in order to ensure that the scheme produces parameterized transport that has large spatial scales.

16.5.3 Ensuring there are no negatively stratified regions

The Gent and McWilliams (1990) scheme assumes a stably stratified column. Our aims in this chapter are to merge their methods into the boundary regions where stratification can be zero or negative. In an ocean model run with convective adjustment, such as the complete adjustment scheme of Rahmstorf (1993), there are no regions of negative stratification. Ensuring nonnegative stratification has been found to be essential when allowing for a nontrivial Gent and McWilliams (1990) quasi-Stokes streamfunction in weakly stratified regions of the model. If negative stratification is allowed, depending on how the quasi-Stokes streamfunction is computed, it can further destabilize the profile, with the resulting simulation rapidly degenerating into unphysical noise.

In MOM4p0, we recommended the use of Rahmstorf (1993) convection as a follow-on to the use of large vertical diffusivities commonly found in mixed layer parameterizations. This approach then ensures proper behaviour of the quasi-Stokes streamfunction in boundary regions. In MOM4p1, we provide an alternative calculation of the vertical stratification so to remove the need to always use Rahmstorf (1993) convection. Here, for purposes of computing the neutral slope, we numerically compute the vertical stratification as

$$\left(\frac{\partial \rho}{\partial z}\right)^{\text{effective}} = \min\left[\left(\frac{\partial \rho}{\partial z}\right), -\epsilon\right]. \tag{16.54}$$

That is, we only employ stable vertical stratification for purposes of computing the neutral slope vector used in the neutral physics scheme. This *trick* facilitates the use of neutral physics for all slopes, without incurring spurious numerical artefacts in those regions of negative stratification. We enable this approach in the neutral physics modules `nphysicsA` and `nphysicsB` (the `nphysicsC` module does not compute neutral slopes).

16.6 Lateral diffusive parameterization

The lateral diffusive parameterization is simpler to characterize than the quasi-Stokes streamfunction, since there is no quadratic transition region. Instead, the diffusive fluxes are linearly tapered from their internal neutral direction form, through the transition regions into the boundary oriented form in the turbulent boundary layers. These considerations lead to the following downgradient lateral diffusive tracer fluxes.

- Surface turbulent boundary layer: $0 \le h \le h_{\text{surf}}$. The diffusive flux is oriented parallel to the surfaces of constant generalized vertical coordinate s, which in MOM4p1 are quasi-horizontal within the upper ocean. Therefore,

$$\mathbf{F}_{\text{surf}} = -A_I \, \nabla_s \, C, \tag{16.55}$$

  where ∇_s is the lateral gradient along surfaces of constant generalized vertical coordinate.

- Surface transition region: $h_{\text{surf}} \le h \le h_{\text{surf}} + D_{\text{surf}}$. The diffusive flux linearly tapers from the interior form to the surface form

$$\mathbf{F}_{\text{surf-trans}} = \left(\frac{h - h_{\text{surf}}}{D_{\text{surf}}}\right) \mathbf{F}_{\text{interior}} + \left(\frac{h_{\text{surf}} + D_{\text{surf}} - h}{D_{\text{surf}}}\right) \mathbf{F}_{\text{surf}}. \tag{16.56}$$

- Ocean interior: $h_{\text{surf}} + D_{\text{surf}} \leq h \leq H_{\text{bott}} - (h_{\text{bott}} + D_{\text{bott}})$. Here, the flux is taken from the small slope neutral diffusion operator (Section 5.2.3)

$$\mathbf{F}_{\text{interior}} = -A_I \left(\nabla_\rho C + \hat{\mathbf{z}}\, \mathbf{S} \cdot \nabla_\rho C \right). \tag{16.57}$$

- Bottom transition region: $H_{\text{bott}} - (h_{\text{bott}} + D_{\text{bott}}) \leq h \leq H_{\text{bott}} - h_{\text{bott}}$. As with the surface transition region, we prescribe a linear tapering from the interior flux to the bottom turbulent boundary layer flux

$$\mathbf{F}_{\text{bott-trans}} = \left(\frac{h - (H^*_{\text{bott}} - D_{\text{bott}})}{D_{\text{bott}}} \right) \mathbf{F}_{\text{bott}} + \left(\frac{H^*_{\text{bott}} - h}{D_{\text{bott}}} \right) \mathbf{F}_{\text{interior}}, \tag{16.58}$$

  where again $H^*_{\text{bott}} = H_{\text{bott}} - h_{\text{bott}}$ is the thickness of water above the bottom turbulent boundary layer.

- Bottom turbulent boundary layer: $H_{\text{bott}} - h_{\text{bott}} \leq h \leq H_{\text{bott}}$. Here, the topography orients the lateral diffusive flux, and so we take

$$\mathbf{F}_{\text{bott}} = -A_\sigma \nabla_\sigma C, \tag{16.59}$$

  where $\sigma = (z - \eta)/(H + \eta)$ is the topography following σ-coordinate, and A_σ is a diffusivity that may be enhanced when dense water lies above light water within the bottom turbulent layer, as prescribed by Beckmann and Döscher (1997). Further details on this method are discussed in Chapter 19.

The diffusive flux in the transition regions can be simplified, and doing so allows for a straightforward numerical implementation. For this purpose, write equation (16.56) in the form

$$\begin{aligned} \mathbf{F}_{\text{surf-trans}} &= \left(\frac{h - h_{\text{surf}}}{D_{\text{surf}}} \right) \mathbf{F}_{\text{interior}} + \left(\frac{h_{\text{surf}} + D_{\text{surf}} - h}{D_{\text{surf}}} \right) \mathbf{F}_{\text{surf}} \\ &= \mathbf{F}_{\text{surf}} + \left(\frac{h - h_{\text{surf}}}{D_{\text{surf}}} \right) (\mathbf{F}_{\text{interior}} - \mathbf{F}_{\text{surf}}). \end{aligned} \tag{16.60}$$

Now substitute the tensor form of the interior flux taken from the small-angle neutral diffusion tensor (see Section 14.1.4 of Griffies (2004)) to find

$$\mathbf{F}_{\text{surf-trans}} = \mathbf{F}_{\text{surf}} - A_I \left(\frac{h - h_{\text{surf}}}{D_{\text{surf}}} \right) \begin{pmatrix} 0 & 0 & S_x \\ 0 & 0 & S_y \\ S_x & S_y & S^2 \end{pmatrix} \begin{pmatrix} C_{,x} \\ C_{,y} \\ C_{,z} \end{pmatrix}. \tag{16.61}$$

Hence, it is only the off-diagonal piece of the flux which is linearly scaled, along with the (3,3) diagonal term. The diagonal piece in the horizontal remains unscaled. In practice, we implement the same relation at the bottom, which means that if sigma transport is used (Chapter 19), we will have both horizontal and sigma oriented diffusion in the bottom turbulent layer.

16.7 Computation of the Rossby radius

The Rossby radius is needed for computing the transition layer thickness using the algorithm described in Section 16.2.2. We detail here the methods used in MOM4p1 for its computation.

Outside an equatorial band of roughly $\pm 5^\circ$, the mth-mode Rossby radius takes the form

$$\lambda_m = \frac{c_m}{|f|}, \tag{16.62}$$

where c_m is the phase speed of the mth-mode ($m \geq 1$) gravity wave in a non-rotating, continuously stratified flat bottom ocean (Gill, 1982). Within an equatorial band of $\pm 5^\circ$, the Rossby radius is given by

$$\lambda_m = \left(\frac{c_m}{2\,\beta}\right)^{1/2}, \tag{16.63}$$

where $\beta = f_{,y}$ is the meridional derivative of the Coriolis parameter. An approximate gravity wave phase speed can be obtained by methods described in Chelton et al. (1998), and it takes the form[5]

$$c_m \approx \frac{1}{m\,\pi} \int_{-H}^{\eta} N \, \mathrm{d}z. \tag{16.64}$$

The squared buoyancy frequency is written

$$\begin{aligned} N^2 &= -(g/\rho)\,(\rho_{,s}\, s_{,z} + \rho_{,\theta}\, \theta_{,z}) \\ &= g\,(\beta\, s_{,z} - \alpha\, \theta_{,z}), \end{aligned} \tag{16.65}$$

where

$$\alpha = \partial_\theta \, \ln \rho \tag{16.66}$$

$$\beta = \partial_s \, \ln \rho \tag{16.67}$$

are the thermal expansion and saline contraction coefficients, respectively. The Rossby radius used in MOM4p1 for the transition layer thickness in Section 16.2.2 is taken to be the first baroclinic wave ($m = 1$) in equaion (16.64).

In addition to computing the Rossby radius as just described, we follow Large et al. (1997) by restricting the computed Rossby radius within the range

$$R_{\mathsf{min}} \leq R_{\mathsf{rossby}} \leq R_{\mathsf{max}}, \tag{16.68}$$

where Large et al. (1997) set

$$R_{\mathsf{min}} \approx 15\mathsf{km} \tag{16.69}$$

$$R_{\mathsf{max}} \approx 100\mathsf{km}. \tag{16.70}$$

16.8 Method for obtaining low pass filtered fields

For determining the upper and lower turbulent boundary layer thicknesses, we take values from other portions of the model, such as the turbulent mixed layer schemes. These schemes produce

[5]Even though the gravity wave speed feels the bottom, since the vertical integral in equation (16.64) extends over the full depth range, the study by Chelton et al. (1998) showed that the Rossby radius over the bulk of the World Ocean, outside of shelf regions, is dominated by the inverse Coriolis dependence (see their Figure 6).

boundary layer thicknesses which have relatively rapid time scales for fluctuations, such as days. In contrast, for the neutral physics scheme, we are interested in low pass or time filtered variations in the boundary layers, on the order of weeks to months. Obtaining the low pass filtered boundary layer information is cumbersome if we aim to save previous time step values and form the traditional time average.

Instead, we prefer a method suggested by Anand Gnanadesikan (personal communication 2005), whereby the low pass, or slow, variable A^{slow} is obtained by solving the first order equation

$$\frac{\partial A^{\text{slow}}}{\partial t} = -\left(\frac{A^{\text{slow}} - A^{\text{fast}}}{\tau_{\text{damp}}}\right), \tag{16.71}$$

where A^{fast} is the rapidly varying boundary layer depth, and τ_{damp} is a damping time on the order

$$\tau_{\text{damp}} \approx 30\,\text{days}. \tag{16.72}$$

Taking a forward time step for this equation leads to the discrete form

$$A^{\text{slow}}(\tau + \Delta\tau) = (1-\gamma)\, A^{\text{slow}}(\tau) + \gamma\, A^{\text{fast}} \tag{16.73}$$

where

$$\gamma = \Delta\tau/\tau_{\text{damp}}. \tag{16.74}$$

We use the same algorithm for evolving the diffusivity computed for the neutral physics scheme based on any of the closure ideas discussed in Section 14.4 of Griffies (2004). In this way, the diffusivity fluctuations are damped in time, with major changes occurring only on the slower time scale set by γ.

16.9 Regularized slopes

In general, a model such as MOM4p1 can realize any value for the density, which contrasts with an isopycnal model where densities are quantized. The continuous range of density allows, in particular, for very fine structure in the vertical. This structure is sometimes the result of numerical methods and roundoff, and can lead to small step-like features in the vertical. In the presence of these steps, the vertical derivative of density, needed to compute the neutral slopes and the buoyancy frequency, can exhibit discontiuous features, with, say, infinite slopes interspersed with finite slopes. This behaviour creates difficulties with the neutral diffusion and skew diffusion fluxes, especially with the quasi-Stokes streamfunction.

To regularize the slopes computed in the neutral physics scheme, we provide two optional forms of smoothing: one in the horizontal (via a Laplacian diffusion) and one in the vertical (via a 1-2-1 filter). The smoothing is performed on the vertical derivative of density prior to computing the slopes. Formally, this smoothing breaks the integrity of the temperature and salinity triads described in Griffies et al. (1998). However, the payoff is to produce neutral fluxes that are well behaved, and perform in a manner consistent with that expected from the physics. Experiments with and without smoothing are encouraged to see if it is needed for a particular simulation.

CHAPTER
SEVENTEEN

Parameterization of form drag

This chapter is a placeholder for documentation of the form drag parameterizations available in MOM4p1. At present, MOM4p1 has implemented the schemes proposed by Greatbatch and Lamb (1990), Aiki et al. (2004), and Ferreira and Marshall (2006). The code is available in the module

`mom4/ocean_param/mixing/ocean_form_drag_mod`.

These schemes are experimental and have not been thoroughly used at GFDL.

17.1 Regarding the TEM approach

We comment here on the relevance of implementing the Gent and McWilliams (1990) scheme via the tracer equation, as traditionally done in MOM as motivated by Gent et al. (1995) and Griffies (1998), versus the alternative, which adds a vertical stress to the horizontal momentum equation, as recently implemented in a global model by Ferreira and Marshall (2006). When adding a stress to the momentum equation, the prognostic velocity variable is interpreted as the residual mean, or effective velocity, rather than the traditional Eulerian mean velocity. This *transformed Eulerian mean* (TEM) interpretation is quite elegant, since it is the residual mean velocity that advects tracers in a coarsely resolved (i.e., no mesoscale eddies) z-model, *not* the Eulerian mean velocity. The elegance is maintained so long as one need not compute the Eulerian mean velocity.

For many purposes, we do not require the Eulerian mean velocity, so the TEM momentum equation provides all the variables required to run an ocean model. However, the following considerations point to a need for the Eulerian mean velocity in cases of realistic ocean climate modeling.

- In computing the air-sea stress in realistic coupled climate models, it is important for many purposes to include the velocity of the ocean currents according to the discussion in Pacanowski (1987). The relevant currents for this calculation are the Eulerian mean currents, not the residual mean.

- When computing the Richardson number commonly required for mixed layer parameterizations, we require the vertical shear of the Eulerian mean velocity, not the vertical shear of the residual mean velocity.

There are two options that one may consider. First, one may choose to ignore the difference between the Eulerian mean and the residual mean velocity. Alternatively, one may choose to diagnose the Eulerian mean from the residual mean. The Eulerian mean velocity is available within a TEM ocean model, given the prognostic residual mean velocity plus a prescribed mesoscale eddy closure to compute the eddy induced velocity. Its calculation requires derivatives of the quasi-Stokes streamfunction to obtain the eddy-induced velocity, and one further derivative to compute the vertical shear. As discussed by Griffies (1998), this calculation can produce a rather noisy eddy induced velocity, especially near boundaries. Furthermore, there is no general principle guiding us in formulating a particular choice of discretization for the eddy induced velocity from a streamfunction. A noisy eddy induced velocity produces a noisy diagnosed Eulerian mean velocity, which then puts noise in the air-sea stress as well as the Richardson number. These numerical sources of noise are unacceptable for realistic climate modeling, and represent a practical barrier to making use of the TEM approach.

CHAPTER
EIGHTEEN

Restratification effects by submesoscale eddies

This chapter documents the MOM4p1 implementation of the parameterization by Fox-Kemper et al. (2008b), with further details discussed in Fox-Kemper et al. (2008a). This scheme parameterizes the restratification effects of submesoscale eddies in the ocean mixed layer. These effects occur on a time scale much shorter than the mesoscale eddies parameterized via the neutral physics scheme (Chapter 16).

18.1 Basics of the scheme

The parameterization is implemented via a vector streamfunction

$$\mathbf{\Psi} = \left(\frac{C_e \, \mu \, h^2 \, g \, \Delta s}{\rho_o \, L_f \, \sqrt{f^2 + \tau^{-2}}} \right) \hat{\mathbf{z}} \wedge \overline{\nabla \gamma}^z . \tag{18.1}$$

In this equation, we have

- $0.06 \le C_e \le 0.08$ is a dimensionless number;
- $\mu = [1 - (1 - 2\,d/h)^2]\,[1 + 5/21\,(1 - 2\,d/h)^2]$ is a non-negative vertical structure function in the mixed layer layer, with zero values outside the mixed layer, where $d \ge h$ and $d \le 0$;
- $d = -z + \eta$ is the depth of seawater, defined as the vertical distance from the ocean free surface;
- η is the deviation of the ocean free surface from the resting state at $z = 0$;
- g is the gravitational acceleration;
- h is the mixed layer thickness;
- $\overline{\nabla \gamma}^z$ is the mixed layer averaged horizontal gradient of locally referenced potential density;
- f is the Coriolis parameter;
- τ is a time scale for the submesoscale eddies (order few days);

- L_f is a length scale for the width of the submesoscale eddies (order 5km);
- Δs is the horizontal grid spacing;
- ρ_o is the constant Boussinesq density.

Written in components, the streamfunction is given by

$$\mathbf{\Psi} = \Gamma\, \mu\, (-\overline{\gamma_{,y}}^z, \overline{\gamma_{,x}}^z, 0), \tag{18.2}$$

where

$$\Gamma = \frac{C_e\, h^2\, g\, \Delta s}{\rho_o\, L_f\, \sqrt{f^2 + \tau^{-2}}} \tag{18.3}$$

is shorthand for the non-negative dimensionful scalar contributions, with physical dimensions $\mathrm{m}^6/(\mathrm{sec\ kg})$. The dimensionless function $\mu(z)$ carries the only vertical dependence of the streamfunction $\mathbf{\Psi}$.

We make the following observations.

- The formulation of Fox-Kemper et al. (2008b) is in terms of the mixed layer, rather than the planetary boundary layer. The reasoning is that the planetary boundary layer can be very small under stable buoyancy forcing. However, the submesoscale eddies remain even in these situations, so long as the mixed layer depth is nontrivial. MOM4p1 has an option for setting h according to either the mixed layer depth, or the planetary boundary layer depth.

- Fox-Kemper et al. (2008b) pose the parameterization in terms of the horizontal buoyancy gradient, which is related to the gradient of the locally referenced potential density via

$$-\rho_o\, \nabla\, b = g\, \nabla\, \gamma \tag{18.4}$$
$$= g\, (\gamma_{,\theta}\, \nabla\, \theta + \gamma_{,S}\, \nabla\, S), \tag{18.5}$$

  where θ is the potential temperature, S is the salinity, and

$$\gamma_{,\theta} = \partial\, \gamma / \partial\, \theta \tag{18.6}$$
$$\gamma_{,S} = \partial\, \gamma / \partial\, S \tag{18.7}$$

  are the density partial derivatives.

- The front length can either be a constant, or computed according to the first baroclinic Rossby radius over the mixed layer

$$L_f = \frac{h\, \overline{N}^z}{f} \tag{18.8}$$

  with $\overline{N}^z$ the buoyancy frequency averaged over the depth of the mixed layer, and h is the mixed layer thickness. Substitution of the front length (18.8) into the streamfunction (18.1) leads to

$$\mathbf{\Psi} = \left(\frac{C_e\, \mu\, h\, g\, \Delta s}{\rho_o\, \overline{N}^z} \right) \left(\frac{f}{\sqrt{f^2 + \tau^{-2}}} \right) \hat{\mathbf{z}} \wedge \overline{\nabla\, \gamma}^z. \tag{18.9}$$

  In this way, the streamfunction goes to zero as the equator is approached.

- The streamfunction can at times become quite large, in which case the model can be prone to instabilities. MOM4p1 thus provides the following means to limit the value of the streamfunction magnitude

$$\mathbf{\Psi}_{\text{limited}} = \text{sign}(\mathbf{\Psi})\ \min[v_{\text{max}}\,\Delta z, \text{abs}(\mathbf{\Psi})], \tag{18.10}$$

  where v_{max} is a namelist-specified velocity scale on the order of 1m/sec, and Δz is the grid cell thickness.

18.2 Skew tracer flux components

We implement the effects of the streamfunction (18.1) on tracer concentration via a skew diffusion, as defined by an anti-symmetric stirring tensor

$$\mathbf{A} = \Gamma\,\mu \begin{pmatrix} 0 & 0 & -\overline{\gamma_{,x}}^z \\ 0 & 0 & -\overline{\gamma_{,y}}^z \\ \overline{\gamma_{,x}}^z & \overline{\gamma_{,y}}^z & 0 \end{pmatrix} \tag{18.11}$$

acting on the gradient of the tracer concentration. The components to the skew tracer flux are given by

$$F^{(x)} = \Gamma\,\mu\,\overline{\gamma_{,x}}^z\,C_{,z} \tag{18.12}$$

$$F^{(y)} = \Gamma\,\mu\,\overline{\gamma_{,y}}^z\,C_{,z} \tag{18.13}$$

$$F^{(z)} = -\Gamma\,\mu\,\overline{\nabla\,\gamma}^z \cdot \nabla\,C \tag{18.14}$$

which can be written in terms of the vector streamfunction

$$F^{(x)} = \Psi^{(y)}\,C_{,z} \tag{18.15}$$

$$F^{(y)} = -\Psi^{(x)}\,C_{,z} \tag{18.16}$$

$$F^{(z)} = -\Psi^{(y)}\,C_{,x} + \Psi^{(x)}\,C_{,y}. \tag{18.17}$$

It is revealing to consider the special case of potential temperature for a linear equation of state

$$\gamma = \rho_o - \alpha\,\theta, \tag{18.18}$$

with $\alpha > 0$ constant. The skew temperature flux components are given by

$$\mathbf{F}^{(h)} = -\Gamma\,\mu\,\alpha\,\theta_{,z}\,\overline{\nabla\,\theta}^z \tag{18.19}$$

$$F^{(z)} = \Gamma\,\mu\,\alpha\,\nabla\,\theta \cdot \overline{\nabla\,\theta}^z. \tag{18.20}$$

With a stable stratification where $\theta_{,z} > 0$, the horizontal flux is directed opposite to the vertically averaged horizontal temperature gradient: $\mathbf{F}^h \propto -\overline{\nabla\,\theta}^z$, and so is downgradient in this sense.

The technology for discretizing the neutral physics operators (e.g., skew diffusion from Gent et al. (1995) as discussed in Griffies (1998)) is useful for rotated diffusion and skew diffusion.

We thus make use of this technology for the present purposes of discretizing the submesoscale closure of Fox-Kemper et al. (2008b). The full tracer transport tensor is thus given by

$$\mathbf{J} = \begin{pmatrix} A_I & 0 & (A_I - \kappa)\, S^{(x)} - \Gamma\, \mu\, \overline{\gamma_{,x}}^z \\ 0 & A_I & (A_I - \kappa)\, S^{(y)} - \Gamma\, \mu\, \overline{\gamma_{,y}}^z \\ (A_I + \kappa)\, S^{(x)} + \Gamma\, \mu\, \overline{\gamma_{,x}}^z & (A_I + \kappa)\, S^{(y)} + \Gamma\, \mu\, \overline{\gamma_{,y}}^z & A_I\, S^2 \end{pmatrix} \tag{18.21}$$

$$= \begin{pmatrix} A_I & 0 & (A_I - \kappa)\, S^{(x)} - \Psi^{(y)} \\ 0 & A_I & (A_I - \kappa)\, S^{(y)} + \Psi^{(x)} \\ (A_I + \kappa)\, S^{(x)} + \Psi^{(y)} & (A_I + \kappa)\, S^{(y)} - \Psi^{(x)} & A_I\, S^2 \end{pmatrix}, \tag{18.22}$$

where A_I is the neutral diffusivity, κ is the GM-diffusivity, and $\mathbf{S}$ is the neutral slope vector. It is straightforward to incorporate the submesoscale closure into the neutral physics module. If doing so, one would then implement the full transport tensor (18.22). However, there are occassions where one does not wish to turn on the neutral physics parameterizations. For example, in mesoscale eddying simulations, one may choose to remove the neutral physics closure, but retain the submesoscale closure. We thus prefer to develop a separate module for the submesoscale closure, taking only what we need from the neutral physics module.

18.3 Eddy induced transport

The streamfunction (18.1) gives rise to an eddy induced velocity

$$\begin{aligned} \mathbf{v}^* &= \nabla \wedge \mathbf{\Psi} \\ &= (-\partial_z\, \psi^{(y)}, \partial_z\, \psi^{(x)}, \partial_x\, \psi^{(y)} - \partial_y\, \psi^{(x)}) \end{aligned} \tag{18.23}$$

and an associated volume transport within the mixed layer. There is zero net horizontal volume transport

$$\int_{-H}^{\eta} \mathrm{d}z\, \mathbf{u}^* = 0, \tag{18.24}$$

since the streamfunction vanishes at the ocean surface and at the base of the mixed layer. A zero net volume transport is also the case for the eddy induced transport from the Gent et al. (1995) scheme, where the GM streamfunction vanishes at the ocean surface and bottom.

For a vertical position z within the mixed layer, the meridional volume transport passing beneath this depth z, zonally integrated within a basin or over the globe, is computed by the integral

$$\begin{aligned} \mathcal{T}^{(y)}(y, z, t) &= \int \mathrm{d}x \int_{-H}^{z} \mathrm{d}z'\, v^* \\ &= \int \mathrm{d}x \int_{-h}^{z} \mathrm{d}z'\, \partial_{z'}\, \Psi^{(x)} \\ &= \int \mathrm{d}x\, \Psi^{(x)}(x, y, z, t) \\ &= -\int \mathrm{d}x\, \Gamma\, \mu\, \overline{\gamma_{,y}}^z \end{aligned} \tag{18.25}$$

since the streamfunction vanishes at $z \leq -h$ (beneath the mixed layer). Likewise, the zonal transport within the mixed layer is

$$\begin{aligned}
\mathcal{T}^{(x)}(x,z,t) &= \int \mathrm{d}y \int_{-H}^{z} \mathrm{d}z' \, u^* \\
&= -\int \mathrm{d}y \int_{-h}^{z} \mathrm{d}z' \, \partial_{z'} \Psi^{(y)} \\
&= -\int \mathrm{d}y \, \Psi^{(y)}(x,y,z,t) \\
&= -\int \mathrm{d}y \, \Gamma \, \mu \, \overline{\gamma_{,x}}^{z}.
\end{aligned} \tag{18.26}$$

Since $\Gamma \, \mu$ is single signed within the mixed layer, the sign of the horizontal transport in the mixed layer is given by the sign of $-\overline{\nabla \gamma}^{z}$. For example, with denser water towards the north, so that $\overline{\gamma_{,y}}^{z} > 0$, the meridional transport passing beneath a depth z within the mixed layer will be negative, $\mathcal{T}^{(y)}(y,z,t) < 0$. This property of the transport provides a useful check that the scheme has been implemented in the model with the proper sign.

It is instructive to compare the volume transport from the submesoscale parameterization to that induced by Gent et al. (1995). For Gent et al. (1995), the horizontal component of the eddy-induced velocity is

$$\mathbf{u}^{\mathrm{gm}} = -\partial_z \left(\kappa \, \mathbf{S} \right), \tag{18.27}$$

with $\mathbf{S} = -\nabla \gamma / \gamma_{,z}$ the neutral slope vector, and $\kappa > 0$ a diffusivity. The meridional transport is given by

$$\begin{aligned}
\mathcal{T}^{(y)}_{\mathrm{gm}} &= \int \mathrm{d}x \int_{-H}^{z} \mathrm{d}z' \, v^{\mathrm{gm}} \\
&= \int \mathrm{d}x \left(\kappa \, \frac{\gamma_{,y}}{\gamma_{,z}} \right),
\end{aligned} \tag{18.28}$$

where we set the streamfunction to zero at the ocean bottom. For a stable stratification with $\gamma_{,z} < 0$, the volume transport is directed opposite to the sign of the meridional density gradient, which is analogous to the case for the submesoscale transport (18.25).

CHAPTER
NINETEEN

Overflow schemes

The purpose of this chapter is to detail various methods available in MOM4p1 for enhancing the transport of dense water downslope. Some of methods are implementations of schemes from the literature, some are unique to MOM4p1, and some remain incomplete methods which are part of MOM4p1 only for use by those actively pursuing research into overflow algorithms. We present our prejudices in Section 19.4, though the user should recognize that much research still is underway towards finding a suitable overflow scheme for global ocean climate modelling.

There are four methods implemented in MOM4p1 described in this chapter, with the following modules containing the code:

`mom4/ocean_param/mixing/ocean_sigma_transport_mod`
`mom4/ocean_param/mixing/ocean_mixdownslope_mod`
`mom4/ocean_param/sources/ocean_overflow_mod`
`mom4/ocean_param/sources/ocean_overexchange_mod`.

19.1 Motivation for overflow schemes

As described by Winton et al. (1998), coarse resolution z-coordinate models generally have difficulty moving dense water from shallow to deep regions. The key problem is that too much dense water spuriously entrains with the ambient lighter fluid. Only when the topographic slope is resolved so that the grid spacing satisfies

$$|\nabla H| \leq \frac{\Delta z}{\Delta s}, \tag{19.1}$$

does the simulation begin to reach negligible levels of spurious entrainment. Resolving a slope of $1/100$ with vertical resolution of $\Delta z = 20$m thus requires horizontal grid spacing $\Delta s \approx 2$km. This resolution is one or two orders finer than the typical resolution of the 1-2 degree ocean climate models commonly used today. Furthermore, refined vertical resolution, desired for representing vertical physical processes, requires one to further refine the horizontal resolution required to resolve the slope. Notably, there is little difference between the representation of steeply sloping features via either full or partial steps in z-models (Section 6.1.2). Hence, steep "cliff" features remain ubiquitous in the typical ocean climate model using vertical coordinates with quasi-horizontal

isosurfaces. Short of respecting the constraint (19.1), traditional tracer transport schemes (i.e., vertical convection; horizontal and vertical diffusion; and horizontal and vertical advection) are generally unable to transport dense waters into the abyss to the extent observed in Nature. This problem with spurious entrainment is shared by the quasi-horizontal vertical coordinates such as those discussed in Chapter 6.

In an attempt to resolve the spurious entrainment problem, modelers have formulated ways to embed terrain following transport schemes into geopotential or pressure coordinate models. These schemes generally assume the bottom ocean region is turbulent, and so well mixed and not subject to geostrophy. The resulting dynamics act to bring water downslope, eventually being entrained at a neutral buoyancy depth.

Some approaches aim to modify both the momentum and tracer equations, with Killworth and Edwards (1999) documenting a most promising approach. Unfortunately, when modifying the momentum equation so that pressure gradients are computed within the bottom boundary layer, difficulties handling this calculation have resulted in nontrivial problems with spurious transport, especially near the equator. It is for this reason that no global ocean climate model presently employs the Killworth and Edwards (1999), or analogous, scheme. Motivated by this difficulty, we *do not* consider any scheme in MOM4p1 that modifies the momentum equation. Instead, we focus exclusively on methods restricted to the tracer equation.

19.2 The sigma transport scheme

This section documents the scheme available in the module

`mom4/ocean_param/mixing/ocean_sigma_transport_mod`

The papers by Beckmann and Döscher (1997) and Döscher and Beckmann (2000) propose a method to incorporate a rudimentary terrain following turbulent layer in z-models, or more generally into any model with vertical coordinates having quasi-horizontal isosurfaces (e.g., pressure based vertical coordinates). They prescribe changes only to the tracer equation, in which there is advection and diffusion within a bottom turbulent layer. We term these transport mechanisms *sigma diffusion* and *sigma advection*, since the sigma vertical coordinate (Section 6.1.5) is terrain following.

By enabling a terrain oriented route for tracer transport, in addition to the usual grid oriented transport, the quasi-horizontal vertical coordinate models are now afforded an extra pathway for transporting dense water into the abyss.

19.2.1 Sigma diffusion

Diffusion oriented according to the bottom topography is referred to as *sigma diffusion* in the following. The diffusive flux between two adjacent cells living at the ocean bottom is given by

$$\mathbf{F}_\sigma = -A \, \nabla_\sigma T, \tag{19.2}$$

with ∇_σ the horizontal gradient operator taken between cells in the sigma layer. Note that this flux vanishes if the tracer concentration is the same between two adjacent cells within the sigma layer. We follow the approach of Döscher and Beckmann (2000) in which sigma diffusion is strong

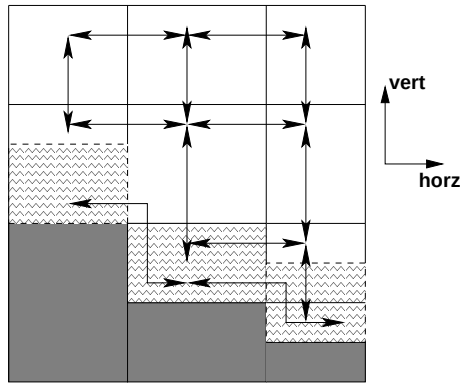

Figure 19.1: Schematic of the along-topography pathway for tracer transport afforded by the sigma transport scheme in MOM4p1. Darkened regions denote land cells, and lightly hatched regions are within the bottom turbulent boundary region. This boundary layer generally can fit within a single bottom cell, as in the left turbulent boundary region; occupy a full cell, as in the middle region; or require more than one of the bottom cells, as in the right region. Tracers communicate with their grid aligned horizontal and vertical neighbors via the usual advection, diffusion, and convective processes. Tracers in the bottom turbulent layer can additionally communicate with their neighbors within the turbulent region via sigma diffusion and sigma advection.

when densities of the participating cells favors downslope motion. That is, the following diffusivity is used

$$A = \begin{cases} A_{\text{max}} & \text{if} \quad \nabla_\sigma \rho \cdot \nabla H < 0 \\ A_{\text{min}} & \text{if} \quad \nabla_\sigma \rho \cdot \nabla H \geq 0, \end{cases} \tag{19.3}$$

where $z = -H(x, y)$ is the bottom depth. Note that in practice, this constraint is applied separately in the two horizontal directions. That is, the zonal diffusivity is large if $\rho_{,x} H_{,x} < 0$ and the meridional diffusivity is large if $\rho_{,y} H_{,y} < 0$. A ratio of the two diffusivities $A_{\text{max}}/A_{\text{min}}$ is a namelist parameter in MOM4p1, with $\approx 10^6$ the default value as suggested by Döscher and Beckmann (2000).

An additional velocity dependent diffusion was also found by Döscher and Beckmann (2000) to be of use. In this case, an added sigma-diffusive flux in the zonal direction is computed using the diffusivity

$$A = \begin{cases} |u| \, \Delta x & \text{if} \quad \rho_{,x} H_{,x} < 0 \ \text{ and } \ u \, H_{,x} > 0 \\ A_{\text{min}} & \text{otherwise.} \end{cases} \tag{19.4}$$

In this expression, $|u|$ is the magnitude of the model's resolved zonal velocity component within the sigma layer, and Δx is the zonal grid spacing. An analogous meridional flux is computed as well.

Sigma diffusion can be specified to occur over an arbitrary layer thickness, even if this layer encompasses a non-integer number of bottom cells. If sigma diffusion is enabled *without* sigma advection, then this bottom layer is time independent.

19.2.2 Sigma advection

In addition to sigma diffusion, MOM4p1 allows for an advective contribution to the bottom boundary layer flow. This portion of the algorithm is experimental, and so *it is not recommended for general use*. We present the discussion here only to expose some initial thoughts on a possible new method, but recognize that the method as discussed here is incomplete. Note that the sigma advection scheme discussed here is distinct from the method proposed by Beckmann and Döscher (1997). Instead, the Campin and Goosse (1999) scheme discussed in Section 19.3 employs an analogous advective transport method which has been implemented in MOM4p1.

In the sigma advection scheme in MOM4p1, there are two ways to determine the advective velocity components acting on tracers within the sigma layer. In both cases, if the deeper parcel within the sigma layer is denser than the shallower parcel, then the sigma advective transport is set to zero. Otherwise, it is active and thus contributes to the downslope tracer transport. This criteria translates into the constraint

$$\nabla_\sigma \rho \cdot \nabla H < 0 \quad \text{for density driven downslope flow,} \tag{19.5}$$

where ρ is the density within the bottom sigma layer. This constraint is the same as used to determine the value for the diffusivity discussed in Section 19.2.1.

19.2.2.1 Sigma velocity derived from resolved velocity

Beckmann and Döscher (1997) and Döscher and Beckmann (2000) determine the advective velocity components acting in the sigma layer from the model's resolved velocity components. In MOM4p1, these velocity components are found by integrating the model's resolved horizontal advective velocity components within the bottom turbulent sigma layer.

19.2.2.2 Sigma velocity from a parameterization

Campin and Goosse (1999) suggest an additional approach to enhance the horizontal velocity available for downslope flow. In MOM4p1, we add this velocity to the resolved velocity within the sigma layer determine as above.

Following Campin and Goosse (1999), assume the dense shallow parcel has a subgrid scale momentum associated with its downslope motion. The zonal momentum is assumed to be proportional to the topographic slope, $H_{,x}$, the acceleration from gravity, g, the amount of fluid within the cell participating in the downslope flow,

$$0 \le \delta \le 1, \tag{19.6}$$

and the density difference

$$\Delta\rho = \mathrm{dx} \left(\frac{\partial \rho}{\partial x} \right)_\sigma \tag{19.7}$$

as measured in the zonal direction within the sigma layer. The momentum is retarded by frictional dissipation, μ (with units of inverse time). These considerations then lead to the momentum balance

$$\rho\, V^{(t)}\, \mu\, u^{\text{slope}} = -g\, \delta\, V^{(t)}\, \Delta\rho\, H_{,x}\ \text{sign}(H_{,x}) \tag{19.8}$$

where

$$V^{(t)} = \texttt{dxt} * \texttt{dyt} * \texttt{dzt}^{\sigma} \tag{19.9}$$

is the volume of the dense parcel within the sigma layer, we assume $\Delta\,\rho\,H_{,x} < 0$, as required for density favorable downslope flow (equation (19.5)), and sign$(H_{,x})$ sets the sign for the downslope velocity. Equation (19.8) is also used to determine a meridionally directed downslope transport, with the meridional topographic slope $H_{,y}$ replacing $H_{,x}$, and $\Delta\rho = \mathrm{d}y\,\rho_{,y}$ the density difference between meridionally adjacent parcels.

Solving equation (19.8) for the velocity component u^{slope} yields

$$\rho\,\texttt{dzt}^{\sigma}\,u^{\text{slope}} = -\left(\frac{g\,\delta}{\mu}\right)\,H_{,x}\,\Delta\rho\,\texttt{dzt}^{\sigma}\ \text{sign}(H_{,x}). \tag{19.10}$$

With the depth H refering to the depth of a tracer cell, the slope $H_{,x}$ is defined at the zonal face of the tracer cell. Hence, the velocity component u^{slope} is likewise positioned at the zonal face. This is the desired position for the zonal advective tracer transport velocity component.

Campin and Goosse (1999) suggest the values for frictional drag

$$\mu = 10^{-4}\,\text{sec}^{-1} \tag{19.11}$$

and fraction of a cell participating in the transport

$$\delta = 1/3. \tag{19.12}$$

These parameters are namelists in MOM4. Using these numbers, with an absolute topographic slope of $|H_{,x}| \approx 10^{-3}$ and density difference $\Delta\rho \approx 1\,\text{kg}\,\text{m}^{-3}$, leads to

$$u^{\text{slope}} \approx .03\,\text{m sec}^{-1} \tag{19.13}$$

and the associated volume transport

$$U^{\text{slope}} = u^{\text{slope}} \times \texttt{thickness_sigma} \times \texttt{dyt}, \tag{19.14}$$

where `thickness_sigma` is the thickness of the sigma layer. With $u^{\text{slope}} \approx .03\text{m}\,\text{s}^{-1}$ corresponding to the speed of fluid within a sigma layer that is one-degree in width and 50m in thickness, we have a volume transport $U^{\text{slope}} \approx 0.2$Sv. Larger values are realized for steeper slopes, larger density differences, larger grid cells, and thicker sigma layers.

19.2.2.3 Maintaining mass conservation

Introducing horizontal advection within the sigma layer necessitates the consideration of mass conservation within this layer. Our focus here is just on the additional mass conservation issues arising from sigma advective transport.

The balance of mass within an arbitrary layer is detailed in Section 7.6. Assuming there is no transport through the bottom of the sigma layer into rock, we are led to the mass budget for the sigma layer (equation (7.102))

$$0 = \partial_t\,(\mathrm{d}z\,\rho) - \mathrm{d}z\,\rho\,\mathcal{S}^{(\mathsf{M})} + \nabla_{\sigma}\cdot(\mathrm{d}z\,\rho\,\mathbf{u}) + (\rho\,w^{(\sigma)})_{\text{top of sigma layer}}. \tag{19.15}$$

Again, each term in this equation is associated *just* with the sigma transport process. Hence, the horizontal velocity $\mathbf{u}$ as that obtained from the considerations given earlier in this section. However, the remaining terms have not been specified yet, and so must be set according to physical arguments and/or convenience.

19.2.2.4 Dia-sigma transport

First, consider the case of zero mass source arising from sigma transport, and a zero time tendency term $\partial_t (\mathrm{d}z\ \rho)$ (such as occurs in the Boussinesq case assuming a constant sigma layer thickness). The mass budget within the sigma layer is thus closed by a dia-sigma transport

$$(\rho\, w^{(\sigma)})_{\text{top of sigma layer}} = -\nabla_\sigma \cdot (\mathrm{d}z\ \rho\, \mathbf{u}). \tag{19.16}$$

This transport measures the amount of water that crosses the sigma layer from the surrounding fluid. This choice was taken by Beckmann and Döscher (1997) and Döscher and Beckmann (2000), and it was also employed by Campin and Goosse (1999).

Furthermore, Beckmann and Döscher (1997) suggest that to reduce the spurious entrainment associated with tracer advection aligned with the model's grid, it is appropriate to reduce, or remove, this advective transport within the sigma layer in favour of the sigma advection transport. Tang and Roberts (2005) also take this approach. Nonetheless, we do not follow this suggestion for the following reasons. First, it complicates the treatment of the advection operator by introducing an *ad hoc* parameter that partitions between sigma advection and grid aligned advection. Second, and primarily, we take the perspective that the sigma advection process is subgrid scale. Hence, it should act only in those cases where the resolved, grid aligned, velocity is unable to provide a sufficient downslope transport. We should thus *not* remove the grid aligned advective transport using an *ad hoc* specification. That is, we do not aim to remedy spurious entrainment arising from grid aligned advective transport by removing this transport altogether.

Given these objections, we do not pursue this approach further in MOM4p1.

19.2.2.5 Mass sources

Next, consider the case where all mass is advected downslope within the sigma layer, with a zero time tendency term $\partial_t (\mathrm{d}z\ \rho)$ and zero dia-sigma transport.[1] This assumption then leads to the sigma layer mass budget

$$\mathrm{d}z\ \rho\, \mathcal{S}^{(\mathsf{M})} = \nabla_\sigma \cdot (\mathrm{d}z\ \rho\, \mathbf{u}). \tag{19.17}$$

That is, the divergent horizontal advective transport within the sigma layer is balanced by a nonzero mass source. The horizontal integral of the mass source over the sigma layer vanishes, since the sigma advection velocity satisfies either the no-normal boundary condition at land/sea interfaces, or periodicity. Hence, the introduction of the nonzero mass source does not corrupt global mass conservation. It does, however, come at the cost of also requiring nonzero tracer sources; the introduction of new fluid locally requires also the introduction of nonzero tracer locally, since the fluid has some tracer content (e.g., a temperature). These tracer sources do not necessarily lead to a zero global net introduction of tracer. This approach is thus unacceptable.

19.2.2.6 Undulating sigma layer thickness

The time tendency $\partial_t (\mathrm{d}z\ \rho)$ represents changes in the density weighted sigma layer thickness. It vanishes for a Boussinesq case if the sigma layer has constant thickness. However, if the sigma

[1] Grid aligned advection generally leads to transport across the sigma layer.

layer can inflate or deflate, this term remains nonzero. That is, without mass sources or without dia-sigma transport, the mass budget within the sigma layer takes the form

$$\partial_t \left(\mathrm{d}z \, \rho \right) = -\nabla_\sigma \cdot \left(\mathrm{d}z \, \rho \, \mathbf{u} \right). \tag{19.18}$$

Hence, the sigma layer undulates according to the convergence or divergence of mass advected within the layer. Its undulations are of just the magnitude needed to keep a zero dia-sigma transport. So the picture is of a blob of heavy fluid moving downslope, causing the sigma layer to undulate in order to accomodate the fluid motion. See Figure 3.5 for an illustration of this fluid motion. This approach is available only for models such as MOM4p1 that allow an arbitrary time dependent thickness for the sigma layer.

During some initial research, we have favoured this approach in MOM4p1 as it avoids objections raised about the previous alternatives. We do make some simplifications, and note that the approach has only recently (as of 2006) been tested, with some unfortunate problems discussed below. Here are some things to note.

- For the nonBoussinesq case, we replace the *in situ* density appearing in the time tendency with the constant Boussinesq density ρ_o. Given uncertainties in many of the scheme's parameters, this replacement is justified.

- The sigma layer thickness is bounded from above and below by user specified values. Allowing the thickness to vary too far can lead to noisy behaviour. Settings bounds amounts to an implicit specification of detrainment whenever the thickness gets too large, and entrainment when it gets to small.

- It has proven useful to smooth the sigma layer thickness. An option is available to smooth the layer thickness with a Laplacian diffusion operator.

19.2.2.7 Problems with the MOM4p1 sigma advection scheme

The most fundamental problem with the MOM4p1 sigma advection scheme, as implemented according to equation (19.18), is that as mass converges to a region to thus expand the sigma layer, there is no corresponding dynamical mechanism to carry this perturbation away, and thus allow for an adjustment process. Instead, by only considering the mass conservation equation, with no dynamical equations, the sigma layer will generally grow without bound in regions where mass converges, or disapper in regions of divergence. This situation is not encountered in an isopycnal model, since these models have dynamical processes to adjust the fluctuating thicknesses.

Absent a dynamical mechanism for the adjustment, the sigma advection scheme must employ artificial limits on the layer thickness. These limiters impose, in effect, a detrainment or entrainment process to keep the layer thickness within the specified bounds. Such processes, however, have not yet been implemented in MOM4p1, so the present scheme is incomplete. Without the entrainment and detrainment processes, the artificial limits, when imposed, allow for the tracer to realize extrema, since its time tendency is artificially altered. This is unacceptable, and so the scheme as presently implemented is unusable.

19.2.3 Implementation of sigma transport

Consistent with Beckmann and Döscher (1997), the turbulent bottom layer momentum equations remain the same as interior k-level cells. We now just allow tracers in the bottom turbulent layer to be affected by transport with their "sigma-neighbors" in addition to their horizontal and vertical neighbors. Figure 19.1 provides a schematic of the extra pathway available with sigma tracer transport.

The bottom turbulent sigma layer in MOM3 was appended to the very bottom of the model, and so effectively lived beneath the deepest rock. This approach is inconvenient for the following reasons.

- It makes for awkward analyses.
- It precludes direct comparison between models run with and without sigma-physics since the grid used by the two models is different.
- It makes it difficult to consider convergence when refining the grid mesh.

For these reasons, the bottom turbulent layer in MOM4 is included within the regular model domain. This is the approach used by Beckmann and Döscher (1997) (e.g., see their Figures 1 and 2).

The disadvantage of the MOM4p0 approach is that the bottom turbulent layer thickness *thickness_sigma* has a generally non-constant thickness and is determined by the thickness of the grid cell next to topography. In particular, with partial bottom steps, the effective turbulent layer thickness could be very thin, in which case thin cells act as a bottle-neck bo bottom transport. This implementation is inconvenient.

In MOM4p1, we allow for an arbitrarily thick bottom turbulent layer. We do so by incorporating the required grid cells into the bottom turbulent sigma layer. This approach requires some added accounting, but it is straightforward. In particular, the tracer concentration within the bottom turbulent layer is computed by

$$T_{\text{sigma}} = \frac{\sum_{\text{sigma}} \rho \, \text{dzt} \, T}{\sum_{\text{sigma}} \rho \, \text{dzt}}, \tag{19.19}$$

where the sum extends over the cells, including cell fractions, contained in the bottom turbulent layer. A time tendency is computed for sigma transport of T_{sigma} within the bottom turbulent sigma layer. The relative fraction of a grid cell participating in the bottom turbulent layer determines the magnitude of the tracer time tendency added to this cell.

19.3 The Campin and Goosse (1999) scheme

This section documents the scheme available in the module

`mom4/ocean_param/sources/ocean_overflow_mod`.

Consider a heavy water parcel sitting on top of a shelf/cliff that is horizontally adjacent to a lighter parcel sitting over a deeper water column. We may expect that the dense parcel will move off the shelf, down the slope, and into the deep. Along the way, entrainment will occur, with many important processes determining the details of the final water mass. This is indeed a

cartoon of an important oceanic process forming much of the deep and intermediate waters in the ocean. Unfortunately, without some extra "engineering" help, Winton et al. (1998) show that coarse resolution z-models are incapable of providing the proper dynamical pathways for this transfer of dense shelf water into the deep. Beckmann and Döscher (1997) suggest one means to enhance the representation of this process, and we discussed this scheme in Section 19.2. Campin and Goosse (1999) propose yet another, which we detail in this section. Both schemes only affect the tracer equation.

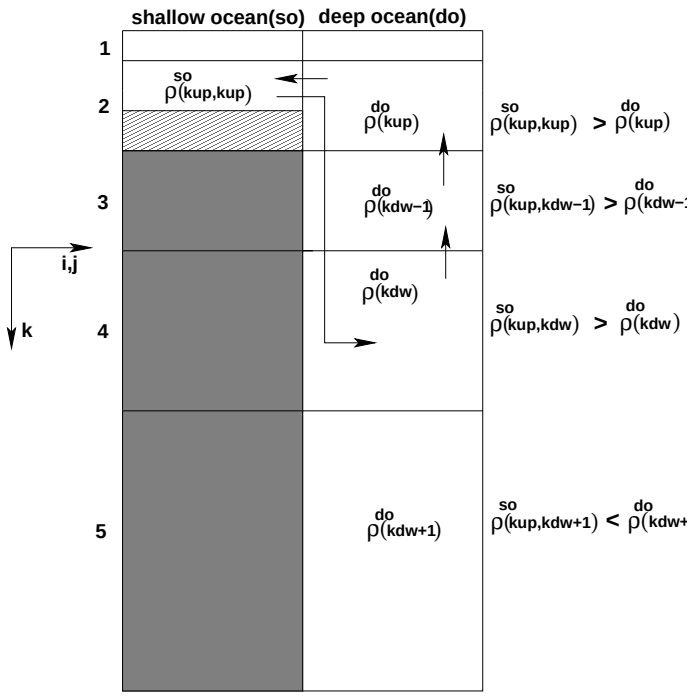

Figure 19.2: Schematic of the Campin and Goosse (1999) overflow method in the horizontal-vertical plane. The darkly filled region represents bottom topography using MOM4's full cells. The lightly filled region represents topography filled by a partial cell. Generally, the thickness of a cell sitting on top of a topographic feature, as the $k = 2$ cell in the "so" column, is thinner than the corresponding cell in the deep-ocean column (the $k = 2$ cell in the "do" column). Shown are tracer cells, with arrows representing the sense of the scheme's upstream advective transport. This figure is based on Figure 1 of Campin and Goosse (1999).

19.3.1 Finding the depth of neutral buoyancy

Figure 19.2 illustrates a typical situation in a horizontal-vertical plane. Here, we see a heavy parcel of *in situ* density $\rho^{so}(k = kup)$ sitting horizontally adjacent to a lighter parcel of *in situ* density $\rho^{do}(k = kup)$. The superscript "so" refers to water in the "shallow ocean" column, whereas "do" refers to water in the "deep ocean" column.

If the heavy parcel is allowed to adiabatically move off the shelf and then vertically within the deep column, it will equilibrate at its depth of neutral buoyancy. To compute the depth of neutral

buoyancy, we evaluate the *in situ* density for the parcel taken at the local value for the *in situ* pressure of the environment where it may potentially equilibrate. For the example shown in Figure 19.2, with (i, j) setting the horizontal position of the shelf parcel and $(i+1, j)$ setting the horizontal position of the deep column, we have

$$\rho^{so}(kup, kup) = \rho(s_{i,j,kup}, \theta_{i,j,kup}, p_{i,j,kup}) \tag{19.20}$$

$$\rho^{so}(kup, kdw-1) = \rho(s_{i,j,kup}, \theta_{i,j,kup}, p_{i+1,j,kdw-1}) \tag{19.21}$$

$$\rho^{so}(kup, kdw) = \rho(s_{i,j,kup}, \theta_{i,j,kup}, p_{i+1,j,kdw}) \tag{19.22}$$

$$\rho^{so}(kup, kdw+1) = \rho(s_{i,j,kup}, \theta_{i,j,kup}, p_{i+1,j,kdw+1}). \tag{19.23}$$

That is, we compute the density at the salinity and potential temperature of the shallow ocean parcel, $(s_{i,j,kup}, \theta_{i,j,kup})$, but at the *in situ* pressure for the respective grid cell in the deep column. The density is then compared to the density of the parcel at the *in situ* salinity, temperature, and pressure of the cells in the deep ocean column.

19.3.2 Prescribing the downslope flow

Following Campin and Goosse (1999), we assume that the dense parcel has a downslope momentum imparted to it. This momentum is proportional to the topographic slope, $H_{,x}$, the acceleration from gravity,g, the amount of fluid within the cell participating in the downslope flow,

$$0 \leq \delta \leq 1, \tag{19.24}$$

and the positive density difference

$$\Delta\rho = \rho^{so}(\mathrm{kup}, \mathrm{kup}) - \rho^{do}(\mathrm{kup}) > 0. \tag{19.25}$$

The momentum is retarded by frictional dissipation, μ (in units of inverse time). These considerations then lead to the momentum balance

$$\rho_o \, V^{(t)} \, \mu \, u^{slope} = g \, \delta \, V^{(t)} \, \Delta\rho \, |H_{,x}| \tag{19.26}$$

where

$$V^{(t)} = \mathtt{dxt} * \mathtt{dyt} * \mathtt{dzt} \tag{19.27}$$

is the volume of the dense parcel's tracer cell. Equation (19.26) is also used to determine a meridionally directed downslope transport, with the meridional topographic slope $\partial_y H$ replacing $\partial_x H$, and $\Delta\rho$ the density difference between meridionally adjacent parcels.

Solving equation (19.26) for the speed u^{slope} yields

$$u^{slope} = \left(\frac{g \, \delta}{\rho_o \, \mu} \right) |\partial_x H| \, \Delta\rho. \tag{19.28}$$

If the depth H refers to the depth of a tracer cell, then the absolute slope $|\partial_x H|$ is naturally defined at the zonal face of the tracer cell. Hence, the speed, u^{slope}, is likewise positioned at the zonal face. This is the desired position for an advective tracer transport velocity.

Campin and Goosse (1999) suggest the values $\mu = 10^{-4}\,\text{sec}^{-1}$ and $\delta = 1/3$. These parameters are set as namelists in MOM4. Using these numbers, with an absolute topographic slope of $|H_{,x}| \approx 10^{-3}$ and density difference $\Delta\rho \approx 1\,\text{kg}\,\text{m}^{-3}$, leads to the speed

$$u^{slope} \approx .03\,\text{m}\,\text{sec}^{-1}. \tag{19.29}$$

Associated with this downslope speed is a volume transport of fluid leaving the cell

$$U^{slope} = u^{slope}\,\texttt{dzt}_{min}\,\texttt{dyt}. \tag{19.30}$$

In this equation, $\texttt{dzt}_{min}$ is the minimum thickness of the shelf cell and the adjacent cell. This minimum operation is necessary when considering MOM4's bottom partial cells, whereby the bottom-most cell in a column can have arbitrary thickness (Figure 19.2). With $u^{slope} \approx .03\text{m}\,\text{s}^{-1}$ corresponding to the speed of fluid leaving a grid cell that is one-degree in width and $50\,\text{m}$ in depth, we have a volume transport $U^{slope} \approx 0.2\text{Sv}$. Larger values are easily realized for steeper slopes, larger density differences, and larger grid cells.

19.3.3 Mass conservation and tracer transport

To conserve mass throughout the system, the mass flux exiting the shelf cell and entering the deep cell must itself be returned from the adjacent cell. This situation then sets up a mass flux throughout the participating cells, where there is zero convergence of the flux and so zero net increase or decrease in mass. For the Boussinesq fluid, mass conservation is replaced by volume conservation. This redirected plumbing is shown in Figure 19.2.

The convergence-free seawater mass flux carries with it tracer mass. If there are differences in the tracer content of the cells, then the tracer flux will have a nonzero convergence, and so it moves tracer throughout the system. We use first-order upstream advective transport as a discretization of this process. First-order upstream advection is the simplest form of advection. Its large level of numerical diffusion is consistent with our belief that the bottom layer flows in the real ocean near steep topography are quite turbulent. Hence, although inappropriate for interior flows, we are satisfied with the use of upstream advection for the overflow scheme.

19.3.4 Implementation in MOM4

This section details the implementation of the Campin and Goosse (1999) scheme in MOM4.

19.3.4.1 Start of the integration

At the start of the model integration, it is necessary to determine those grid points where it is possible to have a downslope flow. For this purpose, we introduce the array `topog_step(i,j,m)`, with $m = 1, 2, 3, 4$ specifying in a counter-clockwise direction the four surrounding columns whose depths are to be compared to that at the central (i, j) point. Figure 19.3 illustrates this notation. If the adjacent column is deeper than the central point, thus representing a possible direction for downslope flow, then `topog_step(i,j,m)` for this value of m is set to unity. Otherwise, `topog_step(i,j,m)` for this m is zero. Note that with partial bottom cells, it is possible for an adjacent column to be deeper yet for the number of vertical cells to be the same in both columns. To initiate the downslope scheme of Campin and Goosse (1999), we insist that there be at least one more grid cell in the adjacent column.

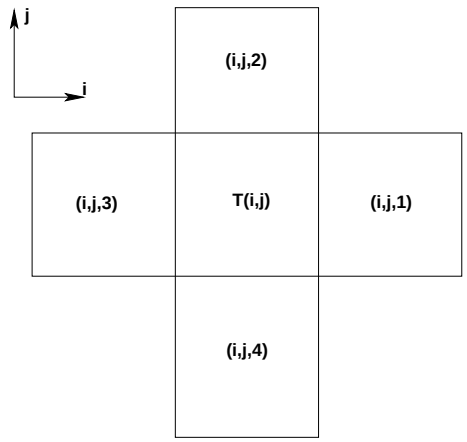

Figure 19.3: Plan view (x-y plane) of a tracer grid cell at (i, j) and its horizontally adjacent tracer cells. We label the adjacent cells $(i+1, j), (i, j+1), (i-1, j), (i, j-1)$ as $m = 1, 2, 3, 4$. Notice that we do not consider downslope flow along a diagonal direction.

19.3.4.2 During a time step

During each time step, we locate where downslope flow is favorable for points sitting on the ocean bottom at $(\mathtt{i}, \mathtt{j}, \mathtt{kmt}(\mathtt{i}, \mathtt{j}))$. For each of the four directions ($m = 1, 2, 3, 4$) where `topog_step(i,j,m)`=1, we check the density difference between the central point and the adjacent point. If the density of the central point is larger, then the Campin and Goosse (1999) scheme is used to initiate downslope transport. For these directions, we locate the depth of neutral buoyancy for the central point according to the discussion in Section 19.3.1, and so specify the number of vertical cells, `kdw`, participating in the transport. Note that we allow for downslope transport to occur in more than one direction, as occurs in those cases for a fixed (i, j) where `topog_step(i,j,m)` has more than a single nonzero element.

Our prescription is mindful of the possibility for the shallow-cell to be a partially filled cell sitting on the topography. For this reason, the convergence-free volume transport associated with the downslope flow is weighted by the minimum vertical thickness of the two cells (equation (19.30)). Otherwise, it would be possible to flood a thin partial cell with a huge amount of tracer (e.g., heat).

We incorporate effects from the Campin and Goosse (1999) overflow scheme into MOM4's tracer time tendency array. To derive the tendency, we proceed as for the river-mixing and cross-land mixing formulations discussed in Griffies et al. (2004) by focusing on the time evolution due to just the overflow process. For the particular zonal-vertical case illustrated in Figure 19.3, we prescribe

$$\partial_t \left(V^{(t)} \rho C\right)^{so}_{i,j,kup} = \rho U^{slope} \left(C^{do}_{i+1,j,kup} - C^{so}_{i,j,kup}\right) \tag{19.31}$$

$$\partial_t \left(V^{(t)} \rho C\right)^{do}_{i+1,j,kup} = \rho U^{slope} \left(C^{do}_{i+1,j,kdw-1} - C^{do}_{i+1,j,kup}\right) \tag{19.32}$$

$$\partial_t \left(V^{(t)} \rho C\right)^{do}_{i+1,j,kdw-1} = \rho U^{slope} \left(C^{do}_{i+1,j,kdw} - C^{do}_{i+1,j,kdw-1}\right) \tag{19.33}$$

$$\partial_t \left(V^{(t)} \rho C\right)^{do}_{i+1,j,kdw} = \rho U^{slope} \left(C^{so}_{i,j,kup} - C^{do}_{i+1,j,kdw}\right), \tag{19.34}$$

where

$$\rho\, U^{slope} = u^{slope}\, \mathtt{rho_dzt}_{min}\, \mathtt{dyt}, \tag{19.35}$$

with

$$\mathtt{rho_dzt}_{(min)} = \min(\mathtt{rho_dzt}_{i,j,kup}, \mathtt{rho_dzt}_{i+1,j,kup}) \tag{19.36}$$

the minimum density weighted thickness of the two cells at $k = kup$. For the Boussinesq case, ρ factors are set to the constant reference density ρ_o. Setting the tracer concentration to the same uniform value leads to vanishing time tendencies in each cell, thus reflecting volume/mass conservation. Additionally, summing these four equations leads to a vanishing right hand side, thus reflecting conservation of total tracer in the system. Since the downslope mixing has the form of an upstream advection, we discretize temporally by evaluating the tracer and density on the right hand side at the lagged time $\tau - 1$.

19.4 Neutral depth over extended horizontal columns

Both Campin and Goosse (1999) and Beckmann and Döscher (1997) provide quasi-physical approaches to the problem of simulating deep water formation near topography. Each provides plumbing routes beyond the local horizontal-vertical routes available in geopotential or pressure models. In this way, these methods afford a new means for *representing* the flows. Questions such as parameterizing the rates of entrainment, volume flux, etc. (e.g., Killworth and Edwards (1999)) are not directly addressed by these schemes, although the present schemes can be extended a bit to include such details.

Climate modelers generally gauge the utility of overflow schemes on the overall results. Namely, do the schemes provide a route for deep water formation near topographic gradients in a manner expected from observations? Details of the transport are often not the first priority. This situation is unsatisfying from a process physics perspective. It may, nonetheless, be the best available for many coarse resolution models.

In this section, we discuss our prejudices with MOM4p1 development. To start, consider the density structure in Figure 19.4. This figure illustrates a case where the sigma transport scheme of Section 19.2 does not prescribe enhanced downslope transport. The reason is that the sigma transport scheme only works with density within the bottom "sigma layer". For this example, density at the bottom of the deeper column is greater than that on the shelf, and so there is no enhanced transport prescribed. In contrast, the Campin and Goosse (1999) scheme prescribes a downslope transport, with the dense shelf water moving to its neutral buoyancy depth. It is for this reason that we favour, in MOM4p1, downslope schemes where the depth of neutral buoyancy is determined, with this depth possibly above the ocean bottom.

Even within this example, however, there remain limitations of the Campin and Goosse (1999) scheme. The limitation is that their scheme only reaches out one grid box in the horizontal. That is, although the scheme is non-local in the vertical, it remains local in the horizontal. What can happen is the dense parcel will find itself denser than any parcel in the adjacent column, and so its resting place, with the Campin and Goosse (1999) algorithm, is at the bottom of the adjacent column, rather than at a neutral buoyancy depth. If given the opportunity to exchange with columns further removed from the central column, the parcel is afforded the opportunity to find a more suitable neutral buoyancy layer. This general result motivates us to consider two experimental schemes, whereby the notions of a neutral buoyancy level motivated from Campin and Goosse (1999) are

extended to columns removed from the central column. As the parcel finds a more suitable resting place, it is assumed to exchange properties with the intermediate parcels, in a manner meant to represent entrainment as it moves downslope. The rates of transport remain a function of the topographic slope and the difference in density, just like the Campin and Goosse (1999) scheme.

There are two methods available in MOM4p1 for realizing these ideas. The first is implemented in the module

`mom4/ocean_param/sources/ocean_overexchange_mod`.

In this scheme, a dense shallow parcel is allowed to be transported horizontally over more than a single column, so long as it continues to remain on the bottom of the adjacent columns, thus affording it more opportunity to find its neutral buoyancy level. The exchange results in no net mass exchange between parcels, and so there is no need for an advective replumbing to be implemented, in contrast to the Campin and Goosse (1999) scheme. Here, the resolved dynamics adjust based on mixing of the water masses and the associated changes in density structure. This process then becomes directly analogous to the cross-land mixing formulation discussed in Griffies et al. (2004) and in Chapter 20. That is, we remove the intermediate cells from the process described in Section 19.3.4.2, and just focus on the single shallow and deep cell, thus leading to

$$\partial_t \left(V^{(t)}\, \rho\, C\right)^{so}_{i,j,kup} = \rho\, U^{slope} \left(C^{do}_{i+1,j,kdw} - C^{so}_{i,j,kup}\right) \tag{19.37}$$

$$\partial_t \left(V^{(t)}\, \rho\, C\right)^{do}_{i+1,j,kdw} = \rho\, U^{slope} \left(C^{so}_{i,j,kup} - C^{do}_{i+1,j,kdw}\right), \tag{19.38}$$

This parameterization is simpler to implement than the Campin and Goosse (1999) scheme, since we omit the intermediate cells from the process. This approach also does not rely on assumptions of a flow that may be set up in response to the exchange of fluid.

The second method is implemented in the module

`mom4/ocean_param/mixing/ocean_mixdownslope_mod`.

In this scheme, exchange of tracer occurs as a partial convective mixing process. We assume that a part of the shallow dense cell is transported downslope, and this then mixes with the intermediate cells with an efficiency proportional to the topographic slope and the density difference. In equations, we compute a combined mass of the mixed water according to

$$M_{\mathsf{sum}} = M(s) + M(d), \tag{19.39}$$

where

$$M(s) = \gamma\, \mathtt{rho_dzt}(s)\; \mathtt{dat}(s) \tag{19.40}$$

is the mass of water in the shallow dense cell participating in the exchange, and

$$M(d) = \delta\, \mathtt{rho_dzt}(d)\; \mathtt{dat}(d) \tag{19.41}$$

is the mass of deep cell participating. In these equations, `dat` is the horizontal area of the cells, γ is the fraction of the shallow dense cell that is assumed to take part in the downslope transport, and δ is proportional to the topographic slope and the density difference between the shallow and deep parcel. If assumed to mix completely over a time step, then the resulting tracer concentration C_{mix} would be given by

$$M_{\mathsf{sum}}\, C_{\mathsf{mix}} = \gamma\, \mathtt{rho_dzt}(s)\; \mathtt{dat}(s)\, C(s) + \delta\, \mathtt{rho_dzt}(d)\; \mathtt{dat}(d)\, C(d). \tag{19.42}$$

Instead of mixing completely, which would require an adjustment process as in convection, we use the tracer concentration C_{mix} to deduce the following time tendencies which drive the cells toward the mixed concentration

$$\texttt{dat}(s)\,\text{tend}(s) = \left(\frac{M(s)\,\gamma}{\Delta t}\right)(C_{\text{mix}} - C(s)) \tag{19.43}$$

$$\texttt{dat}(d)\,\text{tend}(d) = \left(\frac{M(d)\,\delta}{\Delta t}\right)(C_{\text{mix}} - C(d)). \tag{19.44}$$

Given the mixed tracer concentration (19.42), we have

$$\texttt{dat}(s)\,\text{tend}(s) + \texttt{dat}(d)\,\text{tend}(d) = 0, \tag{19.45}$$

which reflects the conservation of tracer.

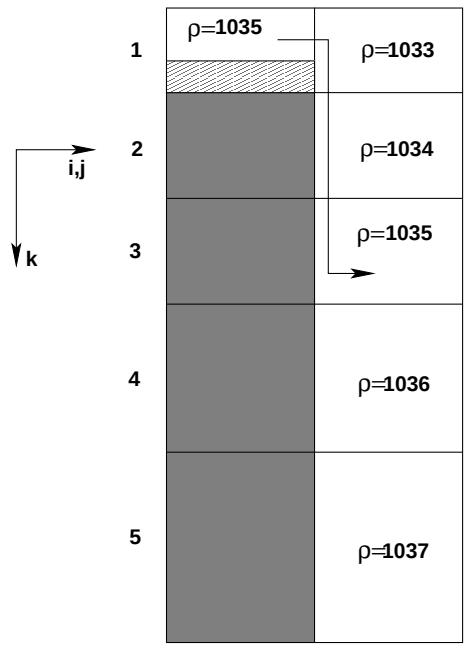

Figure 19.4: Schematic of a situation where a dense parcel sits on a shelf next to a column whose upper portion is light, but whose deeper portion is denser than the shelf. For this case, the Campin and Goosse (1999) scheme prescribes a transport between the shelf water at level 1 and the deeper water at level 3, with water bubbling upward to conserve mass as shown in Figure 19.2. In contrast, the sigma transport scheme will not prescribe any enhanced transport, since here the bottom of the deep column is denser than the shelf.

19.5 Sigma friction

The previous schemes introduce a new transport pathway for tracers. Nothing is done to the momentum equation. Another idea is to consider an enhancement of the vertical friction acting

near to the bottom, with the friction introduced via a vertical viscosity. The effects of vertical friction are related, through geostrophy, to those from Gent et al. (1995), whereby density slopes are reduced without mixing of density classes (Greatbatch and Lamb, 1990). Alternatively, enhancing the vertical viscosity next to the bottom increases the Ekman layer thickness next to the bottom, and this breaks geostrophy, thus allowing for an easier downslope transit of the fluid. The scheme described in this section is *not* available in MOM4p1. We mention it, nonetheless, as it may prove to be of use for some applications.

Following the scaling from Campin and Goosse (1999) discussed in Section 19.3.2, we define a vertical viscosity according to equation (19.26)

$$\begin{aligned} \kappa^{\sigma} &= \mathtt{dzt}^{\sigma}\, u^{\text{slope}} \\ &= -\left(\frac{g\,\delta}{\mu\,\rho}\right) H_{,x}\, \Delta\rho\, \mathtt{dzt}^{\sigma}\ \text{sign}(H_{,x}). \end{aligned} \tag{19.46}$$

Using the parameters from Section 19.3.2 leads to a vertical visosity of

$$\kappa^{\sigma} = 0.15\,\text{m}\,\text{s}^{-2}, \tag{19.47}$$

with larger values for steeper topographic slopes and stronger density contrasts. We propose to introduce this viscosity throughout the sigma layer, and exponentially decrease it above the layer, with a relatively short decay scale

$$\kappa^{\sigma}_{\text{decay}} = 10\text{m}. \tag{19.48}$$

We suggest computing this viscosity separately for the two horizontal directions, and take the maximum of the two for the parameterization.

CHAPTER
TWENTY

Cross-land mixing

The purpose of this chapter is to present the method used in MOM4 for mixing tracers and mass/volume across land separated points, such as across an unresolved Strait of Gibraltar. The material here is taken from the MOM4 Technical Guide of Griffies et al. (2004), with slight modifications to account for generalized vertical coordinates used in mom4p1.

20.1 Introduction

In climate modeling, it is often necessary to allow water masses that are separated by land to exchange properties. This situation arises in models when the grid mesh is too coarse to resolve narrow passageways that in reality provide crucial connections between water masses. For example, coarse grid spacing typically closes off the Mediterranean from the Atlantic at the Straits of Gibraltar. In this case, it is important for climate models to include the effects of salty water entering the Atlantic from the Mediterranean. Likewise, it is important for the Mediterranean to replenish its supply of water from the Atlantic to balance the net evaporation occurring over the Mediterranean region.

We describe here a method used in MOM4 to establish communication between bodies of water separated by land. The communication consists of mixing tracers and mass/volume between non-adjacent water columns. Momentum is not mixed. The scheme conserves total tracer content, total mass or volume (depending on whether using the non-Boussinesq or Boussinesq versions of MOM4), and maintains compatibility between the tracer and mass/volume budgets. It's only restriction is that no mixing occur between cells if their time independent thicknesses differ. This constraint is of little practical consequence.

20.2 Tracer and mass/volume compatibility

Consider two boxes with fluid masses $M^{(1)} = \rho^{(1)} V^{(1)}$ and $M^{(2)} = \rho^{(2)} V^{(2)}$ and tracer concentrations (tracer mass per mass of fluid) $T^{(1)}$ and $T^{(2)}$ (for a Boussinesq fluid, the density is set to the constant Boussinesq density ρ_o). A mixing process that conserves total tracer mass and total fluid

mass must satisfy

$$\partial_t (T^{(1)}\, \rho^{(1)}\, V^{(1)} + T^{(2)}\, \rho^{(2)}\, V^{(2)}) = 0 \tag{20.1}$$

$$\partial_t (\rho^{(1)}\, V^{(1)} + \rho^{(2)}\, V^{(2)}) = 0. \tag{20.2}$$

Notably, mass conservation can be considered a special case of total tracer conservation when the tracer concentration is uniform and constant: $T \equiv 1$. This result provides an important *compatibility* constraint between the discrete tracer and mass/volume budgets. For constant volume boxes with a Boussinesq fluid, such as considered in rigid lid models, compatibility is trivial. For boxes which change in time, such as the top cells in MOM4p0 free surface or any box in mom4p1, then compatibility provides an important constraint on the methods used to discretize the budgets for mass/volume and tracer. The remainder of this chapter incorporates these ideas into the proposed cross-land mixing scheme.

20.3 Tracer mixing in a Boussinesq fluid with fixed boxes

To start in our formulation of cross-land mixing, let us consider mixing of two volumes of Boussinesq fluid, where the separate volumes remain constant in time

$$\partial_t V^{(1)} = \partial_t V^{(2)} = 0. \tag{20.3}$$

An example is the mixing between two constant volume grid cells. If the mixing takes place instantaneously and between the full contents of both boxes, as in convective adjustment, then the final tracer concentration in both boxes is given by

$$T_{final} = \frac{T^{(1)}\, V^{(1)} + T^{(2)}\, V^{(2)}}{V^{(1)} + V^{(2)}}. \tag{20.4}$$

It is assumed in convective mixing that the volumes of the two boxes remains unchanged. The picture is of an equal volume of water rapidly mixing from one box to the other, without any net transport between the boxes.

Instead of instantaneous and complete convective mixing, consider mixing of the two boxes at a volume rate U. That is, U represents an equal volume per time of water mixing between the boxes, with no net transport. As shown in Figure 20.1, U is chosen based on the observed amount of water exchanged through the passageway. Just as for convective adjustment, the volumes of the two boxes remains fixed. But the tracer concentrations now have a time tendency. One form for this tendency relevant for constant volume cells is given by

$$\partial_t (V^{(1)}\, T^{(1)}) = U\, (T^{(2)} - T^{(1)}) \tag{20.5}$$

$$\partial_t (V^{(2)}\, T^{(2)}) = U\, (T^{(1)} - T^{(2)}). \tag{20.6}$$

Since the volumes are constant, we can write these budgets in the form

$$\partial_t T^{(1)} = \frac{U}{V^{(1)}}\, (T^{(2)} - T^{(1)}) \tag{20.7}$$

$$\partial_t T^{(2)} = \frac{U}{V^{(2)}}\, (T^{(1)} - T^{(2)}), \tag{20.8}$$

This is the form of cross-land tracer mixing used in the rigid lid full cell MOM1.

In the real world, transport is often comprised of stacked flows where deep water flows one way and shallow water oppositely (e.g., see Figure 20.1). Hence, a more refined form of cross-land mixing may consist of upwind advective fluxes acting between non-local points in the model, where the advective velocity is specified based on observations. Such sophistication, however, is not implemented in MOM4. Indeed, it is arguable that one may not wish to have more details than provided by the simpler form above, since more details also further constrain the solution.

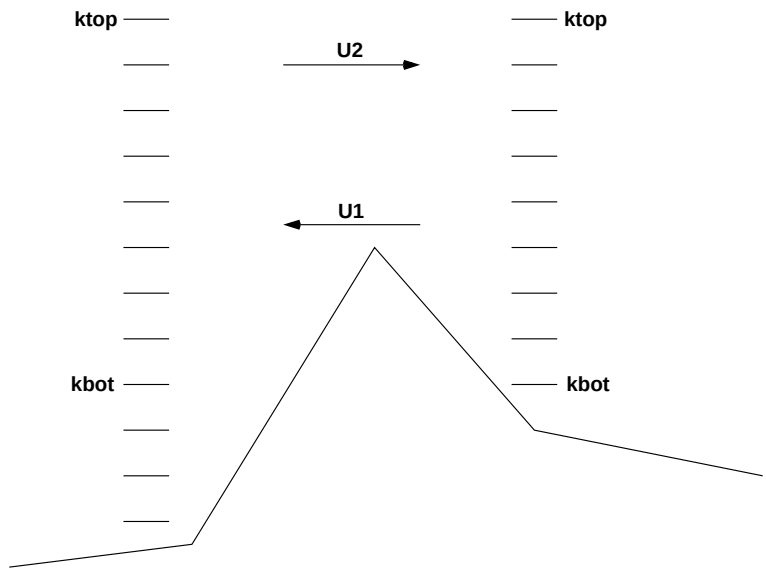

Figure 20.1: Schematic of cross-land mixing. The model's grid mesh is assumed too coarse to explicitly represent the lateral exchange of water masses. For this schematic, we consider an observed sub-grid scale transport U_1 moving in one direction, and U_2 in another. To represent the mixing effects on tracers by these transports, we suggest taking the exchange rate U in MOM4's cross-land mixing to be the average of the transports $U = (U_1 + U_2)/2$. Cross-land mixing occurs between the user-specified depth levels $k = k_{top}$ and $k = k_{bot}$. If $k_{top} = 1$, then cross-land mixing of volume in the top cell must be considered, in addition to tracer transport, in order to maintain compatibility between volume and tracer budgets.

20.4 Mixing of mass/volume

In a model with a coarse mesh, the Mediterranean is typically land-locked. Hence, the net evaporation experienced over the Mediterranean region will cause the simulated ocean volume in this region to decrease without bound. In a model resolving the Straits of Gibraltar, there is a transfer of mass across the Strait from the Atlantic. This mass transfer creates a change in the height of the free surface.

Our goal is to have a parameterized mass transfer associated just with a difference in the free surface height. That is, if the densities are different yet the free surface heights are equal, then there is no mixing. By transferring masses of water, we must also recognize that the water contains

tracer. Hence, mass and tracer mixing must maintain the compatibility mentioned in Section 20.2. In this section, however, we only introduce a basic form for mass transfer. Full compatibility with tracer transfer is achieved in Section 20.5

20.4.1 Instantaneous and complete mixing

To start by considering what form for mixing is appropriate, consider a convective analog whereby a complete mixing of masses $\rho^{(1)}\,A^{(1)}\,h^{(1)}$ and $\rho^{(2)}\,A^{(2)}\,h^{(2)}$ leaves the final mass per area in both cells given by

$$(\rho\,h)_{final} = \frac{\rho^{(1)}\,A^{(1)}\,h^{(1)} + \rho^{(2)}\,A^{(2)}\,h^{(2)}}{A^{(1)} + A^{(2)}}, \tag{20.9}$$

where $A^{(1)}$ and $A^{(2)}$ are the temporally constant horizontal areas of the two grid cells and $h^{(1)}$ and $h^{(2)}$ are their generally time dependent thicknesses.

There are two problems with this mixing. First, it is too rapid and too complete. We prefer a method that allows for some control in the rate of mixing. Second, it changes the mass within a grid cell in cases where the initial masses per area are equal yet the constant horizontal areas of the cells differ.

20.4.2 A finite time incomplete mixing

A finite time and incomplete mixing is analogous to that taken for the tracers in Section 20.3. Here, we consider the time tendencies for the mass per area within a cell

$$\partial_t(\rho^{(1)}\,h^{(1)}) = \gamma^{(1)}\,(\rho^{(2)}\,h^{(2)} - \rho^{(1)}\,h^{(1)}) \tag{20.10}$$

$$\partial_t(\rho^{(2)}\,h^{(2)}) = \gamma^{(2)}\,(\rho^{(1)}\,h^{(1)} - \rho^{(2)}\,h^{(2)}), \tag{20.11}$$

where $\gamma^{(1)}$ and $\gamma^{(2)}$ are inverse damping times. This proposed mixing results in a transfer of mass only when the mass per area within the two boxes differs. The total mass of the two-box system is conserved if the following constraint is satisfied

$$\partial_t[(\rho\,h\,A)^{(1)} + (\rho\,h\,A)^{(2)}] = (A^{(1)}\,\gamma^{(1)} - A^{(2)}\,\gamma^{(2)})\,(\rho^{(2)}\,h^{(2)} - \rho^{(1)}\,h^{(1)}) = 0. \tag{20.12}$$

This relation places a constraint on the inverse damping times $\gamma^{(1)}$ and $\gamma^{(2)}$

$$A^{(1)}\,\gamma^{(1)} = A^{(2)}\,\gamma^{(2)} \tag{20.13}$$

which is easily satisfied.

The problem with the mixing prescribed by equations (20.10) and (20.11) is that mixing will ensue in the following two undesirable cases. First, if the densities of the two cells are initially the same $\rho^{(1)} = \rho^{(2)} = \rho$, yet the cells have different thicknesses, then density change is driven solely by the difference in cell thicknesses

$$h^{(1)}\,\partial_t\rho^{(1)} = \rho\,\gamma^{(1)}\,(h^{(2)} - h^{(1)}) \tag{20.14}$$

$$h^{(2)}\,\partial_t\rho^{(2)} = \rho\,\gamma^{(2)}\,(h^{(1)} - h^{(2)}). \tag{20.15}$$

Such is acceptable in our scheme only for the surface ocean grid cell.

Another problem with the mixing prescribed by equations (20.10) and (20.11) is seen by considering the situation whereby two top model grid cells have initially equal thicknesses $h^{(1)} = h^{(2)} = h$ yet different densities. The model grid cell thickness will evolve because of the difference in densities

$$\rho^{(1)}\,\partial_t\,h^{(1)} = h\,\gamma^{(1)}\,(\rho^{(2)} - \rho^{(1)}) \tag{20.16}$$

$$\rho^{(2)}\,\partial_t\,h^{(2)} = h\,\gamma^{(2)}\,(\rho^{(1)} - \rho^{(2)}). \tag{20.17}$$

However, as stated at the beginning of this section, we aim to prescribe a mixing process that occurs only when the tracer concentration and/or free surface heights differ. Therefore, we must consider an alternative to equations (20.10) and (20.11)

20.4.3 A finite time incomplete mixing for surface cells

We consider the following prescription for the surface grid cells, in which mixing occurs only when the surface heights differ

$$\partial_t(\rho^{(1)}\,h^{(1)}) = \gamma^{(1)}\,\overline{\rho}\,(h^{(2)} - h^{(1)}) \tag{20.18}$$

$$\partial_t(\rho^{(2)}\,h^{(2)}) = \gamma^{(2)}\,\overline{\rho}\,(h^{(1)} - h^{(2)}). \tag{20.19}$$

When considered over interior model grid cells, then we prescribe no mass transfer. The density factor $\overline{\rho}$ can be given by anything convenient, such as

$$\overline{\rho} = \frac{\rho^{(1)} + \rho^{(2)}}{2}, \tag{20.20}$$

or the even simpler prescription

$$\overline{\rho} = \rho_o. \tag{20.21}$$

20.5 Tracer and mass mixing

The general case of mixing tracers and mass is now considered. The following are the aims of the formulation.

- Total fluid mass in the two boxes is conserved.
- Total tracer mass in the two boxes is conserved.
- In the rigid lid Boussinesq full cell case, the tracer tendency reduces to equations (20.7) and (20.8) used in MOM1.
- Mass is exchanged only between top grid cells, in which case if the tracer concentration in the two boxes is the same yet the mass differs, then mixing of mass will leave the tracer concentrations unchanged.
- The time tendency for the mass exchange in the top cells is proportional to the difference in surface height `eta_t` between the cells, rather than the generally smaller difference between the cell thickness `dzt`.

Mixing that satisfies these constraints is given by the following for the surface grid cells with $k = 1$

$$\partial_t(\rho^{(1)}\, h^{(1)}\, T^{(1)}) = \left(\frac{2\, U\, \rho_o}{A^{(1)}\, (H^{(1)} + H^{(2)})}\right) (h^{(2)}\, T^{(2)} - h^{(1)}\, T^{(1)}) \tag{20.22}$$

$$\partial_t(\rho^{(2)}\, h^{(2)}\, T^{(2)}) = \left(\frac{2\, U\, \rho_o}{A^{(2)}\, (H^{(1)} + H^{(2)})}\right) (h^{(1)}\, T^{(1)} - h^{(2)}\, T^{(2)}) \tag{20.23}$$

$$\partial_t(\rho^{(1)}\, h^{(1)}) = \left(\frac{2\, U\, \rho_o}{A^{(1)}\, (H^{(1)} + H^{(2)})}\right) (h^{(2)} - h^{(1)}) \tag{20.24}$$

$$\partial_t(\rho^{(2)}\, h^{(2)}) = \left(\frac{2\, U\, \rho_o}{A^{(2)}\, (H^{(1)} + H^{(2)})}\right) (h^{(1)} - h^{(2)}) \tag{20.25}$$

Likewise, for interior cells with $k > 1$, we prescribe

$$\partial_t(\rho^{(1)}\, h^{(1)}\, T^{(1)}) = \left(\frac{2\, U\, \overline{\texttt{rho_dzt}}}{A^{(2)}\, (H^{(1)} + H^{(2)})}\right) (T^{(2)} - T^{(1)}) \tag{20.26}$$

$$\partial_t(\rho^{(2)}\, h^{(2)}\, T^{(2)}) = \left(\frac{2\, U\, \overline{\texttt{rho_dzt}}}{A^{(2)}\, (H^{(1)} + H^{(2)})}\right) (T^{(1)} - T^{(2)}) \tag{20.27}$$

$$\partial_t(\rho^{(1)}\, h^{(1)}) = 0 \tag{20.28}$$

$$\partial_t(\rho^{(2)}\, h^{(2)}) = 0. \tag{20.29}$$

In these equations, H is the depth of a column with a resting ocean surface. For the $k > 1$ equations, $\overline{\texttt{rho_dzt}}$ is the averaged thickness weighted density for the two cells. For the $k = 1$ equations,

$$h(k = 1) = \texttt{Grd\%dzt}_{\texttt{k=1}} + \texttt{eta_t} \tag{20.30}$$

is the thickness of the top cell for the case of a geopotential vertical coordinate. The general $\texttt{Thickness\%dzt}_{\texttt{i,j,k=1}}$ thickness varies much less rapidly in the horizontal when employing zstar or pstar as the vertical coordinate. In order to employ similar mixing rates for the geopotential model as for the general vertical coordinate models, we prefer the more restricted definition (20.30) of thickness based on the geopotential model. The mass per area equations (20.24) and (20.25) result from the tracer equations (20.22) and (20.23) upon setting the tracer concentrations to a constant, as required for compatible budgets.

20.6 Formulation with multiple depths

We now consider the case where there are multiple boxes in the vertical. We restrict attention to situations where mixing occurs between boxes at the same vertical level, as shown in Figure 20.1.

20.6.1 MOM1 formulation of cross-land tracer mixing

In MOM1, the vertical cells all have time independent thicknesses (i.e., rigid lid geopotential coordinate model), and the fluid is Boussinesq. It is useful to start with this case prior to considering the more general case.

In the full cell rigid lid case, we follow the approach given by equations (20.7) and (20.8), where the relevant volume now becomes that for the respective column. The volumes for the two columns $lx = 1, 2$ are given by

$$V^{(lx)} = A^{(lx)} \sum_{k=kbot}^{ktop} \mathtt{dzt_k} = A^{(lx)}\, H^{(lx)}, \tag{20.31}$$

where

$$A^{(lx)} = \mathtt{dxt_{i,j}}^{(lx)}\, \mathtt{dyt_{i,j}}^{(lx)} \tag{20.32}$$

are the generally different horizontal cross-sectional areas of the tracer cells in the two columns, and $H^{(1)} = H^{(2)}$ is the vertical thickness of the two columns. The top and bottom k-levels for the columns are set by $\mathtt{k} = \mathtt{ktop}$ and $\mathtt{k} = \mathtt{kbot}$. As mentioned earlier, the formulation here allows for mixing only between boxes that live on the same k-level, so $\mathtt{k} = \mathtt{ktop}$ and $\mathtt{k} = \mathtt{kbot}$ are the same for both columns $lx = 1, 2$.

Use of these volumes in equations (20.7) and (20.8) leads to the tracer time tendencies for a particular k-level

$$\partial_t T_k^{(1)} = B^{(1)}\, (T_k^{(2)} - T_k^{(1)}) \tag{20.33}$$

$$\partial_t T_k^{(2)} = B^{(2)}\, (T_k^{(1)} - T_k^{(2)}), \tag{20.34}$$

where

$$B^{(lx)} = \frac{U}{V^{(lx)}} \tag{20.35}$$

represents the rate ($B^{(lx)}$ has units of inverse time) at which the two columns participate in the mixing. Conservation of total tracer is maintained between two horizontally adjacent boxes within the two columns. We see such conservation via multiplying the above tendencies by the respective time independent volumes of the two cells, and adding

$$\partial_t (V_k^{(1)}\, T_k^{(1)} + V_k^{(2)}\, T_k^{(2)}) = (T_k^{(2)} - T_k^{(1)})\, (A^{(1)}\, B^{(1)}\, h_k^{(1)} - A^{(2)}\, B^{(2)}\, h_k^{(2)}) = 0, \tag{20.36}$$

where

$$\begin{aligned} A^{(1)}\, B^{(1)}\, h_k^{(1)} &= U\, (h_k^{(1)}/H^{(1)}) \\ &= U\, (h_k^{(2)}/H^{(2)}) \\ &= A^{(2)}\, B^{(2)}\, h_k^{(2)} \end{aligned} \tag{20.37}$$

was used.

20.6.2 Generalizing to free surface and non-Boussinesq

We now generalize to the case of time varying grid cells with generalized vertical coordinates. Based on the considerations of Section 20.5 and the form used in MOM1, we write for the general case for a surface grid cell with $k = 1$

$$\partial_t (\rho_k^{(1)}\, h_k^{(1)}\, T_k^{(1)}) = \left(\frac{2\, U\, \rho_o}{A^{(1)}\, (H^{(1)} + H^{(2)})} \right) (h_k^{(2)}\, T_k^{(2)} - h_k^{(1)}\, T_k^{(1)}) \tag{20.38}$$

$$\partial_t (\rho_k^{(2)}\, h_k^{(2)}\, T_k^{(2)}) = \left(\frac{2\, U\, \rho_o}{A^{(2)}\, (H^{(1)} + H^{(2)})} \right) (h_k^{(1)}\, T_k^{(1)} - h_k^{(2)}\, T_k^{(2)}), \tag{20.39}$$

where again $H^{(1)}$ and $H^{(2)}$ are the generally different static resting depths of the two columns, and

$$h(k=1) = \texttt{Grd\%dzt}_{\texttt{k=1}} + \texttt{eta_t} \tag{20.40}$$

according to our prescription given by equation (20.30). Setting the tracers to uniform constants leads to the transfer of mass per area between two surface cells

$$\partial_t(\rho_k^{(1)}\, h_k^{(1)}) = \left(\frac{2\,U\,\rho_o}{A^{(1)}\,(H^{(1)}+H^{(2)})}\right)(h_k^{(2)} - h_k^{(1)}) \tag{20.41}$$

$$\partial_t(\rho_k^{(2)}\, h_k^{(2)}) = \left(\frac{2\,U\,\rho_o}{A^{(2)}\,(H^{(1)}+H^{(2)})}\right)(h_k^{(1)} - h_k^{(2)}), \tag{20.42}$$

For interior cells with $k > 1$, we prescribe

$$\partial_t(\rho_k^{(1)}\, h_k^{(1)}\, T_k^{(1)}) = \left(\frac{2\,U\,\overline{\texttt{rho_dzt}}_k}{A^{(1)}\,(H^{(1)}+H^{(2)})}\right)(T_k^{(2)} - T_k^{(1)}) \tag{20.43}$$

$$\partial_t(\rho_k^{(2)}\, h_k^{(2)}\, T_k^{(2)}) = \left(\frac{2\,U\,\overline{\texttt{rho_dzt}}_k}{A^{(2)}\,(H^{(1)}+H^{(2)})}\right)(T_k^{(1)} - T_k^{(2)}), \tag{20.44}$$

where

$$\overline{\texttt{rho_dzt}}_k = \frac{\texttt{rho_dzt}_{\texttt{k}}^{(1)} + \texttt{rho_dzt}_{\texttt{k}}^{(2)}}{2} \tag{20.45}$$

is the average thickness weighted density of the adjacent cells, and

$$h = \texttt{Thickness\%dzt}_{\texttt{i,j,k}} \tag{20.46}$$

is the general thickness of the tracer cell. By inspection, for each k-level this formulation conserves total tracer mass and total fluid mass (recall Section 20.4). Setting the tracers to uniform constants leads to a zero transfer of mass per area between two interior cells.

These budgets can be written in a form familiar from other damping processes, in which for $k = 1$ we have

$$\partial_t(\rho^{(1)}\, h^{(1)}\, T^{(1)}) = \gamma^{(1)}\,\rho_o\,(h^{(2)}\, T^{(2)} - h^{(1)}\, T^{(1)}) \tag{20.47}$$

$$\partial_t(\rho^{(2)}\, h^{(2)}\, T^{(2)}) = \gamma^{(2)}\,\rho_o\,(h^{(1)}\, T^{(1)} - h^{(2)}\, T^{(2)}) \tag{20.48}$$

$$\partial_t(\rho^{(1)}\, h^{(1)}) = \gamma^{(1)}\,\rho_o\,(h^{(2)} - h^{(1)}) \tag{20.49}$$

$$\partial_t(\rho^{(2)}\, h^{(2)}) = \gamma^{(2)}\,\rho_o\,(h^{(1)} - h^{(2)}) \tag{20.50}$$

where the depth label k was omitted for brevity, and

$$\gamma^{(1)} = \frac{2\,U}{A^{(1)}\,(H^{(1)}+H^{(2)})} \tag{20.51}$$

$$\gamma^{(2)} = \frac{2\,U}{A^{(2)}\,(H^{(1)}+H^{(2)})} \tag{20.52}$$

defines the damping coefficients. For interior cells, only tracer concentration is mixed, in which case

$$\partial_t(\rho^{(1)}\, h^{(1)}\, T^{(1)}) = \gamma^{(1)}\,\overline{\texttt{rho_dzt}}\,(T^{(2)} - T^{(1)}) \tag{20.53}$$

$$\partial_t(\rho^{(2)}\, h^{(2)}\, T^{(2)}) = \gamma^{(2)}\,\overline{\texttt{rho_dzt}}\,(T^{(1)} - T^{(2)}), \tag{20.54}$$

with $\gamma^{(1)}$ and $\gamma^{(2)}$ as for the surface cell.

The damping coefficients (20.51) and (20.52) are generally time dependent for cases with mixing in the top cell and where the free surface height is included when computing the column thicknesses $H^{(1)}$ and $H^{(2)}$. One may alternatively be motivated to keep the damping coefficients constant in time by setting $H^{(1)}$ and $H^{(2)}$ to be the time independent depth of the respective columns. This choice is appropriate when using cross-land mixing between columns in shallow regions where the free surface height is some nontrivial fraction of the full column depth. MOM4 generally sets the thicknesses to their time independent depths.

To get a sense for the strength of the mixing, consider the case of a one-degree horizontal grid mesh where the upper thousand meters of the water column is mixed across Gibraltar with $U = 1.75 \times 10^6\,\mathrm{m}^3\,\mathrm{s}^{-1}$, which is a reasonable value. With $H^{(1)} = H^{(2)} \approx 1000m$ we have

$$V^{(1)} \approx V^{(2)} \approx 1.2 \times 10^{13}\mathrm{m}^3, \tag{20.55}$$

and to the damping coefficient

$$\gamma^{(1)} \approx \gamma^{(2)} = \frac{U}{V} \approx 1.5 \times 10^{-7}\mathrm{s}^{-1} \approx 77\ \mathrm{days}^{-1}. \tag{20.56}$$

Just as for any other form of mixing, if the damping coefficients are too large, then it is possible for there to be numerical instabilities. MOM4 provides a check so that no more than one-half of a particular grid cell is mixed per model time step.

20.7 Suppression of B-grid null mode

When mixing the free surface height across an unresolved strait, it has been found essential to mix between two pairs of adjacent columns in order to suppress the checkerboard null mode present on the B-grid (see Chapter 26 of Griffies et al. (2004)). For the Mediterranean example, this means choosing any two adjacent points on each side of Gibraltar and setting the volume transport for each column to $U = (1/2)\,1.75 \times 10^6\mathrm{m}^3\,\mathrm{s}^{-1}$.

CHAPTER
TWENTYONE

Implicit treatment of vertical mixing

The purpose of this chapter is to detail the method used to implicitly time step vertical SGS processes. The material here is based on Section 9.5 of the MOM4.0 Guide (Griffies et al., 2004). There are some novel features discussed here arising from the possibility of including bottom drag implicitly in MOM4p1, which is useful when employing large bottom drags.

When the MOM4 namelist `aidif` is set to unity, vertical mixing of momentum and tracers is time stepped implicitly. When $\texttt{aidif} = 0.0$, vertical mixing is time stepped explicitly. Intermediate values give a semi-implicit treatment, although at present MOM4 does not support semi-implicit treatments. An implicit treatment of vertical mixing allows unrestrained values of the vertical mixing coefficients. An explicit treatment, especially with fine vertical grid resolution, places an unreasonable limitation on the size of the time step. The use of fine vertical resolution with sophisticated mixed layer and/or neutral physics schemes has prompted the near universal implicit treatment of vertical mixing in ocean climate models.

21.1 General form of discrete vertical diffusion

We can write the vertical diffusion equation in the discrete form

$$\partial_t \, (\rho \, \mathrm{d}z \, \phi)_k = -(J^z_{k-1} - J^z_k), \tag{21.1}$$

where J^z_k is the vertical SGS flux entering cell k through the bottom face of the cell, and J^z_{k-1} is the vertical SGS flux leaving cell k through its top face. The field ϕ can be either a tracer concentration or a horizontal velocity component. For an implicit treatment of either vertical diffusion (for tracers) or vertical friction (for velocity), we have time stepped ϕ using all time explicit pieces, and thus produced a field $\phi^*(\tau+1)$, which is the updated field sans the time implicit contributions. So for the purpose of formulating the implicit time stepping portion of the vertical physics, we write the time discrete vertical diffusion equation

$$(\rho \, \mathrm{d}z \, \phi)_k(\tau+1) = (\rho \, \mathrm{d}z \, \phi)^*_k(\tau+1) - \Delta\tau \, \texttt{aidif} \, (J^z_{k-1} - J^z_k), \tag{21.2}$$

where we assumed the preferred MOM4p1 forward time stepping scheme[1], and exposed the dimensionless time-implicit factor `aidif`. Again, for implicit time stepping, $\texttt{aidif} = 1.0$, which

[1] For the leap-frog scheme, the $\Delta\tau$ factor goes to $2\,\Delta\tau$.

is the general case for a simulation with nontrivial vertical physics. The mass per area of a grid cell is updated prior to the tracer concentration or velocity components, thus allowing us to divide equation (21.2) by $\rho\,\mathrm{d}z$ at time $\tau+1$, yielding

$$\phi_k(\tau+1) = \phi_k^*(\tau+1) - \Gamma_k\,(J^z_{k-1} - J^z_k), \tag{21.3}$$

with

$$\Gamma_k = \frac{\mathtt{aidif}\,\Delta\tau}{(\rho\,\mathrm{d}z)(\tau+1)}. \tag{21.4}$$

21.2 Discretization of vertical fluxes

The vertical flux J^z_k is located at the bottom of the kth tracer or velocity cell. A positive value for J^z_k leads to an increase in $\phi_k(\tau+1)$. Away from surface and bottom boundaries, we assume that this flux takes the downgradient form

$$J^z_k = -\rho_o\,\kappa_k\left(\frac{\phi_k(\tau+1) - \phi_{k+1}(\tau+1)}{\mathtt{dzwt}_k}\right). \tag{21.5}$$

The factors of ϕ are evaluated at time $\tau+1$ because of the implicit treatement. The vertical mixing coefficient κ_k has a general space-time dependence set by a vertical mixing scheme. As for the flux itself, the diffusivity κ_k is situated at the bottom of the tracer or velocity cell, depending on whether ϕ is a tracer field or velocity component. The factor of ρ_o is needed for dimensional consistency, and by our assumption that κ is a kinematic viscosity or diffusivity. The array $\mathtt{dzwt}_k$ represents the vertical distance between tracer points at time τ. For vertical mixing of velocity, `dzwt` becomes the distance between velocity points `dzwu`.

At the ocean surface, the vertical flux is given by the surface boundary condition $sflux$ placed on the velocity or tracer. For a tracer,

$$J^z_{k=0} = -\mathtt{stf}, \tag{21.6}$$

with `stf` MOM4's surface tracer flux array with units of velocity times density times tracer concentration. The minus sign arises from the MOM4 convention that associates a positive `stf` with an increase in tracer within the $k=1$ cell. In contrast, the present discussion assumes a convention for the flux J^z whereby a positive $J^z_{k=0}$ is associated with a decrease in tracer within the $k=1$ cell. For velocity,

$$\mathbf{J}^z_{k=0} = -\mathtt{smf}, \tag{21.7}$$

with `smf` the surface momentum flux with units of density times squared velocity. At the ocean bottom, a similar condition leads to

$$J^z_{k=\mathtt{kmt}} = -\mathtt{btf} \tag{21.8}$$

for bottom tracer fluxes, and

$$\mathbf{J}^z_{k=\mathtt{kmu}} = -\mathtt{bmf} \tag{21.9}$$

for bottom momentum fluxes. The minus signs again represent a difference in convention between MOM4 and the present discussion. In MOM4, a negative `btf` represents the passage of tracer from solid rock into the ocean domain, as in geothermal heating. For velocity, a positive `bmf` represents a drag on the ocean momentum field due to SGS interactions with the solid earth.

21.3 A generic form: Part A

To develop the solution algorithm, it is necessary to put the vertical diffusion equation into a generic form. For this purpose, let us consider in sequence the equation for surface cells $k = 1$, interior cells with $k > 1$, and bottom cells with $k = \texttt{kmt}$.

21.3.1 Surface cells

For surface cells with $k = 1$ we have

$$\begin{aligned}\phi_k^*(\tau+1) &= \phi_k(\tau+1) + \Gamma_k(\tau)\,(J_{k-1}^z - J_k^z)\\ &= \phi_k(\tau+1) - \Gamma_k(\tau)\,(\texttt{stf} + J_k^z)\\ &= \phi_k(\tau+1) - \Gamma_k(\tau)\,\texttt{stf} + \Gamma_k(\tau)\,\rho_o\,\kappa_k\left(\frac{\phi_k(\tau+1) - \phi_{k+1}(\tau+1)}{\texttt{dzwt}_k}\right),\end{aligned} \tag{21.10}$$

which leads to

$$\phi_k^*(\tau+1) + \Gamma_k(\tau)\,\texttt{stf} = \phi_k(\tau+1)\left(1 + \frac{\Gamma_k(\tau)\,\rho_o\,\kappa_k}{\texttt{dzwt}_k}\right) - \phi_{k+1}(\tau+1)\left(\frac{\Gamma_k(\tau)\,\rho_o\,\kappa_k}{\texttt{dzwt}_k}\right). \tag{21.11}$$

For velocity mixing, `stf` becomes `smf`, and `dzwt` becomes `dzwu`.

21.3.2 Interior cells

For interior cells,

$$\begin{aligned}\phi_k^*(\tau+1) &= \phi_k(\tau+1) + \Gamma_k(\tau)\,(J_{k-1}^z - J_k^z)\\ &= \phi_k(\tau+1) - \Gamma_k(\tau)\,\rho_o\,\kappa_{k-1}\left(\frac{\phi_{k-1}(\tau+1) - \phi_k(\tau+1)}{\texttt{dzwt}_{k-1}}\right)\\ &\quad + \Gamma_k(\tau)\,\rho_o\,\kappa_k\left(\frac{\phi_k(\tau+1) - \phi_{k+1}(\tau+1)}{\texttt{dzwt}_k}\right)\end{aligned} \tag{21.12}$$

which leads to

$$\begin{aligned}\phi_k^*(\tau+1) &= \phi_k(\tau+1)\left(1 + \frac{\Gamma_k(\tau)\,\rho_o\,\kappa_{k-1}}{\texttt{dzwt}_{k-1}} + \frac{\Gamma_k(\tau)\,\rho_o\,\kappa_k}{\texttt{dzwt}_k}\right)\\ &\quad - \phi_{k-1}(\tau+1)\left(\frac{\Gamma_k(\tau)\,\rho_o\,\kappa_{k-1}}{\texttt{dzwt}_{k-1}}\right) - \phi_{k+1}(\tau+1)\left(\frac{\Gamma_k(\tau)\,\rho_o\,\kappa_k}{\texttt{dzwt}_k}\right).\end{aligned} \tag{21.13}$$

21.3.3 Bottom cells

Bottom cells with $k = \texttt{kmt}(i, j)$ have

$$\begin{aligned}\phi_k^*(\tau+1) &= \phi_k(\tau+1) + \Gamma_k(\tau)\,(J_{k-1}^z - J_k^z)\\ &= \phi_k(\tau+1) + \Gamma_k(\tau)\,(J_{k-1}^z + \texttt{btf})\\ &= \phi_k(\tau+1) + \Gamma_k(\tau)\,\texttt{btf} - \Gamma_k(\tau)\,\rho_o\,\kappa_{k-1}\left(\frac{\phi_{k-1}(\tau+1) - \phi_k(\tau+1)}{\texttt{dzwt}_{k-1}}\right),\end{aligned} \tag{21.14}$$

which leads to

$$\phi_k^*(\tau+1) - \Gamma_k(\tau)\,\mathtt{btf} = \phi_k(\tau+1)\,\left(1 + \frac{\Gamma_k(\tau)\,\rho_o\,\kappa_{k-1}}{\mathtt{dzwt}_{k-1}}\right) - \phi_{k-1}(\tau+1)\,\left(\frac{\Gamma_k(\tau)\,\rho_o\,\kappa_{k-1}}{\mathtt{dzwt}_{k-1}}\right). \tag{21.15}$$

21.3.4 Form appropriate for Numerical Recipes

Introducing the notation

$$A_k = \begin{cases} -\Gamma_k(\tau)\,\rho_o\,\kappa_{k-1}/\mathtt{dzwt}_{k-1} & \text{if } k > 1 \\ 0 & \text{if } k = 1 \end{cases} \tag{21.16}$$

$$C_k = \begin{cases} -\Gamma_k(\tau)\,\rho_o\,\kappa_k/\mathtt{dzwt}_k & \text{if } k < \mathtt{kmt} \\ 0 & \text{if } k = \mathtt{kmt} \end{cases} \tag{21.17}$$

$$B_k = 1 - A_k - C_k \tag{21.18}$$

$$\Phi_k^* = \begin{cases} \phi_k^*(\tau+1) + \Gamma_k(\tau)\,\mathtt{stf} & \text{if } k = 1 \\ \phi_k^*(\tau+1) & \text{if } 1 < k < \mathtt{kmt} \\ \phi_k^*(\tau+1) - \Gamma_k(\tau)\,\mathtt{btf} & \text{if } k = \mathtt{kmt} \end{cases} \tag{21.19}$$

renders

$$\Phi_k^* = A_k\,\phi_{k-1}(\tau+1) + B_k\,\phi_k(\tau+1) + C_k\,\phi_{k+1}(\tau+1). \tag{21.20}$$

The solution is arrived at by performing a decomposition and forward substitution. The details are taken from pages 42 and 43 of Press et al. (1992).

21.4 A generic form with implicit bottom drag

We deviate from the previous approach to present here the formulation assuming the bottom boundary fluxes are computed implicitly. Such is important for the case of a bottom drag

$$\mathbf{J}^z_{k=\mathtt{kmu}} = -\rho_o\,C_d\,\mathbf{u}\,\sqrt{\mathbf{u}_{res}^2 + \mathbf{u}^2}, \tag{21.21}$$

where a large bottom drag coefficient C_d, or large residual velocity $\mathbf{u}_{res}$ require a time implicit solution method. For the global one-degree class of models typically run at GFDL, $C_d > 0.002$ generally requires an implicit treatment of bottom drag. Implicit bottom drag is enabled in MOM4p1 by setting the appropriate namelist logical inside *ocean_bbc_nml*.

To time step bottom drag implicitly requires a nonlinear solver. Rather than take that route, we take the simpler approximate approach, also employed when the diffusivity or viscosity is a nonlinear function of the flow. That is, we time discretize the bottom drag as

$$\mathbf{J}^z_{k=\mathtt{kmu}} = -\rho_o\,C_d\,\mathbf{u}(\tau+1)\,\sqrt{\mathbf{u}_{res}^2 + \mathbf{u}^2(\tau)}. \tag{21.22}$$

Hence, for the purpose of formulating the time implicit algorithm, we write the bottom drag

$$\mathbf{J}^z_{k=\mathtt{kmu}} = -\gamma\,\mathbf{u}(\tau+1), \tag{21.23}$$

where

$$\gamma = \rho_o\,C_d\,\sqrt{\mathbf{u}_{res}^2 + \mathbf{u}^2(\tau)} \tag{21.24}$$

is a nonlinear function of velocity at time τ. We can now modify the steps detailed in Section 21.3, using the nonlinear bottom drag (21.23). As this situation arises in practice for the momentum equation, we employ velocity cell labels where appropriate.

21.4.1 Surface cells

For surface cells with $k = 1$ we have

$$\begin{aligned}\phi_k^*(\tau+1) &= \phi_k(\tau+1) + \Gamma_k(\tau)\,(J_{k-1}^z - J_k^z)\\ &= \phi_k(\tau+1) - \Gamma_k(\tau)\,(\mathtt{smf} + J_k^z)\\ &= \phi_k(\tau+1) - \Gamma_k(\tau)\,\mathtt{smf} + \Gamma_k(\tau)\,\rho_o\,\kappa_k\left(\frac{\phi_k(\tau+1) - \phi_{k+1}(\tau+1)}{\mathtt{dzwu}_k}\right),\end{aligned} \tag{21.25}$$

which leads to

$$\phi_k^*(\tau+1) + \Gamma_k(\tau)\,\mathtt{smf} = \phi_k(\tau+1)\,\left(1 + \frac{\Gamma_k(\tau)\,\rho_o\,\kappa_k}{\mathtt{dzwu}_k}\right) - \phi_{k+1}(\tau+1)\,\left(\frac{\Gamma_k(\tau)\,\rho_o\,\kappa_k}{\mathtt{dzwu}_k}\right). \tag{21.26}$$

21.4.2 Interior cells

For interior cells,

$$\begin{aligned}\phi_k^*(\tau+1) &= \phi_k(\tau+1) + \Gamma_k(\tau)\,(J_{k-1}^z - J_k^z)\\ &= \phi_k(\tau+1) - \Gamma_k(\tau)\,\rho_o\,\kappa_{k-1}\,\left(\frac{\phi_{k-1}(\tau+1) - \phi_k(\tau+1)}{\mathtt{dzwu}_{k-1}}\right)\\ &\quad + \Gamma_k(\tau)\,\rho_o\,\kappa_k\,\left(\frac{\phi_k(\tau+1) - \phi_{k+1}(\tau+1)}{\mathtt{dzwu}_k}\right)\end{aligned} \tag{21.27}$$

which leads to

$$\begin{aligned}\phi_k^*(\tau+1) &= \phi_k(\tau+1)\,\left(1 + \frac{\Gamma_k(\tau)\,\rho_o\,\kappa_{k-1}}{\mathtt{dzwu}_{k-1}} + \frac{\Gamma_k(\tau)\,\rho_o\,\kappa_k}{\mathtt{dzwu}_k}\right)\\ &\quad - \phi_{k-1}(\tau+1)\,\left(\frac{\Gamma_k(\tau)\,\rho_o\,\kappa_{k-1}}{\mathtt{dzwu}_{k-1}}\right) - \phi_{k+1}(\tau+1)\,\left(\frac{\Gamma_k(\tau)\,\rho_o\,\kappa_k}{\mathtt{dzwu}_k}\right).\end{aligned} \tag{21.28}$$

21.4.3 Bottom cells

Bottom cells with $k = \mathtt{kmu}(i, j)$ have

$$\begin{aligned}\phi_k^*(\tau+1) &= \phi_k(\tau+1) + \Gamma_k(\tau)\,(J_{k-1}^z - J_k^z)\\ &= \phi_k(\tau+1) + \Gamma_k(\tau)\,(J_{k-1}^z + \mathtt{bmf})\\ &= \phi_k(\tau+1) + \Gamma_k(\tau)\,\gamma\,\phi_k(\tau+1) - \Gamma_k(\tau)\,\rho_o\,\kappa_{k-1}\left(\frac{\phi_{k-1}(\tau+1) - \phi_k(\tau+1)}{\mathtt{dzwu}_{k-1}}\right),\end{aligned} \tag{21.29}$$

which leads to

$$\phi_k^*(\tau+1) = \phi_k(\tau+1)\,\left(1 + \gamma\,\Gamma_k(\tau) + \frac{\Gamma_k(\tau)\,\rho_o\,\kappa_{k-1}}{\mathtt{dzwu}_{k-1}}\right) - \phi_{k-1}(\tau+1)\,\left(\frac{\Gamma_k(\tau)\,\rho_o\,\kappa_{k-1}}{\mathtt{dzwt}_{k-1}}\right). \tag{21.30}$$

21.4.4 Form appropriate for Numerical Recipes

Introducing the notation

$$A_k = \begin{cases} -\Gamma_k(\tau)\,\rho_o\,\kappa_{k-1}/\mathtt{dzwu}_{k-1} & \text{if } k > 1 \\ 0 & \text{if } k = 1 \end{cases} \tag{21.31}$$

$$C_k = \begin{cases} -\Gamma_k(\tau)\,\rho_o\,\kappa_k/\mathtt{dzwu}_k & \text{if } k < \mathtt{kmu} \\ 0 & \text{if } k = \mathtt{kmu} \end{cases} \tag{21.32}$$

$$B_k = \begin{cases} 1 - A_k - C_k & \text{if } k < \mathtt{kmu} \\ 1 + \gamma\,\Gamma_k(\tau) - A_k - C_k & \text{if } k = \mathtt{kmu} \end{cases} \tag{21.33}$$

$$\Phi_k^* = \begin{cases} \phi_k^*(\tau+1) + \Gamma_k(\tau)\,\mathtt{smf} & \text{if } k = 1 \\ \phi_k^*(\tau+1) & \text{if } 1 < k \leq \mathtt{kmu} \end{cases} \tag{21.34}$$

renders

$$\Phi_k^* = A_k\,\phi_{k-1}(\tau+1) + B_k\,\phi_k(\tau+1) + C_k\,\phi_{k+1}(\tau+1). \tag{21.35}$$

The solution is arrived at by performing a decomposition and forward substitution. The details are taken from pages 42 and 43 of Press et al. (1992).

21.5 Implicit bottom drag again

Again considering an implicit bottom drag implementation, we first compute the update of the bottom cell *just* due to the implicit bottom drag

$$\phi(\tau+1) = \phi^*(\tau+1) - \Gamma\,\gamma\,\phi(\tau+1), \tag{21.36}$$

which leads to the trivial inversion

$$\phi(\tau+1) = \frac{\phi^*(\tau+1)}{1+\Gamma\,\gamma}. \tag{21.37}$$

Thereafter, we update the remainder of the implicit vertical physics using the tridiagonal inversion as in Section 21.3, however with the bottom boundary condition set to zero, and with the modified coefficient B_k as follows

$$A_k = \begin{cases} -\Gamma_k(\tau)\,\rho_o\,\kappa_{k-1}/\mathtt{dzwu}_{k-1} & \text{if } k > 1 \\ 0 & \text{if } k = 1 \end{cases} \tag{21.38}$$

$$C_k = \begin{cases} -\Gamma_k(\tau)\,\rho_o\,\kappa_k/\mathtt{dzwu}_k & \text{if } k < \mathtt{kmu} \\ 0 & \text{if } k = \mathtt{kmu} \end{cases} \tag{21.39}$$

$$B_k = \begin{cases} 1 - A_k - C_k & \text{if } k < \mathtt{kmu} \\ -A_k - C_k & \text{if } k = \mathtt{kmu} \end{cases} \tag{21.40}$$

$$\Phi_k^* = \begin{cases} \phi_k^*(\tau+1) + \Gamma_k(\tau)\,\mathtt{smf} & \text{if } k = 1 \\ \phi_k^*(\tau+1) & \text{if } 1 < k \leq \mathtt{kmu} \end{cases} \tag{21.41}$$

21.6 Caveat for implicit bottom drag

A puzzling instability exists in the global 1-degree configuration distributed with the MOM4p1 code. When incorporating bottom drag implicitly in time, and when using pressure or p^* vertical coordinates, the model soon goes unstable, even when using bottom drag coefficients that are stable with an explicit treatment. No such instability appears with geopotential or z^* vertical coordinates. Interestingly, with pressure or p^*, one can run with an explicit treatment of bottom drag using a much larger bottom drag coefficient than available with geopotential or z^*. The cause of this strange behaviour remains under investigation.

PART IV
Diagnostic capabilities

The purpose of this part of the manual is to describe some of the diagnostic capabilities in MOM4p1.

CHAPTER
TWENTYTWO

Streamfunctions

The purpose of this chapter is to present the mathematical formulation of streamfunctions commonly used to summarize the overturning circulation as well as the vertically integrated circulation. This chapter is updated from that presented in the MOM4.0 manual of Griffies et al. (2004).

22.1 Brief on notation

In this chapter, we employ generalized orthogonal coordinates, in which the horizontal grid increments are given by

$$\mathrm{d}x = h_1 \, \mathrm{d}\xi^1 \tag{22.1}$$

$$\mathrm{d}y = h_2 \, \mathrm{d}\xi^2. \tag{22.2}$$

The stretching functions h_1 and h_2 are generally dependent on the horizontal position on the sphere, but independent of vertical position and independent of time. In spherical coordinates,

$$\mathrm{d}x = R \, \cos\phi \, \mathrm{d}\lambda \tag{22.3}$$

$$\mathrm{d}y = R \, \mathrm{d}\phi, \tag{22.4}$$

with R the earth's radius, λ the longitude, and ϕ the latitude.

22.2 Meridional-overturning streamfunction

The meridional overturning streamfunction is commonly used to diagnose features of the thermohaline circulation. The purpose of this section is to formulate an expression for this streamfunction, and in turn to highlight its limitations.

22.2.1 Summary of mas conservation for a finite region

In Section 3.6, we developed the conservation equations for scalar fields over a finite size region, such as a model grid cell. In particular, the mass budget for a grid cell (equation (3.166)) is written

$$\partial_t(\mathrm{d}z \, \rho) = \mathrm{d}z \, \rho \, \mathcal{S}^{(\mathsf{M})} - \nabla_s \cdot (\mathrm{d}z \, \rho \, \mathbf{u}) - (\rho \, w^{(s)})_{s=s_{k-1}} + (\rho \, w^{(s)})_{s=s_k}. \tag{22.5}$$

In the following, we neglect mass sources $\mathcal{S}^{(\mathsf{M})}$ for brevity, but they may be easily reintroduced if present as part of a model's subgrid scale parameterization.[1] As noted by equation (3.167), the divergence operator acting on the flux of mass per unit horizontal area takes the form

$$\nabla_s \cdot (\mathrm{d}z\, \rho\, \mathbf{u}) = \frac{1}{\mathrm{d}y} \frac{\partial}{\partial x} (\mathrm{d}y\, \mathrm{d}z\, \rho\, u) + \frac{1}{\mathrm{d}x} \frac{\partial}{\partial y} (\mathrm{d}x\, \mathrm{d}z\, \rho\, v), \tag{22.6}$$

which leads to the expanded form of mass conservation

$$\boxed{\begin{aligned} \partial_t (\mathrm{d}x\, \mathrm{d}y\, \mathrm{d}z\, \rho) = &- \mathrm{d}x \frac{\partial}{\partial x} (\mathrm{d}y\, \mathrm{d}z\, \rho\, u) - \mathrm{d}y \frac{\partial}{\partial y} (\mathrm{d}x\, \mathrm{d}z\, \rho\, v) \\ &- (\mathrm{d}x\, \mathrm{d}y\, \rho\, w^{(s)})_{s=s_{k-1}} + (\mathrm{d}x\, \mathrm{d}y\, \rho\, w^{(s)})_{s=s_k}. \end{aligned}} \tag{22.7}$$

This result follows by assuming the horizontal area $\mathrm{d}x\, \mathrm{d}y$ of a grid cell is independent of time and depth.

22.2.2 Zonally integrated mass transport

We now consider the integrated mass transports

$$\mathcal{V} = \int_{\xi^1_a}^{\xi^1_b} \mathrm{d}x\, (v\, \rho\, \mathrm{d}z) \tag{22.8}$$

$$\mathcal{W} = \int_{\xi^1_a}^{\xi^1_b} \mathrm{d}x\, (w\, \rho\, \mathrm{d}y), \tag{22.9}$$

which provide the meridional and vertical transport of mass (kg/sec) integrated along a line of constant generalized zonal coordinate ξ^1. Integration endpoints ξ^1_a and ξ^1_b are assumed to be at land-sea boundaries, where u vanishes, or over a periodic domain. As in the spherical coordinate case, we refer to $\mathcal{V}$ as the generalized meridional transport, though the generalized coordinates need not be aligned with the geographical latitude/longitude coordinates.

Now consider the meridional derivative of the meridional transport

$$\begin{aligned} \partial_y \mathcal{V} &= \frac{\partial}{\partial y} \left(\int_{\xi^1_a}^{\xi^1_b} \mathrm{d}x\, (v\, \rho\, \mathrm{d}z) \right) \\ &= \frac{1}{h_2\, \partial \xi^2} \left(\int_{\xi^1_a}^{\xi^1_b} \mathrm{d}x\, (v\, \rho\, \mathrm{d}z) \right) \\ &= \frac{1}{h_2} \int_{\xi^1_a}^{\xi^1_b} \frac{\partial}{\partial \xi^2} (\mathrm{d}x\, v\, \rho\, \mathrm{d}z). \end{aligned} \tag{22.10}$$

[1] The cross land scheme of Chapter 20 introduces mass source and sink terms.

In the last step, we alllowed for the partial derivative operator $\partial/\partial\xi^2$ to commute with integration over paths with constant generalized zonal coordinate ξ^1. This result follows since the generalized horizontal coordinates (ξ^1, ξ^2) are independent. Correspondingly, we may introduce the increment $\mathrm{d}\xi^2$ inside and outside of the integral to render

$$\partial_y \mathcal{V} = \frac{1}{\mathrm{d}y} \int_{\xi^1_a}^{\xi^1_b} \mathrm{d}y \, \frac{\partial}{\partial y}(\mathrm{d}x \, v \, \rho \, \mathrm{d}z). \tag{22.11}$$

We now use the mass conservation equation (22.7) to find

$$\partial_y \mathcal{V} = \frac{1}{\mathrm{d}y} \int_{\xi^1_a}^{\xi^1_b} \Big(-\partial_t(\mathrm{d}x \, \mathrm{d}y \, \mathrm{d}z \, \rho) - (\mathrm{d}x \, \mathrm{d}y \, \rho \, w^{(s)})_{s=s_{k-1}} + (\mathrm{d}x \, \mathrm{d}y \, \rho \, w^{(s)})_{s=s_k} \Big), \tag{22.12}$$

where we cancelled the zonal transport term $u \, \rho \, \mathrm{d}y \, \mathrm{d}z$, since it either vanishes at the zonal boundaries (ξ^1_b, ξ^1_a), or exhibits periodicity. Introducing the vertical transport (22.9) yields

$$\boxed{\mathrm{d}y \, \partial_y \mathcal{V} + \delta_k \mathcal{W} = - \int_{\xi^1_a}^{\xi^1_b} \partial_t(\mathrm{d}x \, \mathrm{d}y \, \mathrm{d}z \, \rho)} \tag{22.13}$$

with

$$\delta_k \mathcal{W} = \mathcal{W}_{k-1} - \mathcal{W}_k \tag{22.14}$$

the vertical finite increment of the vertical transport.

Equation (22.13) is a direct result of the mass conservation equation (22.7) applied to a zonal integral. It says that the divergence of the zonally integrated meridional and vertical transport equals to the zonally integrated tendency of mass. This result is the basis for our next step, which is to define a streamfunction.

22.2.3 Mass transport streamfunction

A streamfunction can be defined for any non-divergent transport. For the zonally integrated mass transport, equation (22.13) says there is zero divergence if the zonal integral of the time tendency of mass vanishes. Zero time tendency arises if the top and bottom grid cell boundaries are set according to constant hydrostatic pressure surfaces, so that $\rho \, \mathrm{d}z = -g^{-1} \, \mathrm{d}p$. In this case, the mass within a cell is constant in time. Analogously, there is also a zero divergence of the volume transport for a Boussinesq fluid using geopotential vertical coordinates, in which case the volume of fluid in a cell is constant. In more general cases, however, there is no guarantee that the mass within a cell is constant. Additionally, in the presence of water crossing the ocean boundaries, mass will change, again leading to a nonzero divergence. Even with these caveats, the streamfunction defined below provides a very useful measure of the zonally integrated mass transport, thus motivating its near ubiquitous use as a model diagnostic.

In the case of a non-divergent zonally integrated mass transport, a mass transport streamfunction Ψ can be introduced according to the following specifications[2]

$$\mathcal{V} = -\delta_k \Psi \tag{22.15}$$

$$\mathcal{W} = \Psi_{,y}. \tag{22.16}$$

The streamfunction has dimensions mass/time, just as the meridional and vertical transports $\mathcal{V}$ and $\mathcal{W}$. The typical oceanographic dimension for these transports is Sverdrup, where $1\,\mathrm{Sv} = 10^9 \mathrm{kg\,sec}^{-1}$.

To derive a diagnostic expression for the streamfunction, we may start from either of the expressions (22.15) or (22.16). Integration and the use of boundary conditions then leads to expressions for Ψ, with the two expressions equivalent if the zonally integrated mass transport is non-divergent. In many simulations, the meridional transport $\mathcal{V}$ is more easily computed than the vertical transport $\mathcal{W}$, making the specification $\mathcal{V} = -\delta_k \Psi$ the most common starting point. From a finite volume perspective, the relation $\mathcal{V} = -\delta_k \Psi$ says that the discretized streamfunction should be computed at the top and bottom interfaces of grid cells, so that its vertical difference across the cells then leads to the meridional transport through the cell's vertical side walls (see Figure 22.1). Correspondingly, the streamfunction is horizontally co-located with the meridional transport $\mathcal{V}$.[3]

The relation $\mathcal{V} = -\delta_k \Psi$ remains valid if we modify Ψ by any function of horizontal position, since the vertical difference eliminates the arbitrary function.[4] We choose to exploit this ambiguity by specifying the arbitrary function so that the streamfunction has a zero value at the ocean bottom. We are motivated to take this choice since for most oceanographic purposes, there is no mass transport considered between the liquid ocean and solid earth. Consequently, the solid earh boundary condition is time independent, and for convenience we specify that it vanishes.

Let us now develop the streamfunction, starting from the ocean bottom using the definition $\mathcal{V} = -\delta_k \Psi$. For the top surface of the bottom-most cell with $k = kmt$, we have

$$\Psi_{kmt-1} = 0 - \mathcal{V}_{kmt}, \tag{22.17}$$

where $0 = \Psi_{kmt}$ is inserted as a place-holder for the next iteration, and $\mathcal{V}_{kmt}$ is the meridonal transport leaving the vertical side walls within the bottom-most cell. For the next cell up in the column, we have

$$\begin{aligned} \Psi_{kmt-2} &= \Psi_{kmt-1} - \mathcal{V}_{kmt-1} \\ &= -\mathcal{V}_{kmt} - \mathcal{V}_{kmt-1}. \end{aligned} \tag{22.18}$$

Induction leads to the result

$$\boxed{\begin{aligned} \Psi_K &= -\sum_{k=K+1}^{kmt} \mathcal{V}_k \\ &= -\sum_{k=K+1}^{kmt} \left(\int_{x_a}^{x_b} \mathrm{d}x \, (v \, \rho \, \mathrm{d}z) \right)_k , \end{aligned}} \tag{22.19}$$

[2]This definition of Ψ has an associated sign convention, with the opposite convention just as valid mathematically, but chosen less frequently in practice.

[3]We are led to an alternative grid placement for Ψ if starting from the relation $\mathcal{W} = \Psi_{,y}$.

[4]This ambiguity represents a *gauge symmetry*, which can be exploited in whatever manner is most convenient.

with a continuous expression given by

$$\boxed{\Psi(y,z,t) = -\int_{x_a}^{x_b} \mathrm{d}x \int_{-H}^{z} v\,\rho\,\mathrm{d}z'.} \tag{22.20}$$

In the continuous expression, it is important to perform the vertical integral first, since the bottom topography $z = -H(x,y)$ is a function of the horizontal position.

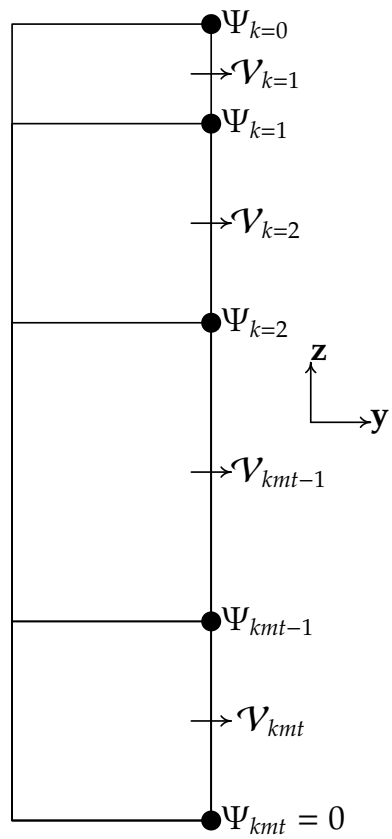

Figure 22.1: This figure illustrates the relation between the meridional-overturning streamfunction Ψ and the meridional transport $\mathcal{V}$, for the particular case of $kmt = 4$ vertical grid cells. The streamfunction is evaluated on the interfaces between the vertical cells, whereas the transport measures the mass leaving the cell in the meridional direction. Note the relatively think bottom cell can arise from the use of bottom partial step representation of topography as used in MOM4.

22.2.4 Transport beneath an arbitrary surface

As shown in Section 40.9 of Pacanowski and Griffies (1999), we can extend the above considerations to the case of generalized vertical coordinates. In this case, we are concerned with the

meridional transport of fluid beneath some generalized vertical coordinate surface. It is a straightforward matter to extend the definition of the overturning streamfunction to this case, where

$$\Psi(y,s,t) = -\int_{x_a}^{x_b} \mathrm{d}x \int_{s(-H)}^{s(z)} v\,\rho\,\mathrm{d}z', \tag{22.21}$$

with $s = s(x,y,z,t)$ the generalized vertical coordinate (see Griffies (2004) for details). Surfaces that are physically of interest include various potential density surfaces, which are especially relevant when the flow is adiabatic. See Section 40.9 of Pacanowski and Griffies (1999) for more discussion.

22.2.5 Transport from GM90

The parameterization of Gent et al. (1995) provides a volume transport in addition to the resolved scale Eulerian mean transport. The total meridional-overturning streamfunction takes the form

$$\Psi^{(tot)}(y,z,t) = -\int_{x_a}^{x_b} \mathrm{d}x \int_{-H}^{z} \mathrm{d}z'\,\rho\,(v + v^{gm}). \tag{22.22}$$

We consider now special cases for the eddy-induced velocity v^{gm}.

22.2.5.1 Boussinesq geopotential coordinates

In the Boussinesq case with geopotential vertical coordinates, the meridional eddy-induced velocity is given by

$$v^{gm} = -\partial_z\,(\kappa\,S_y) \tag{22.23}$$

with $S_y = -\partial_y\rho/\partial_z\rho$ the neutral slope in the y-direction and $\kappa > 0$ a kinematic diffusivity. Performing the vertical integral on the GM90 piece leads to

$$\Psi^{(tot)}(y,z,t) = \Psi(y,z,t) + \Psi^{gm}(y,z,t) \tag{22.24}$$

where

$$\Psi^{gm}(y,z,t) = \rho_0 \int_{x_a}^{x_b} \mathrm{d}x\,(\kappa\,S_y) \tag{22.25}$$

with $\kappa\,S_y = 0$ at $z = -H$, and ρ_0 the reference density for the Boussinesq fluid. Hence, the Gent et al. (1995) parameterization adds a contribution that scales linearly with basin size, isopyncal slope, and diffusivity

$$\Psi^{gm} \sim \rho_0\,L\,S\,\kappa. \tag{22.26}$$

As an example, let $\kappa = 10^3 \mathrm{m}^2\,\mathrm{s}^{-1}$, $S = 10^{-3}$, and $L = 10^7$ m, which yields $\mathcal{T} \approx 10$Sv. Such transport can represent a nontrivial addition to that from the resolved scale velocity field.

22.2.5.2 Non-Boussinesq pressure coordinates

In the hydrostatic non-Boussinesq case with pressure vertical coordinates, the meridional eddy-induced velocity is given by

$$v^{gm} = \partial_p \left(g \, \rho \, \kappa \, S_y \right) \tag{22.27}$$

with $S_y = -\partial_y \rho / \partial_z \rho$ the neutral slope in the y-direction relative to constant pressure surfaces. Performing the vertical integral for the GM90 streamfunction leads to

$$\Psi^{gm}(y, z, t) = \int_{x_a}^{x_b} \mathrm{d}x \, (\rho \, \kappa \, S_y). \tag{22.28}$$

22.2.6 Diagnosing the streamfunction in Ferret from MOM4 output

In MOM4, there are two key diagnostics computed on-line that should be saved in order to determine an accurate expression for the streamfunction:

$$\text{ty_trans} = \mathrm{d}x \, (v \, \rho \, \mathrm{d}z) \tag{22.29}$$

$$\text{ty_trans_gm} = \mathrm{d}x \, (\rho \, \kappa \, S_y) \tag{22.30}$$

Computing the Eulerian streamfunction (22.20) requires the following operations

$$\begin{aligned} \Psi(y, z, t) &= -\int_{x_a}^{x_b} \mathrm{d}x \int_{-H}^{z} v \, \rho \, \mathrm{d}z' \\ &= -\int_{x_a}^{x_b} \mathrm{d}x \int_{-H}^{\eta} v \, \rho \, \mathrm{d}z' + \int_{x_a}^{x_b} \mathrm{d}x \int_{z}^{\eta} v \, \rho \, \mathrm{d}z' \\ &= -\text{ty_trans[i=@sum,k=@sum]} + \text{ty_trans[i=@sum,k=@rsum]}. \end{aligned} \tag{22.31}$$

We must compute the streamfunction in this manner since Ferret's relative sum k=@rsum starts from an assumed zero value at the surface and integrates downward, whereas the streamfunction has a zero boundary condition on the ocean bottom. Hence, without subtracting the term ty_trans[i=@sum,k=@sum], the diagnosed streamfunction will incorrectly have nonzero values at the bottom. A nonzero value for ty_trans[i=@sum,k=@sum] arises from net vertically integrated mass transport through a section. For a rigid lid model, this net transport vanishes.

The GM-streamfunction is simpler to compute, whereby

$$\Psi^{gm}(y, z, t) = \text{ty_trans_gm[i=@sum]}. \tag{22.32}$$

There is no vertical sum required, since the vertical integral has already been performed analytically (equations (22.25) and (22.28)).

22.3 Vertically integrated transport

The purpose of this section is to discuss the streamfunction used to summarize the vertically integrated transport. Only when vertically integrated flow is non-divergent, such as for the Boussinesq rigid lid case, will a streamfunction be sufficient. In general, the streamfunction defined in the following only approximates the flow. However, for many cases it is quite useful.

22.3.1 Summary of the rigid lid

With the rigid lid method of Bryan (1969), it is assumed that the vertically integrated velocity in a Boussinesq fluid is non-divergent $\nabla \cdot \mathbf{U} = 0$. Hence, it can be described via a scalar streamfunction $\mathbf{U} = \hat{\mathbf{z}} \wedge \nabla \tilde{\psi}$. In this case, the vertically integrated advective mass transport between two points is given by

$$T_{ab} = \rho_0 \int_a^b dl \; \hat{\mathbf{n}} \cdot \int_{-H}^{0} \mathrm{d}z \; \mathbf{u} = \psi_a - \psi_b, \tag{22.33}$$

where dl is the line element along any path connecting the points a and b, and $\hat{\mathbf{n}}$ is a unit vector pointing perpendicular to the path in a rightward direction when facing the direction of integration. As written, T_{ab} has units of mass per time, and so it represents a mass transport (Bryan, 1969). Therefore, the difference between the streamfunction at two points represents the vertically integrated mass transport between the two points. It is for this reason that the streamfunction is sometimes called the *mass transport streamfunction*.

22.3.2 General case of divergent flow in non-Boussinesq fluids

The vertically integrated horizontal mass transport

$$\mathbf{U}^{\rho} = \int_{-H}^{\eta} \rho \, \mathbf{u} \tag{22.34}$$

generally has a non-zero divergence due to fluctuations of mass within the vertical column, as seen by the column integrated mass balance (equation (3.21))

$$\partial_t \left(\int_{-H}^{\eta} \mathrm{d}z \, \rho \right) + \nabla \cdot \mathbf{U}^{\rho} = q_{\mathsf{w}} \, \rho_{\mathsf{w}} + \int_{-H}^{\eta} \mathrm{d}z \, \rho \, \mathcal{S}^{(M)}. \tag{22.35}$$

As for the overturning transport, we ignore mass sources in the following, thus considering

$$\nabla \cdot \mathbf{U}^{\rho} = -\partial_t \left(\int_{-H}^{\eta} \mathrm{d}z \, \rho \right) + q_{\mathsf{w}} \, \rho_{\mathsf{w}}. \tag{22.36}$$

In either case, the presence of a nonzero divergence requires the introduction of a streamfunction $\tilde{\psi}$ and a velocity potential χ

$$\mathbf{U}^{\rho} = \hat{\mathbf{z}} \wedge \nabla \tilde{\psi} + \nabla \chi. \tag{22.37}$$

Only for a Boussinesq rigid-lid model with zero fresh water flux will χ vanish. Hence, to compute the precise vertically integrated mass transport passing between two points, a direct evaluation of the integral

$$\boxed{T_{ab} = \int_a^b dl \; \hat{\mathbf{n}} \cdot \mathbf{U}^{\rho}} \tag{22.38}$$

is given. Although accurate and complete, this integral does not readily provide a horizontal map of transport, and so it looses much of the appeal associated with the transport streamfunction used with a rigid lid.

However, for many practical situations, maps of the function

$$\boxed{\psi(x,y,t) = -\int_{y_o}^{y} \mathrm{d}y'\, U^\rho(x,y',t)} \tag{22.39}$$

are quite useful, where the lower limit y_o is taken at the southern boundary of the domain, generally given by a solid wall for ocean climate models. By its definition, the meridional derivative of ψ yields the zonal mass transport

$$\psi_{,y} = U^\rho. \tag{22.40}$$

The zonal derivative, however, does not yield the meridional mass transport due to the divergent nature of the vertically integrated flow. It is for this reason that we denote ψ a *quasi-streamfunction*. Notably, for many cases, especially with long time averages, the divergence is small, thus allowing ψ to present a good indication of the path and intensity of the vertically integrated mass transport.

By construction, ψ reduces to the transport streamfunction in the case of a rigid lid where $\nabla \cdot \mathbf{U} = 0$. However, this is not a unique choice and alternatives do exist. For example,

$$\psi^*(x,y,t) = \psi(x_o,y,t) + \int_{x_o}^{x} \mathrm{d}x'\, V^\rho(x',y,t), \tag{22.41}$$

gives

$$V^\rho = \psi^*_{,x}. \tag{22.42}$$

ψ^* has the advantage that zonal derivatives give the exact meridional transport, yet the meridional derivative in general deviates from the zonal transport. Comparing maps of ψ and ψ^* reveals the degree to which the vertically integrated mass transport is non-divergent. For most purposes of climate modeling at GFDL, we map the streamfunction $\psi = -\int_{y_o}^{y} \mathrm{d}y'\, U^\rho$, as deviations from ψ^* are modest for most applications.

CHAPTER
TWENTYTHREE

Effective dianeutral diffusivity

The purpose of this chapter is to detail a method to quantify water mass mixing in MOM without detailed knowledge of the numerical transport scheme. The method is restricted to experiments configured with the following:

- Boussinesq fluid;
- linear free surface, so that the thickness of a grid cell remains constant in time; alternatively, to the use of z^* vertical coordinate, where each cell has a time independent spacing in z^*-space;
- flat bottom ocean;
- linear equation of state;
- each grid cell has the same volume in $x - y - s$ space, with s the general vertical coordinate;
- zero buoyancy forcing.

Relaxing some of these assumptions is possible, yet not implemented. Momentum forcing via winds is allowed. Much of the fundamentals in this chapter are guided by the work of Winters et al. (1995) and Winters and D'Asaro (1995). Griffies et al. (2000b) applied these methods to various idealized model configurations in a rigid lid version of MOM3.

We assume the linear equation of state for an incompressible fluid is written in the form

$$\rho = \rho_0 \, (1 - \alpha \, \theta), \tag{23.1}$$

where θ is potential temperature, ρ_o is a constant density associated with the Boussinesq approximation, and α is a constant thermal expansion coefficient. The system is open to momentum fluxes yet closed to buoyancy fluxes.

23.1 Potential energy and APE in Boussinesq fluids

The purpose of this section is to introduce the notion of a sorted density profile in the context of potential energy and available potential energy (APE). This profile is of particular relevance when considering the effective mixing occuring throughout a column of sorted fluid in Section 23.2.

Potential energy of the ocean is given by

$$E_p = \int \mathrm{d}V \, \rho \, \mathcal{P}, \tag{23.2}$$

where

$$\mathcal{P} = g \, z \tag{23.3}$$

is the potential energy per mass of a fluid parcel, g is the acceleration of gravity, z is the vertical position of a fluid parcel, and $\rho \, \mathrm{d}V = \rho \, \mathrm{d}x \, \mathrm{d}y \, \mathrm{d}z$ is the parcel mass.

Available potential energy (APE) is the difference between the potential energy of the fluid in its natural state, and the potential energy of a corresponding stably stratified *reference* state. The reference state is reached by adiabatically rearranging the fluid to a state of minimum potential energy, which is a state that contains zero horizontal gradients. This rearrangement, or *sorting*, provides a non-local mapping between the unsorted fluid density and the sorted density

$$\rho(\mathbf{x}, t) = \rho(z^*(\mathbf{x}, t), t). \tag{23.4}$$

The sorting map determines a vertical position field $z^*(\mathbf{x}, t)$ which is the vertical height in the sorted state occupied by a parcel at $(\mathbf{x}, t)$ in the unsorted state. Due to the monotonic arrangement of density in the sorted state, $z^*(\mathbf{x}, t)$ is a monotonic function of density $\rho(\mathbf{x}, t)$.

It is convenient to set the origin of the vertical coordinate at the ocean bottom so to keep potential energy of the unsorted state non-negative. This convention also allows for $z^*(\mathbf{x}, t)$ to be defined as a monotonically decreasing function of density. That is,

$$\rho(\mathbf{x}_1, t) < \rho(\mathbf{x}_2, t) \Rightarrow z^*(\mathbf{x}_1, t) > z^*(\mathbf{x}_2, t). \tag{23.5}$$

Conservation of volume in a flat bottom ocean implies that the sorted fluid state has the same vertical extent as the unsorted fluid, which renders

$$0 \leq z, z^* \leq H, \tag{23.6}$$

where H is the ocean depth.

In the following, it proves convenient to denote the density profile in the sorted reference state using the symbols

$$\rho(z^*, t) = \rho_{ref}(z = z^*, t). \tag{23.7}$$

Given this notation, the non-local sorting map between the unsorted and sorted fluid states provides the equivalence

$$\rho(\mathbf{x}, t) = \rho(z^*(\mathbf{x}, t), t) = \rho_{ref}(z = z^*, t). \tag{23.8}$$

In turn, potential energy for the sorted fluid state can be written in two equivalent manners

$$E_{ref} = g \int \mathrm{d}V \; z \, \rho_{ref}(z, t) \tag{23.9}$$

$$= g \int \mathrm{d}V \, z^*(\mathbf{x}, t) \; \rho(\mathbf{x}, t). \tag{23.10}$$

Equation (23.9) represents an integral over the sorted fluid state, in which the density of this state is a function only of the depth. The horizontal area integral is thus trivial to perform. Equation (23.10) represents an integral over the unsorted fluid state, where the density $\rho(\mathbf{x}, t)$ of an unsorted parcel

is weighted by the vertical position $z^*(\mathbf{x}, t)$ that the parcel occupies in the sorted state. It follows that the APE can be written in two equivalent ways

$$E_{APE} = g \int \mathrm{d}V \; z \; [\rho(\mathbf{x}, t) - \rho_{ref}(z, t)] \tag{23.11}$$

$$= g \int \mathrm{d}V \; \rho(\mathbf{x}, t) \; [z - z^*(\mathbf{x}, t)]. \tag{23.12}$$

23.2 Effective dianeutral mixing

In this section we formulate a method to empirically quantify the effects on water masses arising from various simulated tracer transport processes. A similar application was advocated by Winters et al. (1995) and Winters and D'Asaro (1995) for the purpose of diagnosing mixing in direct numerical simulations of unstable fluid flows. Their focus was on physically motivated mixing such as that occuring with breaking waves. The main focus here is on spurious mixing due to numerical errors. The procedure is identical, however, in that for each case, one considers the evolution of the reference density profile, $\rho_{ref}(z, t)$, in a fluid system closed to buoyancy fluxes

$$\partial_t \, \rho_{ref} = \partial_{z^*} \, (\kappa_{eff} \, \partial_{z^*} \rho_{ref}). \tag{23.13}$$

Again, in this equation z^* is the vertical position in the sorted fluid state. Therefore, constant z^* surfaces represent constant density surfaces in the unsorted state. As such, the effective diffusivity κ_{eff} summarizes the total amount of mixing across constant density surfaces. If the simulation does not change the water mass distribution, then $D\rho/Dt = 0$, the sorted reference density is static $\partial_t \, \rho_{ref} = 0$, and the effective diffusivity is zero. In turn, any temporal change in the reference density represents changes in the water mass distribution. These changes are the result of dianeutral mixing, and so have an associated non-zero $\kappa_{eff}(z^*, t)$. This is the basic idea that is pursued in the following sections.

23.2.1 Global effective dianeutral diffusivity

In addition to the diffusivity $\kappa_{eff}(z^*, t)$, which is local in density space, it is useful to garner a summary of the overall dianeutral mixing occuring in an ocean model. A vertical integral of $\kappa_{eff}(z^*, t)$ would provide such information. A quicker computation of a global effective dianeutral diffusivity can be obtained by inverting the variance equation for the sorted density

$$\partial_t \int \mathrm{d}V \; \rho_{ref}^2 = -2 \int \mathrm{d}V \; \kappa_{eff} \; (\partial_z \rho_{ref})^2. \tag{23.14}$$

This result, derived for a closed fluid system, suggests the introduction of a global effective diffusivity

$$\kappa_{global}(t) = - \left(\frac{\partial_t \int \mathrm{d}V \; \rho_{ref}^2}{2 \int \mathrm{d}V \; (\partial_z \rho_{ref})^2} \right). \tag{23.15}$$

This diffusivity provides one number that can be used to represent the total amount of dianeutral diffusion acting over the full model domain. It vanishes when the simulation is adiabatic, as does the effective diffusivity $\kappa_{eff}(z^*, t)$. However it is generally different from the vertical average of $\kappa_{eff}(z^*, t)$.

23.2.2 Finite difference approximation

In the following, assume that the discrete sorted density is equally spaced in the vertical with a separation Δz^*, and let the vertical coordinate increase upwards from zero at the flat bottom ocean floor. Note that in general, $\Delta z^* << \Delta z$, where Δz is the ocean model's grid spacing. The reason is that *all* the $N_x \times N_y \times N_z$ grid points in the ocean model are sorted into the reference vertical profile, which has a vertical range over the same extent as the ocean model: $0 \leq z, z^* \leq H$. As a consequence, the vertical resolution of the sorted profile is $N_x \times N_y$ times finer than the N_z points resolving the profile at a particular horizontal position in the unsorted state.

On the discrete lattice, the vertical diffusive flux of the sorted density

$$F^{z^*}(z^*, t) = -\kappa_{eff}(z^*, t)\, \partial_{z^*}\, \rho_{ref}(z^*, t) \tag{23.16}$$

is naturally defined at the top face of the density cell whose center is at z^*. As such, the diffusion operator at the lattice point z^*, which is constructed as the convergence of the diffusive flux across a density grid cell, takes the discrete form

$$-\left(\partial_{z^*} F^{z^*}\right)(z^*, t) \quad \approx \quad -\left(\frac{F^{z^*}(z^*, t-\Delta t) - F^{z^*}(z^* - \Delta z^*, t-\Delta t)}{\Delta z^*}\right). \tag{23.17}$$

The time lag is necessary to provide for a stable discretization of the diffusion equation. The discretization of the flux is given by

$$\begin{aligned} F^{z^*}(z^*, t) &= -\kappa_{eff}(z^*, t)\, \partial_{z^*}\, \rho_{ref}(z^*, t) \\ &\approx -\kappa_{eff}(z^*, t)\, \left(\frac{\rho_{ref}(z^* + \Delta^* z, t) - \rho_{ref}(z^*, t)}{\Delta z^*}\right). \end{aligned} \tag{23.18}$$

Since the flux is located at the top face of the density grid cell whose center is at the position z^*, the effective diffusivity is located at this face as well. Each of these difference operators is consistent with those used in MOM when discretizing the diffusion equation for the unsorted fluid.

As with the unsorted tendency, the time derivative in the effective diffusion equation can be approximated using a leap-frog differencing:

$$\partial_t\, \rho_{ref}(z^*, t) \approx \frac{\rho_{ref}(z^*, t+\Delta t) - \rho_{ref}(z^*, t-\Delta t)}{2\Delta t}. \tag{23.19}$$

Piecing these results together yields the expression for the vertical flux at the top of the density cell $z^* + \Delta z^*$

$$F^{z^*}(z^*, t-\Delta t) = F^{z^*}(z^* - \Delta z^*, t-\Delta t) - \frac{\Delta z^*}{2\Delta t}\, [\rho_{ref}(z^*, t+\Delta t) - \rho_{ref}(z^*, t-\Delta t)]. \tag{23.20}$$

This flux can be determined starting from the ocean bottom, where is vanishes, and working upwards. Without surface buoyancy fluxes, it also vanishes at the top of the water column, resulting in conservation of $\int dz^*\, \rho_{ref}(z^*, t)$. After diagnosing the flux from the tendency, the effective diffusivity can be diagnosed from

$$\kappa_{eff}(z^*, t) = -F^{z^*}(z^*, t)\, \left(\frac{\Delta z^*}{\rho_{ref}(z^* + \Delta z^*, t) - \rho_{ref}(z^*, t)}\right). \tag{23.21}$$

The issues of what to do when the density gradient becomes small, as in weakly stratified regions, is discussed in Sections 23.2.3 and 23.2.5.

23.2.3 Relevant vertical stratification range

In the stratified portions of the upper ocean, periods $2\pi/N$ for buoyancy oscillations are roughly 10-30 minutes, smaller in the pycnocline, and in the deep ocean periods are roughly 5-6 hours (see pages 55-56 of Pickard and Emery (1990)). The squared buoyancy frequency for the sorted reference state is given by

$$\begin{aligned} N_*^2 &= -\frac{g}{\rho_o}\,\frac{d\rho_{ref}}{dz^*} \\ &= -\frac{g}{1000\,\rho_o}\,\frac{d\sigma_{ref}}{dz^*}, \end{aligned} \tag{23.22}$$

where $\sigma_{ref} = 1000\,(\rho_{ref} - 1)$ is the sigma value for the sorted density $\rho_{ref}(g/cm^3)$. Working with σ_{ref} is desirable for accuracy reasons. The observed range in buoyancy periods provides a range over the sorted vertical profile's stratification for which a calculation of the model's effective diffusivity will be performed:

$$\frac{d\rho_{ref}}{dz^*} = -\frac{1.035 g/cm^3}{980 cm/sec^2}\,\frac{4\pi^2}{T^2}, \tag{23.23}$$

where $T(sec)$ is the period. With $1 \times 60 secs < T < 6 \times 60 \times 60 secs$ defining the period range, the corresponding vertical density gradient range is

$$10^{-10} g/cm^4 \leq \left|\frac{d\rho_{ref}}{dz}\right| \leq 10^{-5} g/cm^4, \tag{23.24}$$

and the corresponding range for the sigma gradient is

$$10^{-7} g/cm^4 \leq \left|\frac{d\sigma_{ref}}{dz}\right| \leq 10^{-2} g/cm^4. \tag{23.25}$$

23.2.4 A useful test case

When coding the effective diffusivity algorithm, it has been found useful to compare results with those from a different approach. Here, we horizontally average (i.e., homogenize) the density field along a particular depth surface. In a model with stable stratification, rigid lid, flat bottom, no-flux boundary, potential density evolution takes the form

$$\partial_t \langle \rho \rangle^{x,y} = -\partial_z \langle w\,\rho \rangle^{x,y} + \partial_z \langle \kappa\,\rho_{,z} \rangle^{x,y} \tag{23.26}$$

where κ is a vertical diffusivity and the angled-brackets indicate horizontally averaged quantities. With zero advection, evolution occurs solely via vertical diffusion. Hence, backing out an effective diffusivity for this horizontally homogenized system yields κ, regardless the horizontal/vertical stratification. It turns out that this algorithm is far simpler to implement numerically, since it does not require sorting nor interpolation to a prespecified sorted coordinate z^*. Its results are in turn more robust. Yet, importantly, they are relevant only for the case of no-advection, which is not so interesting in general yet serves as a good check for specific cases.

23.2.5 Computational precision

Models run with pure horizontal and/or vertical diffusion theoretically show $\kappa_{eff} \geq 0$ (see Winters and D'Asaro (1995) and Griffies et al. (2000b)). However, if the stratification range given by equations (23.24) or (23.25) is violated by more than roughly an order of magnitude, then spurious values of κ_{eff} tend to arise. These spurious values include unreasonably large values for κ_{eff} in regions of very low stratification, and negative values in regions of very large stratification. However, within the range given by equations (23.24) or (23.25), the computation yields reasonable values. For stratification outside this range, κ_{eff} is arbitrarily set to zero.

Another point to consider is that the stratification of ρ_{ref} shows much fine-scale step-liked structure. Computing an effective diffusivity based on such a profile will in turn show lots of noise. Averaging over the fine scales is therefore necessary to garner robust answers. That is, the spurious mixing diagnostic is smoother when having coarser vertical resolution. An objective means of averaging is to average ρ_{ref} vertically onto the same vertical grid used by the forward model in computing the unsorted density state. If this vertical stratification is itself very fine, then spurious values of κ_{eff} may still result, again due to not enough points of ρ_{ref} averaged into a single layer.

23.2.6 Negative κ_{eff}

Those advection schemes which contain dispersion, such as centered differenced advection, have leading order error terms that are not second order, but rather third order differential operators. Hence, the diagnosis of κ_{eff} for these schemes will likely to contain a fair amount of negative values. In turn, negative κ_{eff} may be interpreted as a sign of dispersion errors, which can create or destroy water masses. Upon introducing convection into the model, much of these *undershoots* and *overshoots* created by dispersion are rapidly mixed. In turn, the resulting κ_{eff} should become positive upon introducing convection.

Another source of negative κ_{eff} apparently can arise simply due to the finite sampling time and discrete grid, even in the case of pure diffusion. For example, if there is a mixing event, and if this event is under-sampled in time, it is possible that the sorted state may have density appear in a non-local manner. Such mixing events will lead to negative κ_{eff}. The ability to realize such values for κ_{eff} motivates a sampling time Δt equal to time step used to evolve the unsorted density.

23.2.7 A comment on convection

Although the relaxation experiments allow for a focus on adiabatic physics, in a z-coordinate model there is no guarantee that an experiment will remain vertically stable, especially if running with a nonzero wind stress. If convective adjustment is then allowed, water mass mixing will occur. Hence, the experiments which focus on advection must remove convective adjustment. In turn, the presence of convection is actually quite an important element in determining the effective amount of spurious water mass mixing occuring in the model. The reason is that certain advection schemes, through dispersion errors, introduce unstable water which is then mixed-out through convection. After determining the effective diffusivity from the pure advection experiments, it is appropriate to then allow convection to occur and to compare the amount of convection appearing with the various advection discretizations.

23.2.8 The experimental design

The framework developed in this section applies most readily to an ocean model with a linear equation of state run without any buoyancy forcing. Since the model is to be run with zero buoyancy forcing, it is necessary to spin-up to some interesting state and perform various relaxation experiments. An interesting alternative is to run with zero buoyancy forcing but nonzero wind forcing, such as in a wind driven gyre.

As a test of the implementation for the algorithm to compute κ_{eff}, it is useful to run a set of tests with pure horizontal and vertical diffusion; no advection or convection. These experiments are necessary to establish a baseline for later comparison. After being satisfied, a set of relaxation experiments should be run with advection and/or other transport processes enabled.

23.3 Modifications for time dependent cell thicknesses

There is presently no formulation of this diagnostic for the general case of a time dependent cell thickness. The problem is that the one-dimensional effective diffusion equation, written as

$$\partial_t \left(\Delta z^* \, \rho_{ref} \right) = F_n^{z^*} - F_{n+1}^{z^*} \tag{23.27}$$

to account for time dependent thicknesses, no longer satisfies the compatibility condition of Griffies et al. (2001). That is, for cases with all fluxes vanishing in the unsorted state, there is no guarantee that fluxes likewise vanish in the sorted state, since the evolution of Δz^* is no longer tied properly to its neighbor.

23.4 An example with vertical density gradients

It is useful to present some examples which can be readily worked through by hand. These examples highlight many of the points raised in the previous discussion, and provide guidance for interpreting the three-dimensional MOM results. Each of these examples considers the dynamics of the unsorted and sorted density fields when the unsorted field is affected by vertical and horizontal diffusion. For simplicity, we assume the thickness of all grid cells remains time independent. Extensions to the more general case were discussed in Section 23.3. We also assume a leap frog time stepping, though the analysis follows trivially for a forward time step, with $\tau - \Delta\tau$ converted to τ, and $2\,\Delta\tau$ converted to $\Delta\tau$.

The first example considers the initial density field shown in Figure 23.1. There are a total of $N = N_x \, N_y \, N_z = (4 \times 1) \times 3$ grid cells in this two-dimensional example. The density field has zero baroclinicity. So the question is: How does this state, and the corresponding sorted density state, evolve under the effects of vertical diffusion? Note the grid dimensions for the two states are related through

$$\Delta z = 4 \, \Delta z^*, \tag{23.28}$$

where z is the vertical coordinate for the unsorted state, and z^* is the vertical coordinate for the sorted state. For the following, it is convenient to define this state as that at time $(t - \Delta t)$. The

potential energies of the unsorted and sorted states are easily computed to be

$$E_p(t-\Delta t) = 56\,\rho_o\,g\,\Delta z\,V \tag{23.29}$$
$$E_{ref}(t-\Delta t) = 56\,\rho_o\,g\,\Delta z\,V \tag{23.30}$$
$$E_{APE}(t-\Delta t) = 0 \tag{23.31}$$

where V is the volume of the grid cells, and ρ_o is the density scale. The zero APE is due to the absence of horizontal density gradients.

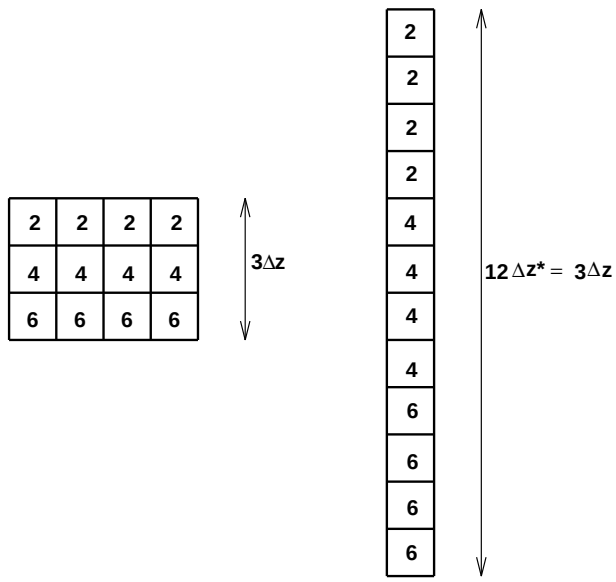

Figure 23.1: The initial density field for the first example. The number in each box represents the density, given in units of ρ_o. The left panel shows the density $\rho(x,z,t-\Delta t)$ in the unsorted fluid state, and the right panel shows the density $\rho_{ref}(z^*,t-\Delta t)$ in the sorted state. Note that the vertical scale $\Delta z^* = \Delta z/4$ for the sorted state has been expanded for purposes of display.

23.4.1 Evolution of the unsorted state

Evolution of the unsorted density is given by the discrete equation

$$\rho(x,z,t+\Delta t) = \rho(x,z,t-\Delta t) - \left(\frac{2\,\Delta t}{\Delta z}\right)\left[F^z(x,z,t-\Delta t) - F^z(x,z-\Delta z,t-\Delta t)\right], \tag{23.32}$$

where the vertical diffusive flux is given by

$$\begin{aligned} F^z(x,z,t) &= -\kappa\,\delta_z\rho(x,z,t) \\ &\approx -\kappa\left(\frac{\rho(x,z+\Delta z,t)-\rho(x,z,t)}{\Delta z}\right). \end{aligned} \tag{23.33}$$

$F^z(x,z,t)$ is defined at the top face of the density grid cell whose center has position (x,z). In the following, it is useful to introduce the dimensionless quantity

$$\delta_{(v)} = 2\,\kappa\,\Delta t/(\Delta z)^2. \tag{23.34}$$

This number arises from the chosen discretization of the diffusion equation. For linear stability of the discretization, $\delta_{(v)} < 1$ must be maintained.

The top panel of Figure 23.2 shows the vertical diffusive flux through the cell faces at time $t - \Delta t$, and the bottom panel shows the resulting density $\rho(z, z, t + \Delta t)$. Density in the middle row does not change, whereas the upper row density increases and the lower row density decreases. The potential energy of this state is

$$E_p(t + \Delta t) = \rho_o \, g \, \Delta z \, V \, (56 + 8 \, \delta_{(v)}). \tag{23.35}$$

This increase in potential energy is a result of the raised center of mass arising from the vertical diffusive fluxes.

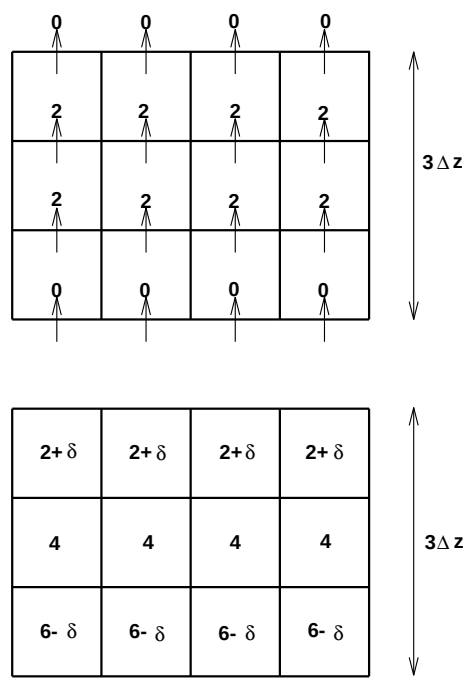

Figure 23.2: Top panel: The vertical diffusive flux $F^z(x, z, t - \Delta t)$, in units of $\rho_o \, \kappa / \Delta z$, passing through the faces of the unsorted density grid cells. Bottom panel: The unsorted density field $\rho(x, z, t + \Delta t)$, in units of ρ_o, where the dimensionless increment δ is given by $\delta = 2\delta_{(v)} = 4 \, \kappa \, \Delta t / (\Delta z)^2$. This density field results from the vertical convergence of the flux $F^z(x, z, t - \Delta t)$.

23.4.2 Evolution of the sorted state

Corresponding to the evolution of the unsorted density, there is an evolution of the sorted density

$$\rho_{ref}(z^*, t + \Delta t) = \rho_{ref}(z^*, t - \Delta t) - \left(\frac{2 \, \Delta t}{\Delta z^*} \right) [F^{z^*}(z^*, t - \Delta t) - F^{z^*}(z^* - \Delta z^*, t - \Delta t)]. \tag{23.36}$$

The dianeutral diffusive flux is

$$\begin{aligned} F^{z^*}(z^*,t) &= -\kappa_{eff}(z^*,t)\ \delta_{z^*}\rho_{ref}(z^*,t) \\ &\approx -\kappa_{eff}(z^*,t)\ \left(\frac{\rho_{ref}(z^*+\Delta z^*,t)-\rho_{ref}(z^*,t)}{\Delta z^*}\right), \end{aligned} \tag{23.37}$$

where $\rho_{ref}(z^*,t)$ is the sorted state's density. $F^{z^*}(z^*,t)$ is defined at the top face of the sorted density grid cell whose center has height z^*. Given the time tendency for the sorted state, the flux is diagnosed through

$$F^{z^*}(z^*,t-\Delta t) = F^{z^*}(z^*-\Delta z^*,t-\Delta t) - \left(\frac{\Delta z^*}{2\Delta t}\right)[\rho_{ref}(z^*,t+\Delta t)-\rho_{ref}(z^*,t-\Delta t)]. \tag{23.38}$$

The left panel of Figure 23.3 shows the sorted density field $\rho_{ref}(z^*,t+\Delta t)$, and the second panel shows the diagnosed vertical diffusive flux $F^{z^*}(z^*,t-\Delta t)$. The third panel shows the vertical density gradient $[\rho_{ref}(z^*+\Delta z^*,t-\Delta t)-\rho_{ref}(z^*,t-\Delta t)]/\Delta z^*$. The fourth panel shows the effective diffusivity $\kappa_{eff}(z^*,t-\Delta t)$, which is diagnosed from the relation

$$\kappa_{eff}(z^*,t-\Delta t) = -F^{z^*}(z^*,t-\Delta t)\left(\frac{\Delta z^*}{\rho_{ref}(z^*+\Delta z^*,t-\Delta t)-\rho_{ref}(z^*,t-\Delta t)}\right). \tag{23.39}$$

The units for $\kappa_{eff}(z^*,t-\Delta t)$ are $(\Delta z^*)^2/\Delta t$. Hence, a value for $\kappa_{eff}(z^*,t-\Delta t)$ of $2\,\delta$ in Figure 23.3 indicates a dimensional value of

$$\begin{aligned} \kappa_{eff}(z^*,t-\Delta t) &= 2\,\delta\,\frac{(\Delta z^*)^2}{\Delta t} \\ &= \kappa\,\frac{4\,\Delta t}{(\Delta z)^2}\,\frac{(\Delta z^*)^2}{\Delta t} \\ &= \kappa/4. \end{aligned} \tag{23.40}$$

This example illustrates a problem with unstratified parts of the sorted profile. As evident from Figures 23.1 and 23.3, the 12 sorted boxes are actually three larger homogeneous boxes, and so the calculation should compute fluxes and diffusivities for these three boxes rather than for the 12 boxes. Figure 23.4 shows such a combined system, where there are three boxes each of height Δz comprising the sorted state. Repeating the previous calculation for this configuration recovers the expected $\kappa_{eff} = \kappa$ on the two interior interfaces. Note that there is no *ad hoc* setting to zero certain values of κ_{eff} associated with unstratified portions of the profile.

As a final note, the potential energy of the sorted state at time $t+\Delta t$ is

$$E_{ref}(t+\Delta t) = \rho_o\,g\,\Delta z\,V\,(56+16\,\delta_{(v)}), \tag{23.41}$$

which is higher than the initial potential energy as a result of the raised center of mass. The APE remains unchanged

$$E_{APE}(t+\Delta t) = 0, \tag{23.42}$$

as it should since there remains zero baroclinicity in the final state.

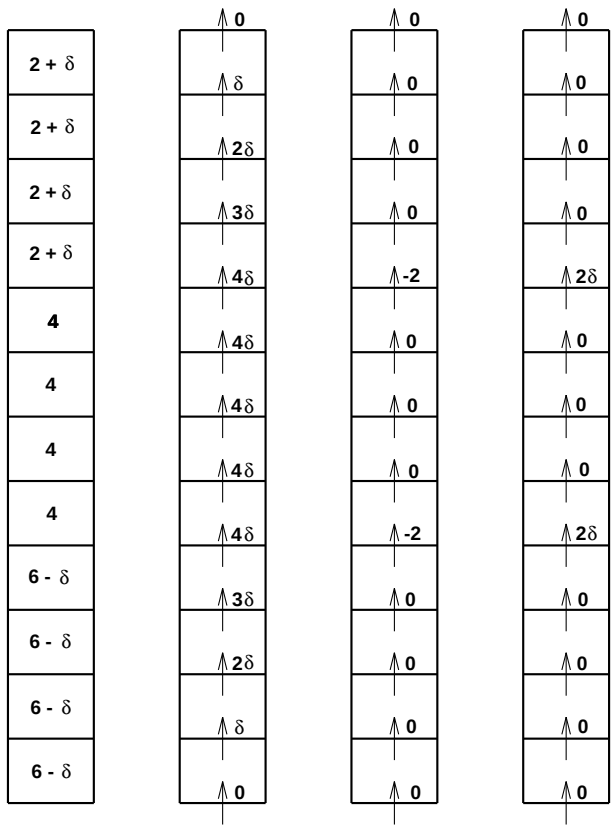

Figure 23.3: First panel (left): The sorted density field $\rho_{ref}(z^*, t + \Delta t)$, in units of ρ_o. Second panel: The vertical diffusive flux $F^{z^*}(z^*, t - \Delta t)$, in units of $\rho_o \, \Delta z^* / (2 \, \Delta t)$, passing through the faces of the sorted density grid cells. Third panel: The vertical density gradient $[\rho_{ref}(z^* + \Delta z^*, t - \Delta t) - \rho_{ref}(z^*, t - \Delta t)]/\Delta z^*$ in units of $\rho_o / \Delta z^*$. Fourth panel: The effective diffusivity $\kappa_{eff}(z^*, t - \Delta t)$ in units of $(\Delta z^*)^2 / \Delta t$.

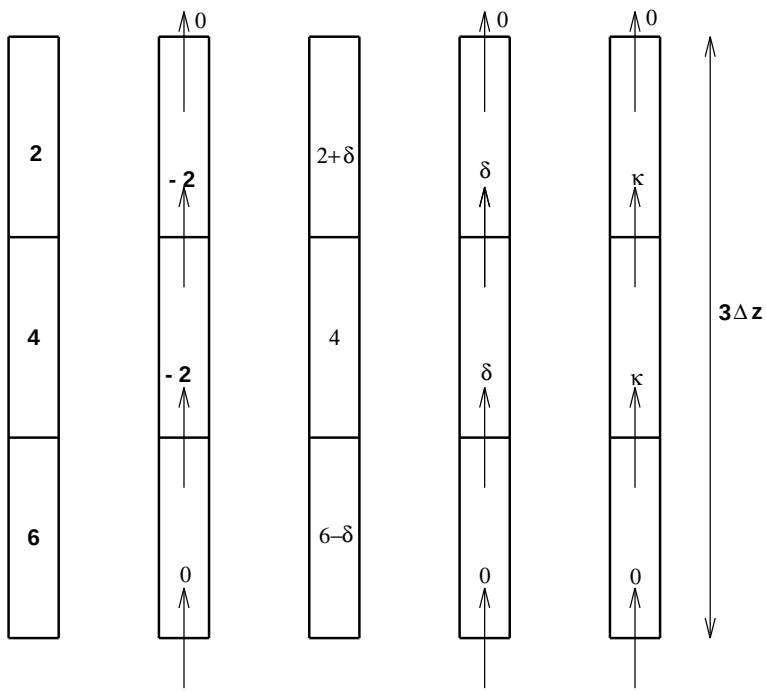

Figure 23.4: First panel (far left): The initial density field $\rho_{ref}(z^*, t - \Delta t)$, consisting of the combination of the three groups of four homogeneous cells. The values are given in units of ρ_o. In this recombined arrangement, $\Delta z^* = \Delta z$. Second panel: The vertical density gradient $[\rho_{ref}(z^* + \Delta z^*, t - \Delta t) - \rho_{ref}(z^*, t - \Delta t)]/\Delta z^*$, in units of $\rho_o/\Delta z^*$. Third panel: The density $\rho_{ref}(z^*, t + \Delta t)$ in units of ρ_o. Fourth panel: The diffusive flux $F^{z^*}(z^*, t - \Delta t)$. Fifth panel (far right): The effective diffusivity $\kappa_{eff}(z^*, t - \Delta t)$.

23.4.3 Caveat about weakly stratified regions

Note that in this example, the same set of boxes are perfectly homogenized at each time step. As such, it is straightforward to combine the boxes in order to derive their effective diffusivities. In general, this simple situation will not be true, and so the effective height of the combined boxes will differ. Furthermore, most cases of homogenization are approximate (Sections 23.2.3 and 23.2.5), which introduces even more time dependence to the interfaces between effectively homogeneous boxes. In order to compute an effective diffusivity, however, our algorithm needs to evaluate all quantities at the same depth level z^*. Time dependent z^* is problematical.

The current example suggestes that one possibile way to account for homogenization is to count the number of nearly homogeneous boxes occuring in a particular section of the sorted column. When the first interface is reached that has a nontrivial stratification, then the effective diffusivity computed for this interface is multiplied by the number of trailing boxes which are homogeneous. This trick works for the example just considered ($\kappa/4 \times 4 = \kappa$). However, in the example considered in Section 23.5.2, it leads to an effective diffusivity which can be larger than the horizontal diffusivity. Such is not possible, and so one is led to reject the proposed patch. A clean way to proceed is to try to resolve as best as possible the stratification within the sorted fluid state. For those regions which are simply too weakly stratified, it must be recognized that the computed effective diffusivity might be smaller than a more refined computation.

An alternative approach is to average the sorted density field onto the discrete levels realized in the unsorted state. Indeed, this resolution of the sorted state is arguably that which is relevant for diagnosing the effective diffusivity. This is the approach taken with the MOM experiments documented in Griffies et al. (2000b).

23.5 An example with vertical and horizontal gradients

This example considers the initial unsorted density configuration is shown in Figure 23.5. There are three rows of four boxes stacked on top of one another, and there are both vertical and horizontal density gradients. Also shown is the corresponding sorted state. As with the example in Section 23.4, the grid dimensions for the two states are related through $\Delta z = 4\,\Delta z^*$, where z is the vertical coordinate for the unsorted state, and z^* is the vertical coordinate for the sorted state. The potential energies are

$$E_p(t-\Delta t) = 110\,\rho_o\,g\,\Delta z\,V \tag{23.43}$$

$$E_{ref}(t-\Delta t) = 98\,\rho_o\,g\,\Delta z\,V \tag{23.44}$$

$$E_{APE}(t-\Delta t) = 12\,\rho_o\,g\,\Delta z\,V, \tag{23.45}$$

where V is the volume of the boxes and ρ_o is the density scale.

23.5.1 Vertical diffusion

Consider first just vertical diffusion acting on the unsorted state. The vertical diffusivity κ acting on the unsorted state is assumed to be uniform and constant.

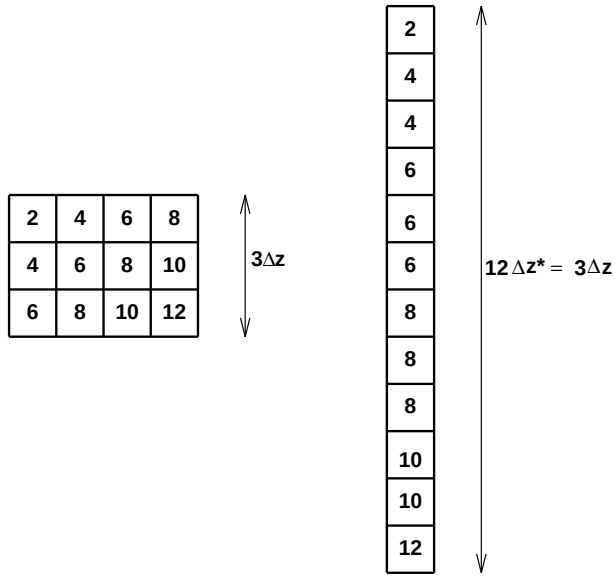

Figure 23.5: The initial density field for the horizontal and vertical diffusion examples. The number in each box represents the density, given in units of ρ_o. The left panel shows the density $\rho(x, z, t - \Delta t)$ in the unsorted fluid state, and the right panel shows the density $\rho_{ref}(z^*, t - \Delta t)$ in the sorted state. Note that the vertical scale $\Delta z^* = \Delta z/4$ for the sorted state has been expanded for purposes of display.

23.5.1.1 Evolution of the unsorted state

Evolution of the unsorted density is given by the discrete equation

$$\rho(x, z, t + \Delta t) = \rho(x, z, t - \Delta t) - \left(\frac{2\,\Delta t}{\Delta z}\right)[F^z(x, z, t - \Delta t) - F^z(x, z - \Delta z, t - \Delta t)], \tag{23.46}$$

where the vertical diffusive flux is given by

$$\begin{aligned} F^z(x, z, t) &= -\kappa\, \delta_z \rho(x, z, t) \\ &\approx -\kappa \left(\frac{\rho(x, z + \Delta z, t) - \rho(x, z, t)}{\Delta z}\right). \end{aligned} \tag{23.47}$$

$F^z(x, z, t)$ is defined at the top face of the density grid cell whose center has height z. The top panel of Figure 23.6 shows the vertical diffusive flux through these faces at time $t - \Delta t$, and the bottom panel shows the resulting density field $\rho(x, z, t + \Delta t)$. Density in the middle row does not change, whereas the upper row density increases and the lower row density decreases. The potential energy of this state is

$$E_p(t + \Delta t) = \rho_o\, g\, \Delta z\, V\, (110 + 16\, \delta_{(v)}), \tag{23.48}$$

which is higher than the initial potential energy as a result of the raised center of mass.

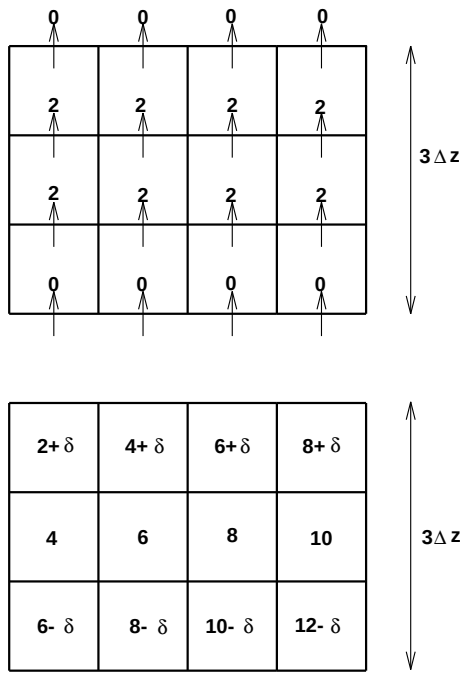

Figure 23.6: Top panel: The vertical diffusive flux $F^z(x, z, t - \Delta t)$, in units of $\rho_o \kappa / \Delta z$, passing through the faces of the unsorted density grid cells. Bottom panel: The unsorted density field $\rho(x, z, t + \Delta t)$, in units of ρ_o, where $\delta = 2\,\delta_{(v)} = 4\,\kappa\,\Delta t/(\Delta z)^2$. This is the density field resulting from the vertical convergence of the flux $F^z(x, z, t - \Delta t)$. The potential energy of this field is $E_p(t + \Delta t) = \rho_o\, g\, \Delta z\, V\, (110 + 16\delta_{(v)})$.

23.5.1.2 Evolution of the sorted state

Corresponding to the evolution of the unsorted density, there is an evolution of the sorted density which is given by

$$\rho_{ref}(z^*, t+\Delta t) = \rho_{ref}(z^*, t-\Delta t) - \left(\frac{2\,\Delta t}{\Delta z^*}\right)[F^{z^*}(z^*, t-\Delta t) - F^{z^*}(z^*-\Delta z, t-\Delta t)]. \tag{23.49}$$

The dianeutral diffusive flux is given by

$$\begin{aligned} F^{z^*}(z^*, t) &= -\kappa_{eff}(z^*, t)\ \delta_{z^*}\rho_{ref}(z^*, t) \\ &\approx -\kappa_{eff}(z^*, t)\ \left(\frac{\rho_{ref}(z^*+\Delta z^*, t) - \rho_{ref}(z^*, t)}{\Delta z^*}\right), \end{aligned} \tag{23.50}$$

where $\rho_{ref}(z^*, t)$ is the sorted state's density. $F^{z^*}(z^*, t)$ is defined at the top face of the sorted density grid cell whose center has height z^*. Given the time tendency for the sorted state, the flux is diagnosed through

$$F^{z^*}(z^*, t-\Delta t) = F^{z^*}(z^*-\Delta z^*, t-\Delta t) - \left(\frac{\Delta z^*}{2\Delta t}\right)[\rho_{ref}(z^*, t+\Delta t) - \rho_{ref}(z^*, t-\Delta t)]. \tag{23.51}$$

The left panel of Figure 23.7 shows the sorted density field $\rho_{ref}(z^*, t+\Delta t)$, and the second panel shows the diagnosed vertical diffusive flux $F^{z^*}(z^*, t-\Delta t)$. The third panel shows the vertical density gradient $[\rho_{ref}(z^*+\Delta z^*, t-\Delta t) - \rho_{ref}(z^*, t-\Delta t)]/\Delta z^*$. Note the regions of zero stratification. The fourth panel shows the effective diffusivity $\kappa_{eff}(z^*, t-\Delta t)$, which is diagnosed from the relation

$$\kappa_{eff}(z^*, t-\Delta t) = -F^{z^*}(z^*, t-\Delta t)\left(\frac{\Delta z^*}{\rho_{ref}(z^*+\Delta z^*, t-\Delta t) - \rho_{ref}(z^*, t-\Delta t)}\right). \tag{23.52}$$

The units for $\kappa_{eff}(z^*, t-\Delta t)$ are $(\Delta z^*)^2/\Delta t$. In addition, consistent with the discussion in Section 23.4.2, the effective diffusivity for the interfaces on top of unstratified water are multiplied by the number of unstratified boxes. A value for $\kappa_{eff}(z^*, t-\Delta t)$ of δ in Figure 23.7 indicates a dimensional value of

$$\begin{aligned} \kappa_{eff}(z^*, t-\Delta t) &= \delta\ \frac{(\Delta z^*)^2}{\Delta t} \\ &= \kappa\ \frac{4\,\Delta t}{(\Delta z)^2}\ \frac{(\Delta z^*)^2}{\Delta t} \\ &= \kappa/4. \end{aligned} \tag{23.53}$$

As a final note, the potential energy of the sorted state at time $t+\Delta t$ is

$$E_{ref}(t+\Delta t) = \rho_o\, g\, \Delta z\, V\, (98 + 7\,\delta_{(v)}), \tag{23.54}$$

which is higher than the initial potential energy as a result of the raised center of mass. The APE is therefore given by

$$E_{APE}(t+\Delta t) = \rho_o\, g\, \Delta z\, V\, (12 + 11\,\delta_{(v)}), \tag{23.55}$$

which is larger than $E_{APE}(t-\Delta t)$ given in equation (23.45).

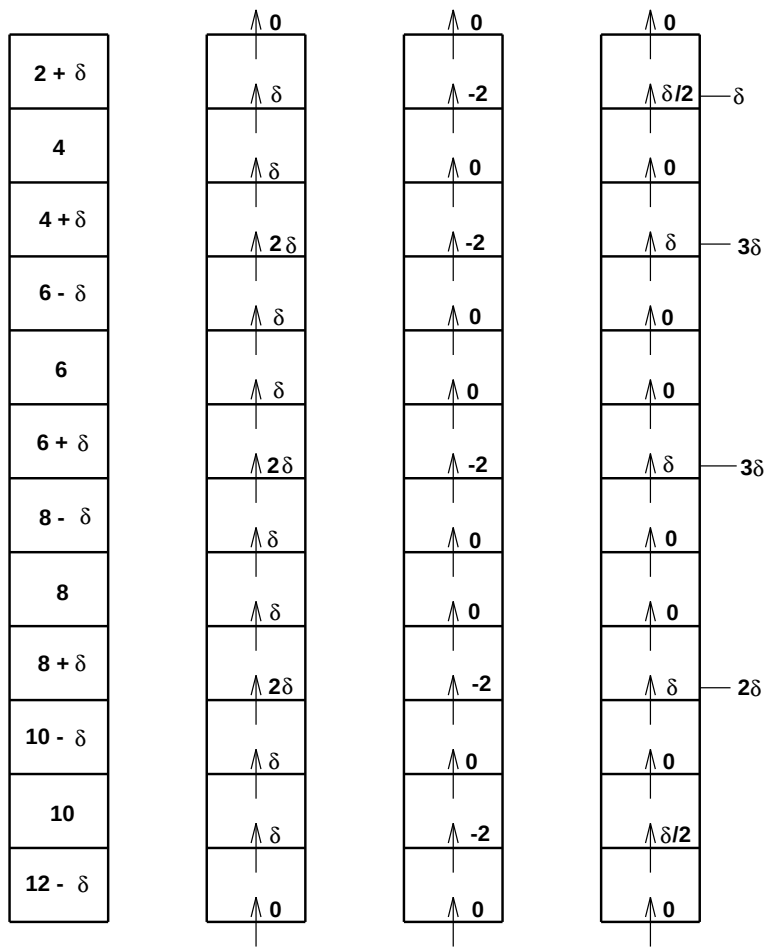

Figure 23.7: Left panel: The sorted density field $\rho_{ref}(z^*, t + \Delta t)$, in units of ρ_o. Second panel: The vertical diffusive flux $F^{z^*}(z^*, t - \Delta t)$, in units of $\rho_o \, \Delta z^* / \Delta t$, passing through the faces of the sorted density grid cells. Third panel: The vertical density gradient $[\rho_{ref}(z^* + \Delta z^*, t - \Delta t) - \rho_{ref}(z^*, t - \Delta t)]/\Delta z^*$ in units of $\rho_o / \Delta z^*$. Fourth panel: The effective diffusivity $\kappa_{eff}(z^*, t - \Delta t)$ in units of $(\Delta z^*)^2/\Delta t$. The four κ_{eff} values which are on top of unstratified portions of the $\rho_{ref}(z^*, t - \Delta t)$ profile have been multiplied by the number of unstratified boxes which lie directly beneath it.

23.5.2 Horizontal diffusion

Consider now just horizontal diffusion acting on the unsorted state. The horizontal diffusivity A acting on the unsorted state is assumed to be uniform and constant.

23.5.2.1 Evolution of the unsorted state

Evolution of the unsorted density is given by the discrete equation

$$\rho(x,z,t+\Delta t) = \rho(x,z,t-\Delta t) - \left(\frac{2\,\Delta t}{\Delta x}\right)[F^x(x,z,t-\Delta t) - F^x(x-\Delta x,z,t-\Delta t)], \tag{23.56}$$

where the horizontal diffusive flux is given by

$$\begin{aligned} F^x(x,z,t) &= -A\ \delta_x \rho(x,z,t) \\ &\approx -A\ \left(\frac{\rho(x+\Delta x,z,t) - \rho(x,z,t)}{\Delta x}\right). \end{aligned} \tag{23.57}$$

$F^x(x,z,t)$ is defined at the east face of the density grid cell whose center has position (x,z). The top panel of Figure 23.8 shows the horizontal diffusive flux through these faces at time $t-\Delta t$, and the bottom panel shows the resulting density field $\rho(x,z,t+\Delta t)$. The potential energy of this state is the same as the initial potential energy, since the horizontal fluxes are parallel to the geopotential

$$E_p(t+\Delta t) = E_p(t-\Delta t) = 110\,\rho_o\,g\,\Delta z\,V. \tag{23.58}$$

23.5.2.2 Evolution of the sorted state

Corresponding to the evolution of the unsorted density, there is an evolution of the sorted density which is given by

$$\rho_{ref}(z^*,t+\Delta t) = \rho_{ref}(z^*,t-\Delta t) - \left(\frac{2\,\Delta t}{\Delta z^*}\right)[F^{z^*}(z^*,t-\Delta t) - F^{z^*}(z^*-\Delta z,t-\Delta t)]. \tag{23.59}$$

The dianeutral diffusive flux is given by

$$\begin{aligned} F^{z^*}(z^*,t) &= -\kappa_{eff}(z^*,t)\ \delta_{z^*}\rho_{ref}(z^*,t) \\ &\approx -\kappa_{eff}(z^*,t)\ \left(\frac{\rho_{ref}(z^*+\Delta z^*,t) - \rho_{ref}(z^*,t)}{\Delta z^*}\right), \end{aligned} \tag{23.60}$$

where $\rho_{ref}(z^*,t)$ is the sorted state's density. $F^{z^*}(z^*,t)$ is defined at the top face of the sorted density grid cell whose center has height z^*. Given the time tendency for the sorted state, the flux is diagnosed through

$$F^{z^*}(z^*,t-\Delta t) = F^{z^*}(z^*-\Delta z^*,t-\Delta t) - \left(\frac{\Delta z^*}{2\Delta t}\right)[\rho_{ref}(z^*,t+\Delta t) - \rho_{ref}(z^*,t-\Delta t)]. \tag{23.61}$$

The left panel of Figure 23.5.2.2 shows the sorted density field $\rho_{ref}(z^*,t+\Delta t)$, and the second panel shows the diagnosed vertical diffusive flux $F^{z^*}(z^*,t-\Delta t)$. The third panel shows the vertical

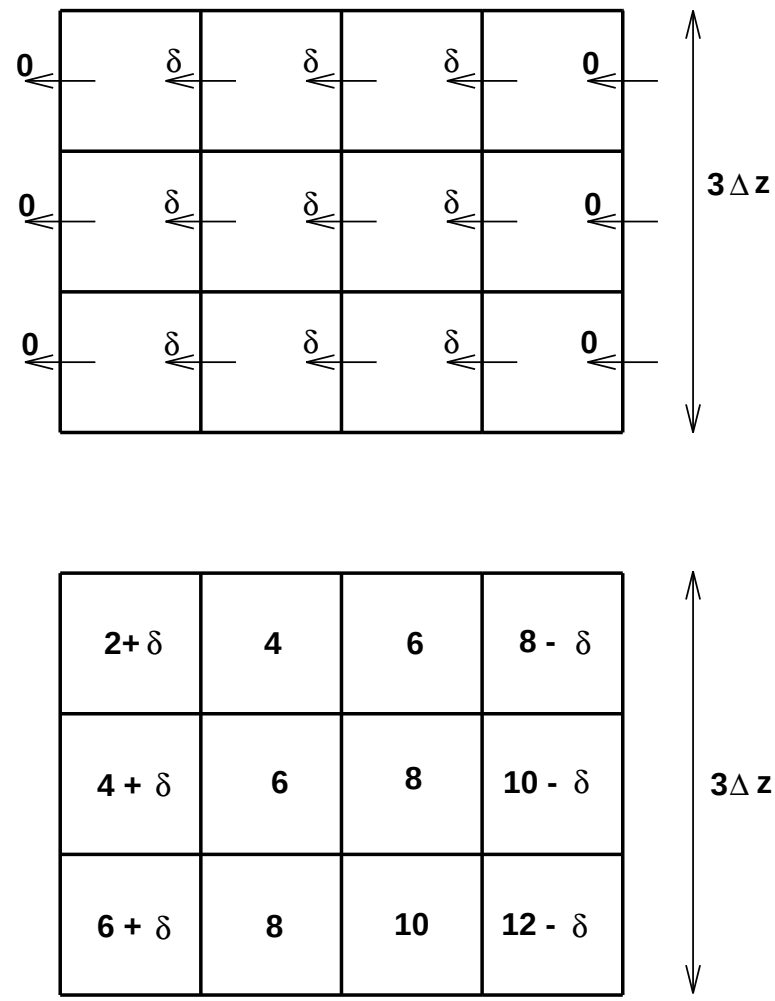

Figure 23.8: Top panel: The horizontal diffusive flux $F^x(x, z, t - \Delta t)$, in units of $\rho_o\, A/\Delta x$, passing through the faces of the unsorted density grid cells. Bottom panel: The unsorted density field $\rho(x, z, t + \Delta t)$, in units of ρ_o, where $\delta = 2\,\delta_{(h)} = 4\,A\,\Delta t/(\Delta x)^2$. This is the density field resulting from the vertical convergence of the flux $F^x(x, z, t - \Delta t)$. The potential energy of this field is $E_p(t + \Delta t) = 110\,\rho_o\, g\, \Delta z\, V$.

density gradient $[\rho_{ref}(z^* + \Delta z^*, t - \Delta t) - \rho_{ref}(z^*, t - \Delta t)]/\Delta z^*$. Note the regions of zero stratification. The fourth panel shows the effective diffusivity $\kappa_{eff}(z^*, t - \Delta t)$, which is diagnosed from the relation

$$\kappa_{eff}(z^*, t - \Delta t) = -F^{z^*}(z^*, t - \Delta t) \left(\frac{\Delta z^*}{\rho_{ref}(z^* + \Delta z^*, t - \Delta t) - \rho_{ref}(z^*, t - \Delta t)} \right). \tag{23.62}$$

The units for $\kappa_{eff}(z^*, t - \Delta t)$ are $(\Delta z^*)^2/\Delta t$. For example, a value for $\kappa_{eff}(z^*, t - \Delta t)$ of $3\delta/2$ in Figure 23.5.2.2 indicates a dimensional value of

$$\begin{aligned} \kappa_{eff}(z^*, t - \Delta t) &= (3\,\delta/2)\ \frac{(\Delta z^*)^2}{\Delta t} \\ &= 6\,A\ \frac{\Delta t}{(\Delta x)^2}\ \frac{(\Delta z^*)^2}{\Delta t} \\ &= 6\,A\ \left(\frac{\Delta z^*}{\Delta x}\right)^2. \end{aligned} \tag{23.63}$$

For the special case of $\Delta x = \Delta z = 4\Delta z^*$, the effective diffusivity is $3A/8$. Note that if the patch proposed in Section 23.4.3 is used, then the $3\delta/2$ diffusivity would become $9\delta/2$, leading to the possibility for an effective diffusivity of $9\,A/8$, which is impossible.

As a final note, the potential energy of the sorted state at time $t + \Delta t$ is

$$E_{ref}(t + \Delta t) = \rho_o\, g\, \Delta z\, V\, (98 + 19\,\delta_{(h)}/2), \tag{23.64}$$

which is higher than the initial potential energy as a result of the raised center of mass. The APE is given by

$$E_{APE}(t + \Delta t) = \rho_o\, g\, \Delta z\, V\, (12 - 19\,\delta_{(h)}/2), \tag{23.65}$$

which is smaller than $E_{APE}(t - \Delta t)$ given in equation (23.45).

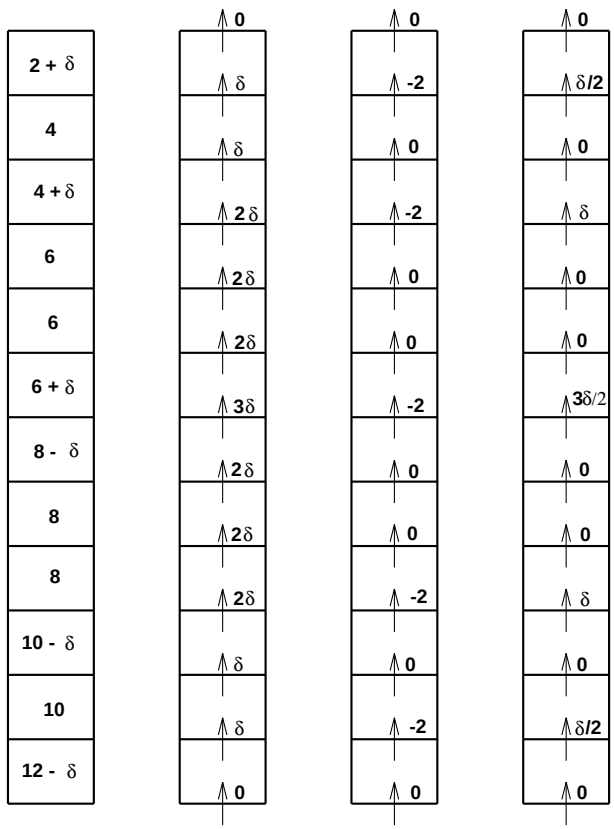

Figure 23.9: First panel (far left): The sorted density field $\rho_{ref}(z^*, t + \Delta t)$ in units of ρ_o. Second panel: The vertical diffusive flux $F^{z^*}(z^*, t - \Delta t)$, in units of $\rho_o \, \Delta z^* / \Delta t$, passing through the faces of the sorted density grid cells. Third panel: The vertical density gradient $[\rho_{ref}(z^* + \Delta z^*, t - \Delta t) - \rho_{ref}(z^*, t - \Delta t)]/\Delta z^*$ in units of $\rho_o / \Delta z^*$. Fourth panel: The effective diffusivity $\kappa_{eff}(z^*, t - \Delta t)$ in units of $(\Delta z^*)^2/\Delta t$. The four κ_{eff} values which are on top of unstratified portions of the $\rho_{ref}(z^*, t - \Delta t)$ profile have been multiplied by the number of unstratified boxes which lie directly beneath it.

CHAPTER
TWENTYFOUR

Spurious dissipation from numerical advection

The purpose of this chapter is to detail a method to locally quantify the level of dissipation (either positive or negative) associated with discretization errors in numerical tracer advection. This method was introduced by Burchard and Rennau (2008), and it provides a valuable complement to the effective dianeutral diffusivity diagnostic detailed in Chapter 23. In particular, the Burchard and Rennau (2008) method can provide a local quantification of the dissipation for any three dimensional model simulation. It cannot, however, generally translate that mixing into a dianeutral diffusivity, since there is no knowledge of neutral directions built into the diagnostic.

24.1 Formulation of the method for Boussinesq fluid

Consider a continuous Boussinesq fluid in the absence of mixing, subgrid-scale fluxes, or sources, in which case the tracer concentration is affected only by advection

$$\partial_t C = -\nabla \cdot (\mathbf{v}\, C). \tag{24.1}$$

Likewise, the squared tracer concentration (indeed, the tracer concentration raised to any power) satisfies the same equation

$$\partial_t C^2 = -\nabla \cdot (\mathbf{v}\, C^2). \tag{24.2}$$

Now consider a space-time discretization of the tracer concentration equation (24.1)

$$C^{n+1} = C^n - \mathcal{D}(C) \tag{24.3}$$

where we assume an explicit two-time level update of the tracer concentration onto discrete time levels $\tau_n = \tau_o + n\,\Delta\tau$. This is the preferred time stepping method in MOM4p1 (see Chapter 8). The discrete operator

$$\mathcal{D}(C) \approx \Delta\,\tau\; \nabla \cdot (\mathbf{v}\, C) \tag{24.4}$$

symbolizes one of the many possible methods used to discretize tracer advection. For later purposes, it is useful to define the right hand side of equation (24.3) as the operator $\mathcal{A}(C)$, so that

$$\mathcal{A}(C) = C^n - \mathcal{D}(C). \tag{24.5}$$

Given the discrete expression (24.3), we can form the square of the updated tracer concentration

$$\begin{aligned}[(C^{n+1})^2]_{(a)} &= [\mathcal{A}(C)]^2 \\ &= (C^n)^2 + [\mathcal{D}(C)]^2 - 2\,C^n\,\mathcal{D}(C).\end{aligned} \tag{24.6}$$

Additionally, another means for computing the updated squared tracer concentration is to discretize the continuous equation for C^2, given by equation (24.2), in which the updated squared tracer concentration is given by

$$[(C^{n+1})^2]_{(b)} = (C^n)^2 - D(C^2). \tag{24.7}$$

Following the definition of the operator $\mathcal{A}(C)$ in equation (24.5), we have

$$[(C^{n+1})^2]_{(b)} = \mathcal{A}(C^2). \tag{24.8}$$

The fundamental question that this diagnostic asks is how well the two approximations for $(C^{n+1})^2$ agree. To answer this question, we simply take the difference

$$\begin{aligned}[(C^{n+1})^2]_{(a)} - [(C^{n+1})^2]_{(b)} &= [\mathcal{A}(C)]^2 - \mathcal{A}(C^2) \\ &= [\mathcal{D}(C)]^2 - 2\,C^n\,\mathcal{D}(C) + D(C^2).\end{aligned} \tag{24.9}$$

A nonzero value for this difference results from nonzero spurious mixing or unmixing due to truncation errors in the advection scheme. Computing this difference requires an evaluation of the advection operator on both the tracer concentration and the squared tracer concentration.

To associate mixing with a particular sign of the difference (24.9), we consider the special case of one-dimensional advection with a constant advection velocity $u > 0$, discretized with first order upstream spatial differences on a uniform grid with spacing Δx. In this case

$$\begin{aligned}[(C^{n+1})^2]_{(a)} &\equiv \mathcal{A}(C)^2 \\ &= (1-\gamma)^2\,(C_i^n)^2 + \gamma^2\,(C_{i-1}^n)^2 + 2\,\gamma\,(1-\gamma)\,C_i^n\,C_{i-1}^n\end{aligned} \tag{24.10}$$

and

$$\begin{aligned}[(C^{n+1})^2]_{(b)} &\equiv \mathcal{A}(C^2) \\ &= (1-\gamma)\,(C_i^n)^2 + \gamma\,(C_{i-1}^n)^2,\end{aligned} \tag{24.11}$$

where $\gamma = u\,\Delta\tau/\Delta x$ is the Courant number, and the discrete advection equation is stable so long as $0 \le \gamma \le 1$. With this chosen discretization, the difference (24.9) takes the form

$$\begin{aligned}\frac{[\mathcal{A}(C)]^2 - \mathcal{A}(C^2)}{\Delta\tau} &= -\left(\frac{\gamma\,(1-\gamma)}{\Delta\tau}\right)\,(C_i^n - C_{i-1}^n)^2 \\ &= -\left(\frac{\gamma\,(1-\gamma)\,(\Delta x)^2}{\Delta\tau}\right)\left(\frac{C_i^n - C_{i-1}^n}{\Delta x}\right)^2 \\ &\approx -\kappa_{\text{eff}}\,(\partial_x\,C)^2 \\ &\le 0,\end{aligned} \tag{24.12}$$

where we identified $(C_i - C_{i-1})/\Delta x$ as a discrete approximation to $\partial_x C$, and defined an effective diffusivity

$$\kappa_{\text{eff}} = \left(\frac{\gamma\,(1-\gamma)\,(\Delta x)^2}{\Delta\tau} \right). \tag{24.13}$$

Hence, the difference between the two approximations to the updated squared tracer concentration takes the form of a discrete dissipation of tracer variance, thus exemplefying the well known dissipative property of first order upwind advection. The effective diffusivity that sets the scale of this dissipation vanishes when the Courant number is either zero, which is the trivial case of no advective transport, or unity, in which case the full contents of cell $i-1$ are transported into cell i over a single time step.

Burchard and Rennau (2008) take the previous result as motivation to define a numerically induced dissipation rate for any advection scheme. We follow their definition, yet introduce a division by $(\Delta\tau)^{-2}$ rather than their use of $\Delta\tau$

$$\begin{aligned} \Sigma &\equiv \frac{\mathcal{A}(C^2) - [\mathcal{A}(C)]^2}{(\Delta\tau)^2} \\ &= \frac{2\,C^n\,\mathcal{D}(C) - [\mathcal{D}(C)]^2 - \mathcal{D}(C^2)}{(\Delta\tau)^2}. \end{aligned} \tag{24.14}$$

The extra $\Delta\tau$ factor is motivated by dimensional arguments given in the discussion following the more general result given by equation (24.29). Again motivated by the one-dimensional upwind advection case, Burchard and Rennau (2008) propose the following identifications

$$\Sigma > 0 \Rightarrow \text{positive dissipation through mixing} \tag{24.15}$$

$$\Sigma < 0 \Rightarrow \text{negative dissipation through unmixing} \tag{24.16}$$

$$\Sigma = 0 \Rightarrow \text{zero dissipation.} \tag{24.17}$$

Regardless whether these identifications are rigorous, they are suggestive and allow one to stratify different advection schemes according to their values of Σ. In general, a key goal of an advection scheme is to have Σ from advection much smaller than the corresponding physically induced dissipation from subgrid scale mixing.

24.2 Formulation for MOM4p1

The previous formulation was based on finite differences applied to a Boussinesq fluid. MOM4p1 is based on a finite volume formulation of the non-Boussinesq fluid. In this section, we generalize the previous considerations to that appropriate for MOM4p1.

For a non-Boussinesq fluid, mass conservation takes the form

$$\partial_t\,\rho = -\nabla\cdot(\rho\,\mathbf{v}). \tag{24.18}$$

Likewise, tracer conservation in the absence of subgrid scale fluxes is given by

$$\partial_t\,(\rho\,C) = -\nabla\cdot(\rho\,\mathbf{v}\,C), \tag{24.19}$$

and the corresponding budget for squared tracer concentration is

$$\partial_t \left(\rho\, C^2\right) = -\nabla \cdot \left(\rho\, \mathbf{v}\, C^2\right). \tag{24.20}$$

MOM4p1 time steps a finite volume tracer budget for a non-Boussinesq fluid using generalized level coordinates, in which case the budget for tracer mass per horizontal area is time stepped. As detailed in Section 3.6, this approach leads to the following tracer advection equation for an interior grid cell

$$\partial_t (C\, \rho\, \mathrm{d}z) = -\nabla_s \cdot (\mathbf{u}\, C\, \rho\, \mathrm{d}z) - (\rho\, w^{(s)}\, C)_{s=s_{k-1}} + (\rho\, w^{(s)}\, C)_{s=s_k}, \tag{24.21}$$

with $w^{(s)}$ the dia-surface velocity component. Following the notation from Section 24.1, we discretize this budget as

$$\begin{aligned} (C\, \rho\, \mathrm{d}z)^{n+1} &= (C\, \rho\, \mathrm{d}z)^n - \mathcal{E}(C) \\ &\equiv \mathcal{B}(C), \end{aligned} \tag{24.22}$$

where the discrete advection operator is written

$$\mathcal{E}(C)/\Delta\tau \approx \nabla_s \cdot (\mathbf{u}\, C\, \rho\, \mathrm{d}z) + (\rho\, w^{(s)}\, C)_{s=s_{k-1}} - (\rho\, w^{(s)}\, C)_{s=s_k}. \tag{24.23}$$

Likewise, the discretized budget for the mass weighted squared tracer concentration is

$$\begin{aligned} (C^2\, \rho\, \mathrm{d}z)^{n+1} &= (C^2\, \rho\, \mathrm{d}z)^n - \mathcal{E}(C^2) \\ &\equiv \mathcal{B}(C^2), \end{aligned} \tag{24.24}$$

where $\mathcal{B}(C^2)$ has dimensions of squared tracer concentration times mass per area.

We follow the steps considered in Section 24.1 to derive an operator that identifies the dissipation due to truncation errors with tracer advection. For this purpose, we consider the square of equation (24.22) as one approximation to the updated squared mass per area of a tracer

$$\begin{aligned} [(C\, \rho\, \mathrm{d}z)^{n+1}]^2_{(a)} &= [\mathcal{B}(C)]^2 \\ &= [(C\, \rho\, \mathrm{d}z)^n]^2 + [\mathcal{E}(C)]^2 - 2\, \mathcal{E}(C)\, (C\, \rho\, \mathrm{d}z)^n. \end{aligned} \tag{24.25}$$

An alternative approximation is obtained from equation (24.24), in which

$$\begin{aligned} [(C\, \rho\, \mathrm{d}z)^{n+1}]^2_{(b)} &= (\rho\, \mathrm{d}z)^{n+1}\, \mathcal{B}(C^2) \\ &= (\rho\, \mathrm{d}z)^{n+1}\, (\rho\, \mathrm{d}z)^n (C^n)^2 - (\rho\, \mathrm{d}z)^{n+1}\, \mathcal{E}(C^2). \end{aligned} \tag{24.26}$$

The difference between these two approximations is given by

$$\begin{aligned} [\mathcal{B}(C)]^2 - (\rho\, \mathrm{d}z)^{n+1}\, \mathcal{B}(C^2) &= (C^2\, \rho\, \mathrm{d}z)^n\, [(\rho\, \mathrm{d}z)^n - (\rho\, \mathrm{d}z)^{n+1}] \\ &\quad + [\mathcal{E}(C)]^2 - 2\, (C\, \rho\, \mathrm{d}z)^n\, \mathcal{E}(C) + (\rho\, \mathrm{d}z)^{n+1}\, \mathcal{E}(C^2). \end{aligned} \tag{24.27}$$

The first term arises from time tendencies in the mass per area of a grid cell

$$\frac{(\rho\, \mathrm{d}z)^n - (\rho\, \mathrm{d}z)^{n+1}}{\Delta\tau} \approx -\partial_t\, (\rho\, \mathrm{d}z), \tag{24.28}$$

and this term has nothing to do with errors in the advection scheme. Notably, it vanishes in two special cases:

- Boussinesq fluid with z-coordinates, in which case the cell thickness $\mathrm{d}z$ is time independent. The only exception is the top level, where the thickness changes due to time tendencies in the free surface height.
- Non-Boussinesq fluid with pressure coordinates, in which case the cell mass per area $\rho\,\mathrm{d}z$ is time independent. The only exception is the bottom cell, where the mass per area changes due to time tendencies in the bottom pressure.

To remove these effects from temporal changes in mass per area of a grid cell, we define the generalized advection dissipation operator

$$\boxed{\Sigma_{\text{general}} \equiv \frac{2\,(C\,\rho\,\mathrm{d}z)^n\,\mathcal{E}(C) - [\mathcal{E}(C)]^2 - (\rho\,\mathrm{d}z)^{n+1}\,\mathcal{E}(C^2)}{(\Delta\tau)^2}.} \tag{24.29}$$

This definition corresponds to the operator Σ defined by equation (24.14). Even though we have ignored the $\partial_t\,(\rho\,\mathrm{d}z)$ term, the operator (24.29) can still be nonzero even if the advection operators are perfect, as occurs when $\rho\,\mathrm{d}z$ has horizontal spatial variations or time variations. Hence, this operator provides insight towards the advection truncation errors only for the special cases listed in the above two bullet points. Indeed, if the mass per area is the same temporal constant on a k-level (as for geopotential coordinates below the surface cell, and pressure coordinates above the bottom cell), we have

$$\Sigma_{\text{general}} = (\rho\,\mathrm{d}z)\,\Sigma \qquad \text{if } \nabla_s\,(\rho\,\mathrm{d}z) = 0, \qquad \text{and } \partial_t\,(\rho\,\mathrm{d}z) = 0, \tag{24.30}$$

where the dissipation operator Σ is defined by equation (24.14).

The extra $\Delta\tau$ factor in the denominator of (24.29), relative to Burchard and Rennau (2008), provides sensible units for the tracer dissipation. In particular, for tracer $C = C_p\,\theta$ being the heat capacity times potential temperature, Σ_{general} has dimensions of $(\text{Watt}/\text{m}^2)^2$. For $C = 1000\,S$ the mass of salt per mass of seawater, Σ_{general} has dimensions of $(\text{kg}\,\text{m}^{-2}\,\text{s}^{-1})^2$.

24.3 Comparing to physical mixing

As a means to gauge the levels of Σ_{general}, we may compare it to tracer dissipation arising from physically motivated subgrid scale mixing processes. For this purpose, we introduce a subgrid scale flux $\mathbf{J}$, so that the tracer concentration and squared tracer concentration satisfy the following equations

$$\partial_t\,(\rho\,C) + \nabla\cdot(\rho\,\mathbf{v}\,C) = -\nabla\cdot\mathbf{J} \tag{24.31}$$

$$\partial_t\,(\rho\,C^2) + \nabla\cdot(\rho\,\mathbf{v}\,C^2) = -C\,\nabla\cdot\mathbf{J}. \tag{24.32}$$

For the squared tracer, write the right hand side in the following manner

$$\begin{aligned}\partial_t\,(\rho\,C^2) + \nabla\cdot(\rho\,\mathbf{v}\,C^2) &= -C\,\nabla\cdot\mathbf{J}\\ &= -\nabla\cdot(C\,\mathbf{J}) + \nabla\,C\cdot\mathbf{J}.\end{aligned} \tag{24.33}$$

Considering a tensor formulation for the subgrid scale tracer flux

$$\mathbf{J} = -\rho\,\mathbf{K}\cdot\nabla C \tag{24.34}$$

leads to

$$\partial_t \left(\rho C^2\right) + \nabla \cdot \left(\rho \mathbf{v} C^2\right) = -\nabla \cdot \left(C \mathbf{J}\right) - \rho \nabla C \cdot \mathbf{K} \cdot \nabla C. \tag{24.35}$$

For a symmetric diffusion tensor,

$$\rho \nabla C \cdot \mathbf{K} \cdot \nabla C > 0, \tag{24.36}$$

in which case the mass weighted squared tracer concentration is dissipated by the sink $-\rho \nabla C \cdot \mathbf{K} \cdot \nabla C$. For the special case of vertical diffusion with diffusivity $\kappa > 0$,

$$\rho \nabla C \cdot \mathbf{K} \cdot \nabla C = \rho \kappa \left(\partial_z C\right)^2. \tag{24.37}$$

A finite volume formulation of the squared tracer equation, focusing just on the dissipation from vertical diffusion, leads to

$$\left(C^2 \rho \, \mathrm{d}z\right)^{n+1} = \left(C^2 \rho \, \mathrm{d}z\right)^n - \Delta\tau \left[\rho \, \mathrm{d}z \, \kappa \left(\partial_z C\right)^2\right]^n, \tag{24.38}$$

which leads to

$$\left[\left(C \rho \, \mathrm{d}z\right)^{n+1}\right]^2 = \left(\rho \, \mathrm{d}z\right)^{n+1} \left(C^2 \rho \, \mathrm{d}z\right)^n - \Delta\tau \left(\rho \, \mathrm{d}z\right)^{n+1} \left[\rho \, \mathrm{d}z \, \kappa \left(\partial_z C\right)^2\right]^n. \tag{24.39}$$

We are thus led to identify the dissipation operator for vertical diffusion

$$\Sigma_{\text{vert-diff}} = \left(\rho \, \mathrm{d}z\right)^{n+1} \left(\rho \, \mathrm{d}z\right)^n \frac{\left[\kappa \left(\partial_z C\right)^2\right]^n}{\Delta\tau}. \tag{24.40}$$

The dissipation operator $\Sigma_{\text{vert-diff}}$ has the same dimensions as Σ_{general} defined for advection in equation (24.29). Importantly, Σ_{general} accounts for dissipation from the three dimensional advection operator, whereas $\Sigma_{\text{vert-diff}}$ accounts for dissipation just from vertical diffusion. That is, the operator Σ_{general} is unable to generally isolate advection induced dissipation associated any particular direction, with the most physically relevant direction being the dianeutral. Furthermore, many of the more promising advection operators are three dimensional, and so we cannot isolate any one of the directions to ascribe a particular effective diffusivity.

Nonetheless, the following are two notable cases where the dissipation operators from advection and diffusion can be directly compared.

- One-dimensional advection-diffusion, which is a rather trivial case, but very useful for prototype development;
- A three-dimensional simulation with just advection and vertical diffusion, using a linear equation of state with density directly proportional to temperature; in this case, the dissipation operators Σ_{general} and $\Sigma_{\text{vert-diff}}$ for temperature are directly comparable.

CHAPTER

TWENTYFIVE

Diagnosing the dianeutral velocity component

The purpose of this chapter is to detail the diagnostic method used in MOM4p1 to compute the dianeutral velocity component. This diagnostic provides a direct measure of the water being transported across neutral directions, and thus can be used to quantify rates of water mass transformation.

25.1 A brief on the model formulation

In developing diagnostic methods to measure levels of dianeutral transfer, we closely follow the numerical methods used to time step the prognostic model variables. This is generally a prudent means for diagnosing terms in a model simulations, and such is especially important when measuring vertical and dianeutral transfer, whose instantaneous values can be quite small. For this purpose, we briefly recall salient elements of the tracer budget discussed in Section 3.6.

Grid cells in MOM4p1 are bounded on the sides by surfaces of constant horizontal coordinates (x, y), and the vertical by surfaces of constant generalized vertical coordinate s (see Figure 25.1). The tracer budget for a cell given by the semi-continuous equation (see Section 3.6.2)

$$\partial_t (C\,\rho\,\mathrm{d}z) + \nabla_s \cdot (C\,\mathbf{u}\,\rho\,\mathrm{d}z) + \Delta_k (C\,w^{(s)}\,\rho) = -\nabla_s \cdot (\mathbf{F}\,\rho\,\mathrm{d}z) - \Delta_k (\rho\,F^{(s)}). \tag{25.1}$$

In this equation, C is the tracer concentration (tracer mass per seawater mass) within the grid cell, $\rho\,\mathrm{d}z$ is the seawater mass per horizontal area, $\mathrm{d}z\,\rho\,(\mathbf{u}\,C + \mathbf{F})$ is the horizontal flux of tracer mass associated with resolved advection through the horizontal velocity $\mathbf{u}$, and subgrid-scale (SGS) processes embodied by $\mathbf{F}$. The time tendency for tracer mass in a grid cell is affected by the horizontal convergence of these fluxes, with ∇_s the gradient operator taken on surfaces of constant s. The fluxes crossing the vertical interfaces of the grid cell are given by $\rho\,(w^{(s)}\,C + F^{(s)})$, and the difference of these fluxes across the top and bottom of the cell is denoted by the operator Δ_k. For Boussinesq vertical coordinates, the density factors are cancelled, whereas they remain for the non-Boussinesq pressure based vertical coordinates.

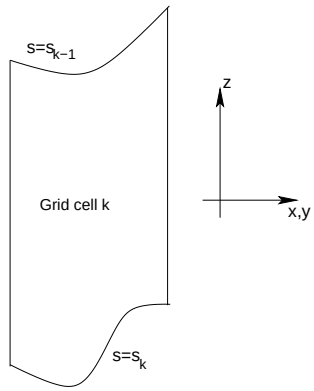

Figure 25.1: Schematic of an ocean grid cell labeled by the vertical integer k. Its sides are vertical and oriented according to $\hat{\mathbf{x}}$ and $\hat{\mathbf{y}}$, and its horizontal position is fixed in time. The top and bottom surfaces are determined by constant generalized vertical coordinates s_{k-1} and s_k, respectively. Furthermore, the top and bottom are assumed to always have an outward normal with a nonzero component in the vertical direction $\hat{\mathbf{z}}$. That is, the top and bottom are never vertical. We take the convention that the discrete vertical label k increases as moving downward in the column, and grid cell k is bounded at its upper face by $s = s_{k-1}$ and lower face by $s = s_k$.

25.2 Dianeutral velocity component

The dia-surface velocity component $w^{(s)}$ is defined by

$$w^{(s)} = z_{,s} \frac{\mathrm{d}s}{\mathrm{d}t}, \tag{25.2}$$

where $s = s(x, y, z, t)$ is an arbitrary smooth surface in the ocean interior, and $\mathrm{d}/\mathrm{d}t$ is the material time derivative. A full discussion of the dia-surface velocity component can be found in Section 6.7 of Griffies (2004), Section 2.2 of Griffies and Adcroft (2008), or Section 3.1.8 of the present document. We encountered $w^{(s)}$ in equation (25.1) when presenting the tracer budget integrated in MOM4p1. In that case, $w^{(s)}$ is the prognostic model's "vertical" velocity component.

For our diagnostic purposes, we are interested in the case where s is determined by a locally referenced potential density surface, symbolized here by γ. Here,

$$\gamma_{,z}\, w^{(\gamma)} = \gamma_{,\theta} \frac{\mathrm{d}\theta}{\mathrm{d}t} + \gamma_{,S} \frac{\mathrm{d}S}{\mathrm{d}t}, \tag{25.3}$$

where $w^{(\gamma)}$ is the *dianeutral velocity component*, S is the salinity, and θ is the potential temperature (or conservative temperature of McDougall (2003)).[1] The partial derivatives

$$\gamma_{,\theta} = \partial\gamma/\partial\theta \tag{25.4}$$

$$\gamma_{,S} = \partial\gamma/\partial S \tag{25.5}$$

[1]Note that the pressure term $\rho_{,p}\, \mathrm{d}p/\mathrm{d}t$, which appears in the material time derivative for *in situ* density ρ, is dropped here since we are focused on the locally referenced potential density γ.

measure how density changes as a function of temperature and salinity. Additionally, the neutral density vertical derivative

$$\gamma_{,z} = \gamma_{,\theta}\, \theta_{,z} + \gamma_{,S}\, S_{,z} \tag{25.6}$$

provides a measure of the vertical stratification, with the squared buoyancy frequency determined by

$$N^2 = -\frac{g}{\gamma}\, \gamma_{,z}. \tag{25.7}$$

In the remainder of this section, we consider two ways to understand $\gamma_{,z}\, w^{(\gamma)}$, and then we describe a finite volume approach relevant for diagnosing the dianeutral velocity component in MOM4p1.

25.2.1 Kinematics

We now expand the material time derivative in equation (25.3) using the generalized vertical coordinate form

$$\frac{\mathrm{d}}{\mathrm{d}t} = \left.\frac{\partial}{\partial t}\right)_s + \mathbf{u} \cdot \nabla_s + w^{(s)}\, \partial_z, \tag{25.8}$$

where again $s = s(x, y, z, t)$ defines the surfaces of constant generalized vertical coordinate. We are thus led to

$$\gamma_{,z}\, w^{(\gamma)} = \gamma_{,\theta} \left(\partial_t + \mathbf{u} \cdot \nabla_s + w^{(s)}\, \partial_z\right) \theta + \gamma_{,S} \left(\partial_t + \mathbf{u} \cdot \nabla_s + w^{(s)}\, \partial_z\right) S \tag{25.9}$$

where the time derivative is taken with s held constant. Dividing by the vertical stratification

$$\gamma_{,z} = \gamma_{,\theta}\, \theta_{,z} + \gamma_{,S}\, S_{,z} \tag{25.10}$$

leads to the following expression for the dia-neutral velocity component

$$\begin{aligned} w^{(\gamma)} &= w^{(s)} + \frac{\gamma_{,\theta}\, \left(\partial_t + \mathbf{u} \cdot \nabla_s\right)\, \theta + \gamma_{,S}\, \left(\partial_t + \mathbf{u} \cdot \nabla_s\right)\, S}{\gamma_{,z}} \\ &= w^{(s)} - \mathbf{S} \cdot \mathbf{u} + \frac{\gamma_{,\theta}\, \theta_{,t} + \gamma_{,S}\, S_{,t}}{\gamma_{,z}} \end{aligned} \tag{25.11}$$

where

$$\mathbf{S} = -\left(\frac{\gamma_{,\theta}\, \nabla_s\, \theta + \gamma_{,S}\, \nabla_s\, S}{\gamma_{,\theta}\, \theta_{,z} + \gamma_{,S}\, S_{,z}}\right) \tag{25.12}$$

is the slope of the neutral direction with respect to constant generalized vertical coordinate surfaces. We can write expression (25.11) in the equivalent manner

$$\rho\, \gamma_{,z}\, w^{(\gamma)} = \rho \left(\partial_t + \mathbf{u} \cdot \nabla_s + w^{(s)}\, \partial_z\right) \gamma, \tag{25.13}$$

by introducing the identities satisfied by neutral density

$$\gamma_{,t} = \gamma_{,\theta}\, \theta_{,t} + \gamma_{,S}\, S_{,t} \tag{25.14}$$

$$\gamma_{,z} = \gamma_{,\theta}\, \theta_{,z} + \gamma_{,S}\, S_{,z} \tag{25.15}$$

$$\nabla_s\, \gamma = \gamma_{,\theta}\, \nabla_s\, \theta_{,z} + \gamma_{,S}\, \nabla_s\, S. \tag{25.16}$$

In either of the expressions (25.11) or (25.13), we are afforded knowledge of the dianeutral velocity component when given the velocity and tracer distributions, the partial derivatives of density with respect to temperature and salinity, and the active tracer time tendencies. Given these fields, we have $w^{(\gamma)}$ even if we know nothing about the physical processes affecting the flow and tracers. It is for this reason that this perspective is termed *kinematic*.

25.2.2 Physical Processes

We now expose the physical processes affecting $w^{(\gamma)}$. For this purpose, rather than expanding the material time derivative in the definition (25.3), we now introduce the subgrid scale (SGS) fluxes for temperature and salinity

$$\rho \frac{\mathrm{d}\theta}{\mathrm{d}t} = -\nabla \cdot \mathbf{J}^{\theta} \tag{25.17}$$

$$\rho \frac{\mathrm{d}S}{\mathrm{d}t} = -\nabla \cdot \mathbf{J}^{S}, \tag{25.18}$$

where ρ is the *in situ* density, and

$$\mathbf{J} = \rho \, \mathbf{F} \tag{25.19}$$

consists of SGS fluxes arising from lateral and dia-surface advective and diffusive processes.[2] In writing the material evolution as in equations (25.17) and (25.18), we have ignored non-local transport, as in the KPP scheme (Large et al., 1994), as well as heat and salt sources. These extra terms can be trivially incorporated to the formalism.

The convergence of the SGS for temperature and salinity determine $\gamma_{,z} \, w^{(\gamma)}$ via

$$\rho \, \gamma_{,z} \, w^{(\gamma)} = -\gamma_{,\theta} \, \nabla \cdot \mathbf{J}^{\theta} - \gamma_{,S} \, \nabla \cdot \mathbf{J}^{S}. \tag{25.20}$$

Defining a SGS flux for locally referenced potential density

$$\mathbf{J}^{\gamma} = \gamma_{,\theta} \, \mathbf{J}^{\theta} + \gamma_{,S} \, \mathbf{J}^{S} \tag{25.21}$$

allows us to write equation (25.20) as

$$\rho \, \gamma_{,z} \, w^{(\gamma)} = -\nabla \cdot \mathbf{J}^{\gamma} + \mathbf{J}^{\theta} \cdot \nabla \, \gamma_{,\theta} + \mathbf{J}^{S} \cdot \nabla \, \gamma_{,S}. \tag{25.22}$$

The non-flux terms on the right hand side of equation (25.22) arise from cabbeling, thermobaricity, and halobaricity (McDougall, 1987). Note that neutral diffusive fluxes for temperature and salinity *do not* contribute to $\mathbf{J}^{\gamma}$ (Griffies et al., 1998). However, other lateral SGS processes, such as eddy advection (Gent and McWilliams, 1990; Gent et al., 1995) or skew diffusion (Griffies, 1998), are nontrivial contributors to $\mathbf{J}^{\gamma}$.

Let us now consider the form of the dianuetral velocity component under certain approximate situations. First, note that the source terms in equation (25.22) from cabbeling, thermobaricity, and halobaricity disappear for a linear equation of state (EOS), in which case

$$\rho \, \gamma_{,z} \, w^{(\gamma)} = -\nabla \cdot \mathbf{J}^{\gamma} \qquad \text{linear EOS.} \tag{25.23}$$

SGS advection is a nontrivial component in ocean climate models that do not explicitly represent mesoscale eddies. Nonetheless, consider the case when we ignore SGS advection, such as may be appropriate in fine resolution eddying models. In this case, we are left just with vertical diffusion

$$\rho \, \gamma_{,z} \, w^{(\gamma)} = -\partial_z \, J_z^{\gamma} \qquad \text{linear EOS and no eddy advection,} \tag{25.24}$$

[2]For depth-based vertical coordinates in MOM4p1, which integrate the Boussinesq equations, the factors of ρ in equations (25.17)-(25.19) are replaced by the constant reference density ρ_o.

with the vertical flux

$$\rho^{-1} J_z^{\gamma} = -\gamma_{,\theta} \kappa_\theta \theta_{,z} - \gamma_{,S} \kappa_S S_{,z} \tag{25.25}$$

where κ_θ and κ_S are vertical diffusivities for temperature and salinity. Finally, equating these two diffusivities, and making the Boussinesq approximation, leads to

$$\gamma_{,z} w^{(\gamma)} = \partial_z (\kappa \gamma_{,z}) \qquad \text{linear EOS, no eddy advection, and Boussinesq.} \tag{25.26}$$

25.2.3 Diagnosing $w^{(\gamma)}$ in finite grid cells

We now have the kinematic expression (25.13)

$$\rho \gamma_{,z} w^{(\gamma)} = \rho \left(\partial_t + \mathbf{u} \cdot \nabla_s + w^{(s)} \partial_z \right) \gamma \tag{25.27}$$

and the physical process expression (25.20)

$$\rho \gamma_{,z} w^{(\gamma)} = -\gamma_{,\theta} \nabla \cdot \mathbf{J}^{\theta} - \gamma_{,S} \nabla \cdot \mathbf{J}^{S} \tag{25.28}$$

providing two equivalent relations for the dianeutral velocity component $w^{(\gamma)}$. To develop a form appropriate for a finite volume grid cell, we make use of the mass continuity equation written for generalized vertical coordinates

$$\partial_t (\rho z_{,s}) + \nabla_s \cdot (\mathbf{u} \rho z_{,s}) + \partial_s (w^{(s)} \rho) = 0. \tag{25.29}$$

Use of this expression in equation (25.27), along with the identities (25.14)-(25.16), lead to

$$\begin{aligned} (\rho z_{,s}) \gamma_{,z} w^{(\gamma)} = \gamma_{,\theta} & \left(\partial_t (\rho z_{,s} \theta) + \nabla_s \cdot (\rho z_{,s} \mathbf{u} \theta) + \partial_s (\rho w^{(s)} \theta) \right) \\ & + \gamma_{,S} \left(\partial_t (\rho z_{,s} S) + \nabla_s \cdot (\rho z_{,s} \mathbf{u} S) + \partial_s (\rho w^{(s)} S) \right). \end{aligned} \tag{25.30}$$

We now integrate over the vertical extent of a grid cell, from $s = s_k$ upwards to $s = s_{k-1}$ (see Figure 25.1). For the left hand side, we have

$$\begin{aligned} \int_{s_k}^{s_{k-1}} \gamma_{,z} w^{(\gamma)} (\rho z_{,s}) \, \mathrm{d}s &= \int_{z_k}^{z_{k-1}} \gamma_{,z} w^{(\gamma)} \rho \, \mathrm{d}z \\ &\approx \gamma_{,z} w^{(\gamma)} \rho \, \mathrm{d}z, \end{aligned} \tag{25.31}$$

where we used $z_{,s} \, \mathrm{d}s = \mathrm{d}z$, and the last approximation defines the finite volume form of the cell integral. For the right hand side, we assume that the density partial derivatives $\gamma_{,\theta}$ and $\gamma_{,S}$ remain constant over the vertical extent of the cells. For the temperature contribution, we have

$$\begin{aligned} & \int_{s_k}^{s_{k-1}} \left(\partial_t (\rho z_{,s} \theta) + \nabla_s \cdot (\rho z_{,s} \mathbf{u} \theta) + \partial_s (\rho w^{(s)} \theta) \right) \mathrm{d}s \\ & = \partial_t \int_{s_k}^{s_{k-1}} (\rho z_{,s} \theta) \, \mathrm{d}s + \nabla_s \cdot \int_{s_k}^{s_{k-1}} (\rho z_{,s} \mathbf{u} \theta) \, \mathrm{d}s + \Delta_k (\rho w^{(s)} \theta) \\ & = \partial_t (\theta \rho \, \mathrm{d}z) + \nabla_s (\theta \mathbf{u} \rho \, \mathrm{d}z) + \Delta_k (\rho w^{(s)} \theta). \end{aligned} \tag{25.32}$$

To reach this result, we noted that the partial time derivative and lateral gradient operator commute with the vertical integral. The vertical integral of the vertical derivative led to the finite difference $\Delta_k\,(\rho\, w^{(s)}\,\theta)$ across the grid cell's top and bottom faces. Bringing these results together yields the finite volume result

$$\begin{aligned}\gamma_{,z}\, w^{(\gamma)}\,\rho\,\mathrm{d}z = \gamma_{,\theta}\,&\Big(\partial_t\,(\theta\,\rho\,\mathrm{d}z) + \nabla_s\cdot(\theta\,\mathbf{u}\,\rho\,\mathrm{d}z) + \Delta_k\,(\theta\, w^{(s)}\,\rho)\Big)\\ &+\gamma_{,S}\,\Big(\partial_t\,(S\,\rho\,\mathrm{d}z) + \nabla_s\cdot(S\,\mathbf{u}\,\rho\,\mathrm{d}z) + \Delta_k\,(S\, w^{(s)}\,\rho)\Big)\,.\end{aligned} \tag{25.33}$$

This result yields a discrete analog to the continuum kinematic expression (25.27). Again, the time derivative represents the local time tendency due to all processes affecting temperature and salinity. Combining the time derivative with the three dimensional advection provides a finite volume expression for the density weighted material time derivative. Finally, substitution of the finite grid cell tracer budget given by equation (3.165) leads to an expression in terms of physical processes

$$\begin{aligned}\gamma_{,z}\, w^{(\gamma)}\,\rho\,\mathrm{d}z = -\,\gamma_{,\theta}\,&\Big(\nabla_s\cdot(\mathbf{F}_\theta\,\rho\,\mathrm{d}z) + \Delta_k(\rho\, F_\theta^{(s)})\Big)\\ &-\gamma_{,S}\,\Big(\nabla_s\cdot(\mathbf{F}_S\,\rho\,\mathrm{d}z) + \Delta_k(\rho\, F_S^{(s)})\Big)\,.\end{aligned} \tag{25.34}$$

In MOM4p1, we have implemented diagnostics that determine the following terms:

- Time tendency of neutral density = $\gamma_{,\theta}\,\partial_t\,(\theta\,\rho\,\mathrm{d}z) + \gamma_{,S}\,\partial_t\,(S\,\rho\,\mathrm{d}z)$
- Advection of neutral density = $-\gamma_{,\theta}\,[\nabla_s\cdot(\theta\,\mathbf{u}\,\rho\,\mathrm{d}z) + \Delta_k\,(\theta\, w^{(s)}\,\rho)] - \gamma_{,S}\,[\nabla_s\cdot(S\,\mathbf{u}\,\rho\,\mathrm{d}z) + \Delta_k\,(S\, w^{(s)}\,\rho)]$
- Vertical diffusion of neutral density = $-\gamma_{,\theta}\,\Delta_k(\rho\, F_\theta^{(s)}) - \gamma_{,S}\,\Delta_k(\rho\, F_S^{(s)})$
- Vertical diffusion of neutral density arising from vertical mixing processes = $-\gamma_{,\theta}\,\Delta_k(\rho\, F_\theta^{(dianeutral)}) - \gamma_{,S}\,\Delta_k(\rho\, F_S^{(dianeutral)})$
- Vertical diffusion of neutral density arising just from the K33 element of neutral diffusion = $-\gamma_{,\theta}\,\Delta_k(\rho\, F_\theta^{(K33)}) - \gamma_{,S}\,\Delta_k(\rho\, F_S^{(K33)})$.
- Nonlocal KPP tendency = $\gamma_{,\theta}\,\delta\theta^{(nonlocal)} + \gamma_{,S}\,\delta S^{(nonlocal)}$
- Tendency from shortwave penetrative heating
- Tendency from crossland mixing (Chapter 20)
- Tendency from cross land insertion (Chapter 20)
- Tendency from smoothing either the surface height or the bottom pressure (Section 8.3)
- Tendency from mixing downslope (Chapter 19)
- Tendency from overexchange (Chapter 19)
- Tendency from sigma transport (Chapter 19)
- Tendency from fresh water forcing (P-E and rivers plus calving).

The corresponding dianeutral velocity components are also saved, via the division of the above tendencies by $\rho\,\mathrm{d}z\,\gamma_{,z}$. As a check that the diagnostics are properly implemented, for the case of zero background horizontal diffusion and zero tracer sources, we should have the following identities satisfied:

$$\text{time tendency} = \text{advection} + \sum \text{processes affecting T/S}$$
$$\text{vertical diffusion} = \text{vertical diffusion dianeutral} + \text{vertical diffusion K33.}$$

25.2.4 Spurious mixing from numerical advection

Expressions (25.33) and (25.34) can be used to define a finite volume version of $\gamma_{,z}\,w^{(\gamma)}\,\rho\,\mathrm{d}z$. If we then divide by $\gamma_{,z}\,\rho\,\mathrm{d}z$, we are led to a finite volume expression for the dianeutral velocity component $w^{(\gamma)}$. There is a caveat, however, which places some restrictions on the extent to which we can employ this particular formulation.

Namely, consider the case of pure advection with a linear equation of state, in which case we drop all subgrid scale (SGS) processes. Expression (25.34) then says that $w^{(\gamma)}$ vanishes. This result is sensible, as the absence of SGS processes with a linear equation of state imply an absence of mixing, which then leads to material time conservation of tracers. Unfortunately, in a discrete model, there can be nonzero sources of spurious mixing that arise from the numerical discretization of advection. If we could extract these spurious mixing terms from the numerical advection operator, the mixing would contribute to a nonzero spurious SGS flux. Hence, even with zero physical SGS fluxes, the spurious numerical fluxes do not generally vanish. The expressions (25.33) and (25.34) fail to account for these spurious terms since we ignored any truncation errors when extracting the approximate finite volume expressions from the exact continous expressions. Accounting explicitly for the truncation errors is generally nontrivial, given the many sophisticated expressions for numerical advection operators. So in practice, one can use the expressions for $w^{(\gamma)}$ only in those cases that the spurious sources of mixing are much smaller than the physical sources. The methods described in Chapter 23 provide one means to empirically diagnose the level of spurious mixing occuring in idealized simulations.

CHAPTER
TWENTYSIX

Diagnosing the contributions to sea level evolution

The purpose of this chapter is to discuss the diagnostic in MOM4p1 that diagnoses the contribution to sea level time tendencies due to changing currents, surface water forcing, and the steric effect. The discussion follows that given in Section 3.4 of Griffies (2004).

26.1 Mass budget for a column of water

Consider a column of mass conserving fluid extending from the ocean bottom at $z = -H$ to the ocean surface at $z = \eta$. The total mass of fluid, M, inside the column is given by

$$M = \int \mathrm{d}A \int_{-H}^{\eta} \rho \, \mathrm{d}z, \tag{26.1}$$

where ρ is the mass density (the *in situ* density) of seawater, and

$$\mathrm{d}A = \mathrm{d}x \, \mathrm{d}y \tag{26.2}$$

is the time independent horizontal area of the column. For a hydrostatic fluid, in which

$$p_{,z} = -\rho g, \tag{26.3}$$

the total mass per area in a column of seawater is given by the difference in pressure at the ocean bottom and the pressure applied at the ocean surface

$$g \int_{-H}^{\eta} \rho \, \mathrm{d}z = p_{\mathrm{b}} - p_{\mathrm{a}}. \tag{26.4}$$

That is, the total mass in the column is

$$M = g^{-1} \int \mathrm{d}A \, (p_{\mathrm{b}} - p_{\mathrm{a}}). \tag{26.5}$$

In Section 7.4, we developed a budget for the mass of fluid in a column. Repeating some of those steps here for completeness, we note that the time tendency of mass within a fluid column

$$M_{,t} = \int \mathrm{d}A \, \partial_t \left(\int_{-H}^{\eta} \mathrm{d}z \, \rho \right) \tag{26.6}$$

arises when a net amount of seawater mass passes across boundaries of the fluid column, or when there are sources within the column. We generally assume in climate modelling that no seawater mass enters through the ocean bottom. Hence, the only means of affecting seawater mass in the fluid column are through mass fluxes crossing the ocean free surface, from the convergence of mass into the column from ocean currents, and from sources within the column. These considerations lead to the time tendency

$$M_{,t} = \int \mathrm{d}A \left(q_{\mathsf{w}} \, \rho_{\mathsf{w}} - \nabla \cdot \int_{-H}^{\eta} \mathrm{d}z \, \rho \, \mathbf{u} \right) + \int \mathrm{d}A \int_{-H}^{\eta} \rho \, \mathrm{d}z \, \mathcal{S}^{(\mathsf{M})}. \tag{26.7}$$

The surface term

$$q_{\mathsf{w}} \, \rho_{\mathsf{w}} \, \mathrm{d}A = \hat{\mathbf{n}}(\eta) \cdot \hat{\mathbf{n}}_w \, (P - E + R) \, \rho_{\mathsf{w}} \, \mathrm{d}A_{(\eta)} \tag{26.8}$$

represents the mass flux of fresh water (mass per unit time per unit horizontal area) crossing the free surface, where ρ_{w} is the *in situ* density of the fresh water. Equivalently, $q_{\mathsf{w}} \, \rho_{\mathsf{w}} \, \mathrm{d}A$ is the momentum density of the fresh water in the direction normal to the ocean surface. The first volume term arises from the convergence of mass into the column from within the ocean fluid, and the second volume term arises from mass sources.

Equating the time tendencies given by equations (26.6) and (26.7) leads to a mass balance within each vertical column of fluid

$$\partial_t \left(\int_{-H}^{\eta} \mathrm{d}z \, \rho \right) + \nabla \cdot \left(\int_{-H}^{\eta} \mathrm{d}z \, \rho \, \mathbf{u} \right) = q_{\mathsf{w}} \, \rho_{\mathsf{w}} + \int_{-H}^{\eta} \mathrm{d}z \, \rho \, \mathcal{S}^{(\mathsf{M})}. \tag{26.9}$$

We can make this equation a bit more succinct by introducing the notation for density weighted vertically integrated horizontal velocity

$$\mathbf{U}^{\rho} = \int_{-H}^{\eta} \mathrm{d}z \, \rho \, \mathbf{u}, \tag{26.10}$$

which then leads to the following expression for mass conservation of a fluid column

$$\partial_t \left(\int_{-H}^{\eta} \mathrm{d}z \, \rho \right) + \nabla \cdot \mathbf{U}^{\rho} = q_{\mathsf{w}} \, \rho_{\mathsf{w}} + \int_{-H}^{\eta} \mathrm{d}z \, \rho \, \mathcal{S}^{(\mathsf{M})}. \tag{26.11}$$

If we assume a Boussinesq fluid, the seawater parcels conserve volume rather than mass. In this case, the budget for volume within a fluid column takes the form

$$\partial_t \left(\int_{-H}^{\eta} \mathrm{d}z \right) + \nabla \cdot \mathbf{U} = q_{\mathsf{w}} \, \rho_{\mathsf{w}} / \rho_o + \int_{-H}^{\eta} \mathrm{d}z \; \mathcal{S}^{(\mathsf{V})} \tag{26.12}$$

where ocean density factors appearing in the mass conservation equation (26.11) have been set to the constant reference density ρ_o, and

$$\mathbf{U} = \int_{-H}^{\eta} \mathbf{u}\, \mathrm{d}z \tag{26.13}$$

is the vertically integrated horizontal velocity.

26.2 Evolution of sea level

The previous discussion provides integral budgets for a column of seawater extending from the surface to the bottom. For many purposes, one may desire an evolution equation for the surface height or sea level. The purpose of this section is to derive relations that isolate the surface height and identify various physical processes affecting this height.

For this purpose, it will be useful to introduce the vertically averaged density

$$\overline{\rho}^z = \frac{1}{H+\eta} \int_{-H}^{\eta} \mathrm{d}z\, \rho. \tag{26.14}$$

This density can be readily computed within the prognostic model. Introducing the column mean density into the column mass budget (26.11) leads to

$$\overline{\rho}^z\, \eta_{,t} = -\nabla \cdot \mathbf{U}^{\rho} + \rho_{\mathsf{w}}\, q_{\mathsf{w}} + \int_{-H}^{\eta} \mathrm{d}z\, \rho\, \mathcal{S}^{(\mathsf{M})} - D\, \partial_t\, \overline{\rho}^z, \tag{26.15}$$

where

$$D = H + \eta \tag{26.16}$$

is the total thickness of the fluid column from the sea surface to the ocean bottom. Dividing equation (26.15) by the vertically averaged density $\overline{\rho}^z$ yields the surface height equation for a mass conserving fluid

$$\boxed{\eta_{,t}^{\mathsf{nonBouss}} = \underbrace{-\left(\frac{1}{\overline{\rho}^z}\right) \nabla \cdot \mathbf{U}^{\rho}}_{\text{dynamics}} + \underbrace{\left(\frac{\rho_{\mathsf{w}}}{\overline{\rho}^z}\right) q_{\mathsf{w}}}_{\text{water forcing}} + \underbrace{\frac{1}{\overline{\rho}^z} \int_{-H}^{\eta} \mathrm{d}z\, \rho\, \mathcal{S}^{(\mathsf{M})}}_{\text{source}} \underbrace{-D\, \partial_t\, \ln \overline{\rho}^z}_{\text{steric}}.} \tag{26.17}$$

The analogous result for the volume conserving Boussinesq fluid follows from equation (26.12), and is given by

$$\boxed{\eta_{,t}^{\mathsf{Bouss}} = \underbrace{-\nabla \cdot \mathbf{U}}_{\text{dynamics}} + \underbrace{\left(\frac{\rho_{\mathsf{w}}}{\rho_o}\right) q_{\mathsf{w}}}_{\text{water forcing}} + \underbrace{\int_{-H}^{\eta} \mathrm{d}z\, \mathcal{S}^{(\mathsf{V})}}_{\text{source}}.} \tag{26.18}$$

The dynamical, surface forcing, and source terms appearing in the two surface height equations (26.17) and (26.18) are directly analogous for both the non-Bousinesq and Boussinesq fluids.

That is, the convergence arises from changes across a column in the vertically integrated fluid column motion (i.e., the "dynamics"). In a non-Boussinesq fluid, the convergence is also affected by variations in density, whereas no such effects are present in the Boussinesq fluid. The fresh water term arises from surface boundary forcing in both the Boussinesq and non-Boussinesq fluids, and the source term arises from mass or volume sources. The term $-D\,\partial_t \ln \overline{\rho}^z$ appearing in the non-Boussinesq surface height equation represents a fundamentally new process that changes the ocean surface height when the vertically averaged density changes. For example, if the vertically averaged density decreases, the surface height increases, and vice versa. This process is commonly called the *steric effect*. It is an important contributor to sea level in the real ocean, and is of particular interest given the observed increases in ocean temperature arising from anthropogenic climate change. Unfortunately, the steric effect is absent from the Boussinesq fluid's prognostic surface height equation (26.18). As discussed in Section 26.3, we propose approximate methods to diagnostically compute the steric effect in Boussinesq models.

26.3 Diagnosing terms contributing to the surface height

In summary, the previous derivations have led to a surface height evolution equation for a mass conserving fluid that can be partitioned into four terms

$$\eta_{,t}^{\text{nonBouss}} = \underbrace{-\left(\frac{1}{\overline{\rho}^z}\right) \nabla \cdot \mathbf{U}^\rho}_{\text{dynamics}} + \underbrace{\left(\frac{\rho_{\text{w}}}{\overline{\rho}^z}\right) q_{\text{w}}}_{\text{water forcing}} + \underbrace{\left(\frac{1}{\overline{\rho}^z}\right) \int_{-H}^{\eta} \mathrm{d}z\; \rho\, \mathcal{S}^{(\text{M})}}_{\text{source}} \underbrace{-D\,\partial_t\, \ln \overline{\rho}^z}_{\text{steric}}. \tag{26.19}$$

Each term on the right hand side is a time tendency that contributes to the evolution of the ocean surface height. For diagnostic purposes, we split the surface height into the non-steric and steric terms

$$\eta^{\text{nonBouss}} = \eta^{\text{nonsteric}} + \eta^{\text{steric}}, \tag{26.20}$$

where the surface heights are defined according to their time tendencies

$$\eta_{,t}^{\text{nonsteric}} = -\left(\frac{1}{\overline{\rho}^z}\right) \nabla \cdot \mathbf{U}^\rho + \left(\frac{\rho_{\text{w}}}{\overline{\rho}^z}\right) q_{\text{w}} + \left(\frac{1}{\overline{\rho}^z}\right) \int_{-H}^{\eta} \mathrm{d}z\; \rho\, \mathcal{S}^{(\text{M})} \tag{26.21}$$

$$\eta_{,t}^{\text{steric}} = -D\,\partial_t\, \ln \overline{\rho}^z. \tag{26.22}$$

We diagnostically time step each of these two surface heights in order to monitor the instantaneous contributions to the full surface height arising from the physically distinct processes.

We next consider the details of how to diagnose these terms within a non-Boussinesq mass conserving version of MOM4p1, using a pressure based vertical coordinate, as well as a Boussinesq version of MOM4p1 using a depth based vertical coordinate. This formulation also provides guidance for diagnosing these terms from commonly saved model output.

26.3.1 Pressure based vertical coordinates

As the pressure based version of MOM4p1 integrates the mass conserving nonBoussinesq equations, each term on the right hand side of equation (26.19) can be diagnosed in a straightforward

manner. The result of the diagnostic calculation for η^{nonBouss} will be, to within numerical truncation error, the same as the model's prognostic calculation, which computes the surface height after having time stepped the bottom pressure (see Section 7.3.4). Verifying that this is realized in the model is a good way to check both the theory and the model formulation.

26.3.2 Depth based vertical coordinates

For a depth based version of MOM4p1, the surface height is determined from a discrete form of equation (26.18), which omits steric effects. However, it is possible to diagnose the terms appearing on the right hand side of the non-Boussinesq surface height equation (26.19), and in particular to approximate the non-Boussinesq surface height. To do so requires some approximations, which we list here.

- For purposes of performing the vertical integrals to compute the depth averaged density $\overline{\rho}^z$, as well as the density weighted horizontal velocity $\mathbf{U}^\rho$, we assume the currents, surface height, and density computed in the Boussinesq model are reasonably close to those computed in a non-Boussinesq model. This approximation is motivated by the results from a careful comparison of non-Boussinesq effects in a steady state coarse resolution model by Losch et al. (2004). The approximation breaks down when (a) currents are ageostrophic as near boundaries and the equator, (b) flows are strongly nonlinear, as in eddying simulations. Nonetheless, for many purposes, especially for large scale patterns, the approximation remains sufficiently accurate. Hence, it is possible to again diagnose the tendency terms appearing on the right hand side of equation (26.19) as in the non-Boussinesq model.

- To further approximate the calculation, we employ the constant Boussinesq density ρ_o when computing the dynamical contribution, and drop the density ratio when computing the water forcing term and source term. Hence, the only place than *in situ* density is maintained is for computation of the steric term.

In summary, we propose the approximation

$$\eta^{\text{nonBouss}} \approx \eta^{\text{Bouss}} + \eta^{\text{steric}}, \tag{26.23}$$

where η^{Bouss} is the prognostic surface height computed by the Boussinesq model,

$$\eta^{\text{Bouss}} \approx \eta^{\text{nonsteric}} \tag{26.24}$$

and η^{steric} is the steric sea level diagnosed in the Boussinesq model, as described above.

26.4 Global averaged sea level

The previous discussion aimed to identify contributions to sea level change at each point in the ocean. For many purposes, it is of primary interest to measure changes in global mean sea level. We can answer this question by considering a horizontal area mean of the previous diagnostic terms. However, it is cleaner to start from an even more basic perspective, whereby we consider the following relation between the total mass of liquid seawater, total volume of seawater, and global mean seawater density,

$$\mathcal{M} = \mathcal{V} \langle \rho \rangle, \tag{26.25}$$

where $\mathcal{M}$ is the total liquid ocean mass

$$\mathcal{M} = \sum \mathrm{d}x\,\mathrm{d}y\,\mathrm{d}z\,\rho, \tag{26.26}$$

$\mathcal{V}$ is the total ocean volume

$$\mathcal{V} = \sum \mathrm{d}x\,\mathrm{d}y\,\mathrm{d}z, \tag{26.27}$$

and $\langle \rho \rangle$ is the global mean *in situ* density

$$\langle \rho \rangle = \mathcal{M}/\mathcal{V}. \tag{26.28}$$

Temporal changes in total ocean mass are affected by a nonzero net mass flux through the ocean boundaries, so that

$$\partial_t \mathcal{M} = \mathcal{A}\,\langle Q^{\mathsf{w}} \rangle \tag{26.29}$$

where

$$Q^{\mathsf{w}} = \rho_{\mathsf{w}}\, q_{\mathsf{w}} \tag{26.30}$$

is the mass per horizontal area per time of water crossing the ocean boundaries, and

$$\langle Q^{\mathsf{w}} \rangle = \mathcal{A}^{-1} \sum \mathrm{d}x\,\mathrm{d}y\, Q^{\mathsf{w}} \tag{26.31}$$

is the global mean mass per horizontal area per time of water crossing the ocean boundaries. Temporal changes in the ocean volume are associated with sea level changes via

$$\partial_t \mathcal{V} = \mathcal{A}\,\partial_t \langle \eta \rangle, \tag{26.32}$$

where $\mathcal{A} = \sum \mathrm{d}x\,\mathrm{d}y$ is the area of the global ocean surface, and

$$\langle \eta \rangle = \mathcal{A}^{-1} \sum \eta\,\mathrm{d}x\,\mathrm{d}y \tag{26.33}$$

is the global mean sea level. Bringing these results together leads to the evolution equation for the mean sea level

$$\partial_t \langle \eta \rangle = \frac{\langle Q^{\mathsf{w}} \rangle}{\langle \rho \rangle} - \left(\frac{\mathcal{V}}{\mathcal{A}}\right) \frac{\partial_t \langle \rho \rangle}{\langle \rho \rangle}. \tag{26.34}$$

The first term in equation (26.34) is associated with mass fluxes across the ocean surface. The second term arises from temporal changes in the global mean density; i.e., from *steric* effects. The steric effect is missing in Boussinesq models, so that the global mean sea level in a Boussinesq model is altered only by net volume fluxes across the ocean surface.

We can approximate each of the terms in equation (26.34) over a finite time Δt via

$$\Delta \langle \eta \rangle \approx \frac{\langle Q^{\mathsf{w}} \rangle\,\Delta t}{\langle \rho \rangle} - \left(\frac{\mathcal{V}}{\mathcal{A}}\right) \frac{\Delta \langle \rho \rangle}{\langle \rho \rangle}, \tag{26.35}$$

where the Δ operator is a finite difference over the model time step. In a Boussinesq model, we must compute each term on the right hand side in order to develop an accurate time series for the global mean sea level that includes steric effects. For a non-Boussinesq model, $\langle \eta \rangle$ is computed directly from the model's surface height field, since the prognostic model includes steric effects.

In either the Boussinesq or non-Boussinesq case, it is of interest to diagnose the steric term

$$\mathcal{S} \equiv -\left(\frac{\mathcal{V}}{\mathcal{A}}\right) \frac{\Delta \langle \rho \rangle}{\langle \rho \rangle} \tag{26.36}$$

in order to deduce the effect on $\langle \eta \rangle$ associated just with changes in global mean density, as distinct from changes in ocean mass. The steric effect is straightforward to diagnose from a model simulation, given temporal changes in the global mean density.

We now consider the question of how much the steric effect is determined by changes in temperature and salinity. For this purpose, we write the time tendency for global mean density as

$$\partial_t \langle \rho \rangle = \langle \partial_t \, \rho \rangle + \mathcal{V}^{-1} \iint \mathrm{d}x \, \mathrm{d}y \, (\rho(\eta) - \langle \rho \rangle) \, \partial_t \, \eta, \tag{26.37}$$

where $\rho(\eta)$ is the density at the ocean surface. It is the first term in this equation that interests us when considering thermal effects, in which case we write

$$\langle \partial_t \, \rho \rangle = \langle -\alpha \, \rho \, \partial_t \, \theta \rangle + \langle \beta \, \rho \, \partial_t \, S \rangle + \langle c_s^{-2} \, \partial_t \, p \rangle, \tag{26.38}$$

where $\alpha = -\rho^{-1} \, \partial \rho / \partial \theta$ is the thermal expansion coefficient, $\beta = \rho^{-1} \, \partial \rho / \partial S$ is the haline contraction coefficient, and $c_s^2 = \partial p / \partial \rho$ is the squared sound speed. Given this expansion of the density tendency, we identify the thermosteric contribution to sea level as the following finite increment

$$\mathcal{S}^{\text{thermo}} \equiv \left(\frac{\mathcal{V}}{\mathcal{A}} \right) \frac{\langle \alpha \rho \, \Delta(\theta) \rangle}{\langle \rho \rangle}. \tag{26.39}$$

A reasonably accurate approximation can be found by canceling the density factors

$$\mathcal{S}^{\text{thermo}} \approx \left(\frac{\mathcal{V}}{\mathcal{A}} \right) \langle \alpha \, \Delta(\theta) \rangle. \tag{26.40}$$

It is critical to *not* make the further approximation of extracting a constant thermal expansion from the global average:

$$\mathcal{S}^{\text{thermo}} \neq \left(\frac{\mathcal{V}}{\mathcal{A}} \right) \langle \alpha \rangle \langle \Delta(\theta) \rangle. \tag{26.41}$$

The reason to avoid this approximation is that the thermal expansion coefficient varies quite a lot over the World Ocean. Hence, it is important to weight the changes in temperature with the corresponding local value of α.

The halosteric contribution to sea level change is defined analogously

$$\begin{aligned} \mathcal{S}^{\text{halo}} &\equiv - \left(\frac{\mathcal{V}}{\mathcal{A}} \right) \frac{\langle \beta \rho \, \Delta(S) \rangle}{\langle \rho \rangle} \\ &\approx - \left(\frac{\mathcal{V}}{\mathcal{A}} \right) \langle \beta \, \Delta(S) \rangle. \end{aligned} \tag{26.42}$$

The halosteric term becomes more important as increases in melt water from land glaciers dilute seawater. Finally, the difference

$$\mathcal{S}^{\text{pressure}} \equiv \mathcal{S} - \mathcal{S}^{\text{thermo}} - \mathcal{S}^{\text{halo}} \tag{26.43}$$

identifies the steric effects arising from changes in pressure.

CHAPTER
TWENTYSEVEN

Balancing the hydrological cycle in ocean-ice models

The purpose of this chapter is to discuss issues of how to balance the hydrological cycle in ocean-ice simulations using MOM4p1 and the FMS coupler. In particular, we detail how the liquid water flux transferred between sea ice and liquid ocean is diagnosed in MOM4p1, given the salt mass flux transferred between the media.

27.1 Transfer of water between sea ice and ocean

As sea ice forms, water is extracted from the liquid ocean and passed to the solid sea ice. Additionally, there is generally a nonzero salt mass transferred from ocean to ice, thus producing a nonzero salinity for sea ice. Conversely, as sea ice melts, liquid water and salt are added to the ocean.

The GFDL Sea Ice Simulator (SIS) generally simulates sea ice with a nonzero salt content. For example, in the coupled climate model simulations discussed by Delworth et al. (2006), sea ice is assumed to have a salinity

$$\text{S_ice} = \frac{\text{kg salt in sea ice}}{\text{kg sea ice}} \tag{27.1}$$

of S_ice $= 0.005$ (five parts per thousand).

27.2 Balancing the hydrological cycle

When running ocean-ice simulations, we are not explicitly representing land processes, such as rivers, catchment areas, snow accumulation, etc. However, to reduce model drift, it is important to balance the hydrological cycle in ocean-ice models. We thus need to prescribe some form of global normalization to the precipitation minus evaporation plus river runoff. The result of the normalization should be a global integrated zero net water input to the ocean-ice system over a chosen time scale.

How often the normalization is done is a matter of choice. In MOM4p1, we choose to do so at each model time step, so that there is always a zero net input of water to the ocean-ice system. Others choose to normalize over an annual cycle, in which case the net imbalance over an annual

cycle is used to alter the subsequent year's water budget in an attempt to damp the annual water imbalance. Note that the annual budget approach may be inappropriate with interannually varying precipitation forcing.

When running ocean-ice coupled models, it is incorrect to include the water transport between the ocean and ice models when aiming to balance the hydrological cycle. The reason is that it is the sum of the water in the ocean plus ice that should be balanced when running ocean-ice models, not the water in any one subcomponent. As an extreme example to illustrate the issue, consider an ocean-ice model with zero initial sea ice. As the ocean-ice model spins up, there *should* be a net accumulation of water in the growing sea ice, and thus a net loss of water from the ocean. The total water contained in the ocean plus ice system is constant, but there is an exchange of water between the subcomponents. This exchange should not be part of the normalization used to balance the hydrological cycle in ocean-ice models.

27.3 Water mass flux from salt mass flux

Balancing the hydrological cycle in an ocean-ice model run with the FMS coupler requires an indirect method. The reason is that melt water from the ice model is added to the precipitation field prior to being added to the ocean model. So prior to balancing the water fluxes, we must remove the ice melt from the precipitation. The namelist option for performing this normalization is

`zero_net_water_coupler`

found in the module

`mom4p1/ocean_core/ocean_sbc_mod`.

An alternative namelist option is

`zero_net_water_couple_restore`

which balances the water due to precipitation minus evaporation plus runoff plus restoring flux water. Note that in MOM4p0, ice melt was *not* removed from precipitation prior to computing the water normalization using `zero_net_water_coupler`. This bug compromised the integrity of the ocean-ice models run with MOM4p0 which used the option `zero_net_water_coupler`.

To obtain the water mass flux between sea ice and ocean, we could consider two approaches. First, we could alter the FMS sea ice code so that it carries explicit information about the water flux in question. This approach requires modifying code that lives outside of MOM4p1, and so is not desirable from a MOM4-centred perspective. Alternatively, we can make use of the salt mass flux passed between the ocean and sea ice. This approach is limitated to cases where the ice is assumed to have a uniform bulk salinity, as presently assumed in the GFDL sea ice model.

In MOM4p1, we have access to the following salt flux

$$\text{salt_flux_to_ice} = S_{\text{ice}}\, \rho_{\text{sea ice}}\, \frac{T_{\text{ice melt}}}{\Delta t}. \tag{27.2}$$

In this equation, $\rho_{\text{sea ice}}$ is the density of sea ice, taken as $\rho_{\text{sea ice}} = 905\,\text{kg}\,\text{m}^{-3}$ in the GFDL ice model, and $T_{\text{ice melt}}/\Delta t$ is the thickness (in meters) of ice that melts over the time step (in seconds) of the ice model. By convention, this salt flux is positive when there is growth in sea ice,

thus representing a passage of salt from the liquid ocean into the sea ice. Correspondingly, this flux is positive when there is a mass flux of water to the sea ice. Since we are here working from an ocean perspective, we prefer to measure the flux of salt entering the ocean from the melting sea ice

$$\text{salt_flux_to_ocean} = -\text{salt_flux_to_ice}. \tag{27.3}$$

Dividing the salt flux by the salinity of sea ice yields the mass flux of water that melts (i.e., mass flux of water transferred from sea ice to the ocean)

$$\begin{aligned} \text{mass_melt} &= \frac{\text{salt_flux_to_ocean}}{\text{S_ice}} \\ &= \left(\frac{\text{kg ice melt}}{\text{area sea ice} \times T_{\text{ice melt}}}\right)\left(\frac{T_{\text{ice melt}}}{\Delta t}\right) \\ &= \left(\frac{\text{kg ice melt}}{\text{area sea ice} \times \Delta t}\right). \end{aligned} \tag{27.4}$$

This mass of melting sea ice represents a gain of liquid water for the ocean.

CHAPTER
TWENTYEIGHT

Gyre and overturning contributions to tracer transport

The purpose of this chapter is to discuss the diagnostic in MOM4p1 that computes the contribution to advective tracer transport in the j-direction (generalized meridional) associated with gyre and overturning components of the flow. Bryan and Lewis (1979) were amongst the first to make use of this diagnostic, and Peixoto and Oort (1992) (page 342) describe the decomposition in more detail. The gyre component has traditionally been associated with wind driven processes, and overturning associated with thermohaline processes. However, this physical association is not clean, as it is generally not possible to split the transport into two distinct physical processes. For example, removing wind forcing does not necessarily mean the gyre contribution is zero. Nonetheless, this decomposition is commonly performed, and such has provided some physical insight into the flow characteristics. It is for this reason that MOM4p1 provides a subroutine inside `ocean_tracer_advect.F90` to perform this decomposition.

28.1 Formulation

The meridional advective transport of a tracer within a particular ocean basin is given by the integral

$$\mathcal{H}(y,t) = \int_{x_1}^{x_2} \mathrm{d}x \int_{-H}^{\eta} \mathrm{d}z \, \rho \, C \, v, \tag{28.1}$$

where v is the meridional velocity component, ρ is the *in situ* density, C is the tracer concentration, $z = -H(x,y)$ is the ocean bottom, $z = \eta(x,y,t)$ is the ocean surface, and x_1 and x_2 are the longitudinal boundaries of the basin or global ocean. With the generalized horizontal coordinates in MOM4p1, the coordinate y is assumed to be aligned with the j grid lines. For the purposes of this diagnostic, we do *not* perform a rotation of the flow to the geographical longitude and latitude. For the tripolar grid commonly used for global modeling with MOM4p1, generalized zonal integrals along i-lines yield j-transport, and this is sufficient for most diagnostic purposes. Note the term *north* will continue to be used, with this generally denoting the j-direction, which corresponds to the geographical north when j-lines are parallel to longitudes.

In MOM4p1, the density and thickness weighted advective velocity component

$$\mathcal{V} = v \, \rho \, \mathrm{d}z \tag{28.2}$$

is computed and held in the array `vhrho_nt`, where ρ reduces to the constant Boussinesq density ρ_o for the Boussinesq version of MOM4p1, but it remains the *in situ* density for the nonBoussinesq version. The product $\mathrm{d}x\,\mathcal{V}$ measures the mass per time of seawater leaving the north face of the grid cell, with $\mathrm{d}x\,\mathcal{V}\,C$ thus measuring the mass per time of tracer leaving the north face. We now consider the following decomposition of this transport by defining the zonal average transport and zonal average tracer concentration as follows

$$[\mathcal{V}] = \frac{\sum_i \mathrm{d}x\,\mathcal{V}}{\sum_i \mathrm{d}x} \tag{28.3}$$

$$[C] = \frac{\sum_i \mathrm{d}x\,C}{\sum_i \mathrm{d}x}, \tag{28.4}$$

along with the deviations from zonal average

$$\mathcal{V} = [\mathcal{V}] + \mathcal{V}^* \tag{28.5}$$

$$C = [C] + C^*. \tag{28.6}$$

The discrete i-sum extends over the basin or global domain of interest, so that $\sum_i \mathrm{d}x\,\mathcal{V}$ is the total meridional transport of seawater at this zonal band at a particular k-level. The resulting meridional tracer transport becomes

$$\mathcal{H}(y,t) = \sum_i \sum_k \mathrm{d}x\,\mathcal{V}\,C \tag{28.7}$$

$$= \sum_i \sum_k \mathrm{d}x\,\left([\mathcal{V}]\,[C] + \mathcal{V}^*\,C^*\right), \tag{28.8}$$

where the k sum extends over the depth of a column.

We identify three components in the code:

$$\text{merid_flux_advect} = \sum_i \sum_k \mathrm{d}x\,\mathcal{V}\,C \tag{28.9}$$

$$\text{merid_flux_over} = \sum_i \sum_k \mathrm{d}x\,[\mathcal{V}]\,[C] \tag{28.10}$$

$$\text{merid_flux_gyre} = \sum_i \sum_k \mathrm{d}x\,\mathcal{V}^*\,C^*. \tag{28.11}$$

Note that

$$\text{merid_flux_gyre} = \text{merid_flux_advect} - \text{merid_flux_over}. \tag{28.12}$$

This identity follows very simply when the advective flux takes on the simple form of either first order upwind or second order centered differences. It becomes more involved when considering higher order, or flux limited, advection schemes. Nonetheless, we use this as a defintion of the gyre component, so that the advective flux is built from the advection scheme used in the model.

28.2 Enabling the diagnostic

The following is necessary to enable this diagnostic.

- Set the `ocean_tracer_advect_nml` logical

$$\texttt{compute_gyre_overturn_diagnose} = \texttt{.true}.$$

  This logical is introduced since a number of global arrays must be defined, and it is simplest to determine the need for these arrays by setting a single logical.

- Set any of the following within the diagnostic table:

$$\texttt{"tracer"_merid_flux_advect_"basin"}$$
$$\texttt{"tracer"_merid_flux_over_"basin"}$$
$$\texttt{"tracer"_merid_flux_gyre_"basin"}$$

  where "tracer" is the MOM4p1 shortname for the tracer (e.g., "temp" or "salt"), and "basin" is one of the names "global", "southern","atlantic", "pacific", "arctic", or "indian".

- To get the transport diagnostic partitioned into basins in the World Ocean, it is necessary to read in a netCDF basin mask. A sample mask is provided with the OM3-CORE test case discussed in Chapter 37. The logical to read in this mask is

$$\texttt{read_basin_mask} = \texttt{.true}.$$

  The convention is that the basins are defined by the following values in the mask:

$$\begin{aligned} \text{Southern} &= 1.0 \\ \text{Atlantic} &= 2.0 \\ \text{Pacific} &= 3.0 \\ \text{Arctic} &= 4.0 \\ \text{Indian} &= 5.0. \end{aligned}$$

PART V
Test Cases

The purpose of this part of the manual is to introduce the MOM4p1 test cases. Test cases are offered as a means to explore various numerical and physical options, thus allowing the user to verify that the code is performing in a manner consistent with that at GFDL. This form of verification is critical as one adopts the code for his or her particular research purposes. The test cases also provide a sense for some of the options available in the code, though by no means are all options exercised in the test cases. Note that due to resource limitations, the test cases are not always updated.

Regression Testing for Computational Integrity

Output from the test cases provided with the MOM4p1 distribution is based on short integrations that verify the computational integrity of a simulation. The associated runscripts are provided that allow the user to rerun the regressions. These *regression test suites* (RTS) aim to verify that the following identities hold, with precision maintained to all computational bits:

- Stopping and then restarting the integration will not change answers. That is, we insist on the identity

$$\text{X day integration} = \text{X/2 day integration} + \text{X/2 day integration}. \tag{28.13}$$

  This test verifies that all the relevant fields are properly stored in the restart files, and that no spurious reinitialization step is performed during the beginning of the second leg.

- Changing the number of computer processors will not change the answers. This test examines whether the code is properly written for parallel machines. Its satisfaction requires that all message passing be correctly performed so that accessed halo points are filled with their proper values. In the early days of parallel computing with MOM, this test was very tedious to satisfy, since our experience was based on seriel computing. Now, after some years of experience, it is generally straightforward to code in a manner that ensures answers do not change when processor counts change.

Satisfaction of these two tests is critical to maintain computational integrity of the code.

It is important to note that the runscripts for the regressions are distributed with the following settings:

- `diag_step` is set to a small number, such as 1 or 12, in various diagnostic modules. This setting means that various numerical diagnostics are run at a very high frequency. These diagnostics can be expensive. It is therefore strongly recommended that the setting for `diag_step` be increased to a much larger number when running experiments for long periods of simulation time. Otherwise, the model will be unreasonably slow.

- The diagnostic tables are setup to output netCDF diagnostics at a very high frequency, such as daily. Again, this high frequency is unreasonable when running simulations for long periods of time. The output produced will be enormous, and the model will run at a much slower pace. Additionally, a large number of diagnostics are included in the `diag_table`, many of which may not be of interest to the user. Therefore, prior running an experiment, it is important to edit the `diag_table` to refine the desired output.

Comments on the test cases

The chapters in this part of the manual represent a rough guide to the various test cases. We present a sprinkling of model output to allow interested users to run simulations at their institution to verify that the code has been properly ported. Many details of the experiments are omitted, with examination of the supplied runscripts providing more details. Furthermore, a full accounting of the test cases, both their design and simulation characteristics, is beyond the scope of this document. Indeed, a full discussion would constitute a research paper. We thus present a taste, with further details readily found by diving into the model, running experiments, and performing analysis.

Some test cases are based on research experiments conducted at GFDL and elsewhere. They may thus serve as useful starting points for research using MOM4p1. It is nonetheless critical that the user *not* blindly assume that a test case is precisely appropriate for a particular research project. Instead, one is strongly encouraged to scrutinize each option in a test case before concluding that it is relevant.

As there are many options in MOM4p1, it is not feasible to exercise all options with only a few test cases. Hence, some tests are distributed with more options enabled than scientifically appropriate. Conversely, many options are not fully exemplified by the test cases. Omitted options include the *experimental* options sprinkled through MOM4p1, with these options *not* supported for general use. The developers are aware of the limitations in the test cases, but choose to release the incomplete suite of tests in hopes that *something* is preferable to *nothing*.

CHAPTER

TWENTYNINE

Torus test case

The torus test case `mom4_torus` consists of a flat bottom square domain on the F-plane with doubly periodic boundary conditions. It provides an idealized test bed for implementing various numerical schemes, with applications to tracer advection frequently exercised at GFDL. The flow field can be specified to have uniform horizontal velocity. For the illustration considered here, we consider a zonal flow with $(u, v) = (0.25\mathrm{m\,s^{-1}}, 0)$.

There are various options in

`mom4/ocean_tracers/ocean_passive_mod`

for specifying the initial profile of idealized passive tracers. We consider two profiles shown in the top panel of Figure 29.1. The first profile is a square wave or pulse, and the second is a smooth Gaussian bump. The initial tracer concentrations all live within the range $[0, 1]$. Numerical solutions that fall outside this range constitute spurious unphysical results arising from errors in the advection scheme. A perfect advection scheme would advect the profiles without alteration.

The tracer profiles are advected with the following Courant number

$$\begin{aligned} C &= \frac{u\,\Delta t}{\Delta x} \\ &= \frac{0.25\mathrm{m\,s^{-1}} \times 10800\mathrm{s}}{1.04 \times 10^5\mathrm{m}} \\ &\approx 0.5 \end{aligned} \tag{29.1}$$

using the staggered time stepping scheme standard in MOM4p1 (Section 8.2). For the centred 2nd order and 4th order advection schemes, however, stability requires leap-frog time stepping, in which case the Courant number is ≈ 1 since the time step for advection is $2\,\Delta t$. We consider the following advection schemes available with MOM4p1:

- **2nd**: The second order centred differences scheme has been the traditional scheme employed in earlier versions of MOM. It is available only with the leap-frog version of MOM4p1, since it is unstable with a forward time step used with the forward-backward method (Section 8.2).

- **4th**: The fourth order centred scheme also is available only for the leap-frog version of MOM4p1. This scheme assumes the grid is uniformly spaced (in metres), and so is less than fourth order accurate when the grid is stretched, in either the horizontal or vertical.

- **Upwind**: This is a first order upwind scheme, which is highly diffusive yet monotonic.
- **Quicker**: The quicker scheme is third order upwind biased and based on the work of Leonard (1979). Holland et al. (1998) and Pacanowski and Griffies (1999) discuss implementations in ocean climate models. This scheme does not have flux limiters, so it is not monotonic.
- **MDPPM**: The piece-wise parabolic method with flux limiters.
- **Super B**: Multi-dimensional third order upwind biased approach of Hundsdorfer and Trompert (1994), with Super-B flux limiters.[1]
- **Sweby**: Multi-dimensional third order upwind biased approach of Hundsdorfer and Trompert (1994), with flux limiters of Sweby (1984).[2]
- **PSOM unlimited**: The second order moment scheme of Prather (1986).
- **PSOM limited**: The second order moment scheme of Prather (1986) with flux limiters from Merryfield and Holloway (2003).

After 100 days, the tracer concentration profiles have evolved to those in the second, third, and fourth panels of Figure 29.1. There are clear differences between the various schemes.

The 2nd and 4th order schemes exhibit nontrivial extrema for the square pulse. Extrema arise from the dispersion errors intrinsic to these schemes. The errors are especially large when advecting profiles with strong gradients, such as the square pulse. In contrast, they perform much better for the Gaussian pulse, due to the pulse's much more smooth initial profile. The first order upwind scheme produces no extrema, yet it is highly dissipative, with the square pulse nearly as damped as the Gaussian pulse after 100 days. The Quicker scheme is somewhat of a compromise between the upwind scheme and the 2nd and 4th order schemes. It contains diffusion intrinsic to the algorithm, which smooths the profile to help maintain a more reasonable level of boundedness. However, its performance for the square pulse remains unsatisfying, as there remain some nontrivial unphysical extrema.

In the third panel, the Sweby, Super B, and MDPPM schemes all show similar behaviour to each other. In particular, each maintains the tracer within its physical bounds, since these schemes are flux limited. More detailed analysis reveals that MDPPM is a bit less dissipative than the other two schemes, thus allowing for a slightly better maintenance of the square pulse shape. It is interesting that each scheme converts the initially smooth Gaussian pulse into a more square feature over time. Such is a property common to many advection schemes with flux limiters.

The fourth panel shows results for the limited and unlimited PSOM schemes. The unlimited PSOM scheme produces extrema for the square pulse, but with far smaller amplitude than Quicker, 2nd, or 4th order advection. Even so, it does a wonderful job maintaining the shape of the square pulse. The limited PSOM scheme also maintains the square pulse, but clips the extrema thus retaining tracer concentrations within their physically relevant bounds.

[1]This scheme was ported to MOM4 by Alistair Adcroft, based on his implementation in the MITgcm. The online documentation of the MITgcm at `http://mitgcm.org` contains useful discussions and details about this advection scheme.

[2]This scheme was ported to MOM4 by Alistair Adcroft, based on his implementation in the MITgcm. The online documentation of the MITgcm at `http://mitgcm.org` contains useful discussions and details about this advection scheme.

Based on performance in the square pulse test, the limited PSOM scheme appears to be the best if we insist on maintaining boundedness of the tracer, with the unlimited PSOM scheme preferable if slight extrema are allowed. Use of the PSOM schemes come at the price of adding 10 extra three-dimensional arrays for each tracer. This added memory may preclude PSOM for some models, depending on computer platform and number of tracers. One approach to reducing the memory overhead is to employ the PSOM scheme for the active tracers (temperature and salinity), and another scheme, such as MDPPM, for the passive tracers.

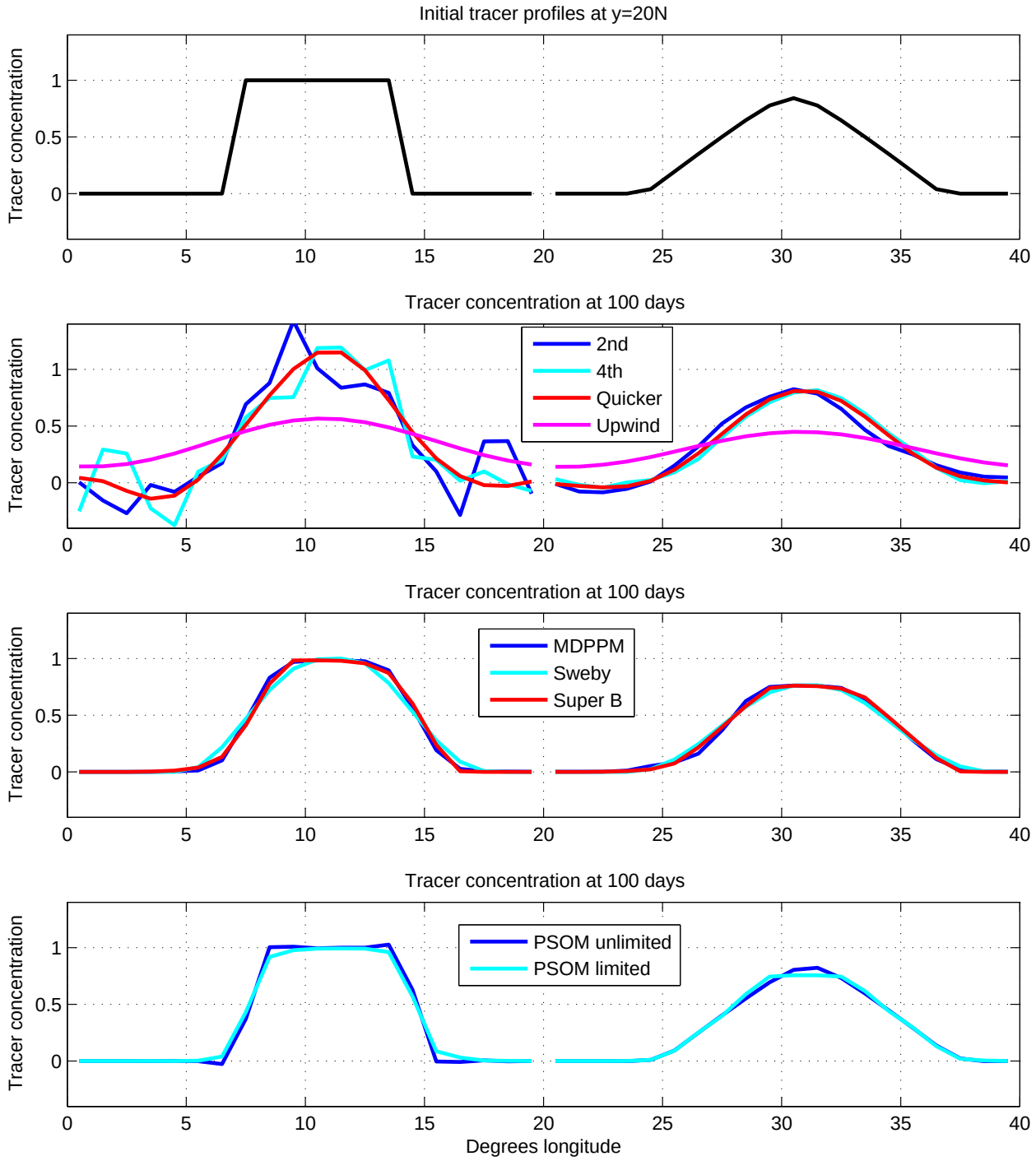

Figure 29.1: Top panel: Initial passive tracer profile for the torus test case. The two profiles are artificially offset in the zonal direction for purposes of clarity in presentation. Shown here is a plot through $y = 20°N$. Second panel: passive tracer profiles after 100 days of integration using 2nd, 4th, Quicker, and Upwind advection schemes. Third panel: Results using MDPPM, Sweby, and Super B. Fourth panel: Results from the limited and unlimited PSOM scheme.

CHAPTER
THIRTY

Symmetric box test case

The symmetric box test case `mom4_symmetric_box` consists of a flat bottom domain which is symmetric across the equator. It has solid walls and is forced with zonally constant forcing. The initial conditions are constant temperature and salinity. The surface restoring fields are show in Figure 30.1. There is zero wind stress applied. Density is determined by the realistic equation of state of Jackett et al. (2006), and the prognostic temperature variable is the conservative temperature of McDougall (2003).

The aim of this test case is to examine numerical methods with respect symmetry across the equator. Small discretization errors which are not symmetric will accumulate and become visible in flow features. This test provides a useful means to measure this accumulation. Consequently, there is a relatively large suite of physical parameterizations enabled, many of which are incompatible with one another. The purpose of enabling so many options is to thoroughly examine symmetry properties of the schemes.

Figure 30.2 shows the surface height and zonally averaged temperature and zonal velocity after 1000 days of simulation. The surface height shows signs of asymmetry, whereas the zonally averaged temperature and zonal velocity are reasonably symmetric.

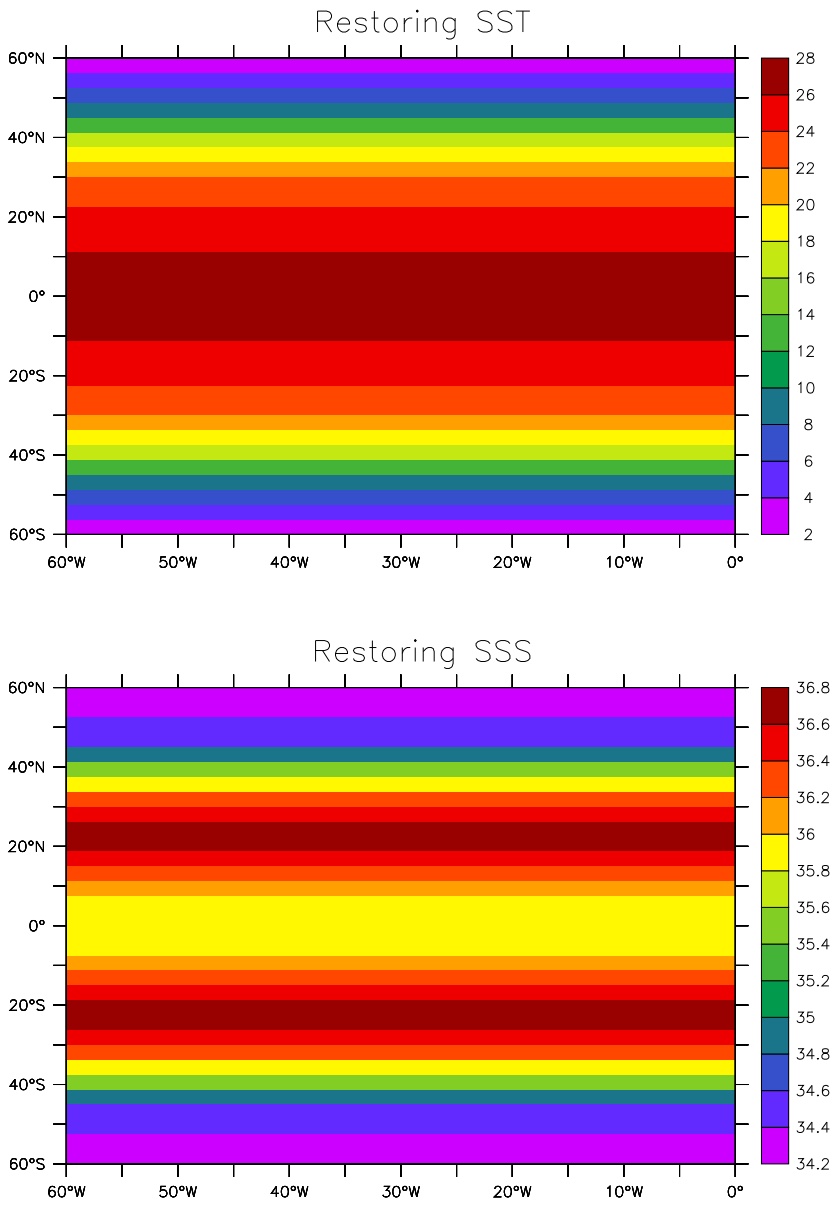

Figure 30.1: Restoring temperature and salinity for the symmetric box test case.

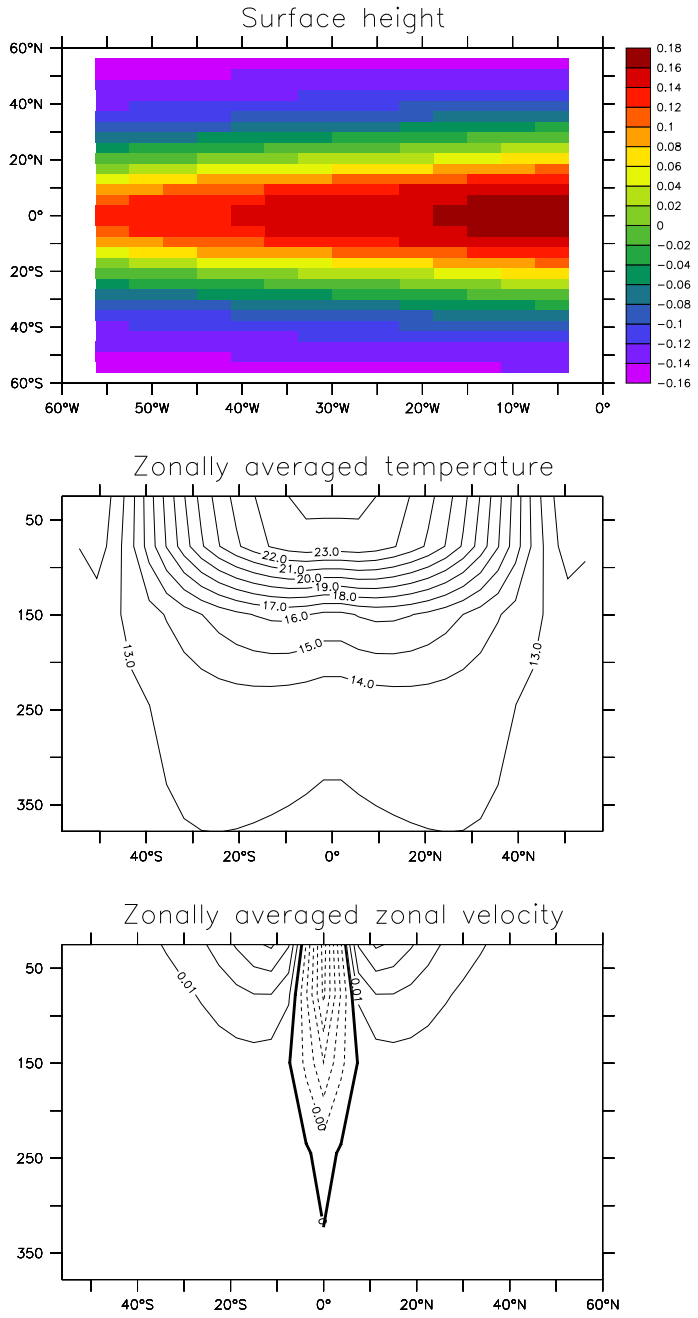

Figure 30.2: Snapshots of simulation features after 1000 days. Top panel: surface height in metres; Middle panel: zonally averaged temperature; bottom panel: zonally averaged zonal velocity.

CHAPTER
THIRTYONE

Box sector test case

The box test case `mom4_box` consists of a flat bottom northern hemisphere sector domain with thermohaline forcing at the upper boundary (Figure 31.1). There is zero wind stress. The initial salinity is constant, and the initial temperature has a nontrivial zonally symmetric thermocline structure (Figure 31.1). Density is a linear function of temperature, and is independent of salinity and pressure.

The domain and grid are of a modest size ($24(x) \times 35(y) \times 18(z)$), thus allowing this test to be run on most any computer. The resulting circulation is driven by density gradients set up by the thermohaline forcing. It exhibits an overturning circulation, with sinking in the north and rising throughout the domain, which is reminscient of many similar idealized simulations run in the 1980s and 1990s.

We illustrate the behaviour of this test with the four following vertical coordinates (see Chapter 6):

- Geopotential vertical coordinate, as in MOM4.0;
- The depth based vertical coordinate

$$z^* = H \left(\frac{z - \eta}{H + \eta} \right) \tag{31.1}$$

- The pressure coordinate;
- The pressure based vertical coordinate

$$p^* = p_{\mathsf{b}}^o \left(\frac{p - p_{\mathsf{a}}}{p_{\mathsf{b}} - p_{\mathsf{a}}} \right), \tag{31.2}$$

  with p_{b}^o the initial bottom pressure, p_{b} the bottom pressure, and p_{a} the applied pressure at the ocean surface, which is set to zero for this suite of tests.

Figures 31.2, 31.3, and 31.4 illustrate the zonal averaged temperature, salinity, and age tracer (see Section 3.6.4), each averaged over years 901-1000. The differences in the simulations is very minor, especially when recognizing the different vertical axes extents for the pressure versus depth based vertical coordinates. Figure 31.5 shows the meridional overturning streamfunction for the simulations, again revealing very minor differences.

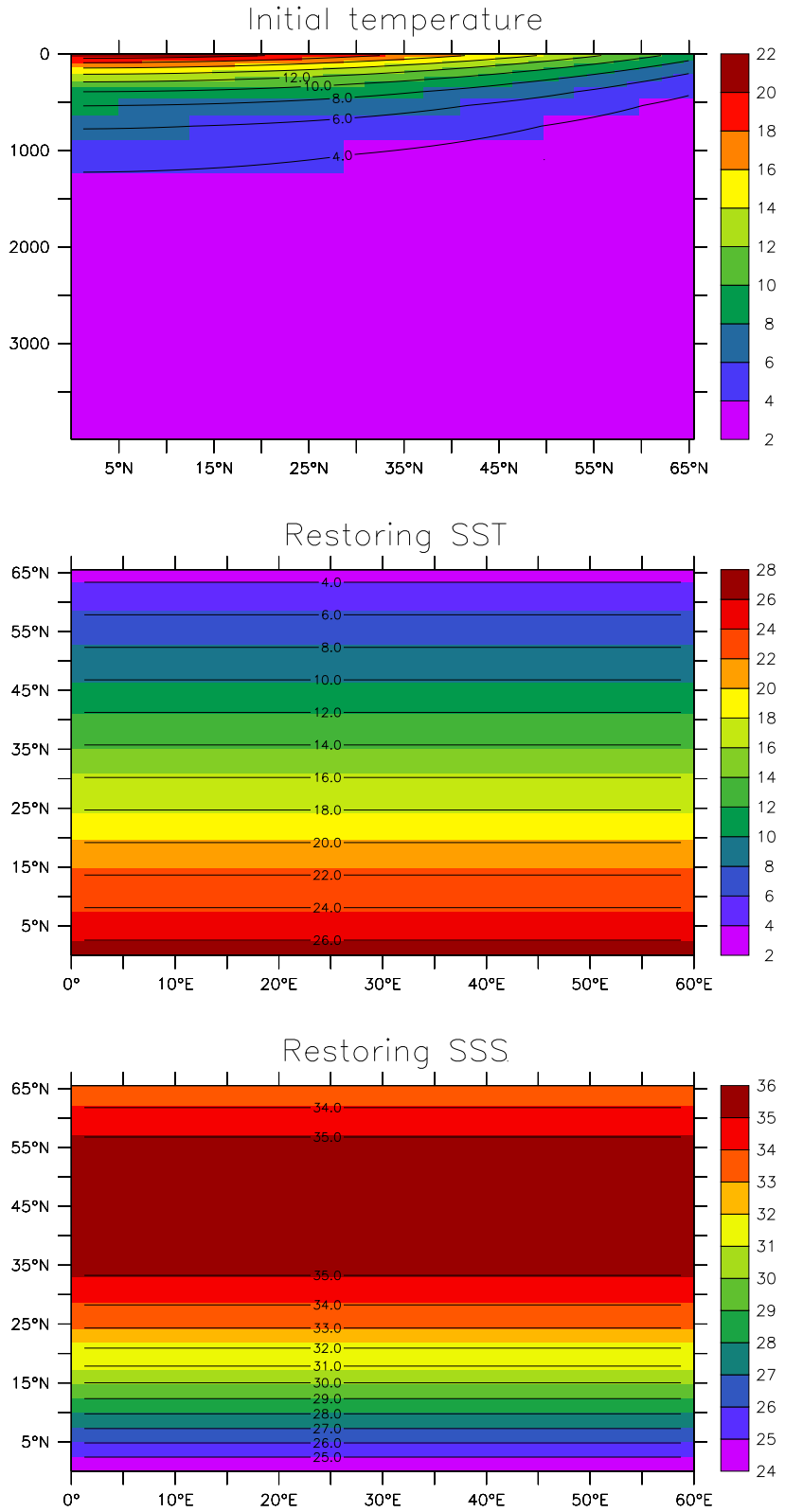

Figure 31.1: Initial and boundary conditions for the box test case. Upper panel: initial temperature. Middle panel: SST used for computing the restoring flux of heat. Lower panel: SSS used for computing restoring flux of salt or fresh water.

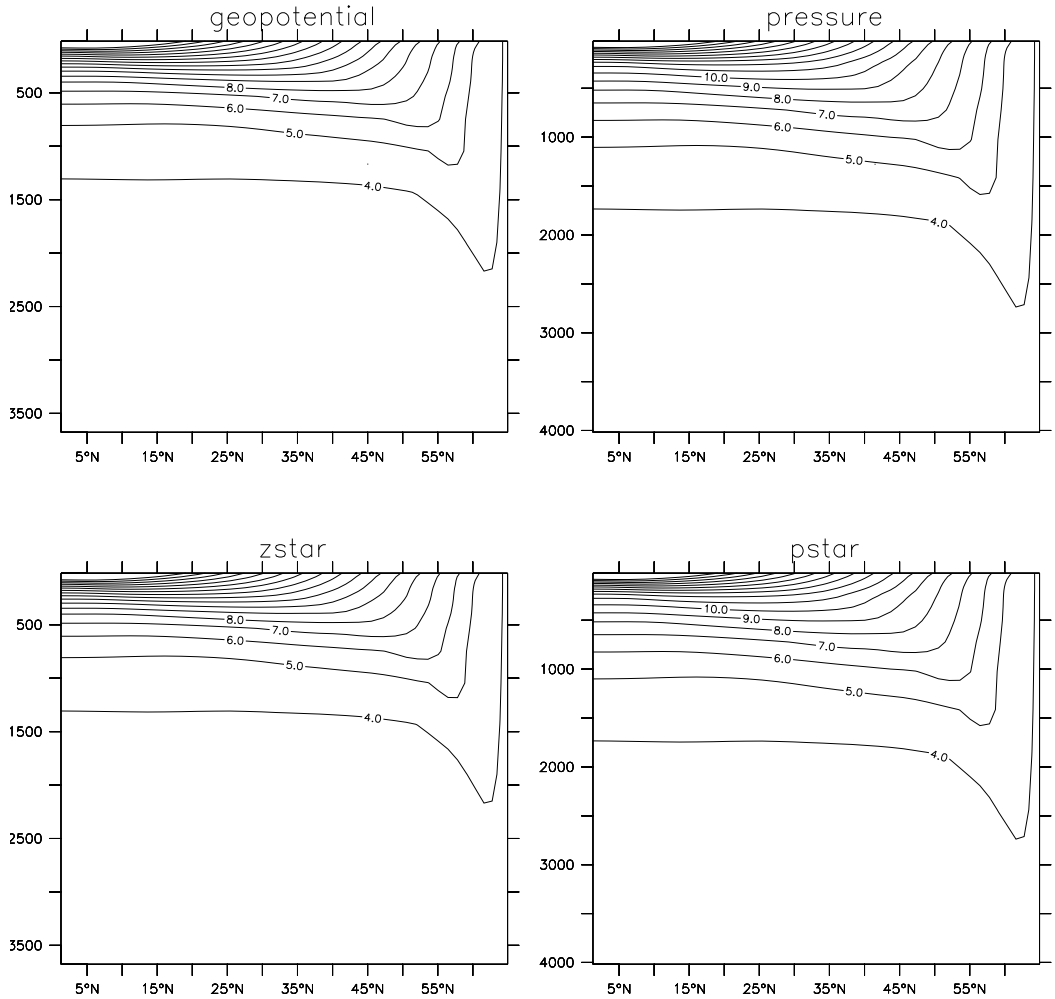

Figure 31.2: Zonal averaged temperature time averaged over the years 901-1000 in the box test case. Shown here are results for the four vertical coordinates considered in this chapter. Note that for the depth based coordinates, the vertical refers to metres, whereas for the pressure based it is dbars. This accounts for the slight offset in the vertical extent of the domains.

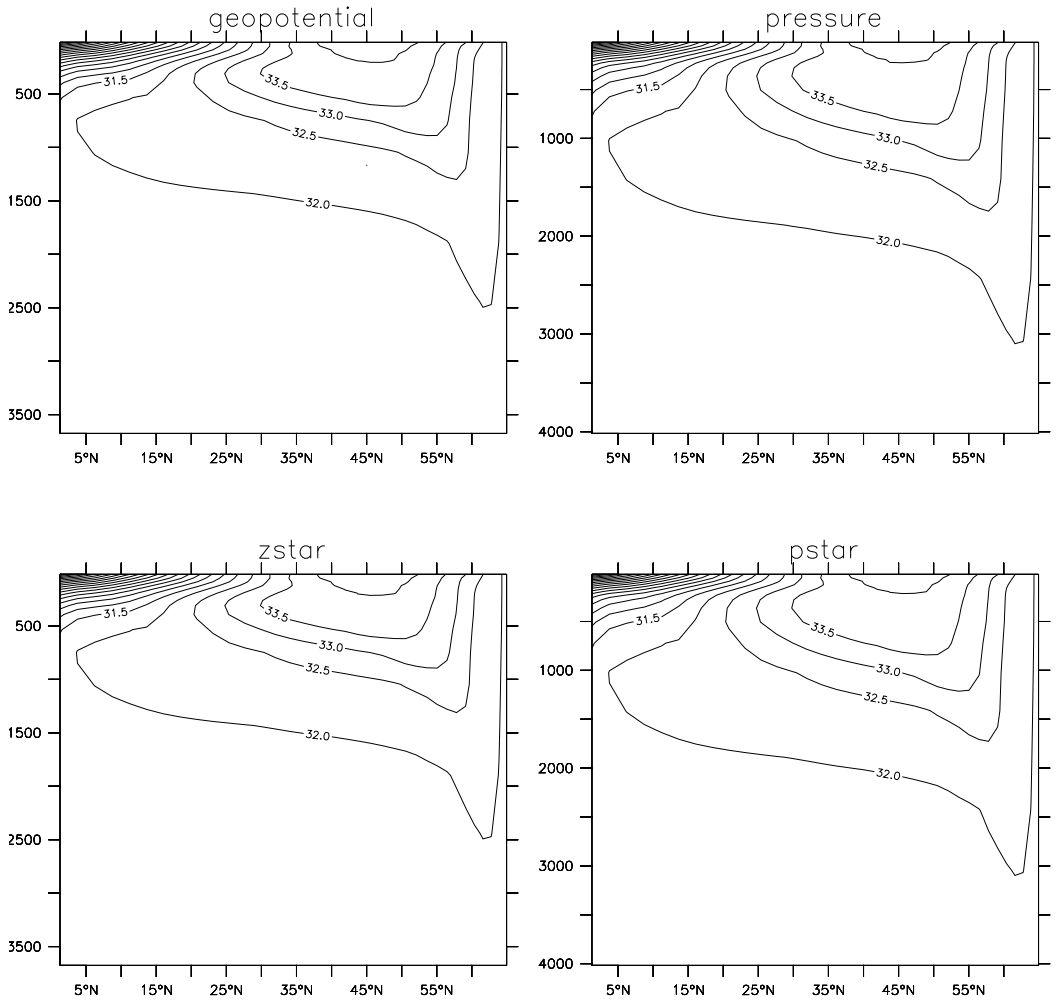

Figure 31.3: As in Figure 31.2, but for salinity.

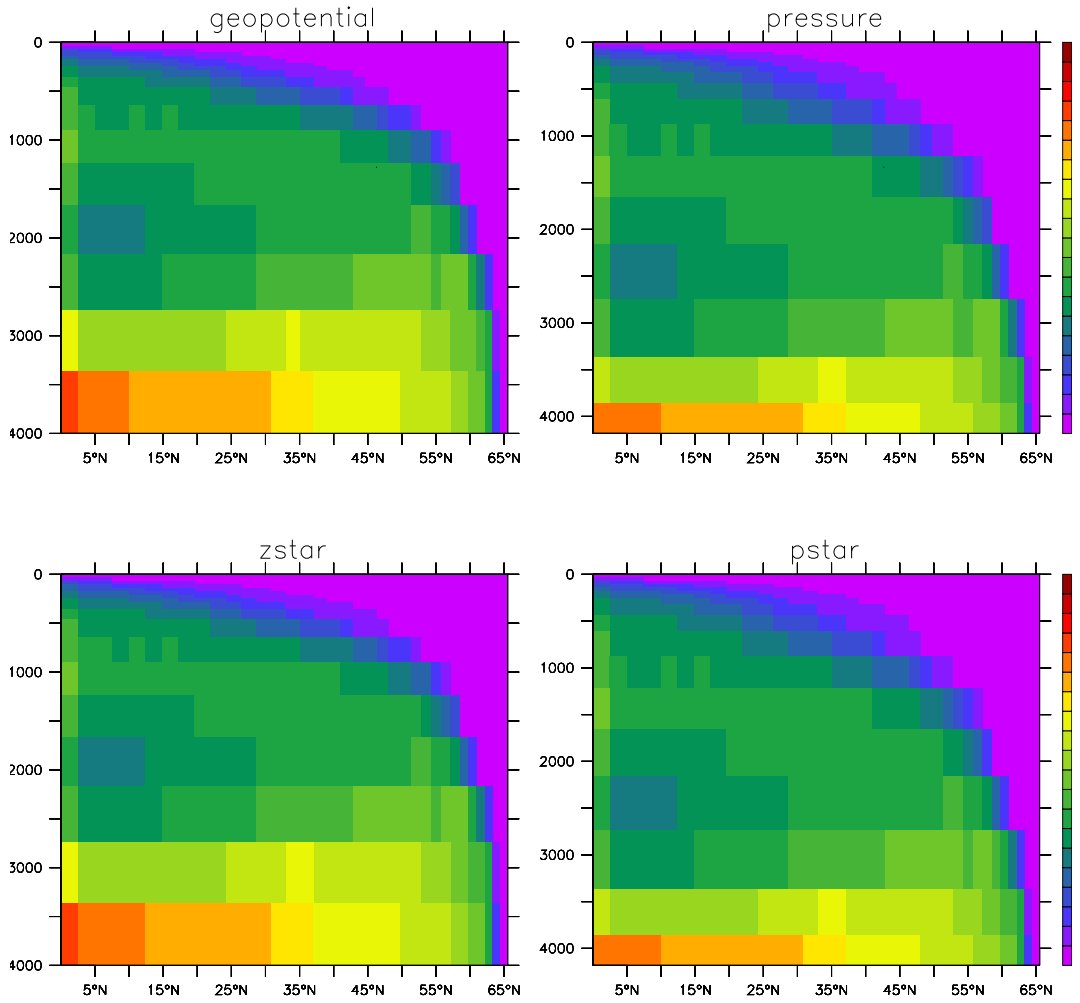

Figure 31.4: As in Figure 31.2, but for the age tracer.

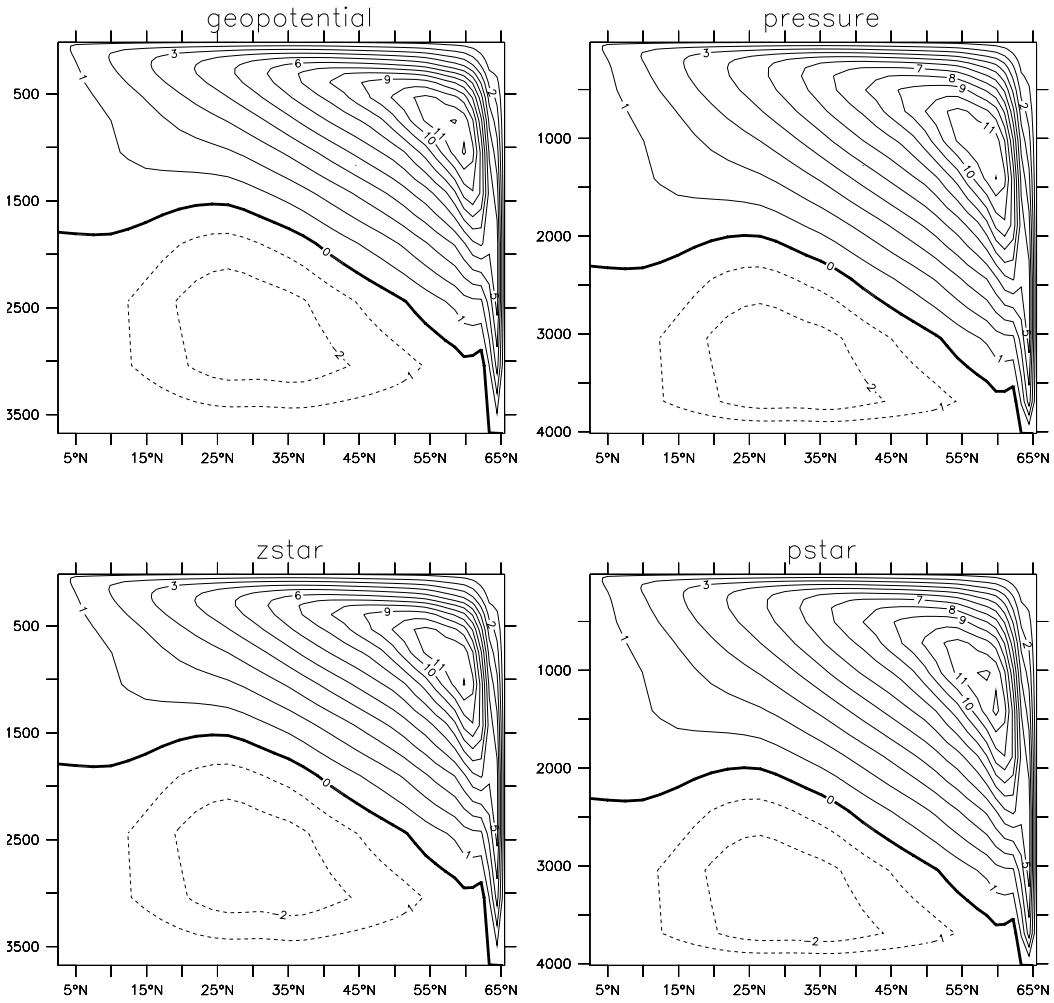

Figure 31.5: As in Figure 31.2, but for the meridional overturning streamfunction.

CHAPTER
THIRTYTWO

Wind driven gyre test case

The test case `mom4_gyre` consists of a flat bottom middle latitude domain driven by a zonal wind stress. The temperature is initially stratified in the vertical (Figure 32.1), with density a linear function of temperature and independent of pressure and salinity. We employ the modified pressure coordinate

$$p^* = p_{\mathsf{b}}^o \left(\frac{p - p_{\mathsf{a}}}{p_{\mathsf{b}} - p_{\mathsf{a}}} \right) \tag{32.1}$$

for the vertical coordinate, with the applied pressure $p_{\mathsf{a}} = 0$, and the static reference bottom pressure

$$p_{\mathsf{b}}^0 = g \int_{-H}^{0} \mathrm{d}z \, \rho^{\mathsf{init}} \tag{32.2}$$

determined by the initial density profile ρ^{init}.

This test case has been used at GFDL for examining the spurious mixing properties of various advection schemes. For this purpose, we initialize to unity a passive tracer on each of the 50 vertical levels, with zero value off the chosen level (Figure 32.1). As the initial temperature profile is independent of horizontal position, the passive tracers are initialized on surfaces of constant density. We use the MOM4p1 MDPPM scheme for the test shown here.

During spinup of the circulation (Figure 32.2), passive tracers are advected around the gyre. Horizontal gradients on a temperature surface arise from inhomogeneous stretching and compression of the surface as a function of the level of eddy activity. The near surface has an Ekman layer, where vertical overturning occurs, as parameterized with convective adjustment. This overturning is in response to the Ekman suction.

Beneath the Ekman layer, spreading of passive tracer across surfaces of constant temperature (Figure 32.3) occurs for two reasons:

- nonzero vertical diffusivity, set here to $10^{-5}\mathrm{m}^2\,\mathrm{s}^{-1}$,
- spurious mixing from numerical advection.

Quantifying levels of spurious mixing is straightforward. We do so by matching the evolution of passive tracer in density space to the evolution achieved with pure vertical diffusion, with a diffusivity fit to match that from the spurious mixing. This approach is a complement to the more complex sorting approach employed by Griffies et al. (2000b) (see Chapter 23).

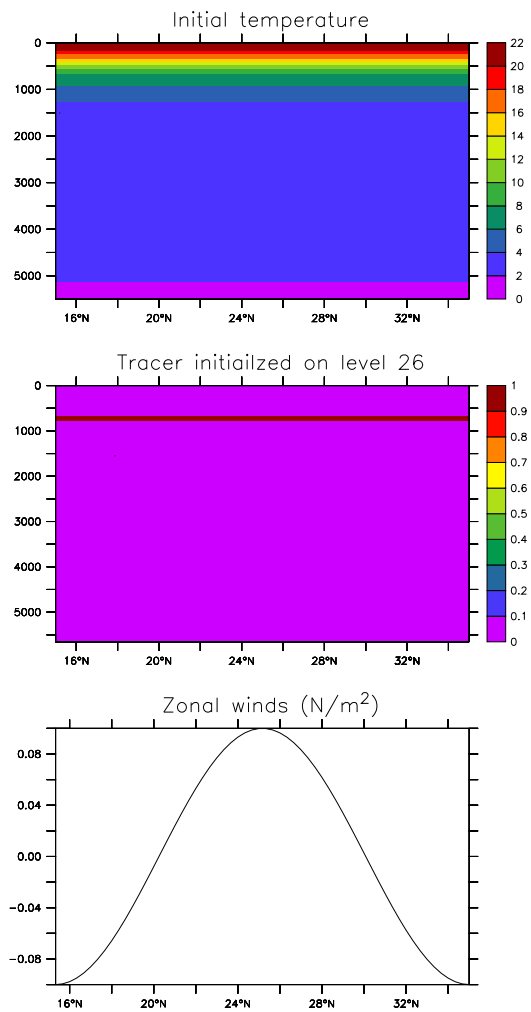

Figure 32.1: Upper panel: Section illustrating the initial temperature for the gyre experiment, with no horizontal variation in the initial temperature field. Middle panel: Illustration of an initial passive tracer, placed in this case on model level 26. Lower panel: The zonal wind stress applied to the gyre model, which spins up a two-gyre circulation within a few years.

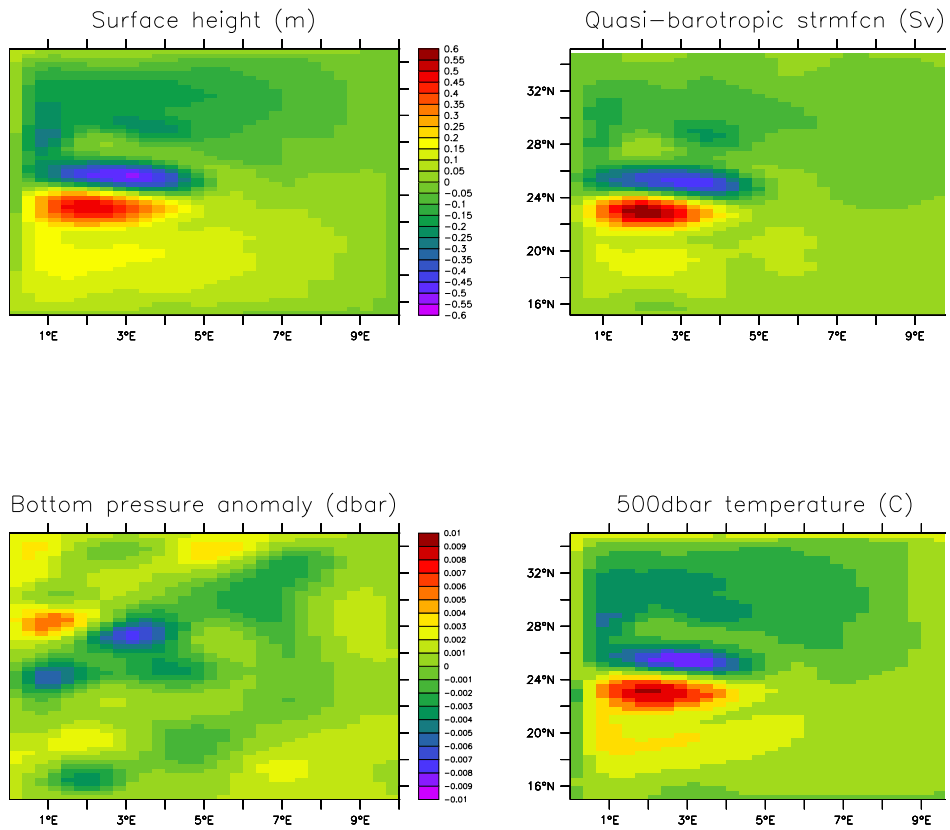

Figure 32.2: Simulation characteristics at 12 months. Shown here are monthly means for the following fields. Upper left panel: surface height (metre); Lower left panel: bottom pressure anomaly (dbar) $p_b - p_b^0$; upper right panel: quasi-barotropic streamfunction; Lower right: Temperature at 500dbar depth. Note the very small bottom pressure anomalies, relative to the surface height undulations, is consistent with the circulation being largely isolated to the upper ocean.

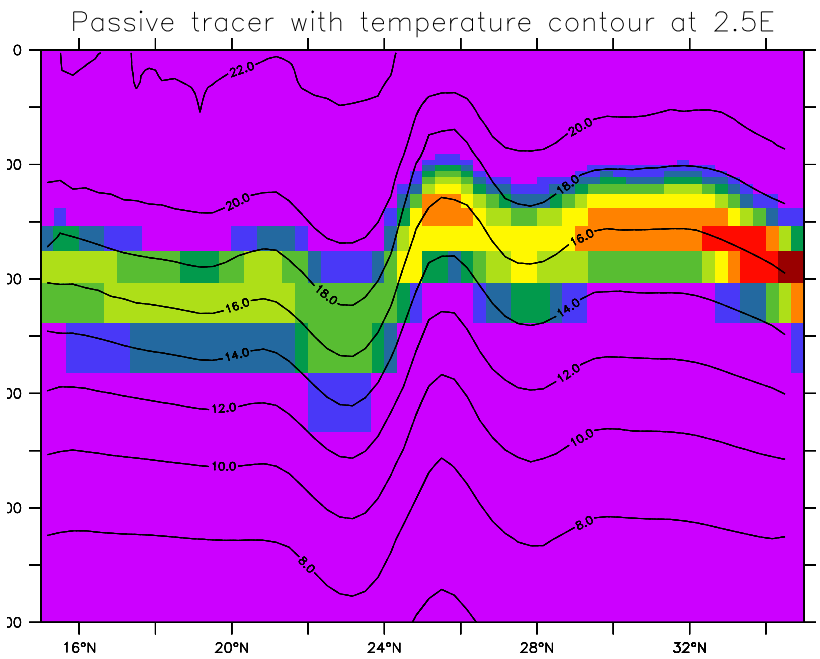

Figure 32.3: Monthly averaged passive tracer at 2.5E, overlaid with contours of constant temperature. Notice how the tracer undulates with the undulating temperature surfaces. Also, the tracer has spread across surfaces of constant density, with this spread associated with the nonzero vertical diffusivity and the spurious mixing from numerical advection errors.

CHAPTER
THIRTYTHREE

DOME test case

The experiment `mom4_dome` is based on the idealized overflow test established for the project Dynamics of Overflow, Mixing, and Entrainment (DOME). Details of the experiment are provided in various published papers, such as Legg et al. (2006).

As with the bowl test case `mom4_bowl` discussed in Chapter 34, the DOME test case provides a means to test various overflow parameterizations. In both tests, the simulations highlight the ability, or inability, of the simulated flow to overcome the geostrophic balance, which aims to align the flow along isobaths. In coarsely resolved level models, spuriously large levels of ambient waters tend to be entrained to the dense pulse, thus compromising the ability of the simulation to form dense deep water, and to feel the effects of the bottom (Winton et al., 1998). The main difference between `mom4_dome` and `mom4_bowl` is that `mom4_dome` allows for a steady state to be achieved, since dense water continues to be injected from the embayment. The `mom4_bowl` test, in contrast, is an adjustment experiment, with no boundary forcing considered.

Coarse resolution level models are notoriously poor at representing overflow processes (Winton et al., 1998). Various approaches have thus been proposed to resolve, or to reduce, the problem. Chapter 19 details the methods available in MOM4p1. For the simulations discussed in this chapter, we employ the quasi-horizontal coordinate p^* detailed in Section 6.2.3. Any of the other quasi-horizontal coordinates, such as z, z^*, or p (Sections 6.1.1, 6.1.4, and 6.2.1) would show similar results. In contrast, the terrain following coordinates $\sigma^{(z)}$ or $\sigma^{(p)}$ (Sections 6.1.5 and 6.2.4) show much more downslope flow, due to their ability to better represent the interaction between the flow and the terrain (not shown).

The configuration consists of a shelf in the north with a shallow embayment. We use $1/2^\circ$ grid resolution in both latitude and longitude, which yields two zonal grid points in the embayment. The vertical grid is the same 50 levels used in the global OM3 configuration described in Chapter 37.

Temperature is initialized with a zonally symmetric profile shown in Figure 33.1. Cold water in the north lives at the bottom of the embayment. It is injected southward by a transport imposed at the embayment's northern boundary. Salinity is initialized to zero everywhere, but it is given a value of unity for water that is injected from the embayment. Density is a linear function of temperature, with no dependence on salinity and pressure. Salinity thus provides a passive marker for injected water that is transported southward and into the abyss. Both temperature and salinity are damped to their initial conditions at the eastern and western boundaries. This damping, applied through a sponge condition, eliminates the Kelvin wave signals. Finally, for tracer advection, we use the

Prather (1986) scheme, employed without flux limiters.

We test the following five cases in this chapter:

- No lateral or downslope parameterization; just advective transport;
- Advection plus sigma diffusion acting in the bottom grid cell;
- Advection plus sigma diffusion acting in the bottom grid cell plus the overflow scheme of Campin and Goosse (1999) (Section 19.3);
- Advection plus sigma diffusion acting in the bottom grid cell plus the overexchange scheme discussed in Section 19.4;
- Advection plus sigma diffusion acting in the bottom grid cell plus the mixdownslope scheme discussed in Section 19.4.

Four months of integration is sufficient to highlight differences between various overflow options available in MOM4p1. Figure 33.2 shows salinity at the bottom of the domain, averaged over the last five days of the four month experiment. The case with pure advection (plus some vertical diffusion) shows little downslope flow, as well as some extrema (values less than zero) arising from the absence of flux limiters on the advection scheme. Adding sigma diffusion allows for salinity to penetrate further south. There are also no tracer extrema, likely due to the smoothing of the otherwise strong gradients near the bottom. Adding the overflow scheme of Campin and Goosse (1999) reduces the depth where salinity penetrates. Apparently it is acting in a manner that handicaps the penetration of dense water southwards, perhaps due to over dilution. In contrast, the *overexchange* scheme allows for the salinity to penetrate further southward and hence deeper. For this test, we applied the *overexchange* scheme in four adjacent grid cells. Finally, the *mixdownslope* also allows for penetration further southward, although with a local extrema a few points away from the embayment, perhaps due to the nonlocal manner of transport. The penetration of salinity southward is reflected in the zonally averaged temperature shown in Figure 33.3. Consistent with the salinity tracer, the densest waters arise from the case with the *overexchange* and *mixdownslope* schemes. The different density profiles give rise to differences in flow characteristics. Figure 33.4 shows the barotropic quasi-streamfunction (see Section 17.2 of Griffies et al. (2004))

$$\psi(x,y) = -\int_{y_{\text{south}}}^{y} \mathrm{d}y'\, U(x,y'), \tag{33.1}$$

where

$$U = \int_{-H}^{\eta} \mathrm{d}z\, u \tag{33.2}$$

is the vertically integrated zonal transport.[1] The vertically integrated transport is far stronger in the cases with dense shelf water penetrating into the deep.

[1] In a rigid lid model, or a free surface model having reached a steady state in the absence of surface boundary fluxes of mass, then ψ is a vertically integrated streamfunction. For the present case, with a transient free surface model, ψ is only a direct correlate to the true vertically integrated transport, hence the qualifier *quasi*.

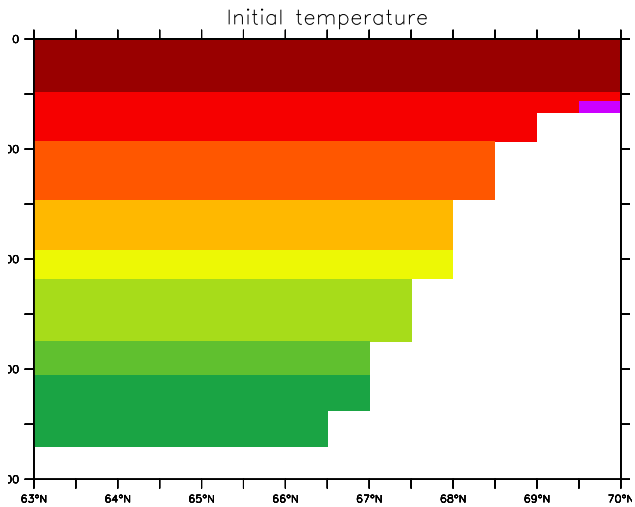

Figure 33.1: Initial temperature for the DOME test case. The cold water in the far north is at the bottom of the embayment. Southward flow is injected from this embayment, allowing for the cold and dense water to leave the embayment and enter the abyss.

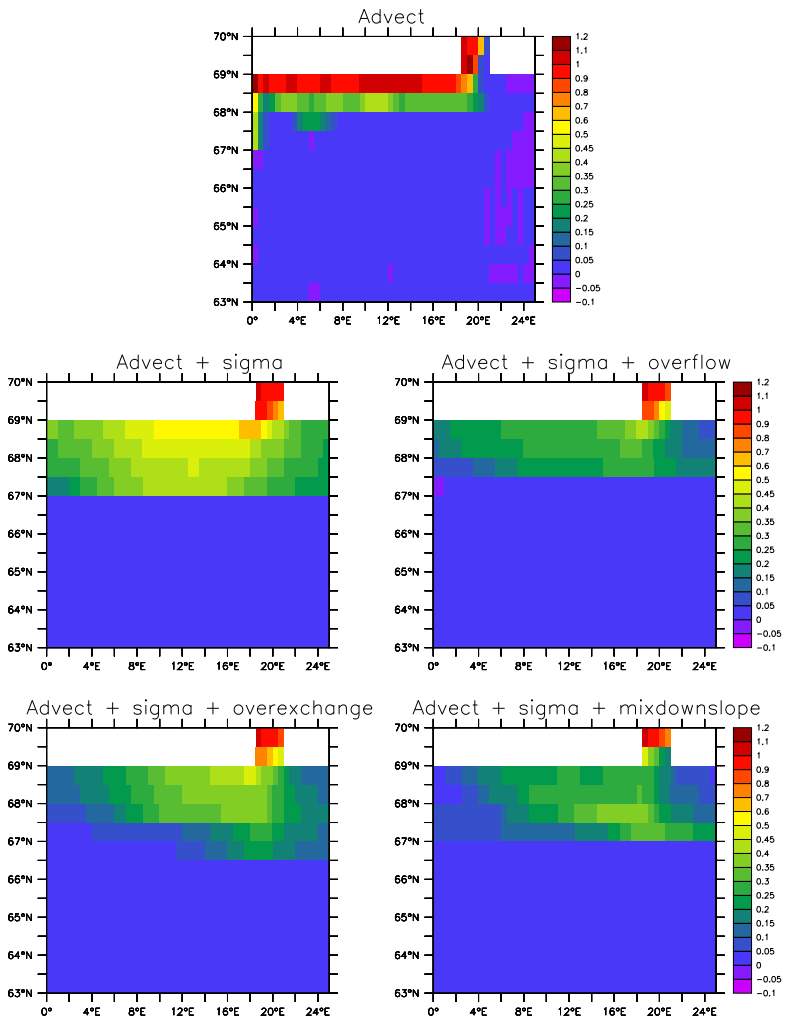

Figure 33.2: Bottom salinity averaged over the last five days of a four month integration. Top panel: no lateral or terrain following parameterization. Middle left: advection plus sigma diffusion applied in the bottom grid cell. Middle right: advection plus sigma diffusion plus the overflow scheme of Campin and Goosse (1999) (Section 19.3). Bottom left: advection plus sigma diffusion plus the *overexchange* scheme (Section 19.4) Bottom right: advection plus sigma diffusion plus the *mixdownslope* scheme (Section 19.4).

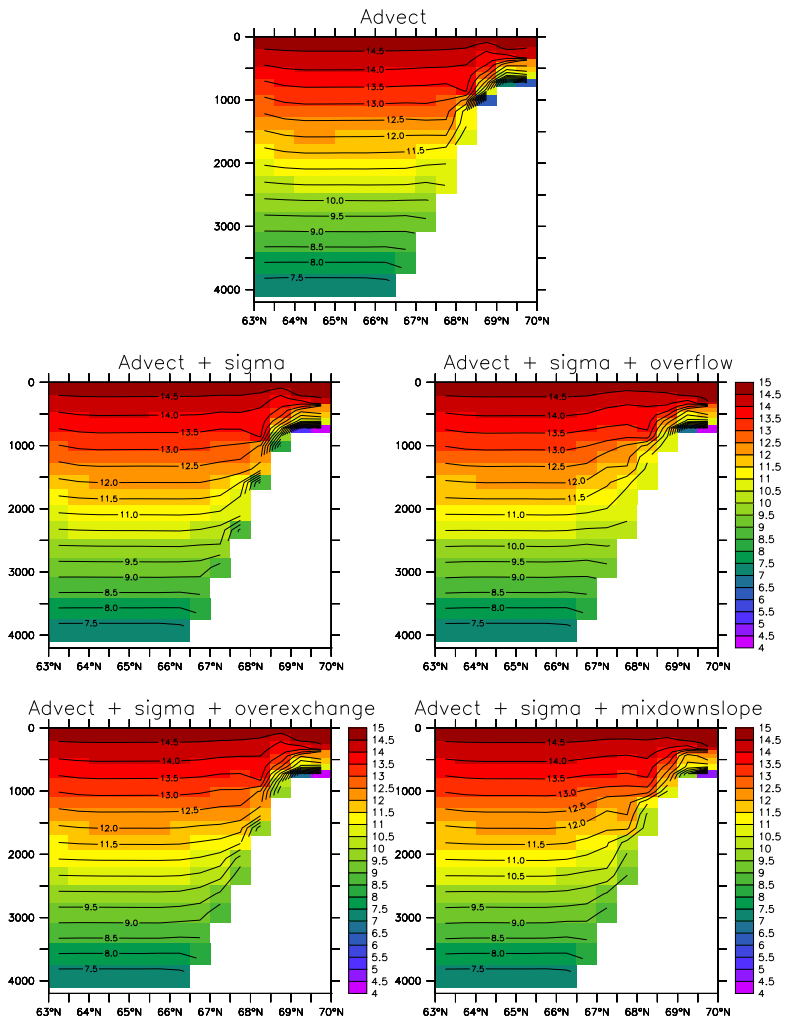

Figure 33.3: Zonally averaged temperature for the DOME test case, with panels corresponding to those in Figure 33.2.

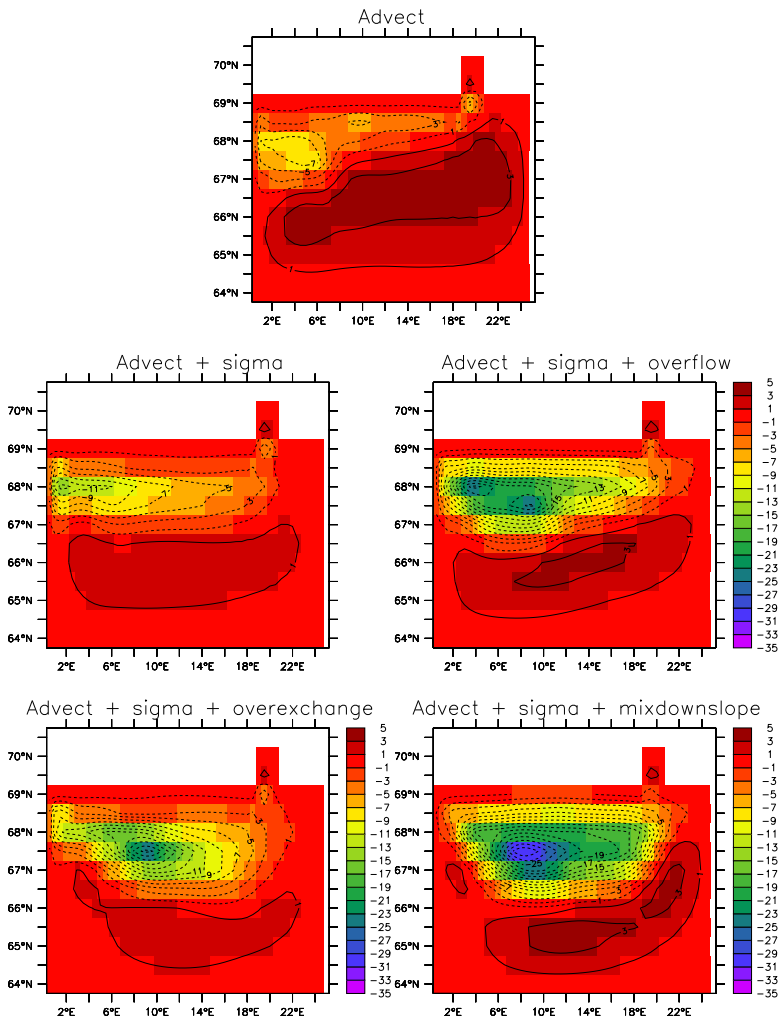

Figure 33.4: Quasi-streamfunction (Sv) for the vertically integrated transport in the four DOME simulations, with panels corresponding to those in Figure 33.2.

CHAPTER
THIRTYFOUR

Bowl test case

The bowl test case `mom4_bowl` is based on a configuration built for studies of overflow processes by Winton et al. (1998). It consists of a shallow shelf in the northern portion of the domain, with a deeper bowl to the south (Figure 34.1). The initial conditions place cold dense water on the shelf (Figure 34.2). Density is a linear function of temperature, and is independent of salinity and pressure.

Integration proceeds with no surface forcing. Hence, this is a relaxation or adjustment experiment, with no steady state realized. The initial pressure forces set up acceleration which causes the water to move off the shelf and into the deeper portion of the domain. The numerical and physical processes active in this relaxation experiment are described by Winton et al. (1998). In particular, the test case is useful to examine the sensitivity of the deep water formed to various numerical and physical options. It can be used in tandem with the test case `mom4_dome` described in Chapter 33.

Level models are notoriously poor at representing overflow processes (Winton et al., 1998). Various approaches have thus been proposed to resolve, or reduce, the problems. Chapter 19 details the methods available in MOM4p1. We test the following four configurations here:

- Terrain following pressure based vertical coordinate

$$\sigma^{(p)} = \left(\frac{p - p_{\mathsf{a}}}{p_{\mathsf{b}} - p_{\mathsf{a}}} \right), \tag{34.1}$$

  with p_{b} the bottom pressure, and p_{a} the applied pressure at the ocean surface, which is set to zero for this suite of tests. For this vertical coordinate, we transport tracer just by advection plus some vertical diffusion.

- Quasi-horizontal pressure based vertical coordinate

$$p^* = p^o_{\mathsf{b}} \left(\frac{p - p_{\mathsf{a}}}{p_{\mathsf{b}} - p_{\mathsf{a}}} \right), \tag{34.2}$$

  with p^o_{b} the initial bottom pressure. In this test, we also just employ advection plus vertical diffusion.

- In this test, we use p^* with the addition of nontrivial sigma diffusion in the bottom cell, as described in Section 19.2.1.

- In this test, we use p^* with the addition of nontrivial sigma diffusion in the bottom cell, as described in Section 19.2.1, as well as the *overexchange* scheme discussed in Section 19.4.

Figures 34.3 and 34.4 show the salinity (a passive tracer) and temperature at the botom of the domain, after one year as averaged over the last five days of the year. Both of the cases without any added subgrid scale methods show advection transporting the tracers southwards along the western boundary. The terrain following $\sigma^{(p)}$ case brings the tracer further into the abyss than the p^* case. When adding sigma diffusion or overexchange to the p^* cases, the bottom signal is greatly diffusved, as expected since these parameterizations are diffusive. They also cause the tracer to bleed into the abyss more uniformly, rather than following the path along the wester wall.

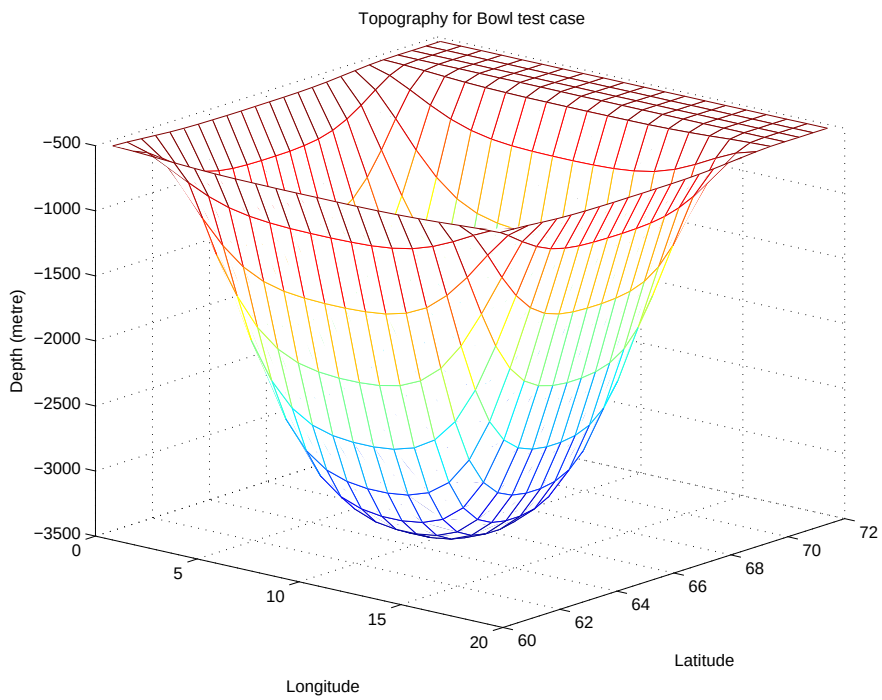

Figure 34.1: Geometry of the bowl test case, with shallow shelf in the north and deeper bowl to the south.

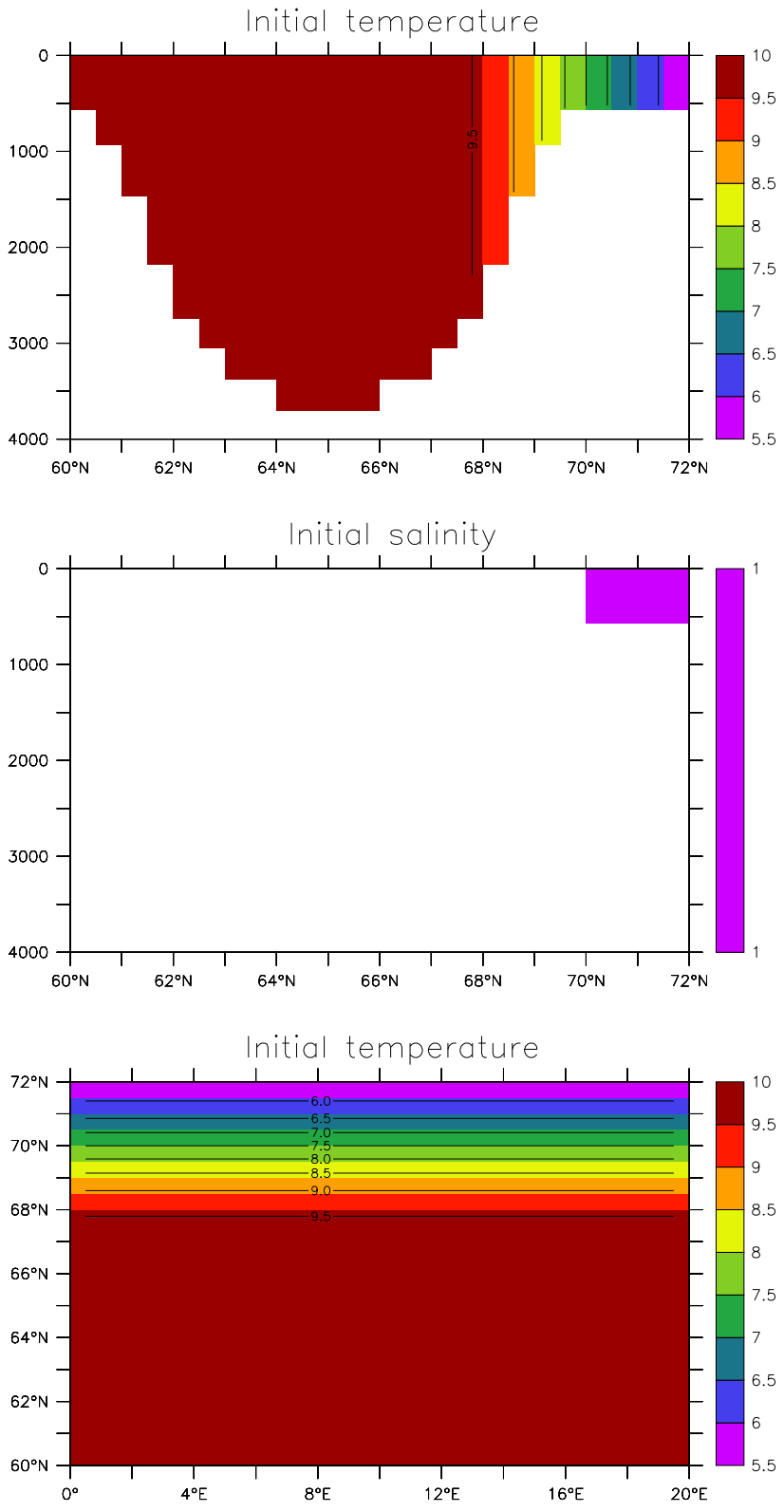

Figure 34.2: Initial conditions for temperature and salinity in the bowl test case. Upper panel: meridional-depth slice of the zonally symmetric initial temperature. Middle panel: Initial salinity, which has a unit value on the shelf and zero elsewhere. Lower panel: Plan view of the initial SST.

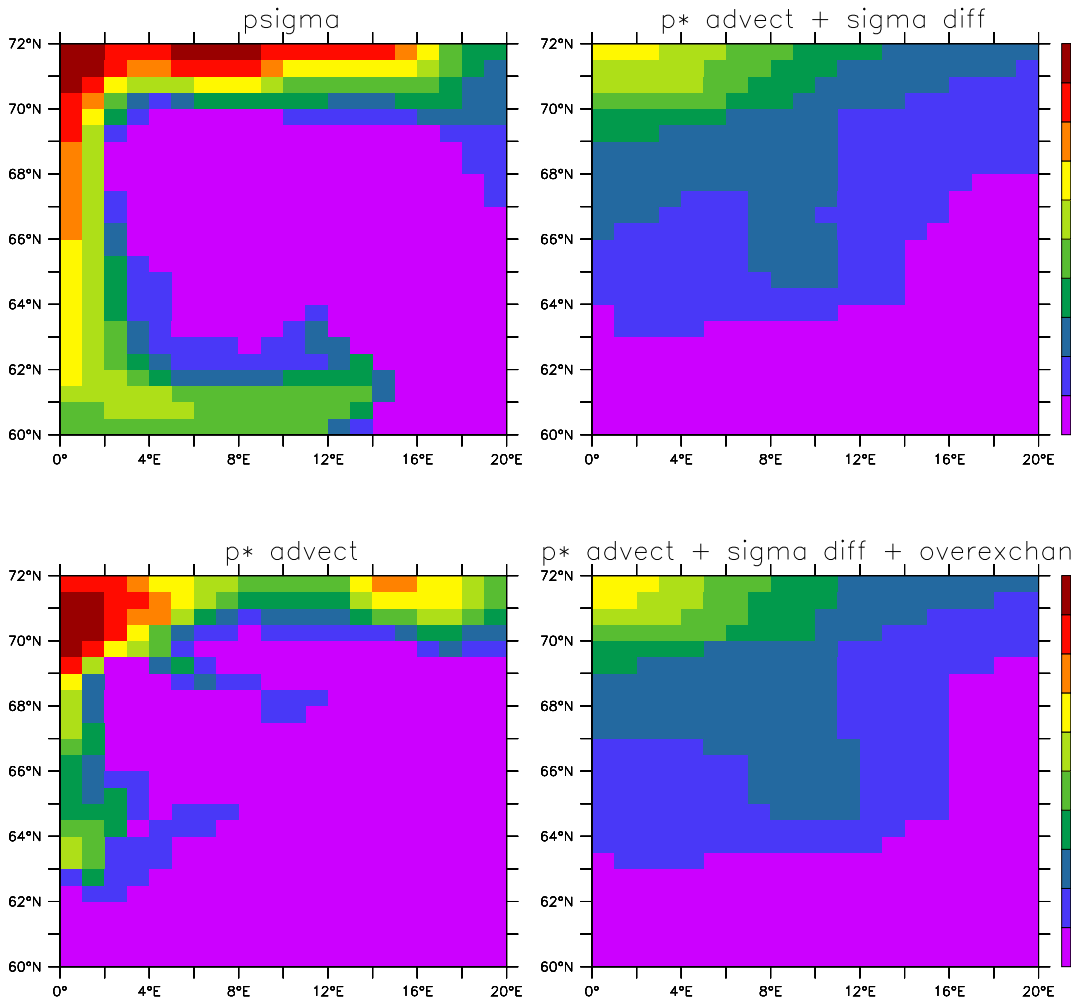

Figure 34.3: Salinity at the bottom of the domain after one year, as averaged over the last five days of the year. Upper left panel: results from $\sigma^{(p)}$ vertical coordinate using advection alone for the tracer transport; Lower left panel: results from p^* vertical coordinate using advection alone for the tracer transport; Upper right panel: p^* with advection and sigma diffusion applied in the bottom cell; Lower right panel: p^* with advection and sigma diffusion applied in the bottom cell and the overexchange scheme.

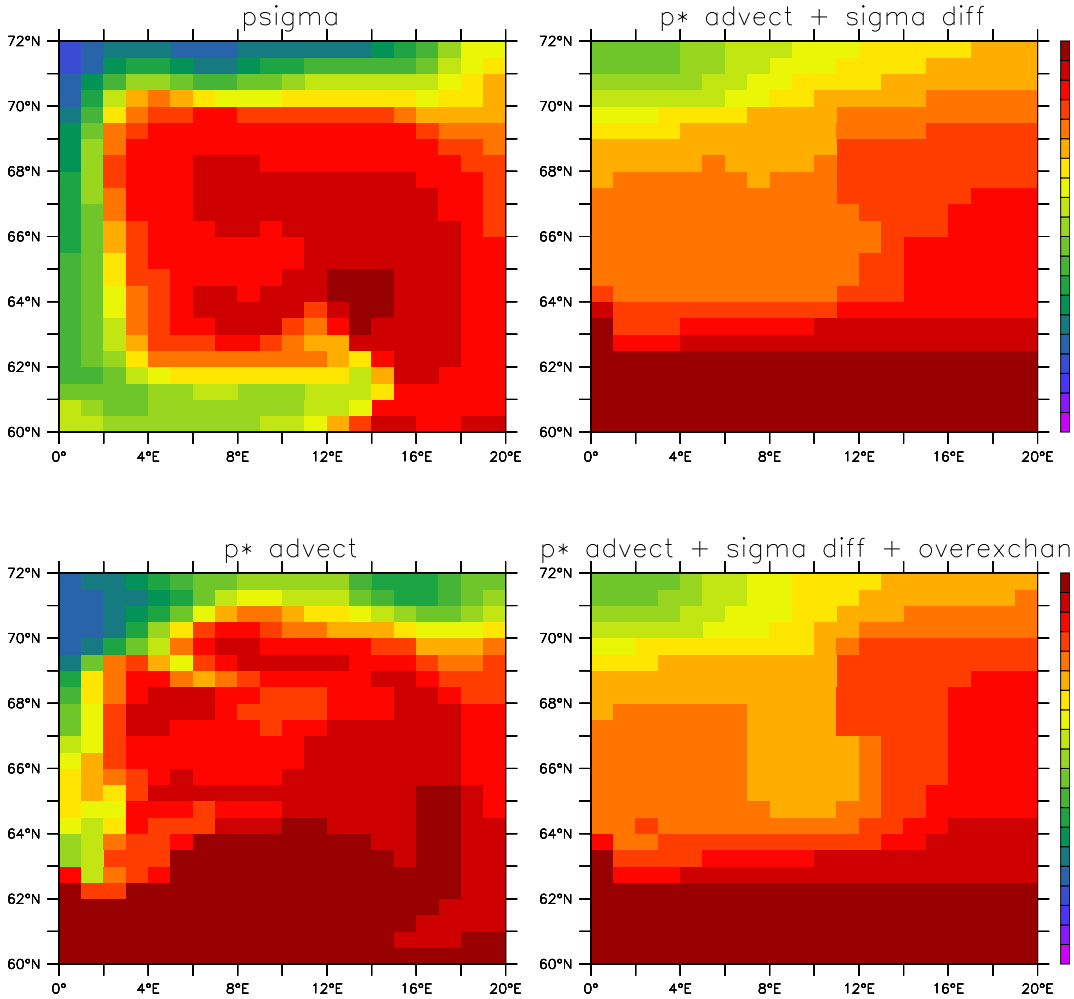

Figure 34.4: As in Figure 34.3, but for temperature.

CHAPTER
THIRTYFIVE

Indian Ocean Model

The test case `mom4_iom` consists of a realistic regional model of the Indian Ocean. The lateral regional boundaries are damped to climatology using sponges. This model was originally developed as part of a course on large scale ocean modelling in Bangalore, India during October 2004. The model remains a useful starting point for certain Indian Ocean research efforts using MOM. It is essentially the MOM4p1 implementation of Version 1.0 of that model configuration. The model is forced with a full suite of realistic atmospheric products, and employs a relatively modern suite of physical parameterizations.

One point of departure from the standard MOM4.0 configuration is to employ the depth based vertical coordinate (Chapter 6)

$$z^* = H\,(z-\eta)/(H+\eta). \tag{35.1}$$

This coordinate is useful in cases where it is desired to refine the vertical resolution in the upper ocean. Such enhanced vertical resolution may be of use for the Indian Ocean, where important vertical gradients exist especially near river mouths.

Figure 35.1 shows the SST, SSS, and surface height fields for the simulation after only two days of integration. As this model is not actively run at GFDL, we have not run it ourselves for much longer periods. Researchers interested in using this model configuration should consult with the MOM4 user community to be able to access the experience of others in running this model.

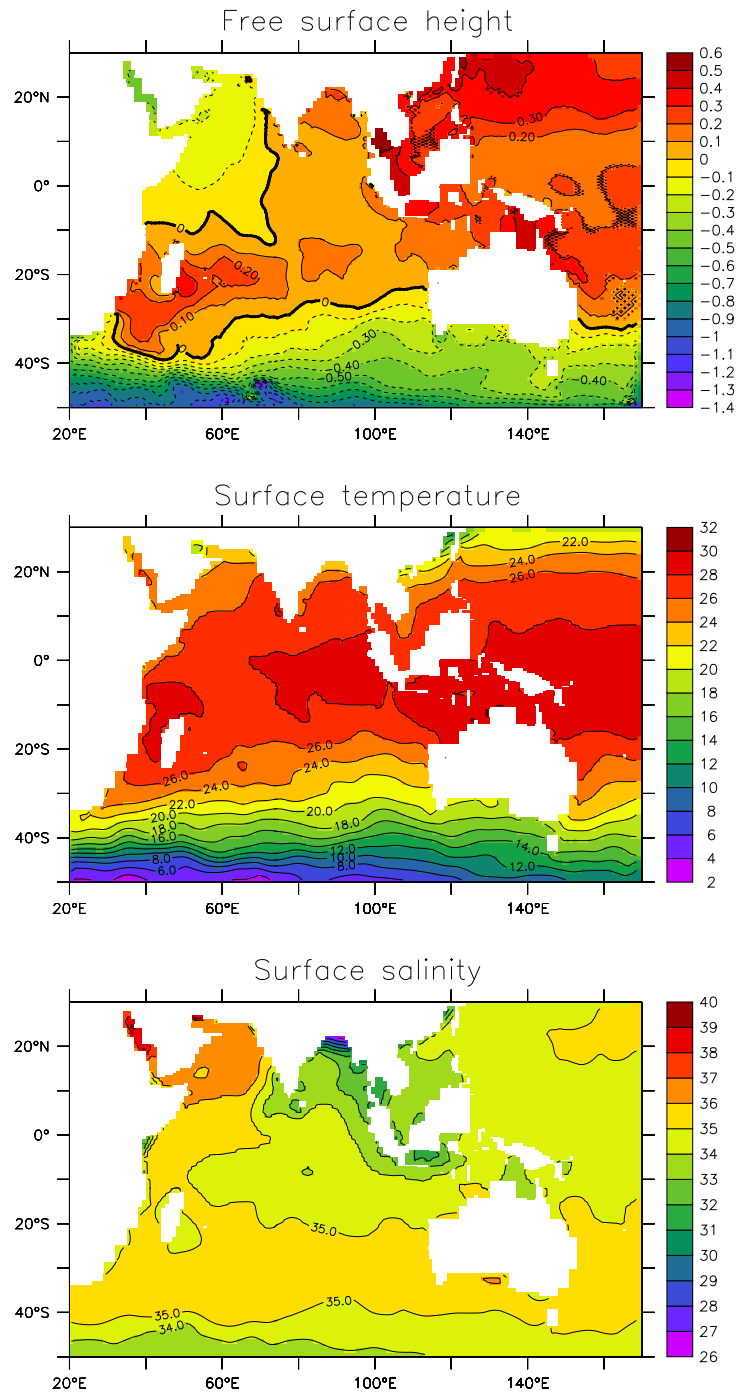

Figure 35.1: Daily averaged surface fields after two days integration of the Indian Ocean Model. Top panel: free surface height (metre); middle panel: surface temperature (C); bottom panel: surface salinity (psu).

CHAPTER

THIRTYSIX

CSIRO Mark 3.5 test

The test case `mom4_mk3p5` consists of a realistic global model with spherical coordinates. This model was developed at the CSIRO Marine and Atmospheric Research in Aspendale, Australia. It is routinely used as the ocean component for the Australian contribution to the IPCC report.

It is notable that this model was originally developed for a rigid lid algorithm in MOM1. For that algorithm, a heavy dose of polar filtering was employed. The present configuration in MOM4p1, employing a free surface, removes all polar filtering, yet it takes a *longer* time step than the polar filtered rigid lid configuration. This result is indicative of the often paradoxical results found with polar filtering. We strongly recommend that all polar filtering be removed from global simulations. Indeed, although a polar filtering module remains as part of MOM4p1, it is *not supported* by GFDL scientists. The main reason is that is breaks local conservation of tracer, thus leading to spurious surface fluxes and poor high latitude simulations.

CHAPTER

THIRTYSEVEN

Global ocean ice model with tripolar grid

The test case `mom4_om3_core` consists of a realistic global ocean and ice model using the tripolar grid of Murray (1996) (Figure 37.1). Griffies et al. (2005) provides extensive details of the model configuration. We thus only provide a brief introduction in this chapter.

The global coupled ocean-ice configuration is very similar to that used as part of the climate model developed at GFDL for the 4th IPCC assessment of climate change (Griffies et al., 2005; Gnanadesikan et al., 2006a). The ocean-ice configuration is also the basis for the GFDL-MOM contribution to the Coordinate Ocean-ice Reference Experiments (COREs) documented in Griffies et al. (2009). These experiments employ the boundary forcing from Large and Yeager (2004), which was developed for the purpose of running global coupled ocean-ice simulations without an interactive atmosphere. This Large and Yeager (2004) dataset is available through the GFDL web site

http://nomads.gfdl.noaa.gov/nomads/forms/mom4/CORE.html.

It has been part of the MOM4 distribution for a few years. In addition to using an updated version of MOM relative to Griffies et al. (2005) and Griffies et al. (2009), some model details have been modified in order to more thoroughly test various features of the simulation for this test case.

37.1 Three different vertical coordinates

In this section, we illustrate certain characteristics after 100 years of integration with focus on results for the three different vertical coordinates (Chapter 6)

$$s = z \tag{37.1}$$

$$s = z^* = H\,(z-\eta)/(H+\eta) \tag{37.2}$$

$$s = p^* = p_{\mathsf{b}}^o \left(\frac{p - p_{\mathsf{a}}}{p_{\mathsf{b}} - p_{\mathsf{a}}} \right). \tag{37.3}$$

We show how results from z and z^* are very close for the full global domain. The p^* differ in some regards that may be attributable to differences in the dynamics and SGS parameterization as treated with Boussinesq and nonBoussinesq models.

37.1.1 Initialization of the p^* simulation

In Section 7.2, we detailed how to initialize the non-Boussinesq models, such as the p^* simulation. In the p^* simulation, the vertical grid is based on increments of p^*, which are pressure increments. Our choice for setting these increments is the simplest approach, whereby the vertical coordinate increment is set according to

$$\mathrm{d}\,s = -g\,\rho_o\,\mathrm{d}z^0. \tag{37.4}$$

The initial vertical depth increment $\mathrm{d}z^0$ is set according to the MOM4 procedure for determining the depth increments in depth-based vertical coordinate simulations.

Through the hydrostatic balance, specifying the pressure increments $\mathrm{d}\,s$ determines mass within a coordinate layer. Placing initial temperature and salinity, such as from the World Ocean Atlas, in these layers then sets the density of the layers. The mass and density of a layer then determines the actual thickness $\mathrm{d}z^{init}$, which is generally different from $\mathrm{d}z^0$. Hence, the sum of thickness $\mathrm{d}z^{init}$ over the column will generally not yield a zero surface height η. This is a problem, since we aim to start the simulation with a zero surface height, as nonzero height anomalies can lead to spurious initial motion of sea ice. It is additionally a problem numerically if the pressure model initializes a bottom partial step that is very thin, or even of negative thickness, in order to fit the mass within the column.

Hence, an iterative process is required, with some modification needed to leave $\eta = 0$ at the initial condition. Our choice, as discussed in Section 7.2, is to modify the bottom depths. To remove the instability possible from thin bottom cells, we deepen those cells that are too shallow to fit the chosen initial column mass, if the bottom partial step is determined to be below a threshold thickness (chosen as 10m for this test case). For columns that can fit the chosen initial mass with the given bottom depth, we do not modify the bottom depth at all. So the initial procedure only deepens some cells. As shown in Figure 37.2, it only deepens cells by a small amount, with the exception of a few cells in the Black Sea. These columns occur in a relatively shallow marginal sea, and contain relatively light water.

37.1.2 Brief analysis for the simulations

We show the following figures on the subsequent pages:

- Figure 37.3: Anamolous surface temperature obtained by time averaging over years 81-100 of the simulation, with anomalies relative to the World Ocean Atlas (WOA).
- Figure 37.4: Anamolous surface salinity obtained by time averaging over years 81-100 of the simulation, with anomalies relative to the World Ocean Atlas (WOA).
- Figure 37.5: Anomalies for SST and SSS for the z^* and p^* simulations relative to the geopotential simulation.
- Figure 37.6: Time series for the temperature and salinity biases relative to WOA, as a function of depth for the geopotential and z^* simulation, and as a function of pressure for the p^* simulation.
- Figure 37.7: Meridional overturning circulation for the Atlantic basin averaged over years 81-100, as well as the time series for the maximum overturning at $45^\circ N$.

In general, differences are small between the geopotential and z^* simulations, whereas they are more noticeable between these two Boussinesq models and the p^* simulation. For surface properties, the main differences are near the boundary current extensions in the Pacific and Atlantic, with this difference signaling a slight shift in the boundary current with the p^* model relative to the depth based models. Overall, the larger spread with the p^* model may be attributed to accumulation of slightly different forcing, where the Boussinesq model normalizes by ρ_o to convert stresses (N/m^2), heating (W/m^2), and hydrological mass fluxes ($kg/(m^2\,s)$) to accelerations, temperature fluxes, and moisture volume fluxes. The p^* model normalizes by the *in situ* surface density of the model. Additionally, the nonBoussinesq equations are slightly different, and accumulation of these differences may be possible for realistic simulations, such as the OM3 CORE test case.

37.2 Age tracer and sensitivity to overflow parameterizations

We saw in Chapter 33 how sigma diffusion acting in the bottom grid cell, plus the overexchange scheme discussed in Section 19.4, affect the transfer of dense water into the abyss in the idealized DOME configuration. We pursue that result here within the OM3 configuration using geopotential vertical coordinate. In particular, we compare three MOM simulations plus an isopycnal simulation using the Hallberg Isopycnal Model:

- Standard configuration using the Sweby advection scheme of Hundsdorfer and Trompert (1994), with flux limiters of Sweby (1984). This configuration employs the sigma diffusion scheme in the model's bottom grid cells.
- Switch from Sweby to the second order moment scheme of Prather (1986).
- Keep Prather (1986) and enable the overexchange scheme discussed in Section 19.4.
- Hallberg Isopycnal Model (HIM): This simulation is analogous to the MOM simulations, with the exception that it employs three times larger restoring of the salinity field. A run with the same restoring is underway and will replace this simulation when available.

All three MOM simulations are quite similar in broad patterns. There are differences when focusing on certain boundary regions, as may be expected from the differences in the overflow parameterization. But the broad scale patterns are quite similar. In contrast, the HIM simulation is far more venitilated, especially in the Southern Ocean. This result is consistent with the coarse resolution results documented by Legg et al. (2006).

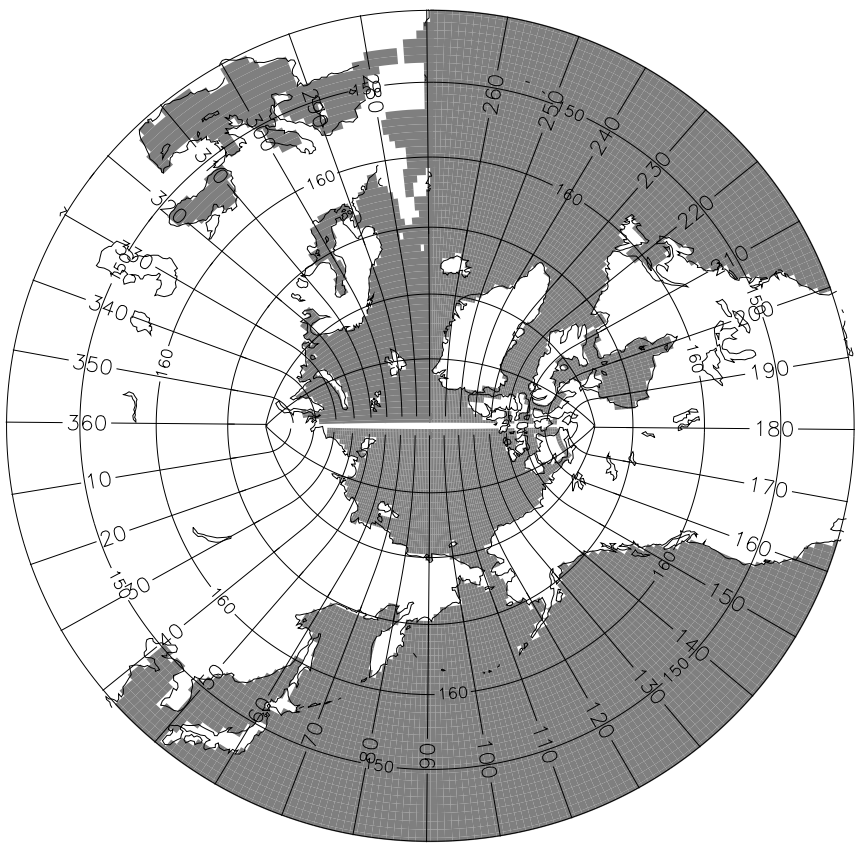

Figure 37.1: Illustration of the bipolar Arctic as prescribed by Murray (1996) (see his Figure 7) and realized in OM3. The transition from the bipolar Arctic to the spherical grid occurs at $65^\circ N$. We denote horizontal grid cells by (i, j) indices. As in the spherical coordinate region of the grid, lines of constant $i-$index move in a generalized eastward direction within the bipolar region. They start from the bipolar south pole at $i = 0$, which is identified with $i = ni$, where ni is the number of points along a latitude circle and $ni = 360$ in OM3. The bipolar north pole is at $i = ni/2$, which necessitates that ni be an even number. Both poles are centered at a velocity point on the B-grid

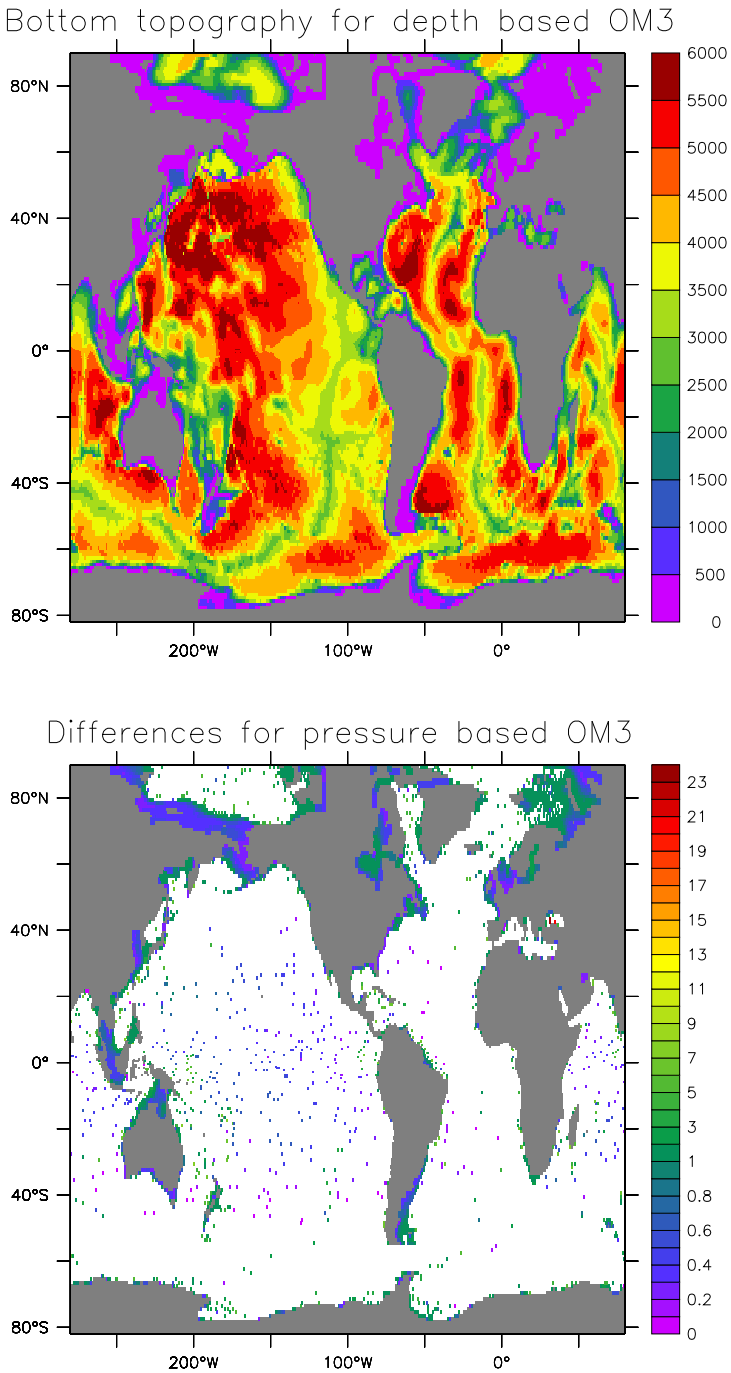

Figure 37.2: Top panel: Topography used in an earlier depth based version of the OM3 test case. Bottom panel: Deepening of the topography required to start the p^* simulation with a zero initial surface height. The modifications are very minor in most of the World Ocean, with a few points in the Black Sea most prominent.

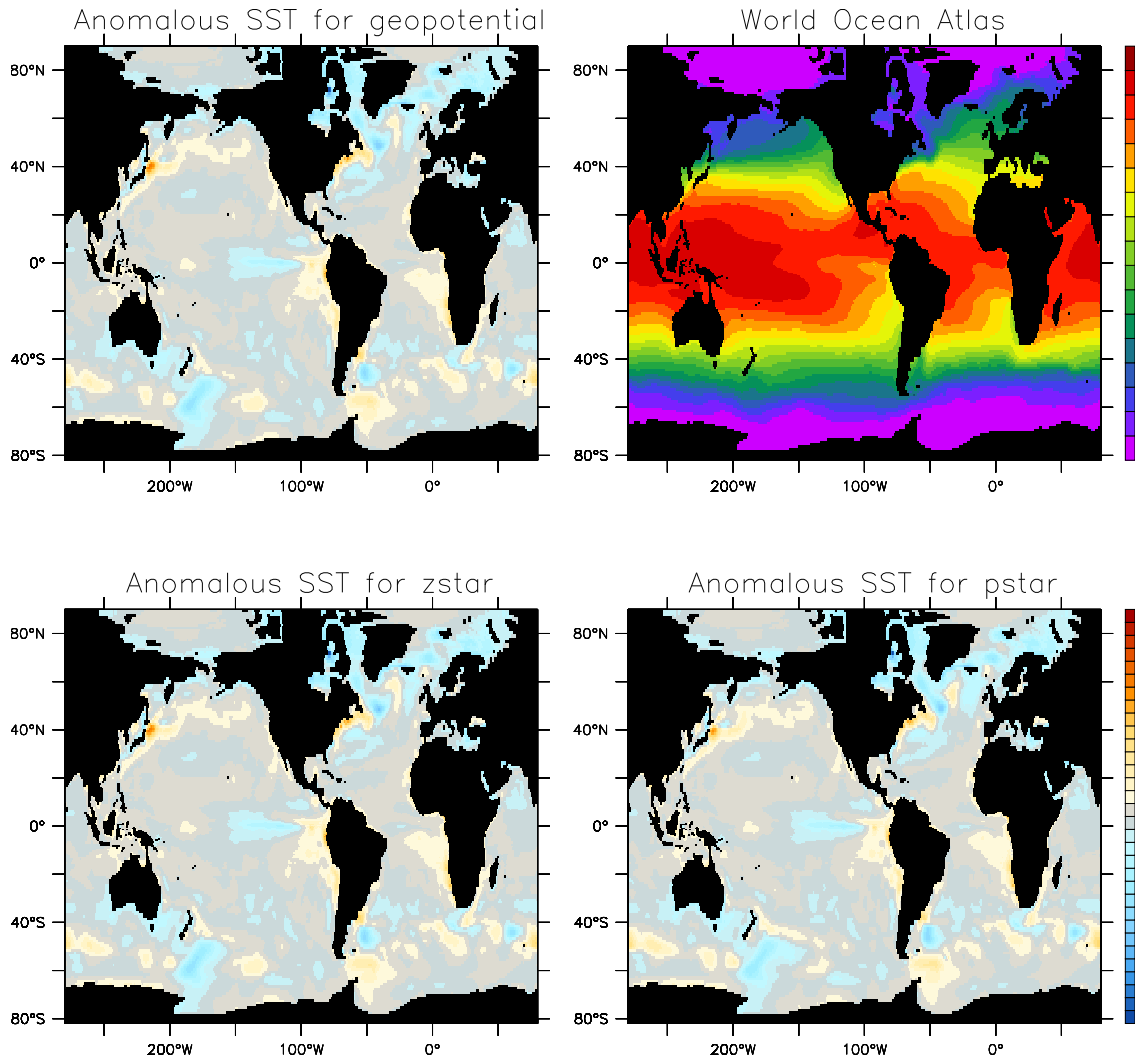

Figure 37.3: Surface temperature anomalies for the depth, z^*, and p^* simulations. Values are computed from 20 year mean over years 81-100.

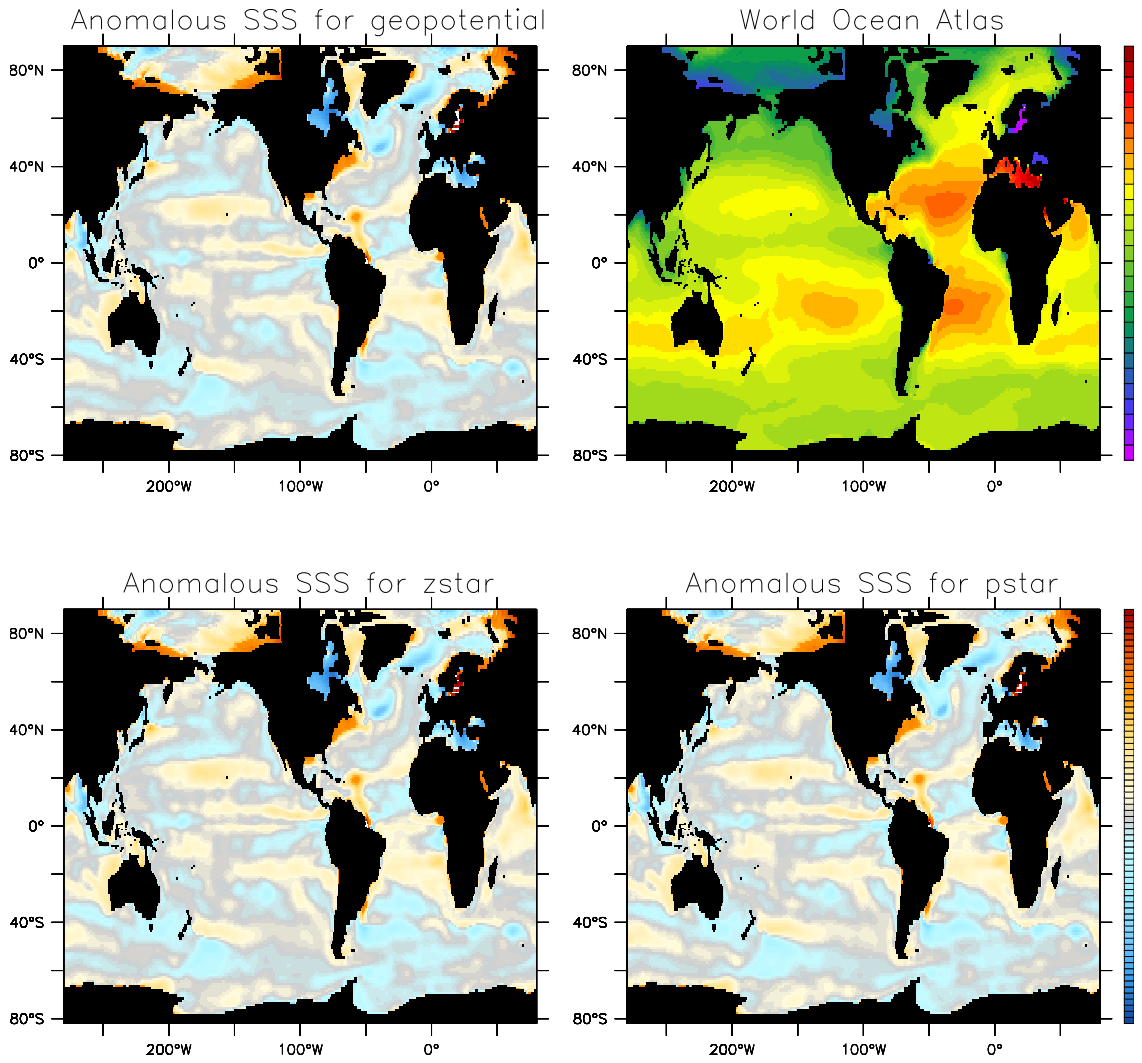

Figure 37.4: Surface salinity anomalies for the depth, z^*, and p^* simulations. Values are computed from 20 year mean over years 81-100.

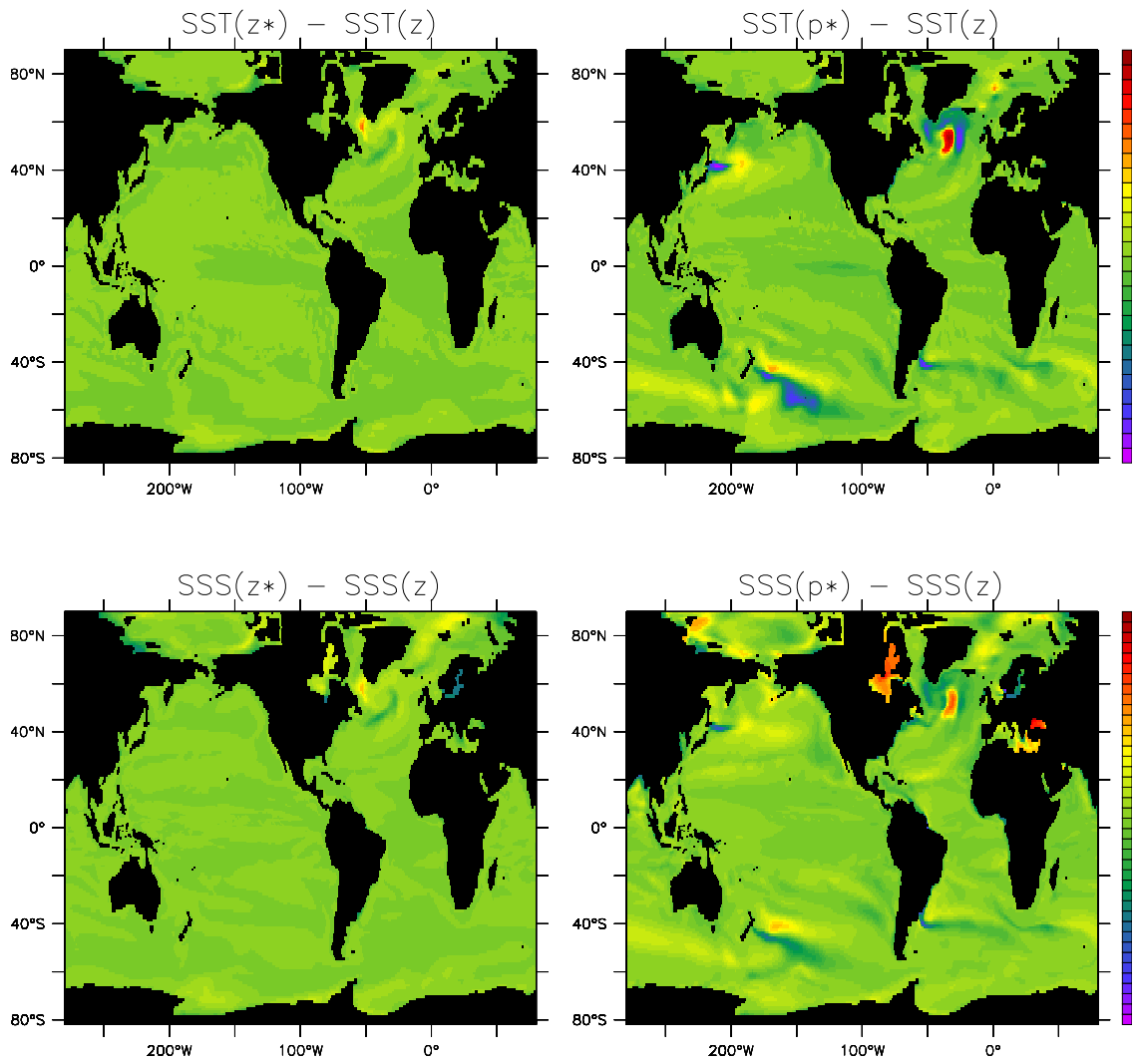

Figure 37.5: Difference in surface temperature and surface salinity between the z^* and geopotential, and p^* and geopotential. Values are computed from 20 year mean over years 81-100.

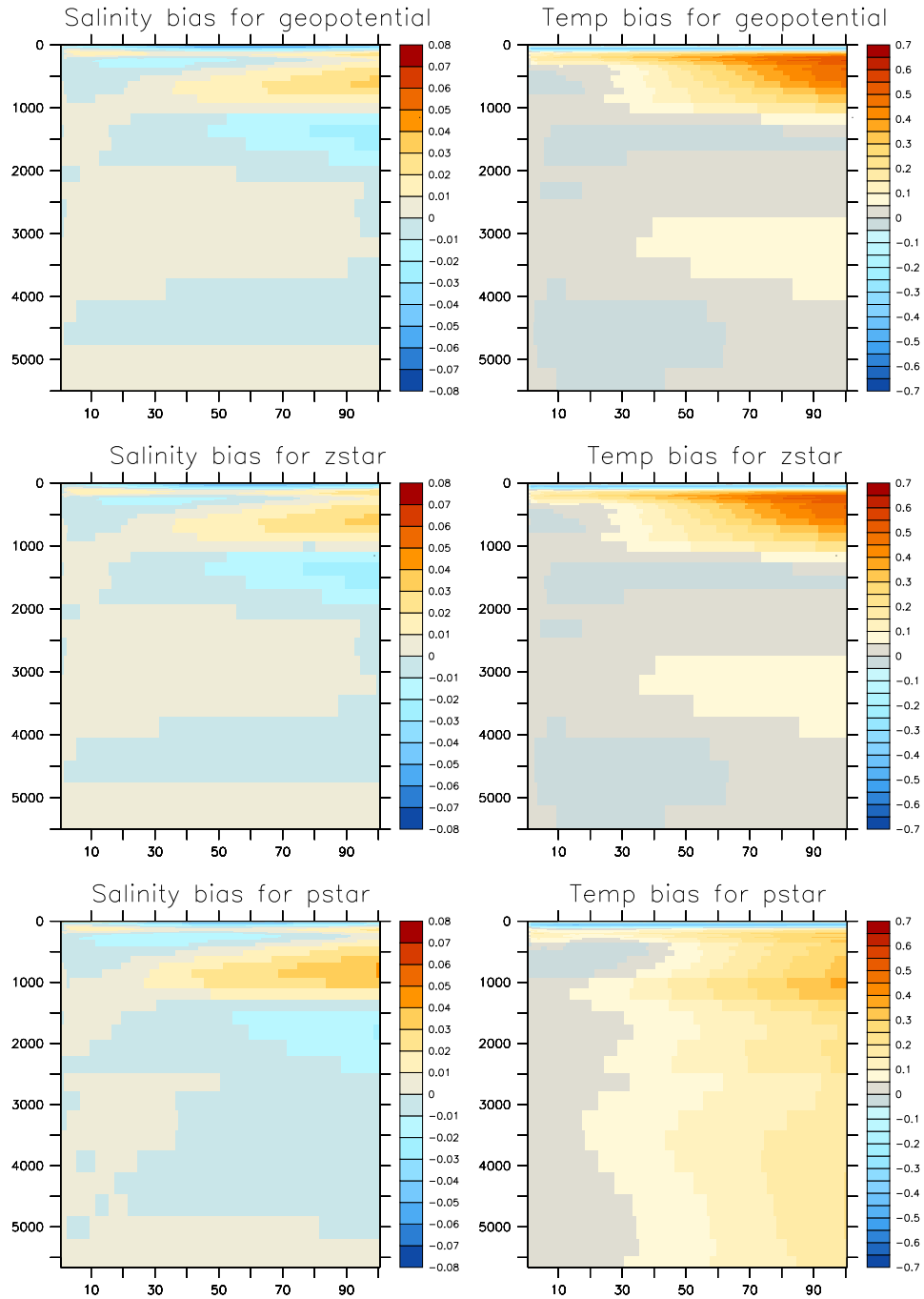

Figure 37.6: Drift for the geopotential, z^*, and p^* simulations in annual mean temperature and salinity as a function of depth and time. This drift is defined as $T_{\text{drift}}(z,t) = \left(\sum_{xy} \mathrm{d}x\,\mathrm{d}y\,\mathrm{d}z\,(T_{\text{model}} - T_{\text{initial}})\right) / \left(\sum_{xy} \mathrm{d}x\,\mathrm{d}y\,\mathrm{d}z\right)$.

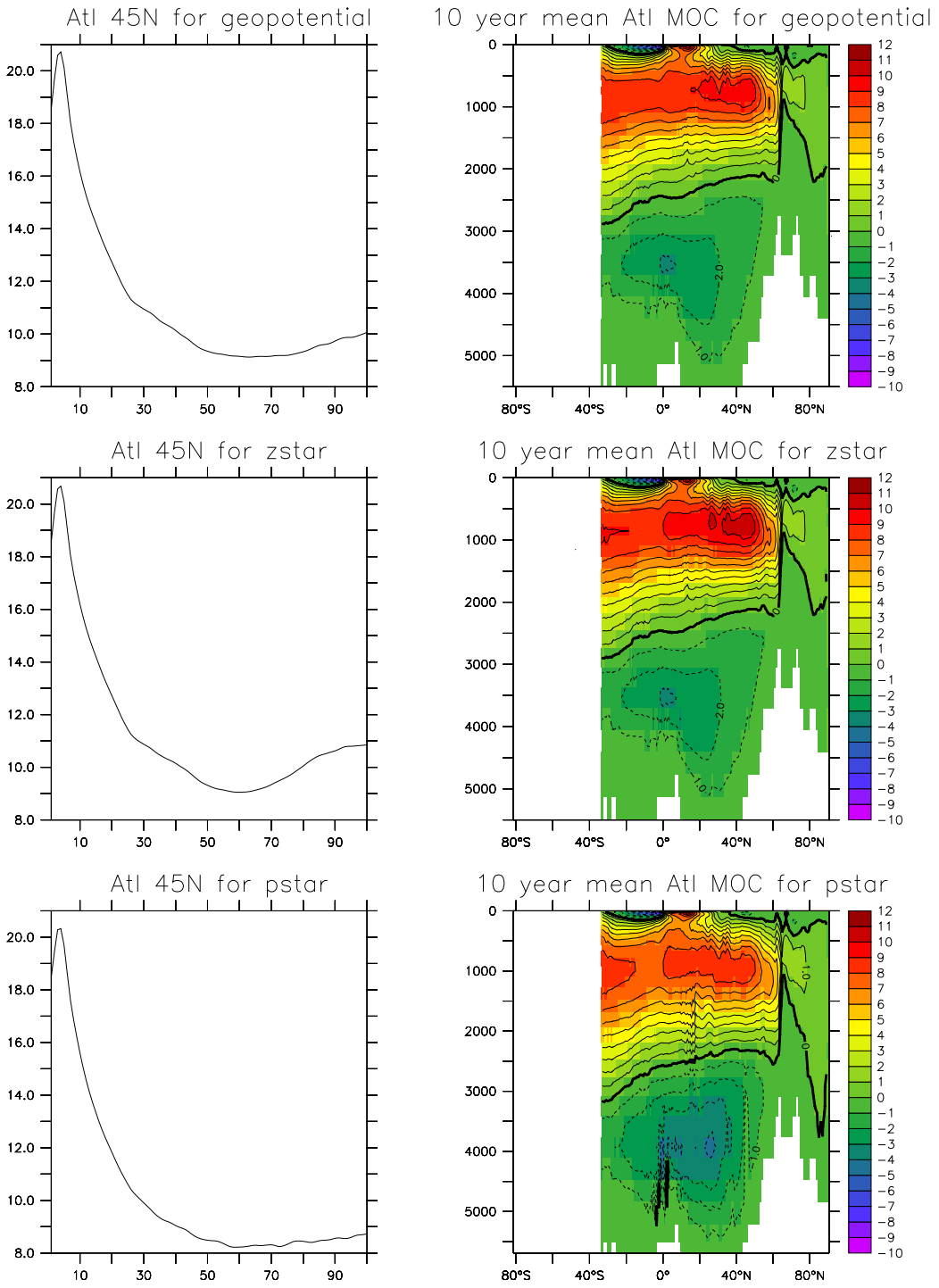

Figure 37.7: Meridional overturning circulation for the Atlantic basin averaged over years 81-100, as well as the time series for the maximum overturning at $45°N$.

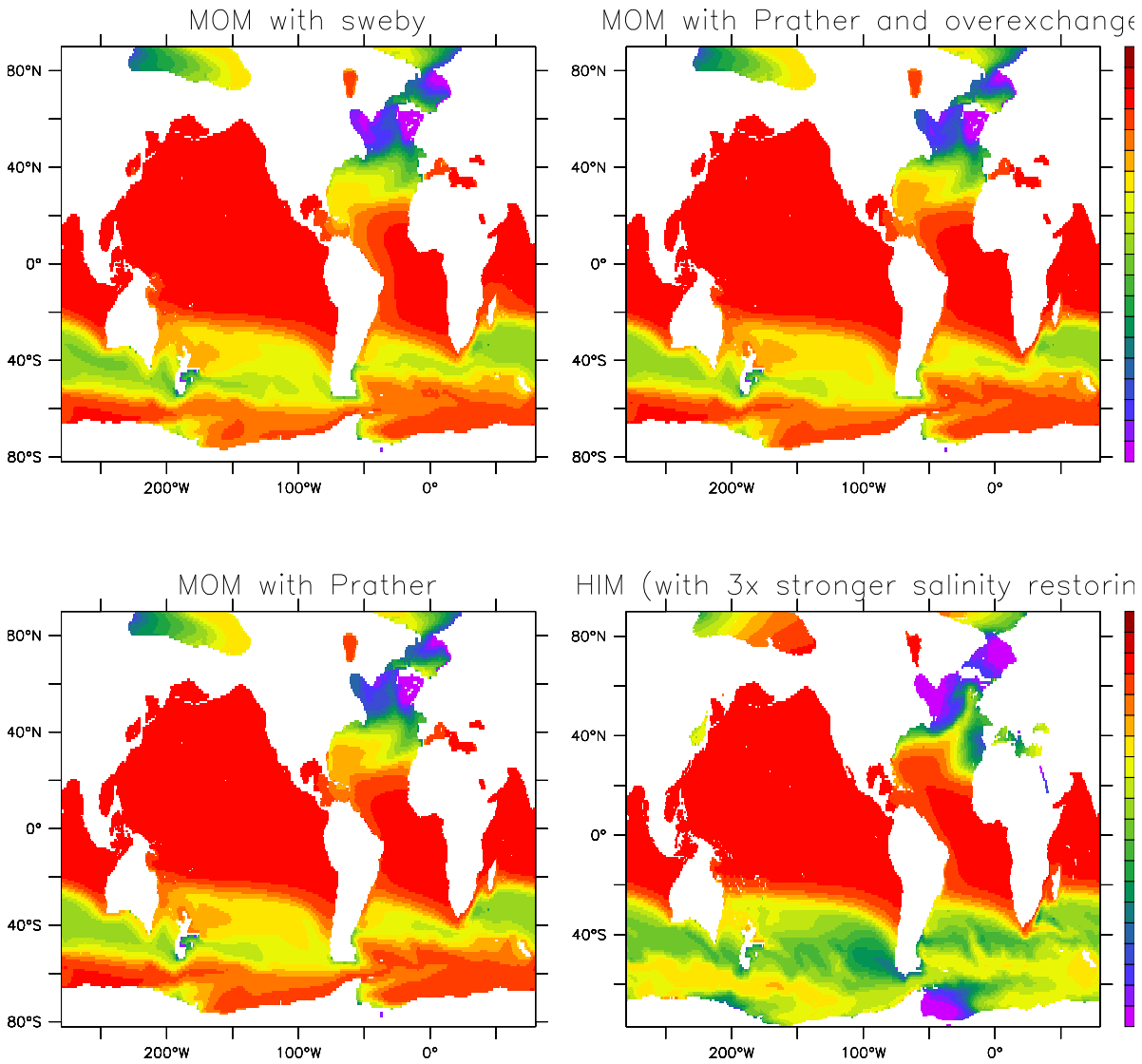

Figure 37.8: Age tracer averaged over the depths 800m-1200m and years 81-100. Top left: Integration with Sweby advection. Bottom left: Prather advection. Top right: Prather with overexchange. Bottom right: HIM.

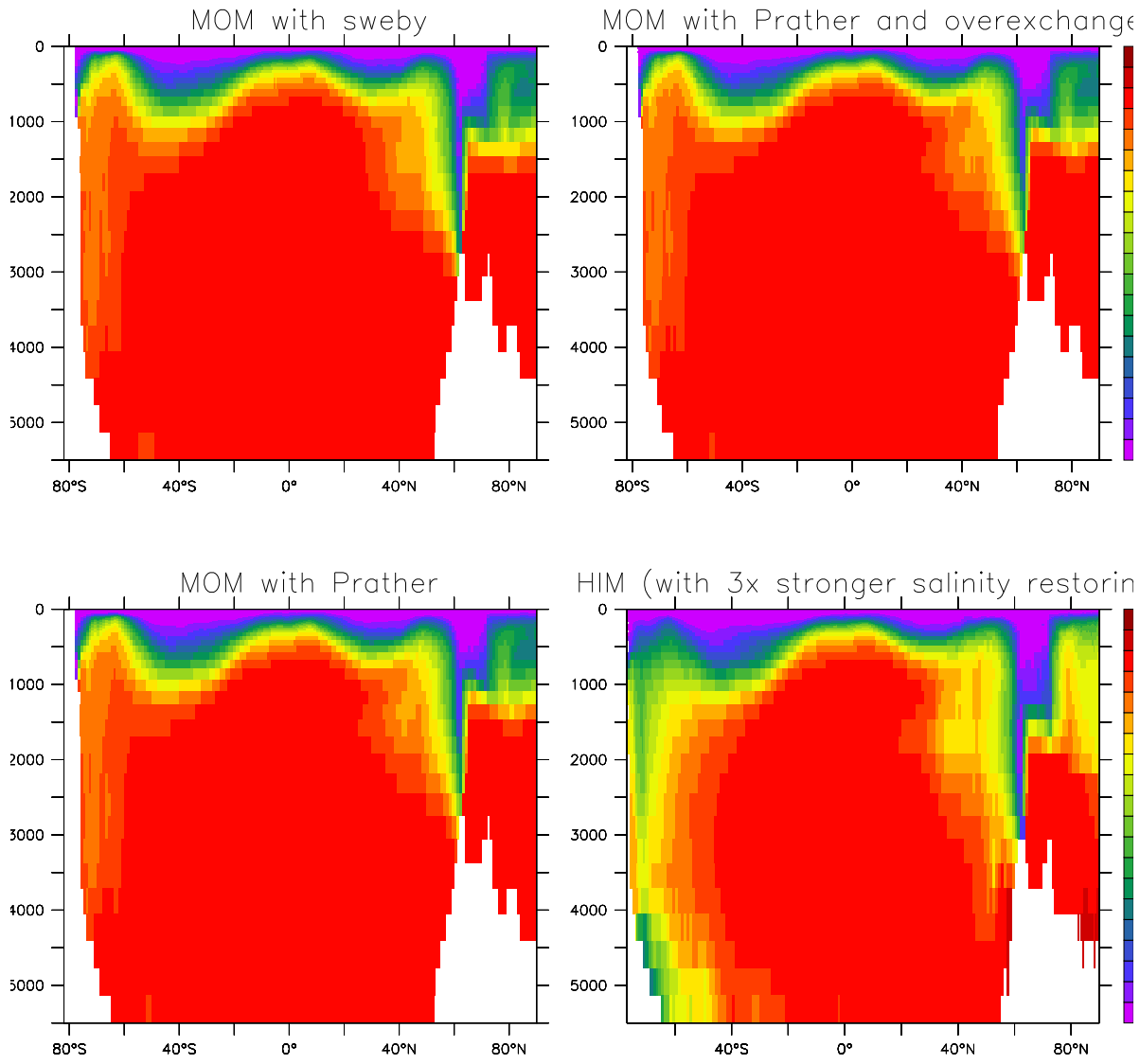

Figure 37.9: Zonally averaged age tracer averaged over years 81-100. Top left: Integration with Sweby advection. Bottom left: Prather advection. Top right: Prather with overexchange. Bottom right: HIM.

CHAPTER
THIRTYEIGHT

Global ocean-ice-biogeochemistry model

The test case `mom4_om3_ecosystem` consists of the same realistic global ocean and ice model used for the `mom4_om3_core` simulation (Chapter 37). The physical components are forced as in `mom4_om3_core`. In addition, we enable the GFDL Ocean Biogeochemistry (GOB) model. This is a model of oceanic ecosystems and biogeochemical cycles which considers 22 tracers including the following:

- three phytoplankton groups
- two forms of dissolved organic matter
- heterotrophic biomass
- dissolved inorganic species for C, N, P, Si, Fe, $CaCO_3$ and O_2 cycling.

The model includes such processes as

- gas exchange
- atmospheric deposition
- scavenging
- N_2 fixation and water column and sediment denitrification
- runoff of C, N, Fe, O_2, alkalinity and lithogenic material.

The phytoplankton functional groups undergo co-limitation by light, nitrogen, phosphorus and iron with flexible physiology. Loss of phytoplankton is parameterized through the size-based relationship of Dunne et al. (2005). Particle export is described through size and temperature based detritus formation and mineral protection during sinking with a mechanistic, solubility-based representation alkalinity addition from rivers, $CaCO_3$ sedimentation and sediment preservation and dissolution.

CHAPTER
THIRTYNINE

Global coupled model CM2.1

The test case `mom4_cm2p1` consists of the same realistic global ocean and ice model used for the `mom4_om3_core` simulation (Chapter 37). In addition, it couples to a realistic atmosphere and land model. This test case is the same configuration used for the GFDL CM2.1 coupled climate model used for the IPCC AR4 assessment, as documented by Griffies et al. (2005), Gnanadesikan et al. (2006a), Delworth et al. (2006), Wittenberg et al. (2006), and Stouffer et al. (2006). This model configuration is being distributed as part of the MOM4p1 code release, in hopes that researchers may find it useful both to develop their own coupled climate models, and to make use of the CM2.1 model as it is presently configured.

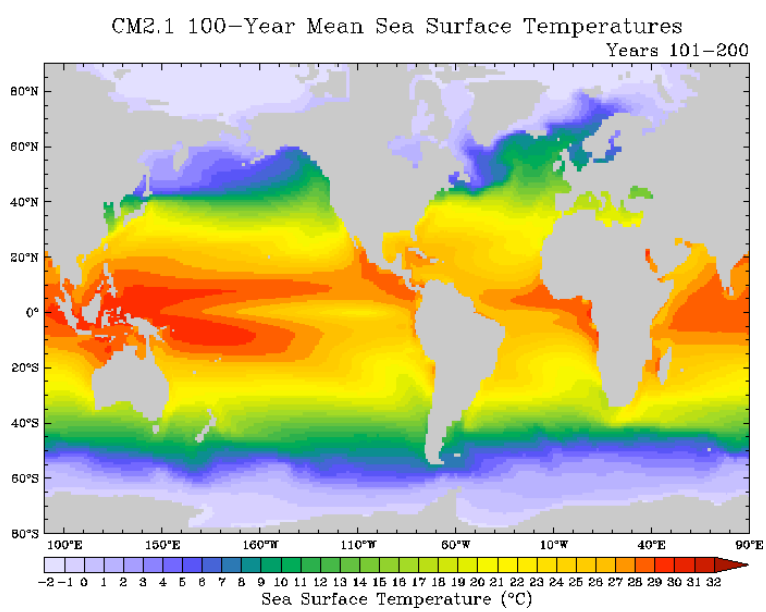

Figure 39.1: Sea surface temperature climatology from the GFDL coupled climate model CM2.1 as documented by Griffies et al. (2005), Gnanadesikan et al. (2006a), Delworth et al. (2006), Wittenberg et al. (2006), and Stouffer et al. (2006).

CHAPTER
FORTY

Eastern upwelling area test case

This chapter was contributed by Martin Schmidt

martin.schmidt@io – warnemuende.de

The test case mom4_atlantic is derived from a regional ecosystem model of the Benguela Upwelling area. It consists of a rectangular box delimited at the eastern side by the Namibian shelf, but by three open boundaries to the south, west and north respectively. The topography is derived from the etopo5 dataset. The circulation in the model area is driven by local wind fields, but is also influenced by coastal trapped waves originating from the equatorial current system. For experiments covering several model years a large model domain is needed, which includes the equatorial current system. However, in the framework of an ecosystem model with many nutrient, phytoplankton and zooplankton variables such a model system appears to be computationally expensive. In detail, it needs to much compute time for sophisticated sensitivity studies. For this purpose, regional sub-models may be of great help and the original purpose of this model configuration is to perform such sensitivity studies. The large model is implemented with MOM-31 as an ecosystem model, but the regional test case configured with mom4_atlantic has only the temperature and salinity tracer enabled.

The circulation at the shelf has three main components, a westward Ekman transport in connection with a coastal jet driven by the trade winds, an intermittent southward undercurrent and an Ekman compensation current which drives deep circulation onto the shelf. The more or less permanent off-shore Ekman transport implies strong coastal upwelling.

The regional model should reproduce these features. The specific boundary conditions at the open model boundaries (OBC) apply for tracer points and involve a radiation condition and relaxation to prescribed values as well. In the ARAKAWA B-grid used with mom4p1, velocity points are internal points, but momentum advection is not well defined and requires approximations. Hence, only information on tracers and sea level is passed from the large model to the regional sub-model.

Grid and topography in the sub-model and the large model are the same in the sub-model domain. Also the atmosphere forcing is similar and this test case could also be considered as a one sides nesting problem. However, the numerical schemes of the large and the regional

model are different. Open boundary conditions are one method to control inconsistency near the boundaries, which eventually may grow large with nesting.

The large model is implemented with MOM-31. It is a regional model itself and covers the area from 10° W to 18° E and 35° S to 8° N. Boundary values for temperature, salinity and sea level are taken from the ECCO-model. The OBC for the large model are very similar to those used in mom4p1. 10 day averages of most model variables can be found at the LAS-server

$$\mathtt{http://las.io-warnemuende.de:8080/las/servlets/dataset}.$$

Some details on the large model will be given below, which may be helpful to understand differences to the regional mom4p1 implementation:

- coupled model with atmosphere data provided from external files,
- leapfrog time stepping with Robert time filter, time step 720 s,
- tracer conserving time stepping scheme as described in Griffies et al. (2001), explicit fresh water flux from rivers and precipitation,
- tracer advection with the quicker scheme, in mom4p1 this is quickermom3,
- vertical diffusion with a modified kpp-scheme. Only that part of the short wave radiation, which is absorbed to a certain depth is added to the non-local vertical heat flux. This avoids numerical artifacts with unstable water column at daytime.
- horizontal diffusion and viscosity using the Smagorinsky closure scheme with a Prandl number of 10, and a Smagorinski factor of 4. Background values for viscosity and mixing are chosen as small as possible.
- Ocean-atmosphere fluxes are updated every hour and are kept constant in-between.
- The wind stress is calculated from composites of three day QuikSCAT based wind fields with high spatial resolution superimposed with a daily cycle derived from NCEP reanalysis data. The wind stress is parametrized following Large and Pond (1981).
- Short wave radiation is calculated from the top atmosphere insolation modified by total cloud cover taken from NCEP reanalysis data. Transmissivity depends on sun angle and absorption is calculated from the optical path length. The albedo is calculated from Fresnel's formula.
- Long-wave upward radiation is calculated from a gray body formula with an emissivity of 0.96. Long-wave downward radiation is taken from a gray body radiation formula with atmosphere 10 m temperature, modified by humidity and cloud coverage.
- Latent heat flux is calculated from virtual air temperature and SST by a usual bulk formula.
- Evaporation is calculated from 2m water vapor pressure. Specific humidity and air temperature are from NCEP reanalysis data. The enthalpy corresponding to the mass flux with evaporation is also taken into account.
- Precipitation data from NCEP reanalysis are used. To calculate the heat flux from precipitation (heavy rain falls are possible in the model domain) the rain temperature is approximated by the air temperature.

- Atmosphere bottom pressure gradients are taken into account from ocean model pressure gradients. This point is important for the performance of the OBC scheme.

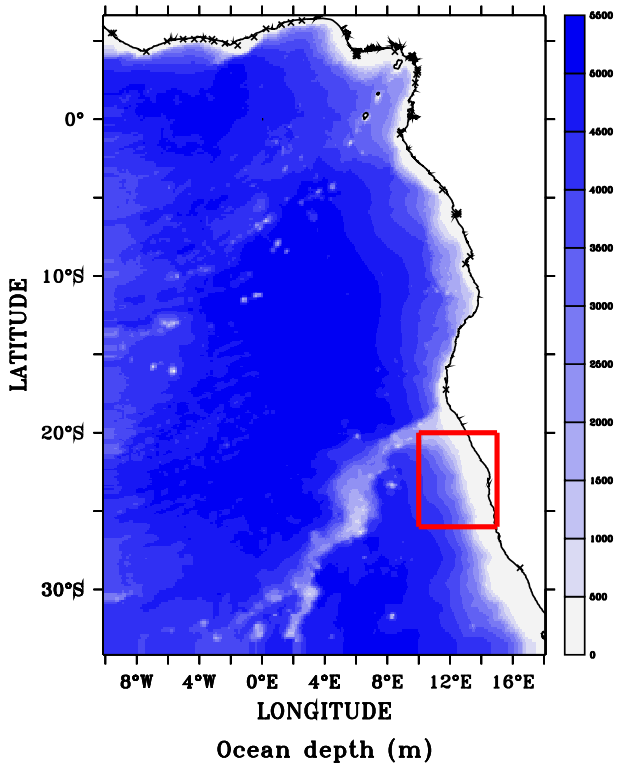

Figure 40.1: The topography of the large model and the embedded region of the sub-model.

Figure 40.1 shows the topography of the large model and the embedded sub-model area for this test case. Along the sub-model boundaries time averages of sea level and tracers were stored every 6 model hours. For the western boundary these data are in the input files *obc_trop_west.dta.nc* and *obc_clin_west.dta.nc*. Similar files are written for the northern and southern boundary. For `mom4p1` a calendar attribute was added to the time axis and the sea level values are transformed to be given in meters.

Subsequently some corner points for the regional `mom4p1` implementation are given. The namelist specifies more details:

- coupled model with atmosphere data provided from external files by data overriding,
- two-level (Adams-Bashford) time stepping with a baroclinic time-step of 1200 s,
- predictor-corrector free surface scheme,
- explicit fresh water flux precipitation, rivers are not in the model domain,
- geopotential coordinates. z^*-coordinates have been also verified to work, but OBC are not ready for pressure coordinates.

- The model domain is an upwelling area. The baroclinic Rossby radius is almost resolved. Hence, `sigma-diffusion` and `neutral physics` are disabled.
- Vertical diffusion is calculated from the `kpp`-scheme. This differs slightly from the method used in `MOM-31`, but the consequences have not been investigated yet.
- Horizontal diffusion is calculated from the Laplacian scheme, with a small value for $vel_micom = 0.001$m s^{-1}.
- Horizontal friction is calculated from the Laplacian Smagorinsky scheme, with a small value for $vel_micom_iso = 0.0005$m s^{-1} and $k_smag_iso = 4.0$.
- Tracer advection is carried out with the `mdfl_sweby`-scheme for all tracers.
- Atmosphere data to calculate ocean atmosphere fluxes are the same as used for the large model. However, in `mom4p1` the ocean surface velocity is taken into account in the wind stress calculation, which is based on Monin-Obukhov similarity theory.
- Downward short- and long-wave radiation is not calculated but overridden from file instead. 6 hourly `NCEP` reanalysis data are used, with a coarse 4 degree spatial resolution. The daily cycle will be represented less accurate than in the large model. Long-wave upward radiation is approximated by a black body formula.

Remarks on file on file preprocessing

The input files of this test case do not fulfill all requirements for `fms` netcdf input files, but they are recognized correctly. A calendar attribute was added to the time axis if missing. Most files are preprocessed with `ferret`,

`http://ferret.pmel.noaa.gov/Ferret/`,

which adds information on axis boundaries. Possibly the *bnds*-specification is not recognized by the `fms` axis tools. For this reason the *bnds*-specification has been removed from all input files.

Plots of the input wind fields in *windx.mom.dta.nc* and *windy.mom.dta.nc* look strange near the coasts. The reason is, that the wind fields are based on scatterometer data with missing values at land points which let the horizontal interpolation tools of `fms` fail. Replacing missing values by zero should be a bad choice. Hence, ocean values are extrapolates into land. This can be done with the function `fill_xy` of `ferret` which is undocumented part of version 6 and later and may be used as follows:

```
use windx_inp.nc                      ! missing values at land
let mask = missing(windx_in,0)*0 + 1 ! do not mask anything
let windx = fill_xy(windx_in,mask,5) ! fill with 5 passes
```

Experiments

The regional model was run with several choices of the namelist parameters over 11 model month. To demonstrate the influence of the wind stress parameterization on the results, the parameterization according the Monin-Obukhov similarity theory and the neutral approximation are used.

Open boundary conditions with a radiation condition and prescribed external data are mathematically ill-posed. Hence, a prefect scheme does not exist and the optimal choice of the boundary

conditions needs experiments with boundary code parameters. It is suggested to vary the parameters used for OBC, especially modify the strength of the relaxation toward external data and to test the different schemes for the calculation of the phase speed of baroclinic and barotropic waves.

Remarks on the wind stress parameterization

The scheme to calculate air-sea fluxes differs in many ways for the large and the regional model. The OBC should be robust against such inconsistency. A detailed discussion of the surface flux schemes in `mom4p1` is out of the scope of this test case, but some details need attention.

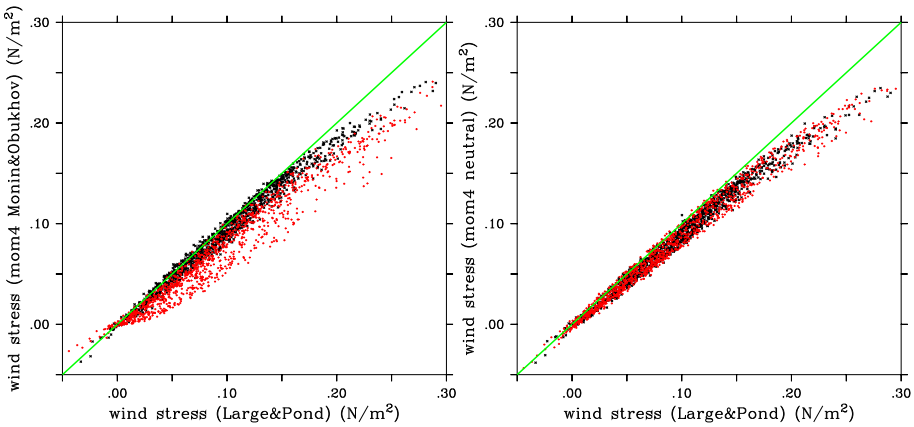

Figure 40.2: Scatter plots of the wind stress calculated in the large model (Large and Pond, 1981) versus the parameterization in `fms`, left: Monin-Obukhov similarity approach, right: neutral approximation. Black dots at 11° E and 21° S, where the boundary layer is often unstable, red dots from 14° E and 25° S in the upwelling area with low SST and a stable boundary layer.

Vertical momentum fluxes in the large model are estimated for a neutral boundary layer. This should be appropriate in a region of more or less permanent trade winds. In the regional model boundary layer stability was taken into account. Because there is no feedback from the ocean to the atmosphere, radiation can drive the SST away from the 2 m air temperature. Indeed this happens, because the cold band of upwelled water near the coast does not have its counterpart in the coarse `NCEP` data. On the other hand, calculated SST appears warmer than in remote sensing based data in the open ocean, which in turn leads to an unstable boundary layer.

Figure 40.2 shows scatter plots of the wind stress from the large scale model (LARGE AND POND, 1981, neutral boundary layer) and the `fms` schemes used in the regional model. Generally, the wind stress in `fms` is lower than in the large scale model. Especially for high wind speed large deviations can be seen. Results from the upwelling area (shown in red) show the influence of the stable boundary layer. It can be suspected, that the coarse `NCEP` reanalysis data do not resolve the narrow upwelling band and have to high atmosphere temperature. This corresponds to a very stable boundary layer in the upwelling band an in the tendency to reduced upwelling compared with a model driven by wind stress calculated for a neutral atmosphere-ocean boundary layer.

Here neither the neutral nor the Monin-Obukhov approach should be favored, but the differences should be mentioned as a source of differences between the large model and the regional model with open boundaries.

The mixing layer depth in the regional model is smaller than in the large model. The vertical

mixing scheme is configured similarly and the differences should be traced back to the different wind stress scheme.

Remarks on the heat flux parameterization
Using the downward radiation from NCEP reanalysis data together with the default heat flux parameterization implemented in fms, the calculated SST becomes to high within several model days. The resulting discrepancy between boundary data and the model interior, drives currents along the boundary. Comparing with the parameterization, used in the large scale model, it seems appropriate to introduce an albedo factor of .9 for the long wave radiation in the data_table. Such a ad hoc correction should be appropriate for a test case and removes the artificial boundary currents.

Mixing layer depth
The mixing layer depth in the regional model is smaller than in the large model. The vertical mixing scheme is configured similarly and the differences should be traced back to the different wind stress scheme.

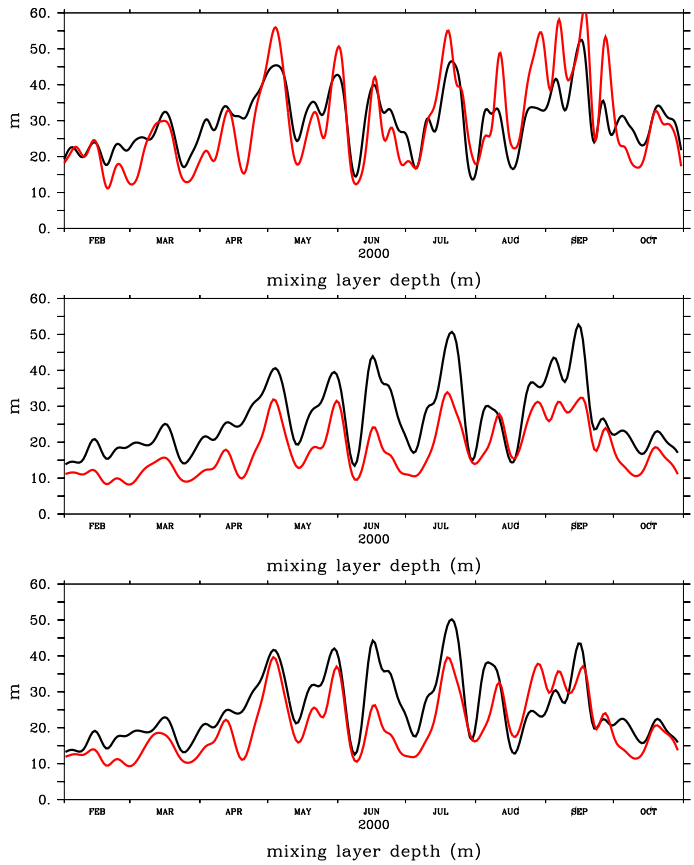

Figure 40.3: The mixing layer depth for the large scale model (upper part), mom4p1 and wind stress from Monin-Obukhov similarity approach (middle) and mom4p1 and wind stress for a neutral boundary layer. Black lines for 11° E and 21° S, where the boundary layer is often unstable, red dots from 14° E and 25° S in the upwelling area with cold SST and a stable boundary layer.

The differences between the large model and the regional model are significant, especially at 14° E and 25° S. The reduced wind stress in the regional model compared with the large scale model should be the major reason. However, a detailed investigation and evaluation with field data will be done elsewhere.

Ekman transport

Figures 40.4 and 40.5 show the wind driven transport in the mixing surface layer. Apparently, the parameterization in `mom4p1` gives smaller results than the large scale model based on `MOM-31`. The eddy like structure appearing in September 2000 are similar in all three models, but the amplitude in `mom4p1` is smaller. Notably, the open boundaries in the regional model permit a smooth solution. An exception is the strong northward current to be seen in September in the model with Monin-Obukhov wind stress at the western boundary at about 24°S, which tends to erode also the salinity field. With a neutral boundary layer the wind stress is enhanced and this feature disappears.

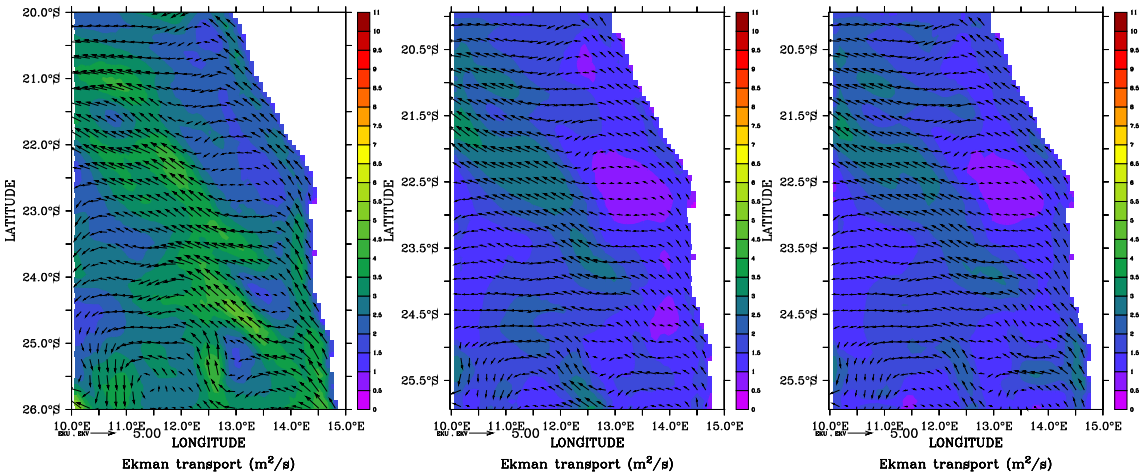

Figure 40.4: The vertically integrated transport in the mixing layer averaged from 2th March 2000 to 12th March 2000. Colours show the modulus. Left hand side the large scale model, middle `mom4p1` with Monin-Obukhov wind stress, right hand side `mom4p1` with neutral wind stress.

Undercurrent at the shelf

A typical feature for eastern boundary currents is an undercurrent at the shelf. Figure 40.6 shows an example. During strong upwelling it merges with the coastal jet and the direction may be reversed as shown in Figure 40.7.

The regional model performs well at the shelf, but the strong salinity signal at the western boundary cannot enter the model domain properly. Instead a strong along boundary current develops, which balances the pressure baroclinic pressure gradient. Again, the regional model with the stronger wind stress (neutral boundary layer scheme) is closer to the large scale model.

The cross shelf circulation

For the Namibian shelf the cross shelf circulation is an essential feature for the ecosystem dynamics. With the cross shelf circulation oxygen is advected onto the shelf which ventilates the shelf bottom water. The ability of the regional model to reproduce this part of the circulation system is

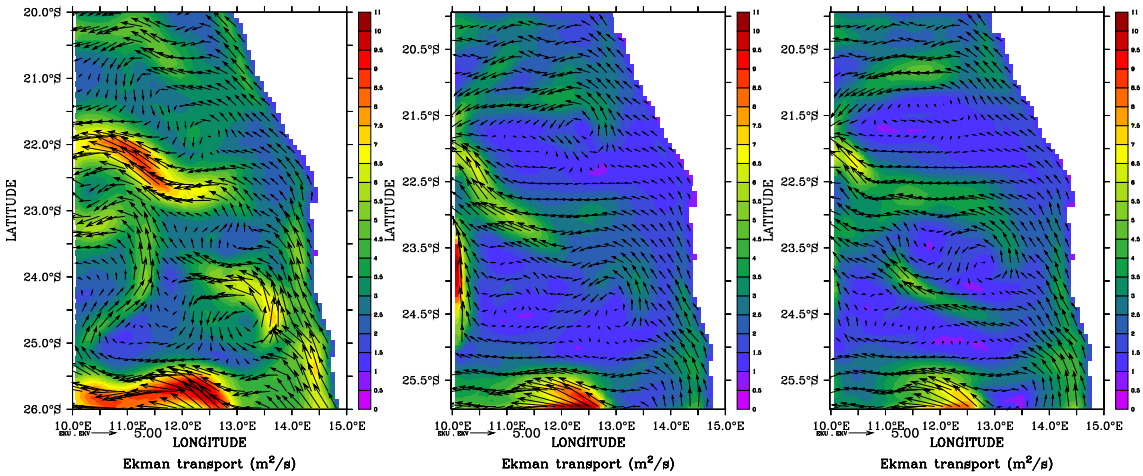

Figure 40.5: The vertically integrated transport in the mixing layer averaged from 2th September 2000 to 12th September 2000. Colours show the modulus. Left hand side the large scale model, middle `mom4p1` with Monin-Obukhov wind stress, right hand side `mom4p1` with neutral wind stress.

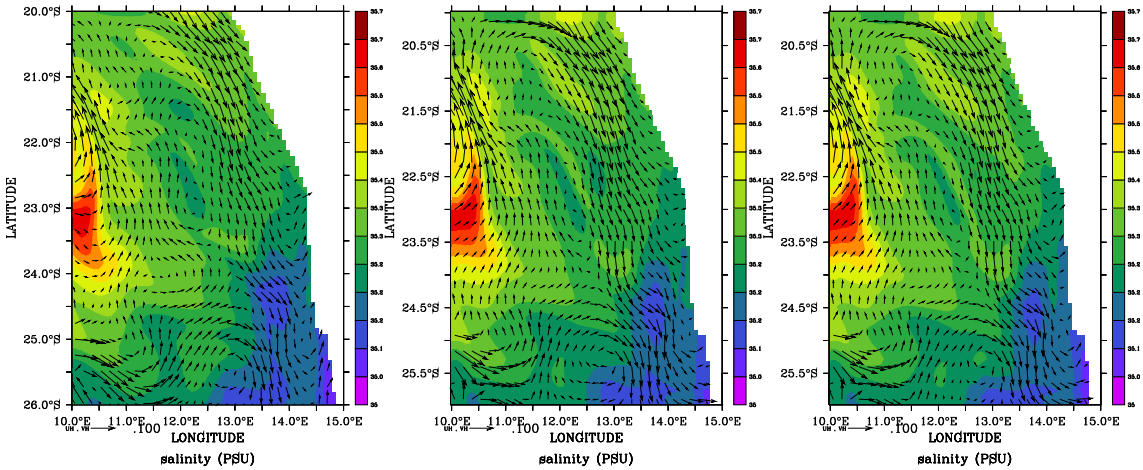

Figure 40.6: Salinity and undercurrent in 80 m depth averaged from 2th March 2000 to 12th March 2000. Left hand side the large scale model, middle `mom4p1` with Monin-Obukhov wind stress, right hand side `mom4p1` with neutral wind stress.

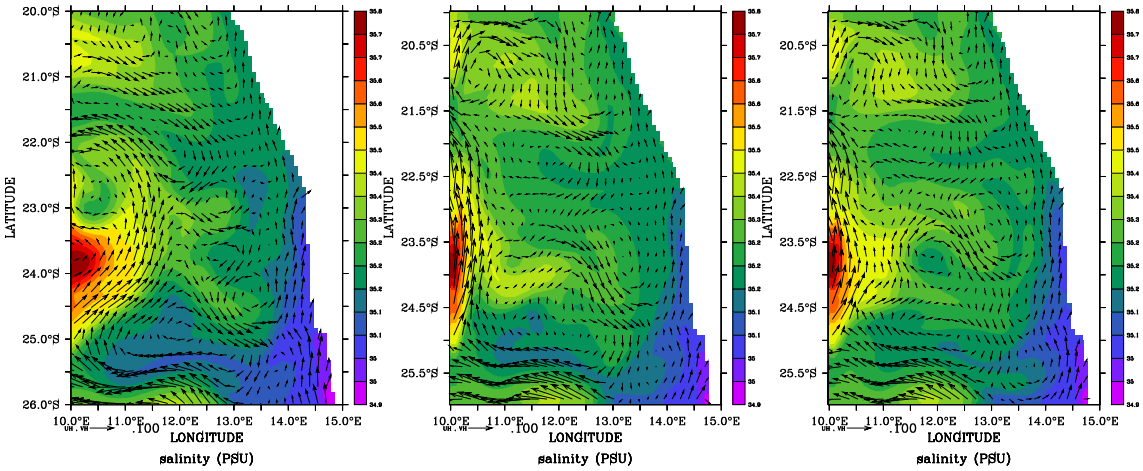

Figure 40.7: Salinity and current in 80 m depth averaged from 2th September 2000 to 12th September 2000. Left hand side the large scale model, middle `mom4p1` with Monin-Obukhov wind stress, right hand side `mom4p1` with neutral wind stress.

very important.

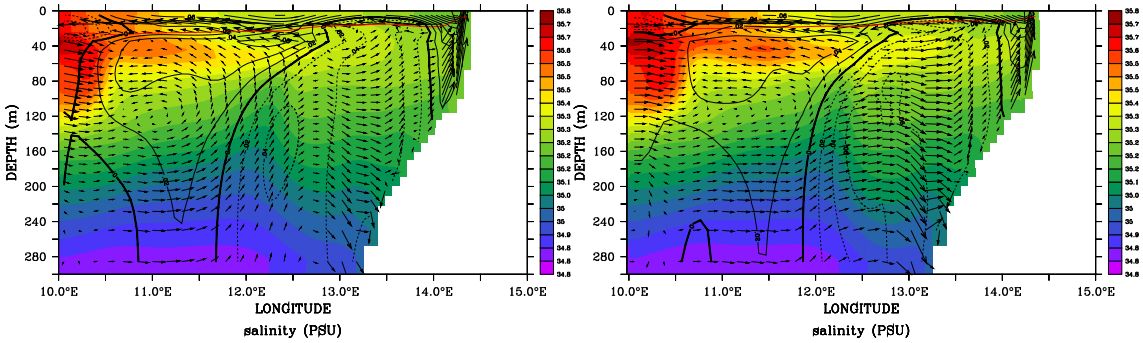

Figure 40.8: Salinity and cross shelf circulation at 23° S averaged from 2th March 2000 to 12th March 2000. Left hand side the large scale model, right hand side `mom4p1` with neutral wind stress. The red line marks the mixing layer depth, the contours the meridional currents. The vertical velocity is scaled with the figures aspect ratio.

Figures 40.8 and 40.9 show a typical upwelling dominated circulation. For March 2000 results from the large scale and the regional model are very similar. Note the tongue of more saline water in 60 m depth generated by the differential advection, which is also verified by field data. Upwelling goes along with a northward coastal jet within a narrow band at the coast. The figures reveal the vertical structure of the poleward undercurrent which is detached from the coast. In September 2000 its deeper parts move off-shore, but there develops a new core near the coast in about 40 m depth. There are differences between the large scale and the regional model in many details, but the general structure of the circulation pattern and the salinity distribution is the same. Especially near the western boundary the saline water appears deflected to the west in the regional model. Some strong upward vertical current develops, which is not in the large scale model. It should stem mostly from the inconsistency in the forcing of both models, which has to be smoothed by

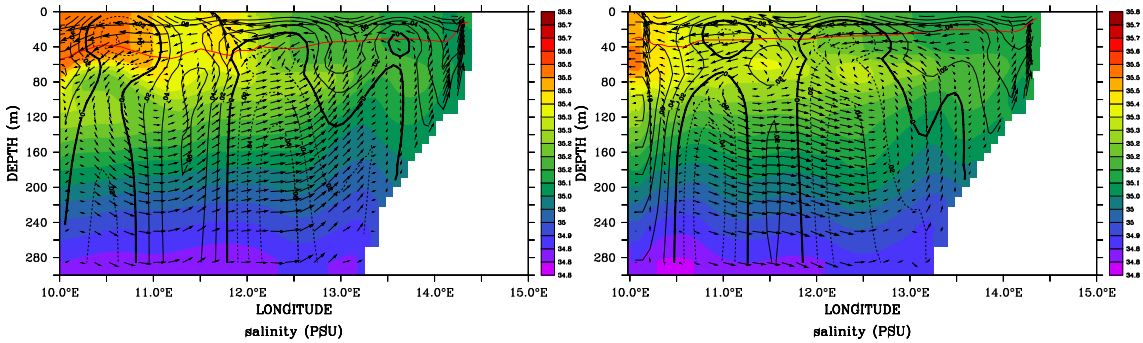

Figure 40.9: Salinity and cross shelf circulation at 23° S averaged from 2th September 2000 to 12th September 2000. Left hand side the large scale model, right hand side `mom4p1` with neutral wind stress. The red line marks the mixing layer depth, the contours the meridional currents. The vertical velocity is scaled with the figures aspect ratio.

the open boundary condition.

A remark about the atmosphere pressure

Inclusion of atmosphere pressure gradients to the surface forcing is often considered as a marginal issue and minor correction because the sea level elevation rapidly adjusts to the air pressure. Slowly varying air pressure gradients are compensated by sea level elevations of the opposite sign and geostrophic currents balanced by surface pressure gradients should not be very different with and without air pressure. However, for a regional model with prescribed sea level elevation at the open boundaries a reference level for the sea level is defined. An air pressure gradient imposed to the model acts in the same manner as a prescribed sea level gradient at the boundary, if the boundary data are not produced consistently with this model configuration. This may happen, when the boundary data come from a model, which does not include air pressure gradients, but the regional model is run with air pressure "switched on", or vice versa.

The regional model of test case `mom4_atlantic` covers parts of the St.-Helena high pressure are, whose persistent pressure gradients are responsible for the permanent trade winds off Namibia. The boundary data from the large scale model consider air pressure, but the default of `mom4p1` is to have air pressure disabled. For the experiments discussed above, it is enabled in *ice_model_nml* defining *slp2ocean=.true.*.

In the surface currents, the influence of the wind stress dominates, but the deeper currents depend strongly on the a consistent treatment of air pressure in the boundary conditions. This should be clearly shown by Figure 40.10, where the regional model drifts away from the large model, when air pressure is not considered. However, in this case the eddy does not appear, which develops near the northern boundary in the regional model with air pressure.

Skills, shortcomings and limitations

The test case demonstrates, that OBC are suitable to drive a regional model with boundary data taken from another model. Many deviations between the results of the large reference model and the regional model can be traced back to different numerics and parameters. The numerical scheme used at the boundaries can be configured, to keep the influence of these deviations small and allows for reliable experiments with the regional model. However, one must be aware,

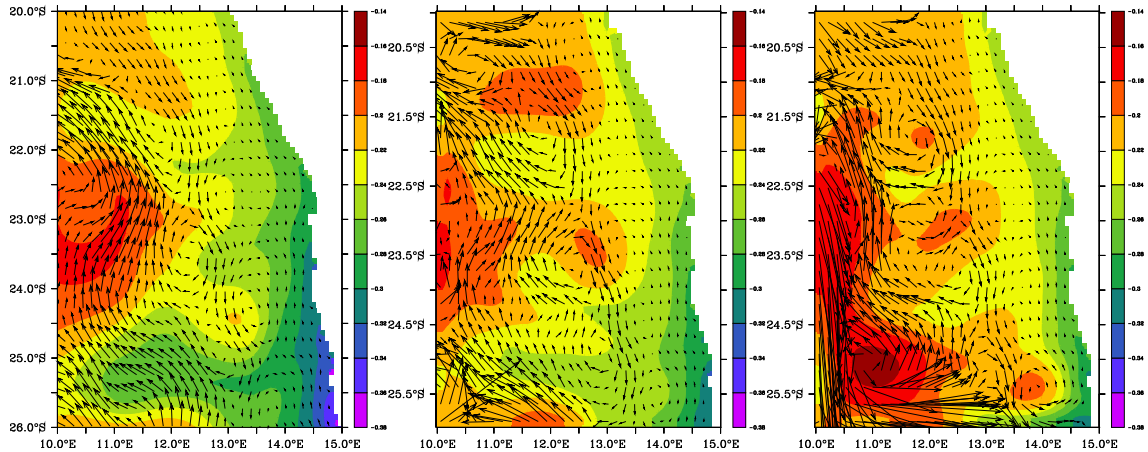

Figure 40.10: The sea level elevation in m and the vertically integrated velocity in $m^2 s^{-1}$ averaged from 2th September 2000 to 12th September 2000. Left hand side the large scale model, middle `mom4p1` with air pressure taken into account, right hand side `mom4p1` with no air pressure gradients in the surface pressure.

that some perturbations generated near the boundaries may propagate as eddies into the model interior. Hence, mesoscale processes may be modified by perturbations from the OBC. The probability of such effects is increasing with the inconsistency between regional model dynamics and prescribed boundary values.

This test case is an extreme application in so far, that the length of open boundaries is large. For a semi-enclosed sea with a small connection to the open ocean the influence of the OBC scheme on the model results should be smaller.

It must be also noted, that the model area is situated within an eastern boundary current. Hence, artificial Rossby waves generated at the open boundaries are leaving the model domain. A similar test case within a western boundary current was not tested yet.

BIBLIOGRAPHY

Adcroft, A. and Campin, J.-M.: Rescaled height coordinates for accurate representation of free-surface flows in ocean circulation models, Ocean Modelling, 7, 269–284, 2004.

Adcroft, A. and Hallberg, R. W.: On methods for solving the oceanic equations of motion in generalized vertical coordinates, Ocean Modelling, 11, 224–233, 2006.

Adcroft, A., Hill, C., and Marshall, J.: Representation of topography by shaved cells in a height coordinate ocean model, Monthly Weather Review, 125, 2293–2315, 1997.

Adcroft, A., Hallberg, R., and Harrison, M.: A finite volume discretization of the pressure gradient force using analytic integration, Ocean Modelling, 22, 106–113, 2008.

Aiki, H., Jacobson, T., and Yamagata, T.: Parameterizing ocean eddy transports from surface to bottom, Journal of Geophysical Research, 31, L19 302, doi:10.1029/2004GL020 703, 2004.

Apel, J. R.: Principles of Ocean Physics, vol. 38 of *International Geophysics Series*, Academic Press, London, 1987.

Asselin, R.: Frequency filter for time integrations, Monthly Weather Review, 100, 487–490, 1972.

Bacon, S. and Fofonoff, N. P.: Oceanic heat flux calculation, Journal of Atmospheric and Oceanic Technology, 13, 1327–1329, 1996.

Beckmann, A. and Döscher, R.: A method for improved representation of dense water spreading over topography in geopotential-coordinate models, Journal of Physical Oceanography, 27, 581–591, 1997.

Black, T. L.: The new NMC mesoscale eta model: description and forecast examples, Weather and Forecasting, 9, 265–278, 1994.

Blumberg, A. and Kantha, L.: Open boundary condition for circulation models, Journal of Hydraulic Engineering, 111, 237–255, 1985.

Bryan, K.: A numerical method for the study of the circulation of the world ocean, Journal of Computational Physics, 4, 347–376, 1969.

Bryan, K.: Michael Cox (1941-1989): his pioneering contributions to ocean circulation modeling, Journal of Physical Oceanography, 21, 1259–1270, 1991.

Bryan, K. and Cox, M. D.: An approximate equation of state for numerical models of the ocean circulation, Journal of Physical Oceanography, 4, 510–514, 1972.

Bryan, K. and Lewis, L. J.: A water mass model of the world ocean, Journal of Geophysical Research, 84, 2503–2517, 1979.

Burchard, H. and Rennau, H.: Comparative quantification of physically and numerically induced mixing in ocean models, Ocean Modelling, 20, 293–311, 2008.

Callen, H. B.: Thermodynamics and an Introduction to Thermostatics, John Wiley and Sons, New York, 493 + xvi pp, 1985.

Camerlengo, A. and O'Brien, J.: Open boundary condition in rotating fluids, Journal of Computational Physics, 35, 12–35, 1980.

Campin, J.-M. and Goosse, H.: Parameterization of density-driven downsloping flow for a coarse-resolution ocean model in z-coordinate, Tellus, 51A, 412–430, 1999.

Campin, J.-M., Adcroft, A., Hill, C., and Marshall, J.: Conservation of properties in a free-surface model, Ocean Modelling, 6, 221–244, 2004.

Chapman, D.: Numerical treatment of cross-shelf boundaries in a barotropic coastal ocean model, Journal of Physical Oceanography, 103(C1), 1060–1075, 1985.

Chassignet, E. P. and Verron, J.: Ocean Weather Forecasting: an Integrated View of Oceanography, Springer Publishers, 2005.

Chelton, D. B., DeSzoeke, R. A., Schlax, M. G., Naggar, K. E., and Siwertz, N.: Geographical Variability of the First Baroclinic Rossby Radius of Deformation, Journal of Physical Oceanography, 28, 433–460, 1998.

Chen, D., Rothstein, L., and Busalacchi, A.: A hybrid vertical mixing scheme and its application to tropical ocean models, Journal of Physical Oceanography, 24, 2156–2179, 1994.

Cox, M. D.: A Primitive Equation, 3-Dimensional Model of the Ocean, NOAA/Geophysical Fluid Dynamics Laboratory, Princeton, USA, 1984.

Danabasoglu, G. and McWilliams, J. C.: Sensitivity of the global ocean circulation to parameterizations of mesoscale tracer transports, Journal of Climate, 8, 2967–2987, 1995.

Danabasoglu, G., Large, W. G., Tribbia, J. J., Gent, P. R., Briegleb, B. P., and McWilliams, J. C.: Diurnal Coupling in the Tropical Oceans of CCSM3, Journal of Climate, 19, 2347–2365, 2006.

DeGroot, S. R. and Mazur, P.: Non-Equilibrium Thermodynamics, Dover Publications, New York, 510 pp, 1984.

Delworth, T. L., Broccoli, A. J., Rosati, A., Stouffer, R. J., Balaji, V., Beesley, J. A., Cooke, W. F., Dixon, K. W., Dunne, J., Dunne, K. A., Durachta, J. W., Findell, K. L., Ginoux, P., Gnanadesikan, A., Gordon, C., Griffies, S. M., Gudgel, R., Harrison, M. J., Held, I. M., Hemler, R. S., Horowitz, L. W., Klein, S. A., Knutson, T. R., Kushner, P. J., Langenhorst, A. L., Lee, H.-C., Lin, S., Lu, L., Malyshev, S. L., Milly, P., Ramaswamy, V., Russell, J., Schwarzkopf, M. D., Shevliakova, E.,

Sirutis, J., Spelman, M., Stern, W. F., Winton, M., Wittenberg, A. T., Wyman, B., Zeng, F., and Zhang, R.: GFDL's CM2 Global Coupled Climate Models - Part 1: Formulation and Simulation Characteristics, Journal of Climate, 19, 643–674, 2006.

DeSzoeke, R. A. and Samelson, R. M.: The duality between the Boussinesq and Non-Boussinesq Hydrostatic Equations of Motion, Journal of Physical Oceanography, 32, 2194–2203, 2002.

Diansky, N., Bagno, A., and Zalensy, V.: Global ocean circulation sigma-model and its sensitivity to the wind stress forcing., Izvestia, Atmospheric and Oceanic Physics, 38, 477–494, 2002.

Döscher, R. and Beckmann, A.: Effects of a bottom boundary layer parameterization in a coarse-resolution model of the North Atlantic Ocean, Journal of Atmospheric and Oceanic Technology, 17, 698–707, 2000.

Dunne, J. P., Armstrong, R., Gnanadesikan, A., and Sarmiento, J.: Empirical and mechanistic models for the particle export ratio, Global Biogeochemical Cycles, 19, doi:10.1029/2004GB002 390, 2005.

Durran, D. R.: Numerical Methods for Wave Equations in Geophysical Fluid Dynamics, Springer Verlag, Berlin, 470 pp, 1999.

England, M. H.: The age of water and ventilation timescales in a global ocean model, Journal of Physical Oceanography, 25, 2756–2777, 1995.

Ezer, T., Arango, H., and Shchepetkin, A. F.: Developments in terrain-following ocean models: Intercomparisons of numerical aspects, Ocean Modelling, 4, 249–267, 2002.

Feistel, R.: Equilibrium thermodynamics of seawater revisited, Progress in Oceanography, 31, 101–179, 1993.

Feistel, R.: A new extended Gibbs thermodynamic potential of seawater, Progress in Oceanography, 58, 43–114, 2003.

Feistel, R. and Hagen, E.: On the Gibbs thermodynamic potential of seawater., Progress in Oceanography, 36, 249–327, 1995.

Ferrari, R., McWilliams, J., Canuto, V., and Dubovikov, M.: Parameterization of eddy fluxes near oceanic boundaries, Journal of Climate, 21, 2770–2789, 2008.

Ferreira, D. and Marshall, J.: Formulation and implementation of a residual-mean ocean circulation model, Ocean Modelling, 13, 86–107, 2006.

Ferreira, D., Marshall, J., and Heimbach, P.: Estimating eddy stresses by fitting dynamics to observations using a residual-mean ocean circulation model and its adjoint, Journal of Physical Oceanography, 35, 1891–1910, 2005.

Fofonoff, N. P.: Physical properties of seawater, in The Sea, edited by M. N. Hill, vol. 1, pp. 3–30, Wiley-Interscience, 1962.

Fox-Kemper, B., Danabasoglu, G., Ferrari, R., and Hallberg, R. W.: Parameterizing submesoscale physics in global models, Clivar Exchanges, 13, 3–5, 2008a.

Fox-Kemper, B., Ferrari, R., and Hallberg, R.: Parameterization of mixed layer eddies. I: Theory and diagnosis, Journal of Physical Oceanography, 38, 1145–1165, 2008b.

Gent, P. R. and McWilliams, J. C.: Isopycnal mixing in ocean circulation models, Journal of Physical Oceanography, 20, 150–155, 1990.

Gent, P. R., Willebrand, J., McDougall, T. J., and McWilliams, J. C.: Parameterizing eddy-induced tracer transports in ocean circulation models, Journal of Physical Oceanography, 25, 463–474, 1995.

Gerdes, R., Köberle, C., and Willebrand, J.: The influence of numerical advection schemes on the results of ocean general circulation models., Climate Dynamics, 5, 211–226, 1991.

Gill, A.: Atmosphere-Ocean Dynamics, vol. 30 of *International Geophysics Series*, Academic Press, London, 662 + xv pp, 1982.

Gnanadesikan, A., Dixon, K. W., Griffies, S. M., Balaji, V., Beesley, J. A., Cooke, W. F., Delworth, T. L., Gerdes, R., Harrison, M. J., Held, I. M., Hurlin, W. J., Lee, H.-C., Liang, Z., Nong, G., Pacanowski, R. C., Rosati, A., Russell, J., Samuels, B. L., Song, S. M., , Spelman, M. J., Stouffer, R. J., Sweeney, C. O., Vecchi, G., Winton, M., Wittenberg, A. T., Zeng, F., and Zhang, R.: GFDL's CM2 Global Coupled Climate Models-Part 2: The Baseline Ocean Simulation, Journal of Climate, 19, 675–697, 2006.

Greatbatch, R. J. and Lamb, K. G.: On parameterizing vertical mixing of momentum in non-eddy resolving ocean models, Journal of Physical Oceanography, 20, 1634–1637, 1990.

Greatbatch, R. J. and McDougall, T. J.: The non-Boussinesq temporal-residual-mean, Journal of Physical Oceanography, 33, 1231–1239, 2003.

Greatbatch, R. J. and Mellor, G. L.: An overview of coastal ocean models, in Coastal Ocean Prediction, edited by C. Mooers, vol. 56 of *Coastal and Estuarine Studies*, pp. 31–57, American Geophysical Union, 1999.

Griffies, S. M.: The Gent-McWilliams skew-flux, Journal of Physical Oceanography, 28, 831–841, 1998.

Griffies, S. M.: Fundamentals of Ocean Climate Models, Princeton University Press, Princeton, USA, 518+xxxiv pages, 2004.

Griffies, S. M.: Some Ocean Model Fundamentals, in GODAE Summer School, edited by E. P. Chassignet and J. Verron, pp. 19–74, Springer/Kluwer, 2005.

Griffies, S. M.: Elements of MOM4p1, NOAA/Geophysical Fluid Dynamics Laboratory, Princeton, USA, 444 pp, 2009.

Griffies, S. M. and Adcroft, A. J.: Formulating the equations for ocean models, in Eddy resolving ocean models, edited by M. Hecht and H. Hasumi, Geophysical Monograph 177, pp. 281–317, American Geophysical Union, 2008.

Griffies, S. M. and Hallberg, R. W.: Biharmonic friction with a Smagorinsky viscosity for use in large-scale eddy-permitting ocean models, Monthly Weather Review, 128, 2935–2946, 2000.

Griffies, S. M., Gnanadesikan, A., Pacanowski, R. C., Larichev, V., Dukowicz, J. K., and Smith, R. D.: Isoneutral diffusion in a z-coordinate ocean model, Journal of Physical Oceanography, 28, 805–830, 1998.

Griffies, S. M., Böning, C. W., Bryan, F. O., Chassignet, E. P., Gerdes, R., Hasumi, H., Hirst, A., Treguier, A.-M., and Webb, D.: Developments in Ocean Climate Modelling, Ocean Modelling, 2, 123–192, 2000a.

Griffies, S. M., Pacanowski, R. C., and Hallberg, R. W.: Spurious diapycnal mixing associated with advection in a z-coordinate ocean model, Monthly Weather Review, 128, 538–564, 2000b.

Griffies, S. M., Pacanowski, R., Schmidt, M., and Balaji, V.: Tracer Conservation with an Explicit Free Surface Method for z-coordinate Ocean Models, Monthly Weather Review, 129, 1081–1098, 2001.

Griffies, S. M., Harrison, M. J., Pacanowski, R. C., and Rosati, A.: A Technical Guide to MOM4, NOAA/Geophysical Fluid Dynamics Laboratory, Princeton, USA, 337 pp, 2004.

Griffies, S. M., Gnanadesikan, A., Dixon, K. W., Dunne, J. P., Gerdes, R., Harrison, M. J., Rosati, A., Russell, J., Samuels, B. L., Spelman, M. J., Winton, M., and Zhang, R.: Formulation of an ocean model for global climate simulations, Ocean Science, 1, 45–79, 2005.

Griffies, S. M., Biastoch, A., Böning, C. W., Bryan, F., Chassignet, E., England, M., Gerdes, R., Haak, H., Hallberg, R. W., Hazeleger, W., Jungclaus, J., Large, W. G., Madec, G., Samuels, B. L., Scheinert, M., Gupta, A. S., Severijns, C. A., Simmons, H. L., Treguier, A. M., Winton, M., Yeager, S., and Yin, J.: Coordinated Ocean-ice Reference Experiments (COREs), Ocean Modelling, 26, 1–46, 2009.

Hallberg, R. W.: Stable split time stepping schemes for large-scale ocean modeling, Journal of Computational Physics, 135, 54–65, 1997.

Hallberg, R. W.: Time integration of diapycnal diffusion and Richardson number-dependent mixing in isopycnal coordinate ocean models., Monthly Weather Review, 128, 1402–1419, 2000.

Haltiner, G. T. and Williams, R. T.: Numerical Prediction and Dynamic Meteorology, John Wiley and Sons, New York, USA, 1980.

Held, I. M. and Schneider, T.: The surface branch of the zonally averaged mass transport circulation in the troposphere, Journal of Atmospheric Sciences, 56, 1688–1697, 1999.

Hendershott, M.: The effects of solid earth deformation on global ocean tide, Geophysical Journal of the Royal Astronomical Society, 29, 389–402, 1972.

Herzfeld, M., Schmidt, M., Griffies, S., and Liang, Z.: Realistic test cases for limited area ocean modelling, Ocean Modelling, submitted, 2010.

Hirsch, C.: Numerical Computation of Internal and External Flows, John Wiley and Sons, 1988.

Holland, W. R., Chow, J. C., and Bryan, F. O.: Application of a third-order upwind scheme in the NCAR ocean model, Journal of Climate, 11, 1487–1493, 1998.

Holloway, G.: Representing Topographic Stress for Large-Scale Ocean Models, Journal of Physical Oceanography, 22, 1033–1046, 1992.

Holloway, G.: Moments of probable seas: statistical dynamics of Planet Ocean, Physica D, 133, 199–214, 1999.

Huang, R. X.: Real freshwater flux as a natural boundary condition for the salinity balance and thermohaline circulation forced by evaporation and precipitation, Journal of Physical Oceanography, 23, 2428–2446, 1993.

Huang, R. X., Jin, X., and Zhang, X.: An oceanic general circulation model in pressure coordinates, Advances in Atmospheric Physics, 18, 1–22, 2001.

Hundsdorfer, W. and Trompert, R.: Method of lines and direct discretization: a comparison for linear advection, Applied Numerical Mathematics, pp. 469–490, 1994.

Jackett, D. R., McDougall, T. J., Feistel, R., Wright, D. G., and Griffies, S. M.: Algorithms for density, potential temperature, conservative temperature, and freezing temperature of seawater, Journal of Atmospheric and Oceanic Technology, 23, 1709–1728, 2006.

Jayne, S. and St.Laurent, L. C.: Parameterizing tidal dissipation over rough topography, Geophysical Research Letters, 28, 811–814, 2001.

Killworth, P. D. and Edwards, N.: A turbulent bottom boundary layer code for use in numerical ocean models, Journal of Physical Oceanography, 29, 1221–1238, 1999.

Killworth, P. D., Stainforth, D., Webb, D. J., and Paterson, S. M.: The development of a free-surface Bryan-Cox-Semtner ocean model, Journal of Physical Oceanography, 21, 1333–1348, 1991.

Klymak, J., Moum, J., Nash, J., Kunze, E., Girton, J., Carter, G., Lee, C., Sanford, T., and Gregg, M.: An estimate of tidal energy lost to turbulence at the Hawaiian Ridge, Journal of Physical Oceanography, submitted, 2005.

Landau, L. D. and Lifshitz, E. M.: Mechanics, Pergamon Press, Oxford, UK, 170 pp, 1976.

Large, W. and Yeager, S.: Diurnal to decadal global forcing for ocean and sea-ice models: the data sets and flux climatologies, NCAR Technical Note: NCAR/TN-460+STR, CGD Division of the National Center for Atmospheric Research, 2004.

Large, W. G. and Pond, S.: Open ocean momentum flux measurements in moderate to strong winds, Journal of Physical Oceanography, 11, 324–336, 1981.

Large, W. G., McWilliams, J. C., and Doney, S. C.: Oceanic vertical mixing: A review and a model with a nonlocal boundary layer parameterization, Reviews of Geophysics, 32, 363–403, 1994.

Large, W. G., Danabasoglu, G., Doney, S. C., and McWilliams, J. C.: Sensitivity to surface forcing and boundary layer mixing in a global ocean model: annual-mean climatology, Journal of Physical Oceanography, 27, 2418–2447, 1997.

Large, W. G., Danabasoglu, G., McWilliams, J. C., Gent, P. R., and Bryan, F. O.: Equatorial circulation of a global ocean climate model with anisotropic horizontal viscosity, Journal of Physical Oceanography, 31, 518–536, 2001.

Ledwell, J. R., Watson, A. J., and Law, C. S.: Evidence for slow mixing across the pycnocline from an open-ocean tracer-release experiment, Nature, 364, 701–703, 1993.

Lee, H.-C., Rosati, A., and Spelman, M.: Barotropic tidal mixing effects in a coupled climate model: Oceanic conditions in the northern Atlantic, Ocean Modelling, 3-4, 464–477, 2006.

Legg, S., Hallberg, R., and Girton, J.: Comparison of entrainment in overflows simulated by z-coordinate, isopycnal and non-hydrostatic models, Ocean Modelling, 11, 69–97, 2006.

Leonard, B. P.: A stable and accurate convective modelling procedure based on quadratic upstream interpolation, Computer Methods in Applied Mechanics and Engineering, 19, 59–98, 1979.

Lin, S. J.: A finite volume integration method for computing pressure gradient force in general vertical coordinates, Quarterly Journal of the Royal Meteorological Society, 123, 1749–1762, 1997.

Losch, M., Adcroft, A., and Campin, J.-M.: How sensitive are coarse general circulation models to fundamental approximations in the equations of motion?, Journal of Physical Oceanography, 34, 306–319, 2004.

Machenhauer, B., Kaas, E., and Lauritzen, P.: Finite-volume methods in meteorology, in Computational Methods for the Atmosphere and the Oceans, edited by R. Temam and J. Tribbia, p. 761, Elsevier, Amsterdam, 2009.

Manizza, M., Le Quere, C., Watson, A., and Buitenhuis, E.: Bio-optical feedbacks among phytoplankton, upper ocean physics and sea-ice in a global model, Geophysical Research Letters, 32, doi:10.1029/2004GL020 778, 2005.

Marchesiello, J. M. P. and Shchepetkin, A.: Open boundary conditions for long-term integration of regional oceanic models, Ocean Modelling, 3, 1–20, 2001.

Marchuk and Kagan: Dynamics of Ocean Tides, Kluwer Academic, 1989.

Marion, J. B. and Thornton, S. T.: Classical Dynamics of Particles and Systems, Harcourt Brace Jovanovich, San Diego, USA, 602 pp, 1988.

Marotzke, J.: Influence of convective adjustment on the stability of the thermohaline circulation, Journal of Physical Oceanography, 21, 903–907, 1991.

Marshall, J. and Schott, F.: Open-ocean convection: observations, theory, and models, Reviews of Geophysics, 37, 1–64, 1999.

Marshall, J., Hill, C., Perelman, L., and Adcroft, A.: Hydrostatic, quasi-hydrostatic, and nonhydrostatic ocean modeling, Journal of Geophysical Research, 102, 5733–5752, 1997.

Marshall, J., Adcroft, A., Campin, J.-M., Hill, C., and White, A.: Atmosphere-Ocean modeling exploiting fluid isomorphisms, Monthly Weather Review, 132, 2882–2894, 2004.

Martinsen, E. and Engedahl, H.: Implementation and testing of a lateral boundary scheme as an open boundary condition in a barotropic ocean model, Coastal Engineering, 11, 603–627, 1987.

McDougall, T. J.: Thermobaricity, cabbeling, and water-mass conversion, Journal of Geophysical Research, 92, 5448–5464, 1987.

McDougall, T. J.: The influence of ocean mixing on the absolute velocity vector, Journal of Physical Oceanography, 25, 705–725, 1995.

McDougall, T. J.: Potential enthalpy: a conservative oceanic variable for evaluating heat content and heat fluxes., Journal of Physical Oceanography, 33, 945–963, 2003.

McDougall, T. J. and McIntosh, P. C.: The temporal-residual-mean velocity. Part II: isopycnal interpretation and the tracer and momentum equations., Journal of Physical Oceanography, 31, 1222–1246, 2001.

McDougall, T. J., Greatbatch, R. J., and Lu, Y.: On conservation Equations in Oceanography: How Accurate are Boussinesq Ocean Models?, Journal of Physical Oceanography, 32, 1574–1584, 2002.

McDougall, T. J., Jackett, D. R., Wright, D. G., and Feistel, R.: Accurate and computationally efficient algorithms for potential temperature and density of seawater., Journal of Atmospheric and Oceanic Technology, 20, 730–741, 2003.

Merryfield, W. J. and Holloway, G.: Application of an accurate advection algorithm to sea-ice modelling, Ocean Modelling, 5, 1–15, 2003.

Mesinger, F.: A method for construction of second-order accurate difference schemes permitting no false two-grid-interval waves in the height field., Tellus, 25, 444–457, 1973.

Mesinger, F. and Arakawa, A.: Numerical Methods used in Atmospheric Models, in GARP Publication Series, vol. 1, p. 66 pages, 1976.

Miller, M. and Thorpe, A.: Radiation conditions for the lateral boundaries of limited-area numerical models, Quarterly Journal of the Royal Meteorological Society, 107, 615–628, 1981.

Morel, A. and Antoine, D.: Heating rate within the upper ccean in relation to its bio-optical state, Journal of Physical Oceanography, 24, 1652–1665, 1994.

Moum, J., Caldwell, D., Nash, J., and Gunderson, G.: Observations of boundary mixing over the continental slope, Journal of Physical Oceanography, 32, 2113–2130, 2002.

Munk, W. and Anderson, E.: Notes on a theory of the thermocline, Journal of Marine Research, 3, 276–295, 1948.

Murray, R. J.: Explicit generation of orthogonal grids for ocean models, Journal of Computational Physics, 126, 251–273, 1996.

O'Brien, J. J.: Advanced Physical Oceanographic Numerical Modelling, D. Reidel Publishing Company, 1986.

Ohlmann, J.: Ocean Radiant Heating in Climate Models, JOC, 16, 1337–1351, 2003.

Orlanski, I.: A simple boundary condition for unbounded hyberbolic flows, Journal of Computational Physics, 21, 251–269, 1976.

Osborn, T. R.: Estimates of the local rate of vertical diffusion from dissipation measurements, Journal of Physical Oceanography, 10, 83–89, 1980.

Pacanowski, R. C.: Effect of equatorial currents on surface stress, Journal of Physical Oceanography, 17, 833–838, 1987.

Pacanowski, R. C.: MOM2 Documentation, User's Guide, and Reference Manual, NOAA/Geophysical Fluid Dynamics Laboratory, Princeton, USA, 216 pp, 1995.

Pacanowski, R. C. and Gnanadesikan, A.: Transient response in a z-level ocean model that resolves topography with partial-cells, Monthly Weather Review, 126, 3248–3270, 1998.

Pacanowski, R. C. and Griffies, S. M.: The MOM3 Manual, NOAA/Geophysical Fluid Dynamics Laboratory, Princeton, USA, 680 pp, 1999.

Pacanowski, R. C. and Philander, G.: Parameterization of vertical mixing in numerical models of the tropical ocean, Journal of Physical Oceanography, 11, 1442–1451, 1981.

Pacanowski, R. C., Dixon, K., and Rosati, A.: The GFDL Modular Ocean Model User Guide, NOAA/Geophysical Fluid Dynamics Laboratory, Princeton, USA, 16 pp, 1991.

Palma, E. and Matano, R.: On the implementation of passive open boundary conditions for a general circulation model: The barotropic mode, Journal of Geophysical Research, 103(C1), 1319–1341, 1998.

Palma, E. and Matano, R.: Dynamical impacts associated with radiation boundary conditions, Journal of Sea Research, 46, 117–132, 2001.

Peixoto, J. P. and Oort, A. H.: Physics of Climate, American Institute of Physics, 520 + xxxix pp, 1992.

Pickard, G. L. and Emery, W. J.: Descriptive Physical Oceanography, Pergamon Press, Oxford, 5th edn., 1990.

Polzin, K. L., Toole, J. M., Ledwell, J. R., and Schmitt, R. W.: Spatial variability of turbulent mixing in the abyssal ocean, Science, 276, 93–96, 1997.

Prather, M.: Numerical advection by conservation of second-order moments, Journal of Geophysical Research, 91, 6671–6681, 1986.

Press, W. H., Teukolsky, S. A., Vetterling, W. T., and Flannery, B. P.: Numerical Recipes in FORTRAN: The Art of Scientific Computing, Cambridge University Press, Cambridge, 2nd edn., 963 + xxvi pp, 1992.

Rahmstorf, S.: A fast and complete convection scheme for ocean models, Ocean Modelling, 101, 9–11, 1993.

Ray, R. D.: Ocean self-attraction and loading in numerical tidal models, Marine Geodesy, 21, 181–192, 1998.

Raymond, W. and Kuo, H.: A radiation boundary condition for multidimensional flows, Quaterly Journal of the Royal Meterological Society, 110, 535–551, 1984.

Redi, M. H.: Oceanic isopycnal mixing by coordinate rotation., Journal of Physical Oceanography, 12, 1154–1158, 1982.

Robert, A.: The integration of a low order spectral form of the primitive meteorological equations, Journal of the Meteorological Society of Japan, 44, 237–244, 1966.

Roed, L. and Cooper, C.: A study of various open boundary conditions for wind-forced barotropic numerical ocean models, in Three-dimensional Models of marine and Estuarine Dynamics, edited by J. Nihoul and B. Jamart, pp. 305–335, Elsevier, 1987.

Shchepetkin, A. and McWilliams, J.: A method for computing horizontal pressure-gradient force in an ocean model with a non-aligned vertical coordinate, Journal of Geophysical Research, 108, 35.1–35.34, 2002.

Simmons, H. L., Jayne, S. R., St.Laurent, L. C., and Weaver, A. J.: Tidally driven mixing in a numerical model of the ocean general circulation, Ocean Modelling, 6, 245–263, 2004.

Smith, K. S. and Vallis, G. K.: The scales and equilibration of midocean eddies: forced-dissipative flow, Journal of Physical Oceanography, 32, 1699–1721, 2002.

Smith, R. D. and McWilliams, J. C.: Anisotropic horizonal viscosity for ocean models, Ocean Modelling, 5, 129–156, 2003.

Sommerfeld, A.: Partial differential equations. Lectures in Theoretical Physics 6, Academic Press, New York, 1949.

Stacey, M. W., Pond, S., and Nowak, Z. P.: A Numerical Model of the Circulation in Knight Inlet, British Columbia, Canada, Journal of Physical Oceanography, 25, 1037–1062, 1995.

Stevens, D. P.: On open boundary conditions for three dimensional primitive equation ocean circulation models, Geophysical and Astrophysical Fluid Dynamics, 51, 103–133, 1990.

Stevens, D. P.: The open boundary conditions in the United Kingdom Fine-Resolution Antarctic Model, Journal of Physical Oceanography, 21, 1494–1499, 1991.

St.Laurent, L. C., Toole, J., and Schmitt, R.: Buoyancy forcing by turbulence above rough topography in the abyssal Brazil Basin, Journal of Physical Oceanography, 31, 3476–3495, 2001.

St.Laurent, L. C., Simmons, H., and Jayne, S.: Estimating tidally driven energy in the deep ocean, Geophysical Research Letters, 29, 2106–2110, 2002.

St.Laurent, L. C., Stringer, S., Garrett, C., and Perrault-Joncas, D.: The generation of internal tides at abrupt topography, Deep-Sea Research, 50, 987–1003, 2003.

Stouffer, R. J., Broccoli, A., Delworth, T., Dixon, K., Gudgel, R., Held, I., Hemler, R., Knutsn, T., Lee, H.-C., Schwarzkopf, M., Soden, B., Spelman, M., Winton, M., and Zeng, F.: GFDL's CM2 Global coupled climate models: Part 4: idealized climate response, Journal of Climate, 19, 723–740, 2006.

Sweby, P.: High-resolution schemes using flux limiters for hyperbolic conservation-laws, SIAM Journal of Numerical Analysis, 21, 995–1011, 1984.

Sweeney, C., Gnanadesikan, A., Griffies, S. M., Harrison, M., Rosati, A., and Samuels, B.: Impacts of shortwave penetration depth on large-scale ocean circulation and heat transport, Journal of Physical Oceanography, 35, 1103–1119, 2005.

Tang, Y. and Grimshaw, R.: Radiation boundary conditions in barotropic coastal ocean numerical models, Journal of Computational Physics, 123, 96–110, 1996.

Tang, Y. and Roberts, M.: The impact of a bottom boundary layer scheme on the North Atlantic Ocean in a global coupled climate model, Journal of Physical Oceanography, 35, 202–217, 2005.

Thiele, G. and Sarmiento, J. L.: Tracer dating and ocean ventilation, Journal of Geophysical Research, 95, 9377–9391, 1990.

Treguier, A. M., Held, I. M., and Larichev, V. D.: On the parameterization of quasi-geostrophic eddies in primitive equation ocean models, Journal of Physical Oceanography, 27, 567–580, 1997.

Umlauf, L., Burchard, H., and Bolding, K.: GOTM: source code and test case documentation: version 3.2, 231pp, 2005.

Wahr, J.: Body Tides on an elliptical, rotating, elastic and oceanless earth, Geophysical Journal of the Royal Astronomical Society, 64, 677–703, 1998.

Winters, K. B. and D'Asaro, E. A.: Diascalar flux and the rate of fluid mixing, Journal of Fluid Mechanics, 317, 179–193, 1995.

Winters, K. B., Lombard, P. N., Riley, J. J., and D'Asaro, E. A.: Available potential energy and mixing in density-stratified fluids, Journal of Fluid Mechanics, 289, 115–128, 1995.

Winton, M., Hallberg, R., and Gnanadesikan, A.: Simulation of density-driven frictional downslope flow in z-coordinate ocean models, Journal of Physical Oceanography, 28, 2163–2174, 1998.

Wittenberg, A., Rosati, A., Lau, G., and Ploshay, J.: GFDL's CM2 global coupled climate models - Part 3: Tropical Pacific climate and ENSO, Journal of Climate, 19, 698–722, 2006.

Wright, D. G.: An Equation of State for Use in Ocean Models: Eckart's Formula Revisited., Journal of Atmospheric and Oceanic Technology, 14, 735–740, 1997.